



**University of  
Leicester**

The Effect of Thermal Tempering Processes on the  
Sharpness and Injury Potential of Pint Glasses

By Richard W. Earp

A thesis submitted to the University of Leicester  
for the Degree of Doctor of Philosophy

Department of Engineering

Submitted September 2015  
Revised January 2016

# **The Effect of Thermal Tempering Processes on the Sharpness and Injury Potential of Pint Glasses**

Richard W. Earp

## **Abstract**

Glass drinkware is widely used in the UK. However, glasses are sometimes used as impulsive weapons in incidents related to alcohol consumption, particularly with imperial pint glasses (~568 ml). In order to reduce the potential for injury with such glasses, glass manufacturers adapted thermal tempering processes to produce tempered (also referred to as toughened) pint glasses. Tempered glass is known for its dense fracture properties and is considered to be a safer alternative to non-tempered (annealed) glass. Tempered pint glasses are now widely used throughout the UK. However, there is no standard which regulates the quality of tempered drinking glasses. This lack of standardisation has been identified as a cause for varying effectiveness of using tempered drinking glasses to reduce injury potential.

This thesis aimed to examine the injury potential of pint glasses and to provide a foundation for a future standard for tempered drinking glasses. The work included: examination of the fracture properties of annealed and tempered drinking glasses; replication and analysis of physical attacks with pint glasses; and assessments into the sharpness of various glass fragments as an indicator of injury potential.

The base region of tempered pint glasses was found to fracture extensively, limiting certain methods of glass attacks. Fragments from the near-rim region were found to vary significantly in size between glasses due to lower wall thicknesses and residual stress. Replications of glassing attacks indicated high forces are involved with such attacks, although the damage severity is lessened with tempered glasses. Sharpness assessments revealed little significant change in fragment sharpness due to tempering. This suggests that changes in injury potential are more likely due to practical considerations such as reduced fragment size, rather than a change in inherent sharpness properties.

## Acknowledgements

I would like to thank the following people who have helped me throughout my Ph.D.:

My supervisor Professor Sarah Hainsworth for her support, guidance, and for the many opportunities given to me over the years.

The EPSRC for funding the work.

Glass Technology Services Ltd. for their sponsorship of this work, their continued input and assistance, and for reviewing the thesis. In particular: David Eustice, Malcolm Glendenning, Matthew Roberts (now of Utopia Tableware Ltd.), Catherine Robinson, Chris Holcroft, Andrew Broadhurst, Nick Kirk, Daniel Rumsey, Martyn Marshall, and Theresa Green.

All my colleagues at the University of Leicester who have provided guidance and advice during experimental work. In particular: Graham Clark, Vinay Patel, Paul Williams, Dr. Duyao Zhang, Nishad Karim, Dr. Gary Nolan, Dr. Hugo Williams, Dr. Simon Lawes, Dr. Dave Weston, Dr. Simon Gill, Dr. Csaba Sinka, and Prof. Jingzhe Pan.

The technicians from the Engineering department who gave huge thought and time into the many bits and pieces made for this project. In particular: Alan Wale, Keith Stanley, Ian Bromley, Julian Jones, Tony Forryan, Barry Chester, Andy Truman, Luigi Alessandro, and Guiseppe Alessandro.

The undergraduate students who contributed to the work on slapping attacks: Abhishek Gadhvi, Ryan Pitchford, and Dmitry Filimonov.

Members of staff at the University of Leicester for their various contributions, including: Carl Vivian for assistance with high speed video footage; Gayle Nicholson for assistance with edge finishing of glass discs; Dominic Kent for processing a very large number of purchase requests; and Tania Wilkinson and Anita Noray.

Jonathon Kavanagh of Trend Marine Ltd. for chemically tempering glass discs.

My entire family for their smiles and support. Especially my wife for her super dooper support, and for carefully proofreading the entire thesis.

## Table of Contents

Abstract.....	i
Acknowledgements.....	ii
<b>1 Introduction</b>	
1.1 Background and motivation of research.....	1
1.2 Research objectives and thesis structure .....	3
1.3 Chapter references.....	6
<b>2 Strength, tempering, and fracture of glass</b>	
2.1 Introduction .....	8
2.2 Glass production .....	8
2.3 Glass strength.....	13
2.4 Residual stresses in glass.....	16
2.5 Fracture characteristics of glass.....	22
2.6 Current standards for thermally tempered glass products .....	33
2.7 Chapter summary.....	35
2.8 Chapter references.....	36
<b>3 Glass preparation and fracture methodologies</b>	
3.1 Introduction .....	41
3.2 Glass samples .....	41
3.3 Tempering and annealing .....	43
3.4 Residual stress assessment .....	53
3.5 Pre-damaging surfaces.....	57
3.6 Fracture methods.....	62
3.7 Fractographic analysis.....	69
3.8 Chapter summary.....	73
3.9 Chapter references.....	74

<b>4</b>	<b>The fracture of annealed and thermally tempered pint glasses</b>	
4.1	Introduction .....	76
4.2	Structural response of drinking vessels due to external impact.....	76
4.3	Fracture characteristics of pint glasses and other glass drinkware subjected to external impact .....	86
4.4	Quantitative analysis of the wall thickness, residual stress, and impact performance of three pint glasses .....	100
4.5	Summary of key properties and characteristics of thermally tempered pint glasses .....	108
4.6	Chapter summary.....	109
4.7	Chapter references.....	111
<b>5</b>	<b>Physical attacks with pint glasses (glassings)</b>	
5.1	Introduction .....	112
5.2	Dynamics and circumstances of glassing attacks.....	113
5.3	Forces involved in glassing attacks .....	118
5.4	Laceration/ injury patterns associated with glassing attacks .....	133
5.5	Chapter summary.....	144
5.6	Chapter references.....	146
<b>6</b>	<b>Characterisation of the sharpness of glass fragments</b>	
6.1	Introduction .....	148
6.2	Sharpness assessment methods .....	148
6.3	Simulating human skin for cutting .....	153
6.4	Sharpness of broken glass by geometrical considerations .....	155
6.5	Sharpness of broken glass by force and energy considerations .....	163
6.6	Design of Experiments investigation into key fragment geometry parameters for penetration ability.....	174
6.7	Chapter summary.....	181
6.8	Chapter references.....	182
<b>7</b>	<b>Glass fragment sharpness part I: Effect of load and temper level</b>	
7.1	Introduction .....	187
7.2	Sharpness as affected by loading magnitude in flexure .....	188
7.3	Sharpness as affected by temper magnitude .....	199
7.4	Chapter summary.....	218
7.5	Chapter references.....	219

## **8 Glass fragment sharpness part II: Pint glasses, non-uniformly tempered glass, and highly-stressed glass**

8.1	Introduction .....	220	
8.2	Sharpness of pint glass fragments .....	220	
8.3	Sharpness of fragments from non-uniformly tempered glass.....	232	
8.4	Sharpness properties of fragments from thermally and chemically tempered glass.....	242	
8.5	Chapter summary.....	254	
8.6	Chapter references.....	255	
<b>9 Conclusions and further work</b>			
9.1	Key findings and significance .....	256	
9.2	Further work .....	260	
9.3	Concluding remarks .....	261	
Appendix A – Hot wire anemometer measurement of jet velocities .....			262
Appendix B – Drinking glasses fractured for section 4.3 .....			268
Appendix C – Flaw sizes a fracture data from a selection of used drinking glasses .....			271
Appendix D – Eye appraisal of wear on a selection of used pint glasses.....			273
Appendix E – Full fragmentation counts for pint glasses subjected to punch tests.....			277
Appendix F – Dynamometer output for impacts without pint glasses.....			278
Appendix G – Extended dynamometer results for slapping attack replications .....			281
Appendix H – Damage quantification data from section 5.4.3.....			284
Appendix I – Edge profile measurement scripts .....			289
Appendix J – Silicone/foam simulant verification.....			298
Appendix K – Further sharpness data from section 7.2.....			301
Appendix L – Further edge/surface profile plots and sharpness data from section 7.3.....			302
Appendix M – Further edge/surface profile plots and sharpness data from section 8.2.....			304
Appendix N – Further sharpness data from section 8.3 .....			308
Appendix O – Further sharpness data from section 8.4 .....			309
Appendix P – The Effect of Tempering and Wall Thickness on the Fracture of Pint Glasses International Journal of Applied Glass Science, 6 [2] 196–207 (2015) .....			310

## 1 Introduction

### 1.1 Background and motivation of research

Glass is widely used in bars and pubs for drinkware in the UK. Advantages of using glass for drinkware include: its high chemical inertness [1], established infrastructure for recycling [2], and the preference of drinkers for the texture and feel of glass over other materials for drinking vessels [3], [4]. However, drinking glasses and glass bottles (reported together) have been estimated to have been used as an impulsive weapon in 4% of all violent incidents in the UK [5]<sup>1</sup>. These violent incidents which involve glass are colloquially known as “glassings” or “bottlings” [6]. They usually take place at weekends in bars, pubs, and nightclubs [3], [7], [8], and those involved are likely to be under the influence of alcohol [9]–[11]. Glassing incidents involving drinking glasses have been reported to cause more severe injuries than those involving glass bottles, due to the increased likelihood of facial injuries [12]. The type of drinking glass used most frequently in such incidents are imperial pint glasses [7] (~568 ml) (referred to as just pint glasses in this thesis).

One approach to reduce the injury potential of drinking glasses has been to introduce substitute materials, which has been met with varying levels of success. Polycarbonate drinking vessels have commonly been implemented as a glass alternative, with evidence of a reduction in glassing incidents [6], [13], [14]. However, its use has provoked negative reactions from patrons and pub owners [4], [10], [15].

A second approach has been to draw on laminated glass concepts. Following a programme in 2010 involving the Home Office and the Design Council in the UK [4], two new pint glasses were unveiled [16]. These glasses used a resin layer to restrain glass fragments in place should the glass break. However, such glasses have not since been made publicly available, largely owing to their high production costs over conventional alternatives.

A third approach has been to apply thermal tempering processes to glass so that articles break into fragments that are considered less likely to cause injury [17]. In the 1990s, manufacturers began applying thermal tempering processes to drinking glasses at a commercial level in response to safety concerns. Tempered (also referred to as toughened) pint glasses gained

---

<sup>1</sup> Notes on British Crime Statistics: These are reported annually in the Crime Survey of England and Wales (CSEW). Since 2012, figures of violent incidents with drinking glasses and glass bottles have not been reported as a separate category. The referenced figure of 4% is from the most recent inclusion in 2011.

popularity amongst the licensed trade [18] and police forces [19]. The thermal tempering process involves even and rapid cooling of a glass article from temperatures approaching 700 °C [20]. It typically results in articles of increased strength. When broken, these articles produce fragments that are smaller and more evenly-sized than glass cooled slowly from the same temperatures, known as annealed glass (see Figure 1.1). The visual difference between annealed and tempered glass before fracture is almost indiscernible to the naked eye in usual lighting conditions.



**Figure 1.1 – Typical fracture of annealed (left) and tempered (right) pint glasses.**

However, the application of the thermal tempering process to drinking glasses is difficult due to their shape. Achieving even cooling over a curved surface, and preventing the re-circulation of hot air in the inside of a drinking glass, is challenging. Failure to adequately manage these factors can weaken the glass, and render it more likely to break than annealed glass. Furthermore, there are no universally accepted safer breakage criteria amongst glass manufacturers for tempered drinking glasses [21]. Consequently, no standard prescribing the necessary strength and fracture characteristics of tempered drinking glasses has been established. Lack of such standardisation has been identified as a cause for varying effectiveness of using tempered drinking glasses to reduce injury potential [22]. This has also resulted in the use of varying terminology for thermally treated pint glasses, and some glasses are referred to as toughened by manufacturers even when the glasses do not exhibit the fracture characteristics of thermally tempered glass.

This thesis aims to gain an understanding of the fracture of annealed and tempered pint glasses and how this translates into injury potential. Additionally, the thesis considers how tempering processes affect the inherent sharpness of glass fragments. Furthermore, the thesis aims to provide a foundation for the establishment of a standard method for both the testing and the required performance of tempered drinking glasses to minimise their potential for injury should the glass be used as a weapon.

## 1.2 Research objectives and thesis structure

The main objective of this thesis is to present empirical research into the injury potential of broken pint glasses in order to establish how injury potential is affected by design and manufacturing processes. The bulk of the work involved the analysis of annealed and tempered soda-lime-silica (SLS) glass. Individual objectives of the thesis are as follows:

- To develop specific and appropriate procedures to result in comparable fracture patterns of glass samples, involving: thermal processing, replication of surface wear due to handling and general usage, and loading methodologies.
- To conduct in-depth fractographic analyses of broken annealed and tempered pint glasses to develop an understanding of typical fracture characteristics.
- To determine the forces involved with glassing attacks, establish likely patterns of injury and injury severity, and establish how this relates to glass fracture characteristics.
- To develop methodologies that determine the forces required for glass to cut and penetrate skin, and to establish what aspects of fragment geometry are likely to affect these forces.
- To establish how tempering affects the inherent sharpness of glass fragments, and determine how this can be affected by variations in the tempering procedure.

The structure of this thesis is intended to follow a logical order of progression, while also allowing each chapter to be self-contained. Some chapters present short reviews of relevant literature when appropriate, which is in addition to the main review of relevant literature on glass in chapter 2. Similarly a main overview of materials and methods is presented in chapter 3, but some specific methodologies are introduced in other chapters where appropriate. An outline of all chapters is as follows:

- **Chapter 2: Strength, tempering, and fracture of glass**

An introduction to glass and a review of literature relevant to this thesis. This includes introductions to: glass composition and manufacture; influential factors to glass strength; residual stresses in glass; photoelasticity; fractography; and existing standards for thermally tempered glass products.

- **Chapter 3 – Glass preparation and fracture methodologies**

A structured overview of the majority of the materials and methods employed during this study. This includes: tempering and annealing methodologies; details of the novel purpose-built tempering equipment for this study; methods of measuring residual

stresses; methods for pre-damaging glass to simulate wear; fracture methodologies; and equipment used in fractographic analysis.

- **Chapter 4 – The fracture of pint glasses**

A series of investigations into the fracture characteristics of pint glasses and other drinking glasses. It includes: finite element simulations of pint glasses under mechanical loading; an exploratory investigation into the typical fracture characteristics of a variety of drinking glasses; and a systematic fractographic investigation into the fracture of three types of pint glasses, in both annealed and tempered conditions.

- **Chapter 5 – Physical attacks with pint glasses (glassings)**

A series of investigations into the forces involved with glassings, in particular with so-called slapping attacks with pint glasses, and the injury patterns that may be associated with them. This includes: a review and discussion of the dynamics involved with glassing attacks; a quantification of forces involved by controlled replication of the attack with a number of participants; and a systematic replication of slapping attacks using a drop tower methodology for the determination of injury patterns.

- **Chapter 6 – Characterisation of the sharpness of glass fragments**

An introduction to the concept of sharpness, to existing methodologies for characterising sharpness, and to how sharpness can be quantified for glass. This includes: a discussion of relevant geometrical factors that characterise glass sharpness, and how fragment edges can be categorised; outlines of novel methodologies developed to determine the forces involved with cutting and stabbing for glass fragments; and initial investigations into how fragment geometry affects these forces.

- **Chapter 7 – Glass fragment sharpness part I: Effect of load and temper level**

An investigation into how the magnitude of thermal temper stresses affects the sharpness of glass fragments. This includes the use of: optical microscopy, scanning electron microscopy and micro-computed tomography; along with the novel techniques for characterising sharpness introduced in chapter 6.

- **Chapter 8 – Glass fragment sharpness part II: Pint glasses, asymmetrically tempered glass, and highly-stressed glass**

A second chapter on the application of sharpness characterisation techniques, split into three main studies. This includes: the sharpness of fragments from pint glasses; the sharpness of asymmetrically-tempered glass samples; and highly stressed glass

samples subjected to biaxial ring-on-ring loading, including annealed, thermally tempered, and chemically tempered glass.

- **Chapter 9 – Conclusions and further work**

A final discussion on the key findings of the work and their contextual significance. Additionally, suggestions as to how this study could be improved and extended are given.

The following chapter introduces the scientific background of the thermal tempering process; as well as the manufacture, strength properties, and fracture properties of glass. This background provides a foundation for later discussion in this thesis of using the thermal tempering process to reduce injury potential.

### 1.3 Chapter references

- [1] Glass Technology Services Ltd., “Investigation of the Significant Factors in Elemental Migration from Glass in Contact with Food: Final Project Report,” 2002.
- [2] *Making Glass*, 4th Edition, British Glass Manufacturers Confederation, 2007.
- [3] P. Cassematis and P. Mazerolle, “Understanding Glassing Incidents on Licensed Premises: Dimensions, Prevention and Control,” *Brisbane, Australia: Griffith Univ. and Queensland Government*, 2009.
- [4] “Using Design to Reduce Injuries from Alcohol Related Violence in Pubs and Clubs,” *Home Office, Design Out Crime*, 2010.
- [5] R. Chaplin, J. Flatley, and K. Smith, *Home Office Statistical Bulletin: Crime in England and Wales 2010/11*. 2011.
- [6] M. Worthington, J. Mckinney, and P. Percival, “The Glass Debate – It’s Your Choice,” *Entry for the 2008 Tilley Awards*, 2008.
- [7] J. P. Shepherd, M. Price, and P. Shenfine, “Glass Abuse and Urban Licensed Premises,” *Journal of the Royal Society of Medicine*, vol. 83, no. April, pp. 276–277, 1990.
- [8] A. Finney, “Findings 214: Violence in the Night-Time Economy: Key Findings from the Research,” *Home Office, Research, Development and Statistics Directorate*, 2004.
- [9] D. Murdoch and D. Ross, “Alcohol and Crimes of Violence: Present Issues,” *The International Journal of the Addictions*, vol. 25, no. 9, pp. 1065–1081, 1990.
- [10] B. Winder and C. Wesson, “Last Orders for Alcohol Related Violence: Exploring Salient Factors in the Occurrence of Violent Incidents in UK Pubs and Other Late Night Venues. Report to British Glass.,” *Nottingham Trent University*, 2006.
- [11] L. C. Luke, C. Dewar, M. Bailey, D. McGreevy, and H. Morris, “A Little Nightclub Medicine: The Healthcare Implications of Clubbing,” *Emergency Medicine Journal*, vol. 19, pp. 542–546, 2002.
- [12] K. S. Coomaraswamy and J. P. Shepherd, “Predictors and Severity of Injury in Assaults with Barglasses and Bottles,” *Injury Prevention*, vol. 9, no. 1, pp. 81–84, 2003.
- [13] A. J. M. Forsyth, “Banning Glassware from Nightclubs in Glasgow (Scotland): Observed Impacts, Compliance and Patron’s Views,” *Alcohol and Alcoholism*, vol. 43, no. 1, pp. 111–117, 2008.
- [14] Z. Anderson, G. Whelan, K. Hughes, and M. A. Bellis, “Evaluation of the Lancashire Polycarbonate Glass Pilot Project,” *Liverpool: Liverpool John Moores University*, 2009.
- [15] “U-Turn on Glasgow Pub Glass Ban,” *BBC News*, 2006. [Online]. Available: [http://news.bbc.co.uk/1/hi/scotland/glasgow\\_and\\_west/5095956.stm](http://news.bbc.co.uk/1/hi/scotland/glasgow_and_west/5095956.stm). [Accessed: 30-Mar-2015].

- 
- [16] M. Ryan, "Last Orders for Pint Glass As We Know It?," *BBC News Magazine*, 2010. [Online]. Available: <http://news.bbc.co.uk/1/hi/8495617.stm>. [Accessed: 30-Mar-2015].
- [17] "BS EN 12150-1:2000 - Glass in Building. Thermally Toughened Soda Lime Silicate Safety Glass. Definition and Description," *British Standards Institute, UK*, 2000.
- [18] Brewers and Licensed Retailers Association (Now The British Beer & Pub Association), "Toughened Glass: BLRA Press Release, Brewers and Licensed Retailers Association, 42 Portman Square, London," 1997.
- [19] D. Hands, "Toughened Beer Glasses: Safe Glass Safe City Campaign," *Design Against Crime*, 2001. [Online]. Available: <http://extra.shu.ac.uk/dac/beerglass.pdf>. [Accessed: 31-Mar-2015].
- [20] R. Gardon, "Thermal Tempering of Glass," in *Glass: Science and technology, Volume 5, Elasticity and Strength in Glasses*, D. R. Uhlmann and N. J. Kreidl, Eds. Academic Press, New York, 1980, pp. 145–216.
- [21] Glass Technology Services, private communication.
- [22] A. L. Warburton and J. P. Shepherd, "Effectiveness of Toughened Glassware in Terms of Reducing Injury in Bars: A Randomised Controlled Trial," *Injury Prevention*, vol. 6, no. 1, pp. 36–40, 2000.

## 2 Strength, tempering, and fracture of glass

### 2.1 Introduction

The main aim of this thesis is to establish the injury potential of pint glasses when used as an impulsive weapon, and how this is affected by thermal tempering treatments. The literature most relevant to the work in the thesis can be separated into three main categories as follows:

- I. The fracture properties of glass and how this is affected by material properties and the loading conditions at the time of fracture.
- II. The mechanical circumstances and dynamics involved with the use of glass as an impulsive weapon.
- III. The assessment of injury potential of a weapon and the quantification of sharpness.

The largest body of existing literature exists for category I, and is the subject of the current chapter. Additional background on glass composition and production is introduced, and also existing standards for thermally tempered glass products are reviewed. Categories II and III are considered separately in chapters 5 and 6, respectively.

Section 2.2 discusses the typical composition and molecular structure of soda-lime-silica glass, and how drinking glasses are formed. Section 2.3 describes the strength of glass and how it is affected by surface flaws. Section 2.4 introduces residual stress in glass and how this relates to annealing and thermal tempering processes. This section also introduces the measurement of residual stress using photoelastic techniques. Section 2.5 considers the fracture characteristics of glass. It reviews key fracture surface features and the use of fractographic techniques in determining events during crack propagation. Finally, section 2.6 reviews existing standards for thermally tempered glass products. This provides context for some of the assessment methods used in later chapters.

### 2.2 Glass production

This section describes the composition and molecular structure of soda-lime-silica glass in order to give a scientific background for the subsequent overview of drinking glass production.

#### 2.2.1 Soda-lime silica glass and the glass transition

Pint glasses are most commonly made from soda-lime-silica (SLS) glass. In this thesis, any reference to glass can be assumed to mean SLS glass unless stated otherwise. A typical composition of a SLS glass is given in Table 2.1.

Chemical compound	Mass percent (%)
Silicon dioxide (SiO <sub>2</sub> )	69-74
Sodium oxide (Na <sub>2</sub> O)	10-16
Calcium oxide (CaO)	5-14
Magnesium oxide (MgO)	0-6
Aluminium oxide (Al <sub>2</sub> O <sub>3</sub> )	0-3
Others	0-5

**Table 2.1 – Typical composition of soda-lime silica glass [1].**

The main component of SLS glass is silica (SiO<sub>2</sub>), which accounts for almost three quarters of the composition by mass. Although glass can be made from pure silica, it has a high melting temperature (1720 °C). Sodium oxide (Na<sub>2</sub>O) is therefore added to reduce the melting point to a more practical value. However, glass consisting only of SiO<sub>2</sub> and Na<sub>2</sub>O is water-soluble [3] and so it is necessary to add CaO, which increases the chemical durability of the glass. These three components are introduced into the initial glass batch as sand (SiO<sub>2</sub>), soda ash (NaCO<sub>3</sub>), and limestone (CaCO<sub>3</sub>), from which SLS gets its name. Further batch ingredients may include cullet (crushed, recycled glass) and fining agents which improve processing aspects during manufacture [2].

The molecular structure of glass is typically modelled as a random network that lacks long range periodic order, based on original ideas proposed by Zachariasen [4]. A material which lacks a defined crystalline structure is said to be amorphous. A two dimensional schematic of the structure of SLS glass is shown in Figure 2.1. The body of the network is formed by silicon and oxygen atoms, with oxygen atoms arranged tetrahedrally around silicon atoms as shown in the inset of the figure. The connectivity between tetrahedra by oxygen atoms is affected by the addition of sodium atoms. This causes the reduction in melting temperature, and also reduces the melt viscosity.

The amorphous structure of SLS glass is similar to that of a liquid. This is because crystallisation is bypassed during cooling from a liquid melt, which is a process known as supercooling. This is particularly likely to occur with SLS glass due to its high viscosity near the melting temperature (~100 Nsm<sup>-2</sup> [5]). The high viscosity of the melt restricts the mobility of the constituent molecules, which increases the time necessary for it to equilibrate and crystallise at the melting temperature. As the glass cools further, its viscosity increases further and eventually reaches a point at which the structure is no longer time-dependent and behaves mechanically like a solid. The point at which this occurs is known as the glass transition.

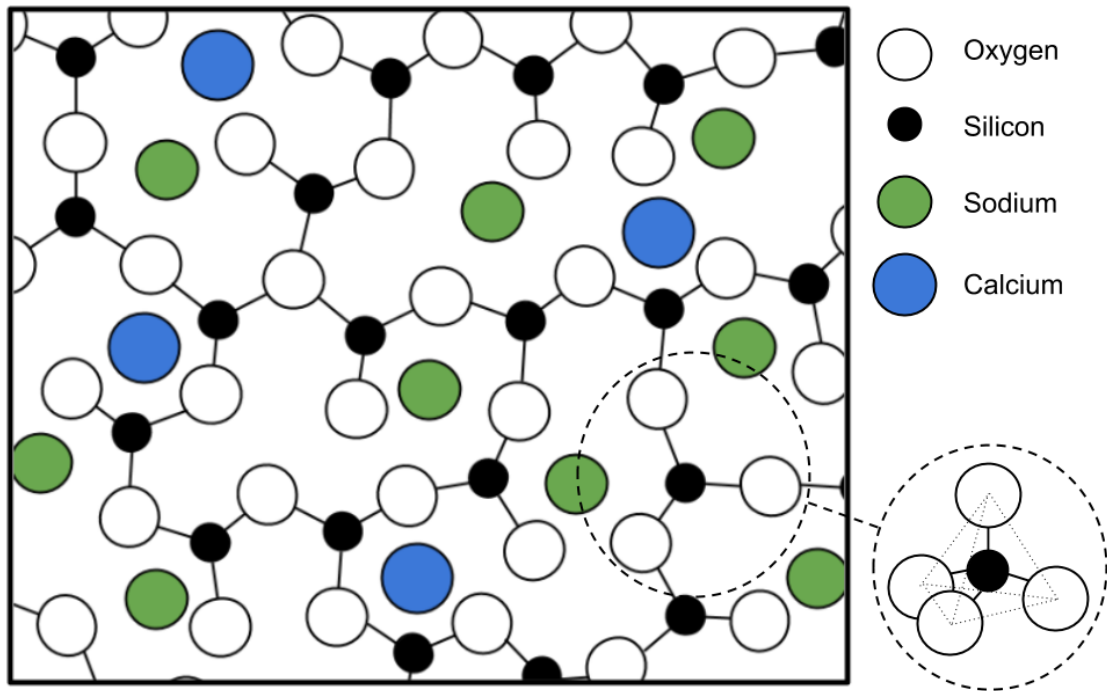


**Figure 2.1 – a: A two-dimensional representation of the molecular structure of SLS glass, after [6] and [7]. Inset: A 3-dimensional representation of a SiO<sub>4</sub> tetrahedron.**

The glass transition occurs over a temperature range that is dependent upon the cooling rate for a particular glass composition. For SLS glass, this typically occurs near to a temperature of  $\sim 580$  °C [8]. The glass transition can be demonstrated in terms of volume-dependence with temperature, as shown in Figure 2.2. When above the melting temperature, the glass melt (red line) has a larger coefficient of thermal expansion than the substance in its solid crystal form (green line). This is shown in the figure by the steeper gradient of the red line. By supercooling (blue line), the substance continues to have the expansivity of its liquid form for some time before the glass transition (purple curves). After the glass transition, the thermal expansivity decreases to a similar value of the crystal form (orange lines).

A consequence of supercooling is that a substance is less dense in its glass form than in its crystalline form. Additionally, rapidly cooled glass is likely to be less dense than slowly cooled glass. As a means to characterise the difference between glasses cooled at different rates, a fictive temperature can be defined. This can be found by extrapolating the glass and supercooled liquid lines (orange and blue lines in Figure 2.2, respectively) [9]. The point at which the lines meet corresponds to the fictive temperature of the glass, as illustrated in the figure.

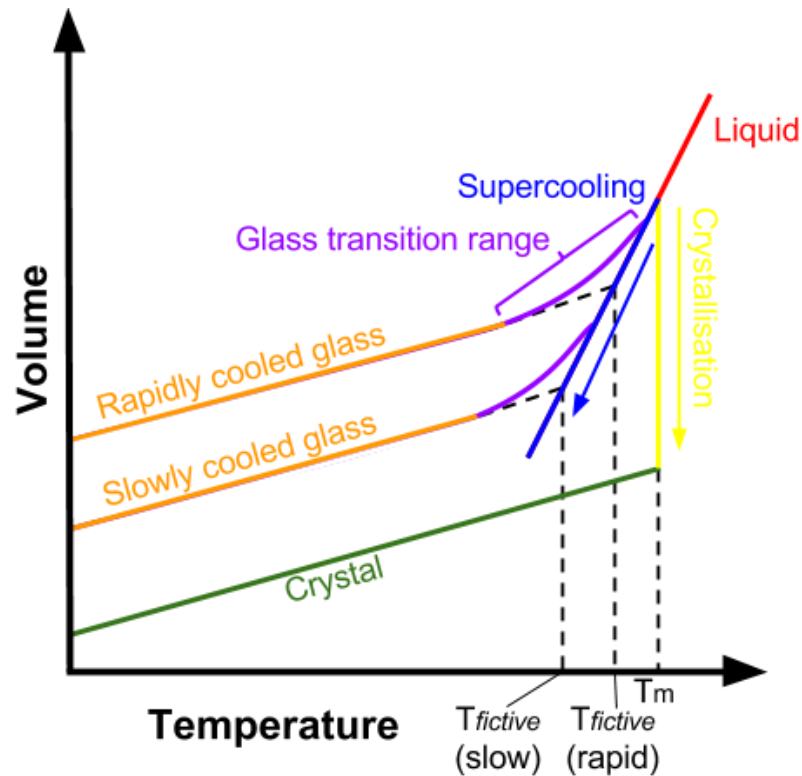
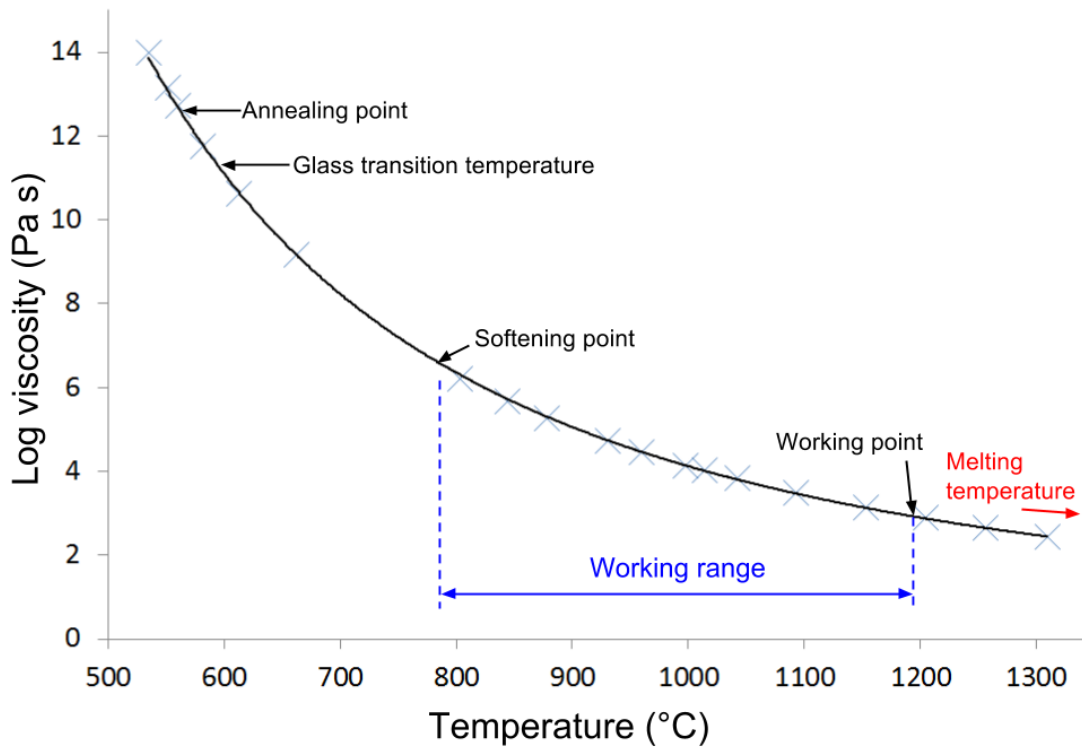


Figure 2.2 – The effect of temperature on volume (or enthalpy) for a glass-forming substance, adapted from [9].

### 2.2.2 Manufacture of pint glasses

The viscosity of glass at temperatures above the glass transition temperature plays a key role in the forming of glass articles. Figure 2.3 shows the effect of temperature on the viscosity of SLS glass, and indicates some critical temperatures to glass manufacture. Of particular significance are the working point and the softening point. The range of viscosity values between these points is known as the working range. The working range is a practical range in which there is an adequate compromise between viscosity and fluidity that allows the glass to be formed into shape, without losing that shape in a short period of time. The melting temperature here is not a true melting point in the sense of the melting of crystals, but rather a practical temperature in which undissolved gases can be removed and homogeneity can be achieved in an acceptable amount of time. It is considered to occur at a viscosity value of 10 Pa·s [10]. The annealing point refers to the temperature at which residual stresses can be relieved in a glass article, and is discussed separately in section 2.4.



**Figure 2.3 – Viscosity dependence on temperature for SLS glass. Values from [11], reference temperatures from [8].**

Commercial pint glasses are made by automated blow moulding processes which are based on traditional glassblowing methods. Three main stages are involved [12], as demonstrated in Figure 2.4:

1. A predetermined mass of molten SLS glass, known as a gob, is gathered from a furnace. The temperature is near to the melting temperature.
2. A preliminary shape is blown from the gob, known as a parison, which vaguely resembles the final shape. The glass temperature is within the working range.
3. The parison is transferred to a cast iron mould, where it is blown to its final shape.

This process is commonly referred to as blow-and-blow [10].

Commercially, drinking glasses are made using the Westlake machine which can produce up to 55,000 articles per day [12]. The machine works by first gathering a SLS gob from a furnace by suction, and then transferring it to a spindle. Compressed air is introduced into the spindle to form the parison and the spindle is rotated towards a wetted mould. The glass is blown with compressed air for a second time in the wetted mould to the required shape [13]. The mould then opens and releases the glass, which is conveyed for further processing.

Greater control over the wall thickness and shape of the glass can be attained by pressing the initial gob with a plunger to form the parison [14], although this is less efficient than purely blow methods [15]. Alternatively, the parison may be formed by placing a flattened gob over a hole so that the centre of the gob sags [15].

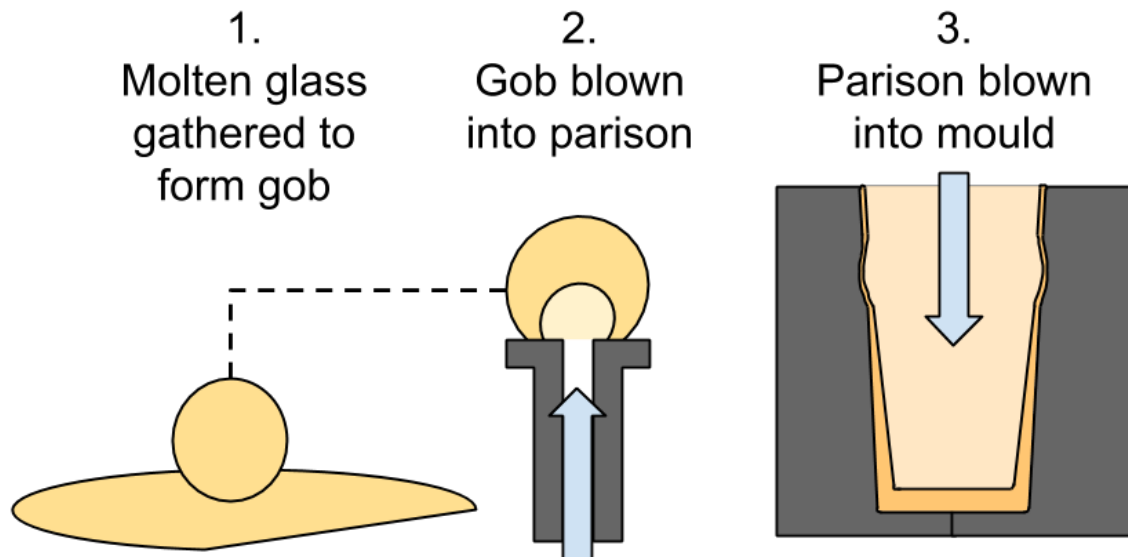


**Figure 2.4 – Three key stages of drinking glass manufacture. Diagram is not meant to be a representation of any particular manufacturing process.**

This section has provided an introduction to the basic properties of glass relevant to production. Additionally, manufacturing methods for drinking glasses have been overviewed.

## 2.3 Glass strength

Throughout this thesis, the fracture of glass articles is assessed to determine injury potential. The fracture event is highly influenced by the state of stress in the glass article at the time of failure. This stress is a combination of two main components: stresses imposed due to an external load, and pre-existing residual stresses in the glass article. These are typically discussed in terms of elastic strain energy [16]. The stresses imposed due to an external load are largely dependent on the strength of the glass article. This is the subject of the current section; residual stress is discussed in section 2.4.

### 2.3.1 Quantifying glass strength

Glass is an isotropic brittle material that can be considered to behave in a linear elastic manner until fracture [17]. As a brittle material, its strength is usually characterised by the maximum far-field tensile load it can withstand,  $\sigma_f$  [18]. This form of loading is also known as mode I loading (see Figure 2.5). However,  $\sigma_f$  is not an intrinsic property of a glass article since it is highly dependent on the presence and size of flaws, particularly those present on surfaces.

These flaws serve as tensile stress concentrators and can vary in size by several orders of magnitude [19].

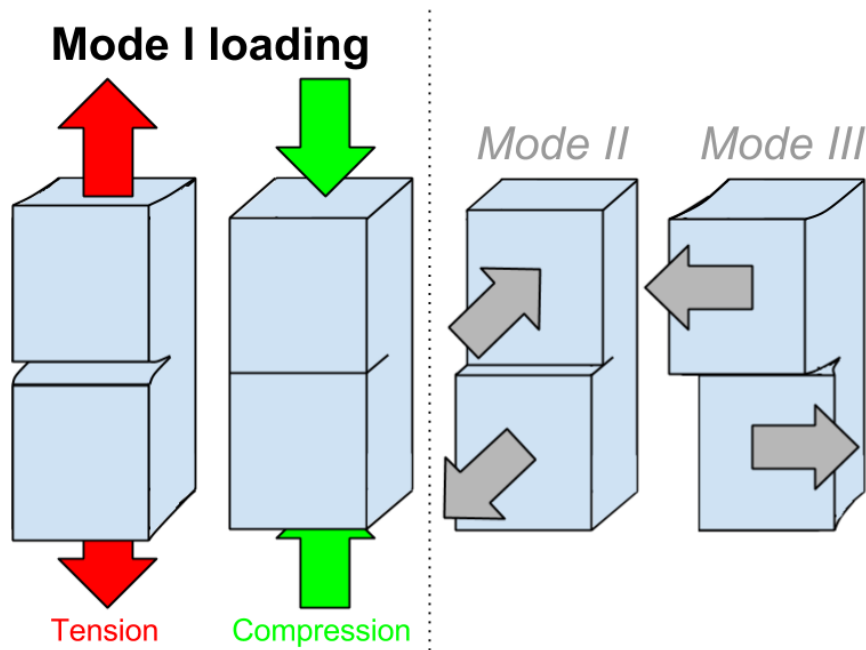


**Figure 2.5 – Three modes of loading, after [18]. Mode I: opening, includes tensile and compressive stresses; mode II: sliding; mode III: tearing.**

The flaw size dependency on glass strength can be expressed by the Griffith equation for brittle materials [20]:

$$\sigma_f = \sqrt{\frac{2E\gamma}{\pi c}} \quad (2.1)$$

where  $\sigma_f$  is the tensile failure stress,  $E$  is the Young's modulus of glass ( $\sim 74$  GPa [21]),  $\gamma$  is the energy required to form a new fracture surface ( $2-4$  J/m<sup>2</sup> [22]), and  $c$  is the maximum radius of the critical flaw from which fracture initiates. The Griffith equation assumes that the critical flaw is a small central crack in an infinitely large plate, and that in order for a fracture to propagate, it must gain the necessary energy to form new fracture surfaces.

Although  $\sigma_f$  is not an intrinsic property of glass, a fracture toughness (also referred to as critical stress intensity),  $K_{Ic}$ , can be defined. This is considered to be an intrinsic material property.  $K_{Ic}$  represents a critical value of stress intensity,  $K_I$ , that can be withstood in any part of a glass article.  $K_I$  takes into account the contributions of both the far field stress ( $\sigma$ ) and  $c$ , as shown in equation 2.2 (assuming the same flaw conditions as in equation 2.1) [16]:

$$K_I = \sigma\sqrt{\pi c} \quad (2.2)$$

Fracture occurs when any combination of  $\sigma$  and  $c$  leads to the condition of  $K_I = K_{Ic}$ . The value of  $K_{Ic}$  for SLS glass is  $\sim 0.7 \text{ MPa}\cdot\text{m}^{-0.5}$  [21]. More precise representation of the flaw shape can be incorporated by the use of stress intensity shape factors.

### 2.3.2 Practical effects of strength dependencies

Practically speaking, equations 2.1 and 2.2 (when adapted for  $K_{Ic}$  and  $\sigma_f$ ) state that the strength (or rather, tensile failure stress) of glass is inversely proportional to the square root of the flaw size. It follows that glasses with larger critical flaw sizes will be weaker. Likewise, small critical flaw sizes will result in higher strengths. This is demonstrated by Figure 2.6. Estimates for the theoretical strength of glass (also known as intrinsic strength) have been made by substituting the interatomic distance for the flaw size in equation 2.1 [23], resulting in values of approximately half the Young's modulus. Such a theoretical strength has not been observed in practice [24].

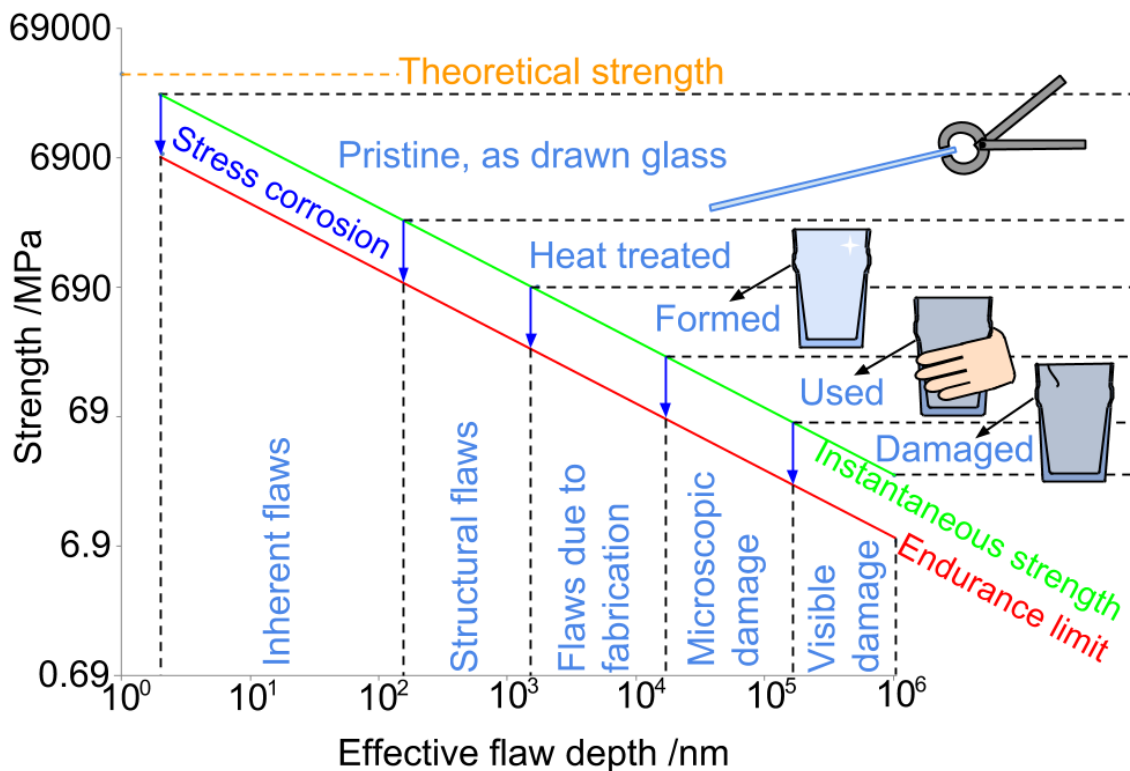


Figure 2.6 – Diagram to illustrate the range of strength values for glass articles as affected by the flaw size, after [19].

The source of flaws in glass is variable and flaw formation is difficult to avoid. Initial flaws present in as-drawn glass may be caused by surface chemical reactions with water in air [25]. Flaws are present in newly-formed glass articles due to contact with moulding equipment, depending on the smoothness of the mould and on the evenness of the mould surface temperature. The strength of glass articles decreases with use, since glass is highly susceptible

to flaws by contact damage because its fracture toughness is relatively low. Other potential causes of flaws in glass include: thermal expansion mismatch stresses due to foreign material inclusions [22], chemical attack particularly due to aggressive dishwasher cycles (for pint glasses) [26], and thermal shock due to rapid and/or uneven cooling [22].

Glass strength is also affected by loading rate. The faster the loading rate, the less time the glass is exposed to stress corrosion processes. As such, higher strength values can be attained by high loading rates or by loading glass samples in an inert environment [27]. This is shown by the green and red lines in Figure 2.6, which show that articles have an instantaneous strength relating to very high stress rates.

This section has addressed the fundamental characteristics of glass strength. The strength and mechanical response of pint glasses to typically applied loads is addressed in chapter 4 of this thesis. An additional influential factor to glass strength is the presence of residual stresses. This is addressed in the following sub-section.

## **2.4 Residual stresses in glass**

Residual stresses in glass are important to this thesis as they are responsible for the distinctive differences in fracture behaviour of annealed and thermally tempered glass. This section provides an introduction to residual stresses in thermally tempered glass and how they may be measured photoelastically.

### **2.4.1 Nature and development of residual stresses by tempering**

Residual stresses are elastic stresses in a material that exist in the absence of external forces [28]. The strength of glass articles can be increased or decreased depending on the magnitude and arrangement of residual stresses.

The failure of a glass article is primarily determined by both the size of surface flaws and the magnitude of far-field tensile stress, as introduced in the previous section. The size of surface flaws is difficult to control. However, the magnitude of far-field tensile stress can be opposed by inducing compressive residual stresses at the glass surfaces. This compressive stress,  $\sigma_c$ , perpetually acts on surface flaws, and must be overcome by a tensile load prior to failure. In theory, this should increase  $\sigma_f$  by  $|\sigma_c|$ . In order to accommodate a compressive surface stress state in a glass article, the interior of the article must have a corresponding tensile stress for the condition of equilibrium. Since the interior is far less susceptible to the development of flaws, this tensile stress can usually be accommodated without failure.

The two most common ways of inducing compressive residual stresses into glass articles are chemical and thermal tempering (also referred to as toughening). An example through-thickness stress distribution resulting from both methods is given in Figure 2.7. It can be seen that the chemically tempered stress distribution results in a greater surface compressive stress and a lesser interior tensile stress than the thermally tempered stress distribution. However, the depth of the compressive layer (known as the case depth) is much greater for thermally tempered glass. The consequences of these differences on the fracture characteristics of both types of tempered glass are detailed in section 2.5.

Most chemical tempering treatments work by replacing alkali atoms local to the glass surface with other alkali atoms that have a larger atomic radius. This typically involves the replacement of sodium ions with potassium ions [29]. Since the chemical tempering process is effective over a small depth, the corresponding interior tensile stress is very low. However, if the depth of the critical surface flaw is greater than the case depth, the compressive surface stress does not provide an effective increase in strength. Furthermore, the process requires long treatment times in comparison to thermal tempering [30], and consequently it has not been commercially applied to drinking glasses.

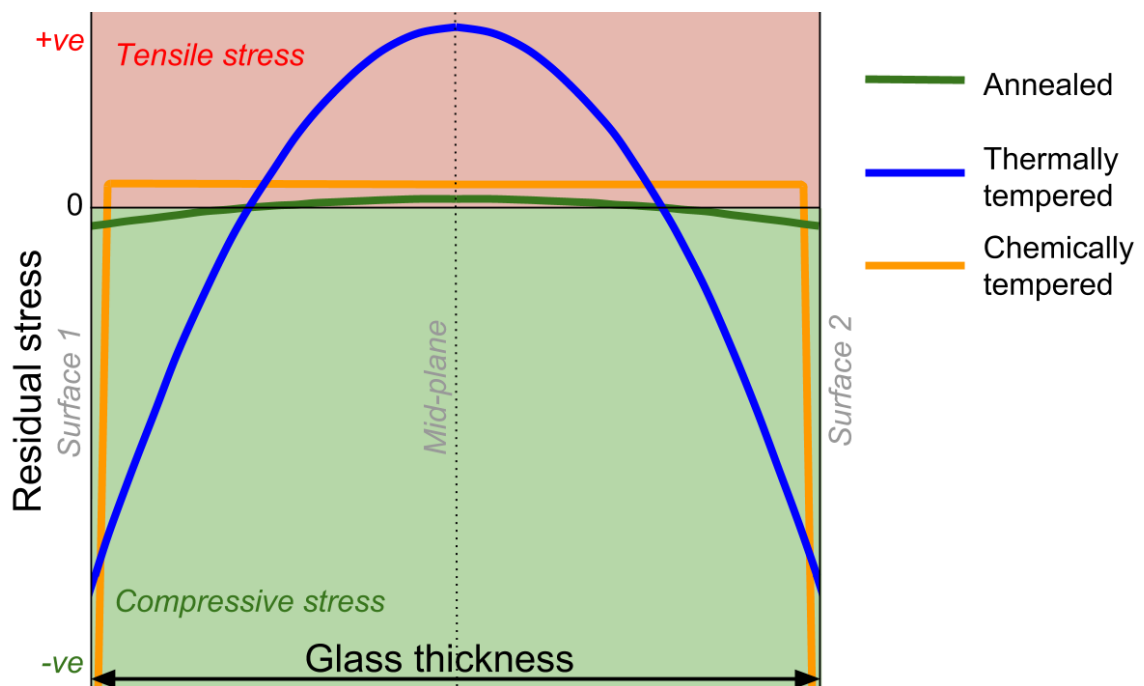


**Figure 2.7 – Illustration of typical through-thickness residual stress distributions for annealed, thermally tempered, and chemically tempered glass, after [31].**

Thermal temper stresses are created when glass is cooled from above the glass transition temperature. The rate at which this occurs affects the magnitude of stresses, with slower

cooling rates resulting in lower overall stresses. When glass is cooled evenly and slowly to minimise the development of residual stress, it is referred to as annealed glass (green profile, Figure 2.7). Conversely, when glass is cooled by rapid quenching at its surfaces, it is referred to as thermally tempered glass (blue profile, Figure 2.7). In practice, the strength of SLS glass has been found to improve by  $1.18 * |\sigma_c|$  after thermal tempering [32].

A simplified explanation of how thermal temper stresses are created in glass articles can be given by considering the temperature during cooling at both the mid-plane and the surfaces of an article [33]. This is demonstrated in Figure 2.8.

**Time i:** Initially, the temperature at the mid-plane of the article ( $T_{mid}$ ), and the temperature at the surfaces of the article ( $T_{surf}$ ), are equal. This temperature is below the working range and above the glass transition temperature range ( $T_g$ ). Within this temperature range, the behaviour of glass is said to be viscoelastic. This means that any stress imposed into the article will be relieved in a finite period of time. Furthermore, as the temperature drops, the viscosity of the glass increases (see Figure 2.3), and the necessary period of time to relieve the same imposed stress increases.

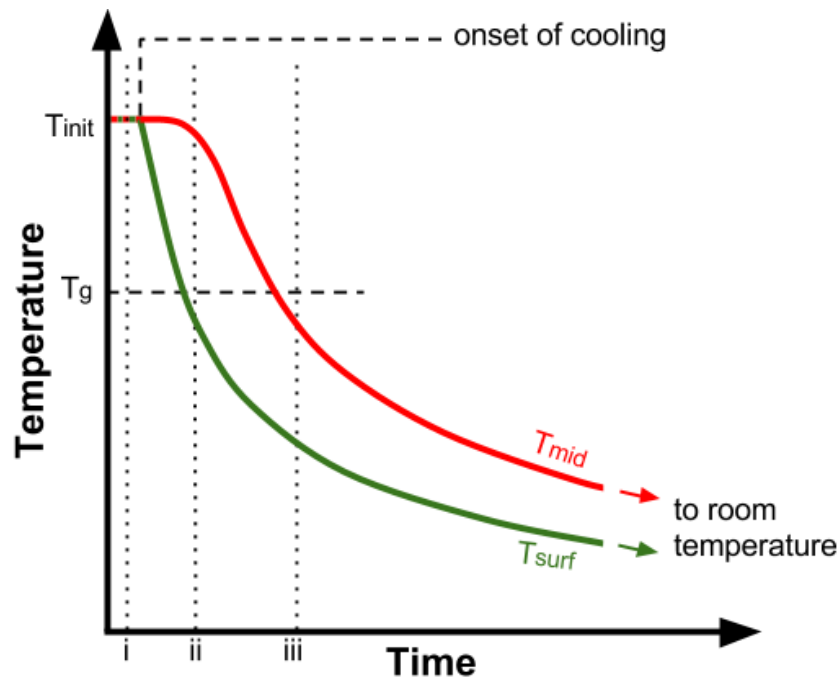


Figure 2.8 – Illustration of mid-plane (red line) and surface (green line) temperature during thermal tempering, after [33].

**Time ii:** Between times i and ii, the cooling process begins by rapidly and evenly quenching the surfaces of the article. Since the surfaces are directly exposed to the quench medium,  $T_{surf}$  begins to decrease while  $T_{mid}$  remains unchanged. At time ii,  $T_{surf}$  has dropped below  $T_g$  and the

region of the glass local to the surface begins to behave as an elastic solid. Since  $T_{\text{mid}}$  is still above  $T_g$ , the region of the glass local to the mid-plane is still viscoelastic. The thermal stresses created due to the contraction of the solidified surface region are therefore relieved by the mid-plane region.

**Time iii:**  $T_{\text{mid}}$  has cooled below  $T_g$ , and the mid-plane region begins to behave as an elastic solid. However, as this region contracts, it is resisted by the already solidified surface region. Consequently, the mid-plane region is put into a state of tension since it is unable to contract to its equilibrium volume. The surface region is simultaneously put into a corresponding state of compression.

Early mathematical treatments of the stresses induced by thermal tempering considered the residual stresses in an article to be equal in magnitude and opposite in sign to the stress relieved near time ii in Figure 2.8 [34]. However, it has since been found that the total residual stress is a result of not just thermal stresses, but also structural stresses. Structural stresses are formed as a result of the effect of cooling rate on density (see Figure 2.2) [35]. Modern mathematical treatment of thermal residual stress formation takes this into account, and requires that the temperature in successive layers of the glass article is considered, rather than just at a surface and the mid-plane [36]–[39].

In addition to the through-thickness stresses as described above, residual stresses can vary laterally across an article. Such stresses are referred to as either membrane stresses or form stresses [33], [40]. Membrane stresses are constant through the thickness of an article, and occur due to lateral variation of the cooling rate.

#### **2.4.2 Photoelasticity for measuring thermal temper stresses**

Throughout this thesis, the measurement of residual stresses in glass articles due to thermal tempering is conducted by the use of non-destructive photoelastic methods. This sub-section provides a basic introduction to photoelasticity in thermally tempered glass. The specific photoelastic methods used in this work are detailed in chapter 3.

Stress measurement by photoelasticity is possible in thermally tempered glass due to its birefringence. This means that when a light beam vibrates in a particular plane and enters a stressed glass article, it splits into two further light beams. These two light beams vibrate in perpendicular planes, the orientation of which coincides with the orientation of principal stresses in the article. The magnitude of each principal stress affects the refractive index of the glass along each plane. Consequently, the two light rays travel through the glass at different

speeds and become out of phase. The orientation of the perpendicular light rays, and the magnitude of the phase difference between the two, permit photoelastic stress analysis. This effect was first observed by Brewster in 1816 [41].

In order to assess residual stresses in glass photoelastically, an instrument called a polariscope is used. Polariscopes have been used in the glass industry for quality control purposes since before the 1930s [42]. The most basic type of polariscope is the plane polariscope. An illustration of the components involved with a plane polariscope and its principle of operation is shown in Figure 2.9.

There are three essential components to a plane polariscope: a light source and two linear polarising filters. They are arranged as shown in Figure 2.9. The first polarising filter (the polariser) is placed in between the light source and the second polarising filter (the analyser). The polariser and analyser are orientated at  $90^\circ$  to each other. The glass sample to be assessed is then placed between the polariser and the analyser. For completely stress-free glass and with 100% efficient polarising filters, no light will pass through the analyser.

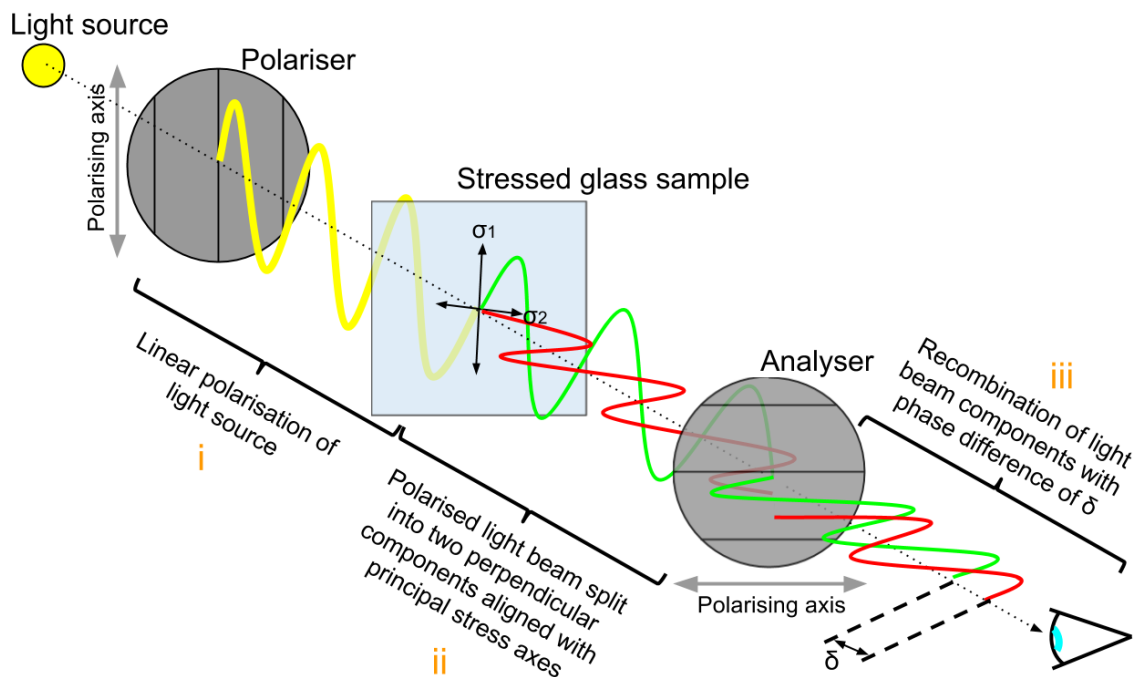


Figure 2.9 – The components and principle of operation of a plane polariscope, after [43].

When a stressed glass sample is placed between the two, the birefringent effect causes the linearly polarised light beam from the polariser to split, re-orientate, and become out of phase (stage ii in Figure 2.9). The light then enters the analyser, and the two light beams recombine in the plane of the analyser with a phase difference between them (stage iii). This phase difference is typically measured in nm and is referred to as optical retardation,  $\delta$ . Assuming

plane stress conditions, the difference in magnitude of the principal stresses can be calculated by equation 2.3 [44]:

$$\sigma_1 - \sigma_2 = \frac{\delta}{Ct} \quad (2.3)$$

where  $\sigma_1$  and  $\sigma_2$  are the principal stress magnitudes,  $t$  is the thickness of the glass sample, and  $C$  is the stress optical coefficient.  $C$  is a material property depending on composition (typically  $2.72 \text{ TPa}^{-1}$  for SLS glass) [43].

When thermally tempered glass is viewed in a plane polariscope from behind the analyser, a series of fringes are observed on the glass on a black background (see Figure 2.10). Black fringes indicate areas where light has been extinguished on entry to the analyser, and therefore had an orientation parallel to the polariser axis. These fringes are known as isoclinic lines or areas, and indicate areas on the glass that have the same principal stress orientation. Rotation of the sample with respect to the polarising filters will result in different isoclinic patterns which repeat every  $90^\circ$ .

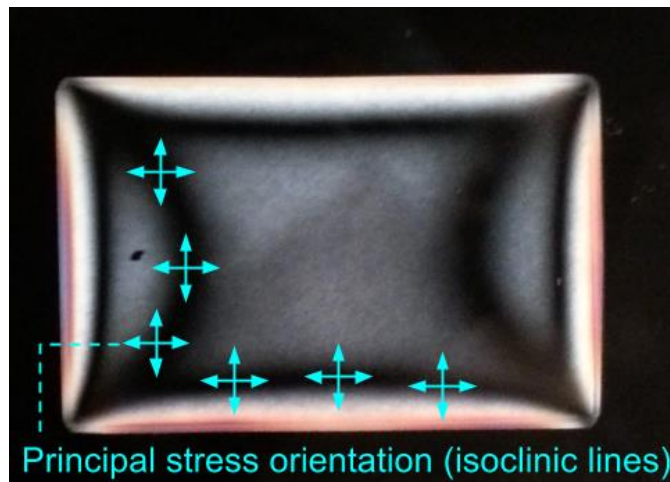


**Figure 2.10 – Photoelastic fringes viewed in a plane polariscope on a rectangular tempered glass sample showing isoclinic lines.**

The use of birefringent plates that produce a known retardation between light beam components can further aid photoelastic assessment. Of these, quarter-wave plates and full-wave plates are the most common, which induce retardations of  $\lambda/4$  and  $\lambda$ , respectively. Quarter-wave plates can be used to remove isoclinic lines. The fringes that remain are known as isochromatic lines, and indicate areas of the glass with the same value of  $(\sigma_1 - \sigma_2)$ . Isochromatic lines do not vary on sample orientation with respect to the polarisation axes. The

use of a full-wave plate in between the glass sample and the analyser improves the colour contrast between fringes without affecting the photoelastic pattern (see Figure 3.9).

This section has introduced residual stresses in glass and how they are produced. This was followed by an introduction to the measurement and assessment of residual stresses by photoelasticity.

## **2.5 Fracture characteristics of glass**

This chapter has so far introduced glass strength and residual stresses in glass. This section considers how these aspects affect the fracture of glass articles. The fracture behaviour of glass is critical to this thesis as it is used as a key indicator of injury potential in several chapters. The study of the fracture characteristics of materials is known as fractography.

This section consists of three sub-sections. Firstly, fractographic axes are introduced and defined. This facilitates the description of fracture features of glass articles. Secondly, typical macroscopic fracture patterns are overviewed with particular focus on annealed and thermally tempered glass. Thirdly, important features observed on fracture surfaces of glass are overviewed.

### **2.5.1 Fractographic axes**

Defining a set of axes based on the orientation of propagated cracks facilitates the description of fracture characteristics of glass articles. An x-y-z co-ordinate system is used in this thesis as illustrated in Figure 2.11, and is based on a system outlined by Bradt [16]. The y-axis follows the main direction of crack propagation. The x-y plane maps the topography of the fracture surfaces in a broken article, which are surfaces formed during the event of fracture. The overall fragmentation pattern traced out by the propagating crack(s) is present on the y-z plane. A full fractographic analysis involves the assessment of features on both the x-y plane and the y-z plane together. Additionally, the x-z plane may be considered as cross-sections of the x-y plane.

These axis definitions are also used for categorisation of the edges on a glass fragment for the assessment of sharpness. This is introduced in chapter 6 of this thesis.

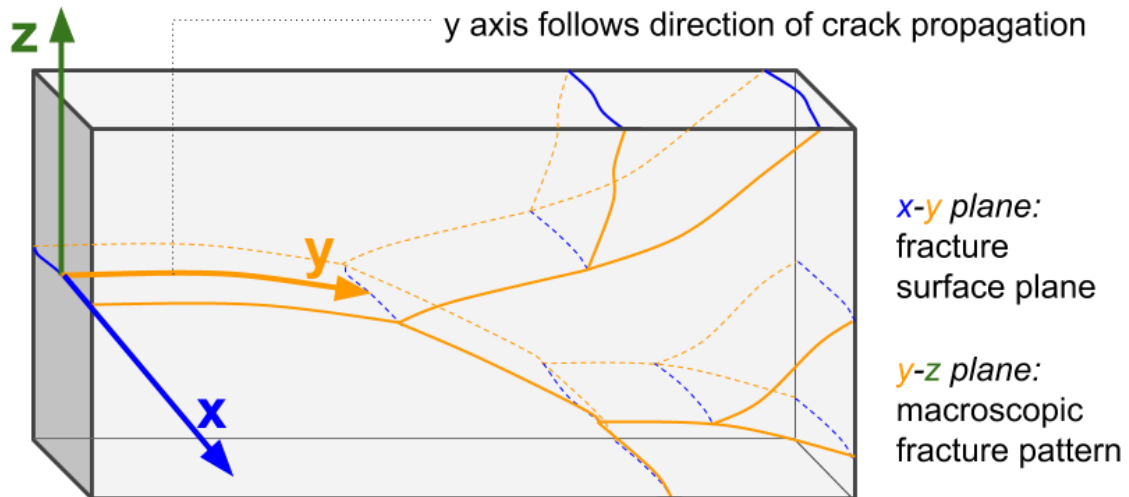


Figure 2.11 – Illustration of fractographic axes on a fractured glass article.

### 2.5.2 Macroscopic fracture pattern (y-z plane)

In this thesis, the macroscopic fracture pattern refers to the fracture pattern present in the y-z plane as shown in Figure 2.11. It can be viewed if the glass article is restrained before fracture in order to hold fragments in place, or if the fractured article is re-assembled. The macroscopic fracture pattern shows how the crack(s) propagated during the event of fracture and gives some information on the stress state of the article at the time of fracture. This sub-section overviews typical y-z plane fracture characteristics of glass and how they are affected by external and residual stresses.

As introduced in section 2.3, the critical conditions for the fracture of glass are quantified by the flaw size, and the magnitude of mode I tensile loading (see Figure 2.5). Mode I loading is also important during crack propagation, as it affects the direction of propagation. This is because cracks in glass have a tendency to orientate themselves so as to minimise the effect of shear loading (modes II and III) [18]. The macroscopic pattern is therefore to a large extent a reflection of the mode I tensile stress state at the time of fracture.

For annealed glass at the time of fracture, the residual stresses are typically very low, in comparison to the external stresses caused by loading. As a result, macroscopic fracture patterns in annealed glass articles reflect the state of tensile stress in the article caused by external loading. Macroscopic fracture patterns of annealed glass can therefore aid assessment of the fracture of glass articles with high levels of residual stress (tempered glass) broken under the same conditions, as the component of the fracture pattern determined by external loading can be separated to some extent. Annealed glass fracture is typically characterised by large fragments of variable size with acute angles as shown in Figure 2.12.

A propagating crack may split into two or more separate cracks. This phenomenon is commonly known as branching, or bifurcation. It occurs when the speed of the crack approaches the terminal velocity in the glass ( $1460\text{--}1600\text{ ms}^{-1}$  for SLS glass [45]). The angle between cracks after bifurcation is commonly referred to as the bifurcation angle and is known to be dependent on the state of stress in the glass article [46].

In thermally tempered glass, the macroscopic fracture pattern is greatly influenced by the residual stresses in the article. It is characterised by typically consisting of small cuboidal fragments and is often referred to as having a diced pattern. An example is shown in Figure 2.12. This fracture behaviour is considered to be safer than annealed glass fracture, and is sometimes referred to as safety glass [47].

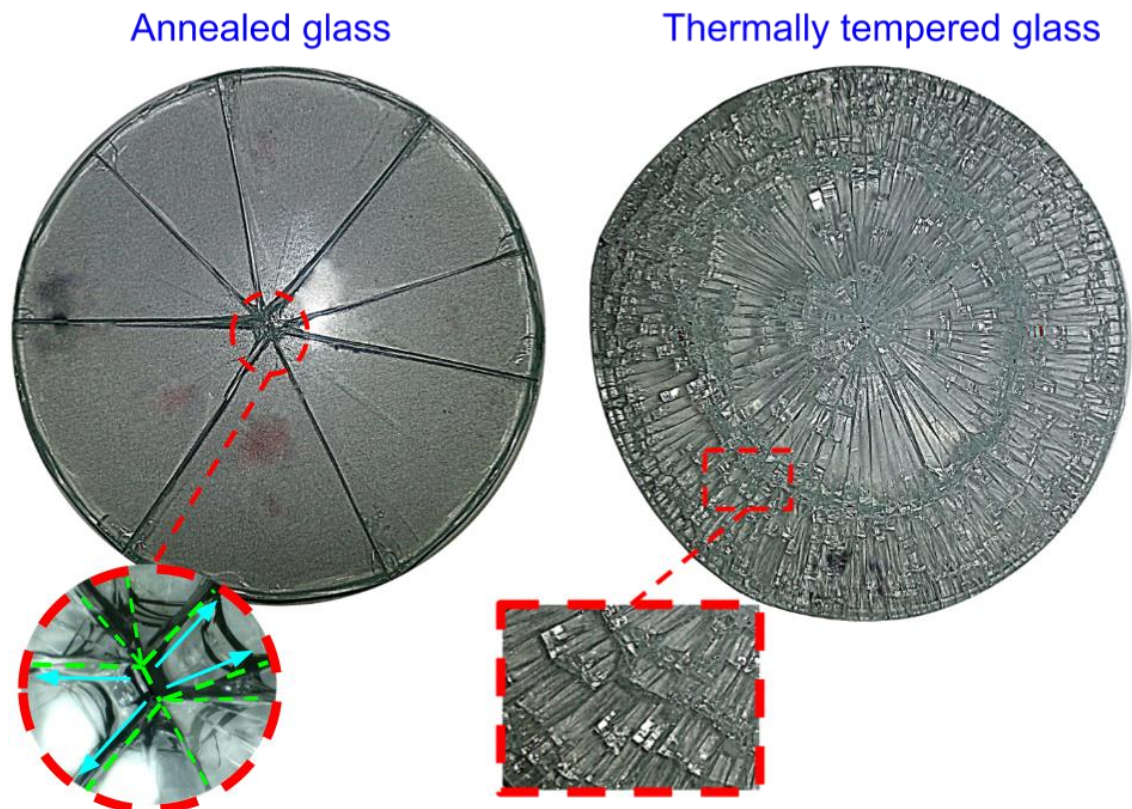


**Figure 2.12** – Examples of annealed and tempered glass fracture patterns in  $y$ - $z$  plane. Both discs broken by equibiaxial ring-on-ring testing. Left inset shows a characteristic breakage pattern near the origin of fracture in an annealed glass article. Right inset is a closer view of some cuboidal fragments in a tempered glass article.

It is possible for tempered glass to break with minimal external stress applied, if a suitably sized flaw is introduced to the interior region, because of its internal tensile stress. When tempered glass is broken in this way, the breakage is often referred to as spontaneous. Gardon [48] found that a threshold residual tensile stress of 47 MPa was necessary to ensure spontaneous breakage in 6 mm thick thermally tempered glass. Values between 34 and 47

MPa were said to be in a transition region which may or may not induce spontaneous breakage.

In usual conditions, the fracture pattern observed for tempered glass is a combination of the effects of both external and residual stresses. Due to its enhanced strength, a greater external load is required to cause fracture. This increases the amount of stored elastic strain energy in the article prior to fracture, which makes more energy available to be converted into fracture surface energy. However, it is likely that not all of the elastic strain energy is released during fracture [49]. Additional fracture can occur in tempered glass due to air humidity, causing secondary cracks that typically propagate at 90° to the main propagating crack [50]. This often results in cube-shaped fragments similar to those shown in Figure 2.13.

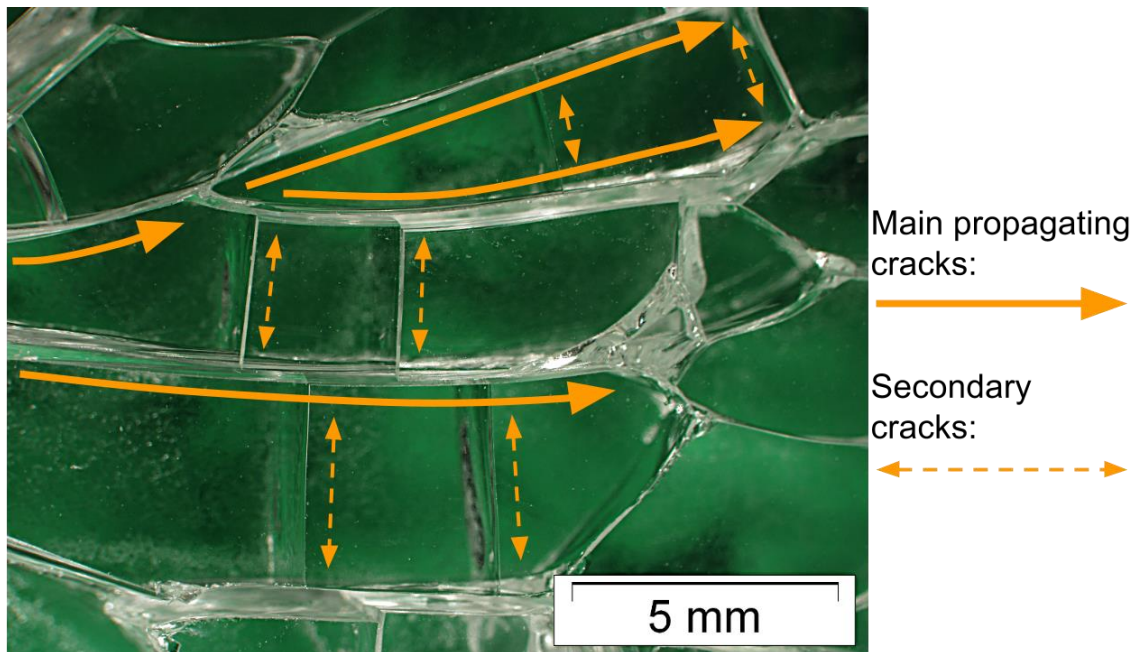


**Figure 2.13 – Secondary cracking in tempered glass resulting in cube-shaped fragments.**

Chemically tempered glass typically has interior tensile stress levels lower than the threshold stress required for spontaneous breakage, despite its high compressive stress. In such cases, the nature of breakage is similar to annealed glass. However, its high compressive surface stress results in higher strength values. This in turn results in high levels of stored elastic strain energy when loaded, and it is therefore likely to have a denser fragmentation pattern than annealed glass.

This section has introduced the typical macroscopic fracture patterns observed on annealed and tempered glasses. The effect of external and residual stresses on the propagated fracture

pattern has been discussed. The patterns observed on the y-z plane correlate with features observed on the x-y plane, which is discussed below.

### 2.5.3 Fracture surface characteristics (x-y plane)

The x-y plane, as shown in Figure 2.11, maps out the topography of the fracture surfaces of a broken glass article. The markings on these surfaces are important as they give information about the nature of the crack event. This sub-section overviews the cause and significance of three common types of fracture surface marking, which are referred to throughout this thesis. These are: the fracture origin region, hackle lines, and Wallner lines.

#### 2.5.3.1 Origin of fracture

The point from which a fracture initiates in a broken glass article is known as the origin. It can be located by either identifying characteristic features on the y-z plane (left inset, Figure 2.12), or by inferring the direction of crack propagation from other fracture surface markings and tracing backwards (see following sub-sections). The immediate region surrounding the origin is the fracture surface area created during the initial phase of propagation. Features in this region give information about the magnitude and state of stress at the point of failure. An example of an origin in SLS glass and the surrounding fracture surface region is shown in Figure 2.14.

Three radial regions centred around the origin flaw can be observed in Figure 2.14: the mirror region (a smooth and featureless region), the mist region (a dimpled region of greater roughness than the mirror), and the hackle region (sharp, strongly defined ridges), as labelled. The roughness of the mirror region has been found to gradually increase, albeit non-linearly, from the origin flaw [51]. However, the change in roughness only becomes discernible by visible light at the mist region. After the hackle region, the propagating crack begins to bifurcate macroscopically. Mist and hackle markings are discussed further in the following sub-section.

The radius of the mirror region,  $r$ , can be used to estimate the tensile failure stress with the following equation [52]:

$$\sigma_f = A/\sqrt{r} \quad (2.4)$$

where  $A$  is a constant which depends on loading conditions and material composition. In this thesis,  $A$  is taken to be  $1.8 \text{ MPa}\cdot\text{m}^{-0.5}$  for SLS glass articles broken by flexure, after Mecholsky [53].

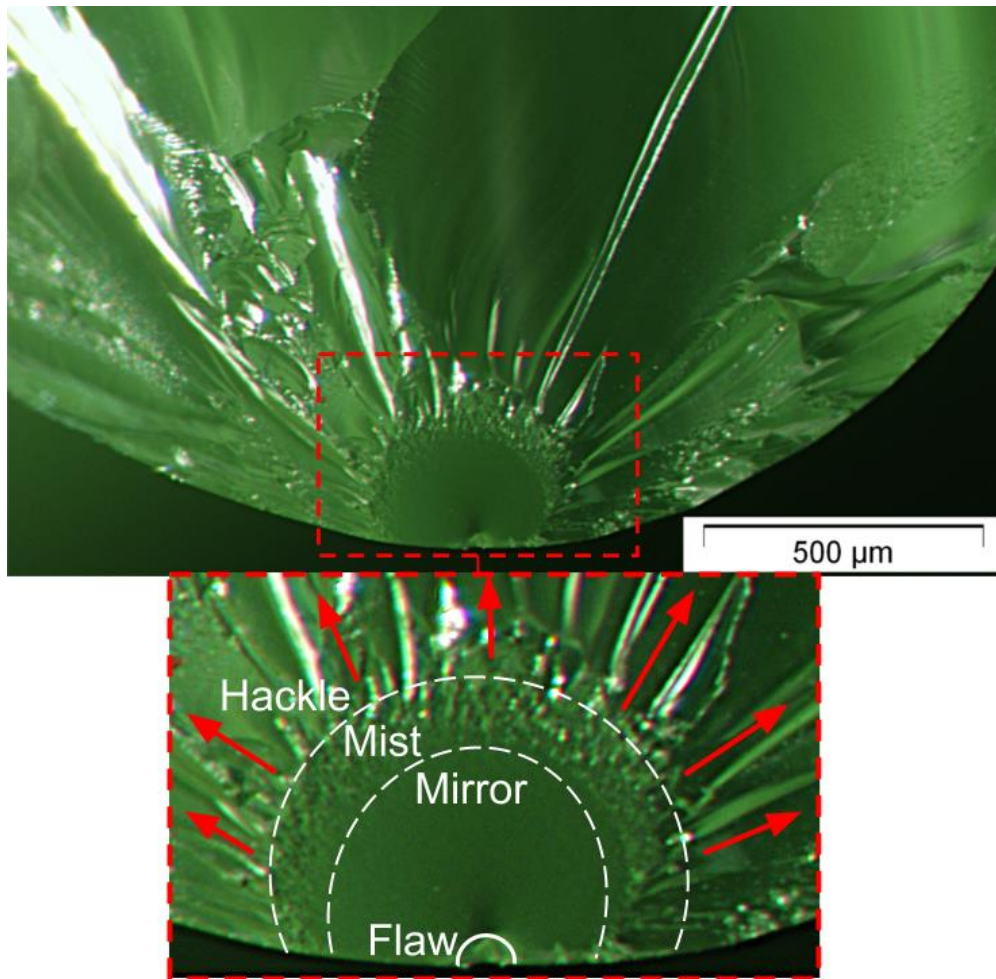


**Figure 2.14** – An optical micrograph of a fracture origin observed from a broken pint glass. Fracture occurred from a flaw at the rim of the glass. Red arrows show direction of the expanding crack front in the hackle region.

The shapes of the mirror, mist, and hackle regions surrounding the origin may differ from those shown in Figure 2.14. If the critical flaw is within the volume, rather than at a surface, the features surrounding the origin may be fully circular and centred around the flaw. The origin region is also very sensitive to residual stresses, and consequently the mirror radius may be variable. Likewise, the mirror region may become elongated if the article is loaded by bending. In cases where the mirror radius is variable, it is usually recommended that the mirror radius is taken by dividing the mirror diameter at the surface by two [54]. For articles broken under very low tensile stress, mist and hackle regions may not develop at all after the origin.

### **2.5.3.2 Hackle lines**

Hackle lines are lines on a fracture surface which run parallel to the local direction of crack growth. They divide areas on the x-y plane which are parallel and are on different Cartesian planes [55]. In general, they are caused by local deviations of the crack front from the main

tensile axis [55]. The circumstances involved during crack development may result in various types of hackle. In this sub-section, three types of hackle are discussed: mist/ velocity hackle, twist hackle, and shear hackle. These are referred to in further chapters of this thesis.

**Mist/velocity hackle** was briefly introduced above as part of the discussion on the fracture origin. The transition from a mirror region, to mist, to hackle, is indicative of a crack accelerating from a low velocity to the terminal velocity in glass. It is therefore observed on fracture surfaces not only near the fracture origin (see Figure 2.14), but also on other fracture surfaces just prior to macroscopic bifurcation.

The mist/velocity hackle region has been shown to consist of similarly-shaped ridges to the larger hackle region [56], but on a smaller scale. The size and frequency of hackle ridges increases with higher crack velocity due to greater magnitude of micro-mechanical activity at the crack front [57].

Examples of mist/velocity hackle on annealed and thermally tempered glass fracture surfaces are shown in Figure 2.15. Both fracture surfaces were created by subjecting the original glass article to flexure. Consequently, one surface of the article was subjected to tensile stress, and the opposite surface was subjected to compressive stress. For the annealed glass, this resulted in the propagating crack front leading at the tensile surface and lagging elsewhere. This is seen in the figure by the presence of mist/velocity hackle at this surface. By contrast, the mist/velocity hackle on the fracture surface of the thermally tempered glass fragment is present at the mid-plane, where the residual tensile stress is expected to be at a maximum.

**Twist hackle** occurs when the propagating crack front encounters mixed mode I/III loading (see Figure 2.5). It is commonly referred to as a river-line pattern [58], however the terminology used in this thesis was chosen to align with ASTM 1256 [54]. It can be seen on both the annealed and thermally tempered fracture surfaces as labelled in Figure 2.15, and also in a closer view in Figure 2.16. The term twist hackle originates from the rotation, or twist, of the main axis of tensile stress. It is typically found near to the side of a glass fragment that was previously subjected to compressive stresses during flexure of the original glass article. The direction of local crack propagation can be inferred from twist hackle as shown in Figure 2.16. Smaller hackle steps coalesce and result in larger and taller hackle steps as the crack propagates under the applied mode I/III load [55].

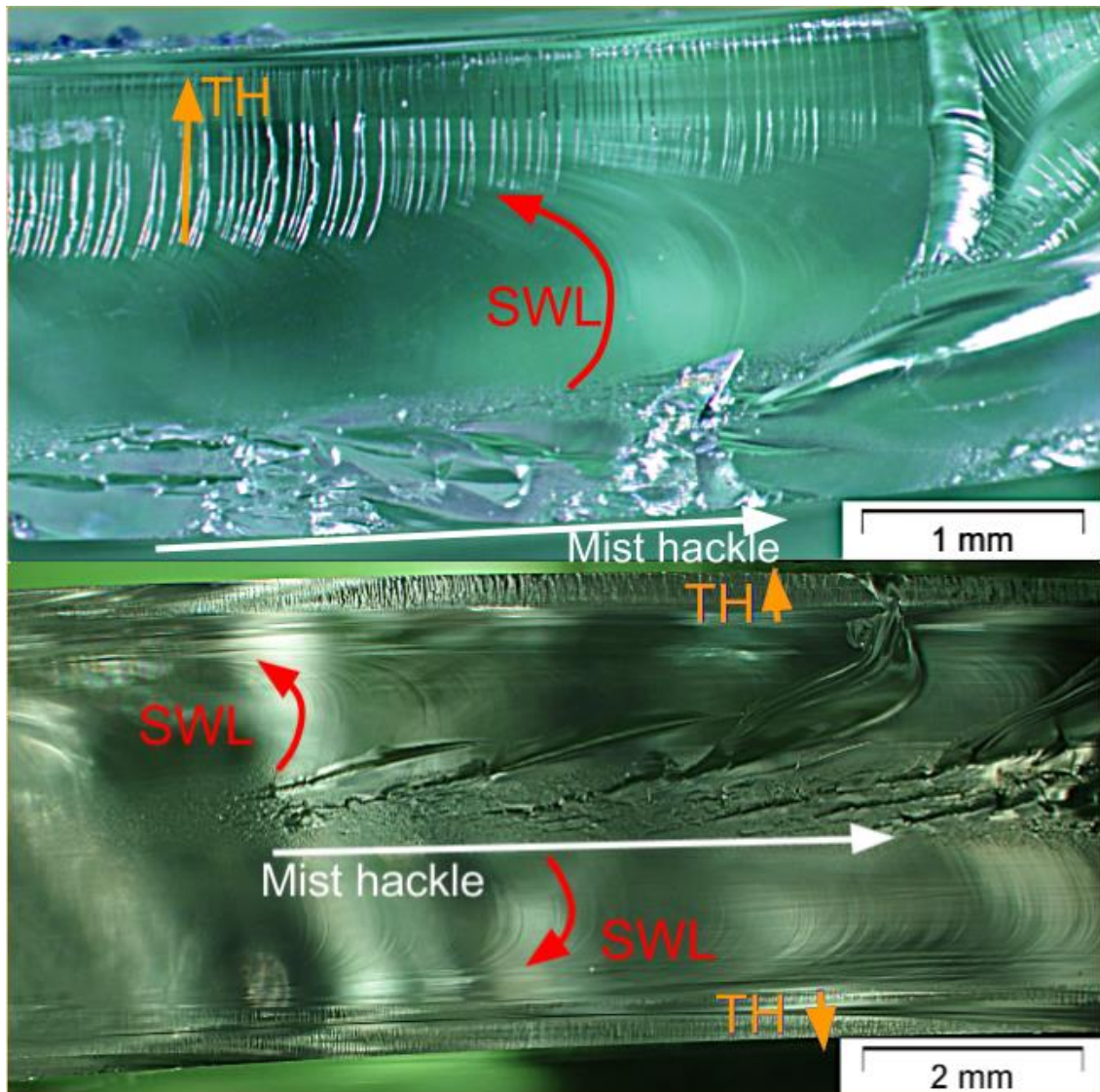


Figure 2.15 – Examples of fracture surfaces from an annealed glass fragment (top) and a thermally tempered glass fragment (bottom), showing key fracture surface markings. Original glass articles were broken by bending. SWL: secondary Wallner line; TH: twist hackle.

**Shear hackle** is a form of hackle that typically occurs far from the fracture origin, and is more common in hollow glass articles [55]. It is found on fracture surfaces where the propagating crack has curved in the  $y$ - $z$  plane, and occurs due to similar loading conditions as those that create twist hackle. An example is shown for an annealed glass in Figure 2.17. Shear hackle may also be referred to as corner hackle [45].

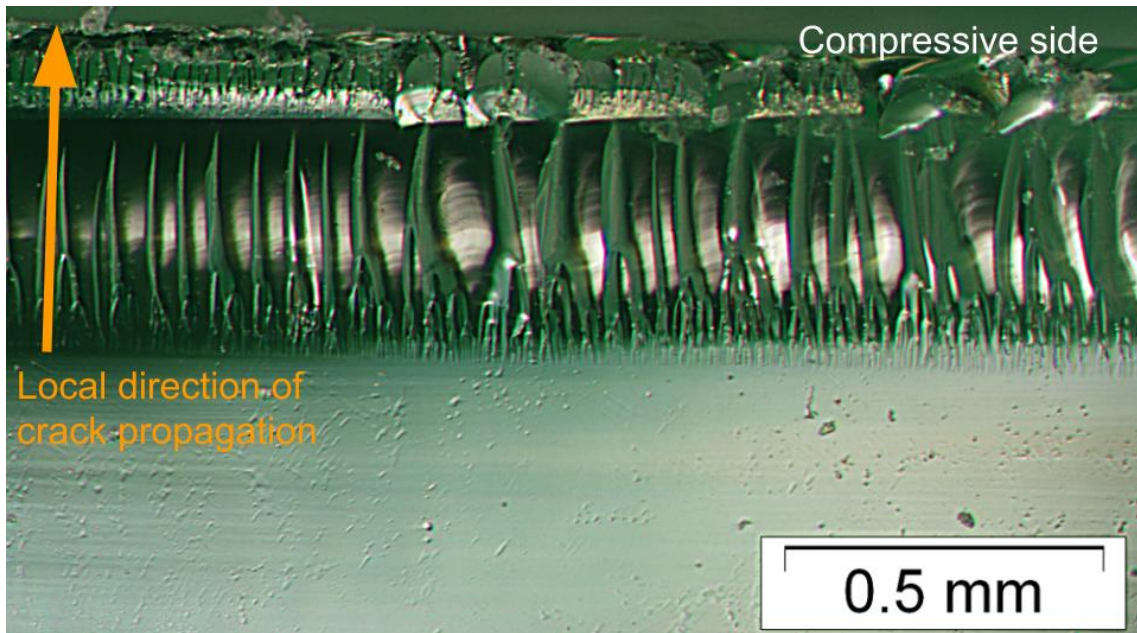


Figure 2.16 – Twist hackle near the compressive surface of an annealed glass disc broken in flexure.

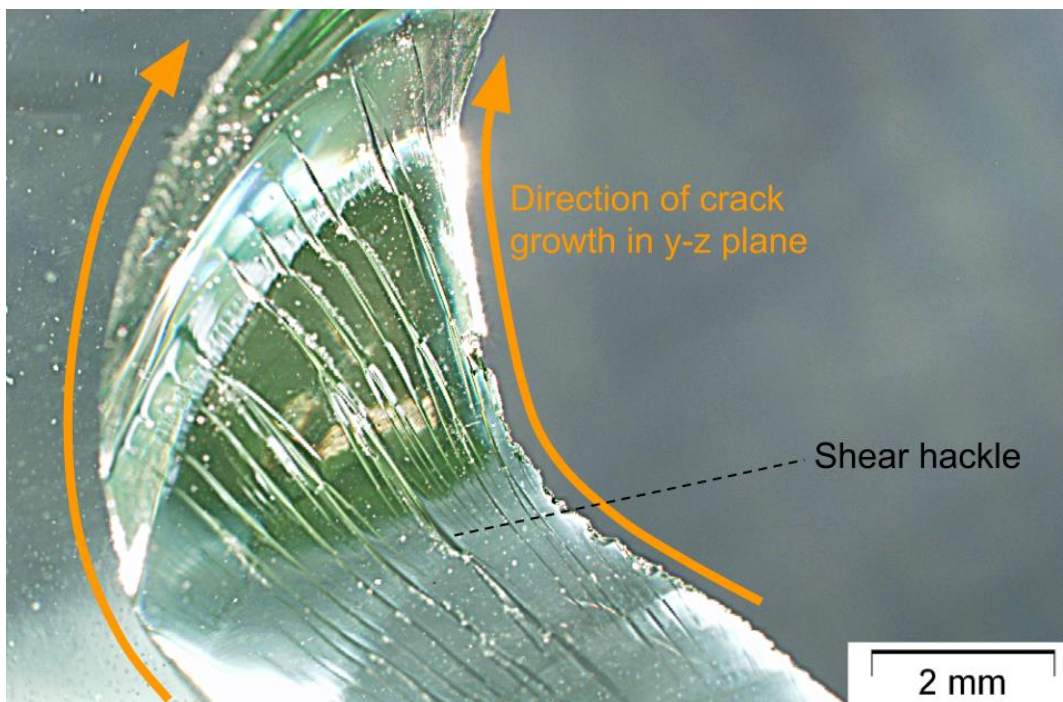


Figure 2.17 – Example of shear hackle on an annealed glass fragment. Due to a change in orientation of the crack growth direction in the  $y$ - $z$  plane.

### 2.5.3.3 Wallner lines

Wallner lines are smooth, curved lines on a fracture surface caused by elastic pulses interacting with the propagating crack front. They can be used to infer the direction of crack propagation, determine the shape of the propagating crack front, and calculate the crack velocity. Wallner lines are categorised according to the source of the elastic pulse that

interacted with the crack front. This section considers so-called primary, secondary, and tertiary Wallner lines, after Wallner [59] and Fréchette [55]. In all cases, the Wallner line is the locus of the intersection of the propagating crack front and the elastic pulse that triggered the line marking [55]. Unlike hackle which is sharp and jagged, Wallner lines are smooth and undular.

**Primary Wallner lines** are created when the propagating crack front encounters a pre-existing flaw in the glass article, which is usually at a surface. Figure 2.18 shows an example.

**Secondary Wallner lines** are created by the propagating crack front encountering a fracture surface feature created by the crack front itself. Secondary Wallner lines typically accompany mist hackle markings as shown in Figure 2.15.

**Tertiary Wallner lines** are created by external elastic pulses, usually created by additional impact or vibration during fracture. Figure 2.19 shows an example.

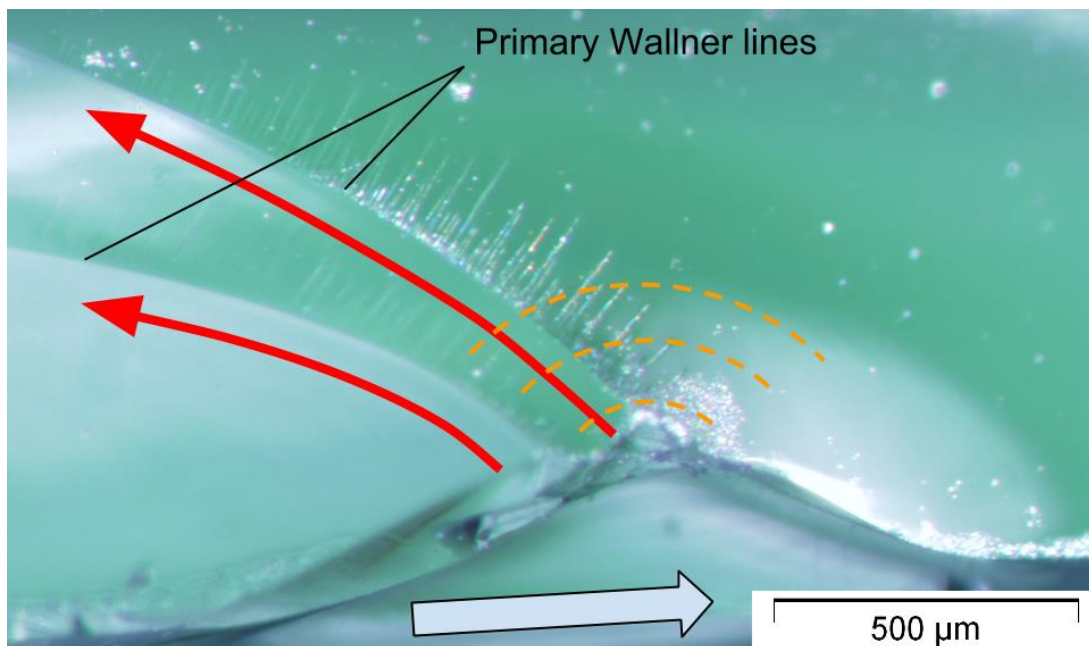


**Figure 2.18 – Two Primary Wallner lines formed on the fracture surface of an annealed glass fragment due to a surface flaw. The elastic pulse created by the propagating crack front encountering the flaw is illustrated with the orange dashed lines. The blue arrow shows the main direction of crack propagation.**

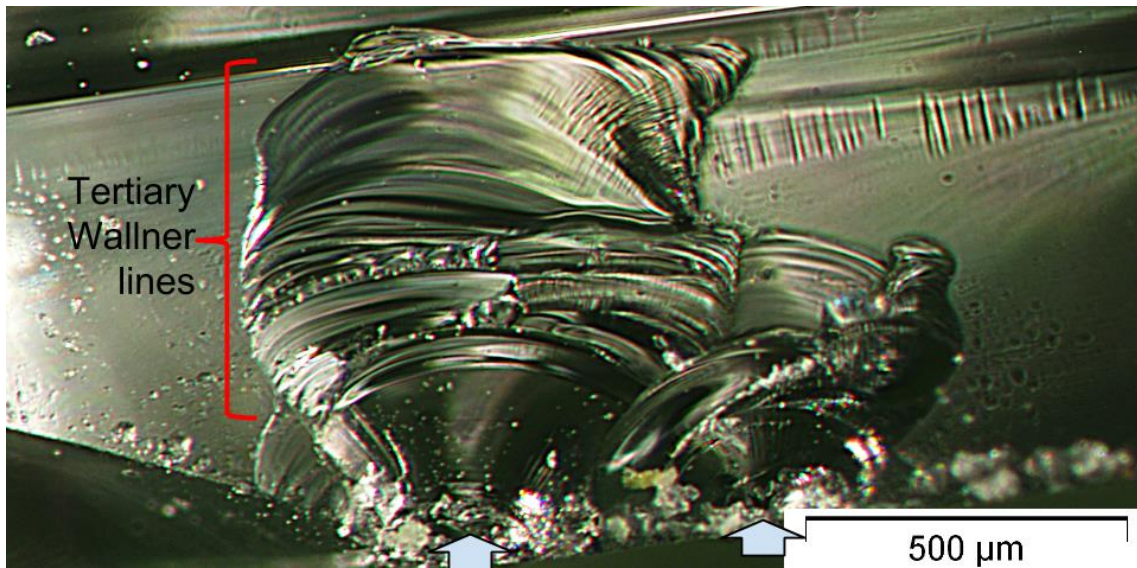
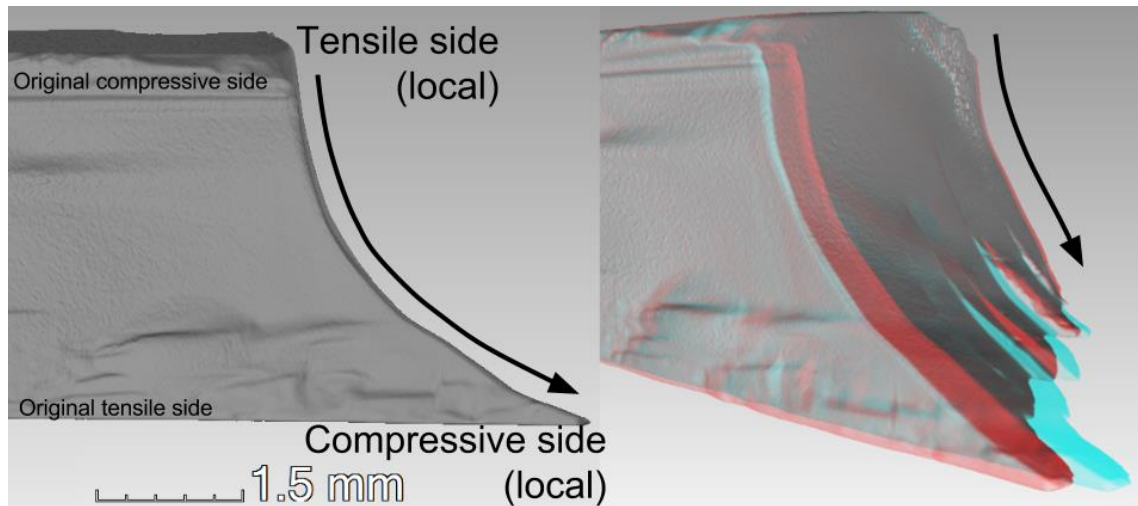


Figure 2.19 – Examples of tertiary Wallner lines caused by external vibrations/impact. Blue arrows show the elastic pulse direction.

#### 2.5.4 Cantilever curl

When glass is subjected to flexure, one surface is primarily subjected to tensile stresses (tensile surface), and the opposing surface is primarily subjected to compressive stresses (compressive surface). A crack running from the tensile surface towards the compressive surface may be diverted by the compressive stress at the compressive surface. This typically results in a gradual curve in the crack propagation direction, which causes the crack to intersect the compressive surface at an oblique angle. This effect is known as cantilever curl [54].

Figure 2.20 shows a micro-computed tomography image of an example of cantilever curl on a glass fragment. In this case the cantilever curl was caused by a contact stress, which was a secondary effect of the main flexure loading. The initial fracture of the glass article originated on the tensile side, and the crack front continued to lead on that side. However, local tensile stress was created on the compressive side due to contact with the flexure loading fixture. This was sufficient to fulfil the condition of  $K_I = K_{Ic}$ . Consequently, cantilever curl occurred, which propagated from what was originally the compressive side. This effect is common in glass articles fractured by impact [60].



**Figure 2.20** (red-cyan glasses required for right image) – Micro-CT images of an annealed glass fragment showing effects of cantilever curl due to flexure by secondary contact stress. Left image shows the direction of crack development from the area of tensile stress to the area of compressive stress. Right image shows an anaglyph of the same sample at a rotated angle.

This section has overviewed fractographic axes in order to assist with the description of fractographic features. Typical fractographic features of annealed and thermally tempered SLS glass were then framed in terms of these axes. Specifically, characteristic macroscopic fracture patterns ( $y$ - $z$  plane), and common fracture surface markings ( $x$ - $y$  plane) were introduced. Additionally, cantilever curl, a common brittle fracture feature encountered by loading in flexure, was introduced.

## 2.6 Current standards for thermally tempered glass products

This section reviews current standards for thermally tempered glass products. Adaptations of some of the assessment methods discussed here are used in later chapters.

There are no accredited standards that prescribe the necessary breakage criteria for tempered pint glasses. However, for annealed glass containers (such as bottles or jars) standard methods exist for testing and assessing the following: the quality of annealing [61]; the performance under thermal shock [62]; and the performance under an internally applied pressure [63]. Additionally, guidelines exist for the sampling of glass containers for performance testing [64]. No standards could be found concerning performance of glass drinking vessels under impact after a review of accredited standards.

Several standards exist for thermally tempered float glass, which evaluate performance criteria based on considerations of human safety [47], [65]–[67]. British Standard 12150 includes a punch test assessment procedure to appraise the acceptability of the fragmentation density. Punch tests introduce a flaw into a glass test piece whilst imposing minimal external stresses,

so as to induce spontaneous fracture in tempered glass. The fragmentation density is usually related to the level of residual stress in an article.

The British Standard punch test assessment procedure specifies that a flat glass pane must be laid flat on a table to avoid bending stresses, and the punch location must be 13 mm inward from the longest edge. The fragmentation is assessed by a fragment count within a 50 mm x 50 mm square area suitably far from the pane edges and punch location (included zone). This is demonstrated in Figure 2.21. The fragment count must be no less than 15 for 3 mm thick glass, and no less than 40 for glass of thickness 4 – 12 mm. Additionally, the length of the largest fragment in the entirety of the included zone must be less than 100 mm.

Safety standards for thermally tempered automobile glazing also include punch tests [68], [69]. The British Standard 857 uses a similar procedure as that outlined above and in Figure 2.21. The ANSI Z26.1 standard specifies that the weight of any fragment from the punch test must not exceed 4.25 g.

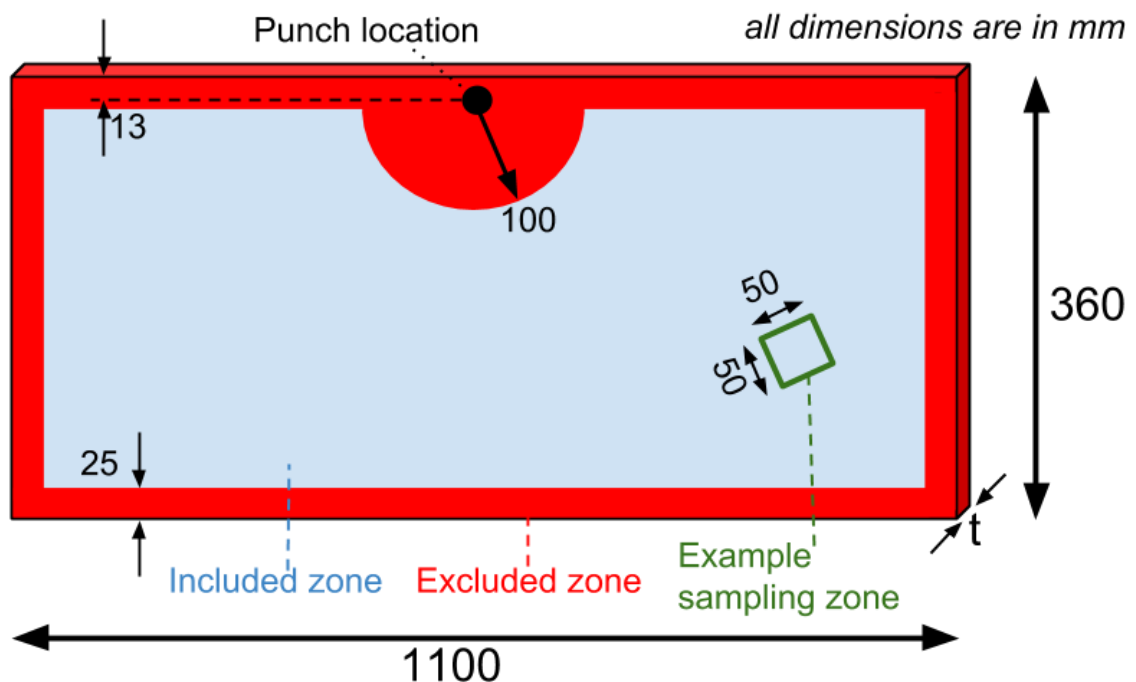


**Figure 2.21** – Illustration of the sample dimensions (not to scale), punch location, and area for appraisal for the fragmentation assessment detailed in British Standard 12150. *t*: thickness.

The performance of thermally tempered float glass under impact is considered in British Standard 12600, and similar tests are detailed in ANSI Standard Z97.1. The glass is impacted using a pendulum method with an impactor incorporating two tyres. Three set drop heights are used consecutively unless fracture occurs. The test specifies that the glass pane must not break, or otherwise break safely. Safe breakage is assessed by weighing the 10 largest crack-

free fragments within 5 minutes of the fracture event. The combined weight must not be greater than the weight of the same glass pane with a face surface area of 6500 mm<sup>2</sup>.

The ASTM C1048 standard specifies that a fully-toughened tempered glass sheet should have a surface compressive stress of no less than 72 MPa. Glass with a compressive surface stress of 24-52 MPa is termed in this standard as heat-strengthened glass. Such glass has a higher tensile failure strength than annealed glass without the full dicing properties of fully-toughened glass. The standard specifies that the compressive surface stress should be measured photoelastically at five set locations across the largest face of the glass sheet.

This sub-section has reviewed standards for thermally tempered glass for safety purposes for products other than glass drinking vessels, and also addressed current standards for glass containers.

## **2.7 Chapter summary**

This chapter has reviewed relevant literature and provided a scientific background to: the composition and production of SLS glass; the flaw-dependent properties of glass strength; the development of, and photoelastic measurement of, residual stresses in glass; macroscopic fracture patterns of broken glass articles; fracture surface markings on glass fragments; and existing standards for thermally tempered glass products. The content of further chapters in this thesis draws on this background, and explores how residual stresses and fracture properties of glass contribute to injury potential.

## 2.8 Chapter references

- [1] “BS EN 572-1:2012 - Glass in Building. Basic Soda Lime Silicate Glass Products. Definitions and General Physical and Mechanical Properties,” *British Standards Institute, UK*, 2012.
- [2] J. E. Shelby, “Glass Melting,” in *Introduction to Glass Science and Technology*, 2nd Edition, The Royal Society of Chemistry, 2009, pp. 26–48.
- [3] “About Glass,” in *Making Glass*, 4th Edition, British Glass Manufacturers Confederation, 2007, pp. 19–40.
- [4] W. H. Zachariasen, “The Atomic Arrangement in Glass,” *Journal of the American Chemical Society*, vol. 54, no. 10, pp. 3841–3851, 1932.
- [5] N. Reid, “Ceramics and Glasses,” in *Materials in Action Series: Structural Materials*, G. Weidmann, P. R. Lewis, J. Briggs, and C. Doyle, Eds. Milton Keynes, U.K. London ; Boston: Materials Dept. Butterworths, 1990, pp. 168–209.
- [6] B. E. Warren, “Summary of Work on Atomic Arrangement in Glass,” *Journal of the American Ceramic Society*, vol. 24, no. 8, pp. 256–261, 1941.
- [7] J. E. Shelby, “Structures of Glasses,” in *Introduction to Glass Science and Technology*, 2nd Edition, The Royal Society of Chemistry, 2009, pp. 72–110.
- [8] J. E. Shelby, “Viscosity of Glass Forming Melts,” in *Introduction to Glass Science and Technology*, 2nd Edition, The Royal Society of Chemistry, 2009, pp. 111–135.
- [9] J. E. Shelby, “Density and Thermal Expansion,” in *Introduction to Glass Science and Technology*, 2nd Edition, The Royal Society of Chemistry, 2009, pp. 138–161.
- [10] ASTM C162-05(2010), Standard Terminology of Glass and Glass Products, ASTM International, West Conshohocken, PA, 2005, [www.astm.org](http://www.astm.org).
- [11] A. Napolitano and E. G. Hawkins, “Viscosity of a Standard Soda-Lime-Silica Glass,” *Journal of Research of the National Bureau of Standards - A. Physics and Chemistry*, vol. 68A, no. 5, pp. 439–448, 1964.
- [12] “The Glass Forming Processes,” in *Making Glass*, 4th Edition, British Glass Manufacturers Confederation, 2007, pp. 33–57.
- [13] M. Cable, “The Mechanisation of Glass Container Production,” *Transactions of the Newcomen Society*, vol. 73, pp. 1–31, 2001.
- [14] H. Griffel, “Lightweighting in the Glass Container Industry,” in *47th Conference on Glass Problems: Ceramic Engineering and Science Proceedings, Volume 8, Issue 3/4*, 1987, pp. 156–170.
- [15] W. J. Zitkus, “Technical Review of the Automated Soda Lime Tableware Industry,” in *Proc XVIII ICG San Francisco, USA*, 1998, pp. 15–26.

- [16] R. C. Bradt, "The Fractography and Crack Patterns of Broken Glass," *Journal of Failure Analysis and Prevention*, vol. 11, pp. 79–96, 2011.
- [17] V. D. Fréchette, "Initiation and Development of Brittle Failure," in *Advances in Ceramics: Failure Analysis of Brittle Materials*, 1990, pp. 3–6.
- [18] B. R. Lawn and T. R. Wilshaw, *Fracture of Brittle Solids*, 1st Edition, London: Cambridge University Press, 1975.
- [19] C. R. Kurkjian, "Mechanical Strength of Glasses—Studies Then and Now," *The Glass Researcher*, vol. 11, no. 2, pp. 1–6, 2002.
- [20] A. A. Griffith, "The Phenomena of Rupture and Flow in Solids," *Philosophical Transactions of the Royal Society A: Mathematical, Physical and Engineering Sciences*, vol. 221, no. 582–593, pp. 163–198, Jan. 1921.
- [21] J. R. Calvert and R. A. Farrar, "Properties of Materials," in *An Engineering Data Book*, 1999, pp. 7–1, 7–2.
- [22] J. E. Shelby, "Mechanical Properties," in *Introduction to Glass Science and Technology*, 2nd Edition, The Royal Society of Chemistry, 2009, pp. 188–200.
- [23] E. Orowan, "Mechanical Strength Properties and Real Structure of Crystals," *Zeitschrift für Kristallographie*, vol. 89, no. 3/4, pp. 327–343, 1934.
- [24] C. R. Kurkjian, P. K. Gupta, R. K. Brow, and N. Lower, "The Intrinsic Strength and Fatigue of Oxide Glasses," *Journal of Non-Crystalline Solids*, vol. 316, pp. 114–124, 2003.
- [25] R. J. Hand and A. B. Seddon, "An Hypothesis on the Nature of Griffith's Cracks in Alkali Silicate and Silica Glasses," *Physics and Chemistry of Glasses*, vol. 38, no. 1, pp. 11–14, 1997.
- [26] "Information for Publicans and Bar Staff," *21st Century Pint - Best Practice Guidelines*, Institute of Materials Minerals and Mining, Materials Knowledge Transfer Network, 2012. [Online]. Available: <http://21stcenturypint.org/information-publicans-and-bar-staff>. [Accessed: 21-Apr-2015].
- [27] H. C. Chandan, R. C. Bradt, and G. E. Rindone, "Dynamic Fatigue of Float Glass," *Journal of the American Ceramic Society*, vol. 61, no. 5–6, pp. 207–210, 1978.
- [28] P. J. Withers and H. K. D. H. Bhadeshia, "Residual Stress. Part 1—Measurement Techniques," *Materials Science and Technology*, vol. 17, no. 4, pp. 355–365, 2001.
- [29] R. F. Bartholomew and H. M. Garfinkel, "Chemical Tempering of Glass," in *Glass: Science and technology, Volume 5, Elasticity and Strength in Glasses*, D. R. Uhlmann and N. J. Kreidl, Eds. Academic Press, New York, 1980, pp. 218–267.
- [30] R. Gy, "Ion Exchange for Glass Strengthening," *Materials Science and Engineering: B*, vol. 149, no. 2, pp. 159–165, Mar. 2008.

- [31] J. S. Olcott, "Chemical Strengthening of Glass," *Science*, vol. 140, no. iv, pp. 1189–1193, 1963.
- [32] A. S. Redner, E. Mognato, and M. Schiavonato, "Correlation Between Strength and Measured Residual Stress in Tempered Glass Products," *Journal of ASTM International*, vol. 2, no. 3, 2005.
- [33] R. Gardon, "Thermal Tempering of Glass," in *Glass: Science and technology, Volume 5, Elasticity and Strength in Glasses*, D. R. Uhlmann and N. J. Kreidl, Eds. Academic Press, New York, 1980, pp. 145–216.
- [34] L. H. Adams and E. D. Williamson, "The Annealing of Glass," *Journal of the Franklin Institute*, vol. 190, no. 6, pp. 835–870, 1920.
- [35] R. Gardon and O. S. NarayanaSwamy, "Stress and Volume Relaxation in Annealing Flat Glass," *Journal of the American Ceramic Society*, vol. 53, no. 7, pp. 380–385, 1970.
- [36] O. S. NarayanaSwamy, "Stress and Structural Relaxation in Tempering Glass," *Journal of the American Ceramic Society*, vol. 61, no. 3–4, pp. 146–152, 1978.
- [37] L. Daudeville and H. Carre, "Thermal Tempering Simulation of Glass Plates: Inner and Edge Residual Stresses," *Journal of Thermal Stresses*, vol. 21, pp. 667–689, 1998.
- [38] J. H. Nielsen, J. F. Olesen, P. N. Poulsen, and H. Stang, "Finite Element Implementation of a Glass Tempering Model in Three Dimensions," *Computers & Structures*, vol. 88, pp. 963–972, Sep. 2010.
- [39] A. Aronen, "Modelling of Deformations and Stresses in Glass Tempering," Tampereen Teknillinen Yliopisto, Julkaisu-Tampere University of Technology, 2012.
- [40] H. Aben and C. Guillemet, "Membrane Stresses," in *Photoelasticity of Glass*, Berlin: Springer-Verlag, 1993, pp. 130–138.
- [41] D. Brewster, "On the Communication of the Structure of Doubly Refracting Crystals to Glass, Muriate of Soda, Fluor Spar, and Other Substances, by Mechanical Compression and Dilation," *Philosophical transactions of the Royal Society of London*, vol. 106, pp. 156–178, 1816.
- [42] F. W. Preston, "The Use of Polariscopes in the Glass Industry," *Journal of the American Ceramic Society*, vol. 13, no. 9, pp. 595–623, 1930.
- [43] H. W. McKenzie and R. J. Hand, *Basic Optical Stress Measurement in Glass*. Society of Glass Technology Sheffield, 2011.
- [44] H. Aben and C. Guillemet, "Basic Photoelasticity," in *Photoelasticity of Glass*, Berlin: Springer-Verlag, 1993, pp. 51–68.
- [45] G. D. Quinn, "Fracture Surface Examination," in *Fractography of Ceramics and Glasses*, National Institute of Standards and Technology, 2007, pp. 5–1 – 5–78.

- [46] F. W. Preston, "The Angle of Forking of Glass Cracks as an Indicator of the Stress System," *Journal of the American Ceramic Society*, vol. 18, no. 1–12, pp. 175–176, 1935.
- [47] "BS EN 12150-1:2000 - Glass in Building. Thermally Toughened Soda Lime Silicate Safety Glass. Definition and Description," *British Standards Institute, UK*, 2000.
- [48] R. Gardon, "Tempering Glass with Modulated Cooling Schedules," *Journal of the American Ceramic Society*, vol. 71, no. 10, pp. 875–878, 1988.
- [49] P. D. Warren, "Fragmentation of Thermally Strengthened Glass," *Ceramic Transactions*, vol. 122, pp. 389–400, 2001.
- [50] R. Tandon and S. Jill Glass, "Fracture Initiation and Fragmentation in Chemically Tempered Glass," *Journal of the European Ceramic Society*, vol. 35, pp. 285–295, Jan. 2015.
- [51] D. Hull, "Influence of Stress Intensity and Crack Speed on Fracture Surface Topography: Mirror to Mist to Macroscopic Bifurcation," *Journal of Materials Science*, vol. 31, no. 17, pp. 4483–4492, 1996.
- [52] L. Orr, "Practical Analysis of Fractures in Glass Windows," *Materials Research and Standards*, vol. 12, no. 1, pp. 21–23, 1972.
- [53] J. J. Mecholsky, "Quantitative Fractographic Analysis of Fracture Origins in Glass," in *Fractography of Glass*, R. C. Bradt and R. E. Tressler, Eds. New York: Plenum Press, 1994, pp. 37–173.
- [54] ASTM C1256-93(2013), Standard Practice for Interpreting Glass Fracture Surface Features, ASTM International, West Conshohocken, PA, 2013, [www.astm.org](http://www.astm.org).
- [55] V. D. Fréchette, "The Fundamental Markings on Crack Surfaces," in *Advances in Ceramics: Failure Analysis of Brittle Materials*, Westerville, Ohio: American Ceramic Society, 1990, pp. 7–29.
- [56] E. K. Beauchamp, "Mechanisms For Hackle Formation and Crack Branching," in *Ceramic Transactions: Fractography of Glasses and Ceramics III. Volume 64*, vol. 64, J. R. Varner, V. D. Fréchette, and G. D. Quinn, Eds. 1996, pp. 409–445.
- [57] D. Hull, "Mirror, Mist and Hackle: Surface Roughness, Crack Velocity and Dynamic Stress Intensity," in *Fractography: Observing, Measuring, and Interpreting Fracture Surface Topography*, Cambridge: Cambridge University Press, 1999, pp. 121 – 155.
- [58] D. Hull, "River Line Patterns," in *Fractography: Observing, Measuring, and Interpreting Fracture Surface Topography*, Cambridge: Cambridge University Press, 1999, pp. 91–119.
- [59] H. Wallner, "Linienstrukturen an Bruchflächen (Line Structures on Fracture Surfaces)," *Zeitschrift für Physik*, vol. 114, no. 5–6, pp. 368–378, 1939.

- [60] V. D. Fréchette, "Common Conditions of Failure," in *Advances in Ceramics: Failure Analysis of Brittle Materials*, no. 28, Westerville, Ohio: American Ceramic Society, 1990, pp. 100–109.
- [61] ASTM C148-14, Standard Test Methods for Polariscopic Examination of Glass Containers, ASTM International, West Conshohocken, PA, 2014, [www.astm.org](http://www.astm.org).
- [62] ASTM C149-86(2010), Standard Test Method for Thermal Shock Resistance of Glass Containers, ASTM International, West Conshohocken, PA, 2010, [www.astm.org](http://www.astm.org).
- [63] ASTM C147-86(2010), Standard Test Methods for Internal Pressure Strength of Glass Containers, ASTM International, West Conshohocken, PA, 2010, [www.astm.org](http://www.astm.org).
- [64] ASTM C224-78(2014), Standard Practice for Sampling Glass Containers, ASTM International, West Conshohocken, PA, 2014, [www.astm.org](http://www.astm.org).
- [65] BS EN 12600:2002 - Glass in Building. Pendulum Test. Impact Test Method and Classification for Flat Glass," *British Standards Institute, UK*, 2003.
- [66] ASTM C1048-12e1, Standard Specification for Heat-Strengthened and Fully Tempered Flat Glass, ASTM International, West Conshohocken, PA, 2012, [www.astm.org](http://www.astm.org).
- [67] ANSI Z97.1-2009, Safety Glazing Materials Used in Buildings - Safety Performance Specifications and Methods of Test, Accredited Standards Committee (ASC) Z97; 800 SW Jackson St. Suite 1500, Topeka, KS 66612-1200.
- [68] "BS 857:1967 Specification for Safety Glass for Land Transport," *British Standards Institute, UK*, 1967.
- [69] ANSI/SAE Z26.1–2007, American National Standard for Safety Glazing Materials for Glazing Motor Vehicles and Motor Vehicle Equipment Operating on Land Highways - Safety Code, American National Standards Institute/Society of Automotive Engineers.

### 3 Glass preparation and fracture methodologies

#### 3.1 Introduction

The work detailed in this thesis involved the fracture of flat glass samples (rectangular and circular in shape) and glass drinking vessels as a means to assess both general fracture characteristics, and those pertaining to potential for injury. The fracture of glass is a dynamic and sensitive process dependent on a large number of variables. Careful procedures are therefore necessary for all sample production processes prior to breakage in order to produce comparable fractured samples. However, control of initial glass production processes (including batch mixing, melting, refining and forming) was beyond the scope of this study.

This chapter details all the steps taken to produce comparable fractured glass samples after the initial production stage, followed by some aspects of post-breakage analysis. These steps include:

- Sample cutting.
- Processing (e.g. annealing, tempering).
- Residual stress assessment (qualitative and quantitative).
- Pre-damaging (abrasion, indentation).
- Sample loading to fracture (by impact, ring-on-ring loading, three point bending).
- Fractographic assessment (macroscopic fracture pattern analysis, origin analysis).

These steps can be considered as preparatory steps taken to produce glass fragments.

A further analysis step for some fragments involved assessing injury potential by consideration of sharpness. However, this is a complex issue and instead merits separate discussion in chapter 6. This chapter follows the order of methodology conducted prior to sharpness assessment, starting with the glass sample type and dimensions. This order is followed in later chapters.

#### 3.2 Glass samples

The following section details the dimensions of the three types of glass sample used in experimentation. These were rectangular flat samples, flat disc samples, and drinking vessels. The former two were cut manually and the latter was procured externally.

### 3.2.1 Flat glass samples

Rectangular glass samples of dimensions 38 x 25 x 4 mm were cut from a sheet of annealed soda-lime-silica glass using a glass cutter with a tungsten carbide tip (Toyo TC10 Oil Glass Cutter, Toyo Glass Co. Ltd., Japan). The surface was scored using a straight edge as a guide, before suitable pressure was applied by hand to enable the glass to break along the score line. The edges of the sample were then ground using a 180 grit diamond polishing disc. The grinding procedure involved first smoothing over the four surfaces with 4 mm width, and then chamfering each edge. Figure 3.1 shows an example edge finish. This process removed particularly large flaws and sharp features created at the edges during cutting. Such an edge finish is termed as “arrissed” according to British Standard 12150 [1].

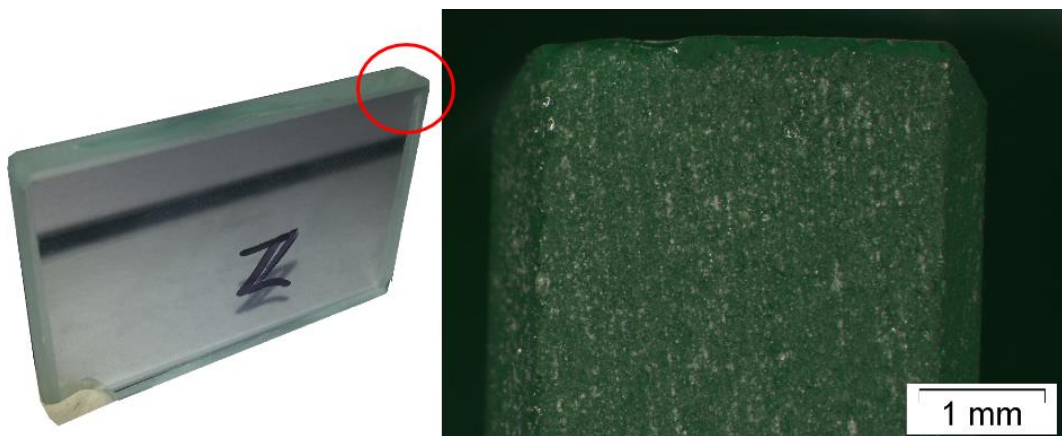


**Figure 3.1 – Example of arrissed edge finish for glass samples. Left: 4mm thick rectangular sample used in experimentation. Right: edge and surface finish of red circled portion.**

Additionally, glass disc samples of 75 mm diameter were cut from 4 mm thick annealed soda-lime-silica glass sheets using a manual circular cutter with a tungsten carbide cutting wheel (65 – 300 mm Circular Glass Cutter, Silverline Tools, UK). The disc edges were polished by a similar process to that outlined in the above paragraph to create an arrissed edge finish. All glass discs were polished using a wet belt sander (Covington 761 Deluxe Commercial Wet Belt Sander, His Glassworks, USA) with a 100 grit silicon carbide belt.

Although the tin-side of each sample was not explicitly identified, the face of each sample relative to the original float glass sheet was noted. This enabled testing processes to be conducted on the same side for each sample relative to the original glass sheet, for the purpose of consistency.

### 3.2.2 Drinking vessels

All glass drinking vessels in this study were obtained new from external suppliers. Of particular interest to this study were two of the most common pint glass shapes, the Nonic and the Tulip,

and also pint glasses developed in response to the 2010 Design Out Crime campaign [2]: the Perfect Pint (Utopia Tableware Ltd., Chesterfield, UK) and the Ultimate Pint (Arc International, Arques, France) (see Figure 3.2). All pint glasses in this study were imperial pint glasses (20 fl. oz., or 568 ml in volume). Additionally, a number of glasses, that were deemed unfit for further use, were donated by pubs and hotels. A discussion of the surface condition of a selection of these glasses included in Appendix D.

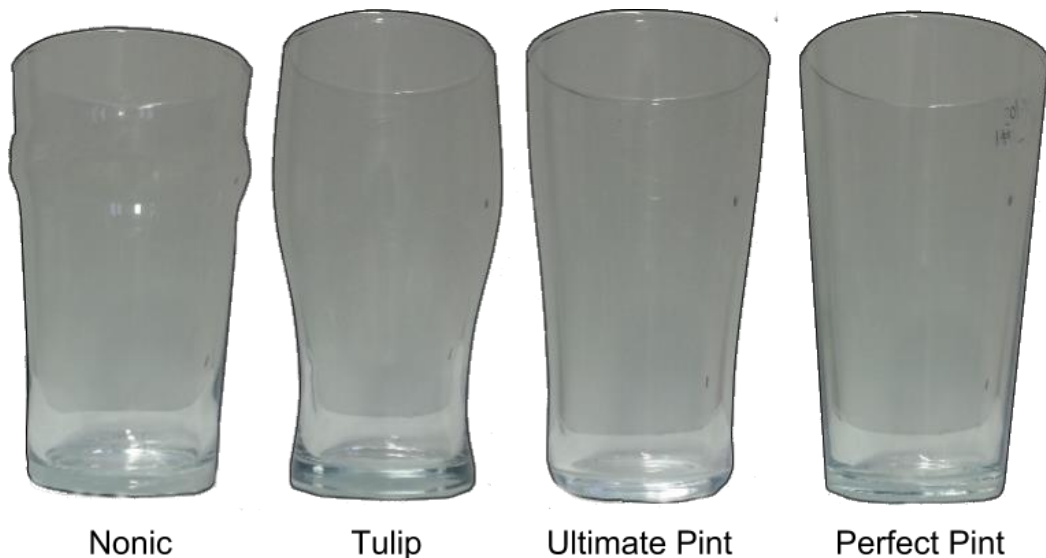


Figure 3.2 – Pint glasses of particular interest to this study.

### 3.3 Tempering and annealing

This section discusses tempering and annealing processes conducted for the glass samples used in experimentation in this study. A custom-built apparatus was designed and developed specifically for the thermal tempering of samples for this study. The parameters selected for tempering are discussed with reference to related available literature, followed by a description of the apparatus and procedures for use. Finally, externally tempered discs used in this study are detailed, as well as annealing procedures conducted on pint glasses. This section is not intended to be an introduction to the thermal tempering process, which is instead covered in chapter 2.

#### 3.3.1 Thermal tempering of glass disc samples with custom-built apparatus

This section overviews the design and procedure of a custom-built apparatus used for the thermal tempering of glass samples in this thesis. It consists of two parts: Firstly, important process parameters for the thermal tempering of glass are discussed, particularly with reference to how these affected the design of the custom-built tempering apparatus. Secondly, the design and operating procedure of the apparatus is detailed. The apparatus

enabled customised control over thermal tempering operations for flat glass rectangular samples and flat glass discs. The level of internal temper was controlled by varying the initial temperature of the glass and the air velocity of impinging jets, and different jet setups were used for each sample type. This enabled investigations into the effect of thermal tempering processes on the sharpness of glass when broken. Glass samples tempered using this rig feature in chapters 7 and 8.

### **3.3.1.1 Process parameters and practical considerations for thermal tempering**

This sub-section reviews important experimental parameters involved in the thermal tempering of glass, and some previous thermal tempering apparatuses. There are very few published studies detailing routine laboratory testing for glass thermal tempering. Table 3.1 presents a summary of relevant experimental details and parameters for four such studies, and for those used in this study for comparison. This sub-section offers a commentary on this table.

**Quench medium:** The most common quenching medium for the thermal tempering of glass is air, due to the low costs involved and the high heat transfer rates that can be achieved in impinging jet configurations [3]. As such, air is used as the quench medium in this study. Higher heat transfer rates can be obtained with the inclusion of water mist into the air, as investigated by Sözbir and Yao [4]. They found the air pressure could be halved for 3 mm and 4 mm thick glass to produce glass of the same temper level, due to the higher heat transfer rate involved with this medium. However, this was accompanied by an increased risk of fracture during cooling because higher transient thermal tensile stresses were imposed on the glass surface. Therefore only air was used for this project.

**Sample dimensions:** The sample dimensions are important because the thickness of the glass determines the maximum attainable through-thickness stress [5]. Additionally, the sample dimensions have an effect on membrane stresses, especially near the edges [6]. The studies included in Table 3.1 used either square- or rectangular-shaped samples with thicknesses ranging from 2.1 to 6 mm. One of the two cooling configurations used in this study involved disc samples to reduce the effect of membrane stresses near corners. A thickness of 4 mm was chosen due to both the availability of 4 mm sheet glass, and that it is similar to mid-wall thickness values for pint glasses (chapter 5). The other cooling configuration used small rectangular-shaped samples which allowed for a simpler jet setup.

Study	Quench medium	Sample dimensions (length x width x thickness) /mm	Sample support method	Transfer method	T <sub>init</sub> /°C	Jet type	Air velocity /ms <sup>-1</sup>	Jet-to-sample distances /mm	HTC \Wm <sup>-2</sup> K
Gardon, 1965 [5]	Air	100x25x6	Held vertically in cage	Vertical transfer by hydraulic ram from tube furnace	640-700	Slot jets	unspecified	100	13-553
Roméro et al., 2001 [7]	Air	200x200x6	Held vertically at bottom of sample	Vertical transfer by collapsible furnace floor	680	Circular jets (hairdryers)	13.5	100	98
Sözbir and Yao, 2004 [4]	Air and water mist	25x25 and 63.5x88.9 for thicknesses 2.1, 2.85, 3.2 and 4	Suspended from top of sample	Horizontal transfer by overhead rail	Glass slid inside oven preheated to 740, soaked for 5 minutes	1. Single jet 2. Array of 7 nozzles	40-90	40	13-2000+
Koike et al., 2012 [8]	Air	100x100x3	Suspended from top of sample	Horizontal transfer by overhead rail	690 soak temperature, 650 at the onset of cooling	Air blast head	unspecified	unspecified	500
Present study	Air	1. 38x25x4 2. Discs of 75 mm diameter, 4 mm thick	Held vertically by steel wire loops	Horizontal transfer by motorised furnace door	620-660 (before transfer)	1. Multi-channel flat fan nozzles 2. 2 arrays of 4 jets	1. 28 – 37 (impinging velocity) 2. 20 – 40 (exit velocity)	1. 85 2. 30-180	N/A

Table 3.1 – Experimental details and parameters for studies using thermal tempering apparatus.

**Sample support method:** The sample support method can affect both the distribution of the heat transfer coefficient by impeding airflow to the sample surface, and can also result in deformation of the glass sample. For example, vertically-tempered flat glass is associated with surface depressions ~20 mm from the edge due to suspension of the glass from tongs [1]. Likewise, prolonged time on rollers during horizontal tempering causes wave-like distortion in the glass [9]. Each of the four studies in Table 3.1 involves vertical tempering. None mention the occurrence of sample distortion due to the sample supporting method. This study used loops of stainless steel wire to hold the rectangular and disc samples, as overviewed in the following section. This was designed to minimise contact with the disc, and maximise surface area exposed to the airflow.

**Transfer method:** This refers to how the glass was transferred from the heating apparatus to the cooling apparatus. An ineffective transfer method may involve erratic movement of the glass sample. This can result in a lower initial temperature than desired, or premature forced convection cooling prior to the actual cooling operation. Koike et al. specify that the glass sample temperature dropped from 690 °C in the heating furnace to 650 °C at the onset of cooling [8]. Gardon [5] does not mention premature cooling effects due to the transfer method, although by measuring the sample temperature by pyrometer after the transfer, his results take this into account. For the studies included in Table 3.1, the transfer involved either horizontal or vertical translation to the cooling apparatus. The transfer method used in this study utilised motorised removable furnace doors, as overviewed in the following sub-section. The transfer to the cooling apparatus was automated to improve reproducibility.

**Initial temperature ( $T_{init}$ ):** This is the uniform temperature of the glass sample at the onset of cooling. In practice, this is likely to vary throughout the body of the sample, and to be lower than the sample temperature obtained in the heating apparatus, due to premature cooling during the transfer to cooling apparatus. Low initial temperatures can result in fracture during cooling by the development of high transient tensile thermal stresses at the surface [5]. High initial temperatures can result in sample deformation, due to the decreased viscosity of the glass.

In this study, only the initial temperature prior to transfer to the cooling apparatus was measured, referred to here as the soak temperature. This was varied between 620 – 660 °C depending upon the cooling configuration, and was measured using a thermocouple placed 5 mm laterally from the centre of each sample. A short investigation into the surface temperature drop was undertaken, which involved placing a thermocouple in contact with the

glass sample. It was found that for a soak temperature of 660 °C, the surface temperature dropped to approximately 628 °C by the time the cooling jets were switched on (door removal to cooling onset times were ~ 3 s). Disc samples were not raised above soak temperatures of 660 °C as higher temperatures were found to result in considerable sample deformation prior to cooling. Soak temperatures less than 620 °C resulted in failure during cooling, or low residual stress levels.

**Jet types:** It can be seen that the studies included in Table 3.1 use a range of jet types. The effect of jet type is discussed in the following sub-section. The apparatus used in this study included arrays of jets to cool glass discs, and multi-channel flat fan nozzles to cool rectangular glass samples. Industrial installations typically involve lateral oscillation of air jets to improve the heat transfer coefficient distribution (see next paragraph) over surface [10], although this was beyond the scope of this study.

**Heat transfer coefficient (h):** This is considered as the combination of the effects of all parameters involved with cooling. It is commonly quoted as the average value over a sample surface [3], and it is useful for predicting the magnitude and distribution of thermally-induced residual stresses. Since the stresses for all samples in this study were evaluated empirically using photoelastic methods, calculations of the heat transfer coefficient were not considered important and were not conducted.

This sub-section has reviewed a range of important parameters involved with the thermal tempering of glass. Apparatuses and test parameters used in other studies have been considered and compared to the apparatus and test parameters used in this study.

### **3.3.1.2 Thermal tempering apparatus and procedure**

This sub-section details the apparatus and procedure used for thermal tempering in this study, which follows from the discussion in the previous sub-section.

The thermal tempering apparatus used in this study used four chamber furnaces (BMF11/7 Economy Chamber Furnace, Elite Furnace Systems Ltd, Leicestershire, UK) simultaneously to heat glass samples. The furnace doors were replaced with customised doors that could be attached to a trolley containing the cooling apparatus. In order to insulate the furnace chamber from the surroundings, a vacuum-formed alumina/silica insulating block (ALTRA KVS 121, Rath USA Inc., Newark, USA) was attached to the furnace doors. Mullite ceramic rods protruded from the doors and served as supports for fixtures to hold glass samples during the heating and cooling processes.

Glass discs were held by two lengths of stainless steel 316L wire of 1 mm nominal diameter, which was bent by hand (Figure 3.3a). The discs slotted into the loops made by the bent wire, which stayed upright by ensuring that the wire fitted tightly onto the ceramic rods. The maximum sample size in this setup was 80 mm diameter, necessitated by the size of the furnace chamber.

Rectangular glass samples were held by two smaller bent lengths of the same wire, which were attached to a centrally-slotted steel plate (Figure 3.3b). The steel plate had grooves on its bottom face so it could sit on the ceramic rods without moving. The wires were bent such that a rectangular sample could be held between the two, with the surfaces perpendicular to the air impingement direction fully exposed. The gripping force to the sample could be adjusted by bending the top wire which acted as a spring. The optimal gripping force that reliably held the sample without it falling, and yet did not result in any significant deformation at the soak temperature of 660 °C, was determined by trial and error.

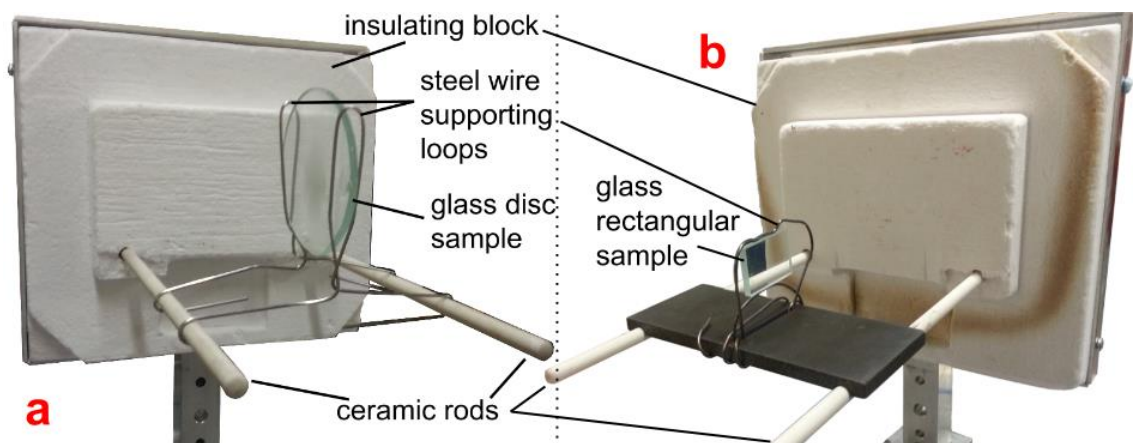


**Figure 3.3 – Two example doors used in the thermal tempering apparatus, with glass sample attachments.**

Figure 3.4 shows the thermal tempering apparatus and demonstrates the tempering procedure. Stage i (as shown in the figure) involved heating the glass samples from room temperature in the furnace chamber. The furnace door was attached to a bracket that held it in place in front of the chamber, and the furnace was then heated to the desired soak temperature (620 °C – 660 °C) at a rate of 10 °Cmin<sup>-1</sup>. Once at temperature, the sample was left to soak for between 5 and 20 minutes depending on the sample dimensions. The temperature was controlled by a Eurotherm 2216e temperature controller (Eurotherm, West Sussex, UK). In addition, a type K thermocouple was used to monitor the temperature of the glass discs during heating, with the probe positioned 5 mm laterally from the centre of the glass sample.

Prior to the end of the soak time at the desired soak temperature, a trolley containing the cooling apparatus was aligned in front of the furnace. This was done by pushing it onto two specifically slotted ramps (a, Figure 3.4) attached to the table supporting the heating furnaces. The trolley castors were then locked in place. The trolley table setup included a small vehicle powered by an electric motor (m) that could travel up and down a straight track (t). A spur gear that was attached to the motor shaft meshed with a linear rack on the straight track. The motor speed was controlled by pulse-width modulation using LabVIEW graphical programming software (National Instruments, Newbury, UK). The vehicle attached to the base of the furnace door leg, which enabled the door to be detached from the bracket holding it against the furnace chamber. This left the door free to travel with the vehicle.

There were two stages to the sample transfer method from the heating furnace to cooling apparatus. These are detailed in Figure 3.4. In stage ii, the door was displaced backwards from the furnace into position in front of the cooling jets (j). This was achieved with the vehicle (m) at a speed of  $\sim 10 \text{ cms}^{-1}$  for rectangular samples and  $17 \text{ cms}^{-1}$  for disc samples.

In stage iii, the cooling jets were moved in towards the sample using pneumatic pin cylinders either side of the sample (p). Rotation of the piston within the cylinder was prevented by attaching the piston to a straight rod which was constrained to only move normal to the air impingement surfaces of the samples. The air was supplied by a compressor with a maximum operating pressure of 0.8 MPa (Airmaster Tiger 8/250 24L Air Compressor, Clarke International, Essex, UK). Solenoid valves (v) were used to control the operation of the pin cylinders and to switch air flow onto the jets. This enabled the entirety of the cooling process to be executed automatically using LabVIEW. Glass samples were cooled until they reached room temperature.

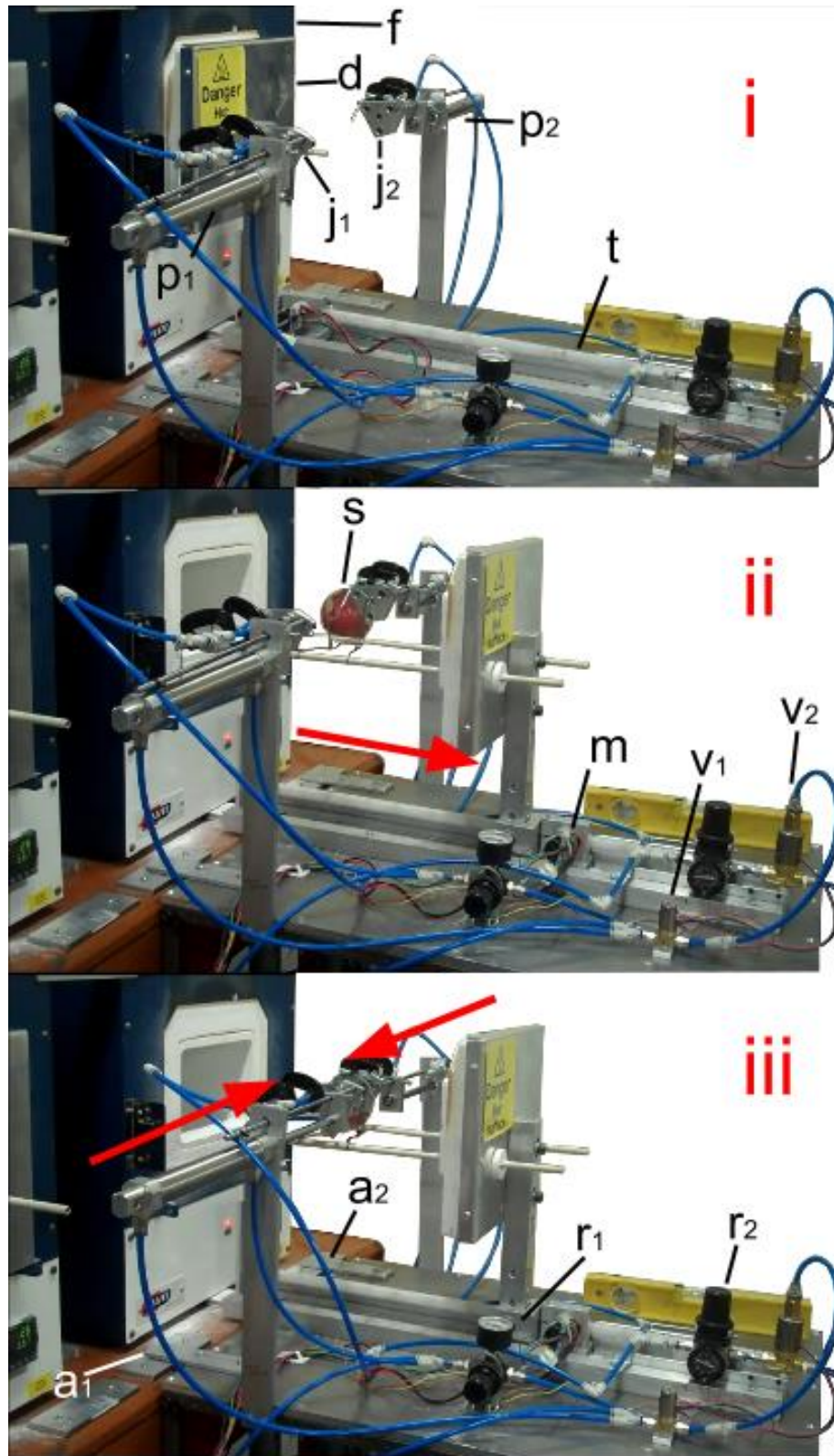
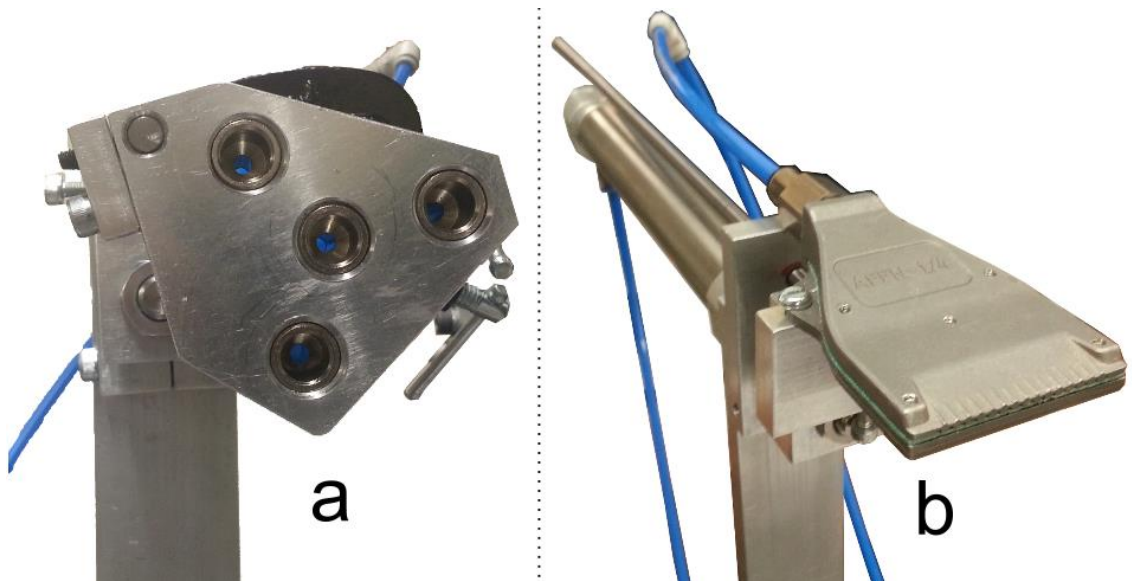


Figure 3.4 – Components and procedure of the thermal tempering apparatus. i: Heating stage: sample in furnace. ii: Transfer stage 1: door moved into position for cooling. iii: Transfer stage 2: Jets moved into position.

f: heating furnace, d: furnace door, j: cooling jets, p: pin cylinders, s: glass sample, m: door displacing vehicle including electric motor and spur gear, t: vehicle track including linear rack to mesh with spur gear, v: solenoid valves, r: regulators, a: positioning ramps.

Two impinging jet configurations were used in this study: arrays of 4 circular jets for tempering disc samples, and multi-channel flat fan nozzles (600.283.42 Multi-Channel Flat Fan Nozzle, Lechler Ltd., Sheffield, UK) for tempering rectangular samples. These are shown in Figure 3.5.



**Figure 3.5 – Air jet configurations used in this study. a: Array of 4 jets. b: Multi-channel aluminium flat fan nozzle.**

**4-jet array:** The 4-jet array split the air flow to each array into 4 new channels. The array pattern was designed to impinge concentrically with the glass disc, so that the central jet impinged the centre of the glass disc. The air velocity 10 mm from each jet was measured using hot wire anemometers at the range of compressor pressures used during testing (0.3 – 0.6 MPa). The air velocity was equalised over each jet in the array by using clamps to regulate the flow, with an accepted standard deviation of  $0.76 \text{ ms}^{-1}$  across all jet outlets. In this configuration, the air velocity upon exit from the jets could be varied from  $\sim 20 \text{ ms}^{-1}$  to  $\sim 40 \text{ ms}^{-1}$ . Appendix A details the measurement and equalisation process. Experimental trials using these jet arrays were typically conducted with a jet-to-sample distance of 30 mm.

**Flat fan nozzles:** The flat fan nozzles divided the air channel into 16 small equally-spaced single air jets, arranged over a 40 mm straight line, similar to slot jets. Each jet orifice was square in shape, with a length of 0.8 mm (Figure 3.6). They were aligned to impinge centrally across the 38 mm length of the rectangular samples. The jet-to-sample distance was set to 85 mm for all test runs.

As with the 4-jet array, the air velocity of the flat fan nozzles was measured using hot wire anemometers, which is detailed in Appendix A. However, since the jet-to-sample distance was fixed, the air velocity at impingement was only dependent on the initial pressure at the time of

the jets being switched on. As such, the air velocity 10 mm from the impinging surface was measured, rather than 10 mm from the jet orifices. The measurements were taken in a grid, in order to quantify the variation of impinging velocity at different locations over the sample surface. The results showed relatively little variation of air velocity over the central length of the rectangular samples (level with the flat fan array), with lower velocities toward the top and bottom edges of the sample. The central impinging velocity ranged from  $27 \text{ ms}^{-1}$  to  $35 \text{ ms}^{-1}$ .

This setup, which used a small-width slot-jet-like nozzle impinging centrally on a 25 mm wide sample, was similar to that of Gardon's [5]. He found that although there was some lateral non-uniformity of quenching rates, it did not affect the degree of temper centrally through the thickness of his samples. The samples tempered with flat fan nozzles in this study are considered in chapter 7 and the sharpness properties of fragments with edges within the central impingement region were of most interest.

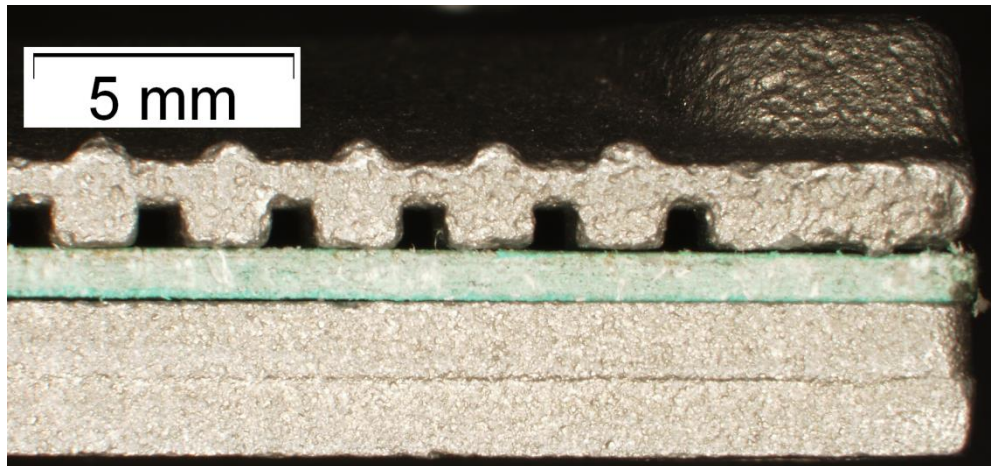


**Figure 3.6 – Optical microscope image of a portion of a flat fan nozzle used for thermal tempering experimentation.**

This section has given an overview of the thermal tempering apparatus used in this study to temper flat glass discs, and has reviewed important thermal tempering parameters and practical considerations for thermal tempering. Glass samples tempered using this apparatus are discussed in chapters 7 and 8.

### **3.3.2 Thermal and chemical tempering of glass disc samples performed externally**

A number of disc samples were tempered by external companies and used for experimentation. Discs of 80 mm diameter with 4 mm thickness were cut and thermally tempered by Piper Glass Ltd. (Piper Glass Ltd., Hertfordshire, UK). These discs had less spatial variation of residual stress across the sample surface than could be obtained with the thermal tempering apparatus outlined in section 3.3.1.2. This permitted a more general assessment of

the sharpness of broken fragments as affected by temper magnitude. The details of how these discs were thermally tempered were not disclosed.

A number of chemically tempered discs were obtained for comparison with thermally tempered glass. These discs had a diameter of 75 mm and a thickness of 4 mm, and were tempered by Trend Marine Ltd. (Trend Marine Products Ltd., Norfolk, UK). The discs were held in a 96% potassium nitrate solution at a temperature between 400 – 480 °C, for a duration of 10 – 18 hours.

Both types of tempered disc were used for the sharpness experimentation discussed in chapter 8.

### **3.3.3 Annealing tempered pint glasses**

All new pint glasses were supplied as tempered. In order to compare the performance of a tempered article to its annealed counterpart, a selection of these glasses were annealed prior to testing which required an appropriate annealing schedule to be determined [11]. The glasses were heated to the annealing point of 550 °C at a rate of 8 °Cmin<sup>-1</sup>, then held at this temperature for an hour, and subsequently cooled at a rate of 2 °Cmin<sup>-1</sup> until the glass was far below its strain point (~500 °C) to prevent the reintroduction of temper stresses.

This section has outlined the tempering and annealing processes conducted on glass samples.

## **3.4 Residual stress assessment**

The residual stress left in glass samples after tempering and annealing processes was characterised using photoelastic techniques. The techniques and equipment used for this varied according to the dimensions of the article under consideration. These techniques and the equipment used are detailed in this section. Photoelastic measurements of pint glasses were interpreted alongside CT scans which provided a measurement of thickness variation in glasses, and this is also detailed in this section. Residual stress and photoelasticity of glass are introduced in chapter 2.

### **3.4.1 Flat glass samples**

#### **3.4.1.1 Photoelastic measurement of residual stresses**

A Scattered Light Polariscopes, or SCALP (SCALP-04, Glasstress Ltd, Talinn, Estonia), was used with thermally tempered flat glass samples to measure the distribution of through-thickness stresses. This is shown in Figure 3.7.

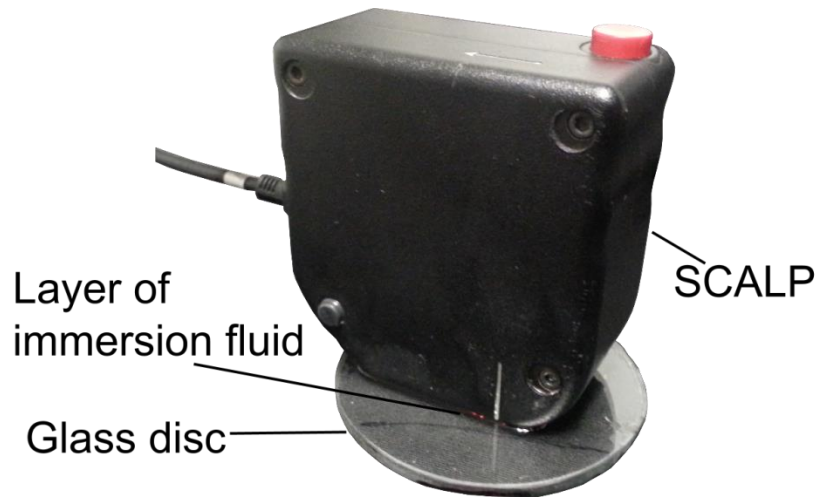


**Figure 3.7 – Scattered Light Polariscope (SCALP) setup.**

The SCALP device consists of a laser that passes through a glass prism, and a camera. The laser passes through the glass sample at an angle of  $45^\circ$  to the surface and the camera records the intensity of the light scattered back vertically to the SCALP device. The intensity of the scattered light throughout the thickness of the glass is then processed with Glasstress proprietary SCALP software (ver 4.5.1.6), from which a plot of retardation through the thickness of the glass can be produced (Figure 3.8, left). The retardation plot is then smoothed by fitting the data to a polynomial of a certain order. All SCALP measurements reported in this study used a third order polynomial with a fit closeness<sup>2</sup> of 0.2. Assuming a laterally isotropic distribution of stress, the stress,  $\sigma$ , at a certain depth,  $z$ , through the thickness can be calculated from the smoothed retardation distribution using the equation:

$$\sigma(z) = \frac{\delta'_z}{C \sin^2 \alpha} \quad (3.1)$$

where  $C$  is the photoelastic constant, usually of the value  $2.7 \text{ TPa}^{-1}$  for soda-lime-silica glass [12];  $\alpha$  is the angle of incidence of the laser beam,  $45^\circ$  for the SCALP; and  $\delta'_z$  is the gradient of the retardation distribution at a depth of  $z$  through the thickness. An example plot of the stress distribution is shown in the rightmost image in Figure 3.8. The surface compressive stresses and central peak tensile stress were recorded from the average of 5 measurements at each measurement location.

<sup>2</sup> The fit closeness refers to the width of the weight function for local regression.

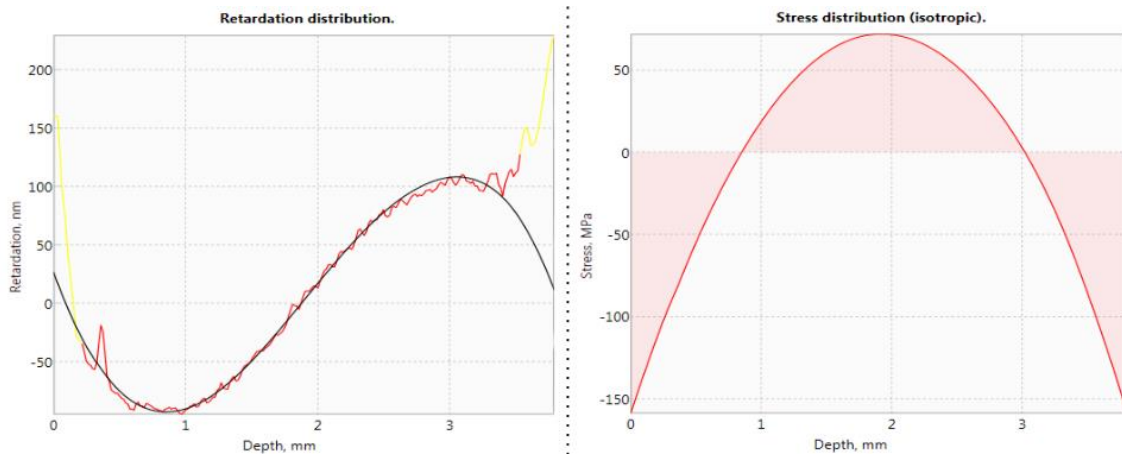


**Figure 3.8 – Outputs from SCALP software taken from a flat thermally tempered glass disc of 4 mm nominal thickness. Left: Measured and fitted retardation curves through the thickness of the glass sample. Right: Residual stress distribution as calculated from the retardation distribution.**

The maximum permissible radius of curvature of the glass for measurement with the SCALP is 300 mm, and so it was not possible to use the instrument with particularly warped samples.

A qualitative assessment of the flat glass samples was also taken with a polariscope equipped with a full-wave plate (tint plate). Examples of glass samples viewed using this setup are shown in Figure 3.9.

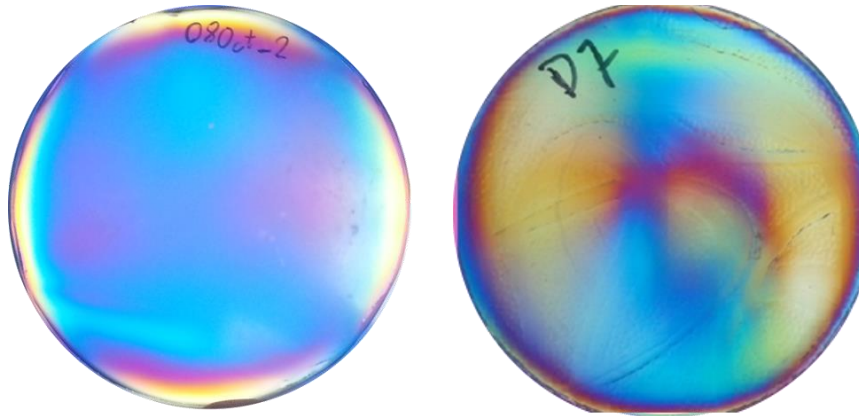


**Figure 3.9 – Examples of two tempered discs viewed with a plane polariscope equipped with a full-wave (tint) plate.**

### 3.4.2 Glass drinking vessels

This section describes techniques to assess the variation of wall thickness in pint glasses and quantitative analysis of the residual stress in the glass walls.

#### 3.4.2.1 Computed tomography for assessing wall thickness variation

The level of internal temper of glass is mainly dependent on the rate of quenching of the outer surfaces, but it is limited by the thickness of the sample [5]. As such, CT scans were conducted

to aid residual stress assessment by determining any circumferential and vertical variation in thickness, using a Toshiba Aquilion 64 detector scanner (Toshiba, Crawley, UK). Each scan was conducted at 120 kV and 100 mA with a 1 mm slice thickness, with reconstructions at 0.5 mm. The images were stored as DICOM files and analysed using OsiriX version 4.1.2 (<http://www.osirix-viewer.com>, last accessed January 2015).

Additionally, some cross sections of annealed pint glasses were prepared by breaking the glass along a scribe line, which were then measured optically.

#### **3.4.2.2 Photoelastic measurement of residual stresses**

In order to measure the magnitude and through-thickness distribution of residual stress in pint glasses, an automated polariscope suited for the measurement of cylindrical articles was used (Automatic Transmission Polariscope AP-07, Glasstress Ltd, Tallinn, Estonia).

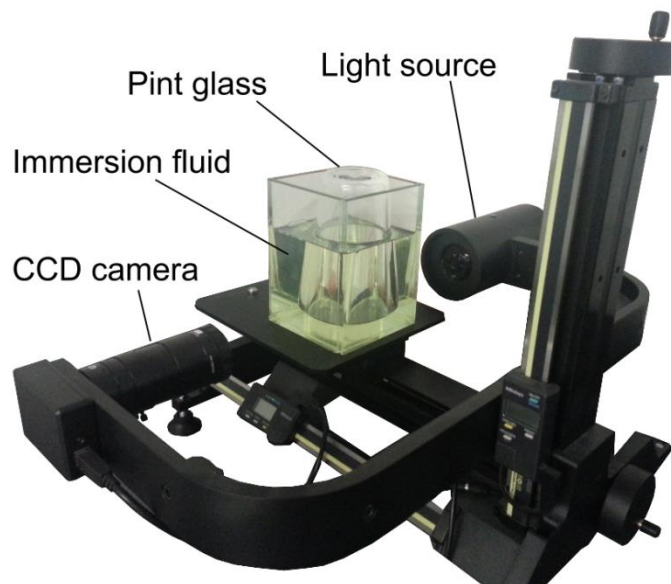


**Figure 3.10 – Automated Polariscope setup for pint glass residual stress quantification.**

Measurement with the automated polariscope was controlled by a computer using Glasstress proprietary software. The apparatus required placing the glass article in an immersion tank, where the immersion fluid was mixed to have the same refractive index as the article. The measurement position could be adjusted up and down the glass wall by adjusting the position of the stand supporting the immersion tank. A beam of polarised light was then shone tangentially through the wall of the glass article and the retardation of the light was recorded using a CCD camera. The polarisation of the light was controlled automatically by a series of polarising filters and quarter-wave plates fitted in a box which contained the light source.

Rotation of these elements was controlled using servo-motors, permitting various photoelastic setups.

When set up to view an axisymmetric article, such as pint glasses, the through-thickness fringe pattern could be observed on screen. Figure 3.11 shows an example of the fringe pattern for a tempered pint glass. This information was then used to compute a stress distribution in the glass wall [13]. As with SCALP measurements, the surface compressive stresses and central peak tensile stress were recorded from the average of 5 measurements at each measurement location.

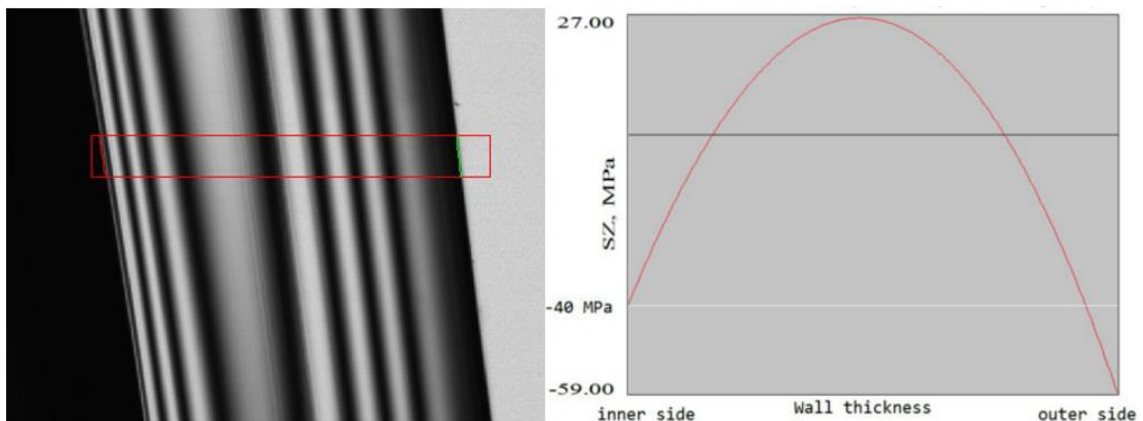


**Figure 3.11 – Outputs from Glasstress automated polariscope software. Left: Fringe pattern observed through a wall of a tempered pint glass. Right: Residual stress distribution as calculated from the digitised intensity of the fringe pattern.**

This section has discussed the methods and equipment used to characterise the state of residual stress in flat glass samples and pint glasses. In some cases, it was useful to then intentionally damage the glass surfaces to mimic surface wear. This is considered in the following section.

### 3.5 Pre-damaging surfaces

The failure strength of a glass article is very sensitive to the condition of the glass surfaces, as discussed in chapter 2. Specifically, the strength is inversely proportional to the square root of the size of the critical flaw from which the fracture initiates. As such, a glass article is likely to be much weaker after use over a prolonged period than immediately after when it was made. Since an aspect of this research is to quantify the sharpness of glass fragments from articles that had been in use, it was necessary to intentionally impart damage onto sample surfaces to mimic this surface wear. This section details the methods by which this was conducted for both flat glass samples (rectangular and disc samples) and pint glasses.

### 3.5.1 Flat glass samples

A number of experiments detailed in this study use Vickers indentation to impart a flaw into the surfaces of flat glass samples. This enabled greater control over the flaw size compared to abrasion techniques. All samples were indented prior to tempering and so residual stresses present due to indentation were not relieved. Indentation into brittle materials with a Vickers indenter results in a well-defined system of cracks that form underneath the indenter tip [14]. This system of cracks is expected to include so-called lateral cracks and median (or radial) cracks (see Figure 3.12). Lateral cracks propagate from some depth below the Vickers impression and travel towards the surface in a curved plane. The lateral cracks labelled in Figure 3.12 have not penetrated the surface. Median cracks usually extend from the corners of the Vickers impression and are visible on the surface of the glass. They are of particular interest as they can be used to mimic the behaviour of naturally occurring surface flaws when subjected to loading [15].

The Vickers indentations were imparted using an Indentec ZHV30-S hardness tester (Indentec Hardness Testing Machines Limited, West Midlands, UK). In most cases a load of 1 kgf was used for indentation, with a dwell time of 10 s. Both the dimensions of the Vickers impression and the length of the median cracks were recorded using ZH $\mu$ .HD software (Indentec Hardness Testing Machines Limited, West Midlands, UK).

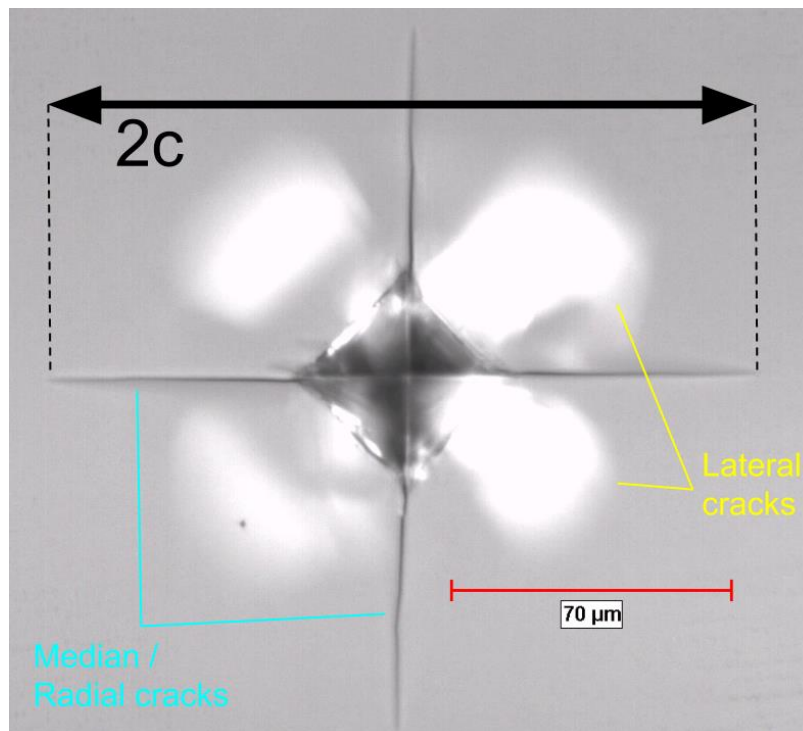


**Figure 3.12** – A micrograph showing an example of a Vickers impression on flat soda-lime-silica glass showing median cracks and lateral cracks. Indentation load was 1 kgf.

Disc samples were indented centrally on one of the flat surfaces (Figure 3.13). They were then subjected to either central impact or equibiaxial ring-on-ring loading until fracture (section 3.6.1). Rectangular samples were indented along the centre of the 25 mm width, and 5 mm away from one of the 25 mm edges. One of the diagonals of the impression was aligned to be parallel to the sample length. This is shown schematically in Figure 3.13. This was to encourage fracture to occur over the central length during 3 point bending (see section 3.6.1.2). Locating the flaw 5 mm laterally from one of the 25 mm edges ensured that edge sharpness effects further from the origin could be investigated.

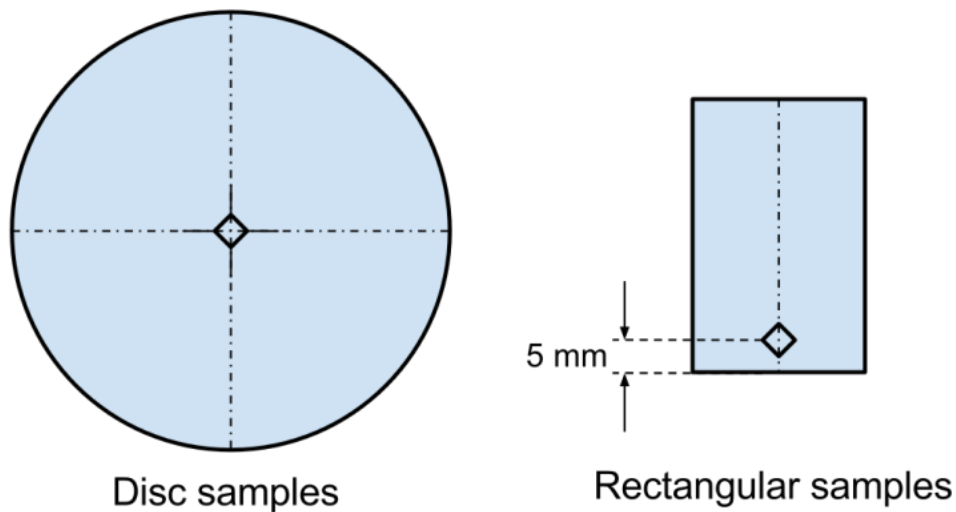


**Figure 3.13 – Schematic to illustrate location of Vickers indentations on flat glass samples. Indent and sample dimensions are for illustration only and are not to scale.**

Some thermally tempered glass samples warped during the cooling process, which meant that they could not be indented without resulting in bending stresses during indentation. Instead, the surfaces of excessively warped samples were pre-damaged by abrading the surface by hand with an applied force of  $\sim 3$  N with 220 grit SiC paper. This was applied over the surface which would be subjected to the largest amounts of tensile stress during loading. The sample was held in one hand, and the SiC paper was moved over the sample in one direction. This was repeated three times.

### 3.5.2 Pint glasses

Both new and used glass drinking vessels were tested during this study. This section details two methods used in this study to damage the surface of new pint glasses, in order to imitate real life wear. The first involves approximately equal abrasion of all the surfaces of a pint glass, and the other involves indentation at a single point to act as the crack-initiating flaw.

### **3.5.2.1 Abrasion**

The majority of pint glasses tested to failure in this study were abraded before loading. All surfaces of each glass were abraded. This was firstly because the stress distribution during loading of a pint glass creates significant tensile stresses on both the inside and outside walls of the glass (see chapter 4), and secondly because the surface damage of a used pint glass varies in location and magnitude (see Appendix D).

Similar to the method described in section 3.5.1 for flat glass discs, this was performed by hand with an applied force of ~3 N with 220 grit SiC paper. The steps were as follows:

1. The glass was held horizontally and the paper was placed along the inside wall profile of the glass from directly below the rim to the base. A hand was pressed on the paper and the glass was rotated fully three times.
2. This process was repeated for the outside wall profile.
3. The rim was abraded by placing a small piece of SiC paper around the circular rim profile and fully rotating the glass three times.
4. The base of the glass was abraded, by holding the glass upside-down and pressing the paper over the base, and then rotating the glass fully three times.

Whilst this does not precisely replicate the wear encountered by the glass in practice, it provides a convenient means of creating a flaw distribution in the article.

### **3.5.2.2 Indentation**

A fixture was designed to enable Vickers indentations to be imparted on the inside surface of the vessel wall. This is shown in Figure 3.14. The fixture was attached to a load frame at one end, and was designed to hold a Vickers indenter at the other. The indenter end protruded from the main axis of the fixture as shown in the figure. This enabled the indenter tip to contact the inside of the glass wall when the glass was laid on its side. Indentations were made at a distance of 10 mm from the rim of the glass.

The indenter was orientated so that one of the diagonals penetrated the glass wall parallel to the wall height axis. The other diagonal therefore penetrated laterally over a concave line. Hardness calculations based on impressions made on concave surfaces are known to underestimate the actual hardness value, and the impressions are likely to be deformed [16]. Furthermore, the actual indentation load could have been reduced by bending of the pint glass indentation fixture in this setup. As such, hardness measurements from indented pint glasses were discarded.

Although indenting the pint glasses in the position shown in Figure 3.14 does not reflect the distribution and magnitude of the wear observed on the used glasses discussed in the previous section, this method meant that the glasses broke with similar energies. This reduced the variability of the fracture pattern caused by large differences in the breaking energy of the glasses.

A load of 50 N was applied during indentation as lower loads could not be accurately reproduced with the given load cell. This ensured that failure occurred from the indentation location when subjected to impact on the outer side of the glass wall, given that the critical criterion for failure (see section 2.3) was not met elsewhere in the article. The method used to impact drinking vessels in this study is outlined in section 3.6.2.

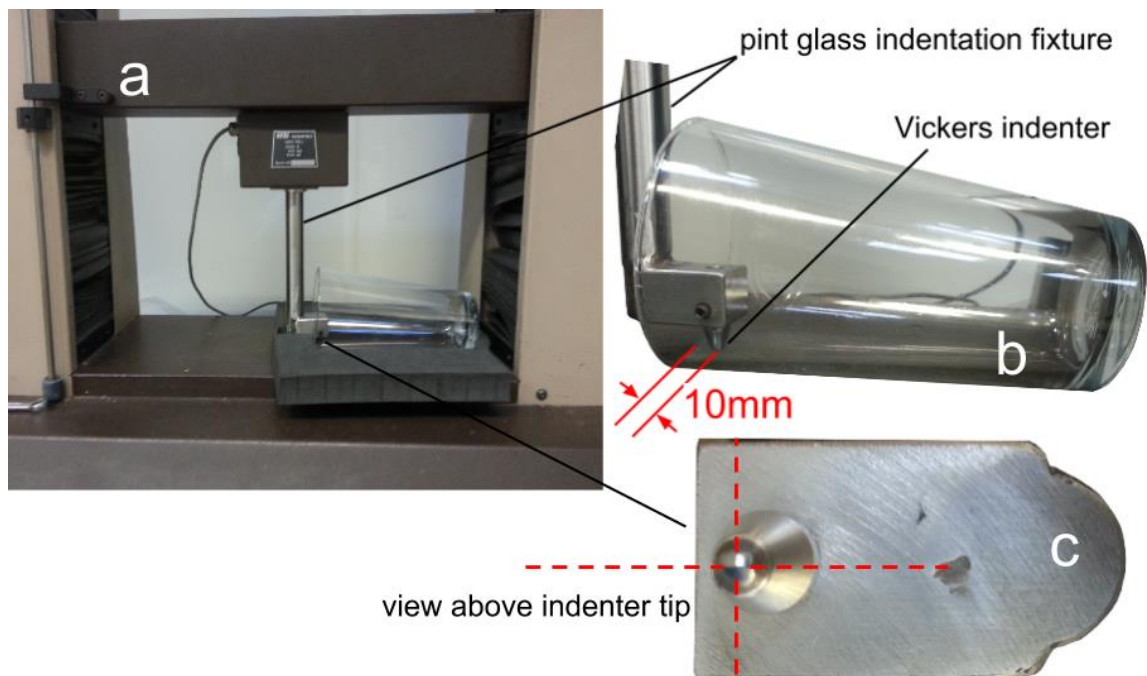


**Figure 3.14 – Method for indenting the inside wall of pint glasses. a: pint glass held in place by foam at base of load frame; b: Closer view of pint glass and indenter without foam; c: view above the Vickers indenter tip, showing the orientation of the indenter.**

### 3.5.3 Optical analysis of Vickers indentations

This sub-section describes the methods used to view Vickers indentations on flat glass samples and pint glasses.

#### 3.5.3.1 Flat glass samples

Micrographs of Vickers indentations made on flat discs were either taken with the on-board microscope on the hardness tester described in the previous section, or taken with a compound microscope (Olympus BX51, Olympus, Southend-on-Sea, UK). Both the lengths of

the indent diagonals, and the lengths of the median cracks were measured. For indentations made using loads in excess of 1 kgf, these measurements were often obscured by the presence of lateral cracks.

### **3.5.3.2 Pint glasses**

Optical measurement of the flaw size was difficult, due to the location of the Vickers impression on pint glasses (see section 3.5.2.2). A USB microscope with maximum magnification of 400x (Veho VMS-004 Deluxe, Veho Europe, Hampshire, UK) was used to view the impressions, as the device could be angled inside the pint glass to focus on the indent. This was used purely as a qualitative measure as the impression was made onto a curved surface and the viewing angle from the microscope was not normal to the impression.

This section has described the methods used in this study to impart flaws into the surface of flat glass samples and pint glass samples. This was done in order to mimic flaw distributions produced on glass articles due to general use, to reduce the energy required to cause fracture of the glass, and to produce comparable fracture patterns. The loading conditions employed to subsequently fracture are overviewed in the following section.

## **3.6 Fracture methods**

The fractographic characteristics of a broken glass article are dependent on the state of stress that the article experienced at the time of fracture. This stress state is a combination of residual stresses present in the glass article at rest, and external stresses brought about by loading conditions. In this section, the loading methods used in this study to fracture the flat glass samples and pint glasses are overviewed.

### **3.6.1 Flat glass samples**

Both glass discs and rectangular samples were tested to failure. Flat glass discs were fractured either by impact using a drop tower, by a ring-on-ring test, or by a punch test. The method of fracture was selected depending on whether the sample was warped and whether the effect of external stress needed to be excluded. Rectangular samples were fractured by a three point flexural test, or a punch test. An overview of the background for each test, and each test procedure is given below.

#### **3.6.1.1 Punch testing of flat glass samples**

Most of the loading methods described in this section involve imposing significant external stresses on the glass, which are additional to the residual stresses that may or may not already be present in the article. Punch tests were also conducted for each sample type. This involves

forcing a sharp point into the glass, without imposing significant external stress. The aim of this test was to create a suitably sized flaw within the tensile zone of residually-stressed glass (usually only thermally tempered), so that the residual stresses provided the majority of the energy for crack propagation. This enabled an assessment of the effects of residual stress on fracture divorced from significant external loading effects.

The punch testing of flat glass samples was conducted using a spring-loaded centre punch with a hardened steel tip. The radius of the tip was checked via optical microscope after every 10 tests. It was ensured that the punch tip radius was never greater than 0.2 mm in order to adhere to a British Standard [1] for conducting punch tests on architectural glass. The punch location was identical to the location for Vickers indentation of flat samples detailed in Figure 3.13. That is, glass discs were punched centrally, and rectangular samples were punched central to the 25mm length of the sample, and 5mm away from one of the 25mm edges. The rectangular samples were not punched centrally due to their relatively small size. The location of the punch enabled assessment of the fragmentation behaviour further from the origin.

### **3.6.1.2 Three-point bending of rectangular samples**

Rectangular samples were tested to failure with a three point bending configuration. A bending fixture was designed to load the rectangular samples directly along the centre line parallel to the longer (38 mm) length. This was instead of a traditional 3 point bending configurations where the sample is loaded along the centre line parallel to the shorter sample length [17]. A schematic of this loading configuration is shown in Figure 3.15. It was designed to encourage fracture to occur over this central line, since this line was expected to have a low residual stress variation due to a low variation of the heat transfer coefficient. This was because the line was aligned to be level with the flat fan nozzle orifices during the thermal tempering operations described in section 3.3.1.2. Glass samples fractured by this method are analysed in chapter 7.

The central loading rod and the two support rods were made from stainless steel, and had a diameter of 8 mm. The test was performed using a universal testing machine fitted with a load cell with a range of 5 kN (Hounsfield H10KM, Tinius Olsen, Ltd., Salfords, UK). The central loading rod was displaced downwards into the sample at a rate of 0.08 mm/min until fracture. This was in order to result in a strain rate of the order of  $10^{-4}$ , as recommended in ASTM C1161 [17]. This was calculated by the following equation:

$$S = \frac{\varepsilon L^2}{6t} \quad (3.2)$$

where  $s$  is the load frame crosshead speed,  $\epsilon$  is the strain rate ( $10^{-4}$ ),  $L$  is the distance between the support rods (18 mm), and  $t$  is the specimen thickness (actual thickness  $\sim 3.82$  mm). The failure stress,  $\sigma_f$ , was calculated using the standard formula for the strength of a beam in 3 point flexure, as given in the ASTM C1161 standard [17]:

$$\sigma_f = \frac{3FL}{2wt^2} \quad (3.3)$$

where  $F$  is the force required to cause fracture,  $w$  is the specimen width (38 mm), and  $L$  and  $t$  are the same as above.

A layer of cellulose tape was applied to the top face of the sample in contact with the central loading rod. This was to ensure that the fragmentation pattern remained intact to aid with fractographic analysis. The top face of the sample was chosen since it was subject to compressive stresses during loading, and was therefore less likely to have any significant effect on the fracture pattern (compared to application of tape on the tensile side of the sample).

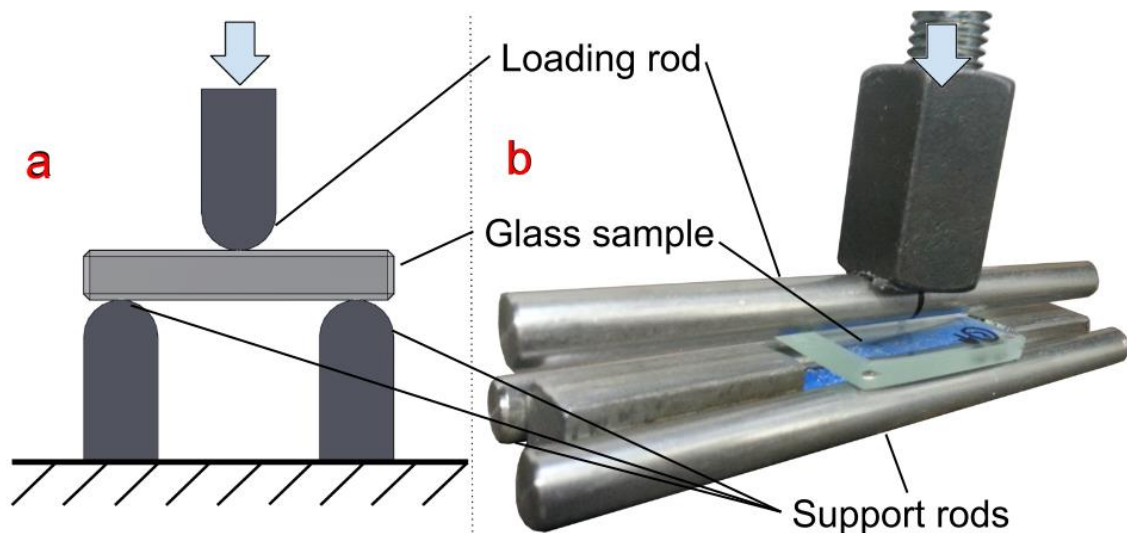


Figure 3.15 – Schematic of the three point bending configuration for testing rectangular samples to failure. a: front view showing position of load and support rods. b: picture of the actual loading configuration, showing that the loading and support rods are aligned parallel to the longer length of the rectangular sample.

### 3.6.1.3 Ring-on-ring loading of glass discs

A number of flat glass discs were loaded to fracture using an equibiaxial ring-on-ring test, conforming to ASTM standard C1499 [18]. The test setup is shown in Figure 3.16. The test provided a reproducible means of fracturing glass discs, and resulted in fragments of various sizes across the article due to the range of stress imposed into the article. Glass discs that were

fractured by this method, and the stress distribution in the disc under loading, are analysed in chapter 8.

The tests involved placing a glass disc sample in between a load ring of 10 mm diameter, and a support ring of 50 mm diameter. The edges of each ring were rounded to a radius of 1 mm and were made of stainless steel. These dimensions were suitable for glass discs of diameter between 48 mm and 88 mm, with maximum thickness of 4 mm. Silicone compliant layers were placed between the rings and the sample to reduce contact stresses between the rings and the glass. As with three point bending tests (see previous sub-section), the side of the sample in contact with the load ring was taped to keep the fracture pattern intact after the fracture event.

The load ring was displaced downwards into the sample at a rate of 2 mm/min until fracture. The force required to cause fracture,  $F$ , was recorded. Provided the origin of fracture occurred within the ring bounds, the failure stress,  $\sigma_f$ , was then calculated using the equation:

$$\sigma_f = \frac{3F}{2\pi t^2} \left[ (1 - \nu) \frac{D_S^2 - D_L^2}{2D^2} + (1 + \nu) \ln \frac{D_S}{D_L} \right] \quad (3.4)$$

where  $t$  is the thickness of the disc;  $\nu$  is the Poisson's ratio (0.22 for soda-lime-silica glass [19]);  $D_S$  and  $D_L$  are the support ring diameter and load ring diameter respectively; and  $D$  is the diameter of the disc [21].

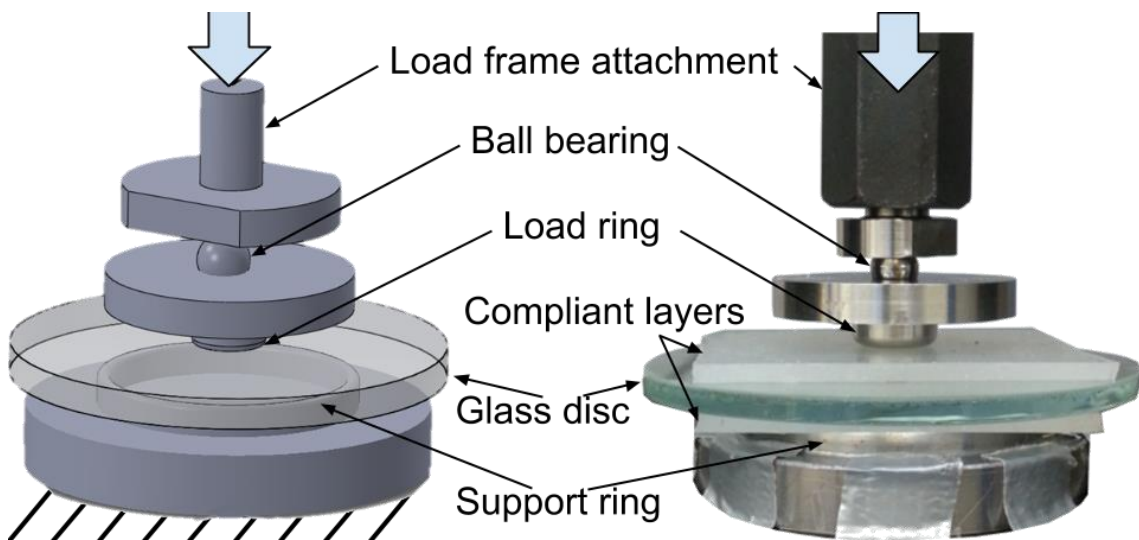


**Figure 3.16 – Components of the ring on ring fixture. Left: fixture schematic to show ring contact area. Right: Actual apparatus.**

The ring-on-ring test was only valid for disc specimens that were within the dimensions stated above, and that did not exceed a flatness tolerance of 0.1 mm in 25 mm. A number of discs

thermally tempered with the apparatus outlined in section 3.3.1.2 did not meet this flatness requirement and were instead loaded by impact, which is considered below.

#### 3.6.1.4 Impact loading of glass discs

An impact loading method was devised as a means of fracturing disc samples that were not eligible for ring-on-ring testing (see previous sub-section). The method involved dropping a steel impactor in a drop tower onto the centre of a glass disc held in a support fixture. The apparatus is shown in Figure 3.17.

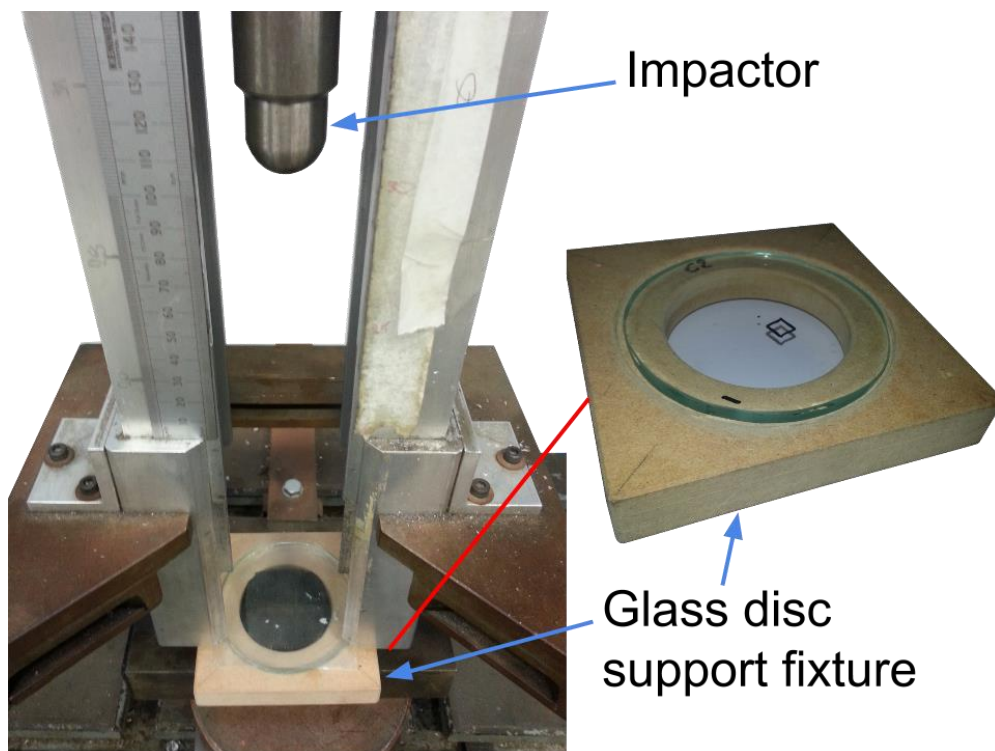


Figure 3.17 – Experimental set up for impact loading of glass discs.

The steel impactor had a round tip of 25 mm diameter. This matched glass vessel pendulum-based impact testing equipment available which use a 25 mm diameter ball bearing to impact the glass wall (Impact Tester, AGR International, Butler, PA). The weight of the impactor was 0.8 kg. The glass support fixture was made from wood, and the inside hole diameter beneath the disc was 55 mm. The support fixture had a recess on its top and bottom surfaces, so glass discs could slot in without lateral movement. One surface had a circular recess of 75 mm, and the opposite surface had a circular recess of 80 mm. This enabled both the 75 mm and 80 mm discs to be tested.

For disc samples that had been abraded or indented, the abraded/indented surface was placed face down in the glass disc support fixture. This ensured that the flaw was present on the side subjected to the most tensile stress. The kinetic energy was calculated using the relation:

$$KE = m \cdot g \cdot h \quad (3.5)$$

where  $m$  is the mass of the impactor,  $g$  is the acceleration on the impactor mass due to gravity, and  $h$  is the height from which the impactor is dropped. Frictional effects were neglected. The drop height (distance between the sample impact point and the impactor tip) was initially 10 mm and was increased in 10 mm intervals until failure. The number of impacts prior to failure was then recorded.

### 3.6.2 Pint glasses

This sub-section outlines the methods used to fracture pint glasses in this study.

#### 3.6.2.1 Impact loading of pint glasses

Pint glasses were tested until fracture using a drop tower and a similar methodology to that outlined for the fracture of disc samples by impact in section 3.6.1.4. This involved systematically increasing the height of an impactor in a drop tower, and subsequently letting it fall by its own weight onto the glass specimen which was loosely restrained by elastic bands onto a wooden block. This enabled a comparative assessment of the strength and fracture characteristics of various glasses. The apparatus for pint glass impact loading is shown in Figure 3.18.

Two impactors of identical dimensions were used. One was made of aluminium and had a mass of 0.5 kg, and the other was made of steel and had a mass of 0.8 kg. The impactor tip radius was 12.5mm, as with the impactor detailed in the previous sub-section. The heavier steel impactor was made and used exclusively to fracture new glasses, as sufficient energy could not be imparted from the aluminium impactor to consistently achieve fracture. The kinetic energy could then be calculated using equation 3.5. As with disc samples, the drop height was initially 10 mm and was increased in 10 mm intervals until failure and the number of impacts prior to failure was recorded. The impact location was changed to suit the needs of each investigation. In section 4.3, impacts were made to various locations along the glass wall in order to ascertain general fracture characteristics of drinking glasses. In section 4.4, the glass was impacted 10 mm from the glass rim throughout the systematic impact testing of 70 pint glasses.



Figure 3.18 – Apparatus used for systematic impact testing. a: Drop tower guide rails extending beyond the top of the picture to a maximum height of 3.5m. b: Glass securing box. c: Cast iron table. d: High speed video camera. e: Light source. f: Enlarged picture of steel impactor from higher up the guide rails.

Each glass was secured in place beneath the drop tower guide rails (Figure 3.18b). For most test runs, the outside walls of the pint glasses were taped to ensure that the fracture pattern remained intact once broken. Additionally, a number of impacts were recorded with a high speed video camera (Olympus i-Speed, Olympus, Southend-on-Sea, UK) (Figure 3.18d) to examine fracture development. This also enabled a more accurate calculation of the energy involved during impact by determining the impactor velocity from the video footage equation 3.6 below.

$$KE = \frac{m \cdot v^2}{2} \quad (3.6)$$

### 3.6.2.2 Punch testing and fragmentation count of pint glasses

The punch test for pint glasses involved hammering a scribe tool with a tungsten carbide tip into the inside wall of the glass until fracture. This is shown in Figure 3.19. The sharp point of the scribe tool was positioned 10 mm from the rim of the glass. Breaking the glass in this way ensures that tensile stresses due to impact of the scribe are more localised than compared to the impact method described in the previous sub-section. This results in the crack being mainly propagated by the residual stresses in the article. The level of fragmentation therefore corresponds to the magnitude of the residual stresses. All glasses broken by punch test were

taped prior to conducting the punch, using adhesive laminating sheets as outlined in the above section. This allowed for the extent of fragmentation in different portions of the glass to be compared.

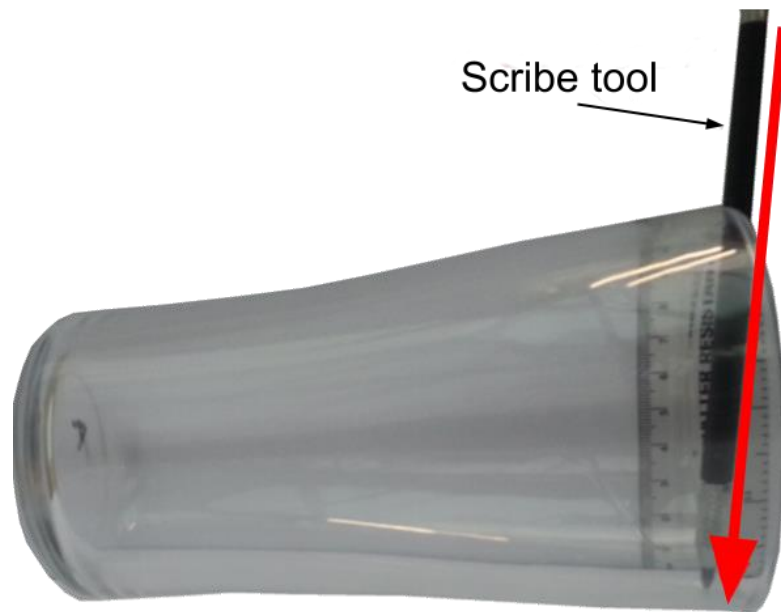


**Figure 3.19 – Set up for a punch test on a pint glass.**

This section has overviewed various methods used in this study to load flat glass samples and pint glass samples to fracture. Additional loading methods were conducted on pint glasses in order to replicate physical attacks with the glasses. This is covered in chapter 5. After fracture, the fractographic features of the samples were analysed. The procedures and equipment used in this analysis are considered in the following section.

### **3.7 Fractographic analysis**

A fractographic analysis was conducted on glass samples after fracture. This involved examination of the macroscopic fracture pattern on the y-z fractographic plane, and examination of the fracture surfaces on the x-y fractographic plane. This section details the equipment used and procedures followed during this process. The section is not intended to be an introduction to fractography, as this is covered in Chapter 2.

#### **3.7.1 Macroscopic examination**

The first stage of the fractographic analysis involved examination of the overall fracture pattern and fracture surfaces by eye. The macroscopic fracture pattern for each sample was photographed using a digital camera (Canon EOS 450D, Canon UK Ltd., Surrey, UK). For pint glasses, this involved taking four photographs of the outside wall orientated 90° from each other, and a picture of the base, to capture the full fracture pattern. The origin and other

fragments of interest were located using these photographs or by visual inspection of the article.

In instances where the fracture stress was an important factor, the origin mirror size was measured and the fracture stress was estimated using equation 2.4. If the location of the origin was unclear, the fracture surfaces were lit by a desk lamp and examined by eye. The direction of crack propagation was inferred by fracture surface markings. This enabled the fracture origin to be identified.

For samples that were taped prior to fracture, fragments of interest were removed with care to not damage fragment edges and fracture surfaces. In most cases the tape could be peeled away. Otherwise, the tape was carefully cut away with a modelling knife. Fracture surfaces of particular interest were then viewed with an optical microscope.

### 3.7.2 Optical microscopy

A stereo microscope (Olympus SZ-X12, Olympus, Southend-on-Sea, UK) was used to examine fracture surfaces, as shown in Figure 3.20. Samples were positioned underneath the objective lens using a modelling clay that dissolved in acetone (Leaf Green Sculpey III Polymer Clay, Polyform Products Company Inc., Illinois, USA). The two eyepieces of the stereo microscope view the sample at slightly different angles. This allowed for a 3-dimensional view of the fracture surfaces. This occasionally meant that some features were more apparent when viewed through the eyepieces than via a live digital camera output on a computer screen. Fracture surfaces were therefore initially viewed through the microscope binoculars. The focus and/or lighting conditions could then be adjusted to emphasise features of interest in a digital snapshot of the fracture surface.

The samples were lit either by using fibre-optic goose-neck guides (Figure 3.20, c), or by a ring light mounted on the objective lens (e). A 150 W halogen bulb was used as the light source. The use of goose-neck light guides allowed for the angle of incidence of the light on the sample to be adjusted. This was useful when viewing shallow fractographic features. For example, Figure 3.21 shows two pictures of the same fracture surface illuminated by different lighting conditions. The left image was taken with a ring light directly above the surface, and the right image was taken with goose-neck guides with the light incident on the surface at a shallow angle. It can be seen in the right image that the Wallner lines are now clearly visible, which are difficult to identify in the left image.

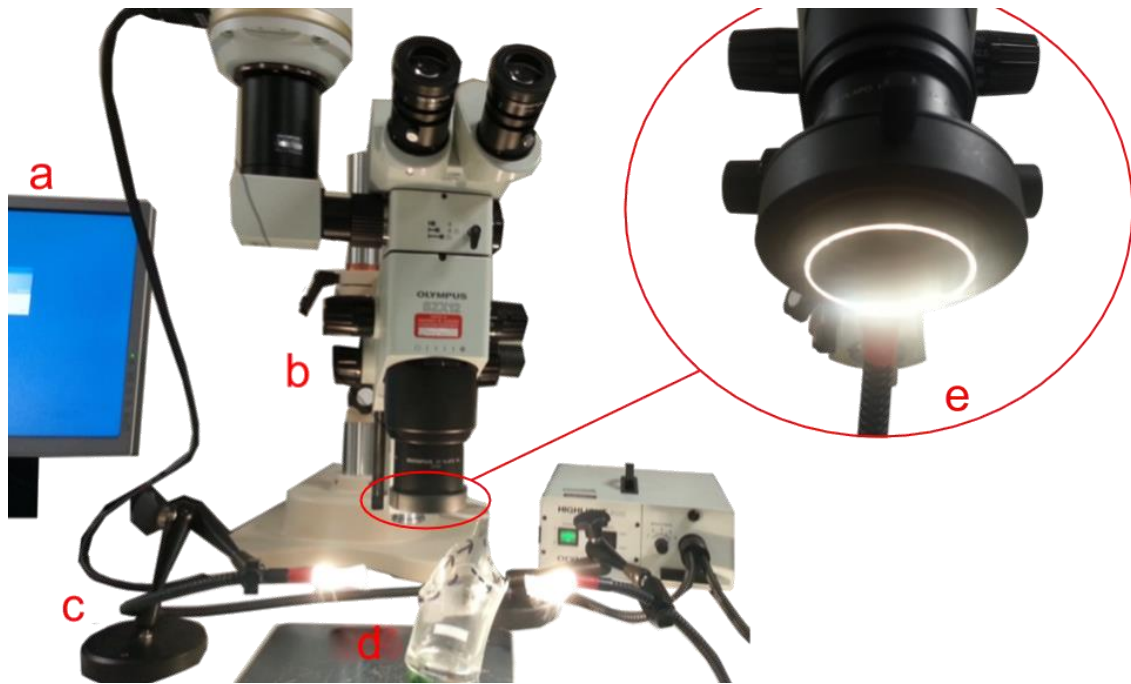


Figure 3.20 – Stereo microscope used for fracture surface examination. a: Computer screen to view and capture live digital images. b: Stereo microscope used for fracture surface examination. c: Goose-neck light guides aimed at glass sample. d: A sample under examination. e: Ring light mounted on the objective lens as an alternate lighting method.

Digital images taken from the stereo microscope were measured and analysed using Olympus proprietary software AnalySIS and stored as TIFF files. Particular surface features of interest were then observed using a scanning electron microscope, as overviewed in the following section.

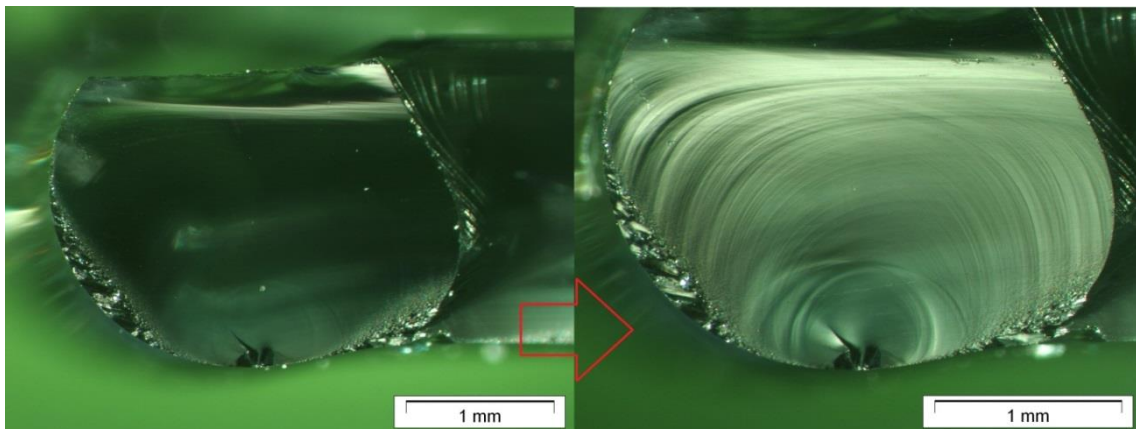


Figure 3.21 – Micrographs to show the effect of lighting conditions on feature visibility. Left: Surface lit from above. Right: Surface lit at a shallow angle.

### 3.7.3 Scanning electron microscopy

Selected surface features of particular interest were viewed using an environmental scanning electron microscope (ESEM) (XL-30, Philips UK Ltd, Surrey, UK) to obtain an image with a higher resolution than that obtained with the stereo optical microscope (see previous sub-

section). SEMs use a beam of electrons to probe a sample surface. Given the shorter wavelength of electrons to that of light, a higher magnification can be obtained. The electron beam scans a rectangular raster over the surface, and an image is constructed by monitoring the position of the beam and the emissions from the sample. Various types of emission from the sample can be measured, each providing different information. Of particular interest in this study were the secondary electron emissions as they give the most topographical detail of the sample.

Use of the ESEM involves placing the sample of interest into a chamber. The chamber is then pumped to create a vacuum, to prevent interaction between the electron beam and the air. Since glass is non-conductive, samples were either viewed in an H<sub>2</sub>O environment in the ESEM chamber, or coated with a thin carbon layer before being placed in the chamber. This reduced surface charge effects on the sample. Measurement and further analysis of fractographic features was conducted using imageJ software version 1.48 (<http://imagej.nih.gov/ij/>, last accessed August 2014).

A drawback of using the SEM and the optical microscope is that the image output is two-dimensional. This may result in mis-representation of three-dimensional features. Therefore some fragments were then imaged using a micro-CT scanner to give a 3-dimensional image. This is considered in the following section.

#### **3.7.4 Micro computed tomography**

A micro-computed tomography (micro-CT) scanner (XTH 225 micro-CT scanner, Nikon Metrology UK Ltd, Derby, UK) was used to generate high-resolution three-dimensional images of selected fragments. Micro-CT involves the combination of many individual radiographs taken of a single sample at different orientations. The radiographs are taken with the X-ray source and detector in fixed positions, with the sample rotated in between the two. Only a rotation of 180° is necessary, but a full rotation of 360° can improve image quality.

Micro-CT offers greater spatial resolution than that possible with clinical computed tomography, however the exact resolution is difficult to quantify as it is dependent on a large number of factors [20]. One factor involves the distance from the X-ray source to the sample, which affects the magnification achieved by the scanner. Glass fragments were placed as close to the X-ray source as possible whilst keeping the entire fragment within the scanning range.

The radiograph data was reconstructed using CT-Pro 2.0 (Nikon Metrology UK Ltd.) and all 3D rendering and subsequent analysis was performed in VGStudio MAX 2.1 (Volume Graphics

GmbH, Germany). The scans were typically conducted with the X-ray voltage and current set at 70 kV and 71  $\mu\text{A}$ , respectively, and no filtration was used. A total of 3016 radiograph images were taken (approximately 1 per  $0.1^\circ$ ).

This section has overviewed the equipment and methodology involved with fractographic analysis in this study. It outlined eye-appraisal of the fracture pattern, optical microscopy, scanning electron microscopy, and micro-tomography. The next analysis step involved assessment of the sharpness of the glass fragments, which is treated separately in chapter 6.

### **3.8 Chapter summary**

This chapter outlined and discussed the steps taken to produce comparable fractured glass samples in this study, and also discussed procedures undertaken for fractographic assessment of the samples. The chapter was arranged by the order that each step needed to be considered. Various sample types were introduced, and the specific preparatory steps for each were discussed. This included: cutting and edge preparation, tempering and annealing processes, residual stress assessment, surface pre-damaging methods, and fracture methods. The following chapter uses a selection of these methods to assess the fracture characteristics of pint glasses.

### 3.9 Chapter references

- [1] “BS EN 12150-1:2000 - Glass in Building. Thermally Toughened Soda Lime Silicate Safety Glass. Definition and Description,” *British Standards Institute, UK*, 2000.
- [2] “Using Design to Reduce Injuries from Alcohol Related Violence in Pubs and Clubs,” *Home Office, Design Out Crime*, 2010.
- [3] R. Gardon and J. C. Akfirat, “Heat Transfer Characteristics of Impinging Two-Dimensional Air Jets,” *Journal of Heat Transfer*, vol. 88, no. 1, pp. 101–107, Feb. 1966.
- [4] N. Sozbir and S.-C. Yao, “Experimental Investigation of Water Mist Cooling for Glass Tempering,” *Atomization and Sprays*, vol. 14, no. 3, pp. 191–210, 2004.
- [5] R. Gardon, “The Tempering of Glass by Forced Convection,” *Proceedings of the 7th International Congress on Glass, National du Verre, Charleroi, Belgique*, no. paper no. 79, 1965.
- [6] R. Gardon, “Thermal Tempering of Glass,” in *Glass: Science and technology, Volume 5, Elasticity and Strength in Glasses*, D. R. Uhlmann and N. J. Kreidl, Eds. Academic Press, New York, 1980, pp. 145–216.
- [7] E. Romero, D. Locheignies, and M. Duquennoy, “Numerical modeling, Experimental Investigations and Stress Control for Flat Glass Tempering,” *Glass Processing Days Proceedings*, pp. 468–471, 2001.
- [8] A. Koike, S. Akiba, T. Sakagami, K. Hayashi, and S. Ito, “Difference of Cracking Behavior due to Vickers Indentation between Physically and Chemically Tempered Glasses,” *Journal of Non-Crystalline Solids*, vol. 358, pp. 3438–3444, Dec. 2012.
- [9] M. Abbott and J. Madocks, “Roller Wave Distortion – Definition , Causes and a Novel Approach to Accurate , On-line Measurement,” *Glass Processing Days Proceedings*, no. June 18–21, pp. 226–230, 2001.
- [10] H. Aben and C. Guillemet, “Membrane Stresses,” in *Photoelasticity of Glass*, Berlin: Springer-Verlag, 1993, pp. 130–138.
- [11] F. V. Tooley and S. R. Scholes, *The Handbook of Glass Manufacture*. New York: Ashlee Publishing Company, 1984.
- [12] GlasStress Ltd., “Scattered Light Polariscope SCALP-04, Instruction Manual ver 4.5.1.” .
- [13] H. Aben, J. Anton, and A. Errapart, “Modern Photoelasticity for Residual Stress Measurement in Glass,” *Strain*, vol. 44, no. 1, pp. 40–48, 2008.
- [14] B. R. Whittle and R. J. Hand, “Morphology of Vickers Indent Flaws in Soda–Lime–Silica Glass,” *Journal of the American Ceramic Society*, vol. 84, no. 10, pp. 2361–2365, 2001.

- 
- [15] B. R. Lawn and D. B. Marshall, "Indentation Fractography: A Measure of Brittleness," *Journal of Research of the National Bureau of Standards*, vol. 89, no. 6, pp. 435–451, Nov. 1984.
- [16] M. S. Drozd, Y. I. Slavskii, and A. A. Baron, "Measuring Vickers Hardness of Components with Curved Surfaces," *Measurement Techniques*, vol. 20, no. 7, pp. 1014–1017, 1977.
- [17] ASTM C1161-13, Standard Test Method for Flexural Strength of Advanced Ceramics at Ambient Temperature, ASTM International, West Conshohocken, PA, 2013, [www.astm.org](http://www.astm.org).
- [18] ASTM C1499-09(2013), Standard Test Method for Monotonic Equibiaxial Flexural Strength of Advanced Ceramics at Ambient Temperature, ASTM International, West Conshohocken, PA, 2013, [www.astm.org](http://www.astm.org).
- [19] J. R. Calvert and R. A. Farrar, "Properties of Materials," in *An Engineering Data Book*, 1999, pp. 7–1, 7–2.
- [20] G. N. Ritty, A. Brough, M. J. P. Biggs, C. Robinson, S. D. A. J. Lawes, and S. V. Hainsworth, "The Role of Micro-Computed Tomography in Forensic Investigations," *Forensic Science International*, vol. 225, no. 1–3, pp. 60–66, Feb. 2013.
- [21] S. P. Timoshenko and S. Woinowsky-Krieger, "Theory of Plates and Shells", 2<sup>nd</sup> Edition, McGraw-Hill, New York, NY, 1959.

## **4 The fracture of annealed and thermally tempered pint glasses**

### **4.1 Introduction**

Tempered drinking glasses, in particular pint glasses, are widely used in bars and pubs in the UK for safety reasons. However, there are few studies which examine and compare the nature of annealed and tempered drinkware fractures. This chapter presents an investigation into the typical fracture characteristics of annealed and tempered soda-lime-silica glass drinkware.

There are four main sections to this chapter:

Section 4.2 considers the structural characteristics of drinking vessels in order to aid the interpretation of fracture patterns later in the chapter. This section includes a review of literature on the loading and fracture of drinking vessels, as well as finite element analyses to investigate the structural response of pint glasses to an applied external load.

Section 4.3 investigates the fracture characteristics of various drinking glasses when subjected to external impact. This includes standard and premium tempered pint glasses purchased as-new from wholesalers, and also a number of used drinking glasses that were donated by various local pubs and hotels.

Section 4.4 presents an investigation into the wall thickness, residual stress level, and impact performance of three types of tempered pint glasses. CT scans were used to analyse the wall thickness. Residual stresses were analysed by the use of photoelastic equipment and punch tests. A drop tower was used to impact pint glasses.

Finally, section 4.5 provides a summary of the key properties and characteristics of tempered pint glasses based on the results of earlier sections. It highlights some key difficulties involved with establishing the standard performance of tempered pint glasses.

### **4.2 Structural response of drinking vessels due to external impact**

This thesis is mainly concerned with the fracture behaviour of pint glasses broken as part of an assault. Methods by which fracture may occur in such incidents are considered in detail in chapter 5 of the thesis. In summary, these methods may be one of the following: impacting the glass onto a hard surface and then using a fragment(s) as a weapon; throwing the glass at a victim so that it fractures on impact; holding the glass in hand and impacting it onto a victim; or holding the glass in hand and thrusting it into a victim [1]. External impact is common to all these breakage methods.

There are two parts to this section. Firstly, previous work on the structural properties of glass bottles is reviewed. Secondly, the structural response of pint glasses to an externally applied load is investigated using finite element analysis. The content of this section is used later in the chapter to aid in the interpretation of drinking vessel fractures.

#### 4.2.1 Stress systems developed in externally impacted glass bottles

There is little published work on the typical fracture characteristics of drinking glasses and on the structural response of drinking glasses to an applied load. However, a number of studies have been conducted on glass bottles. These are considered in this section, and the findings from these studies are extended to pint glasses in following sections.

Preston presented an in-depth overview of the fracture of bottles in 1939 and described the stress systems produced in bottles by thermal shock, internal pressure, and external impact [2]. He noted that propagating cracks could lead at either the inside or outside wall of the bottle, and that a crack front may switch sides due to a different set of stresses in a different portion of the bottle. He also showed that bottles fractured by impact resulted in a series of radiating cracks propagating from the origin. This is similar to the characteristic star-like fracture patterns seen in flat glass subjected to impact [3].

The stress systems caused by impact onto bottles were investigated further by Mould [4]. By using thin brittle coatings that crack under the influence of tensile stress, he identified three key tensile stress systems that developed due to impact on the outside wall of the bottle: inward flexure stress, contact stress, and hinge stresses. These are demonstrated in Figure 4.1. The magnitude of tensile stresses in these stress systems is linearly dependent on the load that originally caused them [5]. Each stress system can serve as the fracture origin source provided that the critical condition for failure ( $K_I = K_{Ic}$ ) is achieved. However, all the stress systems are likely to affect crack propagation once fracture has been initiated [2], [4].

**Inward flexure stress** is induced on the inside wall of the bottle by deflection of the wall during impact. It is present directly beneath the impact point.

**Hinge stresses** become present on the outside wall either side of the impact area. They occur in response to the inward deflection that causes inward flexure stress, which in turn results in two areas of outward deflection. Mould determined that hinge stresses were 5 times lower in magnitude than inward flexure stresses [4]. The location of the maximum hinge stress is dependent on bottle diameter and thickness [5].

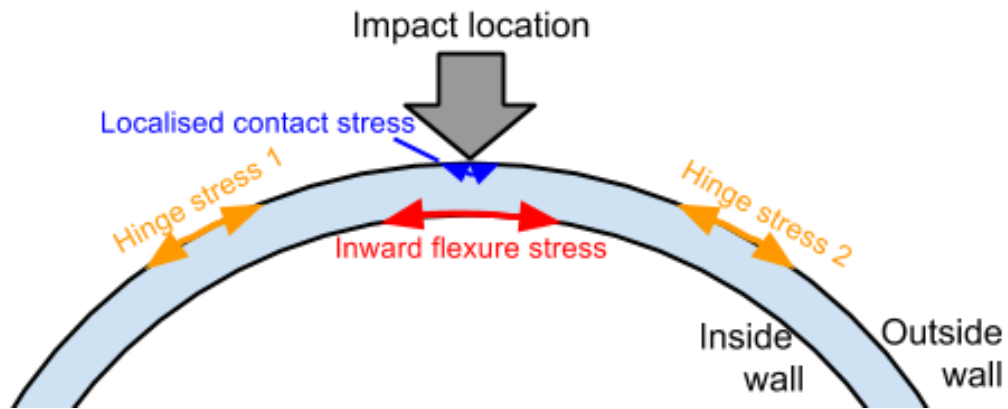


Figure 4.1 – Cross section of stress systems developed on an impacted cylindrical object, after [4].

**Contact stress** (or Hertzian contact stress) is a region of localised tensile stress, which circles the impact location and develops on the impacted surface. The contact stress magnitude is proportional to the glass stiffness [6]. Mould found that the contact stress was 3 times greater in magnitude than the inward flexure stress [4]. However, other stress systems are more likely to be the source of failure due to them having a larger span of tensile stress [6].

This section has introduced key features of the stress systems developed in externally impacted glass bottles. These stress systems are considered in the context of pint glasses in the following sub-section.

#### 4.2.2 Finite element analyses on the structural response of straight-walled and Nonic pint glasses

Existing work on the stress systems developed due to external impact on glass bottles was reviewed in the previous sub-section. The reviewed studies involved the stress systems and fracture characteristics of glass bottles rather than drinking glasses. This sub-section presents a series of finite element analyses on the static loading of pint glasses, in order to characterise their structural response. All analyses were conducted using Abaqus finite element software version 6.12 (Dassault Systèmes UK Limited, Warrington, UK).

There are two parts to this section. Firstly, the 1<sup>st</sup> principal stress systems developed in a straight-walled pint glass, which is loaded at the rim and at the base, are compared in magnitude in section 4.2.2.1. The shape and distribution of the stress regions are also discussed. Secondly, the inward flexure stress in a straight-walled pint glass and a Nonic glass is compared in section 4.2.2.2. This is approached by considering the effect of loading in three different locations on the glass wall.

#### 4.2.2.1 Comparison of stress systems for rim and near-base loading

This sub-section considers the 1<sup>st</sup> principal stress distributions of a straight-walled pint glass subjected to static loading.

**Model properties:** The pint glass CAD model was axisymmetric, and its profile dimensions are given in Figure 4.2. However, the static loading condition was not axisymmetric and so a 3-dimensional analysis was conducted. A mechanical load was considered at two locations, firstly at the rim of the glass and secondly 20 mm from the base of the glass. In both cases, the load was applied diametrically and normal to the outside wall, as demonstrated in Figure 4.2. The glass was rigidly supported on the outside wall opposite the impact location, and was allowed to pivot. This meant that the analysis was symmetrical about the x-y Cartesian plane shown in the figure. As such, only half of the glass was modelled and given a symmetry boundary condition.

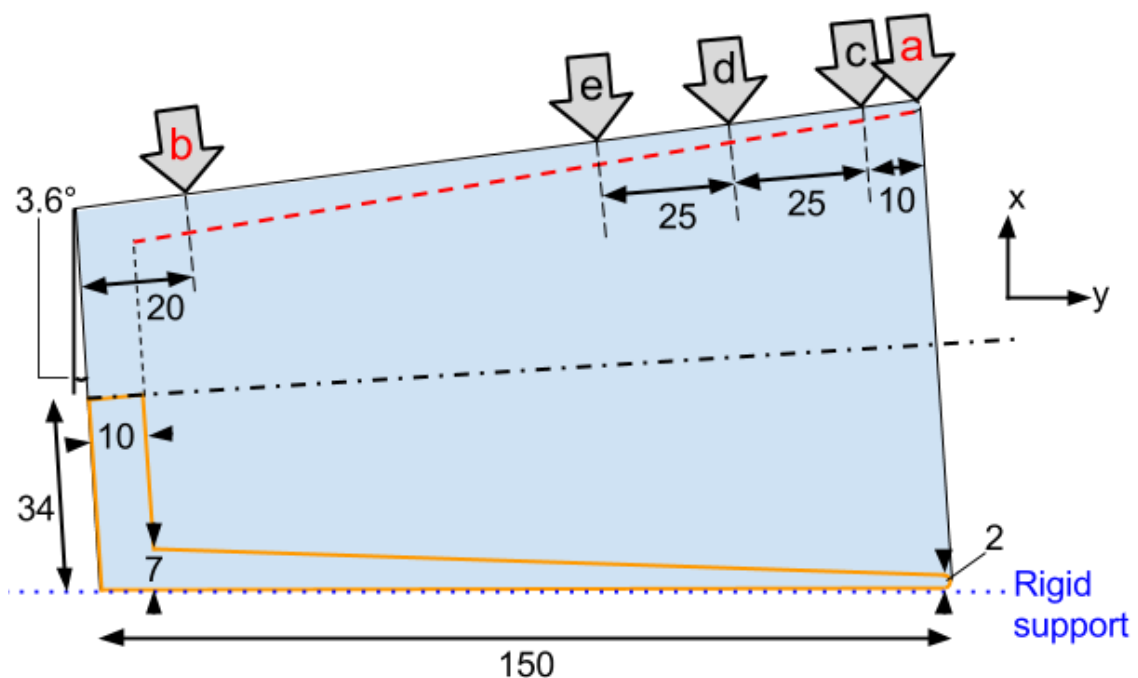


Figure 4.2 – Straight-walled pint glass CAD model profile dimensions for FEA simulations. All dimensions are given in mm. Arrows a and b correspond to rim and near-base loading positions for section 4.2.2.1, respectively. Arrows c, d, and e correspond to loading positions used in section 4.2.2.2.

The applied load for both locations was 7.85 N in magnitude. Since this is a static stress analysis, the stress magnitude scales with the applied load and therefore the choice of a particular load does not have an effect on the stress distribution. The near-base load was applied over a circular area of 6.25 mm radius, and the rim load was applied over a semi-circular area also of 6.25 mm radius. This loading area does not replicate the contact area that

would be achieved with a steel or aluminium impactor as used in section 4.4.5 for impact testing, but may reflect the contact area expected in real-life glassing attacks. The simulation mesh was constructed using 3D stress hex elements (type C3D8R) with a minimum length of 0.6 mm. The Young's modulus and Poisson's ratio were taken as 74 GPa and 0.22, respectively [7], and the glass was assumed to be linearly elastic.

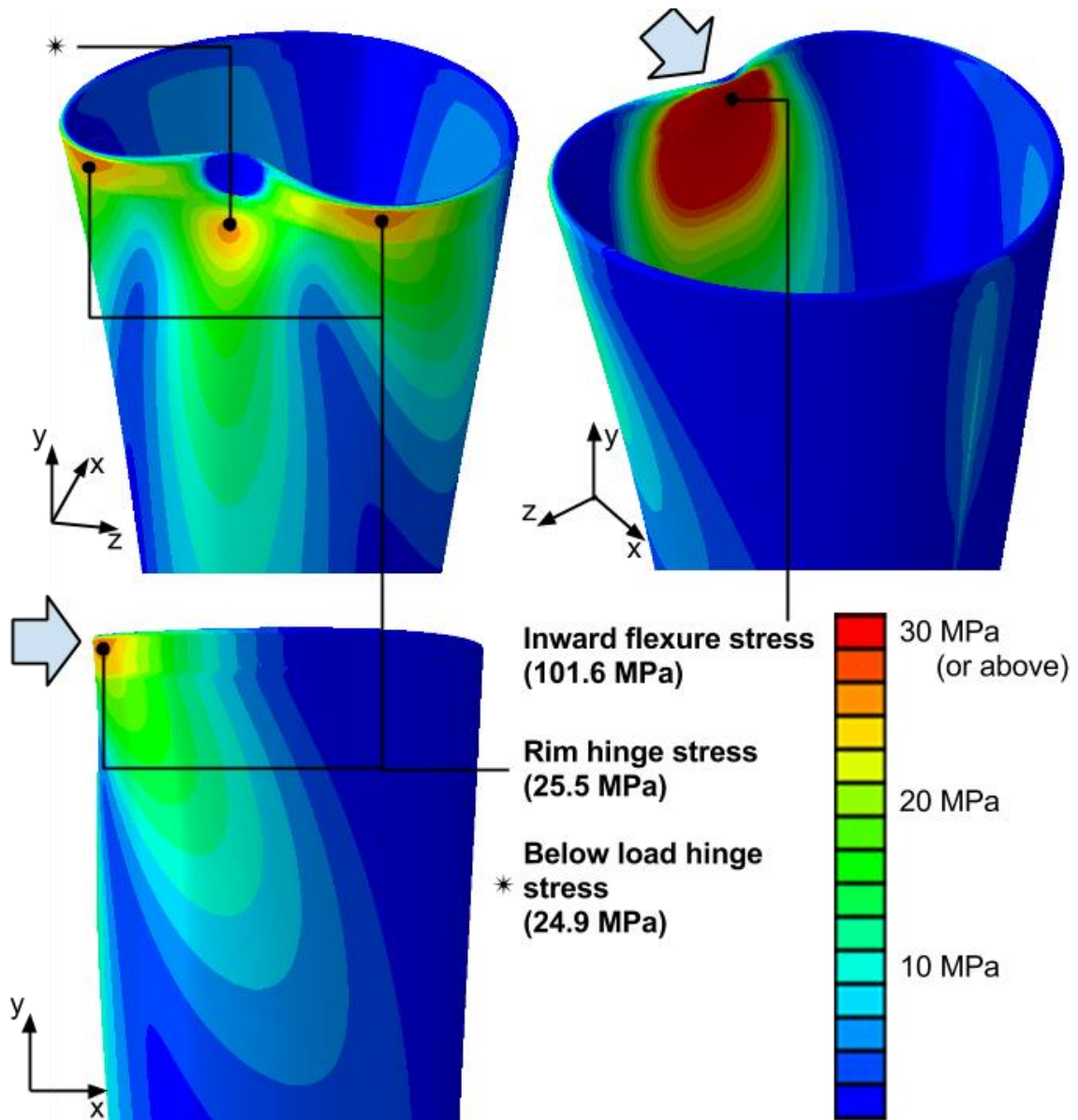


Figure 4.3 – 1<sup>st</sup> principal stress systems developed on a straight-walled pint glass subjected to a static load of 7.85 N at the glass rim. Loading direction is shown by the blue arrows. The deformation scale factor is  $6.42 \times 10^7$ .

**Rim-loaded glass (loading location a):** Various views of the 3D 1<sup>st</sup> principal stress distribution for the rim-loaded glass are shown in Figure 4.3. The maximum 1<sup>st</sup> principal stress magnitude was located within the inward flexure stress system (101.6 MPa). This covered a larger area of the pint glass surface than other stress systems. Three hinge stress areas were identified: one

either side of the loading location (rim hinge stresses), and one beneath the loading location. The maximum 1<sup>st</sup> principal stress in these regions was approximately one quarter of that for inward flexure stress.

The 1<sup>st</sup> principal stress magnitude decreased with vertical distance from the rim for all tensile stress systems. Additionally, rim hinge stress areas spanned an area which rotated around the outside wall of the glass (see bottom-left in Figure 4.3). Further areas of 1<sup>st</sup> principal stress developed on the opposite side of the glass to the loading location on both the inside and outside glass walls. This peaked at ~6 MPa.

The simulations did not show any significant contact stresses. This is most likely due to the following:

- Frictional effects were not included in the model.
- The mesh size could have been greater than the effective area for contact stresses.
- The compliance of the pint glass geometry is likely to be greater than that for a bottle because it has a wider opening at the glass rim.

**Near-base-loaded glass (loading location b):** Two views of the 3D 1<sup>st</sup> principal stress distribution for the near-base-loaded glass are shown in Figure 4.4. Overall, the stresses were much lower in magnitude than for the rim-loaded glass. This is most likely due to the lower compliance of the pint glass when loaded at a location closer to the base.

As with the rim-loaded simulation, the maximum 1<sup>st</sup> principal stress was located within the inward flexure stress system (11.3 MPa). However, this was ~10 times smaller in magnitude than the maximum 1<sup>st</sup> principal stress in the rim-loaded stress system. The next largest stress system was a hinge stress below the loading location which was similar in magnitude to the inward flexure stress. Side hinge stresses were low in magnitude (~1.2 MPa) but covered a large area. Opposite stress regions peaked at 5 MPa in magnitude.

Overall, the glass was far more structurally robust when loaded near to the base. This is most likely due to the higher stiffness in the base region compared to the rim region. Consequently, more of the load was transferred to the formation of compressive stresses. The inward flexure stress system produced with the rim-loaded glass was the largest in magnitude overall, and spanned a large area. This stress system is therefore considered further in the following subsection.

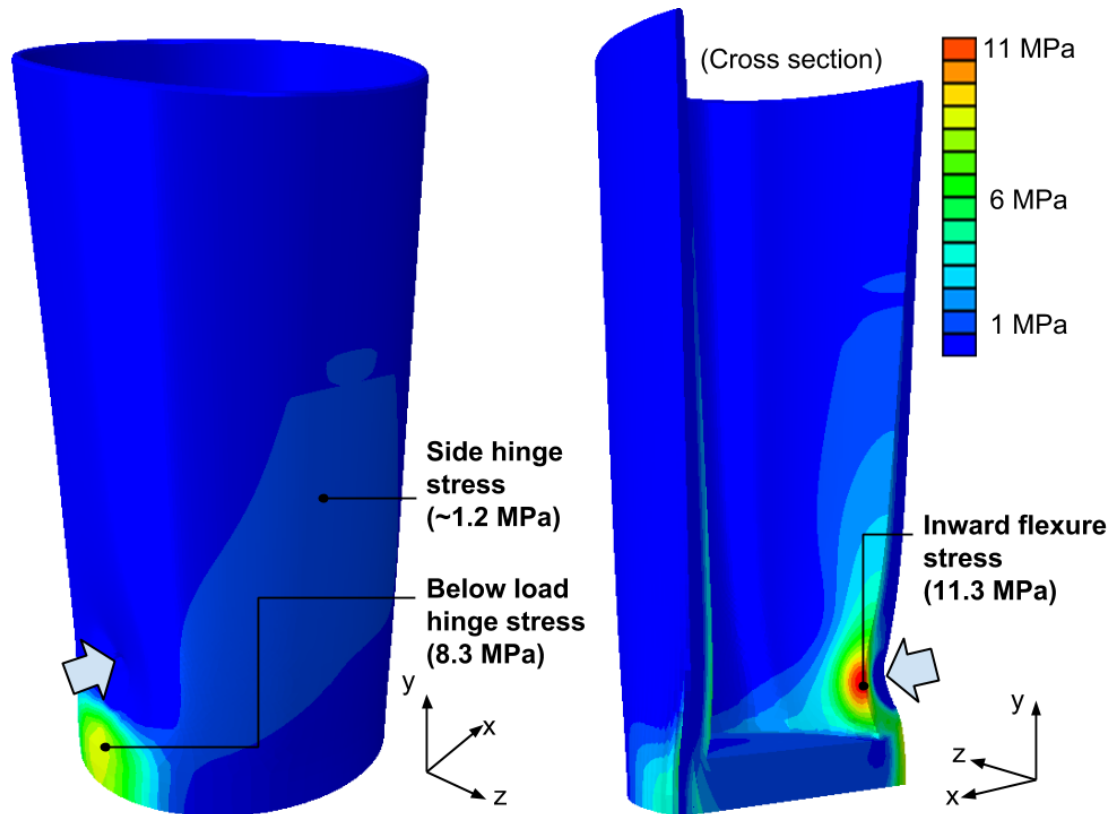


Figure 4.4 – 1<sup>st</sup> principal stress systems developed on a straight-walled pint glass subjected to a static load 20 mm from the glass base. Loading direction is shown by the blue arrows. The deformation scale factor is  $1.53 \times 10^9$ .

#### 4.2.2.2 Comparison of inward flexure stress in straight-walled and Nonic glasses

This sub-section details an investigation into the inward flexure 1<sup>st</sup> principal stress of a straight-walled pint glass and a Nonic pint glass subjected to static loading. The aim of the investigation was to determine whether the glass geometry resulted in significant differences in the magnitude of inward flexure stresses.

Inward flexure stress (defined in Figure 4.1) was selected for further investigation as it was found to result in the largest 1<sup>st</sup> principal stress magnitude caused by static loading in the previous sub-section. Additionally, it spans a significant portion of the inside pint glass wall. This further increases the likelihood that the critical stress intensity will be reached at a flaw within this area. A Nonic glass shape was chosen for investigation due to its extensive use in UK pubs and bars.

**Model properties:** 6 FEA static simulations were conducted with similar model conditions to those detailed in the previous sub-section. The material properties, loading area, and load magnitude were unchanged. The same dimensions for the straight-walled glass were used. The dimensions of the Nonic CAD model are given in Figure 4.5. The radius of curvature of the

Nonic bulge was based on measurements taken from CT scans detailed in section 4.4. All other glass dimensions were retained from those detailed in Figure 4.2 to aid with the comparison of results.

Three loading locations were specified for each glass. These are designated c, d, and e in Figures 4.2 and 4.5. The locations were chosen based on the dimensions of the Nonic CAD model. Load c was applied 10 mm from the glass rim, at the equivalent impact location for impact tests detailed in section 4.4. Load d was applied to the centre of the Nonic bulge, and load e was applied so that it was the same distance from d as location c. The same load location distances (c, d, and e) from the glass rim were used with the straight-walled glass, as shown in Figure 4.2.

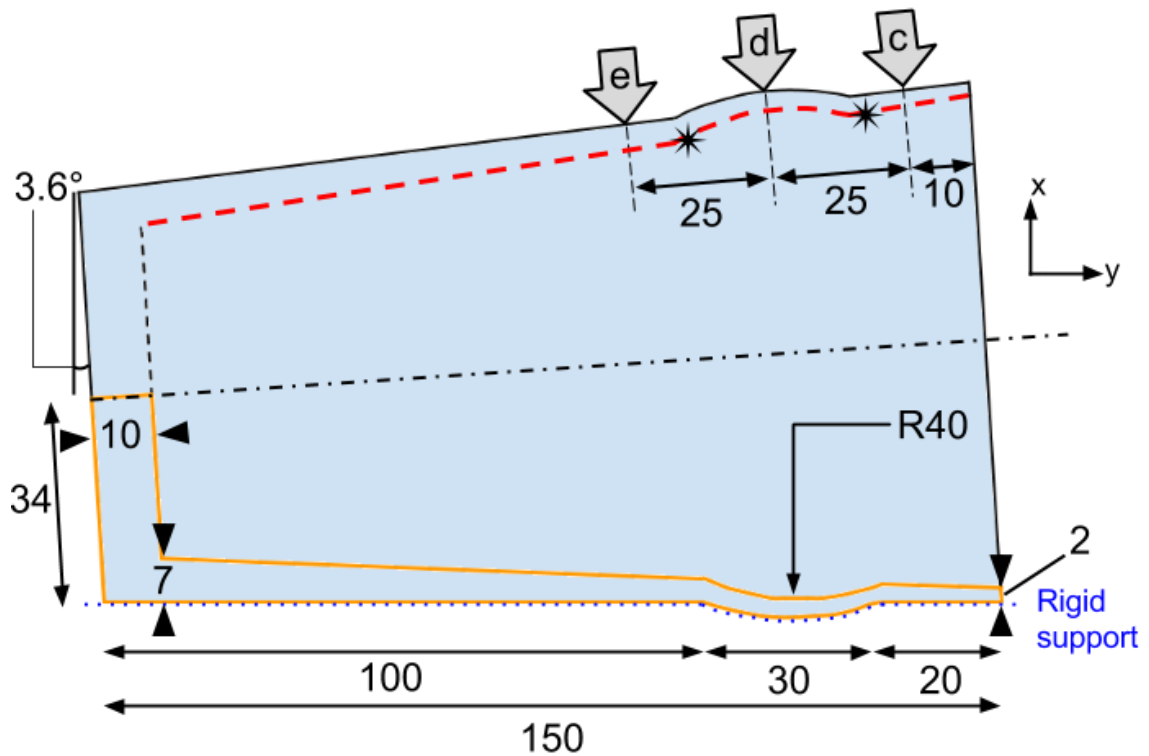


**Figure 4.5 – Nonic pint glass CAD model profile dimensions for FEA simulations in section 4.2.2.2. All dimensions are given in mm. The radius of curvature of the Nonic bulge was 40 mm. Arrows c, d, and e are the 3 loading locations chosen for the investigation.**

**Simulation results:** Graphs of the inward flexure stress distributions along the inside glass wall for each simulation are shown in Figure 4.6. These graphs show the 1<sup>st</sup> principal stress on the inside wall over a line that passes through the inward flexure area from the rim to the inside-base (shown as a red dashed line in Figures 4.2 and 4.5). An inset of the 3D model for each Nonic glass is also shown in Figure 4.6. The deformation of these models is scaled by a factor of  $\sim 10^7$ .

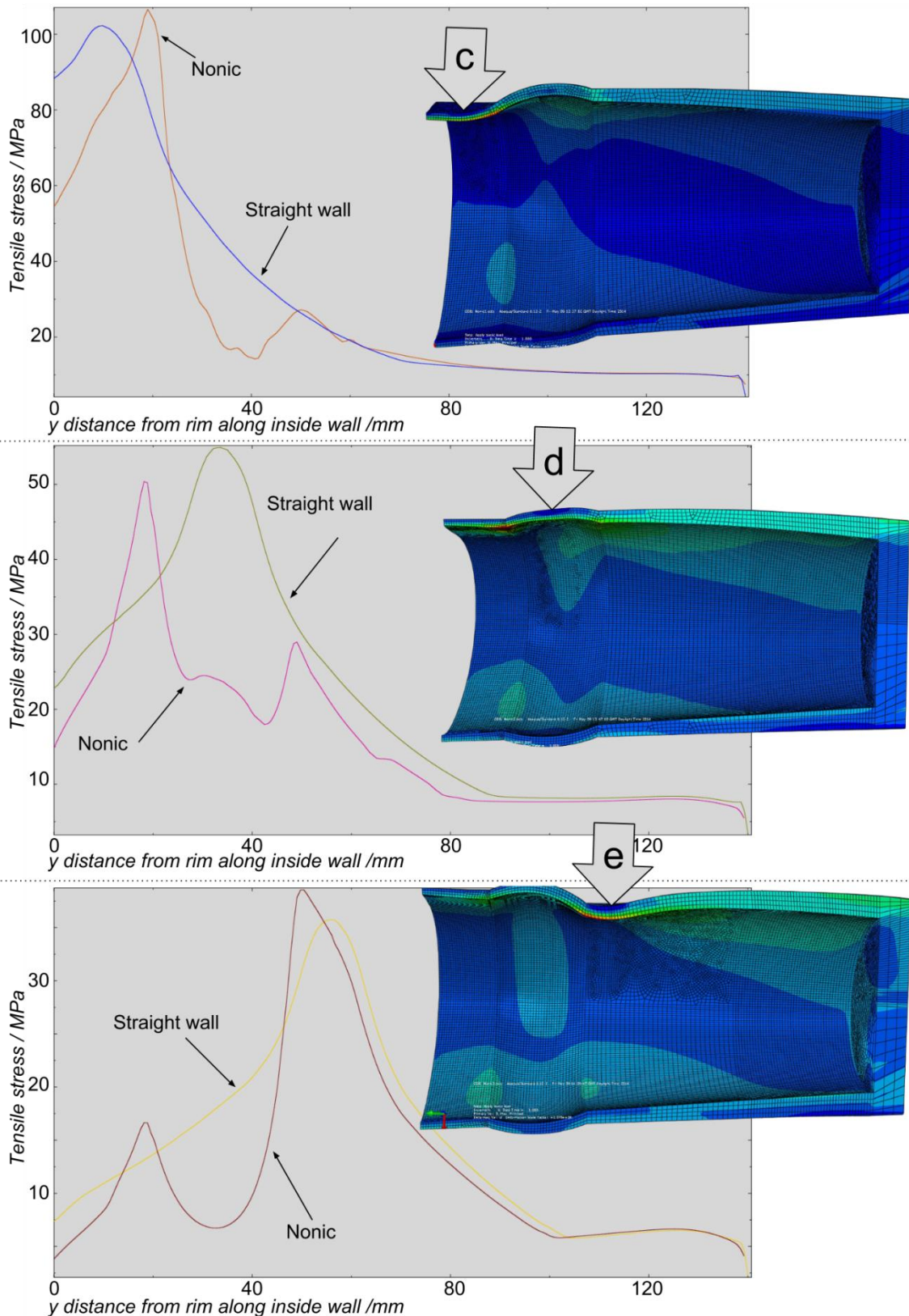


Figure 4.6 – Inward flexure 1<sup>st</sup> principal stress distribution along inside glass walls for FEA simulations detailed in section 4.2.2.2. Loading location is shown by arrows, and corresponds to Figure 4.5. Top, middle, and bottom graphs are the tensile stress distributions for load locations c, d, and e respectively. Each inset is the stress distribution and deformation simulation for the Nonic glass. Scale factor for each inset is of the order of  $10^7$ .

As with the rim-loaded and base-loaded simulations in the previous sub-section, the maximum 1<sup>st</sup> principal stress in the inward flexure area was higher for loading locations closer to the glass rim. For the straight-walled glass, this maximum location was always directly below the loading location. By contrast, the location of the maximum 1<sup>st</sup> principal stress concentration for the Nonic glass was always at one of the two points where the glass bulge intersects the straight-walled region. These points are indicated by asterisks in Figure 4.5. The deformed FEA plots inset into Figure 4.6 suggest that these bulge stress concentration areas serve as additional hinges under loading.

The maximum 1<sup>st</sup> principal stress value for simulations loaded at locations c and e was higher in the Nonic glass than in the straight-walled glass. However, for loading location d, where the Nonic was loaded at the peak of the Nonic bulge, the maximum stress value was greater in the straight-walled glass. The geometry of the bulge is conducive to the development of more compressive stresses, and in all simulations the inward flexure stress at the peak of the bulge was significantly less than the maximum overall 1<sup>st</sup> principal stress. Despite these differences in stress distributions between the two glass shapes, the maximum overall 1<sup>st</sup> principal stress is never more than ~9% greater in one glass loaded at the same location.

The initial loading conditions may be changed as a consequence of the glass geometry. For example, if the glass was loaded by being knocked over onto its side, the straight-walled glass would most likely fall so that its rim impacted the surface. This may result in a stress distribution like that produced in Figure 4.3 (loading location a). By contrast, the Nonic glass may be expected to fall so that the bulge impacts the surface. This may result in a stress distribution like that shown in Figure 4.6 for loading location d. The maximum inward flexure stress in this case is approximately 50% less than that for the straight-walled glass. This would decrease the likelihood of  $K_{Ic}$  being reached for the same uniform flaw distribution.

#### **4.2.2.3 Conclusions**

Section 4.2.2 has shown and discussed the results of 7 FEA analyses into the stress systems produced in pint glasses in static loading scenarios. The main conclusions of this work are as follows:

- Pint glasses are significantly weaker when loaded at the rim as opposed to closer to the base.
- The inward flexure stress system produces the highest 1<sup>st</sup> principal stresses in a pint glass, and spans a larger area than other stress systems. However, contact stresses were not considered in the simulations.

- Hinge stress systems have maximum 1<sup>st</sup> principal stress values of approximately one quarter of that for inward flexure stress systems. An additional hinge stress develops below the impact location.
- For Nonic glasses, the inward flexure stress concentrates at specific locations near the glass bulge. This can make it structurally more robust if loaded on the outside wall at the peak of the bulge (see Figure 4.6).

There are a number of possibilities for further investigation on this work. There are also certain elements of the simulations detailed above that could be improved. Firstly, more realistic loading conditions incorporating friction and velocity impact would allow for contact stresses and time-dependent dynamic effects to be investigated. Secondly, investigating the same loading conditions for more pint glass shapes would further elucidate the effect of glass geometry on stress distributions.

The following section details fractographic investigations into externally impacted pint glasses, and considers the results of the FEA analyses from the above section alongside typical fracture characteristics.

### **4.3 Fracture characteristics of pint glasses and other glass drinkware subjected to external impact**

This section details the results of a fractographic investigation into the fracture characteristics of various glass drinkware. This includes the analysis of standard and premium tempered pint glasses purchased as-new from wholesalers, and also a number of used drinking glasses that had been donated by various local pubs and hotels.

Section 4.3.1 gives an overview of the scope of the fracture investigation. This includes the glasses tested, the testing methods, and preparation techniques. Section 4.3.2 details the general macroscopic fracture characteristics (y-z plane) observed over the course of experimentation. Similarly, section 4.3.3 details general fracture surface characteristics (x-y plane) observed over the course of experimentation. Section 4.3.4 details the fracture characteristics of a number of individual glasses. Section 4.3.5 summarises the main findings of these sections and suggests how the investigation could be improved.

#### **4.3.1 Overview**

A total of 74 glasses were fractured as part of this investigation. A full overview of the drinking glasses, impact locations, and impact methods used in this investigation is given in Appendix B. Appendix B also includes brief descriptions of the fracture characteristics of some glasses not

mentioned in the main text. The majority of glasses were initially taped in order to retain the macroscopic fracture pattern, and then fractured by impact. The source of impact was either by a controlled drop tower impact test (as outlined in section 3.6.2.1) at various locations on the glass wall, or by manual impact. Manual impacts were conducted by holding a glass near the base and hitting part of the exposed glass wall onto the edge of a cast iron table. Appropriate safety equipment was worn for this. Additionally some punch tests were conducted to evaluate residual stress levels.

The involved nature of examining the fracture surfaces of broken glass articles meant that detailed fracture surface investigation was limited to a small number of samples. Therefore a large portion of the discussion in this section focuses on fracture characteristics of individual samples as well as discussion of general fracture trends. A more systematic and quantitative investigation of pint glasses on a larger quantity of samples is detailed section 4.4. The results from this section were used to guide the design of that investigation.

#### **4.3.2 General characteristics of macroscopic fracture patterns (y-z plane)**

The key difference between the behaviour of annealed and tempered pint glasses was the fragmentation characteristics of the base region of the glass. In most annealed fractures, the glass base remained intact with pointed edges travelling outwards (see Figure 4.8c). When tempered pint glasses fractured, the base of the glass invariably underwent extensive fragmentation. The macroscopic fracture patterns in the top region of fractured annealed and tempered glasses were similar, typically showing a star-like fracture pattern centred around the impact location, although there was a slightly higher level of fragmentation in tempered pint glasses. This is shown in Figure 4.7.

A common feature of the fracture pattern for all impacted drinking glasses was the tendency of the cracks to follow the same fundamental pattern. This pattern showed a high degree of symmetry, as seen in Figure 4.7 and in an alternate view in Figure 4.8a. Cracks travelled from the point of impact predominantly upward and downward in a longitudinal direction. Cracks most leftward and rightward of impact deviated towards the circumferential orientation more than other cracks. Subsequently, the cracks attempted to loop back upwards to the longitudinal direction, 180° from the impact point. This produced many boomerang-shaped fragments, as can be seen below the curved arrow in Figure 4.8a and isolated in Figure 4.8b.

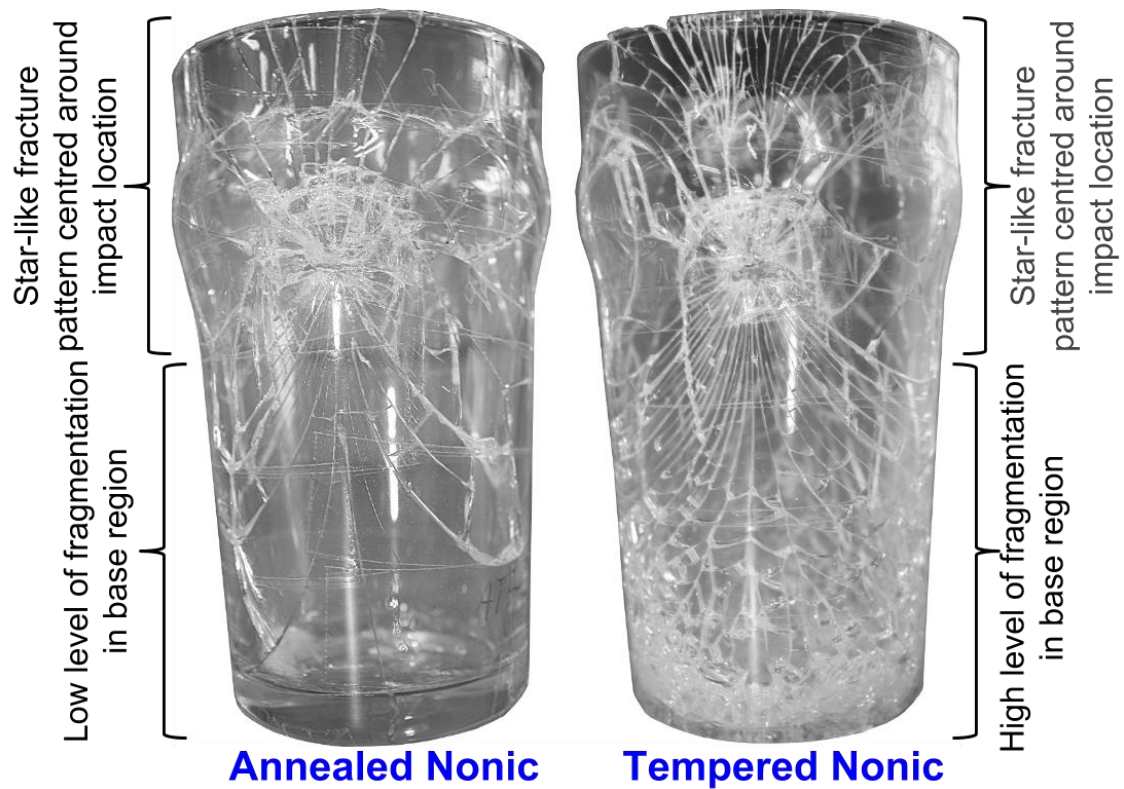


Figure 4.7 – Annealed and tempered Nonic glasses broken by manual impact onto a table edge. Similar fracture patterns can be seen in the top region of the two glasses.

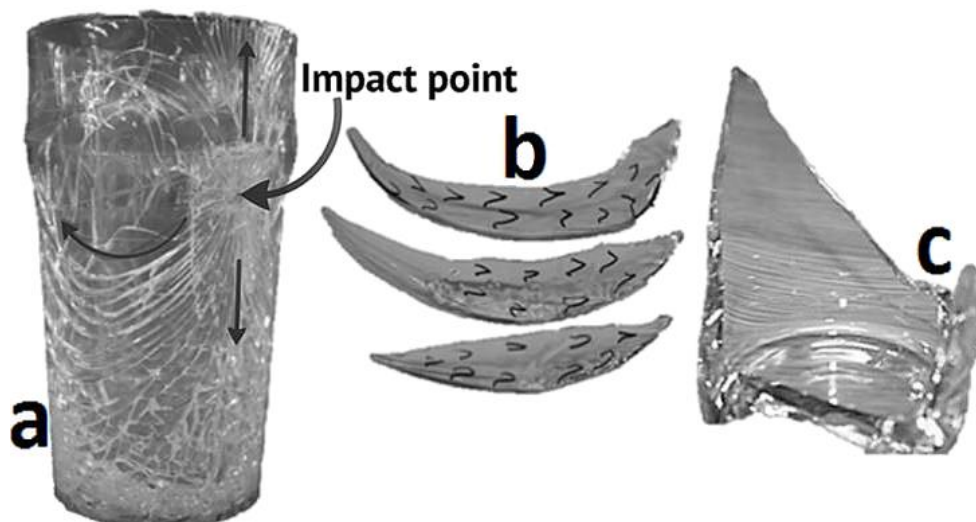
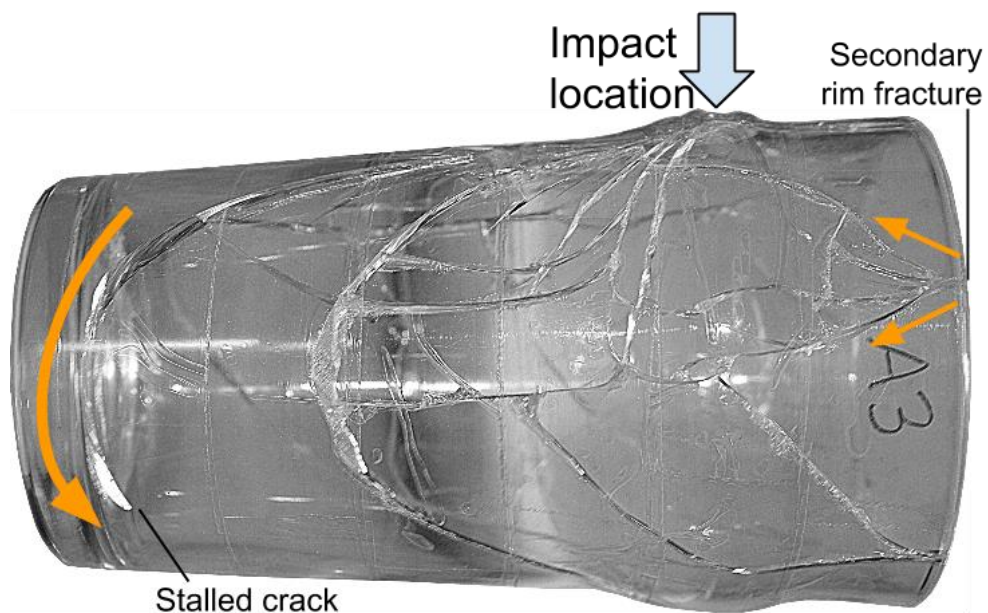


Figure 4.8 – (a) A tempered Nonic glass broken by manual impact. The glass is oriented such that the looping nature of the cracks is emphasized (curved arrow). Longitudinal arrows illustrate the predominantly longitudinal cracking direction. (b) Curved boomerang-shaped shards isolated for emphasis. (c) Half-intact annealed Nonic glass base post-fracture.

Since a crack always propagates normal to the maximum tensile stress at the crack tip, the observed change in propagation direction implies a gradual rotation of maximum tensile stress orientation. Specifically, the tensile stress at the impact location was typically highest in the circumferential (hoop) direction. This switched to the longitudinal direction nearer the hinge

stresses at an acute angle from impact, before becoming predominantly longitudinal again on the opposite side, 180 degrees from impact. A similar description for the rotation of the maximum tensile stress orientation was given by Kepple and Wasylyk for glass containers [5].

Cracks forced to loop around the side of the glass require more energy for propagation. This is because the change in crack orientation necessitates the development of a mode III stress component, as opposed to cracks that propagate directly in the longitudinal direction [8]. Additionally, as the crack travels away from the impact location, the magnitude of tensile stresses caused by loading decreases (see Figure 4.3). Consequently, looping cracks in annealed pint glasses regularly stalled after or during looping (see Figure 4.9).



**Figure 4.9 – Annealed Nonglass fractured due to manual impact, viewed 90° from impact location.**

The most common location for the fracture origin was within the inward flexure stress system, either directly beneath impact or at the glass rim. Additionally, secondary origin fractures occurred on several pre-taped pint glasses 45 – 90° from the impact location due to hinge stresses, as shown in Figure 4.9. These either propagated longitudinally downward from a rim flaw, or longitudinally upward from an already propagated crack.

High speed videos taken of pre-taped pint glasses showed that secondary origin fractures were initiated by the continued imparted energy of the impactor after the primary fracture (see Figure 4.10). They were therefore considered to be an artefact of using tape to retain the fracture pattern, and would not be expected to occur on unrestrained pint glasses. Furthermore, this continued applied force immediately after fracture caused the fracture

surfaces of some fragments to abrade against each other, creating a fine glass dust that accompanied all glass fractures.

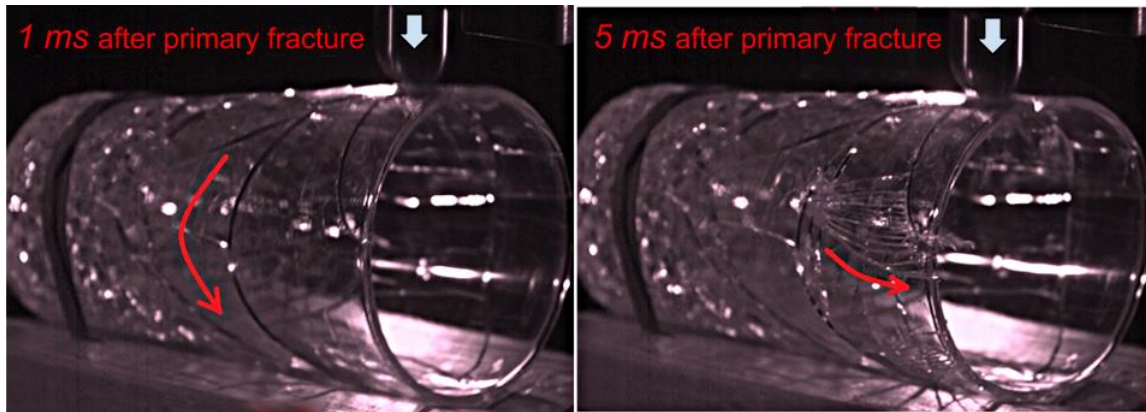


**Figure 4.10** – Frames from high speed video (1000 frames per second) of drop tower impact of a pre-taped Ultimate Pint glass. The left image shows the fracture pattern 1 ms after fracture was initiated. 5 ms after fracture was initiated, additional cracks propagate longitudinally, 90° from the impact location due to continued imparted energy of the impactor.

As-received new glasses required particularly high impact energies to cause fracture, which resulted in a greater level of fragmentation and volume of glass dust after fracture. An example of a new tempered glass fractured with an impact energy of ~20 J is shown in Figure 4.11. Despite the high level of fragmentation, the overall fracture pattern showed the same symmetrical looping characteristics 90° from the impact location.

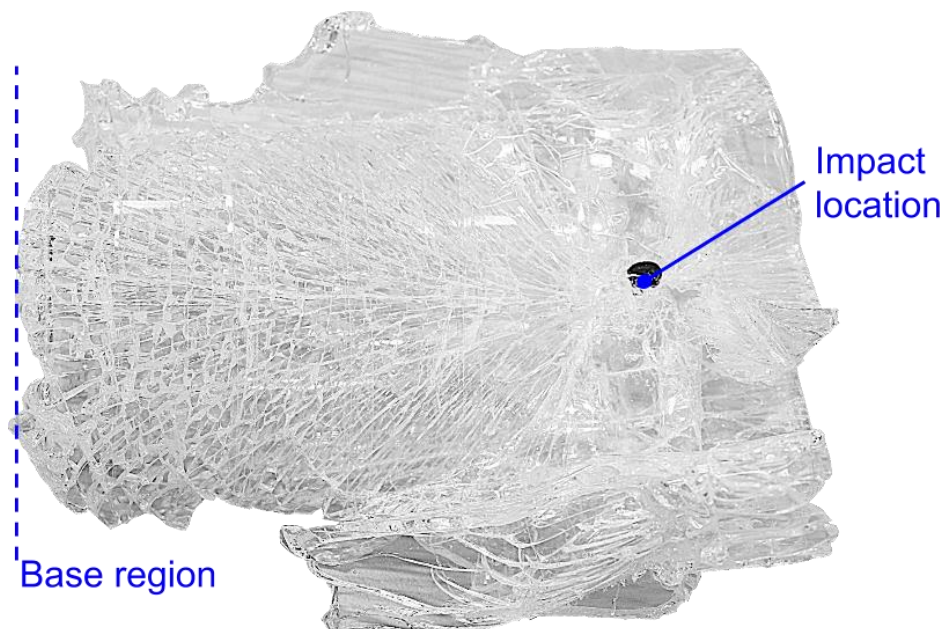


**Figure 4.11** – Fracture pattern of an as-received new Nonic glass broken at high impact energy (~20 J).

In glasses where the fracture originated from the rim, characteristic triangular-shaped fragments were produced that divided the origin. Figure 4.12 shows examples of rim fractures

from two different loading scenarios. The left image in the figure shows an abraded Ultimate Pint glass broken by being dropped from a 1 m tall table onto a concrete floor. The glass landed at the rim, and the fracture subsequently propagated from the rim with the symmetrical looping characteristics described above. The right image in the figure shows an as-received new Ultimate Pint glass broken by manual impact. In this case,  $K_{Ic}$  was reached at the rim rather than directly below the impact location. Since the maximum tensile stress was located beneath the impact location, the cracks propagated towards it before propagating with the same symmetrical looping characteristics.

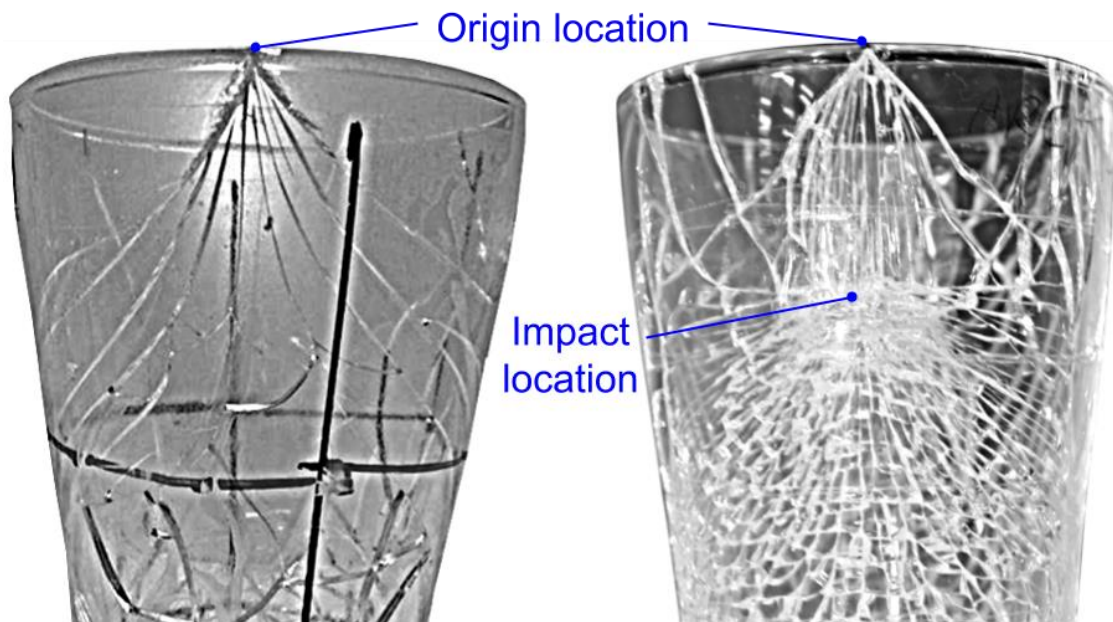


**Figure 4.12 – Ultimate pints with rim-located origins. Left: Abraded glass, dropped from a 1 metre tall table. Right: As-received new glass, broken by manual impact.**

Further details of macroscopic fracture characteristics of individual glasses are given later in this section. The following sub-section continues by overviewing general characteristics of the fracture surfaces of annealed and tempered drinking glasses.

### 4.3.3 General fracture surface characteristics (x-y plane)

In annealed glasses, the main propagating crack led on either the inside or the outside of the glass wall depending on the location of the maximum tensile stresses due to loading. An example of annealed glass fracture surface showing a crack leading on one side is given in Figure 2.15.

For annealed glasses broken due to inward flexure stresses, the crack led on the inside glass wall throughout the fracture event. By contrast, for glasses which broke by hinge stresses, the tensile stress acting on the opposite side to the leading crack was often great enough to see it

change leading sides. The fracture surface in Figure 4.13 shows a point at which a propagating hinge stress crack leading on the outside glass wall switches to the inside wall surface under the influence of inward flexure stress.

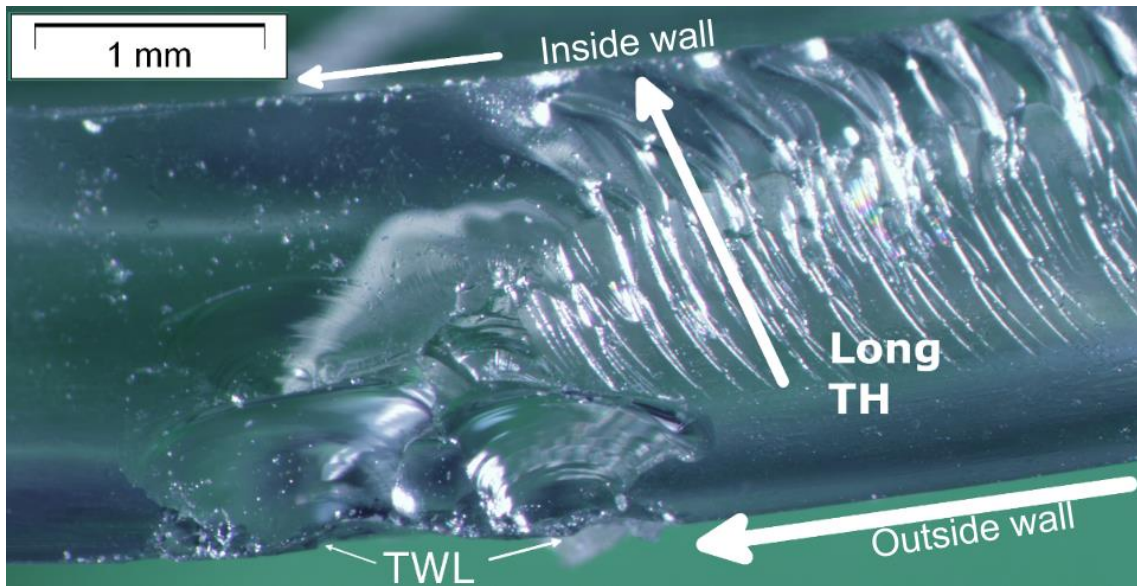


**Figure 4.13** – A fracture surface observed on an annealed Nonic glass fragment broken by manual impact showing a crack leading on one side switch to the other. Travelling right to left, the crack is initially leading on the outside wall surface before switching over to the inside wall surface where the magnitude of tensile stress is greater.

Near to the base of tempered glasses, the crack was seen to have propagated centrally through the thickness, following the tensile mid-plane. An example of a centrally leading crack on a tempered glass fracture surface is shown in Figure 2.15. Near to the rim of the glass, the crack front led closer to a particular side (see Figure 4.14). This is partly due to the greater magnitude of tensile stress caused by external loading in the rim region, but may also be due to a lower magnitude of residual stress in the rim region.

The leading location of the crack front is dependent on a competition between the applied stress and the residual stress. The greater the tensile stress on a particular surface due to external loading, the further the interior band of tensile residual stress tends towards that surface. Towards the bottom of the glass, the interior tensile stress is dominant and the crack is seen to lead and branch near the mid-plane. This is because there is negligible externally applied stress at this point, and the crack propagation is driven almost exclusively by the residual tensile stress.

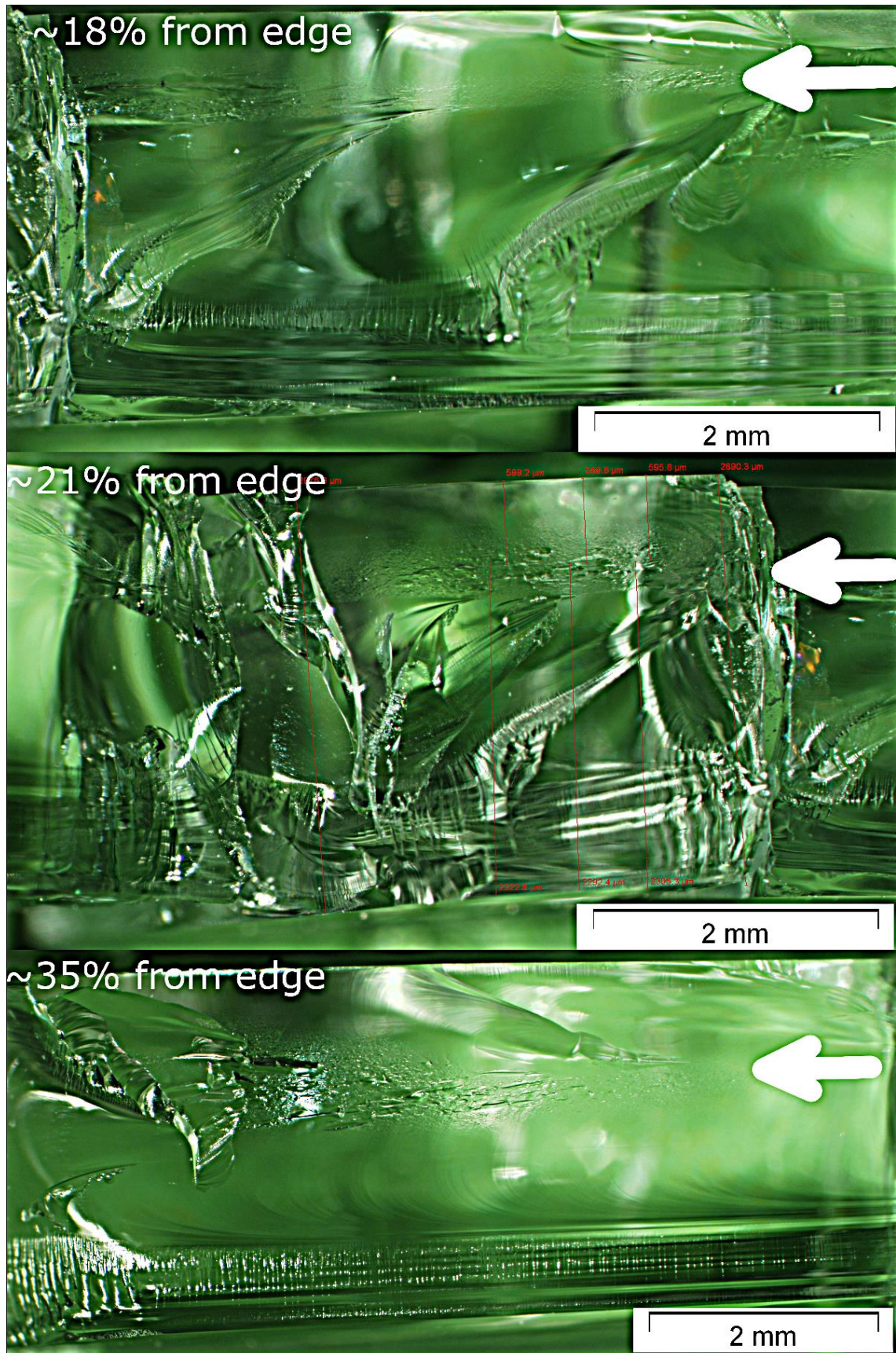
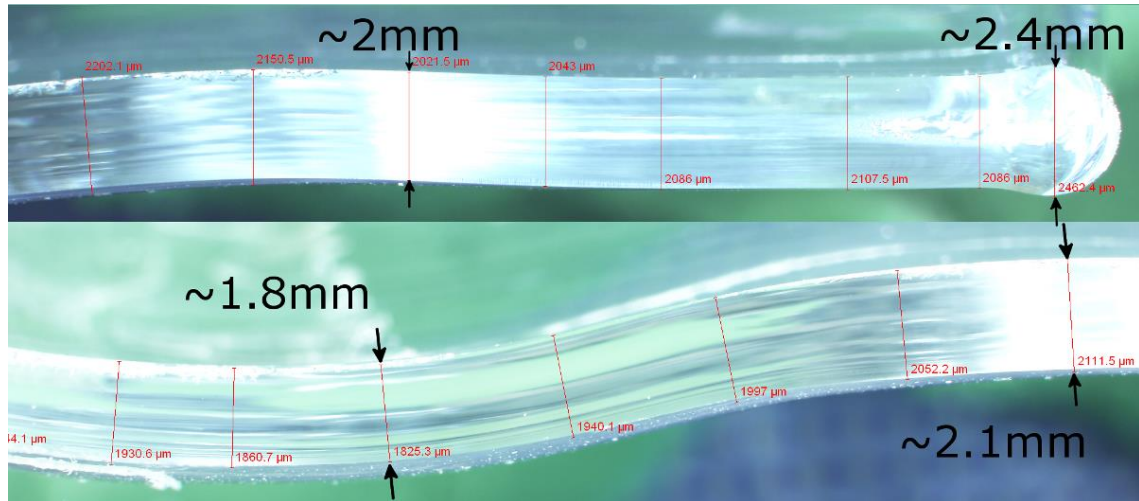


Figure 4.14 – Three fracture surfaces from the same broken tempered pint glass, all showing the crack lead from right to left. Top image is the fracture surface 1.3 mm from the rim of the glass, middle image shows the fracture surface 1.6 mm from the rim, and the bottom image is 2 mm from the rim.

By observation of fracture surfaces of fragments from different portions of the glass, it was clear that the wall thickness was lower near the rim of drinking glasses than near the base. Furthermore, the wall thickness in the bulge region of Nonic glasses was less than in other regions. This is demonstrated by images of the wall profile given in Figure 4.15. The wall thickness of glasses is investigated in further detail with CT scans in section 4.4.



**Figure 4.15 – Optical micrographs of the wall profile of a Nonic pint glass. Top image shows the rim region of the glass, and the bottom image shows the bulge region of the same glass. The wall thickness at the bulge is seen to decrease by ~15%.**

This section has detailed general fracture surface characteristics observed on broken drinking glasses. The following sub-sections compare and overview a number of fracture characteristics of individual glasses.

#### 4.3.4 Fracture characteristics of individual glasses

##### 4.3.4.1 Premium pint glasses

Of the two premium glasses investigated, the Perfect Pint generally broke into smaller, more consistent shards (Figure 4.16, bottom). The Ultimate Pint typically broke with fairly large shards nearer the glass rim (Figure 4.16, middle), with the base in both glasses fragmenting extensively. Fracture surfaces were usually relatively featureless. The majority of visible features were: regions of mist prior to branching; small concentrations of twist hackle at the surfaces; and shear hackle around corners. Further investigation into the wall thickness, residual stress levels, impact performance, and fragmentation density of these glasses is detailed in section 4.4.

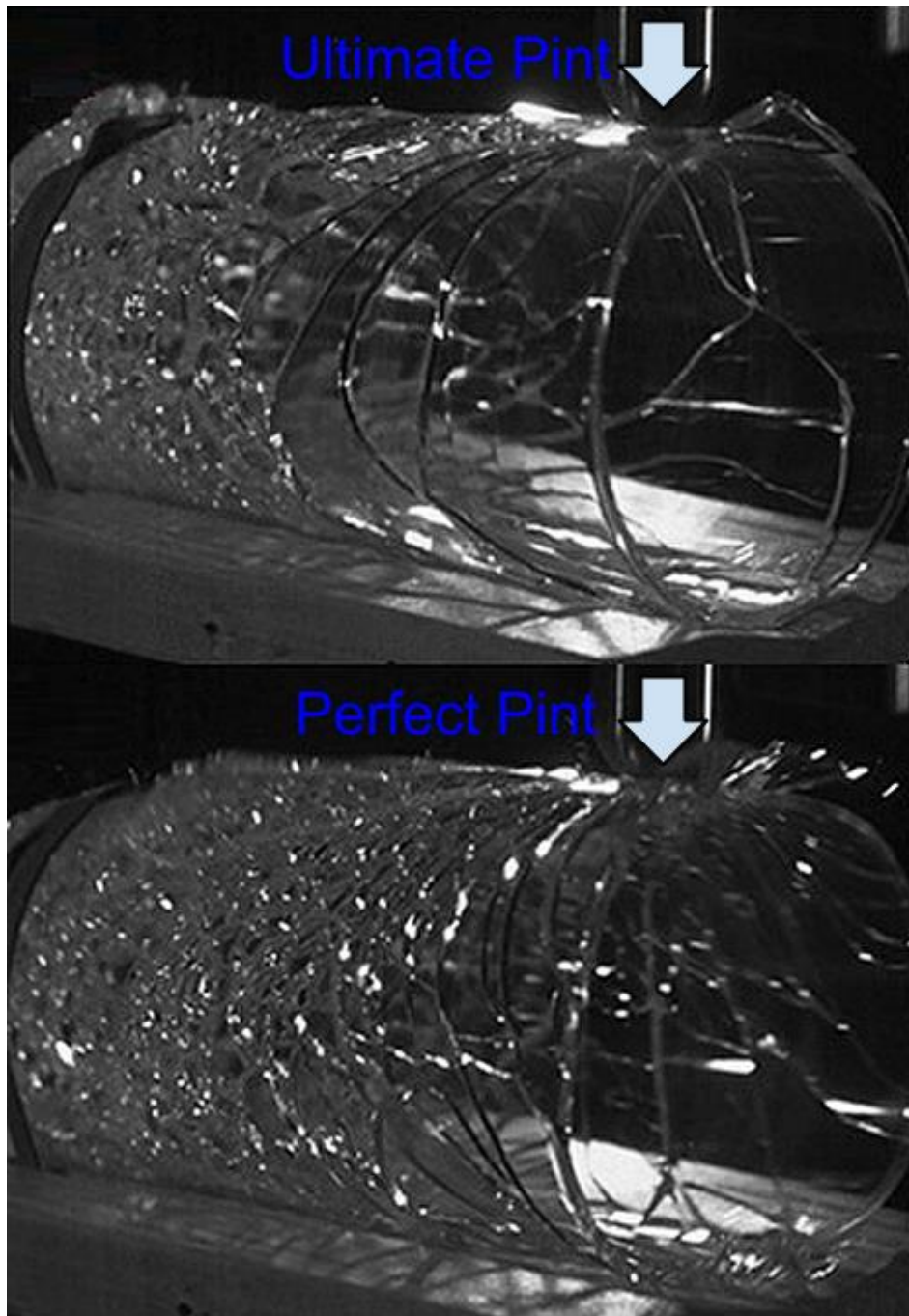


Figure 4.16 – Frames taken from high speed video footage (1000 frames per second) of drop tower impacts to an Ultimate Pint glass (top) and a Perfect Pint glass (bottom). Neither glass was taped prior to impact.

#### 4.3.4.2 Geometrical influence on fracture patterns

**Nonic tempered pint glasses:** An alternative view of the same tempered Nonic glass as shown in Figure 4.8a is given in the left image of Figure 4.17. It can be seen that a series of almost equidistant cracks (parallel to the arrow) are present over the glass bulge, which all branch when the crack front reaches the straight-walled portion of the glass near the rim. This suggests a decrease in stress intensity in the bulge portion before an increase just above it. The

FEA image to the right of Figure 4.17 supports this explanation, showing a region of higher tensile stress occurring at the point of branching.

Additionally, more energy is required to propagate cracks around curves and this may further delay crack branching. The fracture surface across the bulge in Figure 4.17 is shown in Figure 4.18, which shows a large frequency of shear and twist hackle markings. This is indicative of a mode III stress component at the crack tip, as well as high energy expenditure necessary to drive crack propagation.

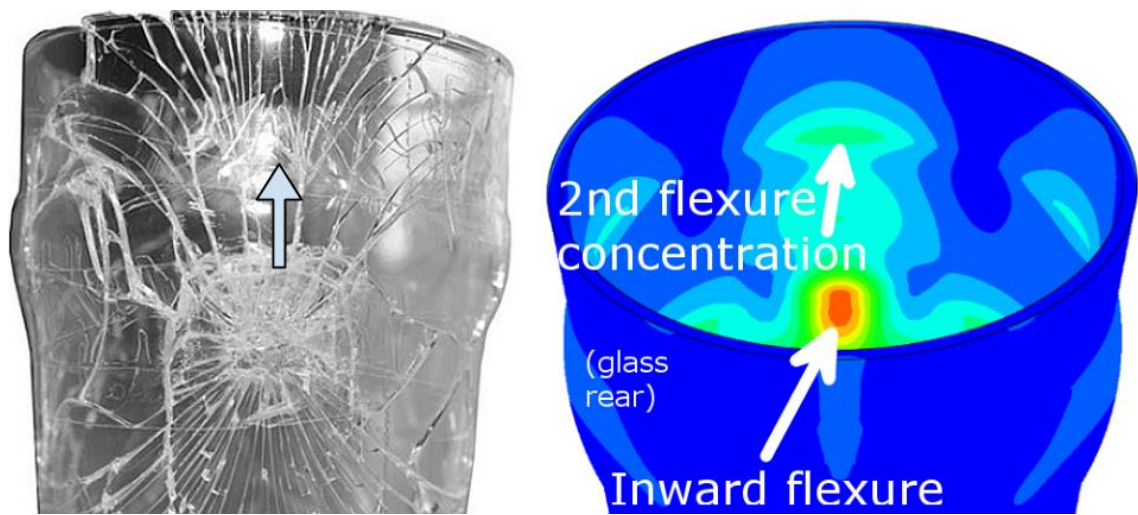


Figure 4.17 – Left: Front view of the impact location of the same broken tempered Nonic glass as that in Figure 4.8a. The fracture surface at the arrow is shown in Figure 4.18. Right: FEA simulation showing the distribution of the inward flexure stress concentrations due to a static load at the location of impact.

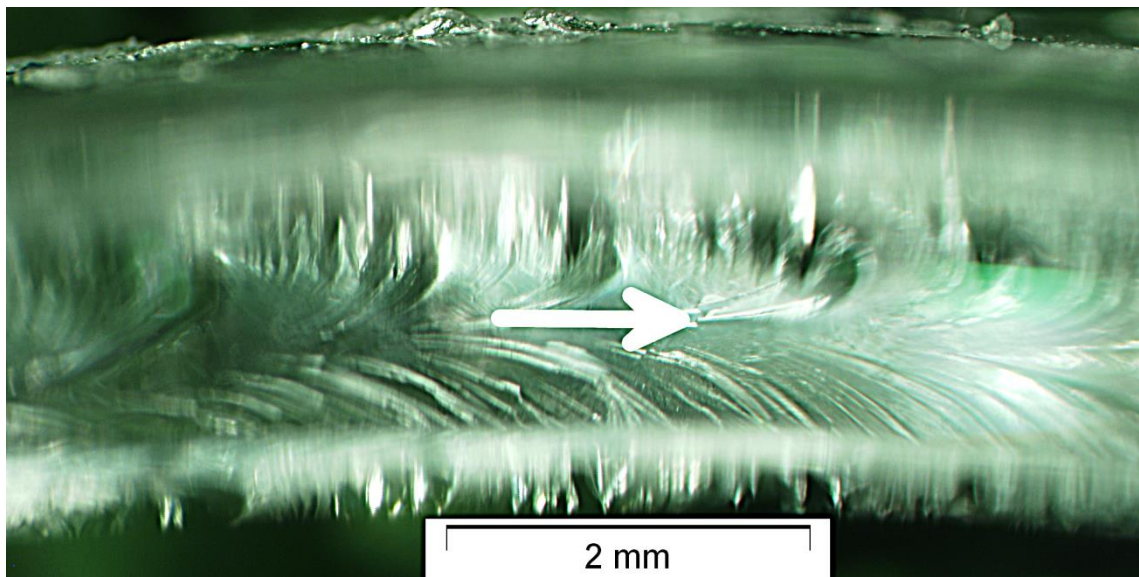
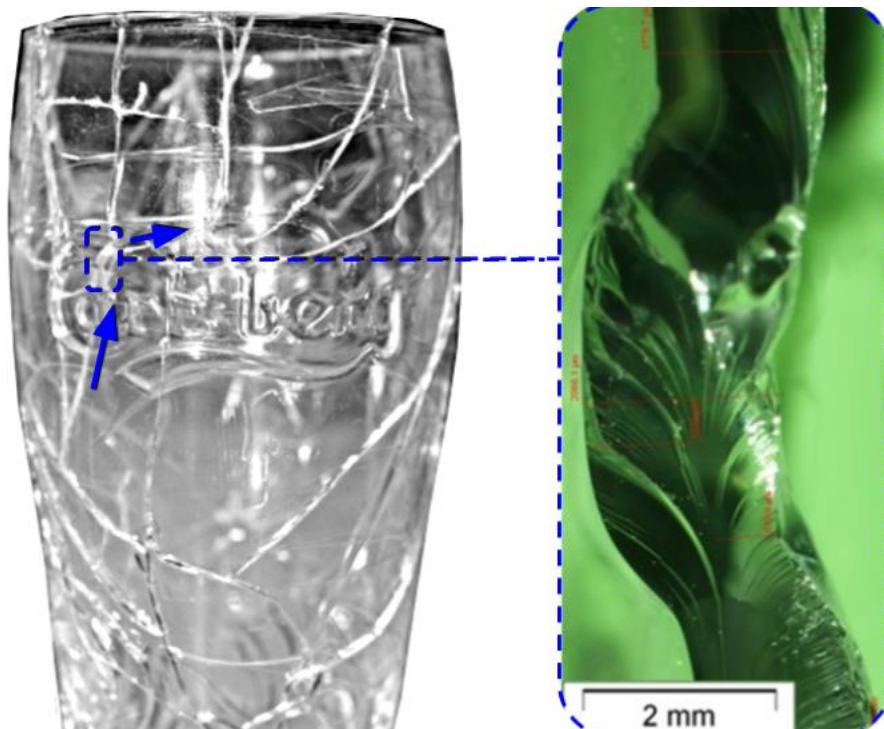


Figure 4.18 – Fracture surface from the tempered Nonic glass as shown in Figure 4.17. The crack leads from left to right with the crack front leading centrally as indicated by the arrow. The top of the figure is out of focus since it lies closer to the microscope lens.

**Embossed tempered pint glasses:** Cracks that propagated through or close to embossed features were often diverted in the y-z plane, as shown in Figure 4.19. In the figure, the propagating crack was diverted whilst passing through an embossed feature. This could be due to the change in local stress conditions at these geometrical features, or locally varying residual stress distributions. However, these effects were minor in comparison to the overall fracture pattern.



**Figure 4.19 – Left: Fracture in an embossed branded tempered pint glass, 90° from impact. Crack is diverted whilst propagating through embossing of the letter ‘C’. Right: Fracture surface from the top of the letter ‘C’ showing shear hackle similar to that shown in Figure 4.18.**

**Stemmed tempered pint glasses:** The branded stemmed pint glasses examined were subjected to: drop tower impact tests (impacted 10 mm from the rim) (x4); punch tests 10 mm from the rim (x2); and longitudinal punch tests (x2) (see Figure 4.20b).

All impact tests resulted in no fracture in the base region, leaving the stem and base fully intact (see Figure 4.20a). This is in contrast to non-stemmed tempered pint glasses where the base fractured extensively (see Figure 4.16). However, the edges appeared macroscopically more rounded than intact bases from annealed glass fractures (compare to Figure 4.8c).

Both punch tests with a punch location of 10 mm from the rim resulted in only localised fragmentation, also leaving the stem and base fully intact. The remaining two glasses were punched longitudinally above the stem to determine whether the base region had been

thermally tempered. This caused spontaneous fragmentation in the cup, stem, and base regions, confirming that thermal tempering was applied to all areas of the glass. However, the stem region remained intact despite cracks being visible. This is most likely due to the high thickness of the stem region in comparison to the wall thickness, as regions of higher thickness are more conducive to the development of residual stresses during tempering. High surface compressive stress values may prevent full fragmentation through the thickness.

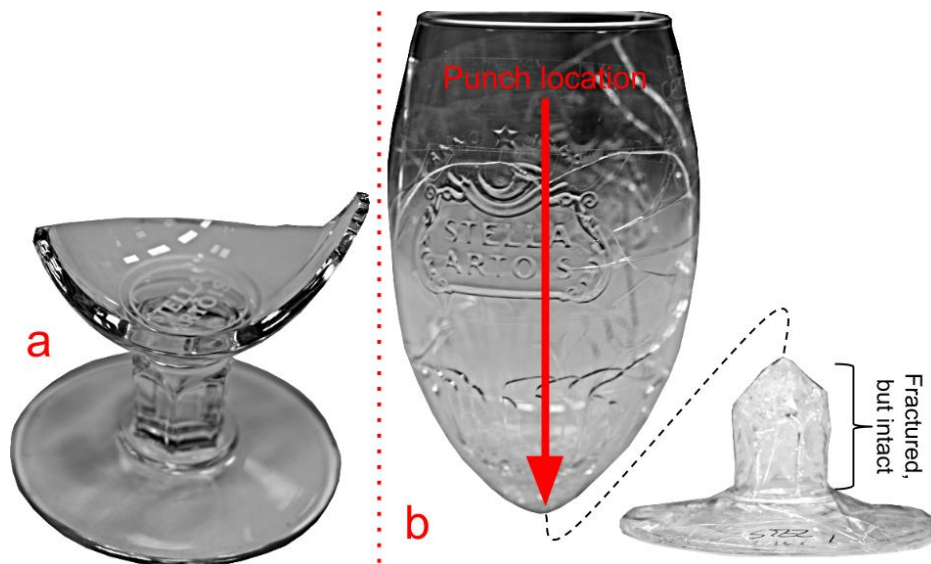


**Figure 4.20 – a: Intact base portion of stemmed branded tempered pint glass after external impact. b: Same type of glass punched on the inside of the glass as shown. Although the stem region fractured, it remained in one piece.**

#### 4.3.4.3 Used glasses

This sub-section overviews the fracture characteristics of 17 used drinking glasses donated by a local hotel. The capacity of the glasses ranged from 170 mL to 280 mL (0.3 to 0.5 imperial pints). The glasses were all subjected to drop tower impact 30 mm from the glass rim along the exterior wall. All glasses were taped prior to impact to retain the fracture pattern.

The location of the primary origin was recorded for each glass, and the width and depth of the origin flaw was measured if recoverable. This gave an indication of the size of flaws that could be expected in used glasses. All recorded data for these glasses is given in Appendix C. Further to this, a brief appraisal of the surface condition of a selection of used pint glasses is detailed in Appendix D. The fracture characteristics of the pint glasses detailed in Appendix D are not considered here as they were used for experimentation in chapter 5 of this thesis.

6 out of the 17 glasses tested had multiple origins. This is likely to be due to continued imparted energy on the fractured article as a result of pre-taping (see Figure 4.10), and/or additional contact with the impactor after the main impact event. Unlike Figure 4.10, all

secondary origins propagated from rim flaws, which were included in the flaw size analysis. In all but one fractures, it was possible to determine the exact location of the primary origin. This was made possible as secondary origin cracks intersected the primary cracks in the macroscopic ( $y$ - $z$ ) fracture plane.

Primary cracks from 10 out of the 17 glasses originated from rim flaws. Two examples of rim flaws are given in Figure 4.21. The remaining 7 primary cracks propagated from flaws on the inside wall due to inward flexure stresses. The depth of flaws varied significantly: from 5  $\mu\text{m}$  to 165  $\mu\text{m}$ . The average flaw depth was 63  $\mu\text{m}$  with a standard deviation of 53  $\mu\text{m}$ . A high variability in the flaw size is to be expected, as this depends on the mechanical history of each individual glass.

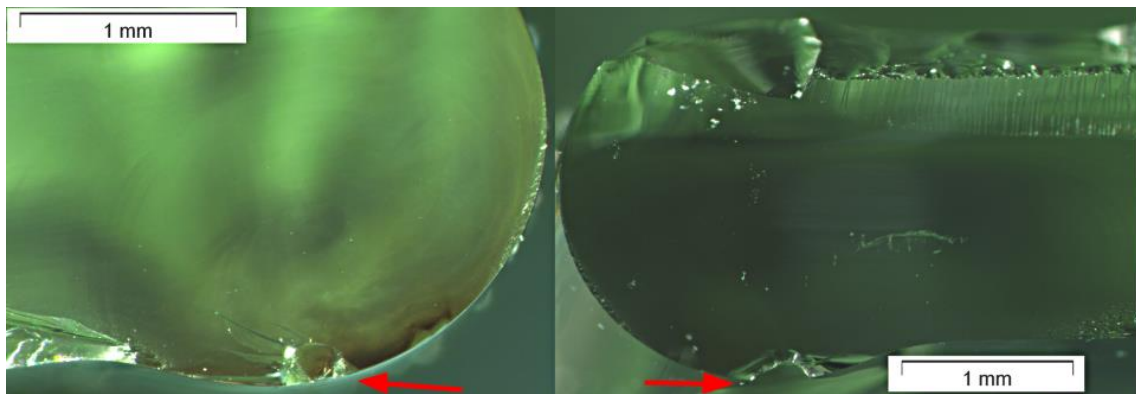


**Figure 4.21 – Examples of relatively large critical flaws present at the rim of used drinking glasses.**

#### 4.3.5 Conclusions

This section has detailed the results of an exploratory investigation into the fracture characteristics of drinking glasses subjected to external impact. The main conclusions from this work are as follows:

- Glasses broken by impact exhibit similar symmetrical fracture patterns. This pattern involves cracks propagating longitudinally near the impact location, looping around the sides of the glass, and propagating longitudinally 180° from the impact location (see Figure 4.8a).
- The base of an annealed glass usually remains intact after fracture. By contrast the base of a thermally tempered glass usually fragments into small cube-shaped pieces (see Figure 4.16). However, for thermally tempered stemmed glassware, the stem and base regions may remain intact after fracture by impact (see Figure 4.20).
- Fragmentation density in the top region (near the glass rim) of annealed and tempered glasses is often similar (see Figure 4.7). For thermally tempered glasses, this means

that fragments in the top region are larger than fragments in the region of the glass base.

- Failure is likely to occur from a critical flaw located within the region of tensile stress opposite the point at which the load is applied (inward flexure), or at the glass rim.
- Rim fractures can typically be identified by characteristic triangular-shaped shards that divide the origin (see Figure 4.12).
- If a propagating crack appears to lead on or close to a particular surface in a tempered glass, this usually means that a very high tensile stress is acting to pull the crack apart at the surface. It may however be the result of uneven or faulty tempering.
- Glasses worn from general usage are likely to have critical flaws located at the glass rim when subjected to external impact (see Figure 4.21).

There are a number of possibilities for further investigation and improvement to this work. Analysing the fracture characteristics of more tempered glass designs would indicate the effectiveness of the thermal tempering process on different glass shapes. Additionally, a larger volume of used glasses would be necessary in order to determine representative typical critical flaw sizes. Ideally, the duration the glasses had been in use and their mechanical history would be known.

Although the investigation was successful in identifying consistent fracture characteristics of drinking glasses broken by impact, the results were largely qualitative. This is addressed in the following section, which involves quantifying the magnitude of residual stress in the walls of a selection of pint glasses, as well as determining impact performance and fragmentation counts in different regions of the glasses.

#### **4.4 Quantitative analysis of the wall thickness, residual stress, and impact performance of three pint glasses**

This section presents the results of a systematic and quantitative investigation into the wall thickness distribution, residual stress levels and distribution, and impact resistance of three types of tempered pint glass. The three glasses were: Nonic glasses (Utopia Tableware Ltd., Chesterfield, UK), Perfect Pint glasses and Ultimate Pint glasses; which were first introduced in section 3.2 of this thesis.

*Perfect Pint* and *Ultimate Pint* are the brand names for premium tempered pint glasses that were developed in response to the Design Out Crime programme on pint glasses [1]. Both glasses are advertised as having safer breakage properties, and retailed for more than twice

the cost of the tempered Nonic glass per unit at the time of purchase (Nonic: 25 pence; Perfect Pint: 80 pence; Ultimate Pint: 60 pence).

There are six parts to this section. Section 4.4.1 details of the number of glasses and the analysis methods used in the investigation. Section 4.4.2 discusses the wall thickness of the three pint glasses which were measured by computed tomography (CT). Section 4.4.3 discusses and presents the results of residual stress measurements made with an automated polariscope. Section 4.4.4 discusses the results of punch tests on the glasses, and considers the fragment count in different portions of the pint glass wall. Section 4.4.5 overviews the results of impact tests on the glasses using a drop tower methodology. Section 4.4.6 concludes the section by bringing together the main findings from the entire investigation.

#### 4.4.1 Testing overview

An overview of all the glasses and analyses used in this investigation is given in Table 4.1.

	Sample breakdown:	Total:
CT scan:	1 x Nonic, 1 x Perfect Pint, 1 x Ultimate Pint	3
Automated polariscope analysis:	1 x Nonic, 1 x Perfect Pint, 1 x Ultimate Pint	3
Punch testing:	10 x Nonic, 10 x Perfect Pint, 10 x Ultimate Pint	30
Impact testing:	30 x Nonic (10 x as-tempered, 10 x as-tempered and abraded, 10 x annealed and abraded)	70
	20 x Perfect Pint (10 x as-tempered, 10 x as-tempered and abraded)	
	20 x Ultimate Pint (10 x as-tempered, 10 x as-tempered and abraded)	

**Table 4.1 – Testing overview for quantitative analysis in section 4.4.**

CT scans and automated polariscope analyses were limited to 3 glasses due to the involved nature of these analyses, and the same glass samples were used for both. Details of the CT and automated polariscope operation are given in sections 3.4.2.1 and 3.4.2.2, respectively. 10 of each of the three glass types in an as-received new condition were subjected to a punch test and fragmentation count, conducted as detailed in section 3.6.2.2.

Impact testing was conducted as per section 3.6.2.1. The impact location was 10 mm from the glass rim for all impacts. Each glass type was tested in an as-received new condition (x10) and an abraded condition (x10). The glasses were abraded as detailed in section 3.5.2.2. Additionally, 10 Nonic glasses were annealed as per section 3.3.3 and abraded prior to testing for comparison. Unlike the majority of impacts conducted in section 4.3 of this chapter which were fully taped prior to fracture, glasses used for impact testing were only partially taped

prior to fracture. This retained the macroscopic fracture pattern local to the impact area for determination of the origin location.

#### 4.4.2 Wall thickness variation

Wall thickness measurements taken from CT scans are shown in Figure 4.22. The measurements show an approximately linear decrease in glass thickness from the base of the glass to the rim (Figure 5). However, the thinnest of the three pint glasses on average, the Nonic, has a minimum wall thickness on the bulge of the glass. The Perfect Pint was seen to be the thickest glass overall. Near-base wall thicknesses ranged between ~6-7 mm, and rim thicknesses ranged between ~2-3 mm.

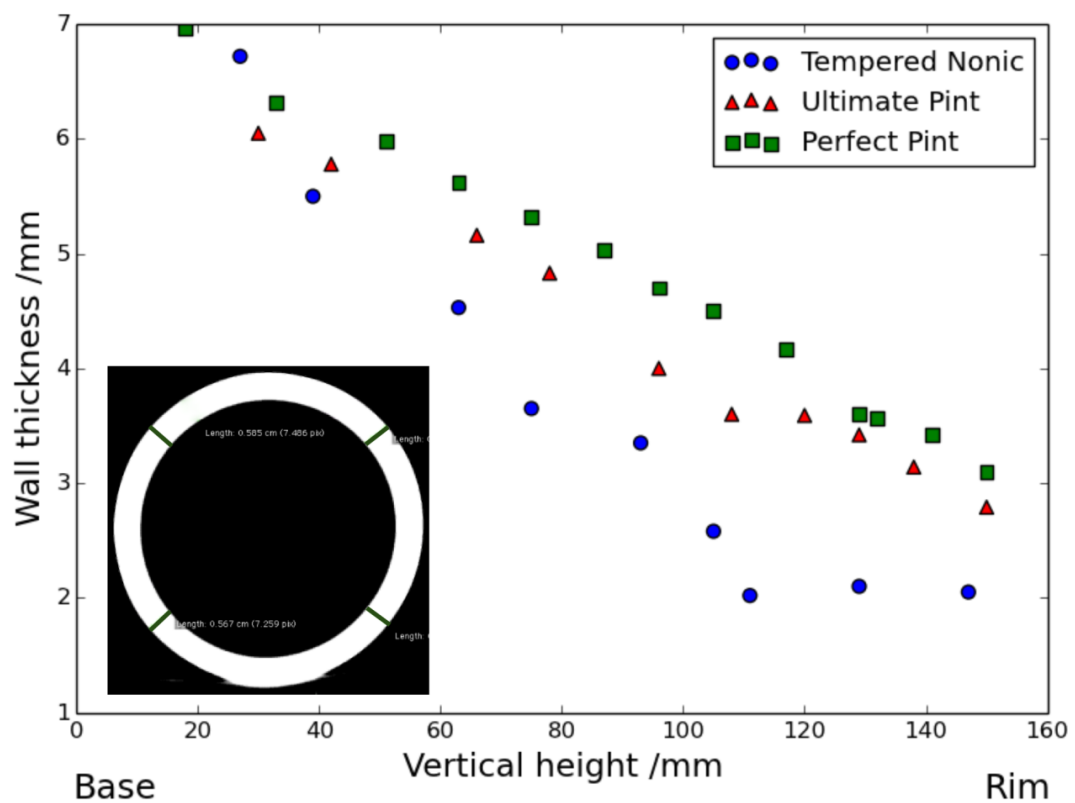
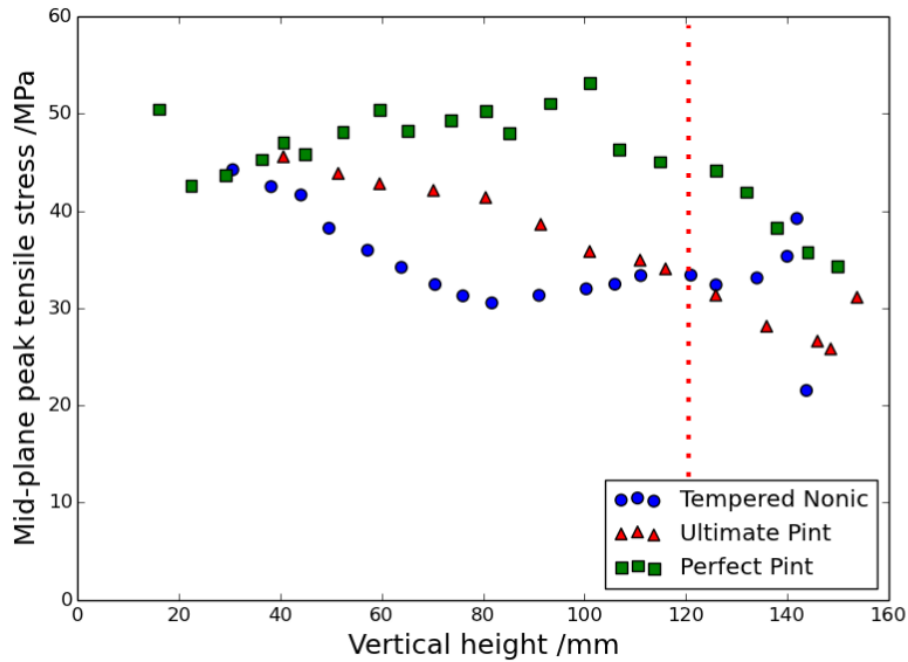


Figure 4.22 – Wall thickness with respect to vertical glass height for each glass from CT data. Inset shows an example cross section from an Ultimate pint, and the 4 averaged wall thickness values.

#### 4.4.3 Residual stress levels

Although the surface compressive stress is generally used to infer the strength of a glass article, it is the magnitude of the tensile mid-plane stress that determines the extent of fragmentation [9]. In Figure 4.23 this is plotted against the height of each glass for one glass wall orientation. The magnitude of tensile mid-plane stress was on average greater for the thicker glasses as determined by CT scans.



**Figure 4.23** – A comparison of the Perfect Pint (squares), Ultimate Pint (triangles), tempered Nonic (circles) and the mid-plane tensile stress from base to rim (left to right). Area to the right of the red dotted line (near the glass rim) indicates data points more likely to be affected by edge effects.

Near to the rim of the pint glasses, photoelastic measurement of stresses became more difficult, resulting in a greater variability of results. However, the Ultimate Pint appears to have a similar magnitude of mid-plane residual tensile stress to the Nonic (~30 MPa) approaching the top 30 mm of the glass. Another study found that 30 MPa tensile mid-plane stress was not sufficient to cause spontaneous breakage (breakage driven mainly by residual stresses and not by external stresses) [10], albeit for 6 mm thick glass.

The magnitude of surface compressive stress increased with the magnitude of mid-plane tensile stress. The inside wall compressive stress was on average ~55 MPa. However, the compressive stress varied considerably between the inside and outside surface. Figure 4.24 shows the difference between the inside and outside compressive stress (inside wall stress – outside wall stress). It should be noted that large variations between the inside and outside wall compressive stresses are not in themselves an indication of whether a glass is suitably tempered. Large variations may exist provided that the compressive surface stresses are of sufficient magnitude.

The inside wall generally had a lower magnitude of compressive stress for all three glasses, particularly near to the base of the Nonic and Perfect Pint glasses. This suggests that the outside wall was subjected to a greater cooling rate than the inside wall during thermal tempering. This is likely to be due to the problem of re-circulating air when air-quenching the

inside of pint glasses. Additionally, the bulge area of the Nonic showed a large difference between inside and outside wall compressive stress, with the inside wall compressive stress dropping to a minimum of  $\sim 30$  MPa. This suggests that the bulge geometry may have also influenced the air-flow during quenching. However, this may pose less of an issue compared to other glass shapes due to the reduced likelihood of contact in this area from stacking glasses on top of each other.

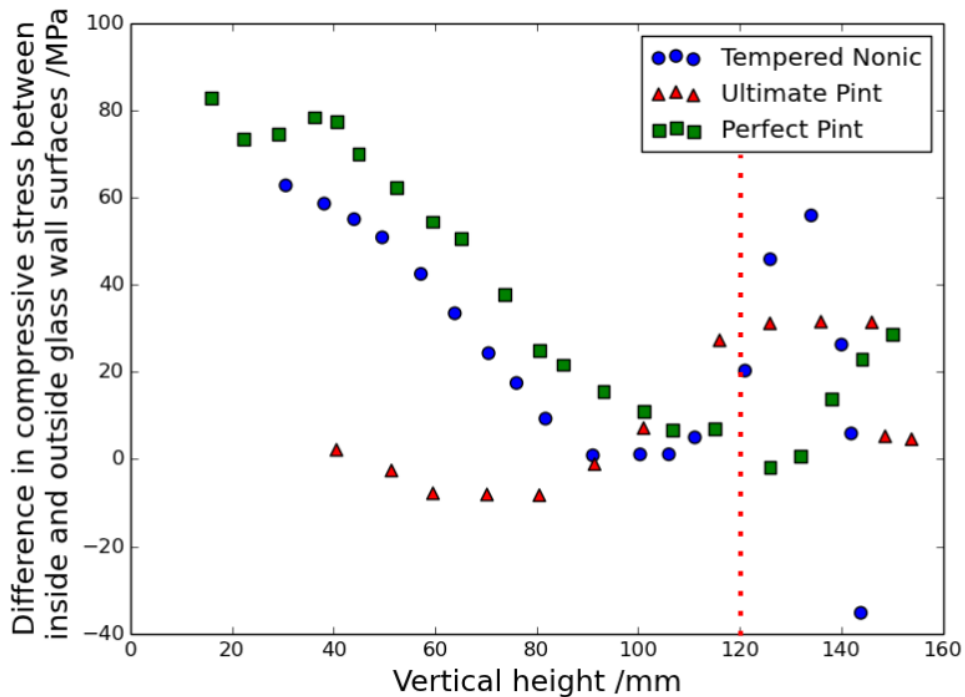


Figure 4.24 – A comparison of the Perfect Pint (squares), Ultimate Pint (triangles), tempered Nonic (circles) and the difference between surface compressive stresses (inner stress – outer stress) from base to rim (left to right). Area to the right of the red dotted line (near the glass rim) indicates data points more likely to be affected by edge effects.

#### 4.4.4 Fragmentation density

A summary table of the fragmentation counts from punch tests is given in Table 4.2. The full fragmentation counts for individual samples are given in Appendix E. For both the Perfect Pint and Nonic glasses, 2 out of the 10 samples did not completely fragment. Instead, localised fragmentation was observed, which was driven mainly by the punch impact stress. By contrast, 6 out of the 10 Ultimate Pint samples did not completely fragment. This suggests that there was a low level of internal tensile stress near to the rim. Alternatively, the punch location may have been in an area of high lateral compressive stress, as the residual stress levels also vary circumferentially.

The fragmentation count method and count regions were outlined in section 3.6.2.2. The top third region of the pint glass wall in each glass resulted in a significantly lower fragment count than the middle and bottom regions. The overall largest fragmentation counts were observed in the Perfect Pint glasses. Figure 4.25 shows a plot of the total fragmentation counts and top third fragmentation counts.

Glass	Samples fully fragmented	Base	Bottom third	Middle third	Top third	Total count	Max. fragment length /mm
Nonic	8/10	166 ± 14	459 ± 15	38 ± 11	8 ± 3	671 ± 28	244 ± 44
Ultimate Pint	4/10	122 ± 18	315 ± 57	212 ± 32	17 ± 7	666 ± 100	126 ± 78
Perfect Pint	8/10	83 ± 9	367 ± 12	410 ± 25	144 ± 8	1004 ± 36	108 ± 41

**Table 4.2 – Summary table for punch test fragmentation counts, showing average counts in different regions of three pint glasses ± the standard deviation. Counts are rounded to the nearest fragment. Only samples which fully fragmented were included in average and standard deviation values.**

The top region of the Nonic pint glasses and Ultimate Pint glasses performed similarly for samples that fully fragmented, although a larger fragmentation count was observed for Ultimate Pint glasses in the middle region. Consequently, larger fragments remained near the glass rim with the Nonic and Ultimate Pint glasses. On a number of occasions, fragments near the glass rim spanned the circumference of the glasses. These results are consistent with the residual stress measurements detailed in the previous section.

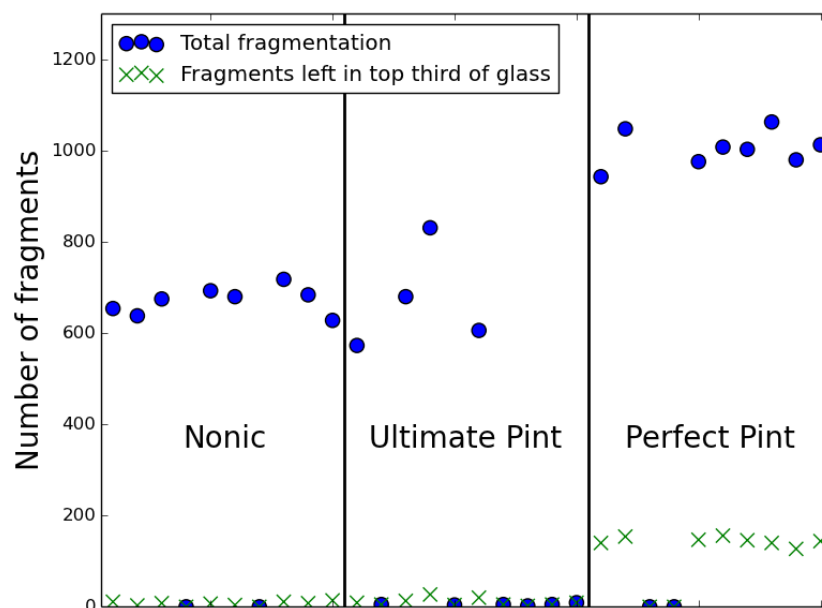


**Figure 4.25 – Values of total fragmentation and top third fragmentation for all punch test samples. Values on the zero line represent instances where the tensile band was not strong enough to initiate total fragmentation of the article.**

#### 4.4.5 Impact resistance

The average energy required to cause macroscopic fracture for each sample set is given in Table 4.3.

The as-received new Perfect Pint glasses required the most impact energy to cause macroscopic fracture during testing (~26 J). The performance of the Ultimate Pint glasses was similar to that of the tempered Nonic glasses (~19 J). This was expected given the relative wall thicknesses and residual stress magnitudes in each glass as detailed in the previous three sub-sections. The abraded glasses fractured at ~3% of the impact energy required to break their as-received new counterparts, although the abrasion process significantly reduced the sample-to-sample variation of the breakage energy.

These breakage energies are considerably different to those found in another study conducted in 1993 with a pendulum impact tester [11]. This found that new and worn tempered Nonics broke at impact energies of ~4 J and 0.18 J, respectively. However, the energy required to break worn Nonics in this case was 4.5% of the energy required to break new Nonics, which is proportionally similar to the data summarised in Table 4.3. This is likely to be due to the difference in compliance of the two impact testing setups, and how securely the pint glass is held. Other pendulum impact testers specifically for testing glass drinkware (e.g. AGR impact tester) would be expected to require far less energy to cause fracture than that reported in the table [12].

Glass type and condition	Average failure energy $\pm$ standard deviation /J	Number of fractures from inward flexure stress regions
Nonic – abraded and annealed	0.3 $\pm$ 0.07	8/10 (2 rim hinge fracture)
Nonic – abraded	0.5 $\pm$ 0.08	9/10 (1 rim hinge fracture)
Ultimate Pint – abraded	0.5 $\pm$ 0.12	10/10
Perfect Pint – abraded	0.7 $\pm$ 0.11	10/10
Nonic – as-received new (steel impactor)	18.8 $\pm$ 3.85	10/10
Ultimate Pint – as-received new (steel impactor)	19 $\pm$ 3.18	10/10
Perfect Pint – as-received new (steel impactor)	25.8 $\pm$ 2.52	10/10

**Table 4.3 – Summary table for impact test breakage energies (10 per sample set) and origin locations.**

#### 4.4.6 Conclusions

Section 4.4 presented the findings of a quantitative investigation into aspects of the properties and performance of three types of tempered pint glasses. The section detailed the results of CT scans, non-destructive and destructive residual stress analyses, and impact tests. The main conclusions from this work are as follows:

- Glasses with thicker walls are able to store more residual stress, thereby giving the possibility of greater strength and fragmentation density.
- The wall thickness of the pint glasses investigated ranged from 6-7 mm near the base, and 2-3 mm near the glass rim. For the Nonic glass, the wall thickness reached a minimum of 1.8 mm at the glass bulge.
- The magnitude of residual stress in the glasses decreased with the wall thickness, and in some cases reached a mid-plane tensile stress of  $\sim 30$  MPa near to the rim of the glass.
- The magnitudes of surface compressive stress on the inside and outside wall were often significantly different, particularly near to the base of glasses.
- A significantly greater number of fragments were created near to the base of the glasses as opposed to near to the rim from a punch test. Consequently, rim-area fragments were comparatively large, often with maximum lengths of  $> 100$  mm.
- Abraded tempered pint glasses fractured at an impact energy of less than 3% of the impact energy required to break as-received new tempered pint glasses on average. Annealed Nonic glasses had even lower breakage energies.
- The vast majority of impacted pint glasses fractured from inward flexure stresses.

There are a number of possibilities for further investigation and improvement to this work, as detailed below.

- A larger volume of samples would be necessary to confirm whether the measurements from CT scans and automated polariscope analyses were representative of the respective pint glass types.
- Further investigation of the circumferential variation of the residual stress in the pint glasses would give a fuller overview of the residual stress distribution.
- A more comprehensive punch test fragmentation analysis could be conducted by assessing the fragmentation with more punch locations.
- Impact testing of glasses worn from regular usage would be necessary to verify whether the abrasion procedure used adequately substitutes this wear.

The results of this section are considered in the following summary section of tempered pint glass properties.

#### **4.5 Summary of key properties and characteristics of thermally tempered pint glasses**

This section gives a summary of the key properties of thermally tempered pint glasses, drawing on the content of previous results from this chapter. Comparisons are made to thermally tempered flat glass in order to highlight the difficulties with applying flat glass standards to pint glasses.

Applying the thermal tempering process to pint glasses is more complicated than to flat glass, due to geometrical differences. It is difficult to achieve even cooling rates over curved surfaces, and to prevent the re-circulation of hot air in the inside of the pint glass. Furthermore, glasses made by commercial blow processes are likely to be thicker near to the glass base than to the rim. This means that the base region is more conducive to the creation of a high magnitude of residual stress, as discussed earlier in this chapter. These factors result in a wider distribution of residual stress magnitude than may be expected in thermally tempered flat glass. Consequently, the assessment of the residual stress and the fracture characteristics is more sensitive to the location chosen for the assessment.

The overall properties and characteristics of impacted thermally tempered pint glasses is summarised schematically in Figure 4.26. This is based on the results of earlier sections in this chapter. Not only does the rim region of the glass have a lower level of internal residual stress, but it is also the region subjected to the highest level of tensile stress due to loading under typical impact conditions. Consequently, larger fragments are created in the top region of the glass than the bottom region when the glass fractures.

Furthermore, the rim is vulnerable to the creation of surface flaws. Such flaws are to a certain extent unavoidable, but the frequency of them may be lessened by geometrical features such as the bulge on a Nonic glass. This feature prevents contact of the rims of two glasses when placed side-by-side, and may also divert tensile stresses due to impact away from the rim (see section 4.2).

In summary, the key differentiating factors of thermally tempered pint glasses to thermally tempered flat glass are:

- A larger variability of thickness throughout the article.

- A larger variability of residual stress throughout the article.
- A larger variability of fragmentation density throughout the article.
- Different regions of the article are known to have different fracture characteristics. Specifically, larger fragments are created in the rim region compared to the base region.
- The rim region is likely to be a key source of flaws.

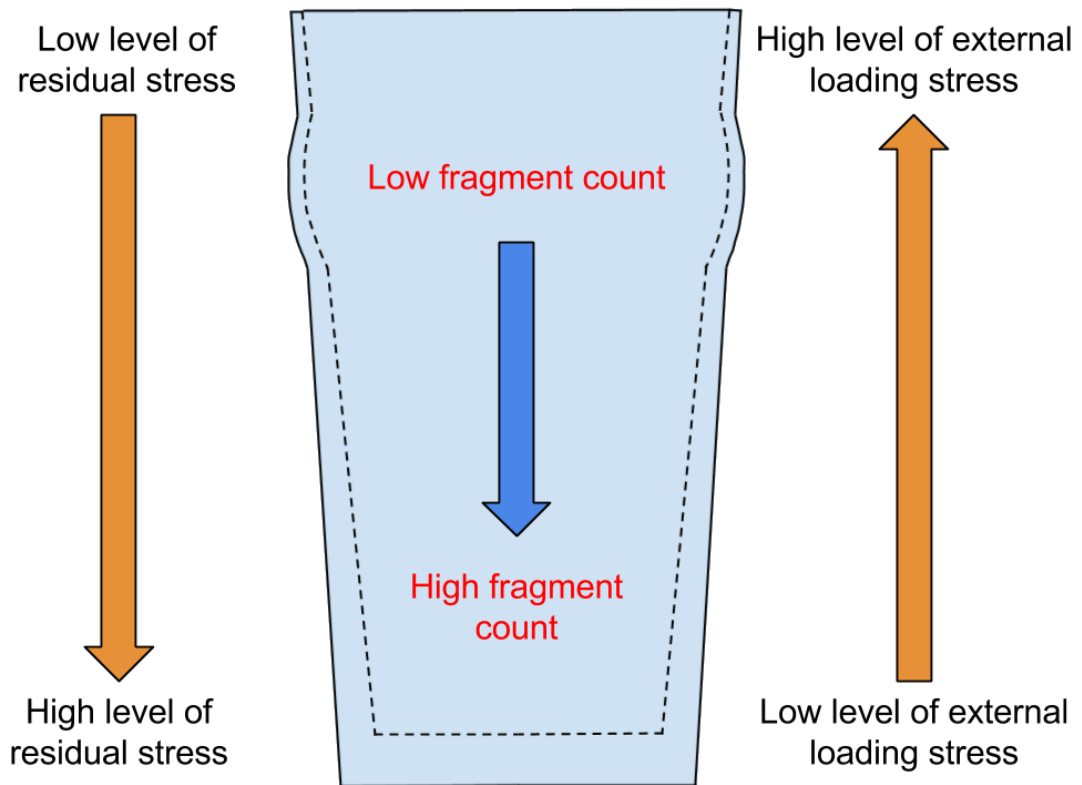


Figure 4.26 – Schematic to show a summary of the results from this chapter for a thermally tempered pint glass broken by impact at the glass rim.

#### 4.6 Chapter summary

This chapter has presented investigations into the structural and fracture characteristics of thermally tempered pint glasses.

Section 4.2 investigated the structural characteristics of pint glasses subjected to static loads by using finite element simulations. These simulations showed that the rim was typically the portion of a glass most likely to develop the highest 1<sup>st</sup> principal stress magnitude under static loading. They also showed the development of a number of individual regions of significant 1<sup>st</sup> principal stress systems present on both the inside and outside surfaces of the glass wall. Additionally, the simulations showed that changes in geometry can affect these stress systems.

Section 4.3 discussed the typical fracture characteristics of a variety of drinking glasses broken by impact to the outside wall. It was shown that the fragmentation characteristics in the top half of some commercially tempered pint glasses were similar to the fragmentation characteristics in the top half of annealed glasses. By contrast, the bases of tempered glasses showed extensive fragmentation whereas the bases of annealed glasses largely remained intact. Additionally, a characteristic symmetrical fracture pattern was identified.

Section 4.4 investigated the fragmentation and impact resistance of three types of tempered pint glasses in further detail. It presented results showing: wall thickness variations from computed tomography scans; residual stress levels from polariscopic measurements; fragmentation counts due to punch tests; and impact resistance due to drop tower impact. It was found that the wall thickness decreased in an approximately linear fashion from the glass rim to the base. The overall magnitude of residual stress followed a similar trend.

Section 4.5 considered the key overall properties of thermally tempered pint glasses and the complexity compared to tempered flat glass, by taking into account the results from earlier sections. However, the extent to which tempered pint glasses are capable of causing injury is unclear. The next chapter addresses this by considering how a pint glass may be used as a weapon, and by determining the extent of the damage caused by assaults with a pint glasses.

## 4.7 Chapter references

- [1] “Using Design to Reduce Injuries from Alcohol Related Violence in Pubs and Clubs,” *Home Office, Design Out Crime*, 2010.
- [2] F. W. Preston, “Bottle Breakage - Causes and Types of Fractures,” *Am. Ceram. Soc. Bull*, vol. 18, no. 2, pp. 35–60, 1939.
- [3] R. C. Bradt, M. Barkey, S. Jones, and M. Stevenson, “Projectile Impact—A Major Cause for Fracture of Flat Glass,” *Journal of Failure Analysis and Prevention*, vol. 3, no. 1, pp. 5–11, 2003.
- [4] R. E. Mould, “The Behavior of Glass Bottles Under Impact,” *Journal of the American Ceramic Society*, vol. 35, no. 9, pp. 230–235, 1952.
- [5] J. B. Kepple and J. S. Wasyluk, “The Fracture of Glass Containers,” in *Fractography of Glass*, R. C. Bradt and R. E. Tressler, Eds. New York: Plenum Press, 1994, pp. 207–252.
- [6] V. D. Fréchette, “Common Conditions of Failure,” in *Advances in Ceramics: Failure Analysis of Brittle Materials*, no. 28, Westerville, Ohio: American Ceramic Society, 1990, pp. 100–109.
- [7] J. R. Calvert and R. A. Farrar, “Properties of Materials,” in *An Engineering Data Book*, 1999, pp. 7–1, 7–2.
- [8] D. Hull, “Cracks Round Bends,” in *Fractography: Observing, Measuring, and Interpreting Fracture Surface Topography*, Cambridge: Cambridge University Press, 1999, pp. 87–90.
- [9] S. T. Gulati, “Frangibility of Tempered Soda-Lime Glass Sheet,” *Glass Processing Days, Tampere, Finland*, pp. 72–76, 1997.
- [10] R. Gardon, “Tempering Glass with Modulated Cooling Schedules,” *Journal of the American Ceramic Society*, vol. 71, no. 10, pp. 875–878, 1988.
- [11] J. P. Shepherd, R. H. Huggett, and G. Kidner, “Impact Resistance of Bar Glasses,” *The Journal of Trauma and Acute Care Surgery*, vol. 35, no. 6, pp. 936–938, 1993.
- [12] Glass Technology Services, private communication.

## 5 Physical attacks with pint glasses (glassings)

### 5.1 Introduction

The previous chapter considered the key breakage characteristics of annealed and tempered pint glasses from a fractographic perspective. This chapter builds on that work by examining how such fracture characteristics may be translated into the patterns and severity of injury that occur if a pint glass is used as a weapon, and builds an understanding of the dynamics involved with such attacks. In particular, it focuses on so-called “slapping” attacks [1], where an intact pint glass is held in an assailant’s hand and slapped on a victim, as demonstrated by Figure 5.1. This chapter aims to address the lack of research on safe breakage characteristics of pint glasses, and to bring more unity as to what should be considered as the necessary breakage criteria for a pint glass standard.



**Figure 5.1 – Schematic of a so-called “slapping” attack with a pint glass.**

There are three components to this chapter. Firstly, the dynamics and circumstances involved with glassing attacks are discussed in section 5.2, in order to provide contextual background and to determine necessary factors for consideration during experimental replication of attacks in following sections. It includes a short investigation into how a pint glass is most likely to be held in a glassing attack.

Secondly, an investigation into the forces and dynamics involved with slapping attacks is presented in section 5.3. This involved the use of a dynamometer to record the force generated during attacks by a number of volunteers. Additionally, high-speed video footage was taken on a number of test runs to assess the manner of approach of pint glasses towards a target.

Thirdly, an investigation into the laceration patterns and severity of cuts in slapping attacks is presented in section 5.4. This involved the modification of a drop tower to hold a pint glass, in order to systematically replicate attacks. The glass was impacted onto layers of synthetic skin, and the distribution, length, and depth of cuts was assessed.

## **5.2 Dynamics and circumstances of glassing attacks**

This section discusses the dynamics and practical circumstances involved with glassing attacks with pint glasses, by reviewing relevant available literature on glass-related assault and framing it in the context of the results of the previous chapter. Specifically, it is concerned with practical factors involved with glassing events, i.e. how the glass is used as a weapon, where the glass is aimed, and how it is held. Psychological factors of individuals involved with the glassing event (i.e. likely demographic, motives, and the effect of alcohol) are not considered.

### **5.2.1 Glassing prevalence and characteristics**

The last estimate for the prevalence of glassing attacks in the UK (with both drinking glasses and glass bottles) in the British Crime Survey (now the Crime Survey of England and Wales) was that it accounted for 4% of all violent incidents [2]. A study based on 5 British Accident and Emergency (A&E) departments found that 72% of glassing incidents resulted in facial injuries, and 23% resulted in hand injuries [3].

The few statistics available on the relative prevalence of the glasses and bottles used vary: some studies provide evidence for drinking glass incidents occurring more frequently than glass bottle incidents [3], [4], and vice versa [5]. However, injuries sustained from drinking glasses have been noted to be characterised by a greater frequency of eye and facial injuries than glass bottles, and therefore a greater level of severity [6]. Furthermore, the difference in shape between drinking glasses and glass bottles affect how the articles are used as impulsive weapons, with bottles being more likely to be used as a clubbing weapon [6], which would lead to blunt force trauma.

This chapter focuses on the injury potential of drinking glasses rather than bottles. Anecdotal evidence from emergency service workers and glassing victims obtained during the 2010 Design Out Crime programme indicated that four main methods are used by assailants in conducting glassing attacks with drinking glasses [1]:

- I. By first breaking a drinking glass and then using the remnants to stab or slash a victim (referred to in this text as a 'break-first' attack).
- II. By throwing an intact pint glass toward a victim (throw attack).

- III. By holding an intact drinking glass in a hand, and slapping it into the face of a victim (slap attack - Figure 5.1).
- IV. By thrusting an intact drinking glass toward a victim in a stabbing action (thrust attack).

Method I is the only one of those listed which involves the fracture of the glass prior to the glassing event. Consequently the nature of the attack is affected by whether the glass has been annealed or tempered. As discussed in the previous chapter, the base of tempered pint glasses typically undergoes dense fragmentation when broken. By contrast, the base of annealed pint glasses typically remains intact with 2 or more protruding edges pointing away from the base. If the glass is held at the base and impacted higher up the glass wall against a surface with sufficient energy to cause fracture; fragments from a tempered glass are likely to fall out of the assailant's grip, whereas the intact base of a broken annealed glass is more likely to remain gripped in hand.

The use of tempered pint glasses may therefore nullify the use of the glass as a weapon for break-first attacks. However, tempered pint glasses with low levels of residual stress may still result in fragments of a comparable size to annealed glass fragments (see previous chapter). It may be possible that these could be retained in hand or subsequently picked up if they fell to the ground, and used as a stabbing or slashing weapon. The use of a glass fragment in such circumstances may also wound the assailant's gripping hand [7], or it may not, possibly depending on the fragment thickness [8], [9]. Additionally, the relief of residual stresses during fracture may affect the sharpness of the fragment edges, even in cases where a tempered pint glass fragment is of comparable size to an annealed pint glass fragment. This is a complex issue and is considered in chapters 7 and 8.

One A&E study found that 84% of victims of glassing attacks with drinking glasses reported that the glass was intact prior to impact [3]. By contrast to method I, methods II, III, and IV, all describe techniques with intact glasses. They are therefore relevant to both annealed and tempered pint glasses. The injuries sustained from such methods are dependent on: the attack dynamics involved; whether or not the glass fractures; and the resulting fracture pattern if the glass fractures. Attacks in which the glass does not fracture will increase the likelihood of the victim sustaining blunt force trauma injuries. Those whereby the glass does fracture will result in an increased risk of sharp force trauma injuries, or both sharp and blunt trauma. The increase in strength provided by tempering (see previous chapter) may therefore increase the risk of blunt force trauma injuries. An increase in strength of drinking glasses has previously

been associated with an overall decrease of injury risk [10]. With thermally tempered glassware there is potential to control the strength so that an appropriate balance can be achieved to minimise both severity and incidence of injury. Chapter 7 investigates whether there is a sufficient level of thermal temper that reduces the potential for injury of glass fragments.

Method II was specified as a throw with an intact pint glass, although throws with partially intact pint glasses may be more likely to cause fatal injury. This was investigated by Sterzik et al., who threw intact drinking glasses at a skull-neck model to investigate the likelihood of such an attack causing a fatal injury to the neck [11]. It was found that throws with an intact pint glass were most likely to cause superficial injuries, if any at all. This depended on: the throw accuracy; whether the base or rim of the glass impacted the target first; and whether or not the glass impacted at a hard surface (skull area) or a soft surface (neck area). It was concluded that the most likely scenario to cause a fatal neck injury was a throw with an intact base of a broken annealed pint glass. However, it is worth noting that these tests involved straight-walled pint glasses of volume 0.3 and 0.5 l (compared to ~0.57 l for pint glasses), and no wear replication techniques were detailed.

Slap and thrust attacks are in many respects similar, and actual attacks may involve aspects of the two. Very little was found in the literature on the occurrence and dynamics of such attacks. Cassematis and Mazerolle assessed reports of 31 glassing incidents on licensed premises, 22 of which specified whether or not the attack involved an article already in hand [4]. All incidents were one-on-one attacks, and most involved drinking glasses. 14 involved glass vessels that were already being held by the assailant, with the remainder of incidents involving an empty glass vessel being picked up (n=8).

Break-first attacks are not discussed further in this chapter because they were considered less relevant for tempered glasses, as discussed above. Methods II, III and IV are discussed in section 5.3.3.1 in an initial investigation. Following this, throw attacks are not discussed further since existing research indicates that the method is of lower risk. The initial investigation detailed in section 5.3.3.1 showed that thrust attacks were less likely to result in breakage of the glass than with slap attacks. For this reason, slap attacks are investigated in greater detail in the remainder of the chapter.

### **5.2.2 Pint glass grip in attacks with glasses intact on impact**

Most glassing attack incidents involve glasses already in hand. This may imply that glasses are held closer to the base in slap and thrust attacks, in accordance with the expected grip when

using the glass as a drinking vessel (referred to as 'drinking position' from here on). In order to investigate pint glass grip further, 11 volunteers were asked how they would hold a Nonic pint glass in such an attack as part of the current study. No instruction was given on how the glass should be held or the method of attack. It was only specified that the attack involved an intact pint glass that may only break on impact with a hypothetical victim. Each participant had not seen how other participants had gripped the glass, and was asked to pick the glass up from a table, rather than being handed the glass. Each grip was then photographed in situ. All photographs are shown in Figure 5.2.

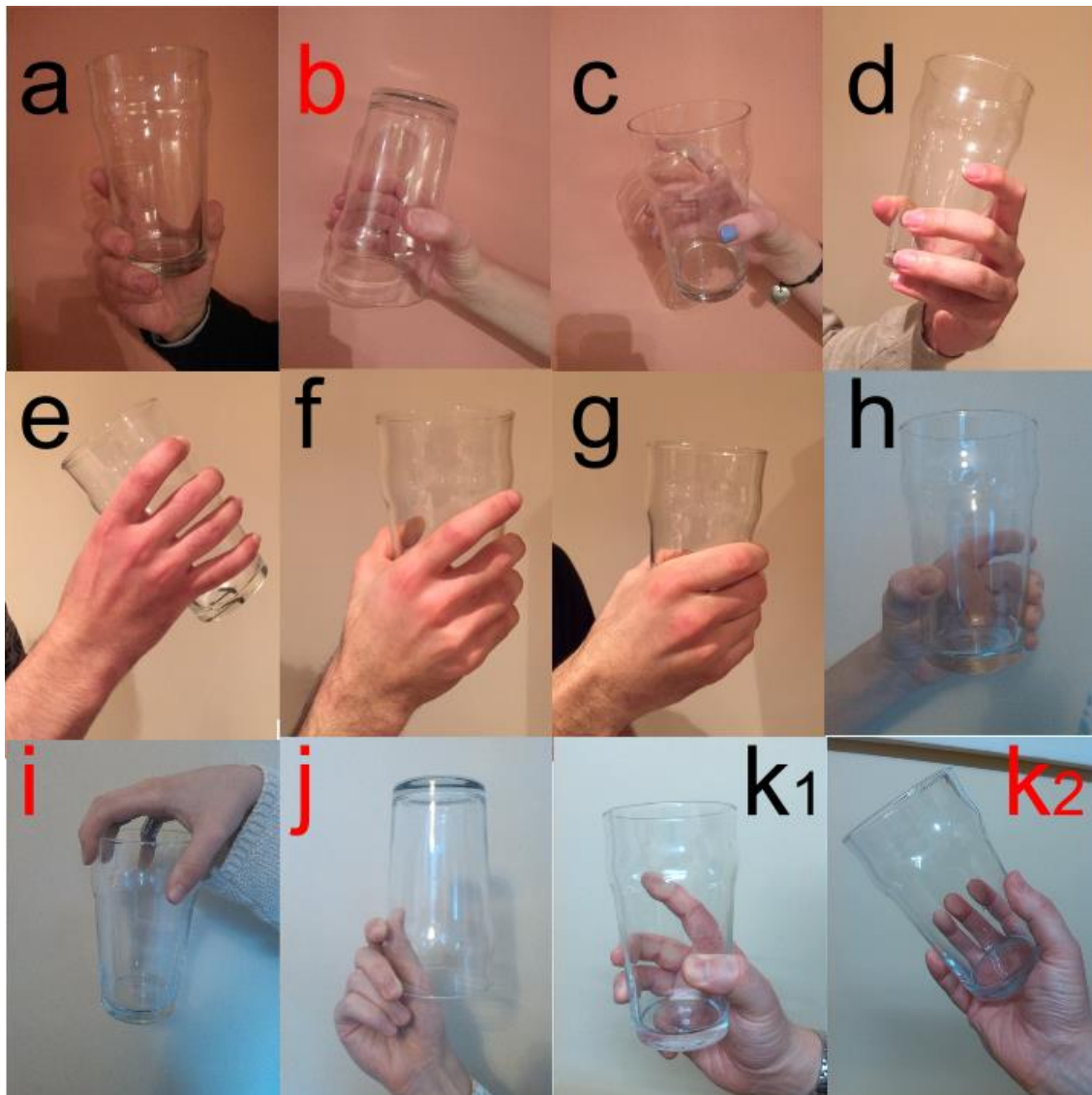


**Figure 5.2 – Photographs of Nonic pint glass grips for a hypothetical glassing attack by 11 volunteers. Red labels indicate incidences where the glass was held considerably differently from a drinking position.**

Eight out of the eleven participants gripped the glass in the drinking position (labelled in black font in the figure). Several participants then asked if they could change their minds, although

only the first grips are shown in the figure. The exception is grip k, which was altered as the second stage of the participant's method of attack. Most participants then went on to describe or allude to the method they would use for the attack. The seven participants who used the drinking position grip for the entirety of the attack described or implied two main methods of attack: a clubbing method where the rim would impact the victim's head or face first in a downward trajectory (a, d, f, g, and h), and a slapping method (c, e) as demonstrated by Figure 5.1. Grips intended for a clubbing method tended to be held closer to the base, whereas the two grips for a slapping method were held midway up the glass height.

A clubbing method was also described by participants b and j, but with the glass inverted so that the base would impact first. Participant i held the glass close to the rim and described a downward attack from above the victim's head. Participant k chose a two stage method of attack, where the glass was picked up using the drinking position ( $k_1$ ) and then shifted grip ( $k_2$ ) to the base to thrust the glass into the victim's face.

Given such a small sample, it was not possible to draw any definitive conclusions as to how a pint glass would be gripped in an actual assault. Furthermore, the investigation did not reproduce the impulsive nature or the circumstances of actual attacks. However, the results do suggest that it may be instinctual to grip the glass in a similar way to the drinking position. Well-tempered pint glasses used in a clubbing attack method may result in small fragments projecting away from the point of impact which may or may not cause sharp trauma. By contrast, if such a glass was used with a slapping attack method, many fragments may become trapped between the assailant's hand and the target with an increased likelihood of causing sharp trauma injuries to both. The overall variation observed for both the gripping position and the intended impact position suggests that no one particular area of a pint glass should be focused on for tempering to reduce injury potential.

The majority of testing in the remainder of this chapter involves the assessment of forces and damage patterns involved with impulsive slapping attack methods (method III). Attacks by break-first methods were not investigated, since they were considered less relevant for tempered glasses. Throw and thrust methods were considered briefly, and provide an opportunity for further testing.

## 5.3 Forces involved in glassing attacks

### 5.3.1 Overview

This section details a series of experimental investigations conducted to determine the forces and general dynamics involved with glassing attacks. These investigations involved the use of a novel dynamometer previously developed in a separate study to quantify the forces involved in stabbings [12]. This, and other equipment to ensure that replication of the attacks could be conducted by volunteers in a safe manner, is detailed in section 5.3.2.1.

The main focus of this section is on slapping attacks with pint glasses, as described in the previous section and demonstrated schematically in Figure 5.1. Attacks by break-first methods were not investigated, since they were considered less relevant for tempered glasses. Throw and thrust methods were considered briefly, and provide an opportunity for further testing. The results from this section contribute to an understanding of the physical dynamics involved with glassings, and were used to guide the development of a systematic and reproducible methodology to determine the potential injury patterns involved with glassings, as detailed in section 5.4.

### 5.3.2 Materials and methods

#### 5.3.2.1 Equipment

Figure 5.3 shows the equipment and the general procedure for the quantification of forces involved in glassing attacks with volunteers. A glass was attached with elastic bands to a 9 mm thick flat platform on a wooden securing fixture, which had a handle attached to the opposing side. This enabled it to be held centrally with a single hand, as shown in Figure 5.4. It was intended that the participant's hand would slide underneath the handle as shown in the figure, rather than being gripped around the handle to imitate a slapping grip. The position of the glass on the fixture could be altered as necessary to change the angle of approach of the glass. The total mass of the fixture was 861 g without a glass attached. A previous iteration of the pint glass securing fixture had raised blocks that sat either side of the pint glass and this was used for the results detailed in section 5.3.3.2.

Safety was a key concern during experimentation, and all participants were required to wear the following personal protective equipment (see Figure 5.3):

- Clear face shield
- Slash-resistant gloves

- Stab vest
- Disposable full body suit (to avoid contamination of clothes with glass particles)
- Disposable shoe covers (as above)

The gloves used had latex palms that allowed for good grip when slid underneath the securing fixture handle.

Over the course of experimentation, several types of pint glasses were used. These included: used tempered Nonic glasses, used tempered Tulip glasses, new abraded Nonic glasses, and new abraded straight-walled glasses. The abrasion method was either by the method outlined in section 3.5.2.2 which used SiC paper, or glasses were scribed on the inside glass wall opposing the impact point.

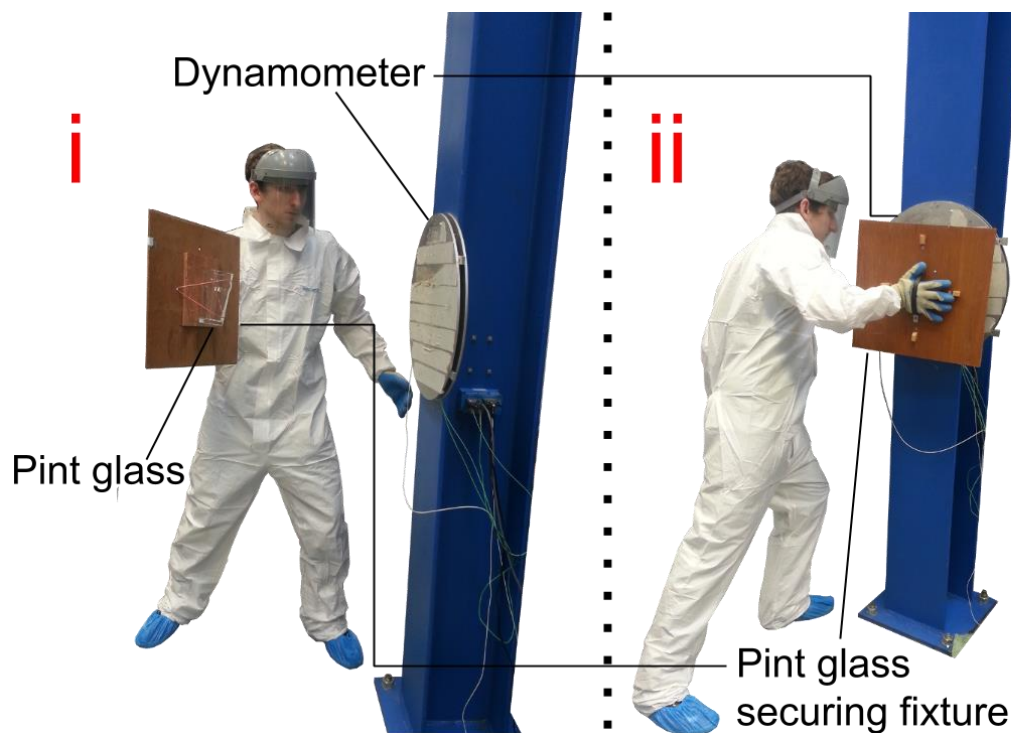


**Figure 5.3 – Equipment and procedure for quantification of glassing forces. Figure depicts chronological procedure to slapping attack (i→ii).**

The dynamometer used during testing was developed as part of a separate study to quantify the forces involved in stabbings [12]. It uses three triangularly-arranged 5 kN load cells (9313AA, Kistler, Hampshire, England) sandwiched between two 6 mm thick circular plates to record forces applied to the plate faces. A single-channel amplifier (ICAM 50731511, Kistler, Hampshire, England) was used to ensure sensitivity over the 5 kN load range. The force output of the dynamometer was recorded 10000 times per second using a LabVIEW program

(National Instruments, Newbury, UK). Results were then logged as force against time and subjected to a zeroing method to ensure the standing force was on average 0.

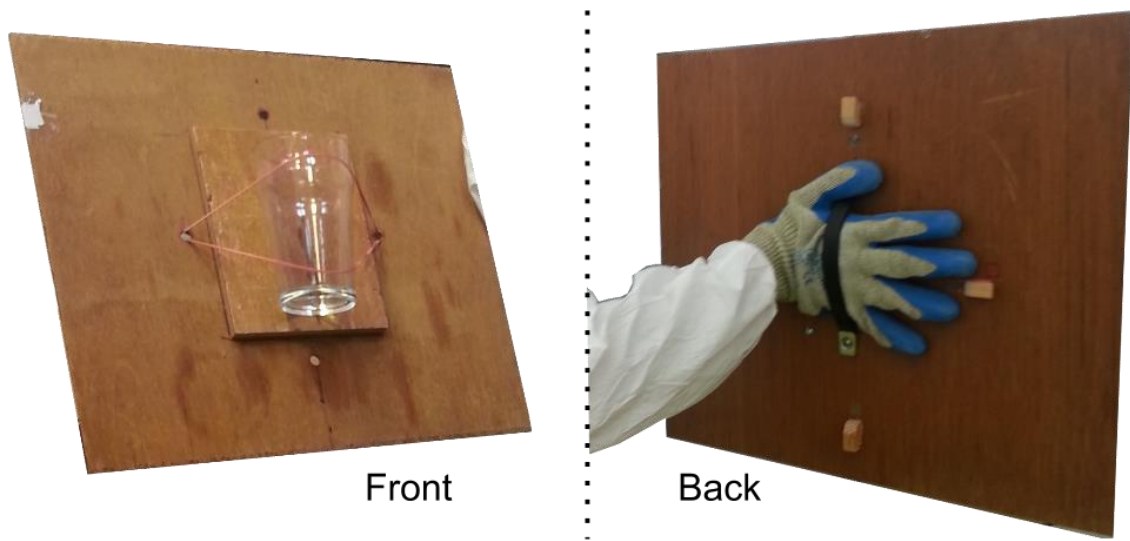


**Figure 5.4 – Pint glass securing fixture used during glassing replications. Pint glass is secured to the front of the fixture with rubber bands in front of a 9 mm thick ply. The fixture is then held by a handle on the opposing side.**

### **5.3.2.2 Interpretation of force-time plots**

A typical force output over a period of 0.5 seconds is shown in Figure 5.5. The force-time output consisted of three main components. The first was glassing peaks, defined as one or more initial peaks directly due to the glassing attack. The second was resonant peaks, defined as numerous subsequent peaks due to dynamic oscillations of the impacted plate, which were indirectly due to the glassing attack. The third was background noise. Resonant peaks and background noise were disregarded during analysis.

The attacks conducted for this study often resulted in more than one glassing peak. Distinguishing between glassing peaks and resonant peaks is complicated since resonant peaks may on occasion be equal in magnitude to glassing peaks. Therefore a methodology was established which consistently defined the portion of the force-time plot that represents the events occurring directly due to the glassing attack (the glassing peaks). This involved the sequential fulfilment of 3 conditions on the force-time plot as follows:

- i. The force deviates by more than 5 N from 0 N.<sup>‡</sup>
- ii. The maximum recorded force over the entire force-time plot is reached.
- iii. The force drops below 0.

<sup>‡</sup> 5 N was chosen as the background force did not exceed this value on 10 test runs conducted without touching the dynamometer.

The bounds of the glassing event were defined as the time at which conditions i and iii were achieved. This is demonstrated in Figure 5.6. The glassing event duration was defined as the time between the achievements of conditions i and iii. The peak force time was defined as the time between the achievements of conditions i and ii.

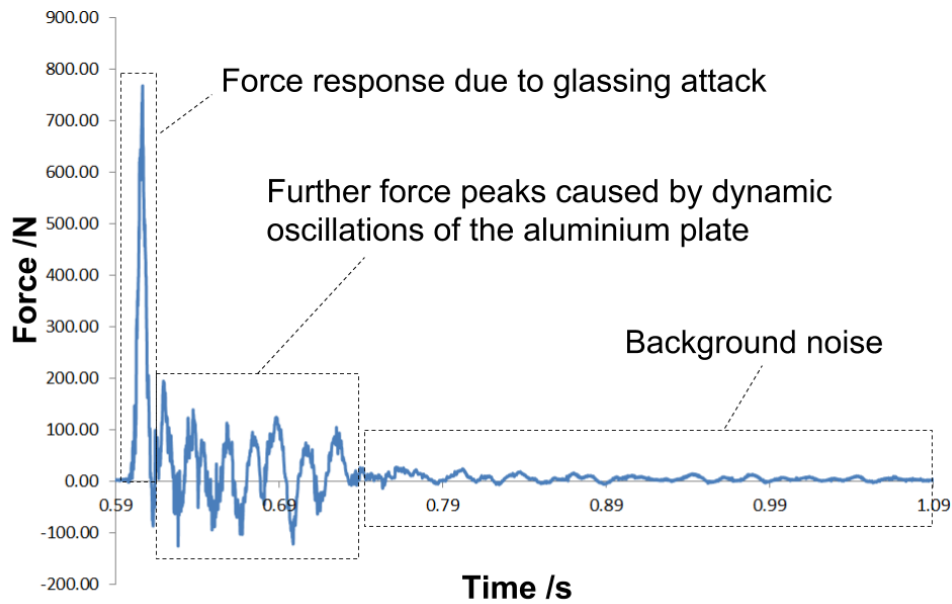


Figure 5.5 – Typical force against time output logged from the dynamometer over a 0.5 s period during a slap attack.

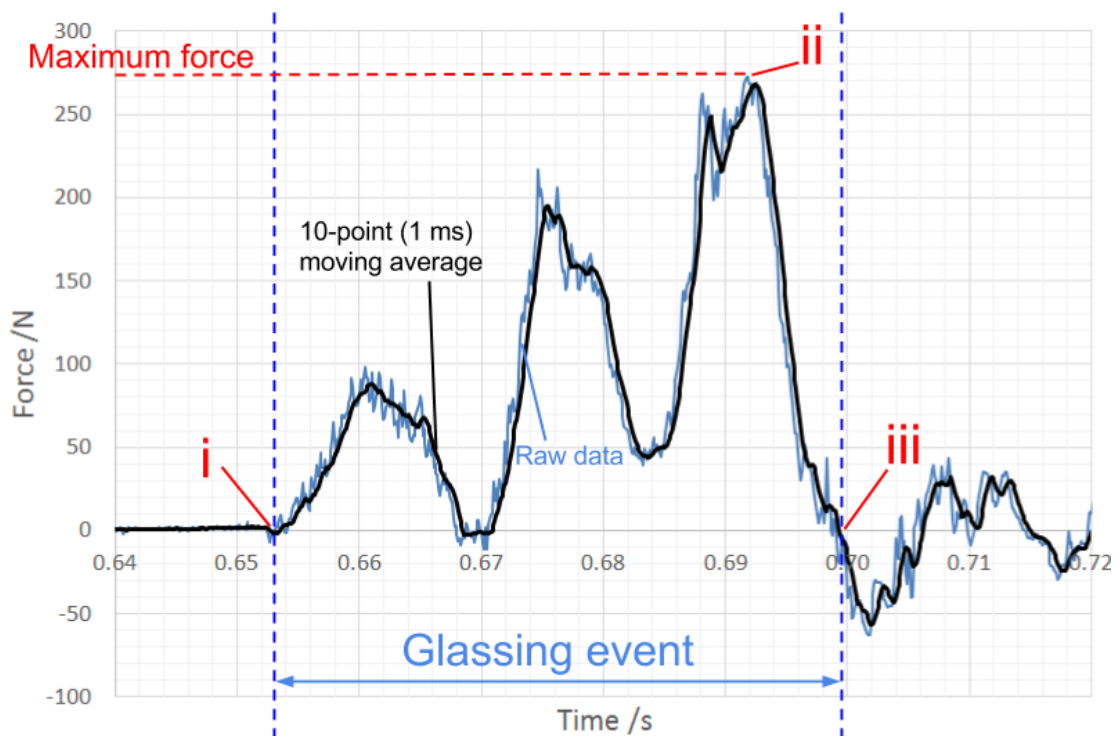


Figure 5.6 – An example force-time plot demonstrating the location of the bounds used to define the glassing event.

In order to aid the analysis of the glassing event, a number of single impacts were conducted onto the dynamometer with a hammer and the securing fixture without a pint glass attached. These were conducted as a comparative measure, and are further detailed in Appendix F. In summary, the average impact event duration was 9.5 ms and 11 ms for the hammer and empty securing fixture, respectively. Additionally, the peak force times were achieved on average at times 2.8 ms and 6.7 ms (31.1% and 60.9% of the average glassing event duration) for the hammer and empty securing fixture, respectively.

This method of determining the glassing event duration may not truly represent the full actual glassing event in circumstances whereby there was a significant time between the peak force time and further impact events due to the glassing attack. This is due to a premature achievement of condition iii.

### **5.3.2.3 Procedure**

In total, 23 volunteers took part in experimentation by performing slapping attacks with the equipment described in the above sub-section. Additionally a small number of thrusts and throws were performed with annealed Tulip glasses (section 5.3.3.1). The general procedure was as follows:

1. If new, glasses were pre-damaged by abrasion (see section 3.5.2.1).
2. The glass was attached to the pint glass securing fixture (with the side-wall flat against the platform for slapping attacks).
3. The volunteer put on the required personal protective equipment, and held the pint glass securing fixture as shown in Figure 5.4.
4. If the attack type was being investigated, the volunteer was asked to perform either a freestyle attack, a hesitant attack, or an aggressive attack. This is detailed further in section 5.3.3.3.
5. The volunteer was counted down from 3 and instructed to perform the glassing attack on 'go'.
6. The force output against time was logged using LabVIEW over a specified time period.
7. After having performed all necessary attacks, the volunteer removed all safety equipment and disposed of the full body suit and shoe covers.
8. Glass was removed from the surrounding area and placed in a sharps bin, which was subsequently taken to a recycling point.

The following was then inferred from each force-time plot (see above sub-section):

- The maximum force attained during the glassing event.
- The glassing event duration.
- The time at which the maximum force was attained (peak force time).

### 5.3.3 Results and discussion

#### 5.3.3.1 Initial tests and observations: throwing, thrusting and slapping

Before investigating glassing attacks by volunteers, a short exploratory study was conducted. This involved the assessment of the recorded force-time output for four attack configurations using annealed straight-walled conical glasses with a single participant. The participant attempted to use a similar force in each attack.

The four attack configurations were based on the methods of attack described in section 5.2.1. Only attacks with intact glasses were investigated, which excluded break-first attacks from the exploratory study. Thrust attacks were investigated in two forms: rim-first and base-first. The four configurations were as follows:

1. A slapping attack as per Figure 5.3.
2. A throw onto the dynamometer face from approximately 5 metres.
3. A thrust with the glass rim impacting the dynamometer first.
4. A thrust with the glass base impacting the dynamometer first.

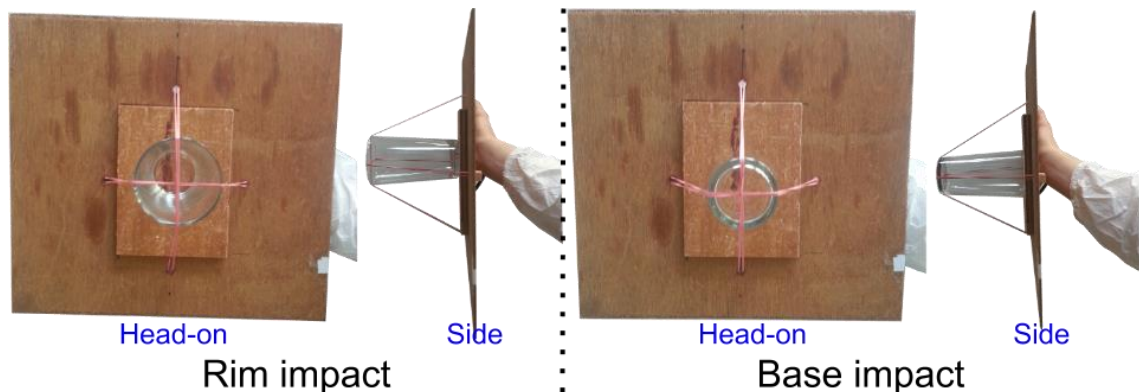


**Figure 5.7 – Pint glass holding configurations for thrust attacks to dynamometer. Slash resistant gloves were worn during actual experimentation.**

Glasses were held in the standard drinking position prior to being thrown. The positioning of the pint glasses on the securing fixture for the thrust attacks is shown in Figure 5.7. These perhaps best represent thrust attacks with the grip  $k_2$  shown in Figure 5.2, rather than those gripped in the standard drinking position. Three glasses were used for each attack configuration, totalling 12 glasses. Glasses which did not break were discarded from

subsequent testing. Key values from the force-time plots are summarised in Table 5.1. Additionally, an example force-time plot for each attack technique over a time period of 35 ms is shown in Figure 5.8.

**Overall forces:** The overall highest forces were observed in base-first thrust attacks. However, the standard deviations of the maximum force for all attack techniques were high (17.86% of the mean on average) and further testing would be required to establish genuine trends. The actual technique employed by the participant was very similar for both slaps and thrusts, and may have been influenced by the limitations imposed by using the pint glass securing fixture. It may be expected that further repeat testing would reveal little statistically significant difference in the maximum forces between thrust and slap attack types. Additionally, the participant may have subconsciously improved/alterd their technique over the test runs. In contrast to slaps and thrusts, maximum forces from throws were significantly lower.

Glassing technique	Repeat #	Maximum force (N)	Glassing event duration (ms)	Peak force time (ms)	% of peak force time to glassing event duration
Slap	1	434	25.7	7.3	28.4
	2	767	14.2	8.9	62.7
	3	712	10.8	3.7	34.3
	$\bar{X} \pm \sigma$	638 ± 146	16.9 ± 6.4	6.6 ± 2.2	41.8 ± 15
Throw	1	123	13.8	6.4	46.4
	2	139	15.2	8.6	56.6
	3	97	23.8	7.9	33.2
	$\bar{X} \pm \sigma$	120 ± 17	17.6 ± 4.4	7.6 ± 0.9	45.4 ± 9.6
Thrust, rim first	1	919	8.7	4.1	47.1
	2	542	8.9	3	33.7
	3	721	13.6	3.5	25.7
	$\bar{X} \pm \sigma$	727 ± 154	10.4 ± 2.3	3.5 ± 0.4	35.5 ± 8.8
Thrust, base first	1	812	15.5	4.2	27.1
	2	1008	14.6	4.4	30.1
	3	745	14.3	3.9	27.3
	$\bar{X} \pm \sigma$	855 ± 111	14.8 ± 0.5	4.2 ± 0.2	28.2 ± 1.4

**Table 5.1 – Key values from force-time plots obtained during initial testing with four glassing techniques with one volunteer. Rows highlighted in green indicate test runs where the glass broke, rows highlighted in red indicate test runs where the glass did not break.**

**Slap attacks:** The force-time plot of the slap attack shown in Figure 5.8a gave a lower overall maximum force value than the further 2 repeat tests, but had the longest glassing event duration measured in this set of experimentation. Additionally, the shape of the plot is significantly different to those obtained from single impact events detailed in Appendix F. A number of peaks are apparent and may correspond to glass breakage and subsequent follow-

through effects of the glass securing fixture. The glassing event duration of repeats 2 and 3 was similar to the empty securing fixture impacts in Appendix F. This may be due to the higher force obtained in these attacks and therefore higher speed of the attacks. This would result in a shorter time between individual peaks relating to impact events, and therefore be more likely to show similarity to a single impact event.

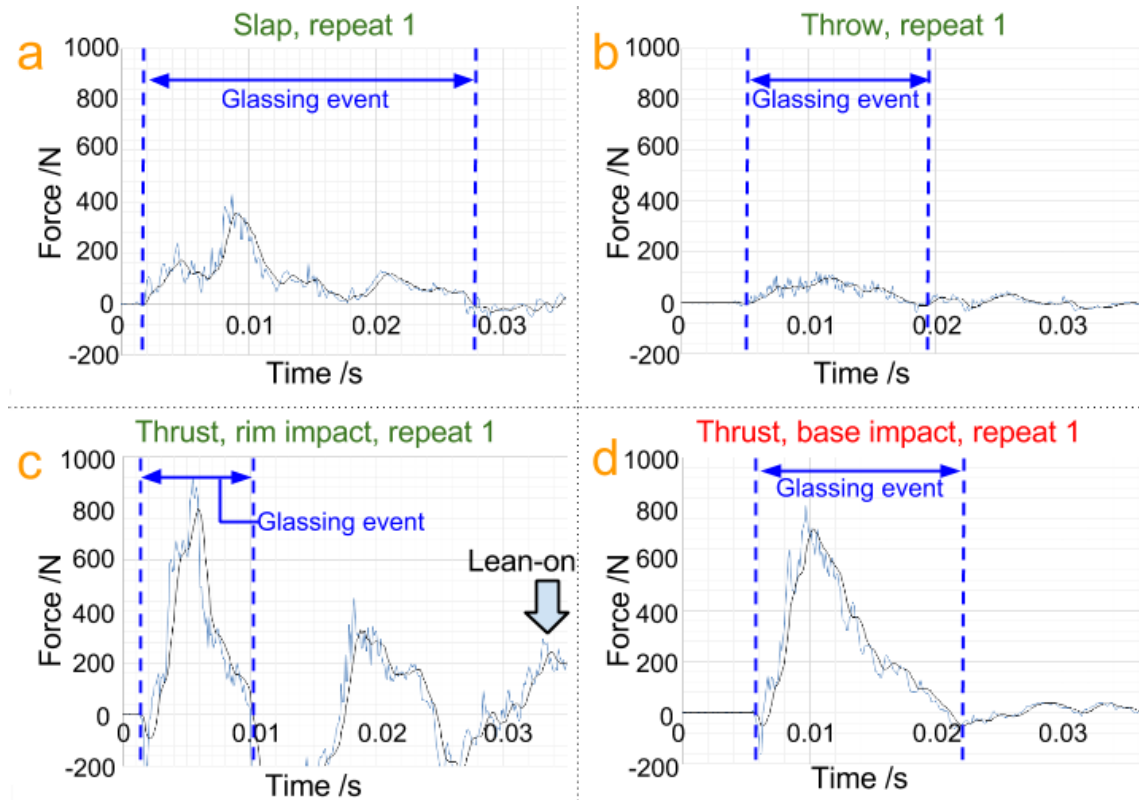


Figure 5.8 – Force-time plots for the first run of each glassing technique conducted during initial testing. Blue line shows the raw data, black line shows the 10 point (1 ms) moving average.

**Throw attacks:** Throw attacks resulted in relatively low maximum force values, although all glasses broke on impact with the dynamometer face. Additionally, throws resulted in the longest glassing event duration on average out of all attacks in this set of experimentation. This may be due to the reduced velocity of glass fragments when following-through to the dynamometer face after initial breakage compared to slapping attacks. Alternatively, this may be due to rotation of the glass after the initial impact – for example, the base of the glass may have impact the dynamometer first without breaking, followed by the glass rotating and the rim impacting the dynamometer.

**Thrust attacks:** 3 out of the 6 thrust tests did not result in fracture of the glass (1 rim-first, 2 base-first). Decreased likelihood of fracture in these attacks was expected since the glass was loaded longitudinally during impact, and was therefore less susceptible to the degree of

bending that is encountered when the glass is impacted normal to the sidewall. All thrust attacks were also characterised by having short glassing event durations and similar force-time plots to impacts with the empty glass securing fixture (see Appendix F).

The participant noted that they leaned on the dynamometer face immediately after repeat 1 of the rim-thrust attacks (Figure 5.8c). This is seen on the force-time plot at the arrow in the figure, after which the force gradually falls down to 0 over an additional period of 18 ms. The lean-on time was not included in the glassing event because the force-time plot dropped below 0 before the lean-on event occurred. Leaning on the target after the initial impact may be representative of real-life instances where the glassing assailant falls onto the victim during the attack.

Further interpretation and conclusions are discussed in section 5.3.4. The forces attained for thrust attacks in this initial investigation may be unrepresentative of thrust attacks held in the drinking position in an actual attack, as the glass may slip out of the assailant's hand. This, combined with the increased likelihood of slapping attacks to result in fracture of the glass, meant that slapping attacks were selected for further investigation. Additionally, high-speed video footage was used for the following sub-section in order to further aid interpretation of the force-time plots and calculate the velocity involved at impact.

### **5.3.3.2 Forces involved in pint glass slapping assaults: 1<sup>st</sup> trial**

This sub-section details an investigation into the forces involved in slapping attacks with used Nonic and used Tulip glasses. 7 volunteers (6 male, 1 female) took part in this round of tests, and each performed 4 slapping attacks onto the dynamometer (2 with a Nonic glass, 2 with a Tulip glass). Participants were instructed to imagine that they were performing a glassing attack by slapping a victim with a pint glass, and held the glass securing fixture with their dominant hand. All attacks were recorded by a high speed video camera (Olympus i-Speed, Olympus, Southend-on-Sea, UK), which captured 1000 frames per second. This allowed for the assessment of: the approach velocity; the angle of glass approach; and the general impact dynamics. A full table of recorded parameters for this investigation is given in Appendix G.

A summary of maximum forces observed, measured velocities, and estimated attack energies is given in Table 5.2. The velocity was measured using high speed video footage. The attack energy was estimated from the combined mass of: the participant's arm, the glass securing fixture (0.861 kg), and the pint glass used (Nonic: 0.338 kg, Tulip: 0.32 kg). The mass of the participant's arm was estimated as 5.77% and 4.97% of total mass for males and females, respectively, according to anthropometric reference tables [13].

#	Nonic			Tulip			
	Maximum force (N)	Approach velocity (ms <sup>-1</sup> )	Estimated energy (J)	Maximum force (N)	Approach velocity (ms <sup>-1</sup> )	Estimated energy (J)	
A	1	887	13.19	455	474	9.35	228
	2	976	12.2	390	474	8.07	170
B	1	1453	12.5	400	678	8.07	166
	2	1322	11.62	346	937	10.7	292
C	1	1247	15	590	1442	13.75	493
	2	936	12.93	438	1208	16.69	727
D	1	1385	12.02	349	1063	12.68	387
	2	992	10.36	259	1362	9.43	214
E	1	265	6	65	401	6.85	84
	2	271	5.78	60	432	8.63	1323
F	1				1008	13.41	599
	2				1283	13.53	610
G	1	1680	11.43	467	949	13.39	639
	2	1492	13.81	681	1070	11.17	443
$\bar{X} (\pm \sigma)$	1076 ( $\pm 432$ )	11.4 ( $\pm 2.71$ )	375 ( $\pm 176$ )	913 ( $\pm 348$ )	11.12 ( $\pm 2.75$ )	370 ( $\pm 207$ )	

**Table 5.2 – Summary table for forces, approach velocities, and estimated energies involved with slapping attacks conducted by participants A-G for section 5.3.3.2. Participant E was female, all other participants were male. No attacks were conducted with Nonic glasses for participant F due to glass availability at the time of testing.**

**Maximum forces and energies:** The average overall maximum force recorded for all attacks was 988 N with a standard deviation of 398 N (~40% of the mean). This was higher than expected, compared to a separate study [12] which investigated slaps by hand onto the dynamometer and determined an average of ~461 N for males. However, this did not involve securing fixtures or a pint glass. The maximum force observed over all attack replications (in Table 5.2) was 1680 N, which is not too distant from the force generated by a punch of a novice boxer (~2381 N) [14]. Measured velocity and subsequently calculated energy values were also higher than expected and were on average: 11.25 ms<sup>-1</sup> and 372 J, respectively. By comparison, the terminal velocity involved in stabbing attacks with knives has been estimated to be in the region of 10 ms<sup>-1</sup>, with a stab conducted overarm being capable of producing an energy of ~115 J [15]. However, this is difficult to compare due to the difference in attacking technique.

The high forces and energies involved with the slap attacks here were likely to have been affected by a number of factors. Firstly, the added mass due to the pint glass securing fixture may have affected the achievable force and enabled a higher terminal velocity, and therefore energy, to be achieved. Secondly, all participants claimed to have some athletic background: participants A, F, and G reported regularly conducting gym work; participant C reported practising martial arts; and participants B, D and E reported playing various sports and general

fitness activities. Thirdly, the tests were performed with all participants present in a group, which may have led to a competitive atmosphere that may have affected the level of the observed maximum forces. However, it is possible that to some extent this would imitate any additional forces generated by the adrenalin involved with an actual impulsive glassing attack.

**Force-time plots:** Student's *t*-tests were performed on the data and did not determine any statistical significance for the difference between the maximum forces or glassing event durations involved with using either Nonic or Tulip pint glasses. The average glassing event duration was 18.7 ms with a standard deviation of 6.2 ms. This is significantly greater than that obtained for empty securing fixture impacts (~11 ms), and suggests that individual events such as glass fracture and fixture follow-through may be involved to increase the glassing event duration. The peak force time occurred on average 60.3% ( $\sigma = 12.7\%$ ) into the glassing event, similar to the average peak force time for empty securing fixture impacts (60.9% into the glassing event).

**High speed video footage:** High-speed video footage revealed that the angle of pint glass approach may also affect the shape of force-time plots. Figure 5.9 shows 3 frames in chronological order from a slap attack by participant G. Although the majority of attacks impacted glass-first, this footage showed the glass securing fixture approaching the dynamometer at an angle with the side of the fixture impacting the face prior to the glass. In further frames the glass and fixture rotate as indicated by the blue dotted line in Figure 5.9. This could result in individual force peaks for: the fixture impact; the glass base impact; the rim/bulge region impact (likely to coincide with the fracture event); follow-through forces of fragments; and follow-through forces of the glass securing fixture. However, it is difficult to determine which peaks are direct responses to the glassing event due to the high velocity of the attacks, and it was not possible to determine from the video footage at what point the glass broke.

Further interpretation and conclusions are discussed in section 5.3.4. Further investigation was required to determine a more representative data set. This necessitated the participation of more volunteers, and the consideration of the forces involved with lower energy attacks. This is addressed in the following sub-section.

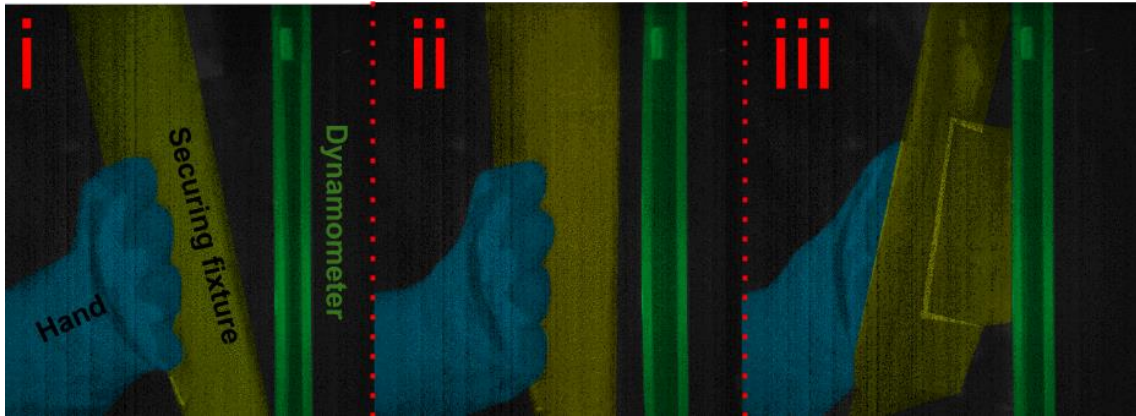


Figure 5.9 – Artificially coloured frames (for enhanced clarity) from high speed video footage of participant G with a Nonic glass in chronological order (i→iii) showing rotation of hand during a slap attack. Hand, glass securing fixture, and pint glass approach from the left. It was not possible to identify the pint glass from the footage.

### 5.3.3.3 Forces involved in pint glass slapping assaults: 2<sup>nd</sup> trial

This sub-section details a further investigation into the forces involved in glassing attacks using a slapping technique. It continues from the previous sub-section and includes a larger and broader group of volunteers (n=15: 10 male and 5 female). None of these volunteers knew of or had taken part in the previous slap attack trials (section 5.3.3.2).

The previous trials found that there was no statistical significance for differences in the force-time output due to the glass shape used. Additionally, the slap-to-slap variation per person was high, which complicated the determination of effects in the force-time output specifically due to glass shape. As such, it was considered reasonable to use a selection of various used pint glasses obtained from a local pub which included both Nonic (of various bulge sizes, see Appendix D) and Tulip glasses.

All participants were instructed to perform 3 slap attacks:

1. A 'freestyle' attack, where participants were not instructed regarding technique for the attack, as per those conducted in the previous sub-section.
2. A 'hesitant' attack, where each participant was asked to imagine pulling away from the attack immediately on impact.
3. An 'aggressive' attack, where the participant was asked to perform the slap attack with full force.

Freestyle attacks were conducted to improve the overall data set detailed in the previous sub-section. Hesitant attacks were conducted to assess the feasibility of performing an attack without follow-through effects. Aggressive attacks were conducted to assess whether the high

forces achieved in the previous trials could be matched by a second group of participants. The area immediately surrounding the dynamometer was covered by a tent in order to reduce the spread of glass fragments. This also meant that participants were not able to watch attacks conducted by others, which reduced the potential for a competitive atmosphere.

**Maximum forces:** A summary table of key average values is given in Table 5.3. A full table of all recorded parameters for this investigation is given in Appendix G. The average maximum force attained over all attacks was 547 N, with a standard deviation of 182 N (~33% of the mean). No statistically significant differences were found between the maximum forces from three attack types by a Student's *t*-test. The overall average maximum forces for freestyle and hesitant attacks were similar (533 N and 531 N, respectively), with aggressive attacks resulting in a larger overall mean (577 N). These values are considerably less (~45%) than the average maximum force value obtained in the previous trials.

Attack type	Gender	Maximum force (N)	Glassing event duration (ms)	Peak force time (ms)	% of peak force time to glassing event duration
Freestyle	M	555 ± 188	48.4 ± 62.9	16 ± 14.3	45.9 ± 18.2
	F	488 ± 222	105.8 ± 103.6	23.4 ± 12.2	41.8 ± 23.7
	Both	533 ± 203	67.6 ± 83.4	18.4 ± 14.1	44.5 ± 20.3
Hesitant	M	575 ± 153	67.7 ± 70.9	22 ± 12.3	48.7 ± 25.7
	F	443 ± 39	46.6 ± 3.1	30.9 ± 5.8	66.3 ± 11.5
	Both	531 ± 142	60.6 ± 58.7	25 ± 11.4	54.6 ± 23.5
Aggressive	M	526 ± 132	28.4 ± 14.7	18.2 ± 10.9	61.5 ± 17
	F	679 ± 244	22.2 ± 13	13.1 ± 11.3	50.2 ± 19.2
	Both	577 ± 191	26.4 ± 14.5	16.5 ± 11.3	57.7 ± 18.6
$\bar{X} (\pm \sigma)$		547 ± 182	51.5 ± 62.1	20 ± 12.8	52.3 ± 21.6

**Table 5.3 – Summary table for key values extracted from the force-time plots recorded during the second set of dynamometer tests. All values are averages, ± the standard deviation.**

Males and females provided similar overall average maximum forces, 552 N and 537 N, respectively. Surprisingly, aggressive attacks performed by male participants provided a lower maximum force on average than freestyle and hesitant attacks. This is in contrast to aggressive attacks performed by female participants, which provided the highest average maximum force value (679 N) out of all groups listed in Table 5.3. The similarity in maximum force attained between each attack type suggests that there is a low level of control involved with glassing attacks by slapping.

**Force-time plots:** Overall, the majority of force-time plots were similar and contained numerous peaks, like that shown in Figure 5.6. The overall average glassing event duration from this set of experimentation was 51.5 ms, although this was less than the standard deviation (62.1 ms). This is more than double the average glassing event duration calculated for the previous trial. The high variation of the glassing event duration was affected by an increased prevalence of participants leaning on the dynamometer immediately after impact. This occurred in ~29% of all attacks. The actual glassing event duration may be greater than that reported here, since it was perceived to end prematurely in ~33% of attacks. This was due to the force falling below 0 N before all glassing events were over, and was a known disadvantage of using the method described in sub-section 5.3.2.2 to characterise the glassing event duration.

Despite the overall similarity in maximum forces attained during this set of experimentation, the glassing event duration in aggressive attacks was significantly less than the other attack types. It was more similar in length to attacks in the previous trial. This was affected by the lower number of perceived lean-on instances immediately after impact (4 out of the 15 aggressive attacks). This suggests that in aggressive attacks, a participant is more likely to quickly remove their hand from the impact area.

Further interpretation and conclusions are discussed in section 5.3.4.

#### 5.3.4 Conclusions

Section 5.3 has detailed investigations into the forces involved in glassing attacks, particularly slapping attacks. There are a number of conclusions that can be drawn from these investigations, which are discussed below.

- The overall average maximum force from all glassing attacks by slapping (23 participants, 74 tests) was 706 N with a standard deviation of 346 N. However, this may be an overestimate of the true force involved with a slapping attack due to the added weight of the fixture used to hold the glasses for safety reasons. Additionally, forces in actual attacks may be lower due to the compliance of the target (e.g. movement of the neck in head attacks and the force absorbed by skin and flesh).
- Attack-to-attack variation and participant-to-participant variation was very high.
- The forces involved with glassing attacks include a number of key events, most likely due to: initial impact force (which may or may not include breakage), a secondary impact with another portion of the glass (if not broken by initial impact force), and the follow-through of glass fragments and the attacking hand. Additional forces may have

been recorded in this study due to impact of the glass-securing safety fixture. Force peaks were more apparent for attacks involving lower forces.

- Calculated energies involved with slapping attacks ranged from 60 J to 727 J. However, this is likely to have been affected by the added weight of the glass-securing safety fixture, and actual energies may be less.
- A glassing slapping attack is unlikely to be well-controlled and may involve leaning on the slapping target immediately after impact. When volunteers were asked to change their style of slapping attack, there was no statistically significant change in maximum force attained. However, aggressive slapping attacks may be less likely to involve any leaning on the target immediately after initial impact.
- Throws with intact pint glasses resulted in significantly less force being produced (~120 N) than in attacks by slapping or thrusting.
- Thrusts with pint glasses were less likely to result in glass fracture.

There are a number of possibilities for further investigation on this work. There are also certain elements of the investigations detailed above that could be improved. These are discussed below.

- The method for holding pint glasses during experimentation could be altered in order to add minimum mass to the hand and be as compact as possible. This would improve the accuracy of forces and energies involved, and reduce the occurrence of irrelevant additional force peaks.
- A larger group of volunteers would improve the data set and would facilitate the determination of trends based on glass type, attack type, and gender. Ideally the group of volunteers should be representative of the general population, for example by reflecting the expected distribution of statures.
- Further tests into the forces involved with other attack types (as described in section 5.2.1) would enable a broader understanding of forces as affected by attack technique. Thrusting attacks would require a new securing fixture or other method to ensure that the glass could be held safely by volunteers in the drinking position (section 5.2.2).
- Further high speed video footage of the attacks taken with better lighting conditions and a higher frame rate would enable the causes of the observed force peaks to be better distinguished, particularly for high velocity attacks. This could then be used along with the data obtained in this study to determine force values for individual events (such as glass breakage and fixture follow-through).

- An improved methodology for determining the glassing event duration would provide more representative values and reduce occurrences of premature ending of the glassing event window.
- Adapting the target to have a similar level of compliance to a human head and neck would result in recorded forces more comparable to actual transferred forces involved in glassing attacks.

## 5.4 Laceration/ injury patterns associated with glassing attacks

### 5.4.1 Overview

This section details a series of investigations into damage patterns caused by and the injury severity of slapping attacks with annealed and tempered pint glasses. This was primarily conducted using a drop tower with modified impacting fixtures, but a number of tests were conducted manually using the pint glass securing fixture detailed in the previous section (Figure 5.4). Glasses were mostly impacted onto a flat target, although some were impacted onto a mannequin head. Injury patterns were assessed by viewing cuts and punctures to silicone layers.

### 5.4.2 Materials and methods

#### 5.4.2.1 Equipment

The equipment used to perform slapping attack replications with a drop tower is shown in Figure 5.10. The drop tower pictured previously in Figure 3.20 was used. Two pint glass holding fixture types were used over the course of experimentation. The first was a simplified gripping hand<sup>§</sup> made from Nylon 6 plastic. This had a total mass of 950 g (b in Figure 5.10) that was designed to have a similar inside diameter (hand length) and width (palm width) to an average male human hand (190.5 mm and 88.9 mm, respectively [16]). The second was a flat surface impactor with a mass of 842 g (c).

The fixtures extended outwards from the drop tower guide rails and attached to drop fixture (a) with four cylindrical roller ball bearings. These had a mass of 1.03 kg and fitted between the guide rails. This ensured that the fixtures fell along the vertical drop path without rotation. Glasses were held in place either by applying a half-cured silicone layer that held the glass once set, or by using elastic bands. On some occasions, additional weight was added to the

---

<sup>§</sup> The gripping hand shown in Figure 5.10 b is the second iteration of the fixture. An original wooden version was used for 2 tests before it fractured.

fixtures to counterbalance the falling assembly. In such cases, the drop height was adjusted accordingly to result in the desired energy at impact using equation 3.5.

The targets used in drop tower testing are shown in Figure 5.11. They were a 381 mm tall polyethylene (PE) mannequin head fitted to an adjustable base, and flat layers of silicone on a wooden platform. Silicone layers were attached to the PE head in most tests. The damage caused to the silicone layers on both targets was used to estimate injury potential.

Quantifying the accuracy of replication of the mechanical behaviour of human skin is complicated due to the variable properties of skin. The properties of skin and the selection of substitute materials for skin is discussed further in section 6.3 of this thesis. For this section decisions were largely guided by consideration of the Shore hardness of the silicones used, since the silicone layers were not subjected to any large strains. Shore hardness is typically used to quantify the hardness of rubbers. It is based on the depth to which a presser foot of standard dimensions penetrates a material at a particular force. Human skin has been reported to have a Shore O hardness of  $25 \pm 5$  [17], which approximately equates to a Shore A hardness of 15-20 [18].

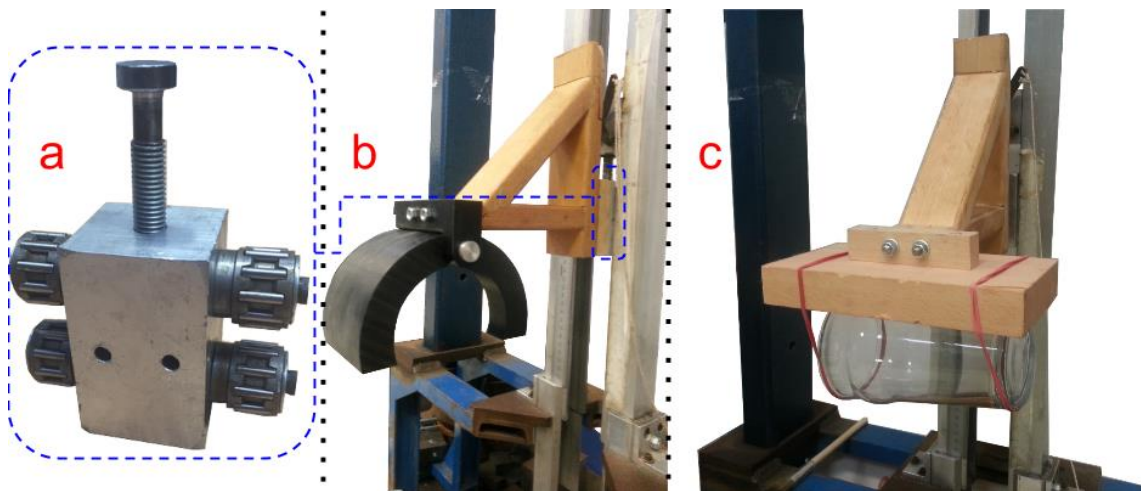


**Figure 5.10 – Modified drop tower impactor equipment used for systematic replication of slapping attacks. a – drop fixture attachment with cylindrical roller ball bearings used to keep movement within guide rails; b – hand/ claw fixture attachment; c – flat surface fixture attachment.**

Two different silicone mixtures were used during experimentation. For coating curved surfaces like the PE head and the impacting gripping hand, it was necessary for the mix to have a fast curing time. For this, a silicone layer referred to in this section as Silicone A was used. This was a silicone with a 6-minute curing time and a Shore A hardness of 10 (PlatSil Gel 10, Mouldlife, Newmarket, England). This was also used as a ~1 mm flat layer in a number of tests. Additionally, a second silicone layer referred to as Silicone B in this section was used. This was

a harder ~2 mm thick silicone sheet with a Shore A hardness of ~55 [19] (Transil 55(B) + Transil 40(A), Mouldlife, Newmarket, England) was mixed for some tests and used as an under-layer. This was used to assess the severity of damage by depth of penetration, with more severe damage penetrating through both layers. A similar method of assessing the damage severity of glass by noting the damage caused through successive layers of material has previously been conducted for assessing the safety of car windscreens [20].



**Figure 5.11 – Targets used in drop tower testing. Left – polyethylene mannequin head on adjustable base; right – silicone layers (layer 1: ~1 mm thick layer of 10A Shore hardness, layer 2: ~2 mm thick layer of ~55A Shore hardness) together on a wooden platform after a test run with an annealed pint glass, showing debris left on the layer.**

#### 5.4.2.2 Procedure

The general procedure for conducting slap attack replications with a drop tower and the equipment described in the above sub-section was as follows:

1. The impact target was positioned on the drop tower table.
2. A pint glass was attached to the drop tower holding fixture.
3. The fixture was raised to the required height to result in the desired impact energy (as determined by equation 3.5).
4. Perspex shielding was erected in place around the drop tower table.
5. The drop tower holding fixture was released and allowed to fall onto the target.
6. Wearing slash-resistant gloves, the shielding was removed and the drop tower holding fixture was raised back up within the guide rails.

7. Main areas of damage regions were marked with a marker pen and documented. A damage region may include a number of cuts and/ or punctures that are located closely together.
8. Glass was removed from the drop tower table and placed in a sharps bin, which was subsequently taken to a recycling point.

For each test, where feasible, the following was recorded on the silicone layer(s):

- The number of cuts, namely those which had not penetrated through the full thickness of each layer.
- The number of punctures, namely those which had penetrated through the full thickness of each layer.

The damage pattern on the silicone layer(s) created by the cuts/punctures was also assessed and related to typical fracture patterns expected of pint glasses broken due to impact.

### **5.4.3 Results and discussion**

#### **5.4.3.1 Initial tests: damage patterns on PE mannequin head**

A pilot study was conducted with a simple impacting glass fixture attached to the drop tower main fixture (Figure 5.10, a) onto the adjustable PE mannequin head (Figure 5.11). An aluminium plate was attached to the impacting fixture, with two suction cups applied to the face of the plate that held the glass. Each glass was held midway between the rim and base. All impacts were made by dropping the fixture from a height of 1 metre, and the majority were made to the top of the PE head.

For each test, a swimming cap was placed onto the mannequin head instead of a silicone layer, and was positioned to be central around the intended impact point. The swimming cap had the effect of exaggerating any cuts made, because the elastic energy used to hold it in place pulled cuts longer. In order to account for this, each impact was recorded with a high speed camera at a rate of 1500 frames per second. This allowed for initial cut patterns to be viewed rather than those with cuts that had propagated after the glass impact.

A total of 17 glasses were tested, which included 5 of each of: tempered Nonics, Ultimate Pints, and Perfect Pints (all first introduced in chapter 3, investigated in detail in chapter 4), and two annealed glasses. Each glass was abraded prior to testing as described in section 3.5.2.2.

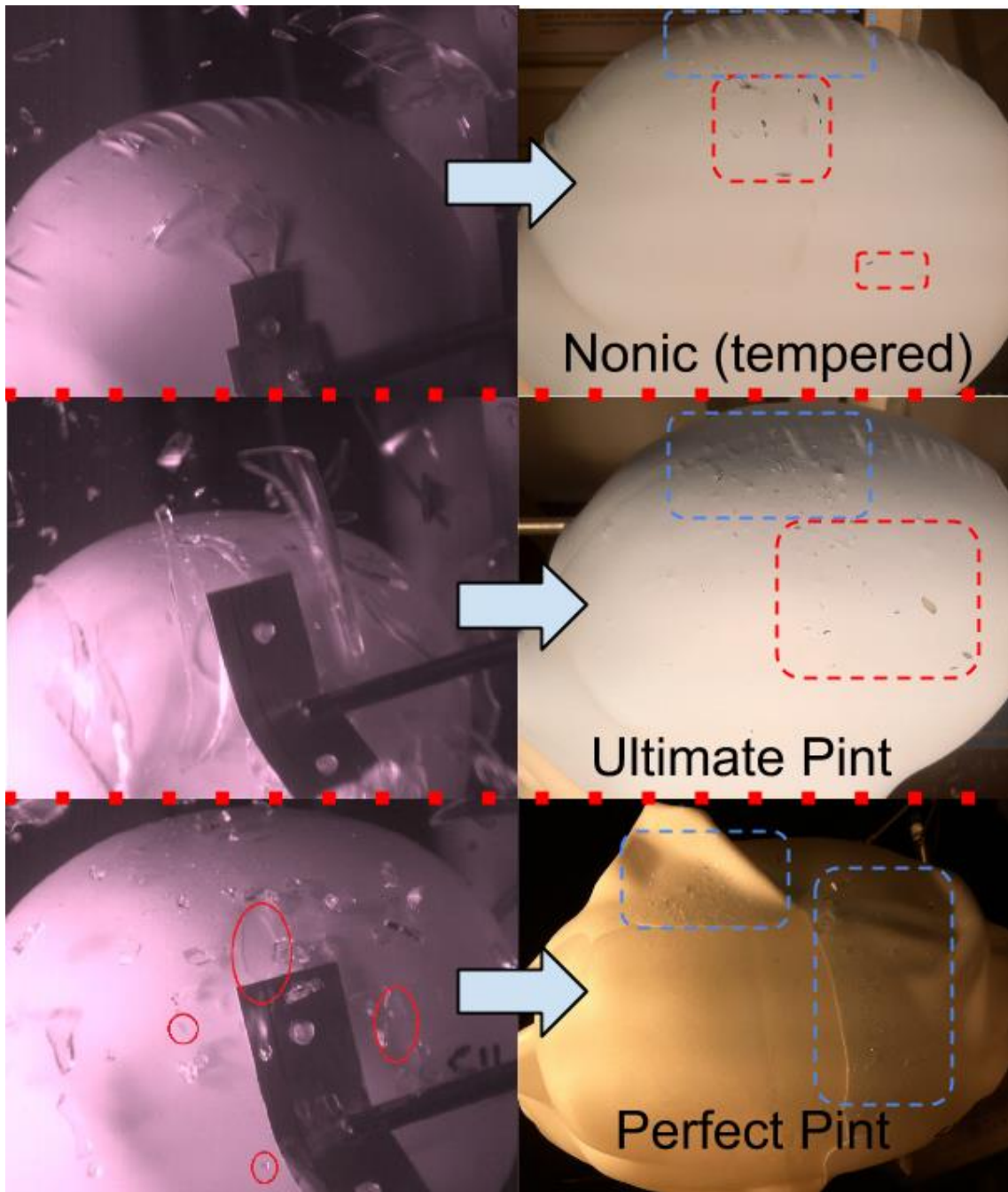
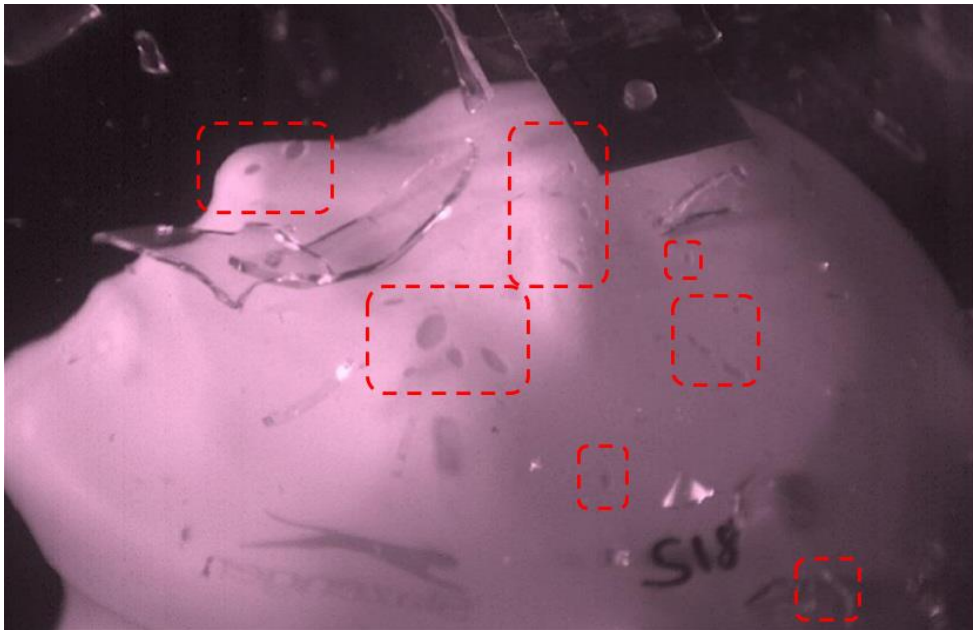


Figure 5.12 – Examples of high speed video frames (left) and subsequent damage to swim cap (right) for one of each tempered Nonic, Ultimate Pint, and Perfect Pint test. Red dashed boxes indicate areas with a high number of cuts (typically in the main impact area), and blue dashed boxes indicate areas with a high number of small glass splinters present on the surface. The cut patterns varied largely between samples and the examples given are not representative of all tests. The ridges seen at the top of the top and middle swim caps were due to the fitting of the cap to the head, and were present prior to testing.

Examples of damage caused by three glasses are shown in Figure 5.12. No general overall cut pattern was found, and the extent of damage varied, with some ripping the swimming cap entirely. Common to all impacts however was a high concentration of cuts within the main area of impact behind the aluminium plate. Small glass particles (splinters) were also

commonly embedded into the cap. The majority of fragments were projected away from the impact area and fell away from the PE head. Overall, very little damage to the head was observed from tempered glasses. Both annealed glasses caused the swim cap to fully rupture, which was caused by one long cut rather than numerous small ones.

A further test was conducted with one tempered Nonic pint glass, which was aimed directly at the PE head face (see Figure 5.13). This showed a wider spread of damage, particularly present at features protruding from the head: the nose, ears, and cheekbone areas. However, these were also areas subjected to high elastic strain by application of the swim cap.



**Figure 5.13 – Frame taken from high speed video of a drop tower slap attack with a tempered Nonic glass impacted to the mannequin face. Red dashed areas indicate areas of damage.**

Two final tests to the PE head were conducted with a simplified hand gripping fixture (Figure 5.10, b) rather than the aluminium plate, in order to better replicate the held area of the glass. Two abraded Tulip glasses were used, one annealed and one tempered. Both the PE head face and inside surface of the gripping fixture were coated in a layer of silicone A of approximately 1 mm thickness. The glass was held around the base region, similar to the drinking position (section 5.2.2). After impact, the silicone layer was peeled away from the simplified hand to facilitate damage review. Two resulting damage patterns from the PE head face and gripping hand are shown in Figure 5.14. Corresponding damage data is given in Appendix H.

A roughly similar distribution of damage occurred to both the head and hand from both attacks. Damage fitted into three main categories. Firstly, scratches that were short in length and minimal in depth. Secondly, cuts that were variable in length with noticeable depth, but

had not penetrated fully through the silicone layer. Thirdly, punctures that were also of variable length but had penetrated fully through the silicone layer. For both glasses, a portion of the silicone area of the hand opposite to the PE head impact point tore away from the hand during the attack event, and was found attached to some fragments that had fallen close to the impact site.

Scratches were typically found in high frequency groups on the PE head for both glasses, and could not feasibly be measured. The annealed Tulip glass caused a greater number of cuts than the tempered glass. Cuts from the annealed glass varied from 4 mm to 20 mm in length, with an average of 10.5 mm, and cuts from the tempered glass were 4-15 mm in length. The tempered Tulip glass resulted in 5 punctures, which ranged from 1 mm to 4 mm without causing any noticeable damage to the PE head or hand fixture. In contrast, the annealed glass resulted in 4 punctures. However, one annealed puncture was 14 mm in length and caused a deep cut into the PE head in the jaw region (region 3 in Figure 5.14, bottom left).

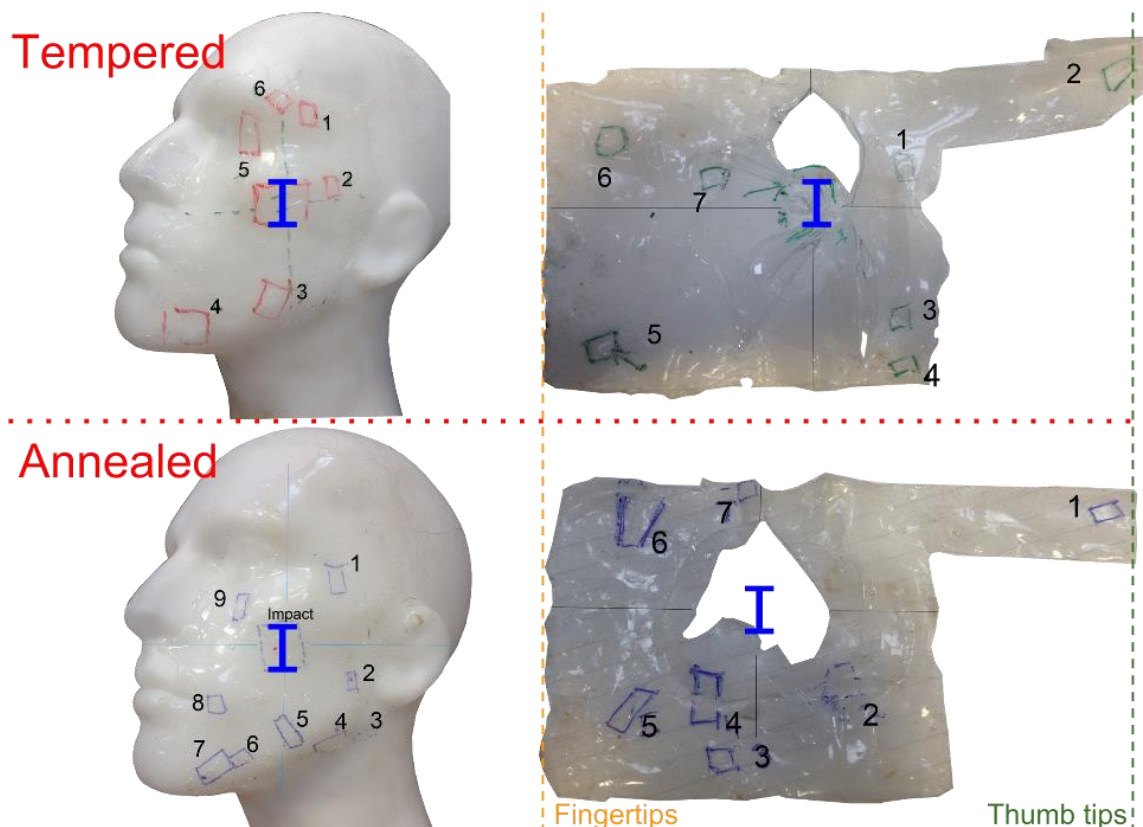


Figure 5.14 – Damage patterns to top layers of the PE head face (left) and the simplified gripping hand (right) resulting from two separate tests. a: abraded tempered Tulip glass, b: abraded annealed Tulip glass. The impact point is labelled with a blue 'I'. The numbers shown correspond to damage areas which were noted in a clockwise order. The frequency and length of cuts in the noted areas is given in Appendix H.

All initial tests showed that the damage spread observed was highly dependent on the dimensions of the holding fixture and target. Further tests utilised flat impactors and targets to better characterise the damage spread, so that the damage spread could then be extrapolated to targets of more complex shape.

#### 5.4.3.2 Damage patterns in manual slapping attacks

This sub-section gives a brief overview of the damage caused by a slapping attack onto a flat target, in order to enable extrapolation to the damage spread on targets of a complex shape. 6 damage assessments were carried out onto single layers of silicone A attached to the flat dynamometer face, by the method outlined in Figure 5.3. This was done by a single participant, with 3 Tulip pint glasses and 3 Nonic pint glasses. 2 of each were tempered (1 new and abraded, 1 used) and 1 of each was annealed as per the method outlined in section 3.3.3. Each damage pattern is shown in Figure 5.15. The corresponding damage data is given in Appendix H.

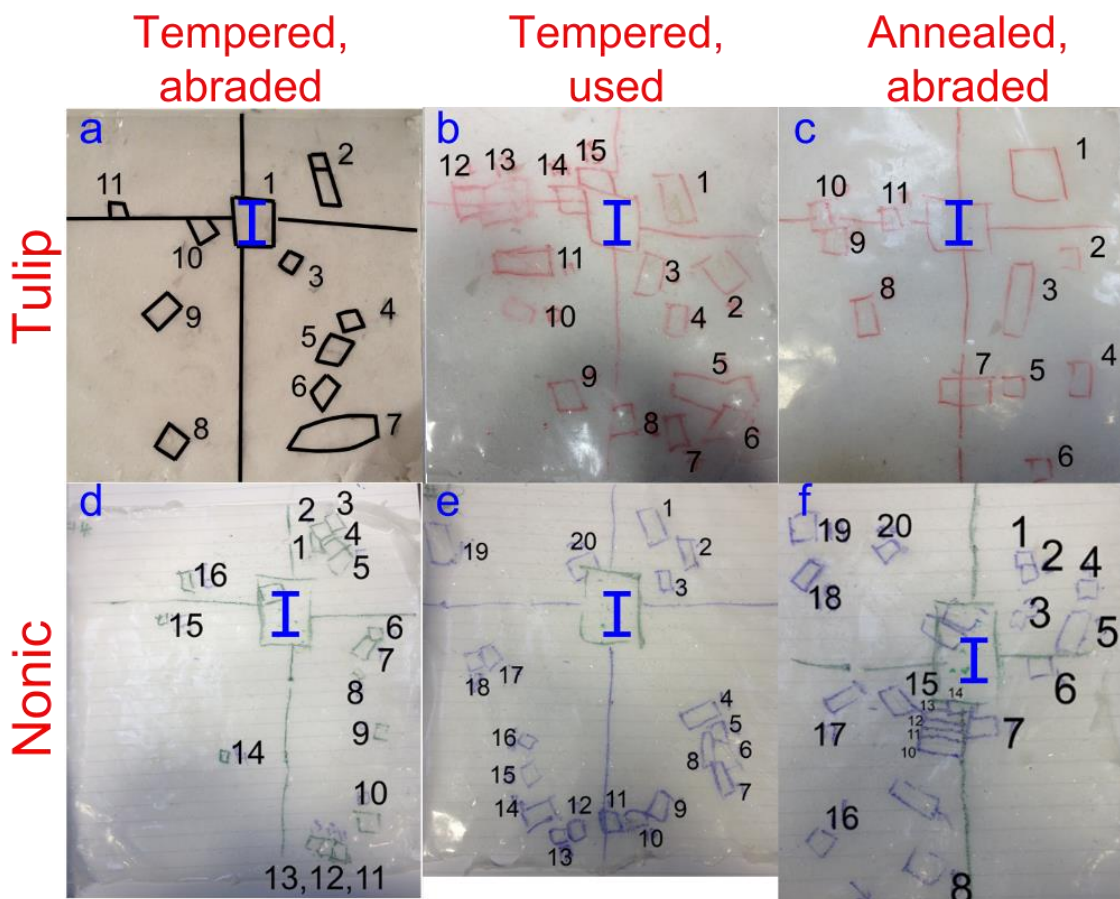


Figure 5.15 – Damage patterns onto single layers of silicone A made by a manual slapping method outlined in Figure 5.3. The impact point is labelled with a blue 'I'. The individual boxes shown are separate damage areas, which are described in Appendix H.

These tests showed a high frequency of damage regions over a wide area surrounding the region of impact. The location of individual damage regions varied significantly between tests. However, damage patterns produced from attacks using tempered glasses (a, b, d, e, in Figure 5.15) showed very little damage directly below the impact region, and to some extent the damage pattern matched the pint glass profile (particularly noticeable in damage pattern e). This is most likely due to the fracture surfaces of the glass fragments being preferentially aligned for penetration of the silicone layer.

It should be noted, however, that the glass securing fixture used in these tests used wooden blocks either side of the glass to hold it in place. This may have restricted the freedom of side fragments and influenced the observed damage pattern. Additionally, the entire glass was pushed into the target by the glass securing fixture. This is likely to have restricted the freedom of fragments that may have otherwise projected away from the target during an attack with a bare hand. This is addressed in the following sub-section. Further interpretation and conclusions are discussed in section 5.4.4.

#### **5.4.3.3 Comparison of damage caused by annealed and tempered glasses**

Section 5.4.3.1 assessed the damage caused in a pint glass slapping attack onto a curved surface with a drop tower methodology, and section 5.4.3.2 conducted manual attacks onto a single flat target. This sub-section presents a systematic investigation into the damage patterns caused by a flat holding fixture with abraded annealed and tempered Nonic glasses (10 of each) onto a flat target.

Impactor type c (see Figure 5.10) was used with the glass held with only the base of the glass supported opposite to impact. This was to replicate a hand holding the glass in the drinking position (see section 5.2.2). Two silicone layers were sat above a flat wooden target as demonstrated by b and c in Figure 5.11. Layer 1 (silicone A) sat above layer 2 (silicone B) and the number and lengths of cuts (damage not penetrating fully through the layer) and the number and lengths of punctures (damage penetrating fully through the layer) in each layer were recorded. This enabled an additional assessment of damage severity by noting the penetration depth by the number of layers that had been penetrated. However, due to the high frequency of cuts to the first layer obtained for all glasses, it was not feasible to measure all cuts on this layer. Additionally, a high frequency of embedded glass debris further obscured the top layer damage.

	Annealed		Tempered	
	Average (range)	Standard deviation	Average (range)	Standard deviation
<b>FIRST LAYER:</b>				
Number of cuts:	Many	-	Many	-
Cut length (mm):	-	-	-	-
Number of punctures:	5 (3 – 8)	1.6	5 (2 – 9)	1.9
Puncture length (mm):	11.8 (3 – 36)	7.1	6.2 (2 – 17)	3.7
<b>SECOND LAYER:</b>				
Number of cuts:	1.1 (0 – 2)	0.7	0.6 (0 – 2)	0.7
Cut length (mm):	9.5 (5 – 21)	4.8	3.5 (2 – 12)	1.7
Number of punctures:	2.3 (1 – 5)	1.2	2.6 (1 – 6)	1.7
Puncture length (mm):	11 (3 – 27)	5.7	4.5 (2 – 12)	2.7

**Table 5.4 – Summary of damage data for silicone layers used as targets in flat target and impactor drop tower tests. Full damage measurement data is given in Appendix H. The range of measured values is given in brackets.**

After ensuring adequate weight counterbalancing, the entire impactor setup had a mass of ~3 kg. The impactor was dropped from a height of 2 metres, corresponding to an impact energy of ~59 J. This corresponded to the lower bound of the energies calculated in section 5.3.3.2 during glassing attack replications. All glasses broke on impact. A summary of the overall data is given in Table 5.4. Full cut and puncture measurement data is given in Appendix H.

Overall, a similar number of damage areas (cut and puncture instances) were noted for both annealed and tempered glasses. The majority of damage occurred near the base region where the glass was supported by the flat impactor, although damage was commonly observed in mid-height areas for both glasses. The base area damage was also the area where most 2<sup>nd</sup> layer penetration was observed. Examples of damage patterns in both layers are shown in Figure 5.16 and Figure 5.17, respectively.

However, the cut and puncture lengths showed significant differences between annealed and tempered glasses on both layers ( $p < 0.01$ ). Annealed glasses typically caused cuts and punctures that were 2-3 times longer than tempered glasses. Damage to the 2<sup>nd</sup> silicone layer usually involved punctures rather than cuts.

Further interpretation and conclusions are discussed in section 5.4.4.

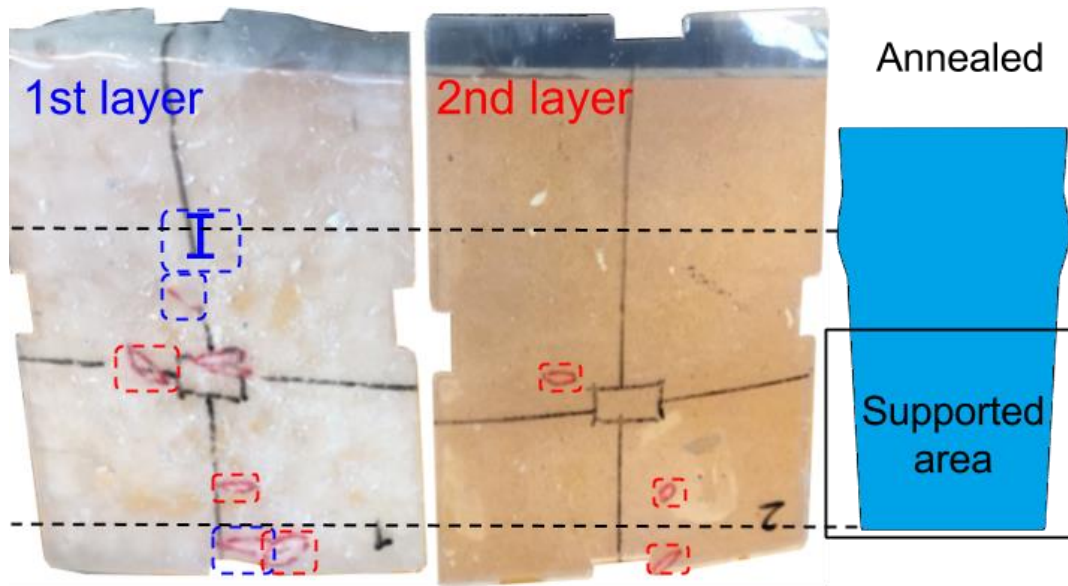


Figure 5.16 – 1<sup>st</sup> and 2<sup>nd</sup> layers of silicone from an annealed Nonic glass impact (sample ref A10 in appendix Table H.4). Damage limited to the top layer is indicated by the dashed blue dashed regions.

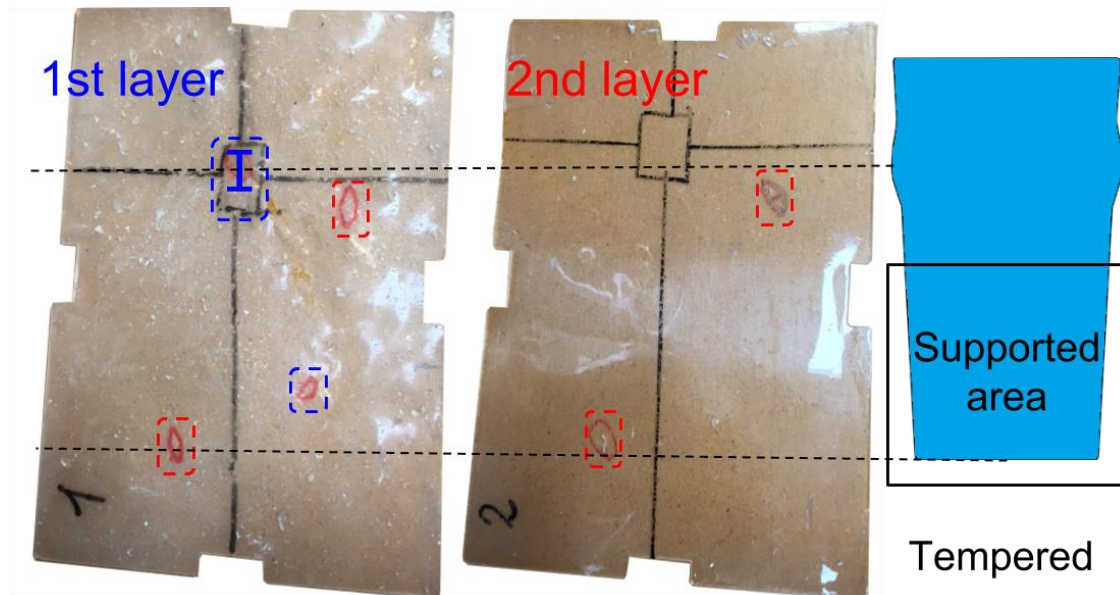


Figure 5.17 – 1<sup>st</sup> and 2<sup>nd</sup> layers of silicone from a tempered Nonic glass impact (sample ref T5 in appendix Table H.5). Damage limited to the top layer is indicated by the dashed blue dashed regions.

#### 5.4.4 Conclusions

Section 5.4 has detailed investigations into the damage patterns associated with slapping attacks. There are a number of conclusions which can be drawn from this work, which are discussed below.

- The majority of damage caused in a pint glass slapping attack is centred around the impact point and is largely affected by the dimensions of the impact target and how the glass is held. Glasses held over a wider area of the glass wall are more likely to

cause a wider spread of damage during the follow-through event of the attack after glass fracture.

- Furthermore, regions of the glass supported by a holding fixture generally caused more deeply-penetrating damage (Figure 5.16), although significant damage could still occur outside this region (Figure 5.17).
- Attacks with tempered pint glasses were seen to result in either more damage areas (section 5.4.3.1) or an equal amount of damage areas (section 5.4.3.2 and section 5.4.3.3) to annealed pint glasses. However, the damage caused by annealed glass resulted in longer cuts and punctures than tempered glass, and resulted in more damage to the equipment used. The maximum cut/ puncture length observed from a tempered glass was 20 mm, and 36 mm from and annealed glass.
- No specific damage patterns related to individual glass shape was observed. However, if the entire glass is supported during an attack the damage may approximately match the glass profile for tempered glasses (section 5.4.3.2).
- All impact events were associated with a high volume of small glass dust (splinters) remaining on the target after fracture.

There are a number of possibilities for further work on the investigations detailed in this section, as well as opportunities for improvement on this work. These are discussed below.

- Further tests by the two silicone layer method outlined in section 5.4.3.3 with various tempered glasses could assist in determining adequate levels of thermal temper for pint glasses by comparison of damage severity.
- A scale to cross-check damage levels through target layers could be developed, which could be used for quality control purposes.
- Further tests based on other glassing attack methods would be necessary to gain a better overall understanding of the damage pattern as affected by attack type.
- A larger volume of tests would be required to confirm the repeatability of particular damage patterns.

## 5.5 Chapter summary

The main aim of this chapter was to build an understanding of the dynamics and damage patterns involved with assaults where drinking glasses are used as an impulsive weapon. Furthermore, it aimed to investigate what features of breakage result in lower levels of damage severity in such assaults.

The chapter firstly considered the prevalence and dynamics of assaults involving drinking glasses in section 5.2. Methods and techniques employed for glassing attacks with pint glasses were discussed. A short survey into how volunteers would hold a pint glass in a hypothetical glassing attack was conducted. It found that the majority of participants would hold the glass as it would be held whilst drinking.

Secondly, the forces involved in glassing attacks were quantified using a dynamometer setup with a number of volunteers in section 5.3. Key force peaks were identified from force-time plots which corresponded to the initial impact, fracture, and follow-through events of the attack. The forces involved with slapping attacks were found to vary largely (265-1680 N), and participants showed a low level of control as to the magnitude of force they produced.

Finally, section 5.4 considered the damage patterns involved with glassing attacks. Novel methodologies were outlined and used to replicate pint glass slapping attacks and to assess damage spread and severity. It was found that the amount of damage caused was dependent on the proportion of the glass held during the attack. This corresponded to the portion of fragments involved in the follow-through stage of the glassing event. It was found that attacks with tempered pint glasses did not decrease the overall spread of damage, but did decrease the severity of damage.

It can be seen from the investigations in this chapter that the lowest potential for injury from a pint glass is likely to result from a fully tempered pint glass. However, since there is wide variability in glassing attacks with a number of factors involved, a tempered pint glass must be tempered with sufficient temper levels throughout the article such that the resulting fragments are of a minimum size. This is due to:

- The variety of methods by assailants in glassing attacks (section 5.2).
- The range of forces and dynamics involved, which in most cases far exceeded the necessary force to penetrate skin (section 5.3).
- That severe damage can occur from fragments from held and free regions of a pint glass during an attack (section 5.4).
- That annealed glass results in more severe damage from a glassing assault (section 5.4).

The following chapter outlines a different approach to assess the injury potential of glass fragments, by considering their geometrical properties and cutting performance relating to sharpness.

## 5.6 Chapter references

- [1] "Using Design to Reduce Injuries from Alcohol Related Violence in Pubs and Clubs," *Home Office, Design Out Crime*, 2010.
- [2] R. Chaplin, J. Flatley, and K. Smith, *Home Office Statistical Bulletin: Crime in England and Wales 2010/11*. 2011.
- [3] J. P. Shepherd, M. Price, and P. Shenfine, "Glass Abuse and Urban Licensed Premises," *Journal of the Royal Society of Medicine*, vol. 83, no. April, pp. 276–277, 1990.
- [4] P. Cassematis and P. Mazerolle, "Understanding Glassing Incidents on Licensed Premises: Dimensions, Prevention and Control," *Brisbane, Australia: Griffith Univ. and Queensland Government*, 2009.
- [5] M. Worthington, J. Mckinney, and P. Percival, "The Glass Debate – It's Your Choice," *Entry for the 2008 Tilley Awards*, 2008.
- [6] K. S. Coomaraswamy and J. P. Shepherd, "Predictors and Severity of Injury in Assaults with Barglasses and Bottles," *Injury Prevention*, vol. 9, no. 1, pp. 81–84, 2003.
- [7] M. A. Rothschild, B. Karger, and V. Schneider, "Puncture Wounds Caused by Glass Mistaken for with Stab Wounds with a Knife," *Forensic Science International*, vol. 121, pp. 161–165, Oct. 2001.
- [8] P. T. O'Callaghan, M. D. Jones, D. S. James, S. Leadbeatter, S. L. Evans, and L. D. M. Nokes, "A Biomechanical Reconstruction of a Wound Caused by a Glass Shard — A Case Report," *Forensic Science International*, vol. 117, pp. 221–231, 2001.
- [9] V. Sterzik, B. Kneubuehl, W. Rupp, and M. Bohnert, "Stab or Throw? Biomechanical studies on the Injuring Potential of Glass Fragments," *Forensic Science International*, vol. 199, pp. e1–e4, 2010.
- [10] A. L. Warburton and J. P. Shepherd, "Effectiveness of Toughened Glassware in Terms of Reducing Injury in Bars: A Randomised Controlled Trial," *Injury Prevention*, vol. 6, no. 1, pp. 36–40, 2000.
- [11] V. Sterzik, B. P. Kneubuehl, D. Ropohl, and M. Bohnert, "Injuring Potential of Drinking Glasses," *Forensic Science International*, vol. 179, pp. e19–e23, 2008.
- [12] G. Nolan, "Quantification of Forces Involved in Stabbings," Ph.D. Thesis, University of Leicester, 2014.
- [13] E. Kreighbaum and K. M. Barthels, *Biomechanics: A Qualitative Approach for Studying Human Movement*, 4th Edition, Allyn and Bacon, 1996.
- [14] M. S. Smith, R. J. Dyson, T. Hale, and L. Janaway, "Development of a Boxing Dynamometer and its Punch Force Discrimination Efficacy," *Journal of Sports Sciences*, vol. 18, no. 6, pp. 445–450, Jan. 2000.

- 
- [15] I. Horsfall, P. D. Prosser, C. H. Watson, and S. M. Champion, "An Assessment of Human Performance in Stabbing," *Forensic Science International*, vol. 102, no. 2, pp. 79–89, Jun. 1999.
- [16] H. Dreyfuss, *The Measure of Man: Human Factors in Design, Revised and Expanded 2nd Edition*. Whitney Library of Design, 1967.
- [17] M. Romanelli and V. Falanga, "Use of a Durometer to Measure the Degree of Skin Induration in Lipodermatosclerosis," *Journal of the American Academy of Dermatology*, vol. 32, no. 1, pp. 188–191, 1995.
- [18] "Shore Durometer Conversion Chart," *Thermal Tech Equipment Co. Inc.* [Online]. Available:  
<http://www.ttequip.com/knowledgelibrary/TechPageShoreDurometerConversionChart.htm>. [Accessed: 08-Apr-2015].
- [19] Mouldlife Ltd., private communication.
- [20] S. E. Kay, J. Pickard, and L. M. Patrick, "Improved Laminated Windshield with Reduced Laceration Properties," *SAE Technical Paper*, paper no. 730969, 1973.

## 6 Characterisation of the sharpness of glass fragments

### 6.1 Introduction

The concept of sharpness is important to this study as it is a means of qualitatively or quantitatively describing the ease at which an object can penetrate a target. Establishing the sharpness of a glass fragment contributes therefore to an understanding of the injury potential of the fragment (i.e. the ease at which a glass fragment can penetrate skin). However, definitions of sharpness can be unclear and determining an appropriate methodology for measuring sharpness is complex. This chapter addresses these issues and suggests methodologies for measuring the sharpness of glass fragments.

In section 6.2, the methods used to classify sharpness in various studies are discussed. In section 6.3, simulants for human skin used in studies relevant to cutting processes are reviewed. Section 6.4 considers the geometrical factors of glass fragments relevant to cutting and outlines a system for categorising cutting edges which is implemented in chapters 7 and 8. The remainder of this chapter describes the methodology employed in this study to quantify the sharpness of glass, and includes an exploratory investigation into the most influential geometrical aspects on fragment penetration ability.

### 6.2 Sharpness assessment methods

This section reviews methods used in other studies to assess the sharpness of various cutting instruments.

An object's sharpness is usually defined either by its ability to cut or by the degree to which its edges are not rounded [1]. These two definitions form the basis of methods used to characterise sharpness. These methods are most commonly conducted in reference to blades (particularly knives) [2]–[11], tools for machining metals [12]–[15] or for surgical instruments [16]–[20]. Studies that aim to quantify the sharpness of glass broken by uncontrolled processes (where the crack path(s) are not pre-determined) are comparatively rare [21], [22], although much attention has been given to specific, controlled glass breakage methods that produce an optimal cutting edge for microtome knives [23]–[25]. It is clear that there is a wide range of possible methods of assessment, which are relevant according to the instrument and/or application being considered.

There are four parts to this section. Firstly, standard methods for characterising the sharpness of implements are discussed. Secondly, a short discussion on qualitative measures for the

assessment of sharpness is presented. Thirdly, quantitative methods to characterise the sharpness of an implement by its geometry are overviewed. Fourthly, quantitative measures of sharpness by measurement of the force or energy required to perform a particular cutting operation are considered.

### **6.2.1 Standard methods for measuring sharpness**

There are very few standard methods that specifically identify sharpness as the main indicator of instrument quality. The British Standard for the sharpness of cutlery (ISO 8442-5:2004) [26] measures sharpness by the depth of cut attained by a knife into a cardboard/silica substrate when the blade is reciprocated forwards and back with a 50 N applied top-load. This reciprocating motion is important as it lowers the force required to penetrate to a particular depth, a phenomenon that is quantified by the “slice-push ratio” [27]. An automatic testing machine has been built to adhere to this standard (Knife and Blade Cutting Test Machine, CATRA, Sheffield UK).

Another standard concerning sharpness, for stainless steel surgical instruments (BS 5194-1:1985) [28], is based on the instrument’s ability to cut through different thicknesses of gauze. Whilst these are useful methods for verifying the performance of their respective instruments, they lack universality. Both the substrate to be cut and the method of cutting are unlikely to be applicable to most other cutting operations. This has led to a wide range of methods being undertaken by researchers to rank the sharpness of various instruments.

### **6.2.2 Qualitative sharpness assessment**

Qualitative assessments for characterising sharpness are generally not preferred since they risk being subjective [4]. These tests typically involve categorising the cutting instrument by how it looks or feels, which has led to various terminologies being used [19]. The quality of the cutting edge has been categorised as either “fine edge”, “burr edge” or “blunt edge” [29]. Placing the tip of a knife on a fingertip and describing the tip as either “blunt”, “moderately blunt” or “sharp” was suggested by Davison as a method for pathologists to assess the sharpness of knives [30].

### **6.2.3 Quantitative sharpness assessment by geometrical considerations**

A simple categorisation of quantitative methods used to characterise sharpness can be made by separating the techniques into those that are based purely on geometrical considerations from those that define sharpness by the force or energy required to perform a particular cutting operation. Non-contact geometrical measurement methods are advantageous in that they do not contaminate or cause damage to the cutting edge. However, such methods are

prone to yielding misleading results, as a measured feature deemed to be sharp may bend or disintegrate on contact, and the same feature may not even be involved in a particular cutting application.

Geometrical assessments typically involve measurement of the tip radius of a cutting instrument and the included angle (or wedge angle) through a cross section of the cutting edge, as defined in Figure 6.1. These measurements are usually taken to complement results from force or energy sharpness assessment techniques, which are considered in section 6.2.4. The tip of a cutting edge is not necessarily circular, so fitting a radius of curvature to the actual tip profile is conducted at the measurer's discretion, but this has still proved to be a useful parameter for sharpness investigations [31]. Depending on how the cutting edge was formed, there may be more than one wedge angle present, leaving a profile that is sometimes termed a 'double wedge angle' [5]. Additionally, the thickness of the blade 1 mm back from the cutting edge has been suggested as a key measurement characteristic [31] to account for changes in the included angle further from the tip. The included angle is typically  $\sim 15^\circ$  for razor blades and between  $30\text{-}40^\circ$  for kitchen knives, and edge radii of  $5\ \mu\text{m}$  and  $17\ \mu\text{m}$  are typical of scalpels and new safety razor blades respectively [31].

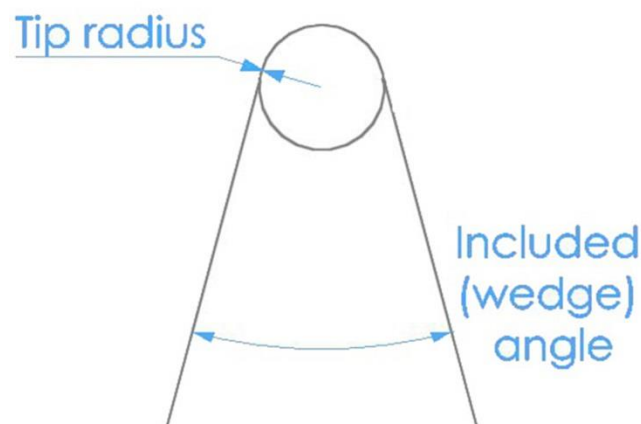


**Figure 6.1 – Typical measurements taken to characterise sharpness, where the diagram shown is a cross section of the cutting edge.**

Taking such measurements solely from a cross section may not be sufficient in circumstances where the cutting profile varies in three dimensions, or where there is not one clear cutting edge. For example, in addition to taking measurements of the tip radius and wedge angle of the cutting edge through the cutting edge cross section of knives, Hainsworth et al. [4] considered the dimensions of the knife point and blunt edge in a study relating to stabbing instances. Knives were dropped using a drop tower in order to impact a foam substrate with

the same kinetic energy. It was found that the knives penetrated deeper into the substrate when values of the blunt edge (the edge of not intended for cutting) tip radius were smaller.

Cross-sectional measurements are typically taken using optical or scanning electron microscopes. In the latter case, it may be necessary to section the tip from the cutting instrument to enable it to fit into a sample chamber. Some researchers have made replicas of the cutting instrument [10], [32] or indented the blade edge into a replica material [32], [33], which were viewed either on a SEM or optical microscope. Laser beam goniometers are also available (Laser Goniometer, CATRA, Sheffield UK) but only give limited information on the edge radius.

In comparison to knives, a glass fragment is likely to have a number of points and edges that could contribute to a cutting operation. Consequently, the methods used to measure the geometrical characteristics of knives are not easily transferrable to glass fragments. In section 6.4, suitable methods for the measurement of glass fragments are discussed.

#### **6.2.4 Quantitative sharpness assessment by cutting force/energy considerations**

The standard methods discussed in section 6.2.1 are examples of quantitative sharpness assessment methods based on the force or energy needed to produce a particular cut. Such methods are advantageous in that they give results based on actual performance. However, they are usually based on specific experimental methods, which are used to quantify the force or energy involved in a particular cutting operation. This section discusses these methods.

Figure 6.2 shows some common cutting methods. Orthogonal cutting (Figure 6.2a) bears most relevance to metal cutting processes where a substrate is moved so that the cutting instrument shaves off a layer, forming an offcut [34]. It is also the method by which specimens are sectioned with microtome knives. In indentation cutting (Figure 6.2b), the cutting instrument penetrates a normally-aligned substrate, where the wedge angle is positioned to be symmetrical about the penetration axis [29]. Using an indentation cutting method, McCarthy et al. [5] derived a dimensionless measure of the sharpness of a blade, termed a “blade sharpness index” (BSI). The BSI relates the energy required to cut to a certain depth to the thickness of a substrate and the substrate’s fracture toughness. This enables the use of different substrate materials in deducing a blade’s BSI. However, the setup requires that the cutting edge penetrates the entirety of the substrate thickness to enable the cutting operation to be treated as a two-dimensional process [6].

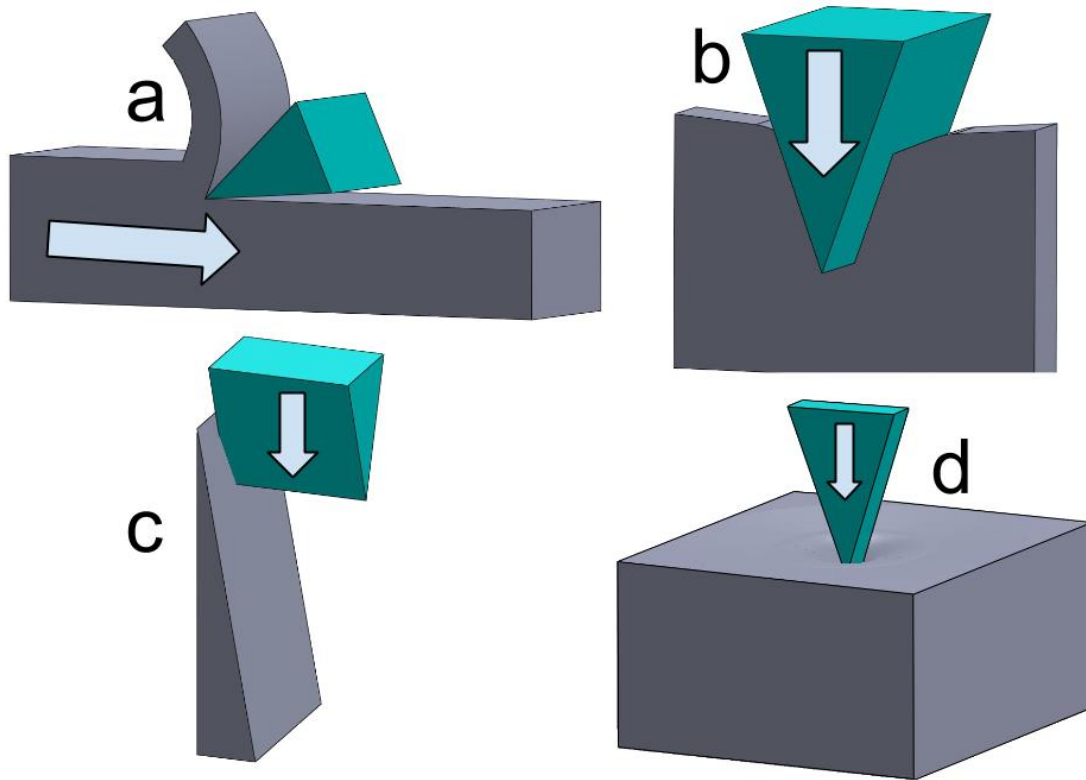


**Figure 6.2 – Schematic of different cutting methods. Substrate is displayed in grey and the cutting instrument in turquoise. a: Orthogonal cutting. b: Indentation cutting. c: ‘Inclined’ cutting. d: Puncture or ‘stab’ cutting.**

Cutting by slashing and stabbing is of particular relevance to forensic investigations. Both are characterised by the morphology resulting wound: a stab causes a wound that has a depth greater than its length, and slashes the opposite [30]. It is likely that a slash would also involve a stabbing aspect [35]. The schematic of an inclined cutting method in Figure 6.2c is based on a rig developed by the Home Office to verify the relative levels of protection to slashing offered by different materials [36]. A constrained blade was dropped onto a surface offset  $2^\circ$  from the drop axis. The blade edge penetrated the substrate attached to the inclined surface, and a spring attached to the back of the missile containing the blade maintained blade contact with the substrate during the slash. McGorry et al. also used an inclined cutting method for testing knife sharpness [9], but instead the knife moved over an inclined plane and penetrated a vertically-restrained fibreglass mesh. The advantage to using this method is that the sharpness over the length of a blade can be assessed by measuring the force levels encountered as the cut is being produced.

Quantification of the forces involved in stabbings is typically carried out using puncture cutting methods (Figure 6.2d) into a substrate material with similar mechanical properties to human skin. A variety of skin simulants have been used across a number of forensic studies and are

discussed in section 6.3.2. Nolan et al. [22] measured the force required for broken glass bottles to penetrate a skin simulant by attaching the necks of the bottles to the crosshead of a universal testing machine. The penetration force was deduced by observation of a peak produced on a force-displacement plot after penetration. Examples of this feature are shown in Figure 6.14. No clear correlation was found between the type of glass bottle and the penetration load. A similar methodology was conducted by Parmar et al. [37] for screwdrivers.

Given the random element involved with fracture in glass, it was necessary to devise cutting methods capable of adapting to different fragment shapes. This is considered in section 6.5. These methods involved the use of a substitute material for human skin. The following section reviews relevant mechanical properties of human skin and the use of substitute materials in other studies.

### **6.3 Simulating human skin for cutting**

This section describes the properties of human skin in relation to penetration by cutting. Materials used to simulate human skin are considered with examples from other studies, which informed the selection of the simulant materials used in this study.

#### **6.3.1 Penetrating human skin**

Quantifying the force required to penetrate human skin is difficult since its properties depend on: age [38]; its location on the body [39]; alignment to the cleavage lines of the skin [40], [41]; moisture content [42]; and loading history [42]. The response of skin to an applied stress is nonlinear, and is known to have a J-shaped stress-strain curve [43]. This occurs as collagen fibres align at higher strain levels resulting in the skin stiffening [44]. Furthermore, its stress-strain response is strain-rate dependent [45].

The forces required to penetrate skin with a given implement are of particular importance within forensic investigations as they can be used as an indication of a deliberate attack, as high attack forces may suggest an incident was intentional [4]. Knight [2] and Green [3] used spring-based instrumented knives to study the force required to penetrate cadavers. They concluded that the knife's tip radius was the most critical parameter in determining the penetration force, and that "no further force" was needed for continued penetration into subcutaneous tissues. O'Callaghan later conducted similar tests with an instrumented knife that was fitted with a piezo-electric force transducer [46]. He highlighted that the use of a spring-based knife would give the impression of no further force being required, since the energy stored in the spring would be released after penetration and then used to cause the

further penetration. His results showed that whilst greater force is required for skin penetration, significant force is still required for further penetration into subcutaneous layers.

Shergold and Fleck [47] considered how the shape of the tip of an instrument affects the mechanism by which it penetrates skin. They found that a “sharp-tipped” punch results in the formation of a mode I planar crack, and a “flat-bottomed” punch penetrates by the formation of a mode II crack that encircles the punch head. Wong et al. [48] arrived at similar conclusions by impacting a silicone skin simulant with rectangular and triangular punches.

### **6.3.2 Simulating skin behaviour**

There are numerous advantages to the use of a substitute to real human skin to assess its biomechanical properties. Ethical and practical issues associated with performing tests on cadavers and amputation specimens are avoided, the batch-to-batch variability is likely to be lessened, and specimens can be more readily available for routine testing.

The use of skin simulants is important in ballistics [49] as well as in quantifying forces involved with stabbings [22], [37], [50]–[53]. Ballistic studies have a history of using gelatine to simulate the properties of flesh and muscle tissue [54], [55]. Additionally, some stabbing studies have used Roma Plastilina (a modelling clay) [21], [51], [53] and/or open-cell foam [4], [53] to simulate the properties of subcutaneous layers. However, by not simulating the outermost skin layers, values for penetration force will not yield comparable results to those occurring in real stabbing events.

To identify an appropriate skin simulant, a candidate material is typically compared to skin in terms of its stress-strain response to tensile loading, its puncture resistance, or its toughness. The choice of relevant parameters for comparison depends on the purpose of the study. A number of studies are available in the literature detailing the mechanical properties of skin [56]–[58]. Jussila et al. [49] identified cowhide as the best simulant from a selection of synthetic rubbers and animal hides by taking into account tensile strength, elongation and threshold velocity. Ankersen et al. compared the tensile strength and puncture resistance of chamois to that of pig skin [52]. They found that although the tensile strength of pig skin was much greater, the two had very similar puncture resistance. Shergold and Fleck conducted a number of tests on silicone rubber [47], [59], and found it to have comparable toughness to skin, albeit having a lower modulus and lower rate of strain hardening.

In this study, the force required for penetration of glass fragments into skin was approximated by using a simulant comprising a silicone layer on top of open-cell foam (section 6.5.1). This

combination has been used in several other studies [22], [37], [48], [50], [60] and has been proved to give reproducible results in stab-penetration tests. An isolated layer of the same silicone is also used in this study to investigate the ability of glass fragments to cause slash wounds (section 6.5.2).

This section has given an introduction into the mechanical properties of human skin, and materials used to simulate its behaviour.

## **6.4 Sharpness of broken glass by geometrical considerations**

This section considers how the sharpness of broken glass is characterised by the assessment of a fragment's geometrical properties. A system for the categorisation of fragment edges is presented, and methods used to measure geometrical parameters of glass fragments are discussed.

### **6.4.1 Formation and categorisation of glass cutting points and edges**

In this study it is assumed that the vertices and edges of a glass fragment determine its cutting ability. These are created by a dynamic crack event that is very sensitive to the state of stress experienced as it progresses. This crack event occurs on a previously intact parent glass article that begins to fracture into two or more pieces when the critical stress intensity factor,  $K_{1C}$ , is exceeded at one or more points on or within the article. One or more cracks then begin to grow in the article under the influence of the stresses present at the crack tip(s). The advancing crack fronts create new fracture surfaces, defining the x-y fractographic plane (see section 2.5), and bifurcate if the crack reaches its terminal velocity. The edges created in these processes and the vertices that connect them are assumed to be the elements involved in cutting operations by the fragment.

The effectiveness of the cutting ability of an edge is determined by the geometrical properties of the edge. In order to facilitate measurement of the geometrical properties of an edge (which are considered in section 6.4.2), this section offers a system of categorising fragment edges. Fragment edges are defined as *x-axis edges* or *y-axis edges*, according to the fractographic axis that the edge is parallel to. Definitions of fractographic axes were given in section 2.5. X-axis edges are categorised according to the direction that the crack travelled in when making the fragment edge, and y-axis edges according to the macroscopic stress state (tensile or compressive) caused by loading.

These categories will be explained using the illustration of a hypothetical fracture in a sheet of flat glass shown in Figure 6.3. The orange arrows show the direction of crack propagation. The

crack is assumed to have propagated fully through the thickness of the sheet, and the x-y plane is assumed to be normal to the y-z plane on all fragments. The fracture pattern on the opposite y-z plane surface is therefore identical to that visible in the figure.

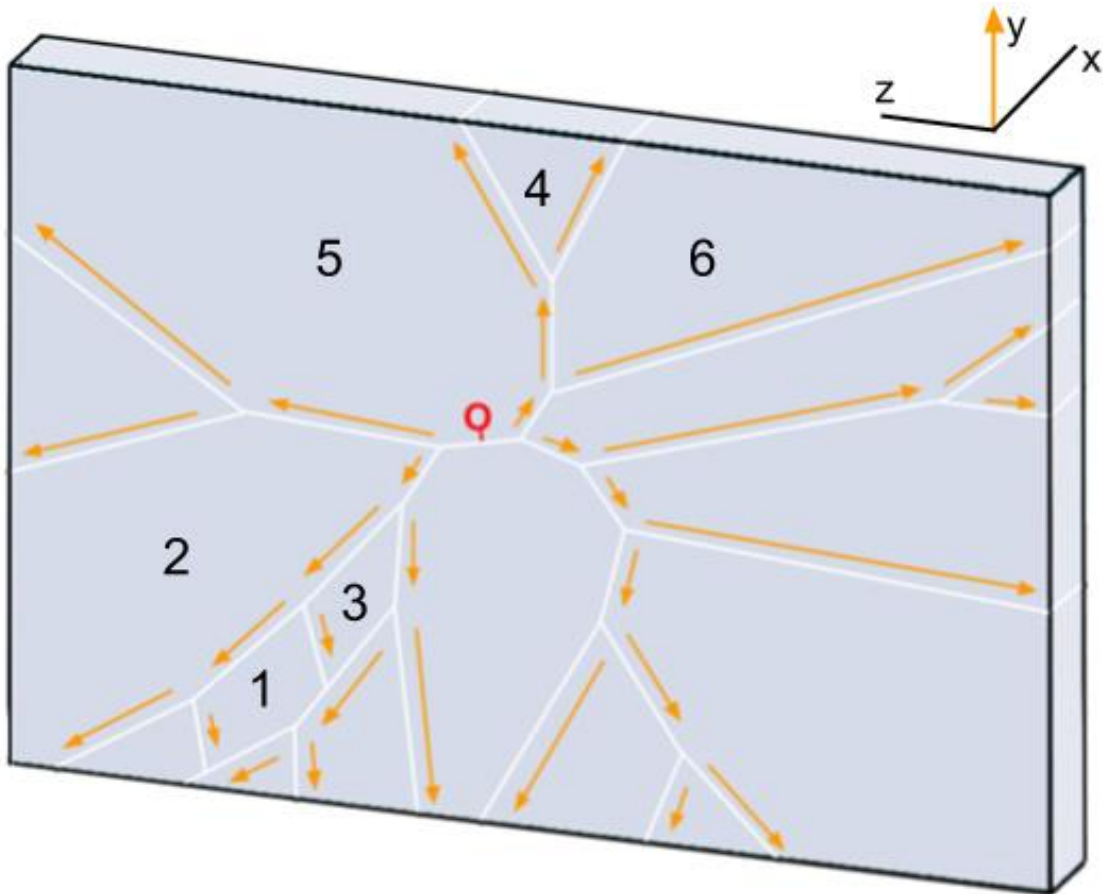
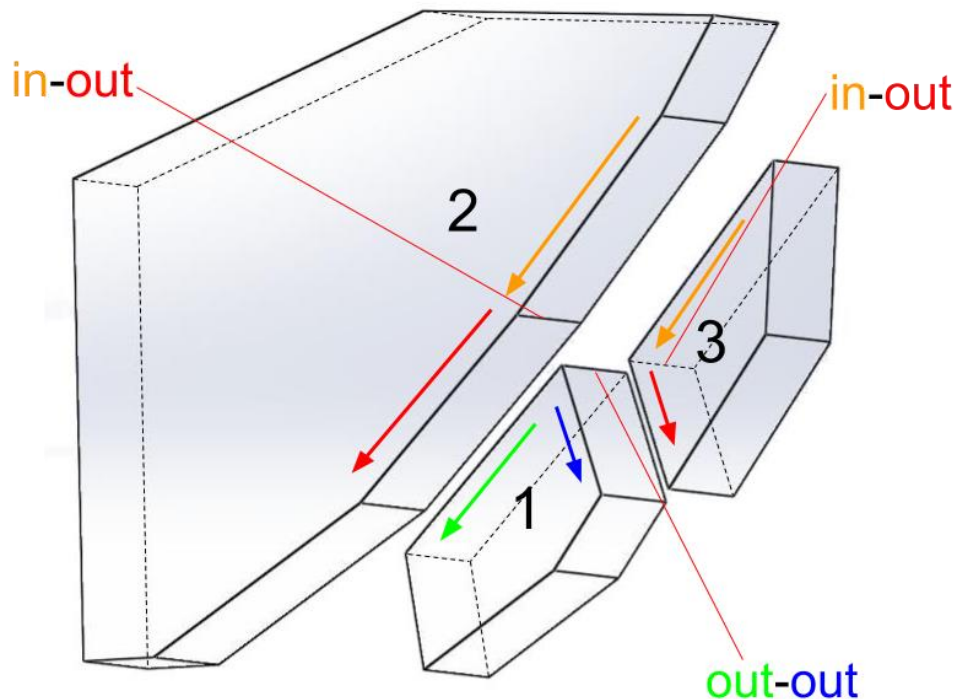


Figure 6.3 – Illustration of a hypothetical fractured sheet of glass, with the directions of crack propagation shown. The fracture origin is labelled 'O'. The numbers are used to reference specific fragments in the text. The y-axis in the legend in the top right corner of the figure is always oriented in the direction of crack propagation (with the z-axis rotating accordingly), but is shown for reference.

#### 6.4.1.1 X-axis edges

X-axis edges are formed during a crack branching event or by a head-on intersection of the crack front with a free surface (which may be a pre-existing free surface or freshly-formed fracture surface). For the hypothetical fracture pattern in Figure 6.3, all of the x-axis edges are straight and parallel to the x-axis, although in practice they typically form a rough profile through the thickness of an article. X-axis edges are categorised according to the overall direction of crack propagation local to the edge, as demonstrated in Figure 6.6. This is inferred from the fracture surface features of one or both of the two intersecting surfaces that form the edge.

Each crack bifurcation event creates an x-axis edge on three fragments. One of these edges is defined as *out-out* and two are defined as *in-out*. An out-out edge is the line of intersection of two fracture surfaces, which both indicate a direction of crack propagation “out” from that edge. An in-out edge is the line of intersection of two fracture surfaces, one of which indicates a direction of crack propagation “in” to the edge, and other “out”. This is illustrated in Figure 6.4, which shows the location of an out-out edge on fragment 1, and the two corresponding in-out edges on fragments 2 and 3.



**Figure 6.4 – Fragments 1, 2, and 3 isolated from the full fracture pattern shown in Figure 6.3, to illustrate the two in-out edges and one out-out edge created in a typical branching event.**

The included angle of an out-out edge as viewed on the y-z plane is commonly referred to in fractographic literature as the branching angle, and is known to vary approximately between 15°-180° depending upon the stress state acting on the crack [61], [62].

When the crack front intersects a free surface head-on, two x-axis edges are created, which are defined as *in-surface* edges. An in-surface edge is the line of intersection of a fracture surface and a free surface (which may be an existing fracture surface), where the fracture surface indicates a direction of crack propagation “in” to the edge. This is illustrated in Figure 6.5, which shows the result of two individual propagating cracks intersecting a free surface. Each intersection with the free surface creates two in-surface edges, as labelled in the figure.

If the free surface is a freshly-formed fracture surface, the edge can be easily mistaken for an in-out edge and may only be identifiable by inference from the y-z plane (free surface) of the reconstructed fracture article.

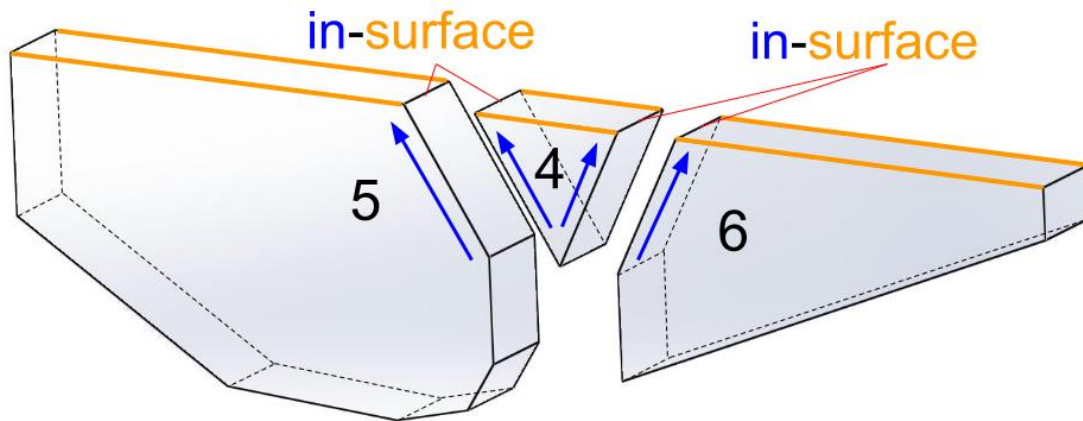


**Figure 6.5 – Fragments 4, 5, and 6 isolated from the full fracture pattern shown in Figure 6.3, to illustrate the two surface-in edges created in each typical head-on intersection of the crack front with a free surface.**

One application of in-surface edges is the cutting edge of glass microtome knives. These are made by scoring a square glass block across one of its diagonals, and then broken by a load applied equally either side of the score line [23]. The accuracy of the score line and the load distribution affect the quality of the edge. A common feature of in-surface edges is that, when the fragment is viewed on the y-z plane just prior to the edge, the crack tends to curve towards 90° to the free surface. This is known in fractographic literature as a “T-intersection” [62], and occurs in order to accommodate the change in stress condition as a crack approaches a free surface. Another feature of in-surface edges is that the edge profile in the x-y plane curves upwards towards the y-z surface that is under compression. Both of these features are undesirable for microtome knives [23].

The edge category for each x-axis edge present on fragments 1 and 4 is labelled in Figure 6.6.

By extension of this naming convention, further edge types can be defined. *Surface-out* edges are created when the critical flaw is present at a surface or edge and the crack propagates into the glass article. *In-in* edges are theoretically possible, but would require two simultaneously propagating crack fronts to intersect head-on. *Surface-surface* edges, i.e. those pre-existing x-axis edges present at the intersection of two free surfaces, are of little interest to this study.

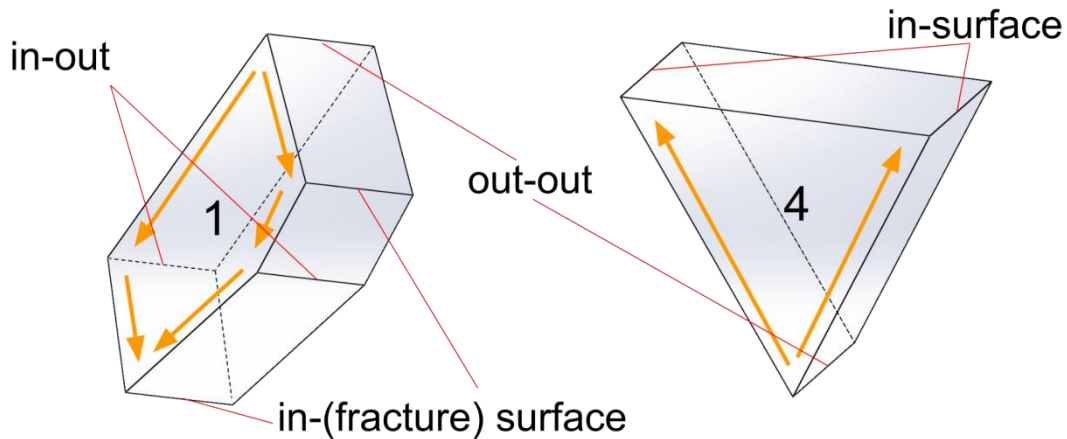


Figure 6.6 – Fragments 1 and 4, isolated from Figure 6.3, with all x-axis edge categories labelled.

#### 6.4.1.2 Y-axis edges

*Y-axis edges* are created simultaneously alongside a propagating crack front and are parallel to the direction of crack growth. For glass of simple geometry broken under known stress conditions, where one side is under tension and the other compression, it is useful to categorise these edges as *tensile edges* and *compressive edges*. This refers to the stresses produced by a bending load (not taking into account contact stress). In annealed glass, the tensile edge is likely to be created by the leading portion of the crack front whilst the creation of the compressive edge will lag behind with the lateral expansion of the crack front.

All x-axis edge profile lengths (i.e. the overall length of the line that follows the x-axis profile route) in an article are likely to be similar to each other if the thickness in the article is constant. However, the y-axis profile lengths are more likely to show large variation between fragments since they will typically have more space and freedom to propagate over the y-z plane.

#### 6.4.2 Parameters for geometrical measurement of fragments

Identification of key glass fragment geometrical parameters for cutting is difficult, since the actual region of a glass fragment involved in a cutting operation varies in three dimensions. In this study, geometrical measurements were taken from two dimensional representations of the actual cutting edge in the interest of simplicity. As such, it was important that geometrical comparisons between fragments were made by selecting 2-D fragment representations in a consistent manner. For example, Figure 6.1 is a cross section of a cutting edge, but in practice this profile varies along the edge length and multiple cross sections may need to be measured to appropriately characterise it. Longer y-axis edges may need to be treated this way. Also, the measurements are affected by the orientation of the plane used to create the cross section.

The region around an x-axis edge is important in stabbing incidents since the intersection of the two corresponding surfaces typically appears to form a point on the free surface y-z plane, as illustrated in Figure 6.7. This free surface may then be treated as having a tip radius and included angle as in Figure 6.1. Similar to y-axis edges, the free surfaces are referred to as the tensile or compressive side in this study, referring to the stresses produced due to a bending load.

In this study, measurement of the x-axis edge profile was conducted so that it was always viewed normal to the centre line of the fragment on one of the free surfaces (Figure 6.7b-c). This avoided potentially large variations in measurements taken either side of the edge profile due to out-of-plane features, and also meant that the profile only needed to be viewed from one side. Geometrical features noted from this viewpoint will be said to be present on the “fracture surface side” from this point onwards.

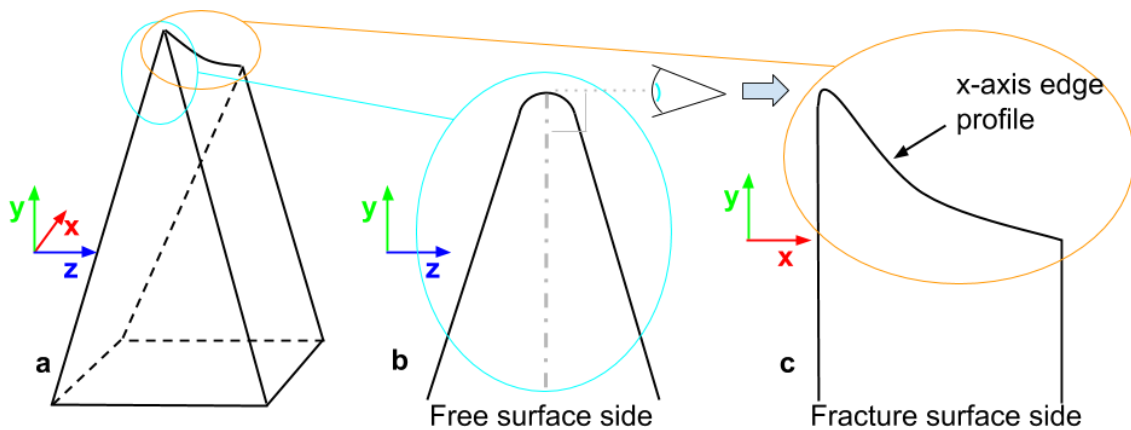


**Figure 6.7 – Illustration of free and fracture surface sides for x-axis edge region measurement. The fracture surface is not parallel to the fracture surface side viewing plane.**

The centre line on the free surface side was assumed to be the axis in which the fragment pierces a target during a stabbing instance. As such, with a fragment aligned as in Figure 6.7c, the section of the x-axis edge profile that protruded most upward was the piercing point and therefore was the point of most interest, and was treated as described in Figure 6.1. However, depending on the degree of deflection of the target substrate during penetration and on the edge profile shape, other sections of the edge occasionally came into contact with the substrate, which altered the state of substrate contact stress. Therefore, additional measurements were taken in this study to characterise the edge profile and are detailed on an example fragment in Figure 6.8.

The included angle of the piercing point is shown by the measurements in red in the example fragment in Figure 6.8. The angle was measured between tangent lines to the profile edge.

These were taken from the two points where edge radius (shown in Figure 6.8 with a blue circle) ceased to follow the actual profile. Additional angular measurements were occasionally taken from tangents further from the tip radius in cases when the profile was likely to curve. The thickness of the glass 1 mm back from the piercing point was recorded to complement these measurements.

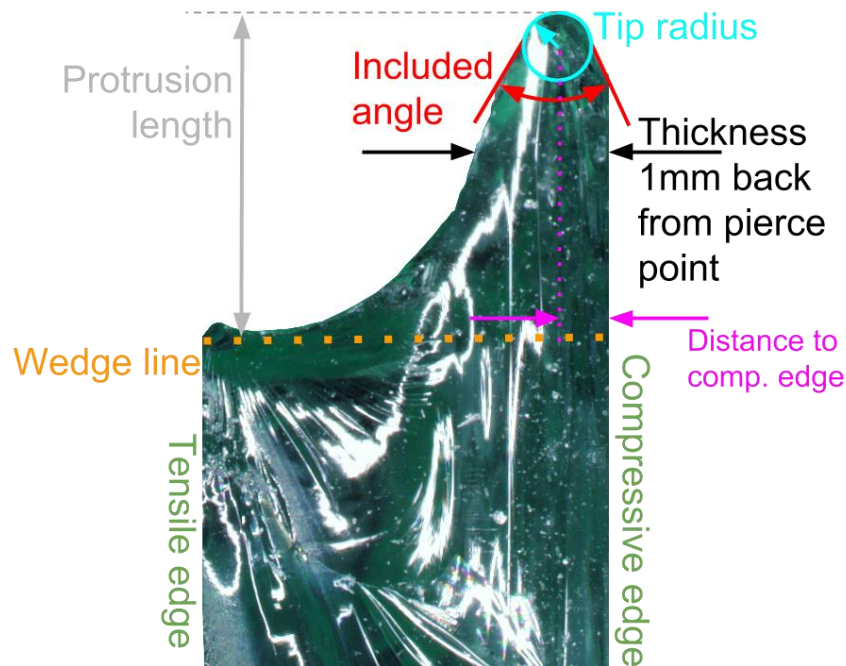


**Figure 6.8 – X-axis edge profile measurements viewed on fracture surface side. The fragment is from a sheet of broken annealed glass. Such a profile is typical for out-out edges of annealed glass fragments.**

A *wedge line* was defined as the line that the edge profile would follow if the fragment's x-axis edge was normal to the y-z plane free surfaces, as in Figure 6.6. This was however more difficult to define for fragments from glass articles that were curved or had a variable thickness. The wedge line was drawn from the lower of the two x-axis edge terminal points when the fragment was viewed in the fracture surface side view. From this, the protrusion length of the piercing point could be measured (Figure 6.8, grey), and also that of any other peaks that were present on the edge profile. The lateral distance between the piercing tip and the compressive y-axis edge was also measured.

In addition to the fracture surface side measurements outlined in Figure 6.8, a measure of the roughness of an edge profile was taken. The roughness here is defined as the average absolute deviation of the x-axis edge profile from the straight line drawn from one x-axis terminal point to the other. This is shown schematically in Figure 6.9a. The roughness of the free surface edge profile was also taken. This was defined as the average absolute deviation of the profile from a line travelling from a point on the profile 1 mm back from the tip, to the tip, and then to a

point 1 mm back from the tip on the other side of the edge profile. This is shown schematically in Figure 6.9b. These roughness calculations were performed by scripts written in Python programming language (Appendix I), which took measurements of 1000 equally spaced points along the edge profile.

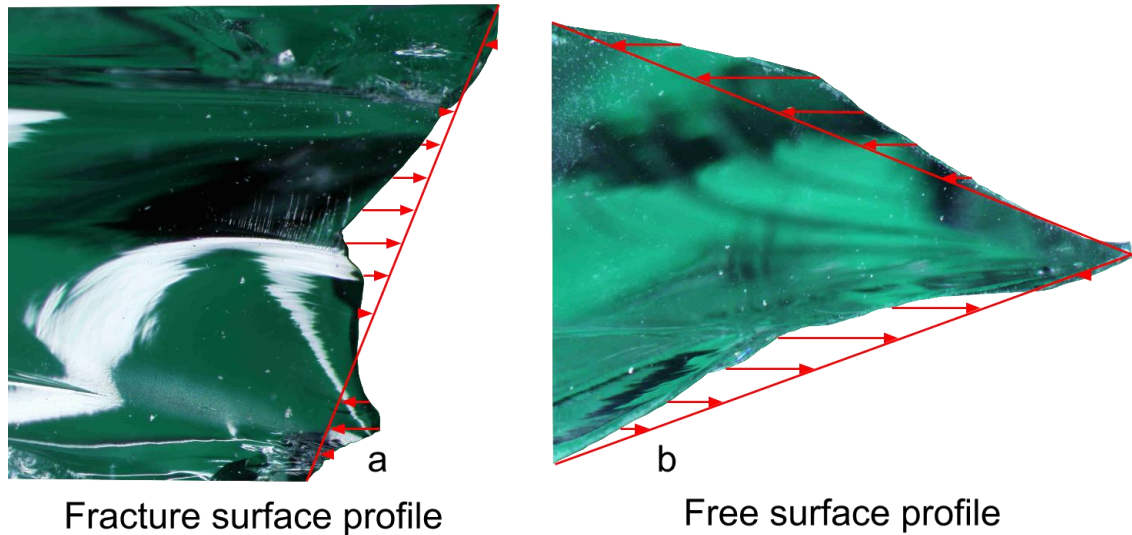


**Figure 6.9 – Diagrams to demonstrate roughness measurement calculations for the fracture and free surface edge profiles. Arrows denote deviation of the actual surface profile to red “smooth” lines. The spacing shown in this figure between deviations is only an illustration.**

#### 6.4.3 Measurement methods

For x-axis edge profile measurement, a centre line was judged using a protractor and drawn on the fragment’s tensile side with a fine permanent pen and straight edge. The fragment was then positioned and aligned relative to the centre line with a small vice clamp so that the fracture surface side could be viewed under a stereo microscope (Olympus SZ-X12, Olympus, Southend-on-Sea, UK). Measurements of the tip radius and included angle of the pierce point were always taken with the microscope at 90X magnification using Olympus proprietary software AnalySIS for both the fracture surface side and the free surface side. The element of subjectivity involved with judgement of an edge radius was reduced by always using the same magnification for tip radius measurement, since all features were being viewed at the same scale. For free surface profile measurements, images were taken at a suitable magnification so that at least the top 1 mm was visible and stored as TIFF images.

The images showing the full profile of the edge were opened in imageJ software version 1.48 (<http://imagej.nih.gov/ij/>, last accessed August 2014). By calibrating the image co-ordinate system to the scale bar, it was possible to then trace a line around the edge profile which could then be saved as a set of coordinates. The coordinates were then passed through to a script

written in Python programming language. The script first linearly interpolated between the coordinates using SciPy (<http://www.scipy.org/>, last accessed August 2014) to ensure that 1000 x-y coordinate sets were present for each profile. The remaining profile measurements were then taken from these coordinate sets (see Appendix I). This saved time collecting multiple time-consuming measurements and reduced the possibility of measurement error caused by manual logging of results.

Measurement of y-axis edge geometrical parameters was conducted by making a replica of the edge in Acrulite casting resin (Rubert, Cheadle, UK), which was later sectioned and polished to leave the edge profile. The section was then viewed in either an optical or a scanning electron microscope for geometrical measurement.

## **6.5 Sharpness of broken glass by force and energy considerations**

In this section, two contact-based experimental methods for characterising the sharpness of glass fragments are detailed. These methods were developed specifically for this study and involve different cutting operations. The first experimental method described represents cutting by penetration (section 6.5.1) and the second represents cutting by slashing (section 6.5.2). These methods are used in chapters 7 and 8.

### **6.5.1 Fragment penetration ability**

#### **6.5.1.1 Overview**

The amount of force required for a glass fragment to penetrate skin was estimated by aligning the edge(s) and point(s) of interest of the fragment and measuring the force required for it to puncture a silicone/foam skin simulant. The puncture load was provided by a universal testing machine fitted with a load cell with a range of 5 kN (Hounsfield H10KM, Tinius Olsen, Ltd., Salfords, UK). Each fragment was positioned and set in casting resin before being attached to the crosshead of the load frame via a specially designed cup fixture (Figure 6.10). The displacement of the crosshead was measured by an on-board optical encoder, and outputs from this and the load cell were logged using Tinius Olsen's proprietary Q-MAT software.

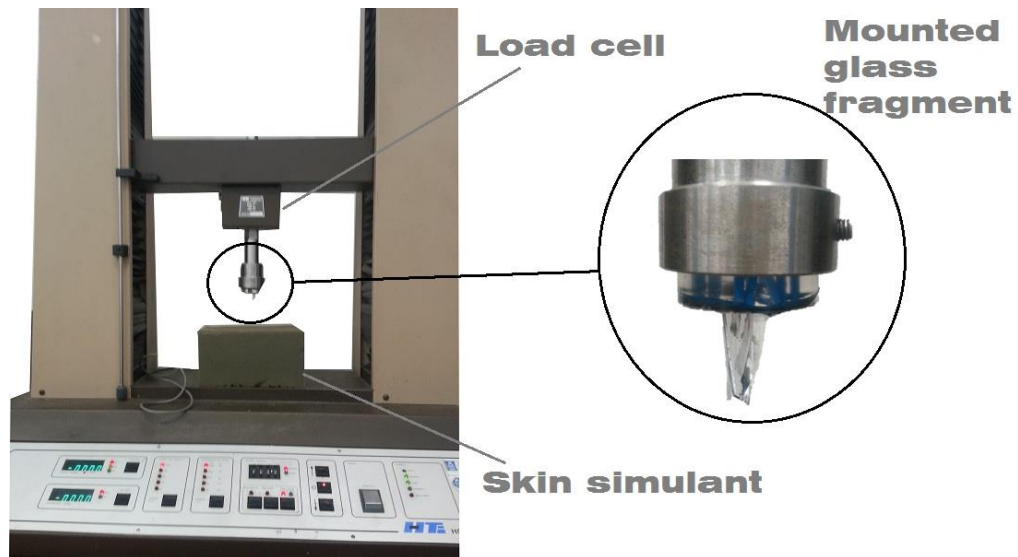


**Figure 6.10 – Apparatus for penetration testing. A fragment mounted in casting resin was secured in a purpose-built cup fixture that screwed into the load cell on the universal testing machine.**

#### **6.5.1.2 Silicone/foam simulant preparation**

Blocks of A4 sized open-cell polyether foam with a depth of 100mm, a density of 23–28 kgm<sup>-2</sup>, and a foam hardness between 125–155 N were obtained externally (Acoustafom, Shropshire, England). The silicone layer was made from a mix of 150 g Transil-55(B) base and 15 g Transil-40(A) curing agent (Mouldlife, Newmarket, England). These were mixed by hand for 5 minutes before being poured into a specifically-sized mould. Once poured, the silicone was spread out evenly and then left to settle for 5 minutes. A weighted foam block was then placed on top of the mould and the fixture was left to set for 24 hours. Once removed from the mould, the silicone layer had a thickness of ~2 mm and was well adhered to the foam. A verification study was conducted on a simulant and is presented in Appendix J.

#### **6.5.1.3 Glass fragment preparation**

Glass fragments were mounted in polyester casting resin (East Coast Fibreglass Supplies Ltd., South Shields, UK) after geometrical measurements had been taken. Once set, this ensured that the fragments remained appropriately aligned during penetration into the skin simulant when attached in the cup fixture. This process was conducted according to the following steps:

- The resin was poured into cylindrical polypropylene moulds of inside radii 10 mm, 20 mm, and 40 mm with removable bases. The choice of mould was governed by the fragment dimensions. This was then placed partly beneath an overhanging ledge on a level surface.
- A glass fragment was then stuck onto the front face of the ledge with a thin piece of adhesive tack and positioned so that a lower portion was dipped into the casting resin

as illustrated in Figure 6.11a. The minimum fragment height used was 10 mm. Since the ledge's front face was normal to the level surface, this aligned the flat glass fragments vertically. For curved fragments, more adhesive tack was used to position the fragment on the ledge, and alignment of the x-axis edge was judged by eye.

- The fragment centre lines applied during the geometrical measurement stage were then aligned to vertical graduation lines that were added to the ledge front face prior to sample preparation as illustrated in Figure 6.11b.
- The resin was then left to set for 24 hours, after which the base was removed from the mould to allow the sample to be gently pushed from beneath, avoiding any damage or contact with the fragment edges.

Figure 6.12 shows examples of the final product. Adaptor moulds were made to allow the smaller samples to attach to the holding cup fixture.

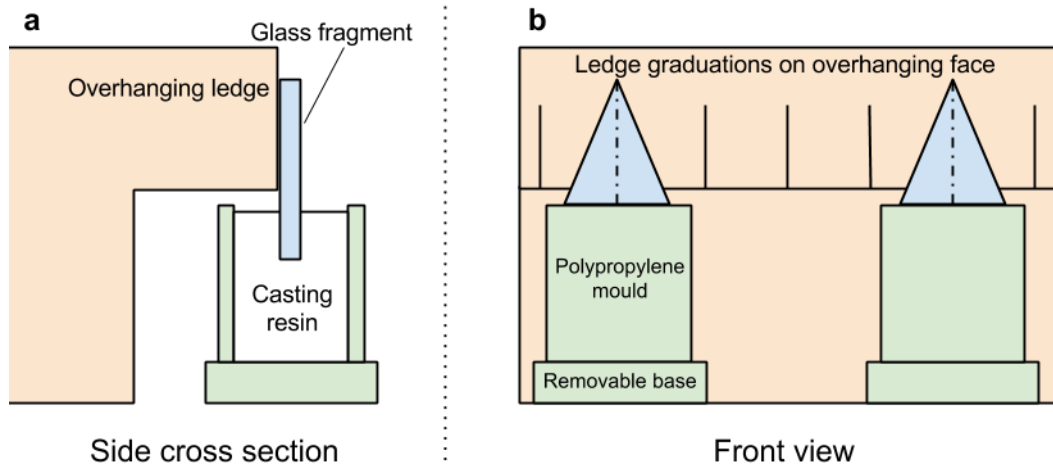


Figure 6.11 – Illustration of setup for alignment of fragments in casting resin for puncture testing.

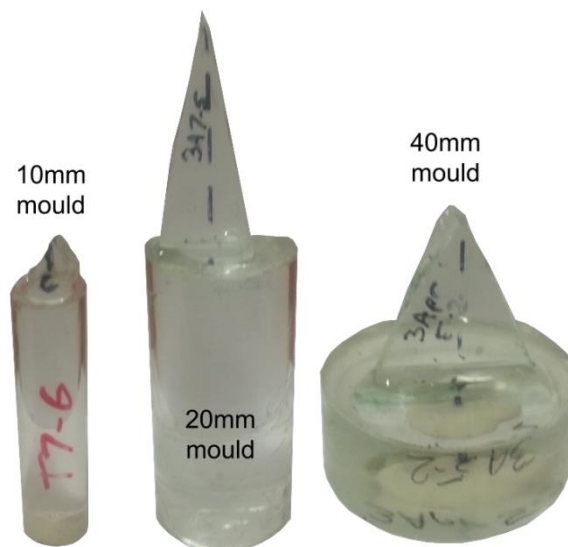


Figure 6.12 – Examples of fragments mounted in resin.

#### 6.5.1.4 Procedure

Following the results of the silicone/foam simulant verification study (see Appendix J), punctures were only made within the  $[x/4, 3x/4, y/4, 3y/4]$  simulant bounds in penetration tests, where  $x$  and  $y$  are the width and length of the silicone layer respectively. This was to avoid edge effects influencing the results.

In order to account for differences in penetration load due to potential thickness variations of the silicone layer, a normalisation procedure was carried out. Prior to each set of experimental runs, punctures were made at the centre and vertices of the bounding rectangle (detailed in the above paragraph) with the machined shard described in Appendix J. The dimensions of the shard were checked on a stereo microscope after every ten simulant blocks for any sign of deterioration. The vertex penetration loads were divided by the central penetration load to give primary correction factors. These factors were then cubically interpolated over the  $[x/4, 3x/4, y/4, 3y/4]$  bounds to create a continuous grid of further correction factors, an example of which is shown in Figure 6.13. This enabled further penetration loads to be normalised with respect to the inherent variation of puncture strength across the block surface, by dividing the raw value with the correction factor associated with the location of puncture.

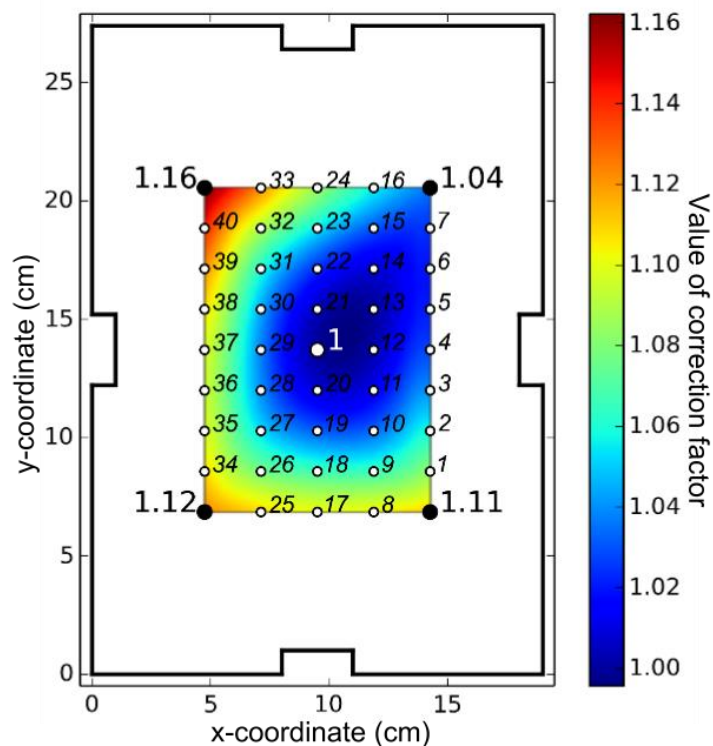
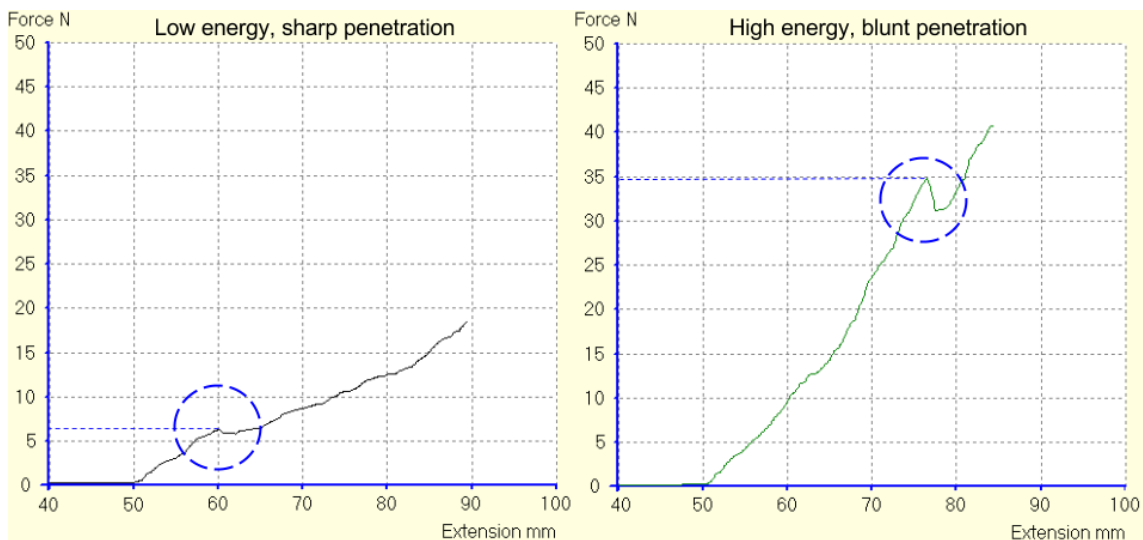


Figure 6.13 – Diagram to demonstrate the test run order, and the use of correction factors for simulant calibration. The correction factors shown are an example from one particular simulant. Cubic interpolation was carried out using SciPy (<http://www.scipy.org/>, last accessed August 2014).

The order and location of experimental runs is indicated by the numbers in small italics and the small white circles respectively in Figure 6.13. The spacing between punctures was  $x/8$  widthways and  $y/16$  lengthways (following from Appendix J) which allowed for 40 penetration tests after the 5 calibration punctures. The order was designed such that each new puncture was surrounded by a minimum of pre-existing punctures. The block was marked prior to any experimental runs. These marks were used to position the simulant before each test run.

A sample was then mounted into the holding cup and secured with a grub screw. Using the universal testing machine's on-board interface, the crosshead was positioned so that it was 50 mm above the simulant. This gave a short period of time before penetration to check that the outputs were being logged properly and that the simulant block was appropriately positioned. The crosshead speed and displacement range were set to 500 mm/min and 100 mm respectively, and the test run was started using the computer user interface. Once the displacement range of 100 mm was reached, the crosshead stopped before returning back to its original position. The penetration load was inferred from a peak or step on a force-displacement plot caused by the release of the elastic strain energy accumulated prior to puncturing (Figure 6.14). The plot was then saved and the mounted fragment was securely stored away for safety purposes.



**Figure 6.14** – Load-displacement graphs obtained from penetration into a skin simulant by glass fragments, showing a peak or step at the time of penetration. (left) Penetration occurs at a low load due to a sharp fragment being used for penetration. (right) Penetration occurs at higher load due to a blunt fragment being used for penetration. The peak is more pronounced due to a greater build-up of elastic strain energy prior to penetration.

## 6.5.2 Fragment slashing ability

### 6.5.2.1 Overview

The ability of a particular fragment to cause a slashing injury was estimated by conducting a repeatable cutting operation with the fragment into a silicone layer. The fragment was then assessed by measuring the cutting depth achieved, and the force that was required to propagate the cut. The test methodology involved the adaptation of a scratch tester to hold a glass fragment in place of a scratching stylus, and an assembly to enable the silicone layer to be fixed onto a rotating wheel. The equipment, sample preparation, and test procedure are detailed in the following sub-sections.

### 6.5.2.2 Equipment

The assembled equipment used for assessing fragment slashing ability is shown in Figure 6.15. The main components of this setup were as follows:

- Scratch tester (ST200, Teer Coatings Ltd., Worcestershire, UK)
- Wheel assembly for mounting flat rectangular silicone cutting substrate
- Holding fixture for mounted glass fragment
- Glass fragment mounted and positioned in resin
- Silicone cutting substrate

The scratch tester used for this test is typically used to assess the performance of coatings on substrates. It is capable of providing a controlled downward force to a specimen fixed onto a table which is capable of lateral motion. The speed of the table movement can be controlled, and is powered by a servo motor. The downward force onto the specimen is usually transmitted by a stylus via a loading shaft. However, for glass fragment slashing tests the stylus was replaced with a fixture that was capable of holding a fragment mounted in resin, similar to that in penetration tests. The mounting fixture was threaded and screwed onto the loading shaft. In order to ensure that the fragment was not forced through the substrate at an angle, the mounting fixture was not fully tightened. This gave the sample the freedom to reorientate so that the optimum cutting plane could be followed.

Additionally, the silicone cutting substrate used was mounted onto a wheel as opposed to being laid flat on the table surface. The wheel was mounted next to a spur gear and fixed onto a shaft which was free to rotate. The ends of the shaft were held by ball bearings in supporting arms positioned either side of the table. The spur gear meshed with a corresponding linear rack fixed onto the scratch tester table. This enabled the table's linear motion to produce

rotary motion of the shaft. A load cell with a 10 N range measured the force opposing the motion of the table. This meant that the cutting ability of various glass fragments could be compared, by applying a constant load to all glass fragments and considering both: the depth of the cut produced, and the force required to propagate the cut. The outputs from both the table load cell and the loading shaft load cell were logged by a purpose-built LabVIEW program (National Instruments, Newbury, UK).

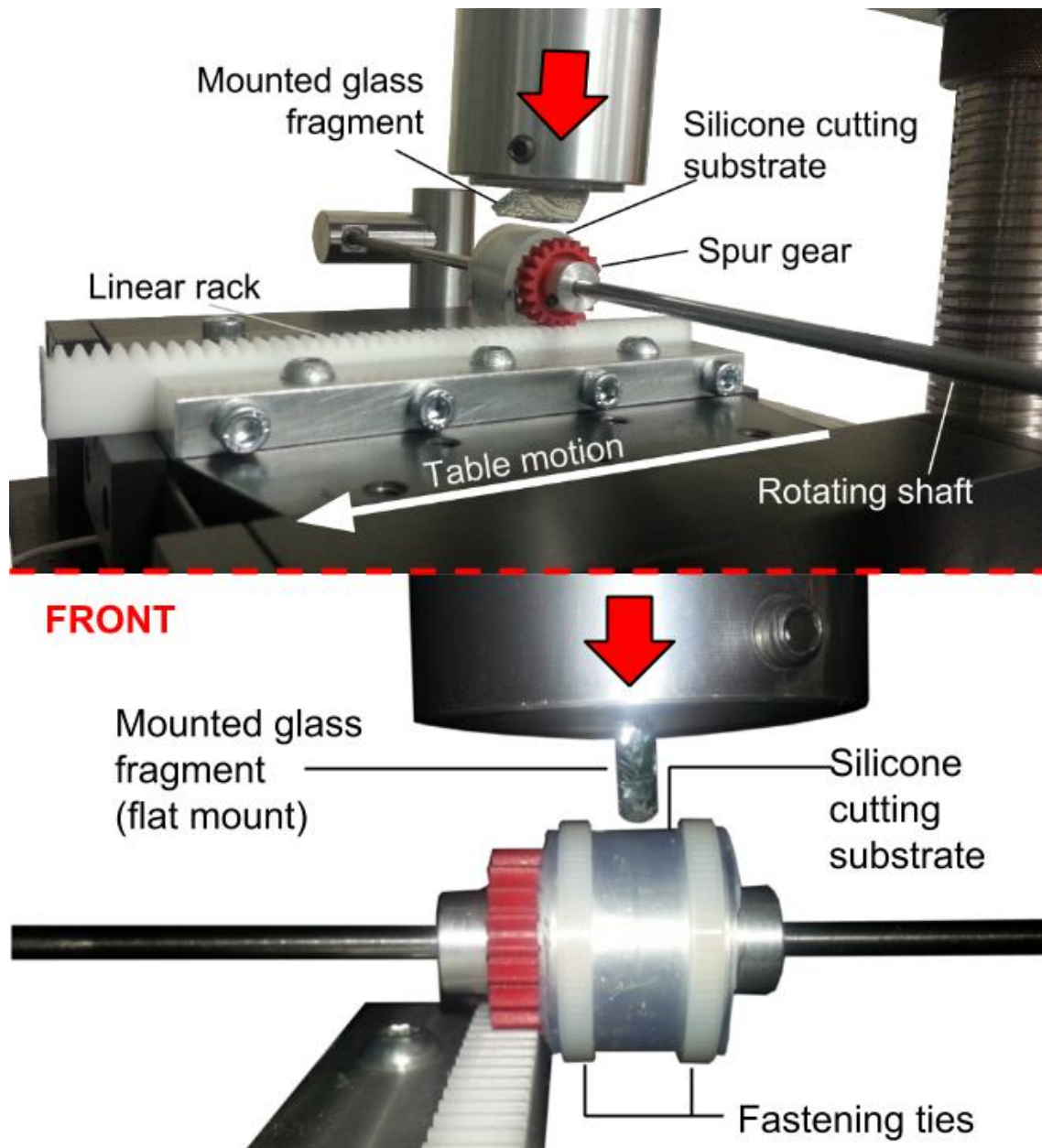


Figure 6.15 – Apparatus for assessing the slashing ability of glass fragments.

The rotary system was developed to increase the versatility of the test, compared to tests with a flat substrate. Specifically, this configuration: enabled edges of more complex geometry to

be tested; avoided large force variations due to material build-up ahead of a flat glass surface; and allowed for specific points along a glass edge to be examined.

### 6.5.2.3 Glass sample preparation

Most resin-mounted fragment samples were prepared using a similar method to that described in section 6.5.1.3, but aligned such that one or more y-axis edges protruded furthest from the mould. Fragments were mounted either with the x-y surface plane horizontal (*flat mount*) or orientated at 45° (*angled mount*) as illustrated in Figure 6.16. Angled mounts allowed for one edge to be isolated for testing. Flat mounts could be aligned using the overhanging ledge method (Figure 6.11). Angled mounts were aligned using a protractor and held in place with modelling clay while the casting resin set.

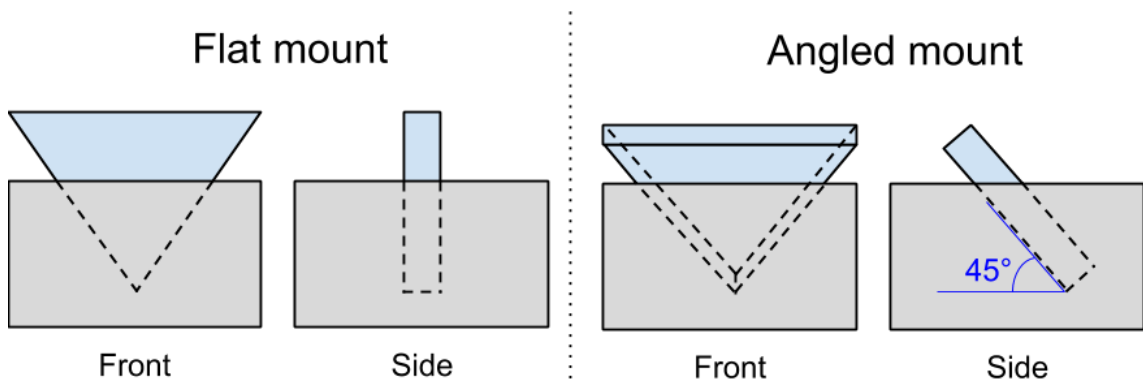


Figure 6.16 – Illustration of fragment mounting configurations in casting resin for slashing samples.

### 6.5.2.4 Silicone cutting substrate preparation

A 20 mm x 50 mm x 2 mm silicone strip was prepared for each test from the same silicone mix as that outlined in section 6.5.1.2. The mix was poured into a large rectangular mould and left to set for 24 hours, resulting in a silicone sheet with a thickness of ~2 mm. A number of strips were then cut to size using scissors.

The silicone samples were then attached to the mounting wheel of the scratch tester wheel assembly with cable ties as shown in Figure 6.15. The clamping force provided by the ties was sufficient to avoid any movement of the silicone during tests. The width and diameter of the mounting wheel were each 20 mm. The cable ties used for experimentation were 3.6 mm in width and 140 mm in length. With the cable ties attached at each end of the wheel as shown in the figure, this allowed for a width of ~12 mm that the fragment could penetrate.

### 6.5.2.5 Assessment of cut depth

The cut depths were assessed by first sectioning the silicone cutting substrates centrally across the cut length. One of the silicone halves was then bent around a cylindrical fixture with a

diameter of 40 mm, and held in place with an elastic band 10 mm from the cross section location. This made the location of the cut apparent. The cut notch was then viewed by optical microscope at 90X magnification and the depth of the notch was measured. This is demonstrated in Figure 6.17.

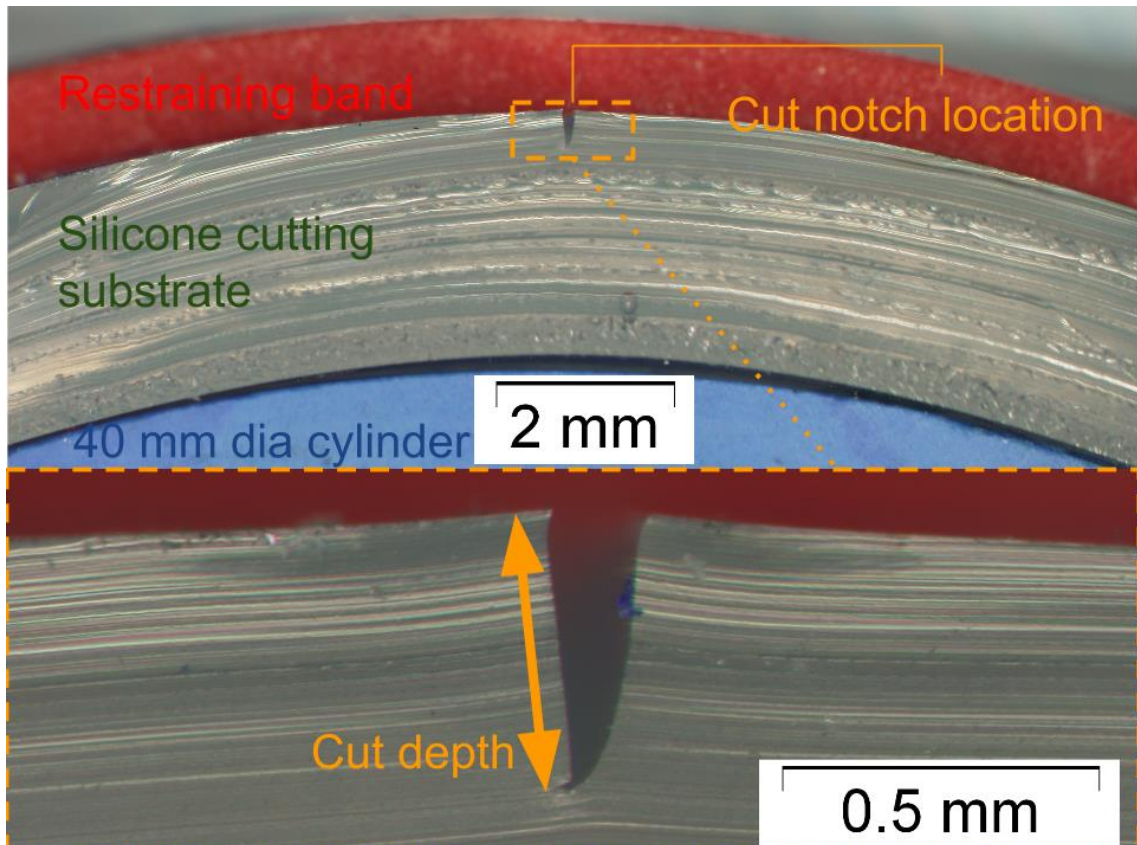


Figure 6.17 – Sectioned silicone strip after slash testing, set up for cut depth measurement.

#### 6.5.2.6 Interpretation of force-distance plots and choice of test parameters

Plots were made for each test of the force measured resisting the rotation of the cutting wheel, against the distance travelled. This was interpreted as the force required to propagate the cut after the initial top load had been applied to the fragment. However, this also included the frictional force involved with turning the wheel assembly. This frictional force was found to account for 0.5 N of the average force with a standard deviation of 0.22 N over 50 tests. This was determined by measuring the force output as the scratch tester table returned to its original position after each test run.

The cutting force measured does not give an indication of the cutting ability alone, because the measured force is also highly sensitive to the cut depth. The cutting force output was therefore always considered alongside the cut depth, as a fragment that penetrated deeply into the silicone may require more force for propagation than one that penetrated shallowly.

Additionally, the cutting force is very sensitive to the chosen top-load applied to the fragment. A top-load of 8 N was chosen, as this was found to provide a good range of cutting forces for a number of test fragments during initial testing. These initial tests also showed that the average steady-state cutting force had a standard deviation of  $\sim 0.52$  N. During these tests, the table was displaced 20 mm at a speed of 20 mm/min. These settings were subsequently used for all further test runs.

An example force-distance plot is shown in Figure 6.18. Three key values were taken from each plot:

- Initial force – The force at the point where the gradient of the side load plot first becomes 0.
- Peak force – The maximum side force load attained during the test. In the majority of cases this coincided with the initial force.
- Average steady cutting force – The average force over the period between the initial force until the removal of the top load.

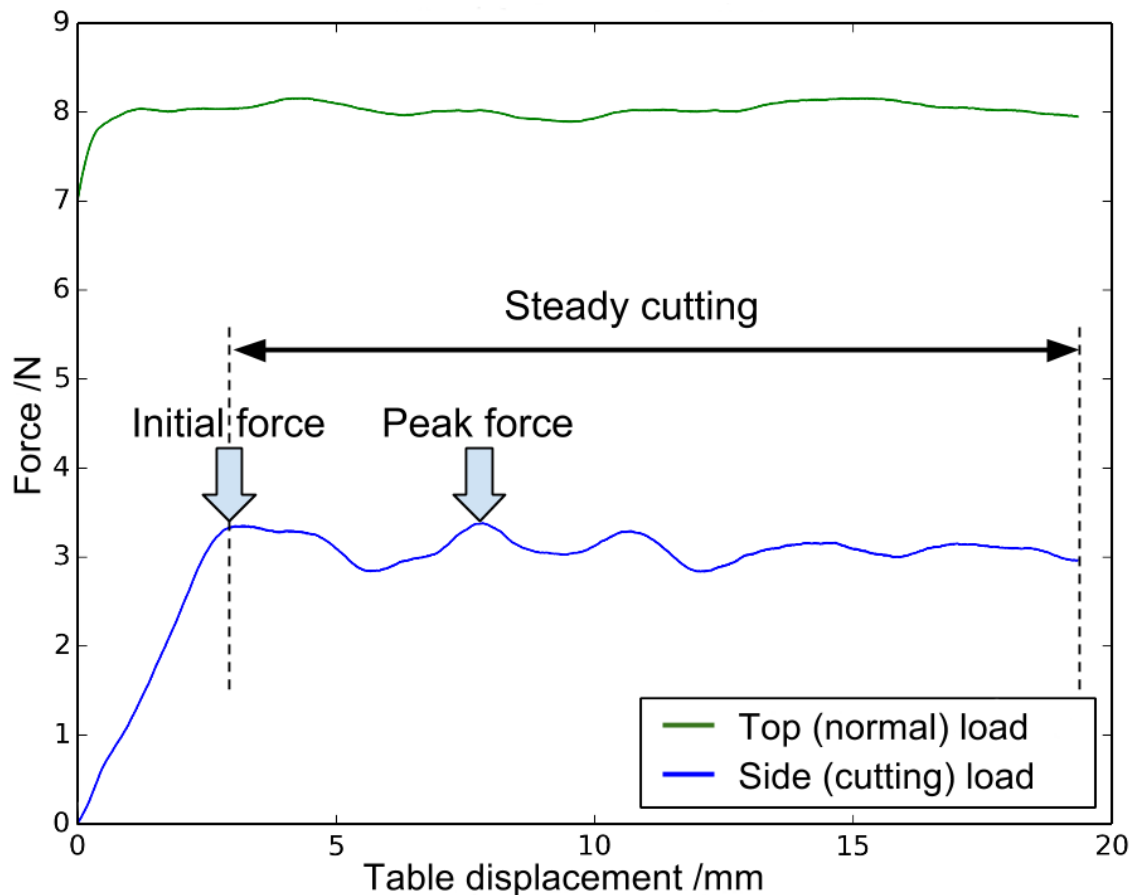


Figure 6.18 – Example force-displacement output from slashing tests for both top and side loads.

**6.5.2.7 Slashing test procedure**

The procedure for performing slashing tests was as follows:

1. A silicone cutting substrate strip (prepared as per sub-section 6.5.2.4) was attached to the wheel assembly with fastening ties as shown in Figure 6.15. Excess length of the ties was cut with scissors.
2. The mounted fragment sample (prepared as per sub-section 6.5.2.3) was then secured in the holding fixture attached to the loading shaft of the scratch tester. The fragment edge(s) were aligned to be parallel to the table movement direction by eye. The height of the fragment edge(s) was then adjusted manually until it was approximately 0.5 mm above the silicone strip.
3. The scratch tester was set to provide a constant top load of 8 N, over a table displacement of 20 mm, at a speed of 20 mm/min. This was done using an on-board interface.
4. The LabVIEW program was then activated and began collecting the output from the load cells at a rate of 50 readings per second, and the test run was started.
5. The loading shaft displaced downwards until a top load of 8 N was achieved. Subsequently, the table displaced 20 mm. Afterwards, the loading shaft returned to its original position, followed by the table. At this point the LabVIEW program was manually shut down and the test output saved.
6. The loading shaft was manually displaced upwards and the mounted fragment was then securely stored away for safety purposes.
7. The fastening ties were cut and the silicone cutting substrate was removed from the wheel assembly.
8. The cut depth was measured as per sub-section 6.5.2.5, and key values were extracted from the force-displacement plot as per sub-section 6.5.2.6.

This section has detailed two contact-based test methodologies developed to assess the cutting performance of glass fragments. The first test was a penetration or stabbing test methodology using a universal testing machine. The second test was a cutting or slashing test methodology using an adapted scratch tester assembly. The following section details an exploratory study conducted to determine the most influential geometrical factors on the penetration force values obtained from penetration tests.

## 6.6 Design of Experiments investigation into key fragment geometry parameters for penetration ability

### 6.6.1 Introduction

In order to gain insight into which geometrical parameters have the greatest effect on penetration loads required, and to enable prediction of the range of penetration loads that may typically be expected, a Design of Experiments (DOE) investigation was undertaken. A DOE approach is useful in circumstances whereby a measured response is dependent on a number of variables. In this case, the measured response is the force required for penetration of a skin simulant and the variables are the geometrical aspects of the glass shard tip.

The parameters investigated were selected for the free surface side according to typical measurements taken to characterise sharpness (Figure 6.1), and for the fracture surface side according to the aspects in Figure 6.8 which could be easily altered. The parameters were: the free surface included angle (at nominal values of 20° and 40°), the free surface tip radius (0.1 mm, 1 mm), the glass thickness (2 mm, 3 mm and 4 mm), and the x-axis edge profile shape (sloped edge, rounded edge, wedge). This yielded a total of 36 geometrical combinations.

Smaller values of each parameter were expected to decrease the penetration load (sharp aspect) and larger values of each parameter were expected to increase the penetration load (blunt aspect). The sharp and blunt aspects of the x-axis edge profile were the sloped edge and the wedge profile respectively, with the rounded edge expected to fall in between. An illustration of these parameters is presented in Figure 6.19, with the actual final measured dimensions.

### 6.6.2 Experimental setup and methodology

Annealed float glass sheets of 2 mm, 3 mm and 4 mm nominal thickness were procured from a local supplier. The actual measured sheet thicknesses were 2.08 mm, 2.84 mm and 3.82 mm respectively. The fragments were first cut as wedges of intended included angle of either 20° or 40°, using a glass cutter with a tungsten carbide tip (Toyo TC10 Oil Glass Cutter, Toyo Glass Co. Ltd., Japan) to score the surface, before manually applying suitable pressure to enable the glass to break along the score line.

The tips were then ground to shape using a 180 grit diamond polishing disc and continually checked for adherence to the desired dimensions with a stereo microscope (Olympus SZ-X12, Olympus, Tokyo, Japan). In some cases it was difficult to machine the glass to the desired fracture profile dimensions without sacrificing the dimensions of the free surface tip profile,

and so some variation between fragment dimensions was accepted, and is shown in Figure 6.19. However, this variation was considered as small in comparison to the difference between the values of the factors investigated. Some examples of the machined fragments are shown in Figure 6.20.

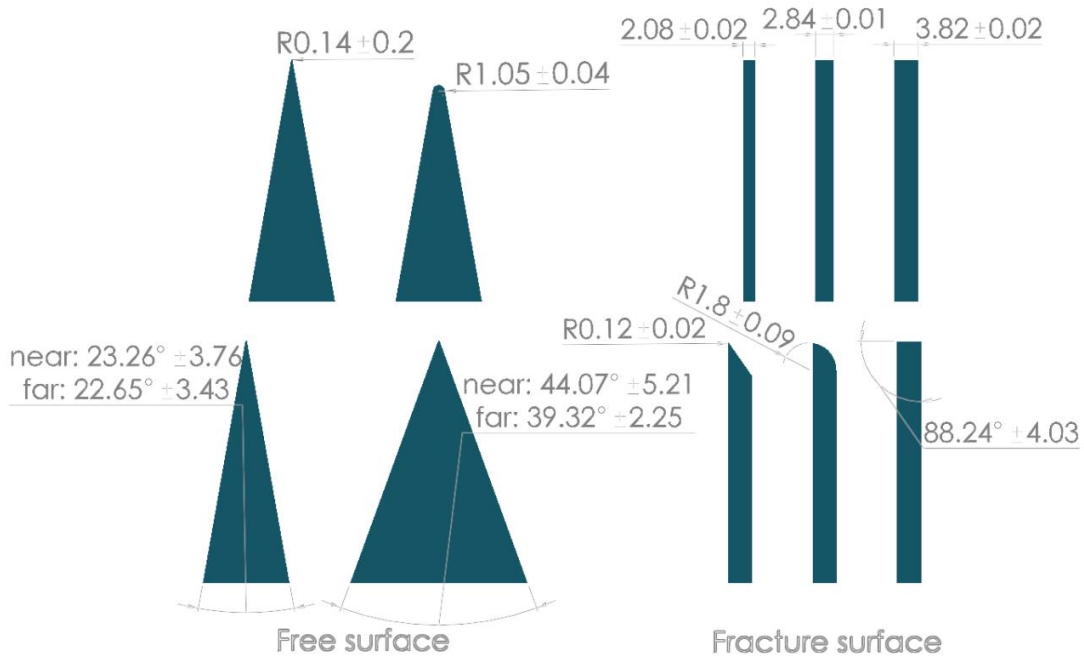


**Figure 6.19 – Tip geometry parameters, along with the actual measured sample values. Dimensions are in mm unless otherwise stated. Value shown is the mean  $\pm$  the standard deviation.**



**Figure 6.20 – Examples of three machined glass fragments used in DOE penetration tests. For each, the free surface profile is shown on the left, and the x-axis edge profile on the right. a: inc. ang.: 20°, tip rad.: 1 mm, thickness: 2 mm, x-profile: wedge. b: inc. ang.: 40°, tip rad.: 1 mm, thickness: 3 mm, x-profile: rounded edge. c: inc. ang.: 20°, tip rad.: 0.1 mm, thickness: 4 mm, x-profile: sloped edge.**

The fragments were then mounted in polyester casting resin using the method outlined in section 6.5.1.3. Each fragment was tested 3 times, giving a total of 108 experimental runs. The order of the runs was randomised using Minitab 16 software (Minitab Ltd, Coventry, UK), which correlated with the positional ordering outlined in Figure 6.13. Three simulant blocks were used in this experiment, and each fragment penetrated each block once. Prior to conducting the experimental runs, five calibration penetrations were done in order to

calculate the correction factors as per section 6.5.1.4. The penetrations were carried out using the equipment and methodology outlined in section 6.5.1. The results were then analysed using Minitab 16 software.

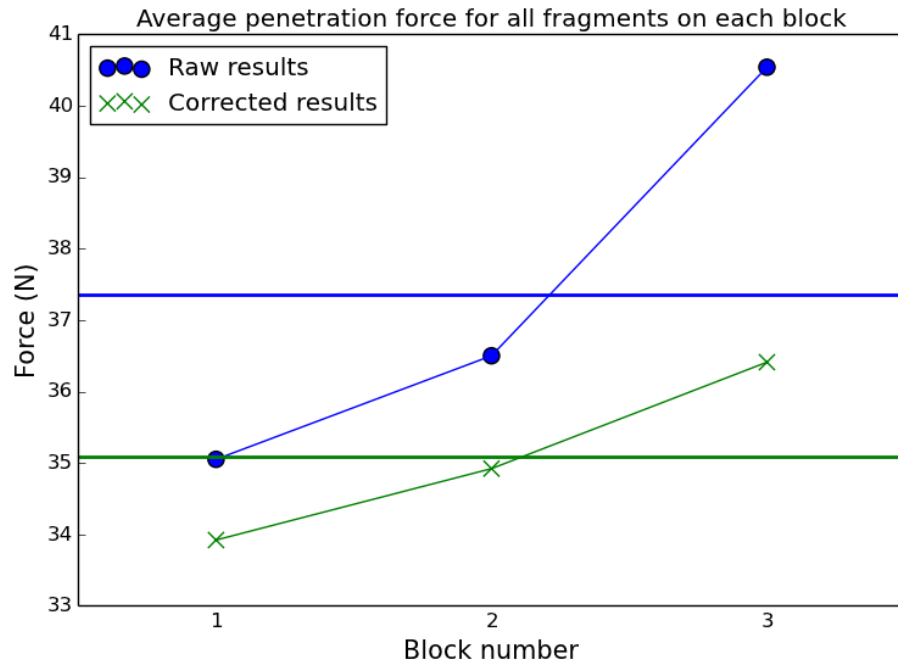
### 6.6.3 Results and discussion

Figure 6.21 shows both the average penetration load and corrected penetration load over all fragments for each block, with the horizontal lines showing the total averages over all runs. It can be seen from the figure that the interpolation reduced the variation between blocks. Additionally, the standard deviation of the average penetration load for each fragment drops from 5.15 N for the raw results to 3.99 N for the corrected results. An overall average increase in penetration load over subsequent tests may be due to cumulative damage to the glass tip during penetration, which may blunt the tip. From this point onwards, only the corrected results are considered.

Figure 6.22 shows the main effects plot for each of the four parameters investigated. The main effects plot displays the average value of the penetration load at each level of a parameter. The change in free surface radius from 0.1 mm to 1 mm displays the greatest step in penetration load (21.9 N). The increase in free surface included angle from 20° to 40° had a similar effect size to the increase in glass thickness from 2 mm to 4 mm (14.5 N and 12.2 N respectively). However, the effect of changing the thickness from 3 mm to 4 mm was smaller than the effect from 2 mm to 3 mm (3.5 N compared to 8.7 N).

Interestingly, the effect of changing the edge profile from sloped edge to rounded edge, and the effect of changing from sloped edge to wedge gave very similar load steps (9.58 N and 9.06 N respectively). This may be because the terminal points of the wedge profile are both sharp and in contact with the simulant during penetration, creating higher localised stress at these points.

Although the rounded edge profile has an obvious protrusion length from the wedge line (as defined in Figure 6.8), stress is dissipated well along its curved profile to give similar penetration load values to the wedge fragments. A semi-circular x-axis profile that gently curves towards the y-axis edges may be expected to yield the highest penetration loads.



**Figure 6.21 – Comparison of the average overall penetration load on each block. The blue and green horizontal lines show the average overall penetration load for the raw and corrected results respectively.**

The Pareto chart presented in Figure 6.23 compares the relative influences of each parameter on the penetration load, along with interaction effects. The “standardised effect” is the step size between mean parameter levels, divided by the standard deviation. This has the effect of scaling each parameter effect regardless of the size of the step change (i.e. a change in free surface angle from 20° to 40° would be expected to have the same standardised effect as a step change from 20° to 50°). The chart suggests that changes in the free surface tip radius have the largest effect on penetration load and changes in x-axis edge profile have the smallest effect.

The interaction effects between two parameters were calculated using the mean effect of different levels of a parameter at different levels of another. Interaction effects indicate whether changes in the two parameters together provoke a different response than if just one parameter was changed alone [63]. For example, the interaction between the free surface angle and free surface tip radius (BC) shows a large interaction effect, as the effect size of changing the free surface angle from 20° to 40° is greater when the free surface radius is 1 mm (18.5 N) than when it is at 0.1 mm (9.5 N), as shown on the inset. The red line in Figure 6.23 represents a line of significance, above which the effect size can be deemed to be significant. In this case, all interaction effects fall very close to this line, with only interactions between glass thickness and x-axis edge profile, and free surface radius and x-axis edge profile, falling below significance.

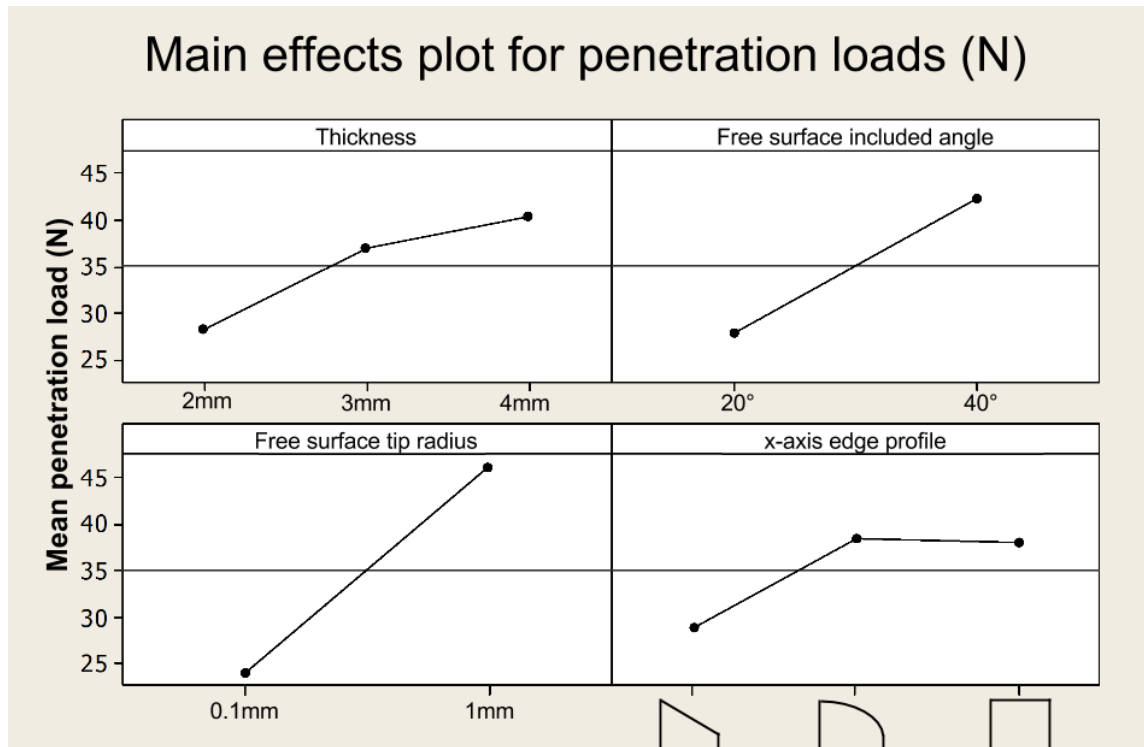


Figure 6.22 – Main effects plot of the penetration load for the four main parameters investigated. The overall mean (~35 N) is represented by the horizontal line in the centre of the figures. Error is considered in the Pareto chart (Figure 6.23).

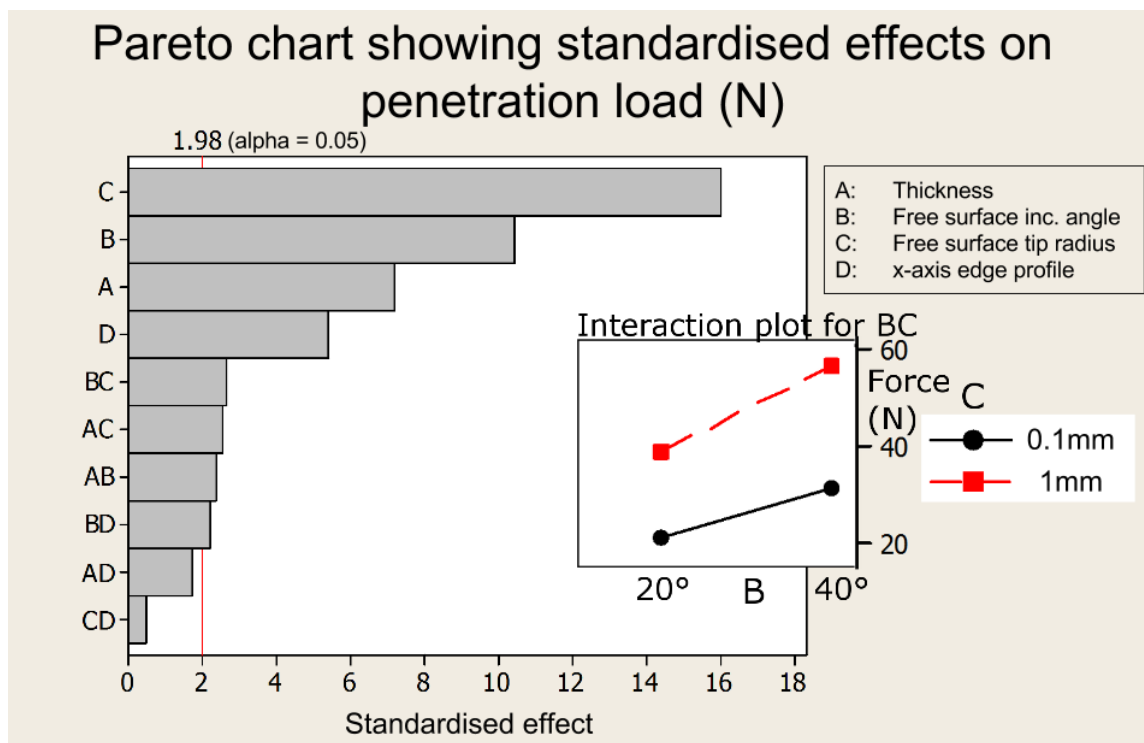


Figure 6.23 – Pareto chart showing the relative effects of each parameter. The inset shows an interaction plot for interaction BC.

Figure 6.24 shows a cube plot as a means of showing the mean penetration load for a number of geometrical combinations. The smallest penetration load is shown in the lower leftmost vertex of the left cube (10.3 N for 2 mm thickness, 20° free surface angle, 0.1 mm free surface radius with an edge point x-axis edge profile) and the largest is found at the higher rightmost vertex of the right cube (66.75 N for 4 mm thickness, 40° free surface angle, 1 mm free surface radius with a wedge x-axis edge profile).

From the cube plot, it is possible to make more specific observations not accounted for in the previous plots. Of particular significance, it can be seen that for low values of the free surface tip radius, a change in thickness has relatively little effect on the penetration load for a fragment with a sloped edge (2.2 N). By contrast, for a fragment with a wedge x-axis edge profile, a change in thickness at the smaller value of the free surface tip radius gives a significant effect size (9.47 N). This is likely to be due to the increased contact length of the x-axis edge profile with the simulant for wedge profiles. Since the sloped edge profile had a distinct piercing point, the stress concentration in the simulant was dependent upon the geometrical properties of the fragment local to the piercing point. It is therefore possible that for sloped edge profiles with very sharp tips, the penetration load is independent of the glass thickness.

The penetration loads for wedge fragments of 2mm thickness with a free surface angle of 40° are lower than expected, giving a negative effect size compared to the equivalent fragments with a sloped edge (-1.11 N). The standard deviation of the penetration load of these fragments does not exceed the average overall standard deviation, and the dimensions were within the standard deviation bounds reported in Figure 6.19. Further tests would be necessary to verify the validity this effect.

A linear regression analysis was performed on the data. This enabled the formulation of regression equations for the prediction of the penetration load for a given glass thickness, free surface included angle, free surface tip radius, and x-axis edge profile. These are shown in Table 6.1. The equations give the penetration load with a standard error of 7.57 N within the range of variables tested.

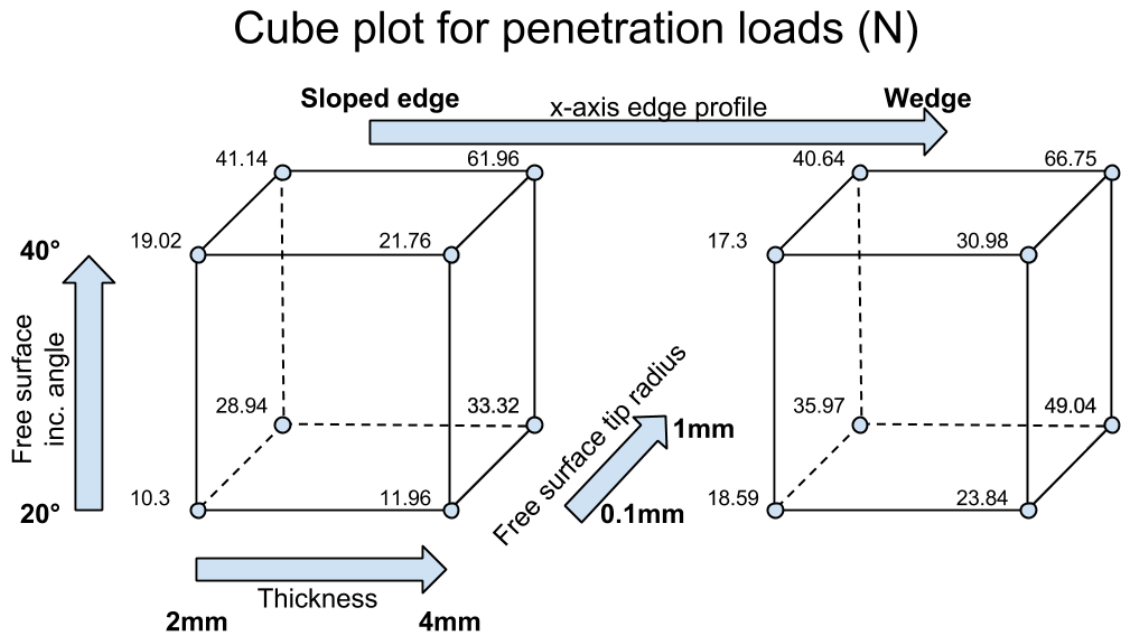


Figure 6.24 – Cube plot showing the penetration load for various geometrical combinations.

Edge profile shape	Regression equation (standard error of 7.57 N, $r^2=0.8$ )		Key
	$F_p = 6.8t + 0.69a + 24.26r - 28.67$	(eq. 6.1)	t: Thickness /mm
	$F_p = 6.8t + 0.69a + 24.26r - 18.92$	(eq. 6.2)	a: Free surface included angle /°
	$F_p = 6.8t + 0.69a + 24.26r - 19.51$	(eq. 6.3)	r: Free surface tip radius /mm

Table 6.1 – Regression equations for prediction of penetration load ( $F_p$ ), based on the results from the DOE study. The calculated results have a standard error of 7.57 N and coefficient of determination of 0.8.

#### 6.6.4 Conclusions

The aim of this DOE investigation was to assess the effect of sharp and blunt geometrical parameters relating to penetration force for the tip of a glass fragment. This involved selecting parameters which were likely to be relevant, and selecting aspects of those parameters which would decrease the penetration load (sharp aspect) or increase it (blunt aspect). In the majority of instances, the inclusion of a blunt aspect on the fragment tip did increase the penetration load. The lowest penetration load was a combination of all sharp geometrical aspects, and likewise, the greatest penetration load was a combination of all blunt geometrical aspects. The force required for penetration ranged from 10.3 N to 66.75 N. Changes in the geometrical parameters on the free surface side (included angle and tip radius) had a greater effect on the penetration load than those on the fracture surface side (thickness and x-axis edge profile).

## 6.7 Chapter summary

This chapter firstly presented a review of previous studies into the sharpness of various implements. The review revealed that methods for assessing sharpness are wide-ranging, and furthermore, there are very few studies assessing the sharpness of glass fragments. Secondly, substitutes for human skin used in forensic studies were considered. Thirdly, methodologies were then presented for measuring the geometrical properties of glass fragments relating to cutting, followed by methodologies to measure the force required for glass fragments to cause stab and slash injuries. These considerations informed the development of the experimental methodologies used in this study to assess the sharpness of glass, which was discussed in section 6.5.

A Design of Experiments investigation into the most influential parameters of a glass fragment for penetration tests concluded the chapter. It found that changes in the tip radius and included angle on the free surface side had the largest effect on the penetration load. The glass thickness and x-axis edge profile also had significant effects. The results of this investigation showed the range of penetration forces that may be expected for glass fragment penetration into human skin, and the results were used for comparison and prediction later in the study.

The methodologies presented in this chapter feature in the following two chapters, and play an important role in quantifying the injury potential of glass fragments from various fractured articles.

## 6.8 Chapter references

- [1] "Sharpness," *CollinsDictionary.com*, 2014. [Online]. Available: <http://www.collinsdictionary.com/dictionary/english/sharpness>, Last accessed July 2014.
- [2] B. Knight, "The Dynamics of Stab Wounds," *Forensic Science*, vol. 6, no. 3, pp. 249–255, 1975.
- [3] M. A. Green, "Stab Wound Dynamics—A Recording Technique for Use in Medico-Legal Investigations," *Journal of the Forensic Science Society*, vol. 18, no. 3, pp. 161–163, 1978.
- [4] S. V. Hainsworth, R. J. Delaney, and G. N. Ritty, "How Sharp is Sharp? Towards Quantification of the Sharpness and Penetration Ability of Kitchen Knives used in Stabbings," *International Journal of Legal Medicine*, vol. 122, pp. 281–291, 2008.
- [5] C. T. McCarthy, M. Hussey, and M. D. Gilchrist, "On the Sharpness of Straight Edge Blades in Cutting Soft Solids: Part I – Indentation Experiments," *Engineering Fracture Mechanics*, vol. 74, pp. 2205–2224, Sep. 2007.
- [6] C. T. McCarthy, A. N. Annaidh, and M. D. Gilchrist, "On the Sharpness of Straight Edge Blades in Cutting Soft Solids: Part II – Analysis of Blade Geometry," *Engineering Fracture Mechanics*, vol. 77, pp. 437–451, Feb. 2010.
- [7] M. D. Gilchrist, S. Keenan, M. Curtis, M. Cassidy, G. Byrne, and M. Destrade, "Measuring Knife Stab Penetration into Skin Simulant using a Novel Biaxial Tension Device," *Forensic Science International*, vol. 177, pp. 52–65, May 2008.
- [8] R. W. McGorry, P. C. Dowd, and P. G. Dempsey, "Cutting Moments and Grip Forces in Meat Cutting Operations and the Effect of Knife Sharpness," *Applied Ergonomics*, vol. 34, pp. 375–382, Jul. 2003.
- [9] R. W. McGorry, P. C. Dowd, and P. G. Dempsey, "A Technique for Field Measurement of Knife Sharpness," *Applied Ergonomics*, vol. 36, pp. 635–640, Sep. 2005.
- [10] R. R. Meehan, J. Kumar, M. Earl, E. Svenson, and S. J. Burns, "The Role of Blade Sharpness in Cutting Instabilities of Polyethylene Terephthalate," *Journal of Materials Science Letters*, vol. 18, pp. 93–95, 1999.
- [11] D. Zhou and G. McMurray, "Modeling of Blade Sharpness and Compression Cut of Biomaterials," *Robotica*, vol. 28, pp. 311–319, Sep. 2009.
- [12] S. Kaldor and P. K. Venuvinod, "Macro-Level Optimization of Cutting Tool Geometry," *Journal of Manufacturing Science and Engineering*, vol. 119, no. 1, pp. 1–9, Feb. 1997.
- [13] Z. J. Yuan, M. Zhou, and S. Dong, "Effect of Diamond Tool Sharpness on Minimum Cutting Thickness and Cutting Surface Integrity in Ultraprecision Machining," *Journal of Materials Processing Technology*, vol. 62, pp. 327–330, 1996.

- [14] J. C. Outeiro, "Influence of tool sharpness on the thermal and mechanical phenomena generated during machining operations," *International Journal of Machining and Machinability of Materials*, vol. 2, no. 3, pp. 413–432, 2007.
- [15] B. R. K. Blackman, T. R. Houtt, Y. Patel, and J. G. Williams, "Tool Sharpness as a Factor in Machining Tests to Determine Toughness," *Engineering Fracture Mechanics*, vol. 101, pp. 47–58, Mar. 2013.
- [16] J. G. Thacker, G. T. Rodeheaver, M. A. Towler, and R. F. Edlich, "Surgical Needle Sharpness.," *American Journal of Surgery*, vol. 157, pp. 334–339, Mar. 1989.
- [17] H. C. Kaulbach, M. A. Towler, W. A. McClelland, K. M. Povinelli, D. G. Becker, R. W. Cantrell, and R. F. Edlich, "A Beveled, Conventional Cutting Edge Surgical Needle: A New Innovation in Wound Closure," *The Journal of Emergency Medicine*, vol. 8, pp. 253–263, 1990.
- [18] F. H. Watkins, S. D. London, J. G. Neal, J. G. Thacker, and R. F. Edlich, "Biomechanical Performance of Cutting Edge Surgical Needles," *The Journal of Emergency Medicine*, vol. 15, no. 5, pp. 679–685, 1997.
- [19] B. Balevi, "Engineering Specifics of the Periodontal Curet's Cutting Edge," *Journal of periodontology*, vol. 67, no. 9, pp. 374–378, 1996.
- [20] C. H. Meyer, Z. Liu, C. K. Brinkmann, E. B. Rodrigues, and T. Bertelmann, "Penetration Force, Geometry, and Cutting Profile of the Novel and Old Ozurdex Needle: The MONO Study," *Journal of Ocular Pharmacology and Therapeutics*, vol. 30, no. 5, pp. 387–391, Jun. 2014.
- [21] P. T. O'Callaghan, M. D. Jones, D. S. James, S. Leadbeatter, S. L. Evans, and L. D. M. Nokes, "A Biomechanical Reconstruction of a Wound Caused by a Glass Shard — A Case Report," *Forensic Science International*, vol. 117, pp. 221–231, 2001.
- [22] G. Nolan, S. D. A. J. Lawes, S. V. Hainsworth, and G. N. Ruddy, "A Study Considering the Force Required for Broken Glass Bottles to Penetrate a Skin Simulant," *International Journal of Legal Medicine*, vol. 126, pp. 19–25, 2012.
- [23] K. Tokuyasu and S. Okamura, "A New Method for Making Glass Knives for Thin Sectioning," *The Journal of Biophysical and Biochemical Cytology*, vol. 6, no. 2, pp. 305–308, 1959.
- [24] K. T. Tokuyasu, "Application of Cryoultramicrotomy to Immunocytochemistry," *Journal of Microscopy*, vol. 143, no. 2, pp. 139–149, Aug. 1986.
- [25] G. Griffiths, K. Simons, G. Warren, and K. T. Tokuyasu, *Biomembranes Part J: Membrane Biogenesis: Assembly and Targeting (General Methods, Eukaryotes)*, vol. 96. Elsevier, 1983, pp. 466–485.
- [26] "BS EN ISO 8442-5 (2004) Materials and articles in contact with foodstuffs Cutlery and holloware part 5: specification for sharpness and edge retention test of cutlery," *British Standards Institute, UK*, 2004.

- [27] T. Atkins, "Slice-Push Ratio: Oblique Cutting and Curved Blades, Scissors, Guillotining and Drilling," in *The Science and Engineering of Cutting: The Mechanics and Processes of Separating, Scratching and Puncturing Biomaterials, Metals and Non-metals*, 2009, pp. 111–140.
- [28] "BS 5194-1:1985 Surgical Instruments. Specification for Stainless Steels," *British Standards Institute, UK*, 1985.
- [29] G. A. Reilly, B. A. O. McCormack, and D. Taylor, "Cutting Sharpness Measurement: A Critical Review," *Journal of Materials Processing Technology*, vol. 153–154, pp. 261–267, Nov. 2004.
- [30] A. M. Davison, "The Incised Wound," in *Essentials in autopsy practice: recent advances, topics and developments.*, G. N. Rutty, Ed. Springer, London, 2003, pp. 187–220.
- [31] T. Atkins, "Sharpness and Bluntness: Absolute or Relative?," in *The Science and Engineering of Cutting: The Mechanics and Processes of Separating, Scratching and Puncturing Biomaterials, Metals and Non-metals*, 2009, pp. 221–243.
- [32] C. Arcona and T. A. Dow, "The Role of Knife Sharpness in the Slitting of Plastic Films," *Journal of Materials Science*, vol. 31, no. 5, pp. 1327–1334, 1996.
- [33] W. M. McKenzie, "Effects of Edge Bluntness in the Cutting of Wood," *Forest Products Journal*, vol. 17, no. 4, pp. 45–50, 1967.
- [34] E. Merchant, "Basic Mechanics of the Metal Cutting Process," *Journal of Applied Mechanics*, vol. 11, no. A, pp. 168–175, 1944.
- [35] A. Bleetman, C. H. Watson, I. Horsfall, and S. M. Champion, "Wounding Patterns and Human Performance in Knife Attacks: Optimising the Protection Provided by Knife-Resistant Body Armour," *Journal of Clinical Forensic Medicine*, vol. 10, pp. 243–248, 2003.
- [36] C. Malbon and J. Croft, "HOSDB Slash Resistance Standard for UK Police, Publication No. 48/05." Home Office Scientific Development Branch, 2006.
- [37] K. Parmar, S. V. Hainsworth, and G. N. Rutty, "Quantification of forces required for stabbing with screwdrivers and other blunter instruments.," *International Journal of Legal Medicine*, vol. 126, no. 1, pp. 43–53, Jan. 2012.
- [38] C. H. Daly and G. F. Odland, "Age-Related Changes in the Mechanical Properties of Human Skin," *The Journal of Investigative Dermatology*, vol. 73, no. 1, pp. 84–87, 1979.
- [39] T. Sugihara, T. Ohura, K. Homma, and H. H. Igawa, "The Extensibility in Human Skin: Variation According to Age and Site," *British Journal of Plastic Surgery*, vol. 44, no. 6, pp. 418–422, 1991.
- [40] K. Langer, "On the Anatomy and Physiology of the Skin," *British Journal of Plastic Surgery*, vol. 31, no. 4, pp. 277–278, 1978.

- [41] H. T. Cox, "The Cleavage Lines of the Skin," *The British Journal of Surgery*, vol. 29, no. 114, pp. 234–240, 1941.
- [42] G. L. Wilkes, I. A. Brown, and R. H. Wildnauer., "The Biomechanical Properties of Skin," *CRC Critical Reviews in Bioengineering*, vol. 1, no. 4, pp. 453–495, 1973.
- [43] S. V. Hainsworth, "How Much Force?," in *Essentials of Autopsy Practice*, G. N. Rutty, Ed. Springer London, 2013, pp. 151–170.
- [44] C. Edwards and R. Marks, "Evaluation of Biomechanical Properties of Human Skin," *Clinics in Dermatology*, vol. 13, pp. 375–380, 1995.
- [45] R. C. Haut, "The Effects of Orientation and Location on the Strength of Dorsal Rat Skin in High and Low Speed Tensile Failure Experiments," *Journal of Biomechanical Engineering*, vol. 111, no. 2, pp. 136–140, May 1989.
- [46] P. T. O'Callaghan, M. D. Jones, D. S. James, S. Leadbeatter, C. A. Holt, and L. D. M. Nokes, "Dynamics of Stab Wounds: Force Required for Penetration of Various Cadaveric Human Tissues," *Forensic Science International*, vol. 104, pp. 173–178, 1999.
- [47] O. A. Shergold and N. A. Fleck, "Experimental Investigation Into the Deep Penetration of Soft Solids by Sharp and Blunt Punches, With Application to the Piercing of Skin," *Journal of Biomechanical Engineering*, vol. 127, pp. 838–848, 2005.
- [48] B. Wong, J. A. Kieser, I. Ichim, M. Swain, V. Livingstone, N. Waddell, and M. Taylor, "Experimental Simulation of Non-Ballistic Wounding by Sharp and Blunt Punches," *Forensic Science, Medicine, and Pathology*, vol. 4, pp. 212–220, Jan. 2008.
- [49] J. Jussila, A. Leppäniemi, M. Paronen, and E. Kulomäki, "Ballistic Skin Simulant," *Forensic Science International*, vol. 150, pp. 63–71, May 2005.
- [50] G. Nolan, S. V. Hainsworth, and G. N. Rutty, "Forces Required for a Knife to Penetrate a Variety of Clothing Types," *Journal of Forensic Sciences*, vol. 58, no. 2, pp. 372–379, Mar. 2013.
- [51] J. Ankersen, A. Birkbeck, R. Thomson, and P. Vanezis, "The Effect of Knife Blade Profile on Penetration Force in Flesh Simulants," *Technology, Law and Insurance*, vol. 3, pp. 125–128, Jun. 1998.
- [52] J. Ankersen, A. E. Birkbeck, R. D. Thomson, and P. Vanezis, "Puncture Resistance and Tensile Strength of Skin Simulants," *Proceedings of the Institution of Mechanical Engineers, Part H: Journal of Engineering in Medicine*, vol. 213, pp. 493–501, 1999.
- [53] E. K. J. Chadwick, A. C. Nicol, J. V. Lane, and T. G. F. Gray, "Biomechanics of Knife Stab Attacks," *Forensic Science International*, vol. 105, pp. 35–44, 1999.
- [54] M. L. Fackler and J. A. Malinowski, "Ordnance Gelatin for Ballistic Studies. Detrimental Effect of Excess Heat Used in Gelatin Preparation," *American Journal of Forensic Medicine and Pathology*, vol. 9, no. 3, pp. 218–219, 1988.

- [55] J. Jussila, "Preparing Ballistic Gelatine —Review and Proposal for a Standard Method," *Forensic Science International*, vol. 141, no. 2, pp. 91–98, 2004.
- [56] L. H. Jansen and P. B. Rottier, "Some Mechanical Properties of Human Abdominal Skin Measured on Excised Strips," *Dermatology*, vol. 117, no. 2, pp. 65–83, 1958.
- [57] C. Jacquemoud, K. Bruyere-Garnier, and M. Coret, "Methodology to Determine Failure Characteristics of Planar Soft Tissues using a Dynamic Tensile Test," *Journal of Biomechanics*, vol. 40, no. 2, pp. 468–475, Jan. 2007.
- [58] A. Ní Annaidh, K. Bruyère, M. Destrade, M. D. Gilchrist, and M. Otténio, "Characterization of the Anisotropic Mechanical Properties of Excised Human Skin," *Journal of the Mechanical Behavior of Biomedical Materials*, vol. 5, no. 1, pp. 139–148, 2012.
- [59] O. A. Shergold, N. A. Fleck, and D. Radford, "The Uniaxial Stress Versus Strain Response of Pig Skin and Silicone Rubber at Low and High Strain Rates," *International Journal of Impact Engineering*, vol. 32, pp. 1384–1402, Sep. 2006.
- [60] K. Whittle, J. Kieser, I. Ichim, M. Swain, N. Waddell, V. Livingstone, and M. Taylor, "The Biomechanical Modelling of Non-Ballistic Skin Wounding: Blunt-Force Injury," *Forensic Science, Medicine, and Pathology*, vol. 4, pp. 33–39, Jan. 2008.
- [61] F. W. Preston, "The Angle of Forking of Glass Cracks as an Indicator of the Stress System," *Journal of the American Ceramic Society*, vol. 18, no. 1–12, pp. 175–176, 1935.
- [62] G. D. Quinn, "General Examination and Fracture Patterns," in *Fractography of Ceramics and Glasses*, National Institute of Standards and Technology, 2007, pp. 4–1 – 4–44.
- [63] J. Antony, "Understanding Key Interactions in Processes," in *Design of Experiments for Engineers and Scientists*, Elsevier, 2003, pp. 17–28.

## **7 Glass fragment sharpness part I: Effect of load and temper level**

### **7.1 Introduction**

In the previous chapter, the concept of sharpness and its relation to injury potential was discussed, and methodologies for assessing the sharpness of glass fragments were outlined. This chapter is the first of two chapters that use these methodologies to characterise the sharpness of a variety of glass fragments both qualitatively and quantitatively. In this chapter, a 3 point bending (3PB) configuration is used to fracture annealed and tempered rectangular glass samples in order to determine how the loading magnitude and temper level affect properties pertaining to sharpness and injury potential.

Determination of a minimum temper level for a glass article, that yields fragments with a suitably low risk of causing injury once broken, has both economical and preventative benefits. It removes the need to over-temper glass articles to comfortably ensure safety standards are met, and decreases the likelihood of the glass article being used as an effective impulsive weapon.

The design of the experiments was intended to replicate the stress conditions of a portion of a pint glass wall in close proximity to the fracture origin or loading area. This is demonstrated in Figure 7.1. Stress distributions of pint glasses subjected to typical loading conditions were discussed in chapter 4. Using rectangular samples as opposed to pint glasses simplified many aspects of the investigation, including: tempering processes, initial flaw alignment, loading alignment, and fragment retrieval.

A further aim of the chapter is to test whether fragments from tempered glass have blunter geometrical aspects than those of annealed glass. Thermally tempered glass is considered to have safer breakage behaviour than annealed glass [1], but whether this is due to inherent fragment sharpness, or practical considerations due to the reduced fragment size, is not entirely clear.

Experimentation is split into two main sections: firstly, an investigation into the effect of loading magnitude on sharpness properties using annealed glass samples is presented (section 7.2); and secondly an investigation into how the level of thermal temper affects sharpness properties using 3 thermal temper levels is presented (section 7.3). The format of each section is similar and consists of two main parts: the pre-sharpness assessment analysis, and the sharpness assessment of the glass fragments. The involved nature of conducting sharpness

assessment means it does not feasibly lend itself to a high volume of tests. As such, many features are discussed on a sample-by-sample basis.

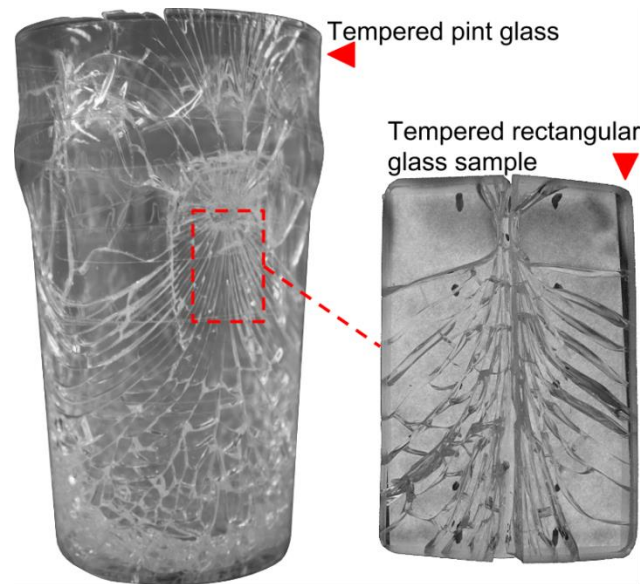


**Figure 7.1 – A tempered pint glass broken by impact from chapter 4 (left) and a tempered rectangular sample broken by 3PB. The dashed red rectangle indicates the location (in relation impact location) on the pint glass wall with stress conditions most similar to that in the current set of experiments.**

The pre-sharpness assessment section follows the order of methodology outlined in chapter 3. It consists of the residual stress assessment; hardness and strength data; and macroscopic fracture analysis. The sharpness assessment section first outlines the choice of procedures for sharpness analysis (as discussed in the previous chapter). This is followed by the results of sharpness assessments for x-axis edges and y-axis edges (definitions of x-axis and y-axis edges are based on fractographic axes and are detailed in the previous chapter). Each sharpness section ends with an overview of the main conclusions from the investigation. Where appropriate, conclusions between sections 7.2 and 7.3 are drawn in section 7.3. The overall results of this chapter are then summarised in section 7.4.

## **7.2 Sharpness as affected by loading magnitude in flexure**

### **7.2.1 Introduction**

This section details an investigation into how the sharpness of y-axis edges of glass fragments is affected by the magnitude of mode I stress induced by bending. This is in order to provide a foundation for divorcing edge morphology features due to loading effects from those due to residual stresses. Loading by flexure was conducted to reflect the bending stresses encountered by pint glasses under typical loading conditions prior to fracture (see Figure 7.1 and chapter 4).

Since the minimisation of the effects of residual stresses was desirable, annealed glass samples were used. Flat rectangular samples were used to simplify the investigation, and were broken by three point bending (3PB) as outlined in section 3.6.1.2. It was intended that this loading configuration would result in a crack that would run underneath and parallel to the loading rod, thus producing two fragments. Since this is unlikely to result in significant crack branching (a main cause of x-axis edges, see chapter 6), the focus of this investigation was mainly on y-axis edges. Different bending loads at fracture were achieved by variation of the initial flaw size on the glass surface by imparting Vickers indents at three different loads.

The following sub-section overviews the pre-sharpness assessment procedures conducted, and provides the background for the sharpness assessments. Conclusions are then drawn in sub-section 7.2.5.

## 7.2.2 Pre-sharpness assessment analysis and sample fracture

### 7.2.2.1 Overview

A summary of the pre-sharpness analysis stage of this investigation is given in Table 7.1.

Glass samples:	15 x flat rectangular (25 x 38 x 3.82 mm)
Tempering/annealing processes:	As-received (annealed)
Residual stress assessment:	SCALP
Surface pre-damaging:	0.2, 0.5, and 1 kgf Vickers indentation as per sub-section 3.5.1 for rectangular samples
Fracture method:	Three point bending (3PB) as per sub-section 3.6.1.2

**Table 7.1 – Pre-sharpness assessment summary table for investigation of sharpness with loading magnitude.**

A total of 15 flat annealed rectangular glass samples was used in this investigation. Confirmation of low residual stress levels was conducted using a Scattered Light Polariscope (SCALP). Variation of the loading magnitude (and by extension, tensile failure stress) was achieved by imparting Vickers indentation flaws of various sizes. For this, indentation loads of 0.2, 0.5 and 1 kgf were used on 5 samples each. Fracture was then achieved by 3PB with the indented side in contact with the support rods (the tensile side – see Figure 3.15).

### 7.2.2.2 Photoelastic measurements

The central region of the sheet of annealed float glass from which the rectangular samples were cut was subjected to through-thickness residual stress measurement prior to cutting. This was conducted using a Scattered Light Polariscope (SCALP). Five measurements were taken, which gave a mean surface stress of -9 MPa ( $\sigma = 2$  MPa), and a mean peak core stress of 4 MPa ( $\sigma = 2$  MPa). This surface compressive stress is ~13% of the minimum prescribed surface

stress for fully tempered glass (69 MPa) [2], and a peak core tensile stress of 4 MPa is ~12% of that required to cause spontaneous fracture propagation (34 MPa) [3]. This was deemed suitable for the current investigation.

### 7.2.2.3 Flaw morphology and mechanical data

The indentation data, flaw size (2c) data, and strength data from 3PB loading are tabulated in Table 7.2.

Indentation load /kgf	Vickers hardness /GPa	Flaw size (2c) / $\mu\text{m}$	% full MR crack developed	Failure stress in 3PB /MPa	Mirror tensile failure stress /MPa
0.2	$5.2 \pm 0.2$	$44 \pm 6$	60	$86.5 \pm 12.9$	-
0.5	$5.7 \pm 0.2$	$103 \pm 4$	100	$93.2 \pm 15.8$	$77.5 \pm 0.6$
1	$5.7 \pm 0.2$	$175 \pm 4$	100	$67.6 \pm 6.2$	$56.8 \pm 1.1$

**Table 7.2 – Indentation data and strength data for annealed rectangular glass samples. Values shown are the mean  $\pm$  the standard deviation. Mirror tensile failure stress values only considered for samples that failed from Vickers indent flaw.**

The morphology of all 15 imparted Vickers indent flaws is shown in Figure 7.2. The orientation of the micrographs is shown in the top right inset of Figure 7.2, with the horizontal (D1) and vertical (D2) indentation diagonal parallel to the length and width of the rectangular sample, respectively. Since the length of D1 was located beneath the loading rod in the 3PB configuration, the tensile stress due to loading mainly acted on this diagonal. As such, only the median/radial (MR) cracks propagating from the corners of D1 are considered for the initial flaw size (2c). Furthermore, in Table 7.2, 2c is only considered as the horizontal length of the crack, as opposed to the actual crack length. Therefore, if a MR crack deviated by any angle from the horizontal axis, the actual crack length would be greater than 2c. The percentage of indentations which had visible MR cracks propagating from both corners associated with diagonal D1 is given in Table 7.2.

Indents made with loads of 0.2 kgf showed the greatest level of variation, both dimensionally and by the number/orientations of the MR cracks. Indentation loads of 0.5 and 1 kgf showed less variation and resulted in similar hardness values. 1 kgf indents showed the least overall variation of 2c, and the MR cracks showed little overall deviation from the sample central line.

The overall average tensile failure strength of the 0.2 kgf indent samples was not as expected, as these samples required less load for fracture overall than those with 0.5 kgf indents. This could be due to a change in stress concentration from the edges towards the Vickers indent flaw for samples with larger values of 2c. Macroscopic fracture analysis (see following sub-

section) revealed that this was due to  $2c$  being too small, and samples instead failed from an edge flaw.

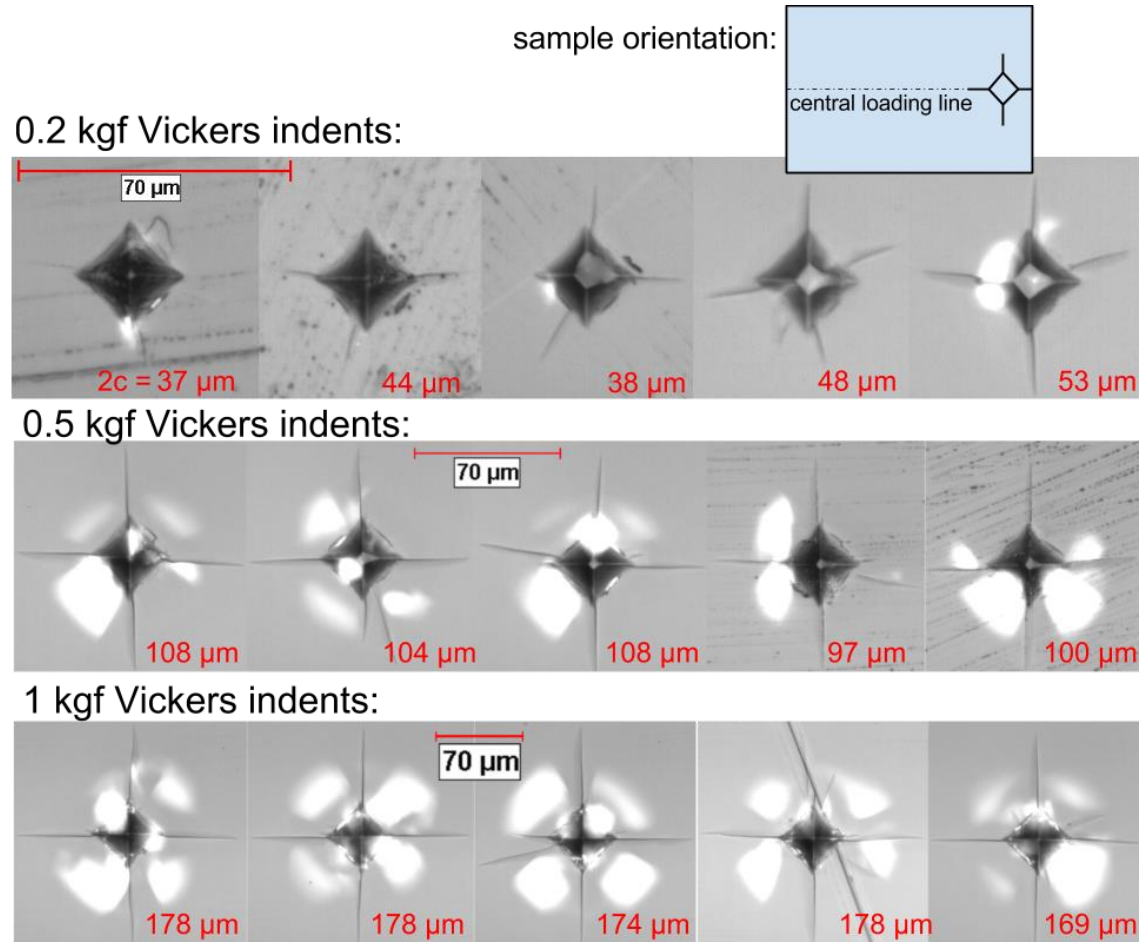


**Figure 7.2 – Micrographs of all 15 Vickers indentation flaws imparted onto rectangular samples for investigation 7.2. The flaw size ( $2c$ ) for each indent is shown in red. Top right inset illustrates the orientation of all micrographs relative to the sample dimensions. Order of indents correlates to Figure 7.3. All micrographs were taken a minimum of 30 minutes after indentation.**

Failure stress was also calculated by consideration of the mirror size using equation 2.4 for samples that successfully fractured with the Vickers indent as the initiating flaw (see Table 7.2). These values were on average less than those calculated with equation 3.3, and showed significantly less variation. This could be due to the limited ability to control precise alignment of samples during testing with the 3PB fixture, and/or the alignment of the Vickers indent with sample centre line.

However, since the objective of this investigation was to determine the change in sharpness properties across the sample length due to applied load, the 3PB failure stress was considered the more important value. The mirror tensile failure stress only gives an indication of the surface stress level local to the indentation, whereas the 3PB failure stress is directly proportional to the overall load applied to the sample.

### 7.2.2.4 Macroscopic fracture and fracture surface analysis

The macroscopic fracture patterns of all annealed rectangular samples are shown in Figure 7.3.

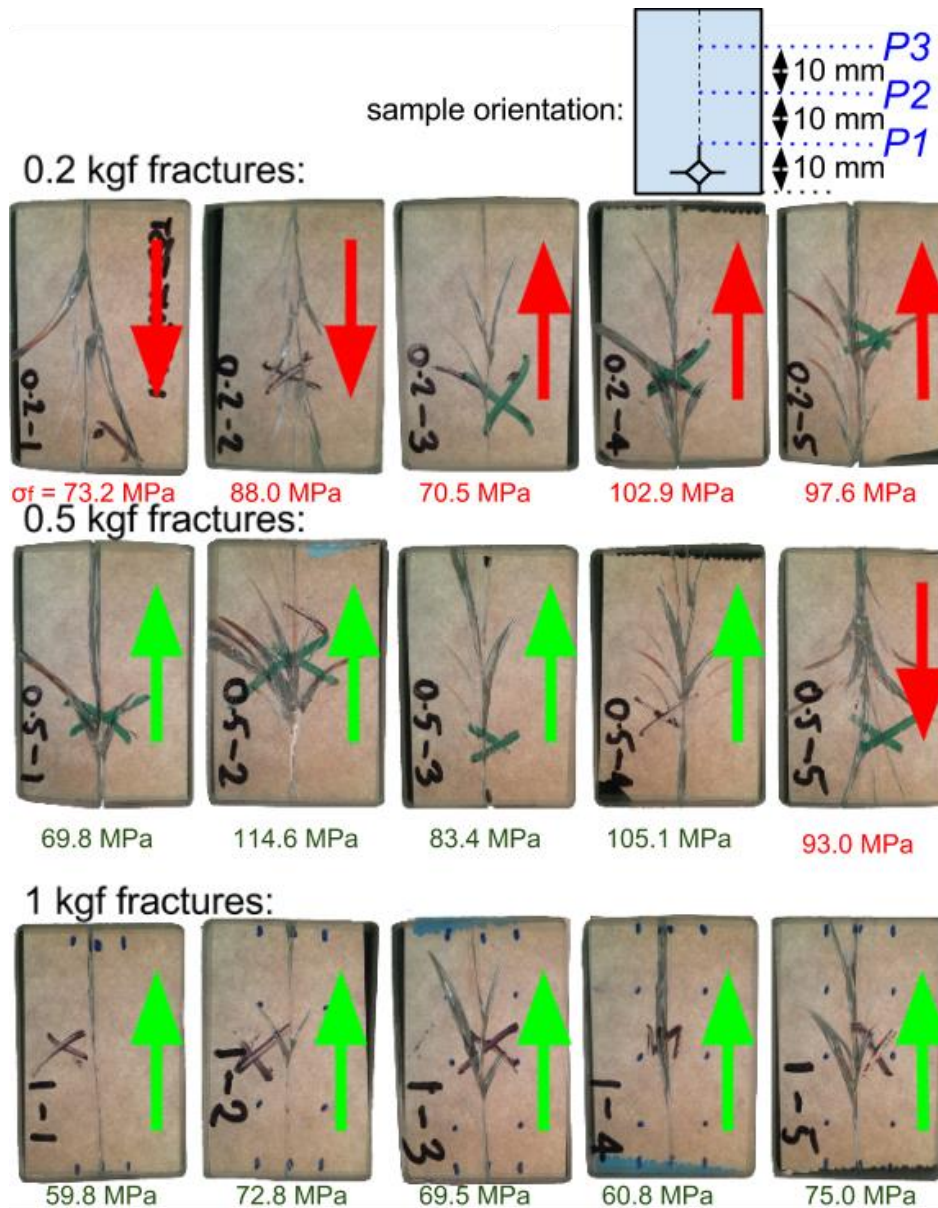
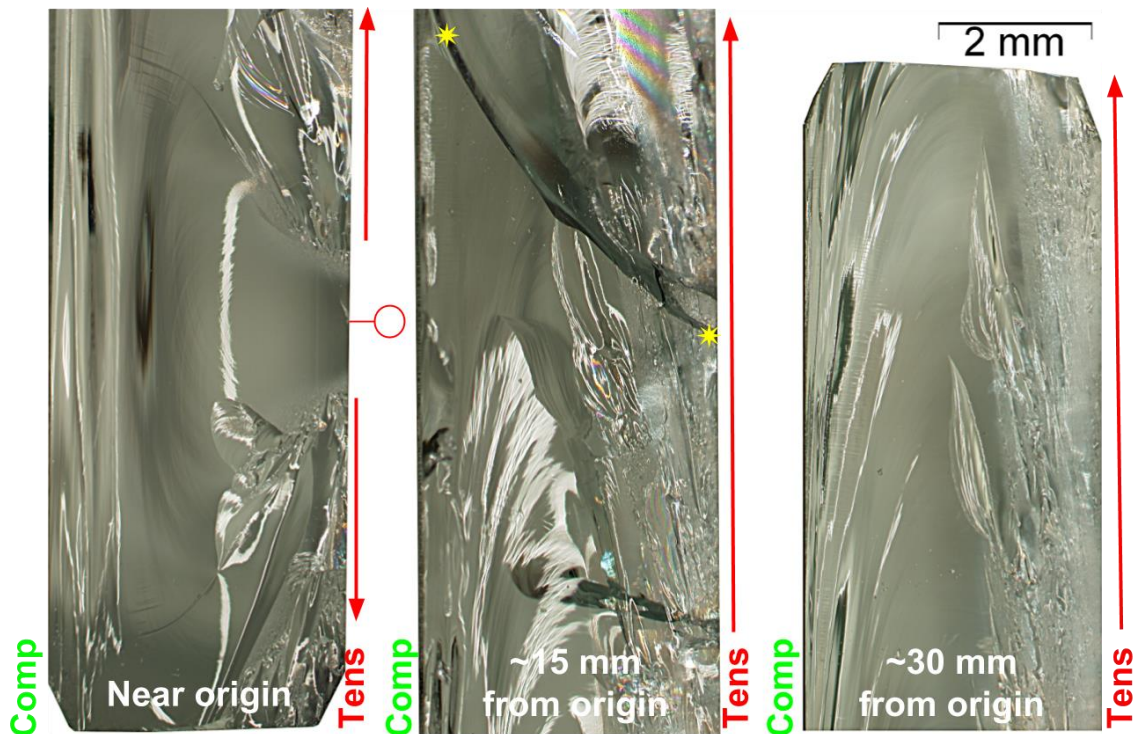


Figure 7.3 – Fracture patterns for all annealed rectangular samples broken by 3PB, with individual failure stresses shown. The top right inset indicates the orientation of the samples relative to the Vickers flaw location. The arrows indicate the direction of crack propagation. Green arrows indicate that fracture initiated from the Vickers flaw, and red arrows indicate that fracture initiated from an edge flaw. Order correlates to indent micrographs in Figure 7.2.

The 3PB failure stresses are shown beneath each sample for convenience, but were summarised in the previous sub-section. 6 out of the 15 samples did not fracture from the Vickers flaw, as indicated by the red arrows. This included all samples with indents made with a 0.2 kgf load, and one sample with an indent made with a 0.5 kgf load.

In 3PB, the maximum imposed tensile stress lies beneath the loading rod, on the face in contact with the support rods. The imposed stress then decreases laterally toward the longer edges of the rectangular samples. For the samples that fractured with sufficient load to cause branching, cracks that began to propagate away from the central loading line were therefore typically arrested prior to terminating at a free surface in the x-y fractographic plane. This was observed in samples that had a calculated tensile failure strength of above 69 MPa.



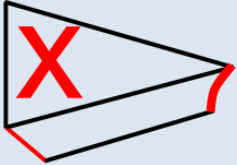
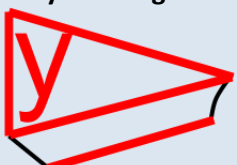
**Figure 7.4 – Three example fracture surfaces of annealed rectangular fragments broken by 3PB (0.5 kgf fractures) with tensile and compressive sides labelled, at various propagation lengths. Red circle denotes Vickers origin flaw location. Yellow asterisks superposed to the central fracture surface indicate a crack on the surface due to branching (see Figure 7.3).**

The fracture surfaces formed by the central crack that ran below the loading rod were observed via a stereo optical microscope for 0.5 kgf and 1 kgf indented samples. 0.2 kgf indented samples were not considered for further testing due to the fractures not initiating from the imparted indent flaws. The fracture surface features of the observed samples were similar, and an example is shown in Figure 7.4. The origin mirror region was open as opposed to semi-circular, which is common for glass broken by bend loading [4]. The crack front then led on the tensile surface until it intersected a free surface, forming a band of mist hackle on the tensile side that was thicker for higher-energy fractures.

This section has summarised the pre- and post-breakage analysis processes conducted prior to sharpness assessment of annealed flat rectangular glass samples. The results are used as a foundation to the sharpness analysis study that follows.

### 7.2.3 Sharpness assessment: overview

A summary of the sharpness assessment tests and analyses conducted on fragments from flat annealed rectangular glass samples is given in Table 7.3 below.

 <p><b>x-axis edges</b></p>	<p>Optical profile analysis</p> <p>SEM analysis (tip radii)</p> <p>Penetration testing</p>	<p>None</p> <p>None</p> <p>None</p>
 <p><b>y-axis edges</b></p>	<p>Micro-CT cross sections (included angles)</p> <p>Replica sections (edge radii)</p> <p>Slash test</p>	<p>0.5 and 1 kgf samples (10)</p> <p>0.5 and 1 kgf samples (10)</p> <p>0.5 and 1 kgf samples (10)</p>

**Table 7.3 – Sharpness analysis summary table for investigation of sharpness with loading magnitude.**

Only the y-axis edges of fragments were assessed in this investigation because only a small amount of crack branching occurred. Only samples indented with loads of 0.5 kgf and 1 kgf were subjected to edge assessment, because samples indented with loads of 0.2 kgf did not fracture successfully from the imparted Vickers flaw. The samples typically broke into two halves which had a high degree of symmetry, and presented comparable geometrical features. This enabled one half to be used for micro-CT scans and replica edge casting, and the other half to be used for slash tests.

The included angles of the fragment edges were measured from micro-CT scans at three cross-sectional locations. These three locations are indicated on the inset of Figure 7.3 as P1, P2, and P3; and were 10 mm, 20 mm, and 30 mm from one of the 25 mm edges of the samples respectively.

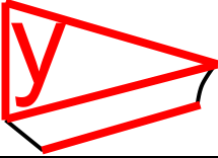
Replica casts were made of fragments after micro-CT scans were conducted. As discussed in section 6.4.3, difficulties encountered during preparation meant that only a small number of tip radii measurements from these casts were valid. The number of samples that average tip radii measurements are based on are therefore given in the text where appropriate.

Slash tests were conducted on the central region of the y-axis tensile side edge. The tensile edge was chosen for testing rather than the compressive edge due to concerns over the

condition of the compressive edges after fracture. Since the compressive side was in contact with the adhesive tape used to retain the fragments, any further bending of the glass sample after fracture may have caused damage to the compressive edges.

#### 7.2.4 Sharpness assessment: y-axis edges

A summary of all y-axis edge parameters collected in this investigation is given in Table 7.4. This sub-section discusses the results in the order of this table.

	0.5 kgf samples	1 kgf samples	All
<b>Micro-CT cross sections</b>			
Near (1% into thickness) tensile side included angle /°	95.2 ± 4.5 (5)	99.3 ± 7.3 (7)	97.2 ± 6.4 (7)
Far (10% into thickness) tensile side included angle /°	92.4 ± 10.4 (11)	91.2 ± 6.7 (7)	91.8 ± 8.7 (9)
Near (1%) compressive side included angle /°	98.1 ± 20.1 (20)	114.3 ± 17.4 (15)	106.2 ± 20.5 (19)
Far (10%) compressive side included angle /°	83.8 ± 20.9 (25)	84.2 ± 15.8 (18)	84.0 ± 18.5 (22)
<b>Replica tip radii measurements</b>			
Tensile side tip radius /μm	~1-3 (n = 2)	None	~1-3 (n = 2)
Compressive side tip radius /μm	~2-3 (n = 2)	None	~2-3 (n = 2)
<b>Fragment cutting/slashing tests</b>			
Penetration depth /mm	0.45 ± 0.19 (42)	0.62 ± 0.33 (53)	0.53 ± 0.28 (53)
Average load in steady state /N	3.8 ± 0.5 (13)	4.3 ± 0.9 (21)	4.0 ± 0.8 (20)
Friction coefficient	0.45 ± 0.07 (16)	0.51 ± 0.10 (20)	0.48 ± 0.09 (19)

**Table 7.4 – Summary of parameter data collected y-axis edges of annealed indented rectangular sample fragments. In each case the average value is shown ± one standard deviation. The percentage of the standard deviation compared to the average value is shown in parentheses. For tip radii measurements, the number of samples tested is shown in parentheses instead. All parameters listed in this table are described and illustrated in section 6.4 in the previous chapter.**

**Cross sections (micro-CT):** Edge included angle measurements were taken from the micro-CT cross sections for both the compressive and tensile sides. As introduced in section 6.4, *near* and *far* included angles were measured. These correspond to when the edge included angle is measured between the side and a point 1% or 10% into the profile, respectively. Student's *t*-tests were conducted to determine any significant differences between near and far measurements, and between measurements of the tensile and compressive side included angles. The full results of these analyses are given in Appendix K.

No significant differences were found between 0.5 kgf and 1 kgf samples. It was found that far included angles were significantly closer to  $90^\circ$  than near included angles, with the latter being in the region of  $\sim 100^\circ$  on average. Obtuse near included angles could be a sign of damage to the edges. Additionally, significant differences were found between the compressive and tensile side included angles. Far compressive side included angles were on average acute, and far tensile side included angles were on average obtuse.

These trends are reflected in the shape of the average cross section plots given in Figure 7.5. These plots were obtained by digitally tracing fragment cross sections and averaging the coordinates, and effectively show the average cross-sectional edge profile. The plots show evidence of a cantilever curl effect occurring (see section 2.5.4). This is highlighted by the higher standard deviation of the plots near the compressive side.

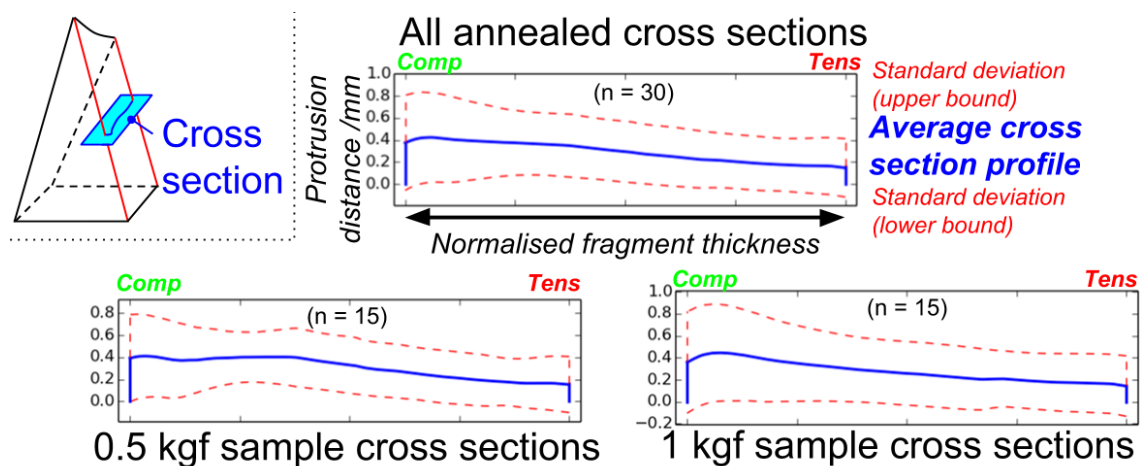


**Figure 7.5 – Average cross section profile morphology the annealed indented rectangular samples shown in Figure 7.3. Vertical axes are in units of mm. Average profiles are plotted with a solid blue line. Upper and lower standard deviation profile bounds are plotted with dashed red lines. 3 cross sections were assessed per fragment. Inset shows y-axis/cross section profile context. The scale of the figures shows the thickness normalised to 4 mm.**

**Tip radii measurements:** Only two of each of the tensile side and compressive side tip radii were valid for measurement. SEM micrographs of these tips are shown in Figure 7.6. Approximate tip radii measurements ranged from 1-3  $\mu\text{m}$ . This is smaller than that of new surgical scalpels ( $\sim 5 \mu\text{m}$ ) [5].

**Fragment cutting/slashing tests:** As with other geometrical parameters measured, no significant differences were found between 0.5 kgf samples and 1 kgf samples for fragment performance during slash tests. An average cut depth of 0.53 mm was measured when the applied top load of 8 N was used. On average, the force required to propagate the cut was

found to be approximately half of the top load. The cross sections of the cut profiles showed straight, non-ragged cuts. An example is shown in Figure 7.7.

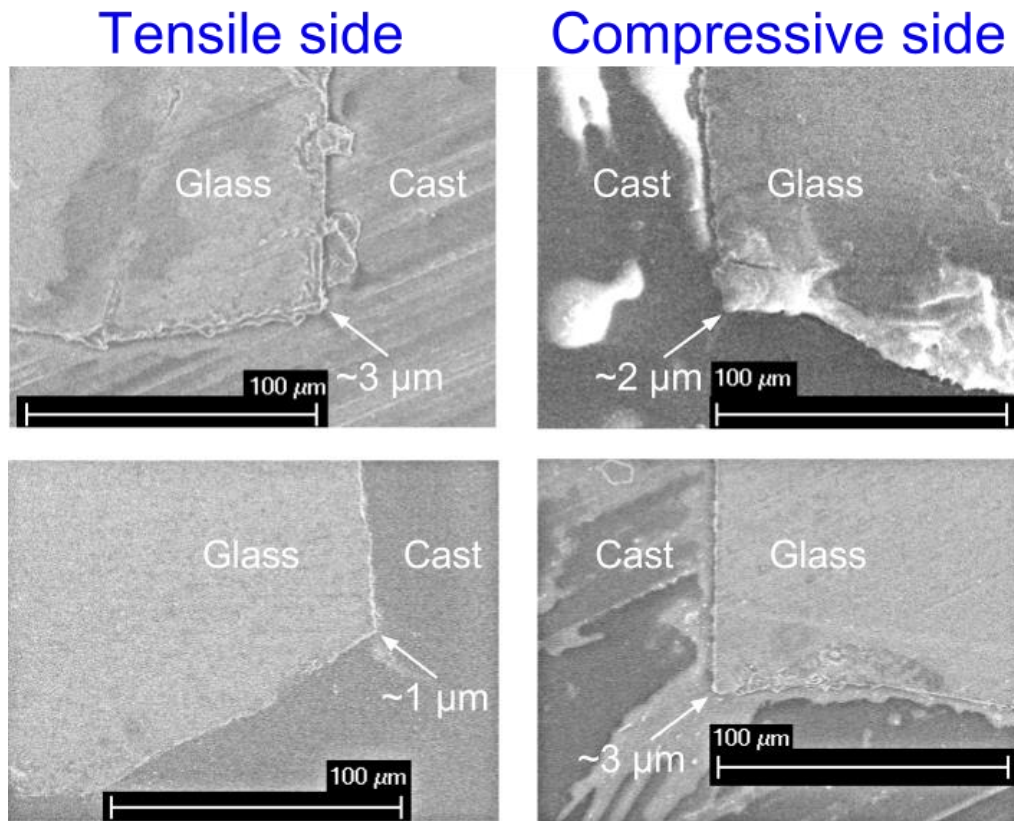


Figure 7.6 – SEM micrographs showing tensile and compressive side tip radii measurements.

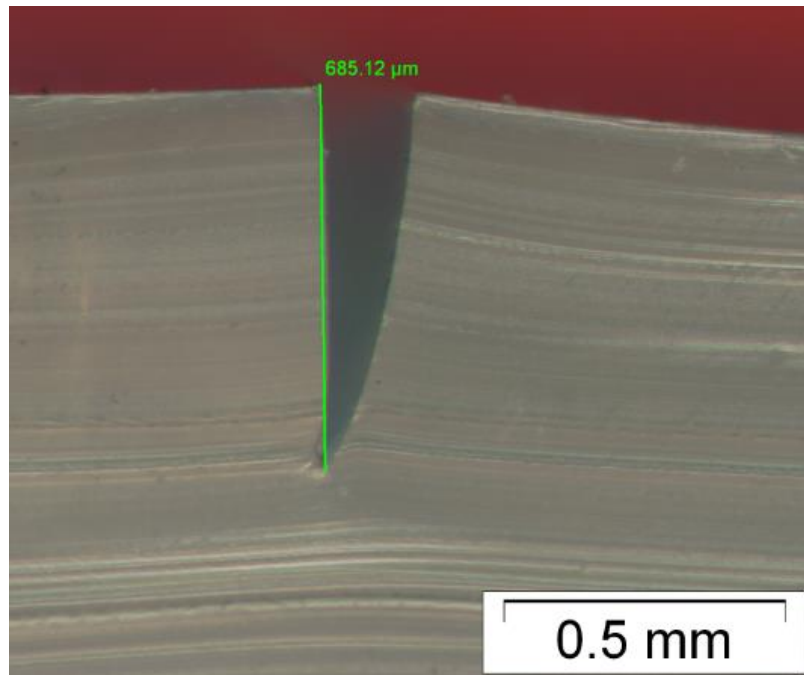


Figure 7.7 – Example cut profile cross section from an annealed fragment slash test.

Although  $\sim 1.4$  times the stress was required to fracture the 0.5 kgf indented samples compared to the 1 kgf indented samples, these results suggest that this does not result in a significant change in sharpness properties or cutting performance.

This sub-section has presented and discussed the main results from this sharpness investigation. The following sub-section overviews the main conclusions from this work.

### **7.2.5 Conclusions**

Section 7.2 has presented and discussed the results of pre-sharpness assessments, fracture pattern observations, and the results of  $\gamma$ -axis sharpness assessments of annealed glass fragments broken by 3-point bending. The aim of the investigation was to determine how the sharpness properties of annealed glass fragments are affected by the magnitude of the applied load at the time of fracture.

The main conclusions of this investigation are as follows:

- The indentation technique for controlling the fracture load was successful in producing two sample sets with a difference of  $\sim 25$  MPa failure stress. However, no statistically significant differences were found between these two data sets for edge geometrical features or cutting performance.
- Cantilever curl effects were observed on the cross sections of both sample sets, with the cross section profile curving near to the compressive side of the samples. This resulted in greater variation of the included angle at the compressive side than at the tensile side.
- On the small number of sample edge radii viewed by scanning electron microscopy, the tip radii were measured to be between 1 and 3  $\mu\text{m}$ .
- All tensile  $\gamma$ -axis edges subjected to slash tests made straight, non-ragged cuts, and the cut was propagated with a friction coefficient of  $\sim 0.48$ .

Recommendations for how the investigation could be improved or extended are given below:

- By indenting samples with greater loads, the sharpness properties of samples broken at lower bending loads could be assessed. This would give a broader range of failure loads and potentially make any trends between failure load and sharpness properties more apparent.
- A greater number of samples would be necessary to determine typical edge radii of annealed glass fragments.

- Testing the slash test performance of compressive y-axis edges would enable comparisons to be drawn with the equivalent performance of tensile y-axis edges.
- Testing the slash test performance of fragments at different orientations would more fully characterise the slash performance, since in actual cutting scenarios the angle of approach is likely to be more complex than that tested here.

The overall results are compared to the equivalent results for tempered rectangular samples in the following section.

### **7.3 Sharpness as affected by temper magnitude**

#### **7.3.1 Introduction**

This section details an investigation into how the magnitude of thermal temper affects the geometrical properties of glass fragments pertinent to sharpness. Specifically, it aims to assess whether an increase in the magnitude of temper results in an increase in the bluntness of fragments.

The investigation focuses on tempered samples broken by a significant applied bending load, as opposed to spontaneous propagation induced by a punch test (or equivalent). As such, it is applicable to fragments in close proximity to the fracture origin or loading area in bending scenarios. Additionally, some fragments from punched samples are analysed.

As with section 7.2, rectangular samples were tested. These samples were tempered using the equipment detailed in section 3.3.1.2. All samples were cooled by air at room temperature with one of three different cooling rates (see Appendix A). These had initial air velocities of: 28, 34, or 36 ms<sup>-1</sup>; corresponding to a 'low', 'medium', or 'high' temper level, respectively. The initial glass temperature in all cases was 680 °C.

The central loading line in the 3PB configuration corresponded to the line of impingement of the flat fan jets (see Appendix A), and therefore corresponded to the line of maximal consistent heat transfer during cooling. All samples were indented at the same location along this line and under the same conditions after tempering and prior to fracture. This was done to attempt to normalise the failure stress so that the residual stress could be treated as an independent variable (separate from the effects of applied bending load) when considering sharpness.

Unlike the investigation detailed in section 7.2, the high frequency of crack branching due to residual stress facilitated sharpness assessment of both x-axis edges and y-axis edges (as

defined in chapter 6). However, the small fragment sizes meant that they were not eligible for cutting performance assessments (penetration and slash testing).

The following sub-section overviews the results from the pre-sharpness assessment analysis. This is followed by the sharpness assessment results for the fragment surfaces, x-axis edges, and y-axis edges.

### 7.3.2 Pre-sharpness assessment analysis and sample fracture

#### 7.3.2.1 Overview

A summary of the pre-sharpness analysis stage of this investigation is given in Table 7.5. The procedure was for the most part similar to that of section 7.2.2.

Glass samples:	18 x flat rectangular (25 x 38 x 3.82 mm)
Tempering/ annealing processes:	Low, mid, and high cooling rate using flat fan nozzles (see Appendix A), from an initial temperature of 680 °C
Residual stress assessment:	SCALP, plane polariscope, and punch test
Surface pre-damaging:	1 kgf Vickers indentation as per sub-section 3.5.1 for rectangular samples
Fracture method:	Three point bending (3PB) as per sub-section 3.6.1.2

**Table 7.5 – Pre-sharpness assessment summary table for investigation of sharpness with temper magnitude.**

Each cooling rate was designated 6 samples, totalling 18 samples. Of these, 5 were subjected to 3PB loading, and 1 to a punch test. The residual stress state was characterised both quantitatively and qualitatively by: conducting SCALP measurement, observing photoelastic patterns, and conducting punch tests. An indentation load of 1 kgf was chosen for all samples, since this resulted in the lowest variation of 2c out of the loads conducted for the previous section.

#### 7.3.2.2 Residual stress assessment

Once tempered, all rectangular glass samples were first viewed in a plane polariscope equipped with a tint plate. This gave a qualitative indication of the lateral spread of temper stresses, rather than an indication of the magnitude of through-thickness stress. Samples were photographed at orientations of 0°, 22.5°, 45°, and 67.5° with respect to the polariser axis in order to characterise the nature of the isoclinic fringes. It was found that the overall photoelastic pattern remained relatively unchanged with temper level.

An example of this pattern for a sample with a mid-temper is shown in Figure 7.8. An approximately 16 mm central square area remained fairly uniform in colour over a full 90°

rotation. This indicates a uniform lateral temper level in this region. The bordering area is highly affected by its close proximity to the sample edges, and therefore shows more fringes. The change in fringe shape with orientation is due to isoclinics, which implies that the orientation of the principal stresses shifts around the sample periphery.

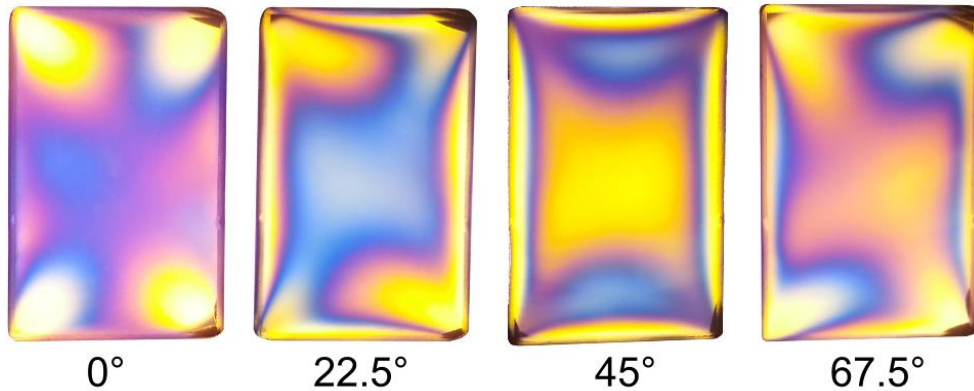


**Figure 7.8 – Photoelastic patterns observed of a mid-tempered sample for different orientations relative to the polariser in a plane polariscope setup with a tint plate \*\*.**

Measurements of through-thickness stresses in the centre region were then conducted using a SCALP for 15 tempered samples (5 per cooling rate). The results are summarised in Table 7.6.

	Low cooling rate	Medium cooling rate	High cooling rate
Surface compression (MPa)	86 ± 5 (2.8)	96 ± 6 (2.3)	108 ± 5.97 (2.6)
Central tension (MPa)	31.3 ± 4.6 (1.4)	37.6 ± 5.0 (1.2)	44.1 ± 4.0 (0.8)
SC/CT	2.75	2.55	2.44

**Table 7.6 – SCALP measurement data for tempered rectangular samples. Values shown are the mean ± the standard deviation. Values in parentheses indicate the mean standard deviation per individual sample (5 measurements were conducted per sample). SC/CT is the ratio of surface compression to central tension.**

The surface compressive stress for each temper level was above the level which constitutes fully toughened glass (69 MPa [2]). The central tensile stress values of 31, 38, and 44 MPa almost cover the span of critical tensile stress thresholds for fragmentation density outlined by Gardon for 6 mm thick glass [3] (<34 MPa: no dicing; 34 -47 MPa: transition; >47 MPa: fine dicing).

The ratio of surface compression to central tension (SC/CT) is higher than that typically expected for tempered glass (~2.2 [3]). SC/CT is known to be dependent on the variation of the glass cooling rate during tempering. Specifically, a well-timed change from a higher cooling

\*\* The pattern observed at 45° is similar to that observed by Brewster for jelly parallelepipeds held in tension during setting [8] (his Fig. 24).

rate to a lower cooling rate can increase the value of SC/CT. This would explain the SC/CT values presented in Table 7.6, given the measured decrease of the air velocity with time (see Appendix A).

One sample of each temper level was subjected to a punch test. The punch was conducted as per section 3.6.1.1. Photographs of these samples after the punch test was conducted are shown in Figure 7.9. Fragment counts corresponded to the increase in temper level, with actual fragment counts for low, medium, and high tempers of 7, 11, and 24, respectively. This is different to the observed fragment count (parentheses, Figure 7.9), as some fractures had not propagated fully through the sample thickness. Some x-axis profiles of these punched samples are assessed in sub-section 7.3.4.1.

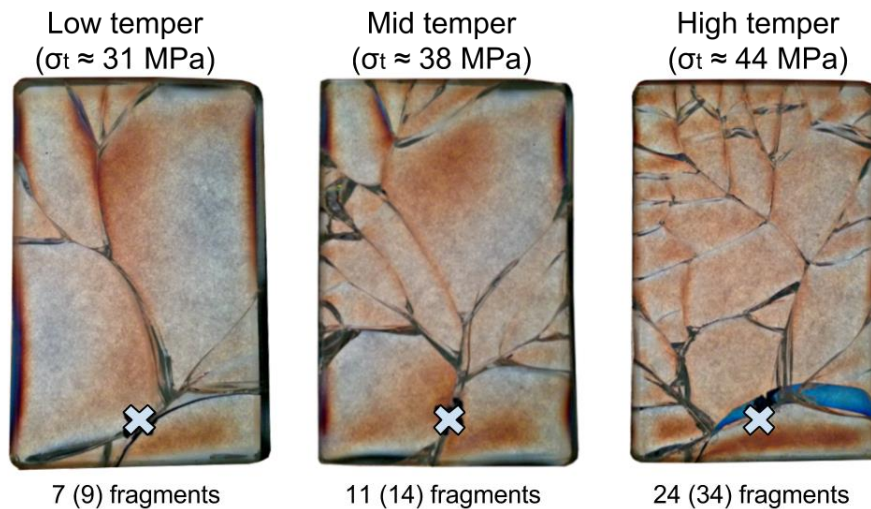


**Figure 7.9 – Fracture patterns of punched tempered rectangular samples held together by transparent adhesive tape. Central tensile stress, and actual and observed fragment count for each temper level is given. Punch locations are indicated by crosses. Pictures taken in a plane polariscope - with darker orange areas giving an indication of residual stress unreleased during the fracture event.**

### 7.3.2.3 Flaw morphology and mechanical data

The indentation data, flaw size (2c) data, and strength data from 3PB loading for tempered rectangular samples are tabulated in Table 7.7.

Mean surface compression /MPa	Vickers hardness /GPa	Flaw size (2c) / $\mu\text{m}$	% full MR crack developed	Failure stress in 3PB /MPa	Mirror tensile failure stress /MPa
86.1	$5.5 \pm 0.2$	$105 \pm 8$	100	$122.5 \pm 14.7$	$58.7 \pm 6.2$
96.0	$5.2 \pm 0.4$	$117 \pm 15$	100	$121.7 \pm 8.3$	$55.9 \pm 3.5$
107.6	$5.7 \pm 0.4$	$105 \pm 7.4$	100	$129.7 \pm 11.9$	$57.4 \pm 3.7$

**Table 7.7 – Indentation data and strength data rectangular glass samples. Values shown are the mean  $\pm$  the standard deviation.**

The morphology of all 15 imparted Vickers indent flaws is shown in Figure 7.10. As with section 7.2, the indent orientation is shown in the top-right inset in the figure, and only the MR crack length parallel to the central loading line was considered for values of  $2c$ .

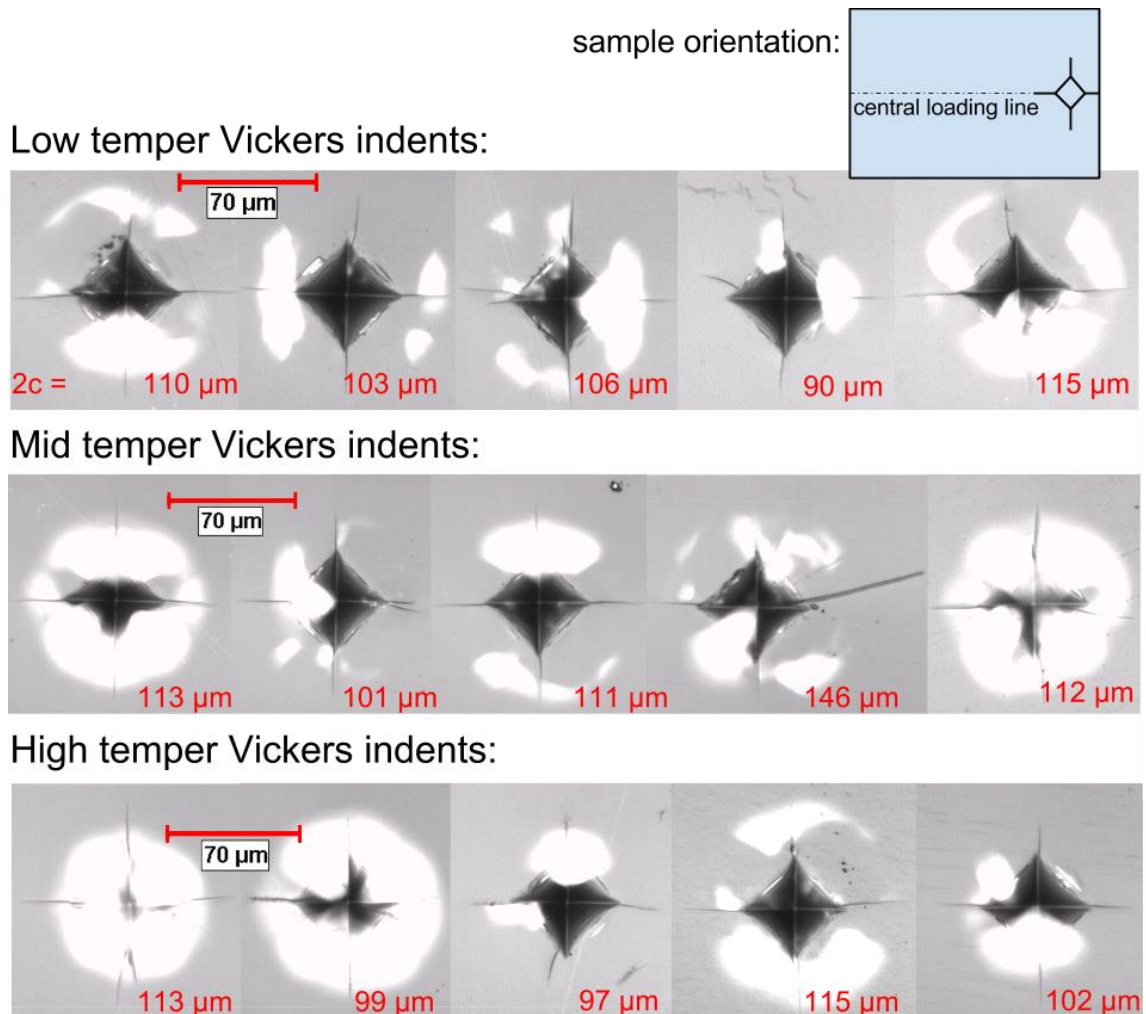


**Figure 7.10 – Micrographs of all 15 Vickers indentation flaws imparted onto rectangular samples for investigation 7.3. The flaw size ( $2c$ ) for each indent is shown in red. Top right inset illustrates the orientation of all micrographs relative to the sample dimensions. Order of indents correlates to fractures in Figure 7.11. All micrographs were taken a minimum of 30 minutes after indentation.**

The value of  $2c$  for all tempered samples was similar:  $\sim 109 \mu\text{m}$  on average with a standard deviation of  $\sim 12 \mu\text{m}$ . This is significantly less than that for annealed samples with the same indent load ( $\sim 175 \mu\text{m}$ ). This is to be expected as the tensile stresses that act to propagate the MR cracks must work against the surface compressive stress. Larger sample sets would be necessary to establish relationships between  $2c$  and the thermal temper levels used here.

As with the initiating crack size, the failure stress was similar for all tempered samples:  $\sim 125 \text{ MPa}$  on average with a standard deviation of  $\sim 12 \text{ MPa}$ . Although the high temper samples did show an overall average increase in failure stress, the magnitude of the increase from mid

temper samples ( $\sim 8$  MPa) was less than the standard deviation observed for the high temper sample set ( $\sim 12$  MPa).

The overall average tensile failure stress as determined by the mirror size was  $\sim 57$  MPa (standard deviation =  $\sim 5$  MPa). This value is not indicative of the actual tensile stress imposed due to loading since it only indicates the net tensile stress local to the origin [6] (i.e. the loading stress + the surface compressive stress). By subtracting this value from the average tensile failure stress as determined by equation 3.3, an estimate of the average surface compressive stress near the critical flaw of  $\sim 67$  MPa can be attained. This is less than the surface compression values obtained by SCALP measurement, which is likely to be due to the effect of local tensile stresses imposed during indentation. The mirror sizes were similar to those obtained from annealed glass with the same indent load ( $\sim 57$  MPa), despite the values of  $2c$  being much smaller. This indicates that there may have been some degree of stable crack growth of the MR cracks prior to full fracture.

#### **7.3.2.4 Macroscopic fracture patterns and fracture surface analysis**

The macroscopic fracture patterns of all tempered rectangular samples are shown in Figure 7.11. The 3PB failure stresses are shown beneath each sample for convenience, and are summarised in the previous sub-section. All fractures initiated from the imparted Vickers flaw.

All samples showed considerable branching, and a slight increase in fragmentation density can be observed from the low temper fractures to the high temper fractures. As with the annealed samples, cracks branching from the central loading line curved laterally towards the longer sample edges. The fragments containing the fracture origin were distinctively shaped, and were usually the largest fragments in each sample.

After fracture, each sample folded in half along the central loading line but remained attached by adhesive tape applied to the compressive side prior to loading. This facilitated further analysis stages as the sample presented itself for fracture surface examination along this centre line. Examples of typical observed fracture surface features observed on tempered rectangular samples are shown in Figure 7.12.

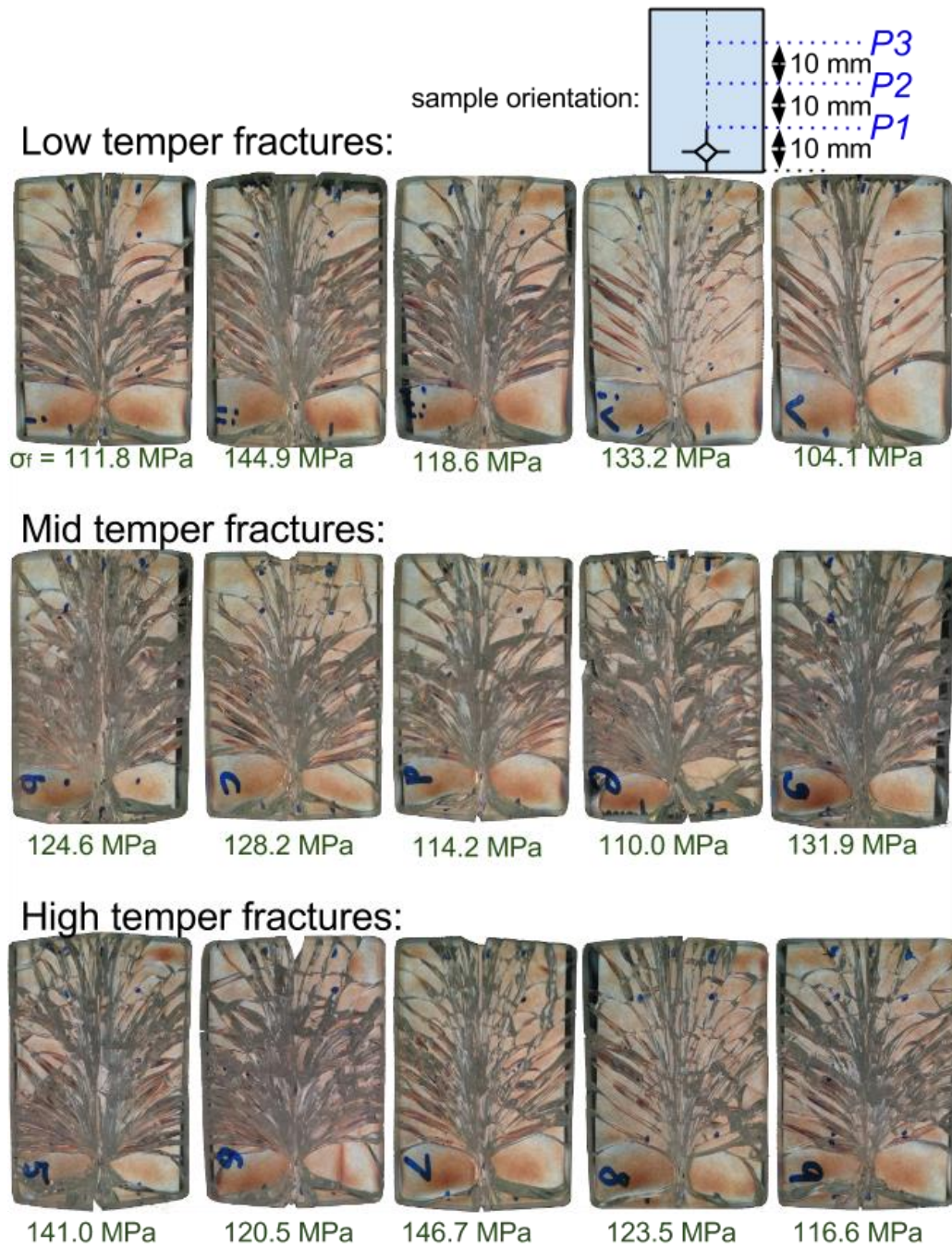


**Figure 7.11 – Fracture patterns for all tempered rectangular samples broken by 3PB, with individual failure stresses shown. The top right inset indicates the orientation of the samples relative to the Vickers flaw location. All fractures originated from the Vickers flaw. Order correlates to indent micrographs in Figure 7.10. Pictures taken in a plane polariscope - with darker orange areas giving an indication of residual stress unreleased during the fracture event. P1, P2, and P3 on the inset correspond to sampling locations used during sharpness assessment.**

The fracture surfaces for all samples appeared similar regardless of thermal temper level. Unlike the annealed rectangular fragments detailed in the previous section, the origin mirror was closed and semi-circular as a result of the higher tensile failure stress. After initiating on the tensile surface at the imparted Vickers flaw, the crack front appeared to tend towards the

mid-plane as it propagated away from the origin. This is similar to the tempered pint glasses detailed in section 4.3.3.

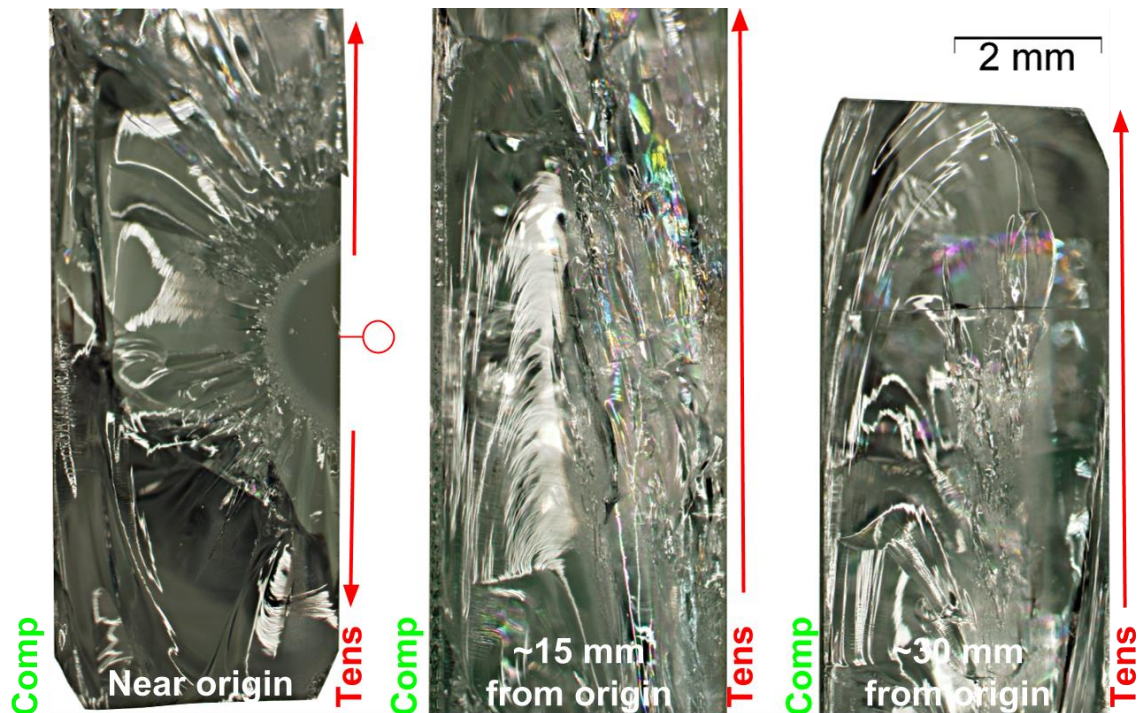


Figure 7.12 – Three example fracture surfaces of tempered rectangular fragments broken by 3PB with tensile and compressive sides labelled, at various propagation lengths. Red circle denotes Vickers origin flaw location.

This section has summarised the pre- and post-breakage analysis processes conducted prior to sharpness assessment of tempered flat rectangular glass samples. The results were used as a foundation for the sharpness analysis study that follows.

**7.3.3 Sharpness assessment: overview**

A summary of the sharpness assessment tests and analyses conducted on fragments from flat thermally tempered rectangular glass samples is given in Table 7.8 below.

<p>x-axis edges</p>	Optical profile analysis	3 per 3PB sample if available (38) + fragments from punch tests (21)
	SEM analysis (tip radii)	Selected fragments
	Penetration testing	None
<p>y-axis edges</p>	Micro-CT cross-sections (included angles)	All 3PB samples (15)
	Replica sections (edge radii)	All 3PB samples (15)
	Slash test	None

Table 7.8 – Sharpness analysis summary table for investigation of sharpness with loading magnitude.

**X-axis edges:** The majority of the x-axis sharpness assessment was conducted optically, as opposed to by penetration tests. This was because the majority of the fragments were shorter than the minimum permissible fragment length (10 mm – see chapter 6) when aligned for resin-mounting. Only out-out edges were assessed in this analysis because they were observed to have the smallest included angles from macroscopic fracture analysis, and may therefore pose the greatest injury potential.

Firstly, the tempered rectangular samples broken by a punch test (see Figure 7.9) were assessed. All available out-out edges (21) were viewed optically and their fracture surface profiles were digitised by the methodology outlined in section 6.4.3. This was conducted in order to assess the morphology of the x-axis profiles created in the absence of high external loads.

Secondly, three fragments were taken for testing from each sample fractured by 3PB at the three sampling locations outlined in the inset of Figure 7.11 (P1, P2, P3). The fragment with the nearest out-out x-axis edge to each sampling location was taken. No fragment was taken if there was no out-out x-axis edge available within a 5 mm radius of the sampling location.

Additionally, a small number of x-axis profiles of interest were viewed using a scanning electron microscope.

**Y-axis edges:** As with penetration testing, slash tests were not viable due to the majority of fragments having edges shorter than the minimum permissible length of 10 mm. Therefore only cross section analysis via micro-CT scans was conducted, alongside SEM analysis of mounted tip radii.

The included angles of the fragment edges were measured from micro-CT scan images at three cross-sectional locations in the same manner as described in section 7.2.3 at locations P1, P2 and P3 (see Figure 7.11). This was conducted on one of the two sample halves that were restrained using adhesive tape. Replica casts were made of fragments after they were subjected to micro-CT scans as discussed in section 7.2.3.

#### **7.3.4 Sharpness assessment: x-axis edges**

This sub-section discusses the results of sharpness assessments of x-axis edges conducted for tempered rectangular samples.

### 7.3.4.1 x-axis profile morphology: fragments from punch tests

Figure 7.13 shows plots of the overall average x-axis profile morphology for out-out edges of punch test fragments. Additionally, average plots from low, mid, and high temper profiles are shown. The average profile shapes did not appear to change with temper level and appeared to be relatively flat. However, further examination revealed three characteristic protrusion regions: two near the free surface sides and one at the profile centre. These protrusion regions are more clearly visible with an exaggerated protrusion axis as shown in Figure 7.14a, and were more pronounced on some x-axis edges than others. Two examples of actual profiles are shown in Figure 7.14.

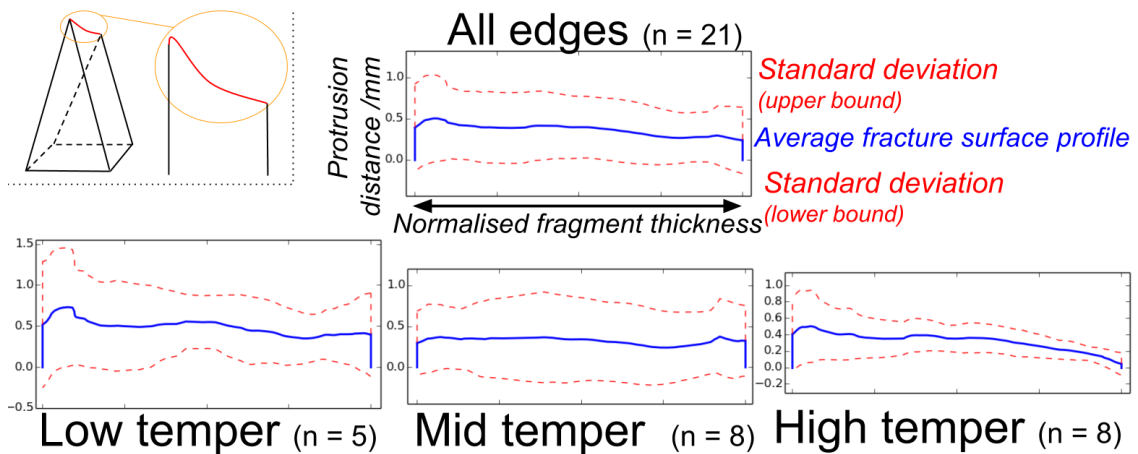


Figure 7.13 – Average x-axis profile morphology of out-out edges from the tempered rectangular samples shown in Figure 7.9. Vertical axes are in units of mm. Average profiles are plotted with a solid blue line. Upper and lower standard deviation profile bounds are plotted with dashed red lines. Inset shows x-axis profile context. The scale of the figures shows the thickness normalised to 4 mm.

The exaggerated average profile shape is similar to the shape of the propagating crack front in thermally tempered glass shown in high-speed video images taken by Nielsen [7]. These showed the crack front leading centrally, followed by the sides, with the regions in between lagging behind. This may suggest a strong dependence of the out-out profile shape on the crack front shape.

It was found from the DOE study detailed in section 6.6 that flat horizontal x-axis edges ('wedge' fragments) required greater force to penetrate a skin simulant than for fragments with sloped x-axis edges. Furthermore, the average free surface included angle for punch test fragments was  $\sim 65^\circ$ , which was greater than the included angles tested in section 6.6. Although the tip radii of these fragments were not measured, the observed free surface included angles and fracture surface profile shapes may contribute to a large penetration force.

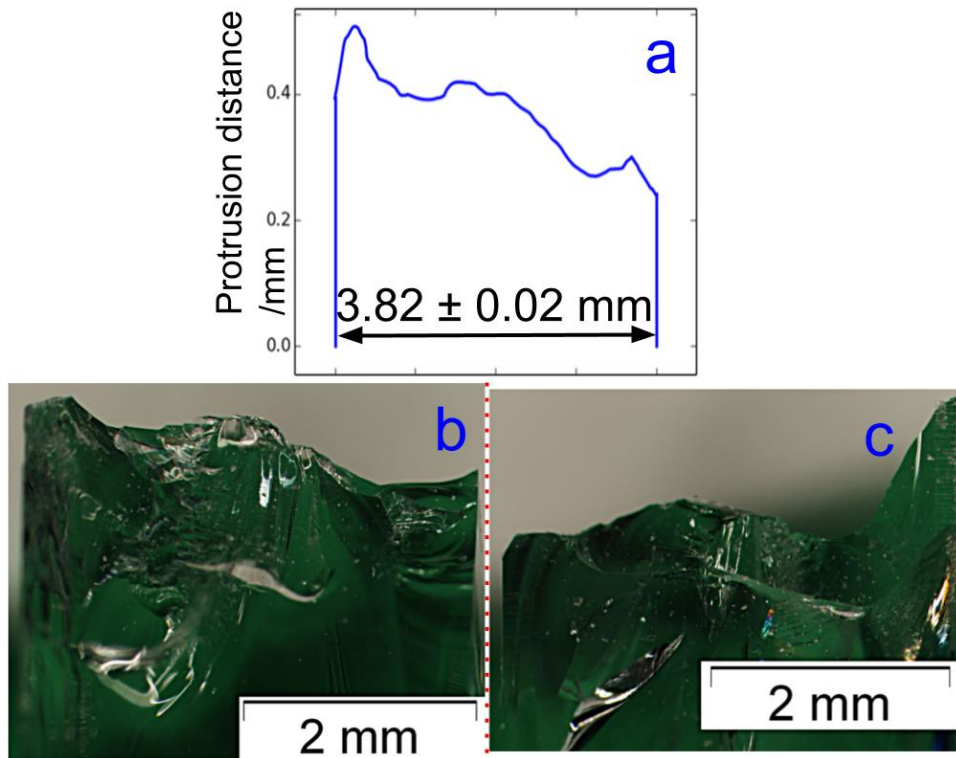


Figure 7.14 – a: overall average edge profile morphology ( $n = 21$ ) with exaggerated protrusion scale to emphasise profile trend. b: optical micrograph of an out-out edge from a mid-temper punched sample. c: optical micrograph of an out-out edge from a low-temper punched sample.

The average edge profile shapes from punched samples are compared to those broken by 3PB in the following sub-section.

#### 7.3.4.2 *x-axis profile morphology: fragments from 3PB loading*

A summary of measured geometrical parameters for x-axis edges of tempered rectangular samples broken by 3PB is shown in Table 7.9. The results in the table are categorised according to temper level and sampling position as well as showing the overall combined average values.

An overall large variation of parameter measurements was observed. The highest level of variation was encountered with tip radii measurements, which ranged from  $\sim 2 \mu\text{m}$  to  $\sim 3.4$  mm. This is likely to be due to the fragility of the tips, which are particularly prone to damage during the fracture event and during sampling of fragments. Additionally, tip radii measurements were conducted manually, and so the results may have been affected by any subjectivity involved with fitting a radius of curvature to the edge profile (this is discussed in chapter 6).

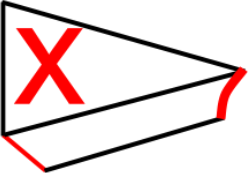
Student's *t*-tests were conducted to determine whether there were any significant differences in parameter values due to the temper level or the sampling location. The full results of the *t*-tests are given in Appendix L. No significant differences were found between the recorded free

surface profile parameters, or between the three sampling locations investigated. However, two instances of significant differences between mid and high temper fracture surface profile sample parameters were observed which is discussed after a consideration of the average fracture surface profile shapes.

Plots of the average x-axis profiles for each tempering level and sampling location are shown in Figure 7.15. The typical shape of each plot is similar, curving towards the compressive side in a cantilever curl fashion (see section 2.5.4). It is clear that the stresses due to external loading had a significant effect on the fracture surface profiles when compared to Figure 7.13. It is difficult to identify whether the characteristic protrusion regions identified in the previous subsection are present in some form on these profiles, due to the added influence of external stresses. Since the cantilever curl direction tends towards the overall direction of primary crack propagation, the most protruding portion of the fracture surface profile appears relatively flat. It would be expected that the corresponding edges of adjacent fragments would have a well-defined fracture surface protrusion point with a small included angle at the compressive side. However, since the corresponding edge would be an in-out edge, the free surface included angle may be expected to be greater and therefore pose less potential for injury.

Fragments from mid-temper rectangular samples were observed to have significantly greater average fracture surface protrusion lengths than high-temper samples. This is reflected in the average profile shapes shown in Figure 7.15, where the mid-temper profile is noticeably longer than the high temper profile. The average protrusion length was defined using the lower terminal point of the fracture surface profile, and was therefore very sensitive to the magnitude of cantilever curl of the fracture surfaces. This suggests that the effect of cantilever curl is lessened by the higher residual stress levels in the high-temper samples.

The shape of the average fracture surface profiles was similar to the rounded fracture surface profile investigated in the exploratory study into geometrical effects on penetration force (section 6.6). This permitted the use of the regression equation 6.2 in order to provide an estimate for the expected penetration force of these fragments, using the free surface tip radius and far included angle, with a thickness of 3.82 mm. These estimated values are listed in Table 7.9. The average calculated penetration force was 40 N with a standard deviation of 17 N. However, since the fragments were too small for penetration tests, they may also be too small to grip for use as a stabbing weapon, and would be unlikely to cause fatal injury.

	Low temper (n = 14)	Mid temper (n = 11)	High temper (n = 13)	Loc. P1 (n = 15)	Loc. P2 (n = 14)	Loc. P3 (n = 9)	All (n = 38)
<b>Fracture surface profile parameters</b>							
Tip radius / $\mu\text{m}$ (manual)	255 $\pm$ 343 (135)	366 $\pm$ 952 (260)	72 $\pm$ 136 (189)	68 $\pm$ 66 (97)	207 $\pm$ 323 (156)	512 $\pm$ 1041 (203)	224 $\pm$ 571 (255)
Near included angle / $^\circ$ (manual)	99.1 $\pm$ 46.3 (47)	86.4 $\pm$ 43.5 (50)	82.0 $\pm$ 37.6 (46)	94.5 $\pm$ 40.8 (43)	87.4 $\pm$ 44.6 (51)	84.7 $\pm$ 44.4 (52)	89.6 $\pm$ 43.3 (48)
Thickness 1mm from piercing point /mm	2.8 $\pm$ 1.0 (36)	2.5 $\pm$ 0.8 (32)	2.9 $\pm$ 0.9 (31)	2.7 $\pm$ 0.8 (30)	2.8 $\pm$ 0.9 (32)	2.8 $\pm$ 1.2 (43)	2.8 $\pm$ 0.9 (32)
Protrusion length /mm	2.6 $\pm$ 1.8 (69)	3.1 $\pm$ 1.4 (45)	2.0 $\pm$ 1.1 (55)	2.4 $\pm$ 1.0 (42)	2.6 $\pm$ 1.7 (65)	2.6 $\pm$ 1.9 (73)	2.6 $\pm$ 1.5 (58)
Average protrusion length /mm	1.7 $\pm$ 1.2 (71)	2.2 $\pm$ 1.1 (50)	1.3 $\pm$ 0.7 (54)	1.6 $\pm$ 0.8 (50)	1.8 $\pm$ 1.2 (67)	1.7 $\pm$ 1.2 (71)	1.7 $\pm$ 1.1 (65)
Lateral distance to comp. edge /mm	2.7 $\pm$ 1.3 (48)	2.9 $\pm$ 0.8 (28)	2.9 $\pm$ 1.1 (38)	3.0 $\pm$ 1.0 (33)	2.8 $\pm$ 1.1 (39)	2.5 $\pm$ 1.3 (52)	2.8 $\pm$ 1.1 (39)
Root mean square roughness, Rq /mm	0.67 $\pm$ 0.46 (69)	0.86 $\pm$ 0.45 (52)	0.46 $\pm$ 0.25 (54)	0.64 $\pm$ 0.40 (63)	0.72 $\pm$ 0.46 (64)	0.57 $\pm$ 0.39 (68)	0.65 $\pm$ 0.42 (65)
<b>Free surface profile parameters</b>							
Tip radius / $\mu\text{m}$ (manual)	60 $\pm$ 94 (157)	239 $\pm$ 636 (266)	267 $\pm$ 637 (239)	33 $\pm$ 39 (118)	189 $\pm$ 572 (303)	425 $\pm$ 724 (170)	183 $\pm$ 518 (283)
Near included angle / $^\circ$ (manual)	57.8 $\pm$ 30.8 (53)	54.4 $\pm$ 37.1 (68)	62.1 $\pm$ 27.4 (44)	62.7 $\pm$ 29.6 (47)	52.1 $\pm$ 28.2 (54)	60.5 $\pm$ 38.4 (63)	58.3 $\pm$ 31.8 (55)
Far included angle / $^\circ$	47.0 $\pm$ 29.6 (63)	41.7 $\pm$ 26.1 (63)	34.7 $\pm$ 16.2 (47)	43.1 $\pm$ 17.2 (40)	45.7 $\pm$ 31.0 (68)	31.3 $\pm$ 23.8 (76)	41.3 $\pm$ 25.2 (61)
Thickness 1mm from piercing point /mm	1.2 $\pm$ 0.5 (42)	1.4 $\pm$ 0.6 (43)	1.3 $\pm$ 0.6 (46)	1.1 $\pm$ 0.3 (27)	1.5 $\pm$ 0.7 (47)	1.4 $\pm$ 0.8 (57)	1.3 $\pm$ 0.6 (46)
Root mean square roughness, Rq /mm	0.18 $\pm$ 0.11 (61)	0.19 $\pm$ 0.09 (47)	0.18 $\pm$ 0.11 (61)	0.15 $\pm$ 0.07 (47)	0.19 $\pm$ 0.09 (47)	0.23 $\pm$ 0.14 (61)	0.18 $\pm$ 0.11 (61)
Estimated penetration force /N (calculated with eq. 6.2)	41 $\pm$ 19 (46)	42 $\pm$ 18 (43)	38 $\pm$ 14 (37)	38 $\pm$ 12 (31)	43 $\pm$ 21 (49)	39 $\pm$ 18 (46)	40 $\pm$ 17 (44)

**Table 7.9 – Summary of parameter data collected for out-out x-axis profiles of tempered rectangular sample fragments. In each case the average value is shown  $\pm$  the standard deviation. The percentage of the standard deviation compared to the average value is shown in parentheses. All parameters listed in this table are described and illustrated in section 6.4 in the previous chapter.**

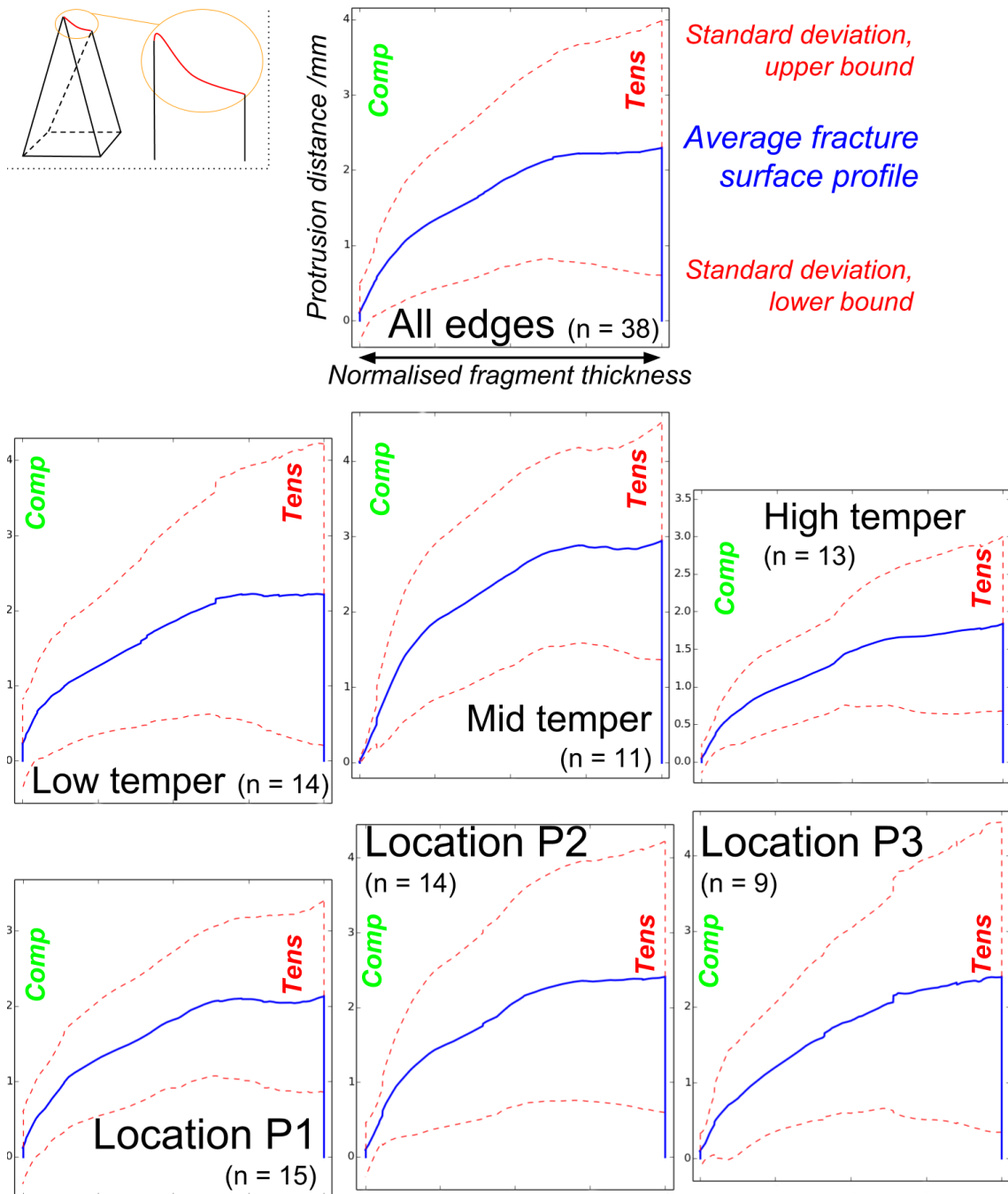


Figure 7.15 – Average x-axis profile morphology of out-out edges from the tempered rectangular samples shown in Figure 7.11. Vertical axes are in units of mm. Average profiles are plotted with a solid blue line. Upper and lower standard deviation profile bounds are plotted with dashed red lines. Inset shows x-axis profile context.

#### 7.3.4.3 SEM analysis of selected x-axis profile tip radii

The tips of a small number of fragments were viewed by scanning electron microscopy in addition to being viewed optically, as in the previous sub-section. This was done in order to form a comparison with tip radii viewed at a lower magnification and to assess the tip morphology at a higher magnification. As discussed in section 6.4, optical microscopy was

chosen for the measurement of parameters for the majority of testing because scanning electron microscopy of all glass fragments was not feasible.

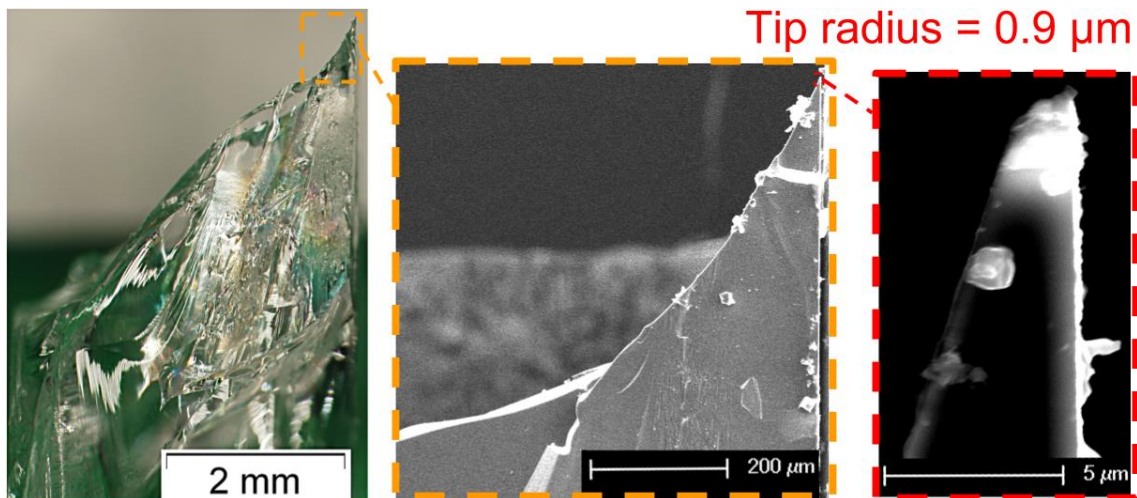


Figure 7.16 – Optical and scanning electron micrographs of a tip of a fracture surface profile of high temper rectangular sample. Optically measured tip radius was 1.75  $\mu\text{m}$ .



Figure 7.17 – Optical and scanning electron micrographs of a tip of a free surface profile of a low temper rectangular sample. Optically measured tip radius was 6.1  $\mu\text{m}$ .

Micrographs of an example fracture surface side fragment tip and an example free surface side fragment tip are shown in Figure 7.16 and Figure 7.17, respectively. In both cases the optically measured tip radius was greater than the tip radius measured from SEM images: 1.75  $\mu\text{m}$  compared to 0.9  $\mu\text{m}$  for the fracture surface profile; and 6.1  $\mu\text{m}$  compared to 4.5  $\mu\text{m}$  or 0.76

$\mu\text{m}$  for the free surface profile, depending on the portion of the tip chosen for measurement as indicated in the figure.

Some difference between tip radii and tip morphology at different magnification levels is to be expected, since further magnification enables a finer level of profile roughness to be distinguished. However, finer measured features may be practically insignificant in a cutting operation. It was not possible to say whether the optically measured tip radii or the tip radii measured from scanning electron micrographs give the best indication of cutting ability without further practical testing to determine at what scale features are most determinate of performance.

This sub-section has detailed the results gathered from sharpness assessments of x-axis profiles of fragments obtained by 3PB loading. The y-axis sharpness assessments conducted on fragments from the same samples are detailed in the following sub-section. The main conclusions from this investigation are summarised in section 7.4.

### **7.3.5 Sharpness assessment: y-axis edges**

This sub-section presents and discusses the results of sharpness assessments of y-axis edges conducted for tempered rectangular samples. All cross section measurements and y-axis edge tip radii measurements taken for this investigation are shown in Table 7.10. Student's *t*-tests were conducted to determine whether there were any significant differences between all included angle measurements, and between measurements for different temper levels. Full *t*-test results are given in Appendix L.

Near compressive side angles were found to be significantly greater than far compressive side angles. Specifically, near compressive side angles were on average obtuse ( $\sim 105^\circ$ ) and far compressive side angles were on average acute ( $\sim 79^\circ$ ). This indicates a change in gradient sign of the profile near to the compressive side edge. This is reflected in the average cross section profile plots given in Figure 7.18. These plots generally show a greater standard deviation near the compressive side, which is likely to be a cantilever curl effect. This same cantilever curl effect is shown by the example actual micro-CT cross sections shown in Figure 7.19.

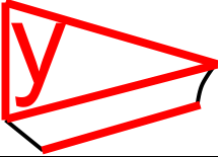
	Low temper	Mid temper	High temper	All
<b>Micro-CT cross sections</b>				
Near (1% into thickness) tensile side included angle /°	94.4 ± 7.8 (8)	96.8 ± 13.8 (14)	106.4 ± 22.0 (21)	99.2 ± 16.5 (17)
Far (10% into thickness) tensile side included angle /°	91.1 ± 13.9 (15)	90.2 ± 10.1 (11)	93.2 ± 14.8 (16)	91.5 ± 13.1 (14)
Near (1%) compressive side included angle /°	100.7 ± 21.4 (21)	107.2 ± 27.1 (25)	107.9 ± 24.7 (23)	105.3 ± 24.7 (23)
Far (10%) compressive side included angle /°	72.2 ± 36.2 (50)	85.8 ± 36.0 (42)	79.8 ± 23.5 (29)	79.3 ± 32.9 (41)
<b>Replica tip radii measurements</b>				
Tensile side tip radius /μm	3-5 (n = 2)	2-10 (n = 4)	4 (n = 1)	5 ± 2
Compressive side tip radius /μm	4-9 (n = 3)	3-11 (n = 5)	7 (n = 1)	6 ± 3

Table 7.10 – Summary of parameter data collected y-axis edges of tempered rectangular sample fragments. In each case the average value is shown ± one standard deviation. The percentage of the standard deviation compared to the average value is shown in parentheses. For tip radii measurements, the number of samples tested is shown in parentheses instead. All parameters listed in this table are described and illustrated in section 6.4 in the previous chapter.

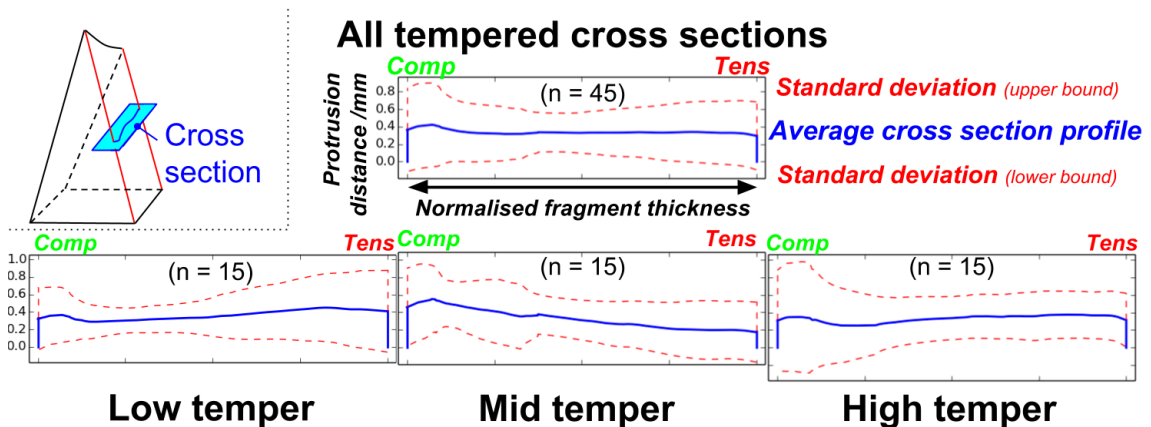
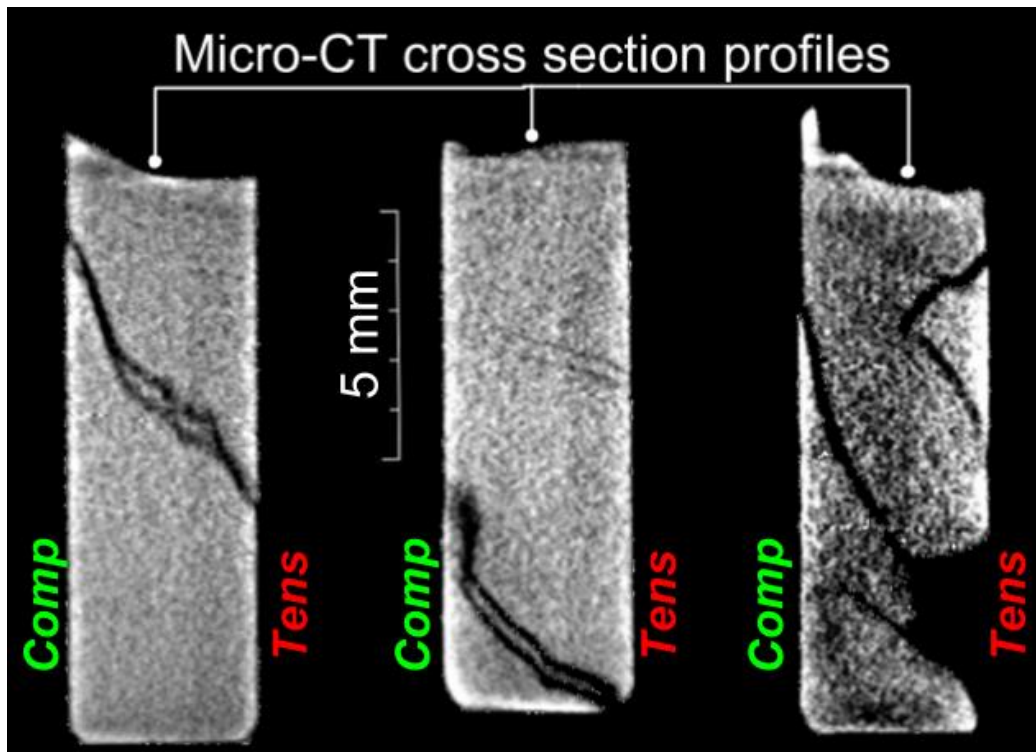


Figure 7.18 – Average cross section profile morphology of out-of edges from the tempered rectangular samples shown in Figure 7.11. Vertical axes are in units of mm. Average profiles are plotted with a solid blue line. Upper and lower standard deviation profile bounds are plotted with dashed red lines. Inset shows y-axis/cross section profile context.

No statistically significant differences were found for the included angle measurements between different temper levels, or even between all tempered and all annealed fragments. Given that the failure stresses of all tempered sample types were similar, these results suggest that the residual stress does not cause a significant change in the included angles or cross section profile shapes. However, the range of temper levels tested was narrow (surface

compressive stresses ranging from  $\sim 86$  MPa to  $\sim 108$  MPa), and so it is not possible to comment on whether higher temper levels may cause significant profile or parameter changes. Changes to the cross section profile shape may be expected for fragments further from the maximum bending load location assessed in this investigation. Fragments from spontaneously fractured tempered glass far from the location of the maximum externally applied stress are less likely to be significantly affected by cantilever curl effects.



**Figure 7.19** – Three examples of tempered rectangular fragment cross sections taken with micro-CT scanner. Cross section profiles are the top edges as labelled.

Overall tip radii measurements ranged from  $\sim 2$ - $11$   $\mu\text{m}$ . Given the small number of these measurements, it is not possible to determine whether the edges of annealed glass fragments are sharper or blunter than the edges of thermally tempered glass fragments. However, based on this small sample set, the edge radii appear to be similar. It should be noted however that this is based on the assessment of fragments close to the location of maximum externally applied stress. The majority of fragments from a fractured thermally tempered glass article are likely to have had an external stress applied to them at the time of fracture of a small fraction of the maximum externally applied stress.

This sub-section has presented and discussed the main results from this sharpness investigation. The following sub-section overviews the main conclusions from this work.

### 7.3.6 Conclusions

Section 7.3 has detailed and discussed the pre-sharpness assessment results, fracture patterns, and sharpness assessment results of thermally tempered rectangular samples broken by three point bending. The aim of this investigation was to determine whether differences in the sample residual stress magnitude affects the sharpness properties of sample fragments once broken. Additionally, it was of interest to determine whether the sharpness of annealed and tempered glass fragments was inherently different.

The main conclusions of this investigation are as follows:

- The fracture of all tempered samples was too dense to permit fragment cutting performance tests by stabbing and slashing. However, this is a reflection of the practical limits to using fragments from thermally tempered glass as a weapon, since they may be too small to hold or grip.
- Additionally, the notable difference in the fracture pattern of tempered samples and annealed samples from section 7.2 limited the scope for comparison between the two sample types. A greater number and variety of x-axis edges were present on fragments from tempered glass samples.
- There is little evidence of statistical significance to show that the change in temper level of samples affects the fragment geometrical properties pertaining to sharpness. Additionally, the equivalent measured geometrical parameters of annealed fragments from section 7.2 were not found to be significantly different. This may be because all sharpness assessments were conducted at the location of maximum bending stress.
- The x-axis fracture surface profile shapes of punched samples (low externally applied stress) showed a characteristic pattern which appeared to reflect previously reported crack front shapes for tempered glass. This pattern was not apparent on equivalent profiles from observed fragments in three point bending. These profiles curved towards the compressive edge in a cantilever curl fashion.
- Limited SEM tip radii measurements showed the tip radii of x-axis edges to be of the order of 1  $\mu\text{m}$ , and the tip radii of y-axis edges to range between  $\sim 2\text{-}11$   $\mu\text{m}$ . This is similar to the SEM tip radii measurements in section 7.2.
- Cross sections of fragments taken from micro-CT scans were similar in shape to equivalent cross sections from annealed fragments from section 7.2.

Recommendations for how the investigation could be improved or extended are given below:

- Testing of samples with a greater range of temper levels could make any change in sharpness properties due to temper level more readily apparent.
- Assessing the sharpness of fragments further from the loading location could give a more accurate reflection of the sharpness of fragments of thermally tempered glass articles. This is because in typical fracture conditions, particularly for the fragments of tempered pint glasses, the majority of fragments are created with an external stress that is a small fraction of the maximum loading stress.
- A greater number of SEM measurements would be necessary to determine any changes in the tip radii of tempered fragments due to temper level.

#### **7.4 Chapter summary**

This chapter has presented two investigations into the sharpness properties and cutting performance of fragments from annealed and thermally tempered glass samples broken by the same 3 point bending conditions. It aimed to determine whether changes in failure load magnitude and changes in the residual stress in an article affected properties pertaining to the sharpness of fragments once broken. The measurement of sharpness of glass fragments is a complicated problem, and this chapter presents one approach for doing so.

Section 7.2 presented an investigation into loading magnitude effects on sharpness using annealed glass samples. Samples were indented at different loads using a Vickers indenter in order to control the failure load. However, no statistically significant difference in sharpness properties was found between fragments broken at the different loads tested. Fragment cross sections showed evidence of a cantilever curl effect which resulted in differences in geometrical sharpness factors between the tensile and compressive sides. The fragments produced similar straight non-ragged cuts during slash tests.

Section 7.3 presented an investigation into the effect of residual stress level on sharpness using glass samples cooled at different rates. All samples were indented at the same load using a Vickers indenter in order to normalise the failure load to some extent. There was little evidence to show that the change in residual stress level significantly affected sharpness properties. Additionally, there were no statistically significant differences between the cross section profiles of annealed and tempered fragments taken at the same points relative to the fracture origin.

The following chapter continues from this chapter by further utilising the sharpness assessment techniques detailed in chapter 6.

## 7.5 Chapter references

- [1] “BS EN 12150-1:2000 - Glass in Building. Thermally Toughened Soda Lime Silicate Safety Glass. Definition and Description,” *British Standards Institute, UK*, 2000.
- [2] ASTM C1048-12e1, Standard Specification for Heat-Strengthened and Fully Tempered Flat Glass, ASTM International, West Conshohocken, PA, 2012, [www.astm.org](http://www.astm.org).
- [3] R. Gardon, “Tempering Glass with Modulated Cooling Schedules,” *Journal of the American Ceramic Society*, vol. 71, no. 10, pp. 875–878, 1988.
- [4] ASTM C1256-93(2013), Standard Practice for Interpreting Glass Fracture Surface Features, ASTM International, West Conshohocken, PA, 2013, [www.astm.org](http://www.astm.org).
- [5] T. Atkins, “Sharpness and Bluntness: Absolute or Relative?,” in *The Science and Engineering of Cutting: The Mechanics and Processes of Separating, Scratching and Puncturing Biomaterials, Metals and Non-metals*, 2009, pp. 221–243.
- [6] G. D. Quinn, “Stresses from the Mirror Size,” in *Fractography of Ceramics and Glasses*, National Institute of Standards and Technology, 2007, pp. 7–10 – 7–13.
- [7] J. H. Nielsen, J. F. Olesen, and H. Stang, “The Fracture Process of Tempered Soda-Lime-Silica Glass,” *Experimental Mechanics*, vol. 49, pp. 855–870, Dec. 2008.
- [8] D. Brewster, “On the Communication of the Structure of Doubly Refracting Crystals to Glass, Muriate of Soda, Fluor Spar, and Other Substances, by Mechanical Compression and Dilation,” *Philosophical transactions of the Royal Society of London*, vol. 106, pp. 156–178, 1816.

## **8 Glass fragment sharpness part II: Pint glasses, non-uniformly tempered glass, and highly-stressed glass**

### **8.1 Introduction**

This chapter follows the previous chapter by detailing the results from three further investigations into the sharpness of glass fragments, using the methodologies described in chapter 6. The three investigations were as detailed below.

Firstly, fragments from annealed and thermally tempered pint glasses broken by the same impact loading conditions are considered in section 8.2. This involved the use of a Vickers indentation technique to the inside surface of the glasses, as a means to provide a reproducible pre-damaging procedure.

Secondly, the effect of a non-uniform tempering process on fragment sharpness is considered in section 8.3. This was done by thermally tempering of glass disc samples by arrays of 4 single jets, which resulted in a variable level of convective heat transfer across the circular disc surfaces. The glass discs were then broken by impact.

Thirdly, fragments from annealed, thermally tempered, and chemically tempered glass samples broken by ring-on-ring tests are considered in section 8.4. The thermally and chemically tempered glass samples in this investigation were tempered by external companies. The chemically tempered glass samples were used for an assessment of the effect of very high compressive stresses at the sample surfaces on sharpness properties.

The structure of each investigation is presented in a similar way to the previous chapter. A summary of the pre-sharpness assessment is presented, which follows a similar order to the methods in chapter 3 of this thesis. This is followed by an overview of the sharpness assessment procedures conducted, and the results from these assessments.

The main conclusions of the chapter are summarised in section 8.5.

### **8.2 Sharpness of pint glass fragments**

#### **8.2.1 Introduction**

This section details an investigation into the sharpness of fragments from annealed and thermally tempered pint glasses. The specific aims of this investigation were to:

- Provide estimates for the force required to penetrate skin with pint glass fragments, using a skin simulant for the investigation.
- Ascertain how the sharpness of tempered glass fragments is affected by the location of the fragment on the pint glass.
- Compare the sharpness of looping fragments from annealed glass and tempered glass.
- Compare the sharpness of different fragment edge categories.
- Assess the working use of a Vickers indentation technique onto pint glasses as a reproducible pre-damaging method.

The variable level of residual stress and thickness, and the typical resulting fracture characteristics of pint glasses, were introduced in chapter 4. Fragments were selected for analysis based on their distance from the glass base, their orientation relative to the impact location, and the x-axis edge category of interest. Looping fragments refers to fragments roughly 90° from the impact location where the longest edges are curved in shape (as introduced in chapter 4).

All glasses were broken by impact with the same impact energy. The pint glasses investigated here were pre-damaged by a Vickers indentation at a pre-determined location on the interior glass wall. This aimed to provide greater control over the strength of the glasses, and is in contrast to the fractured pint glasses in chapter 4, which were pre-damaged by an abrasion technique.

The following sub-section overviews the pre-sharpness assessment analysis conducted on the pint glass samples. Following this, the sharpness analysis results are presented and discussed. Conclusions are made in sub-section 8.2.6.

### 8.2.2 Pre-sharpness assessment analysis and fracture

A summary of the pre-sharpness analysis stage of this investigation is given in Table 8.1.

Glass samples:	10 x Utopia Perfect Pints
Tempering/annealing processes:	As-received (tempered), annealed as per sub-section 3.3.3
Residual stress assessment:	Automated polariscope, punch test (see chapter 4)
Surface pre-damaging:	50 N Vickers indentation as per sub-section 3.5.2.2
Fracture method:	Impact as per sub-section 3.6.2.1

**Table 8.1 – Pre-sharpness analysis summary table for investigation of sharpness of pint glass fragments.**

10 Perfect Pint glasses were selected for testing. These pint glasses were introduced in chapter 3 of this thesis, and their typical fracture characteristics were discussed in chapter 4. Perfect

Pints were chosen for this investigation because they have straight walls. This suited the pre-damaging method (Vickers indentation) because it reduced the likelihood of significant bending stresses occurring during the indentation event. After indentation, glasses were all fractured by impact at the same energy of 0.6 J. The impact location was directly above the Vickers indent location on the opposite side of the glass wall. 0.6 J was chosen as this was found to be sufficient to break a selection of test glasses indented prior to this investigation.

**Residual stress measurements:** 5 glasses were selected for an annealing procedure (as per sub-section 3.3.3), and 5 were left in their as-received thermally tempered condition. The residual stress distribution in the 5 tempered glasses was assessed with an automated polariscope (as detailed in sub-section 3.4.2.2) at 4 orientations (0°, 90°, 180°, and 270° from the impact location) at a distance of 30 mm from the glass rim. A summary of these measurements is given in Table 8.2. The measurements showed a high level of consistency between glasses.

Central tensile stress /MPa	Interior surface compression /MPa	Exterior surface compression /MPa
43.8 ( $\pm 0.7$ )	-82.9 ( $\pm 1.3$ )	-94.8 ( $\pm 2.1$ )

**Table 8.2 – Summary of residual stress measurements for 5 tempered Perfect Pint glasses 30 mm from the glass rim. Values shown are the average measurement over 4 glass wall orientations. Values in brackets are the standard deviation values.**

**Vickers indentations:** The Vickers indentation method for the pint glasses was outlined in sub-section 3.5.2.2. Vickers hardness values were not calculated because the development of lateral cracks at the high load used (50 N) complicated the identification of the indent diagonal locations, along with other factors discussed in sub-section 3.5.2. Examples of indents imparted onto annealed and tempered glasses are shown in Figure 8.1. All indentations were imparted successfully without causing macroscopic failure of the glasses.

**Macroscopic fracture patterns:** All 10 pint glasses successfully fractured from the imparted Vickers flaw. The fracture patterns were similar to those reported in chapter 4. All annealed glasses broke with the bases remaining intact, and all tempered glasses showed extensive fragmentation. The pattern of propagating cracks looping around the sides of the glasses detailed in chapter 4 was also observed here. Examples of fractured annealed pint glasses and fractured tempered pint glasses local to the fracture origin are given in Figure 8.2.

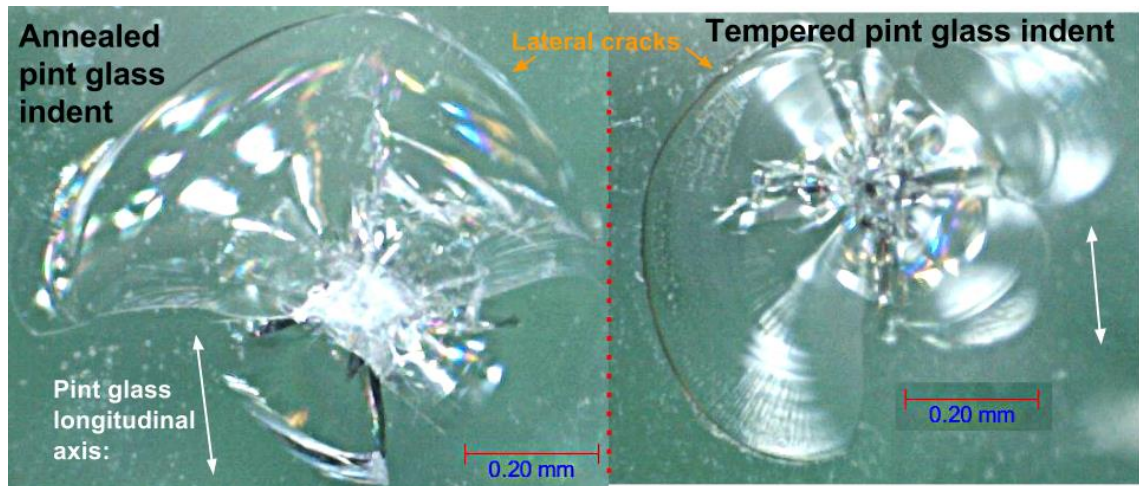


Figure 8.1 – Example micrographs of Vickers indentations imparted on to annealed pint glasses (left) and tempered pint glasses (right).

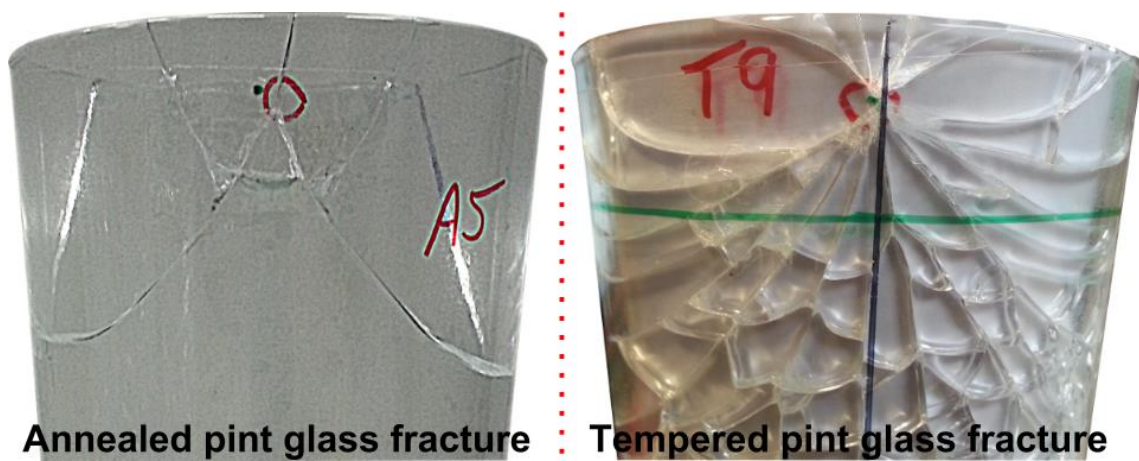
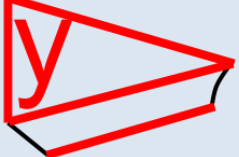


Figure 8.2 – Example fracture patterns of indented annealed pint glasses (left), and indented tempered pint glasses (right) local to the fracture initiation location (circled in red in the figure).

This sub-section has detailed the pre-sharpness assessment analysis conducted for indented pint glasses. Results from the sharpness assessments are detailed in the following sub-section.

### 8.2.3 Sharpness assessment: overview

A summary of the sharpness assessment tests and analyses conducted on pint glass fragments is given in Table 8.3 below.

 <p>x-axis edges</p>	Optical profile analysis	Selected fragment profiles (37)
	SEM analysis (tip radii)	None
	Penetration testing	Selected fragments (37)
 <p>y-axis edges</p>	Micro-CT cross-sections (included angles)	Selected fragment (1)
	Replica sections (edge radii)	Selected fragments (14)
	Slash test	Selected fragments (10)

**Table 8.3 – Sharpness analysis summary table for investigation of sharpness of pint glass fragments.**

**X-axis edges** were assessed by profile analysis and subsequent penetration testing. Comparison of the x-axis edges of annealed and tempered pint glasses was complicated by the lack of crack branching in annealed glasses. For this reason, the majority of the analysis focuses on the assessment of edges from tempered glass fragments at various heights along the pint glass. A small number of available x-axis edges from annealed pint glasses were also observed. These included 4 in-surface edges at locations where the crack intersected the rim after looping around the side of the glass, and 8 cantilever curl edges created by the continued force of the impactor after the initial fracture of the glass (see sub-section 2.5.4).

The tempered glass fragments were selected using a defined sampling procedure. For each glass, 9 sampling locations were defined, which were relative to the impact/indentation location (see Figure 8.3). Additionally, 3 x-axis edge categories were chosen for investigation: in-out, out-out, and in-surface (see sub-section 6.4.1 for definitions). A fragment from each sampling location was taken, and one x-axis edge was selected from each for testing. The edge category to be assessed for each fragment was pre-determined so that 3 of each category would be assessed per pint glass.

The assignment of an edge category to a sampling location was done at random with a python code for each glass. It was ensured that each x-axis category was used no more than twice for each sampling location. Edge categories were determined by viewing the macroscopic fracture pattern by eye. In some cases, the identified fragment edge of interest was not eligible for testing, since the crack had not propagated fully through the thickness at that point. In these cases, the nearest eligible x-axis edge of interest was selected within a 20 mm radius. If there were still no eligible x-axis edges of interest, no fragment was taken from that sampling location. The full sampling matrix for this investigation is shown in Table 8.4.

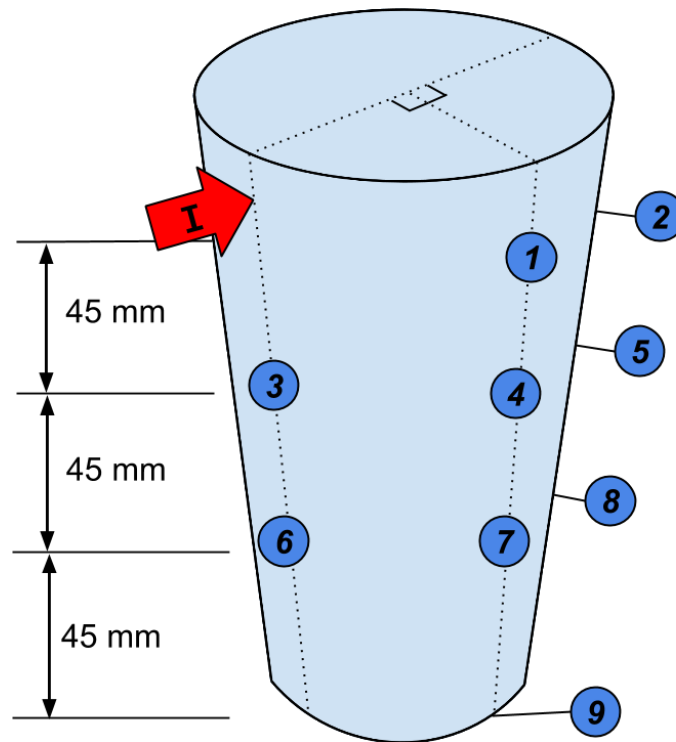


Figure 8.3 – Illustration of sampling locations for pint glass sharpness assessment. Not to scale. Arrow I represents the impact location. Circled numbers represent sampling locations. Locations 3 and 6 are oriented  $0^\circ$  from the impact location. Locations 1, 4, and 7 are oriented  $90^\circ$  from the impact location. Locations 2, 5, and 8 are oriented  $180^\circ$  from the impact location. Location 9 is central to the glass base. Locations 6, 7, and 8 are 45 mm vertically from the glass base. Locations 3, 4, and 5 are 90 mm vertically from the glass base. Locations 1 and 2 are 135 mm vertically from the glass base.

Glass ref:	Sampling location								
	1	2	3	4	5	6	7	8	9
A	I-S	O-O	I-O	I-O	I-O	I-S	O-O	O-O	I-S
B	O-O	I-S	O-O	I-O	I-O	I-S	I-S	I-O	O-O
C	I-O	I-O	I-S	O-O	I-S	O-O	I-O	O-O	I-S
D	I-O	O-O	I-O	I-S	O-O	O-O	I-S	I-S	I-O
E	I-S	I-S	I-S	O-O	O-O	I-O	I-O	I-O	O-O

Table 8.4 – x-axis edge category sampling matrix. I-O: in-out; O-O: out-out; I-S: in-surface. Red highlight: none eligible within 20 mm radius; orange highlight: fragment damaged during preparation.

**Y-axis edges** of looping fragments from annealed and tempered pint glasses were assessed by measuring tip radii of sectioned samples, and by performing slash tests. Looping fragments were chosen from the side  $90^\circ$  anticlockwise to the impact point. Fragments closest to 135 mm vertically upwards from the base were chosen, as looping fragments were available near this location for both annealed and tempered glasses. These were analysed at the lowest part of the loop on the convex side of the fragment. Additionally, a small number of base fragments were taken for SEM cross-section measurement for comparison to fragments from other areas of the glass.

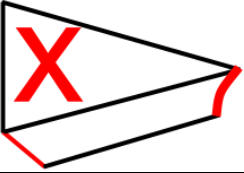
#### 8.2.4 Sharpness assessment: x-axis edges

A summary of measured geometrical parameters for x-axis edges from indented tempered pint glasses broken by impact are shown in Table 8.5. The results in the table are categorised according to the sampling locations shown in Figure 8.3: locations 1 and 2 are referred to as the top region; locations 3, 4, and 5 are referred to as the middle region; and locations 6, 7, and 8 are referred to as the bottom region.

A large level of variation was observed for each parameter value measurement and the largest variation was found for tip radii measurements, similar to other x-axis profile analyses in this thesis. Reasons for tip radii variation were discussed in sub-section 7.3.4.2. Tip radii measurements for top region fragments were however significantly smaller than in other regions. This may be an effect of the greater ease at which the top region fragments could be removed from the restrained fractured article, and therefore of the decreased likelihood of fragment damage during sampling.

Student's *t*-tests were conducted to determine whether there were any significant differences in parameter values due to the sampling location height. The full results of the *t*-tests are given in Appendix M. The penetration load was found to be significantly lower for top region fragments compared to lower region fragments (~16 N compared to ~48 N on average). This penetration load was comparable to the average penetration load for the annealed x-axis edges tested (~21 N on average).

The low penetration load for fragments from the top region is likely to have been affected by three factors. Firstly, the near included angle, the thickness 1 mm from the pierce point, and the tip radius on the fracture surface side were found to be significantly lower for top region fragments. The free surface near and far included angles were also notably lower for top region fragments. Secondly, the thickness of the fragments was lower in the top region. Thirdly, proportionally fewer in-out fragments were tested from the top region than for other regions due to availability. Overall it was found that in-out edges required on average ~1.8 times more force than other edge categories in this investigation. The fragment geometrical parameters and penetration loads categorised by edge category are given in Appendix M, along with further average profile plots.

	Top region (n = 7)	Middle region (n = 13)	Bottom region (n = 15)	All tempered fragments (n = 37)	Annealed fragments (n = 12)
Thickness /mm	3.17 ± 0.11 (3)	4.47 ± 0.43 (10)	5.67 ± 0.54 (10)	4.69 ± 1.12 (24)	3.09 ± 0.08 (3)
<b>Fracture surface parameters</b>					
Tip radius /µm (manual)	77 ± 61 (79)	1111 ± 754 (68)	2036 ± 1897 (93)	1438 ± 1703 (118)	678 ± 965 (142)
Near included angle /° (manual)	95.0 ± 47.1 (50)	155.8 ± 18.5 (12)	110.2 ± 52.4 (48)	126.4 ± 48.5 (38)	42.8 ± 33.9 (79)
Thickness 1mm from piercing point /mm	2.9 ± 0.3 (10)	4.4 ± 0.4 (9)	4.6 ± 1.9 (41)	4.3 ± 1.4 (33)	1.4 ± 1.0 (71)
Protrusion length /mm	0.6 ± 0.3 (50)	0.6 ± 0.3 (50)	1.4 ± 1.1 (79)	0.9 ± 0.8 (89)	3.0 ± 1.8 (60)
Average protrusion length /mm	0.2 ± 0.4 (200)	0.3 ± 0.2 (67)	0.8 ± 0.6 (75)	0.5 ± 0.5 (100)	1.6 ± 0.7 (44)
Lateral distance to comp. edge /mm	0.8 ± 1.1 (138)	1.7 ± 1.2 (71)	2.6 ± 2.0 (77)	1.8 ± 1.7 (94)	2.2 ± 0.9 (41)
Root mean square roughness, Rq /mm	0.37 ± 0.14 (38)	0.28 ± 0.14 (50)	0.65 ± 0.58 (89)	0.44 ± 0.42 (95)	0.67 ± 0.31 (46)
<b>Free surface parameters</b>					
Tip radius /µm (manual)	60 ± 68 (113)	108 ± 167 (155)	286 ± 439 (153)	166 ± 315 (190)	76 ± 78 (103)
Near included angle /° (manual)	63.4 ± 32.6 (51)	93.4 ± 25.8 (28)	93.7 ± 34.9 (37)	86.3 ± 33.4 (39)	86.1 ± 20.1 (23)
Far included angle /°	59.5 ± 31.6 (53)	80.9 ± 31.3 (39)	74.0 ± 36.3 (49)	72.8 ± 33.8 (46)	63.7 ± 14.3 (22)
Thickness 1mm from piercing point /mm	1.6 ± 1.6 (100)	2.6 ± 1.1 (42)	2.6 ± 1.7 (65)	2.4 ± 1.5 (63)	1.7 ± 0.4 (24)
Root mean square roughness, Rq /mm	0.08 ± 0.04 (50)	0.10 ± 0.05 (50)	0.12 ± 0.07 (58)	0.10 ± 0.06 (60)	0.11 ± 0.07 (64)
<b>Penetration testing</b>					
Penetration load /N	16 ± 7 (44) (n = 9)	48 ± 18 (38) (n = 12, *)	47 ± 11 (23) (n = 12, **)	40 ± 18 (45) (n = 35)	21 ± 17 (81) (n = 12)

**Table 8.5 – Summary of x-axis profile parameter data of tempered pint glass fragments. Results are categorised by: top region fragments (locs. 1 and 2), middle region fragments (locs. 3, 4, and 5), and bottom region fragments (locs. 6, 7, and 8). Tests on cantilever curl and in-surface fragments from annealed glasses are also shown. In each case the average value is shown ± one standard deviation. The percentage of the standard deviation compared to the average value is shown in parentheses. All parameters listed in this table are described and illustrated in section 6.4.2. \* 1 fragment damaged during preparation. \*\* 1 fragment damaged during preparation, 2 fragments failed to penetrate.**

A regression model was fitted to the data, in order to determine the most influential geometrical parameters on the penetration load. The full results of the regression analysis are given in Appendix M. Alongside the fragment thickness, four geometrical parameters were

found to have a significant effect on the penetration load: the free near angle, the free far angle, the free root mean square roughness ( $R_q$ ), and the fracture surface profile thickness 1 mm back from the pierce point. This is consistent with the exploratory study on influential factors on penetration load conducted in chapter 6, which found that free surface geometrical parameters had the greatest effect.

The lesser effect of fracture surface parameters on penetration load is emphasised by the average profile plots of fragments from the top, middle, and bottom regions shown in Figure 8.4. These plots show little change in profile shape between different regions, regardless of the significant differences in penetration load.

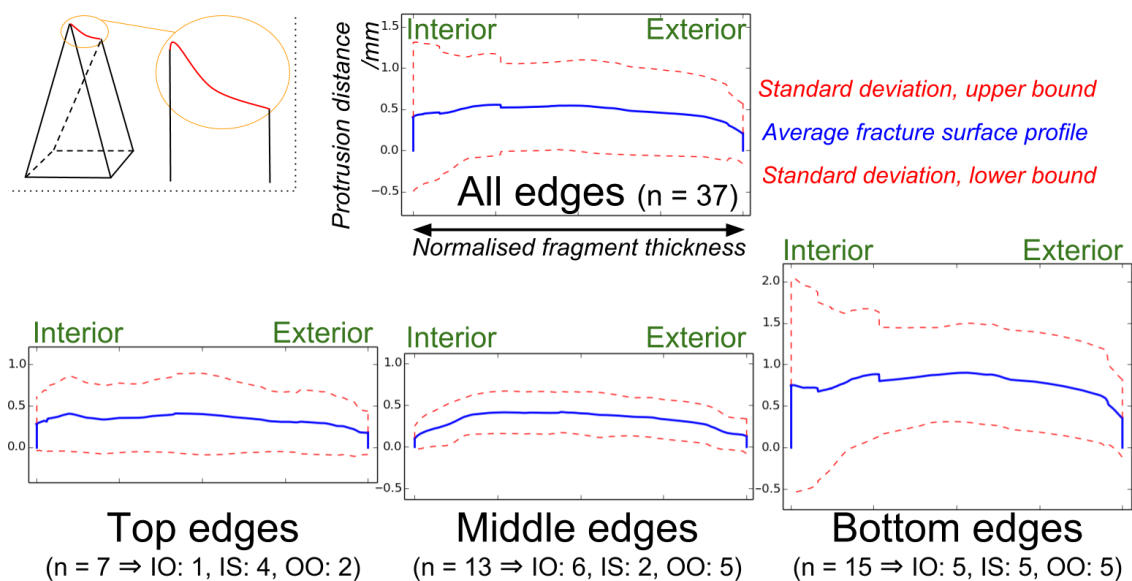


**Figure 8.4 – Average profile morphology of x-axis edges from selected pint glass fragments. Vertical axes are in units of mm. Top edges: from locations 1 and 2; Middle edges from locations 3, 4, and 5; Bottom edges from locations 6, 7, and 8 (see Figure 8.3). Average profiles are plotted with a solid blue line. Upper and lower standard deviation profile bounds are plotted with dashed red lines. Interior and exterior surfaces of the pint glass are as labelled. Inset shows x-axis profile context. The vertical step in the average profile occurs due to a feature on an irregular surface profile and is not the result of noise in the measurement.**

The average cantilever curl and in-surface x-axis profile plots of annealed glass fragments were notably different in shape and are shown in Figure 8.5. The in-surface profiles were rounded since the x-axis edge represented the intersection of the crack front with the rim of the glass. By contrast, the cantilever curl profiles were pointed and had small included angles. Unlike the tempered pint glass fragments, the two edge types had similar free surface included angles but required significantly different penetration loads ( $\sim 40$  N for in-surface edges compared to  $\sim 12$  N for cantilever curl profiles). This therefore represents a case where the fracture surface profile does have a significant effect on the penetration load.

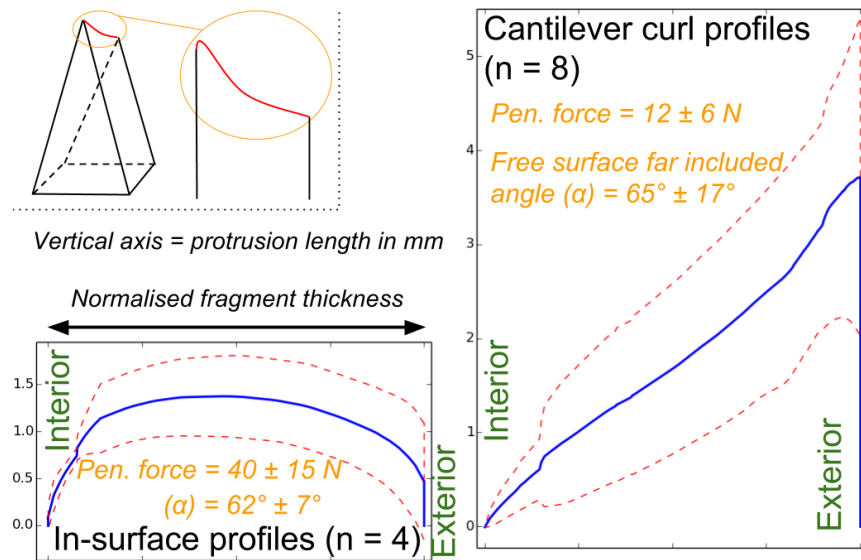


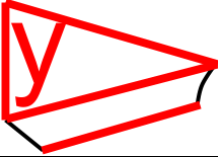
**Figure 8.5 – Average profile morphology of x-axis edges from selected annealed pint glass fragments. Vertical axes are in units of mm. Average profiles are plotted with a solid blue line. Upper and lower standard deviation profile bounds are plotted with dashed red lines. Interior and exterior surfaces of the pint glass are as labelled. Inset shows x-axis profile context.**

This section has discussed the results of x-axis edge analyses conducted on fragments from tempered and annealed pint glass fragments. The conclusions from these analyses are summarised in sub-section 8.2.6.

### 8.2.5 Sharpness assessment: y-axis edges

This sub-section presents and discusses the results of sharpness assessments of y-axis edges of looping pint glass fragments. Such fragments are found in both annealed and tempered glasses from a location  $\sim 90^\circ$  from the impact point, and are introduced in chapter 4. All y-axis edge tip radii measurements and slash test results gathered for this investigation are shown in Table 8.6.

SEM tip radii measurements were found to vary between  $\sim 1\text{-}6\ \mu\text{m}$ , although measurements of  $12\ \mu\text{m}$  and  $24\ \mu\text{m}$  were also found at the interior side for individual annealed and tempered looping fragments respectively. The trend of blunter geometrical characteristics on the interior side compared to the exterior side of the loops was most pronounced for annealed fragments. A cross section obtained by micro-CT of an annealed sample is shown in Figure 8.6 which has a protruding feature with an acute included angle near to the exterior side of the fragment.

	Annealed loops	Tempered loops	Base fragments
<b>Replica tip radii measurements</b>			
Interior side tip radius / $\mu\text{m}$	5-24 (n = 2)	4-12 (n = 2)	~1-2 (n = 3)
Exterior side tip radius / $\mu\text{m}$	3-4 (n = 2)	2 (n = 1)	2-6 (n = 3)
<b>Fragment cutting/slashing tests (n=5 each)</b>			
Penetration depth /mm	$1.22 \pm 0.28$ (22)	$0.26 \pm 0.20$ (77)	N/A
Average load in steady state /N	$7.4 \pm 1.9$ (26)	$4.0 \pm 0.8$ (20)	N/A
Friction coefficient	$0.89 \pm 0.23$ (26)	$0.48 \pm 0.10$ (21)	N/A

**Table 8.6 – Summary of parameter data collected y-axis edges of looping fragments from annealed and thermally tempered pint glasses, and tip radii of base fragments from tempered pint glasses. In each case the average value is shown  $\pm$  one standard deviation. The percentage of the standard deviation compared to the average value is shown in parentheses. For tip radii measurements, the number of samples tested is shown in parentheses instead. All parameters listed in this table are described and illustrated in section 6.4.**

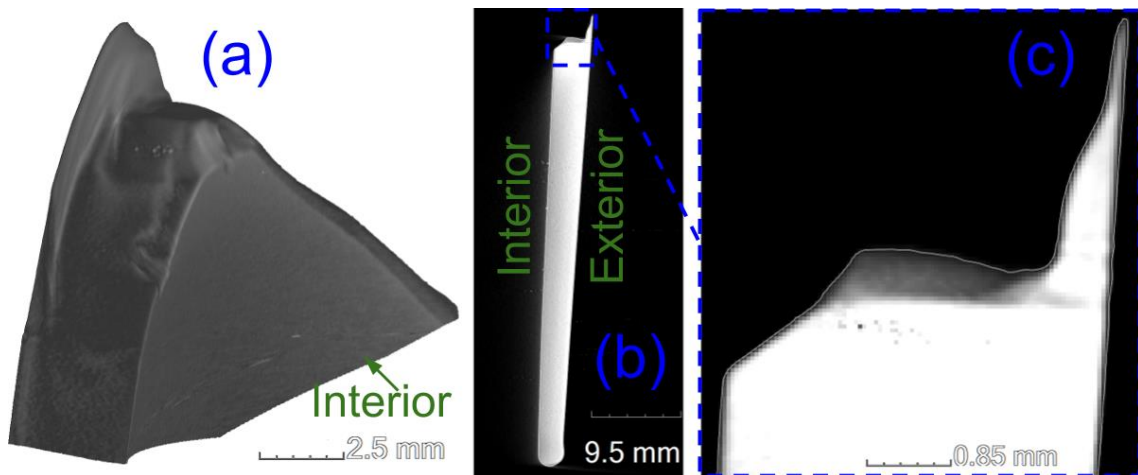


**Figure 8.6 – Micro-CT images of an annealed looping fragment (oriented upside-down). (a): 3D render of a portion of the fragment. (b) Entire cross section. (c) Enlarged tip of cross section showing protruding point near the exterior side.**

The difference in slash test performance between annealed and tempered looping fragments was found to be significant from Student's *t*-tests. Annealed looping fragments achieved a greater penetration depth on average than tempered looping fragments (1.22 mm compared to 0.26 mm). It is therefore difficult to compare the slashing behaviour between the two fragment types as the annealed fragments propagated deeper cuts. This accounts for the significantly larger steady propagation force for the annealed fragments. The cut profiles were however similar in profile, if not in depth. These profiles were similar to those shown in Figure 7.7, and were straight and non-ragged.

This sub-section has presented the main results from this sharpness investigation. The following sub-section overviews the conclusions from this work.

### 8.2.6 Conclusions

Section 8.2 has discussed the results of pre-sharpness assessments, fracture patterns, and sharpness assessments of annealed and tempered pint glass fragments broken by impact.

The main conclusions of this investigation are as follows:

- The Vickers indentation technique used to reproducibly pre-damage the glass was successful in producing the origin location for each impacted pint glass. However, comparisons between annealed and tempered pint glass fragments were complicated by the lack of crack branching in annealed glasses.
- The average forces required to penetrate a skin simulant varied from 16 N to 48 N. The lowest average penetration forces were recorded for fragments from annealed pint glasses and fragments from near to the rim of tempered pint glasses. Fragments closer to the base required ~3 times more force to penetrate the simulant. This is consistent with the fragment sizes noted in chapter 4, where fragments near to the rim of tempered pint glasses were regularly comparable in size to those of annealed glasses. It should be noted however that the observed near-rim fragment sizes from tempered glasses tested in this investigation were consistently smaller than corresponding fragments from annealed glasses.
- In-out type x-axis edges required significantly more force to penetrate a skin simulant compared to out-out and in-surface x-axis edge categories.
- Free surface x-axis edge parameters were found to bear more influence on the penetration force than other measured geometrical parameters.
- Annealed looping fragments penetrated to a depth 4-5 times greater than tempered looping fragments during slash tests. Annealed fragments were also associated with distinctive protruding portions of the fracture surface with acute included angles near to the exterior side (see Figure 8.6).

Recommendations for how the investigation could be improved or extended are given below.

- The use of lower indentation loads for the flaws imparted to the interior wall would ensure that greater loads were required to fracture the glasses. This could result in a greater frequency of crack branching in annealed glasses and permit further comparisons between annealed and tempered glasses.

- Testing tempered pint glasses of different temper levels would allow for greater refinement of the effect of temper stresses on the sharpness properties of pint glass fragments. This could be achieved by subjecting tempered pint glasses to varying short annealing procedures to partially anneal the glasses.

### 8.3 Sharpness of fragments from non-uniformly tempered glass

#### 8.3.1 Introduction

This section details an investigation into the effect of membrane temper stresses on the sharpness of fragments from broken non-uniformly tempered glass. Membrane stresses (also referred to as form stresses) are components of the total residual stress and are constant through the thickness of an article, but vary laterally across the surfaces. This is in contrast to the through-thickness temper stresses measured by automated and scattered light polariscopes elsewhere in this thesis. Membrane stresses are caused by lateral non-uniformity of heat treatment during thermal tempering, and usually reflects the spacing of cooling jets [1].

As with through-thickness temper stresses, membrane stresses can have desirable or undesirable effects on the strength and fracture of an article. Deliberate non-uniform tempering has been practised for car windscreen manufacture [1]. This was done to deliberately control fragment sizes to ensure visibility through the windscreen if broken, whilst still retaining the safety characteristics of tempered glass. However, a large lateral variation in membrane stresses in an article may occur incidentally, and can lead to undesired residual tensile stresses and weaken the article.

The specific aims of this investigation were to:

- Appraise how membrane stresses affect the fracture properties of glass samples and relate the fracture patterns of non-uniformly tempered glass to injury potential.
- Investigate the sharpness properties of fragments from broken non-uniformly tempered glass.

Glass disc samples were tempered using the custom-built apparatus detailed in sub-section 3.3.1.2. An array of 4 single jets (see Figure 3.5) was used to temper the samples from various initial temperatures with various subsequent cooling rates. This resulted in a spatially-dependent cooling rate on the glass disc surfaces, due to the distance between the individual jets.

The following sub-section overviews the pre-sharpness assessment stage of the investigation. The sharpness assessment tests conducted are detailed in subsequent sub-sections. An overall discussion of the results is presented in sub-section 8.3.6.

### 8.3.2 Pre-sharpness assessment analysis and fracture

A summary of the pre-sharpness analysis stage of this investigation is given in Table 8.7 below.

Glass samples:	29 x flat discs (75 mm diameter x 3.82 mm thickness) cut as per sub-section 3.2.1.
Tempering/annealing processes:	Low and high cooling rate procedures
Residual stress assessment:	Plane polariscope, and punch test
Surface pre-damaging:	Abrasion as per sub-section 3.5.1
Fracture method:	Impact as per sub-section 3.6.1.4

**Table 8.7 – Pre-sharpness analysis summary table for investigation of sharpness as affected by lateral temper stresses.**

A total of 29 flat disc samples were thermally tempered during this investigation. 19 samples were used during the initial phase of testing to explore the effects of three test parameters on the fracture properties of the sample. These test parameters were: the jet-to-sample distance; the jet air velocity; and the initial temperature of the glass at the onset of cooling. From this, two specific tempering procedures were defined and termed as *low* and *high* cooling rates. Both cooling rate procedures involved jet-to-sample distances of 30 mm, and initial air velocities of  $30 \text{ ms}^{-1}$ . The initial temperature was  $650 \text{ }^{\circ}\text{C}$  and  $670 \text{ }^{\circ}\text{C}$  for low and high cooling rate procedures, respectively. 5 discs were tempered by each cooling rate procedure. 3 discs of each tempering procedure were then subjected to an impact test (as per sub-section 3.6.1.4), and the remaining 2 were subjected to a punch test.

A high degree of warping was encountered by the discs from the tempering procedures, which meant that the discs were unsuitable for pre-damaging by Vickers indentation. Therefore, the surfaces of each sample were subjected to an abrasion procedure (described in sub-section 3.5.1) prior to loading.

**Residual stress assessment:** All samples tempered by low and high cooling rate procedures were observed in a plane polariscope with a tint plate prior to abrading the surfaces. As with the tempered rectangular samples in section 7.3, a similar photoelastic pattern developed for each sample regardless of tempering procedure with the jet array. An example pattern at orientations of  $0^{\circ}$ ,  $22.5^{\circ}$ ,  $45^{\circ}$ , and  $67.5^{\circ}$  relative to the polariser axis is shown in Figure 8.7. The patterns had a highly mottled appearance, which appeared to correspond to the location and

spacing of the impinging jets as indicated in the figure. This is a typical effect of using arrays of jets for a tempering procedure [1].

A low level of fragmentation was observed for punched samples, as shown in Figure 8.8. The punch location was at a point 10 mm from an edge, on a line that passed through the central jet impingement location and one other jet impingement location (referred to as the lateral jet), as indicated on the figure. Punching at a position near the edge meant that it was simpler to avoid unwanted bending stresses due to the degree of warping of the samples.

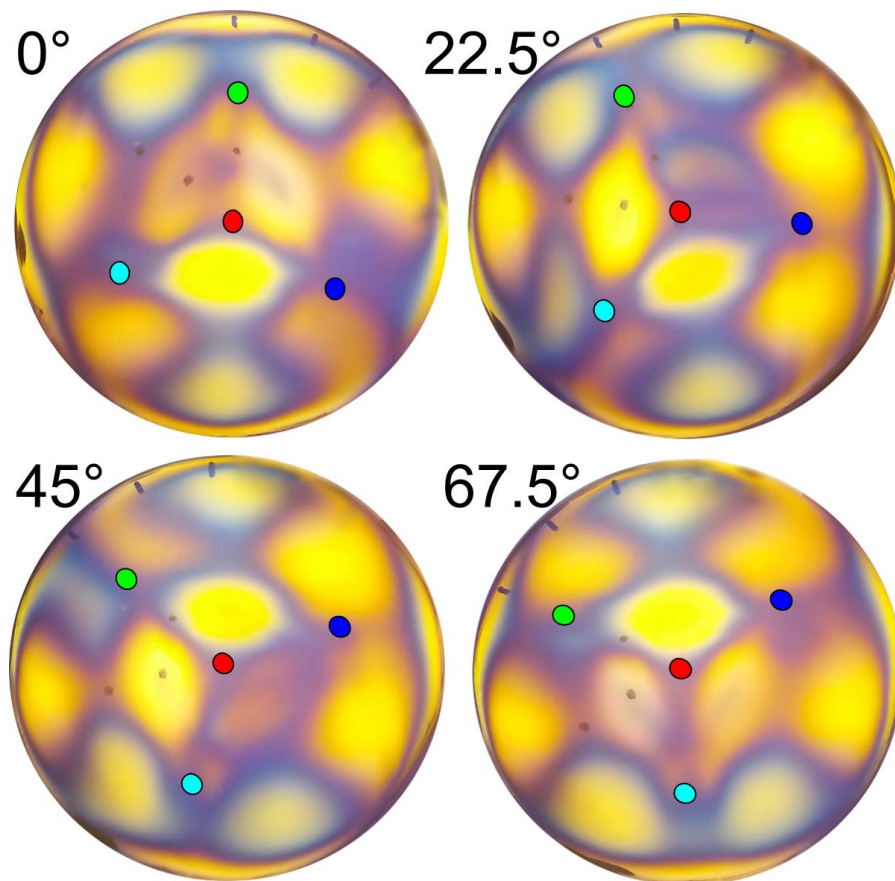


**Figure 8.7 – Photoelastic patterns observed of a disc sample subjected to a low cooling rate procedure during initial testing. Numbers denote rotation of the disc relative to the polariser axis. Circles have been superimposed at the jet impingement locations.**

The general trend for the punch samples involved the initial crack propagating from the punch location towards the lateral jet impingement location. The crack subsequently bifurcated either at, or before, it reached the lateral jet impingement location. The cracks then curved away from the central region of the disc, and intersected the sample edge  $\sim 90^\circ$  from the punch location. The majority of the sample remained intact, which included the central region of the sample. This indicates that a high magnitude of compressive membrane stress was present within this region that acted to divert the crack path. Additionally, the plane polariscope

pictures in Figure 8.8 indicate that this compressive stress was not fully released during the fracture event.

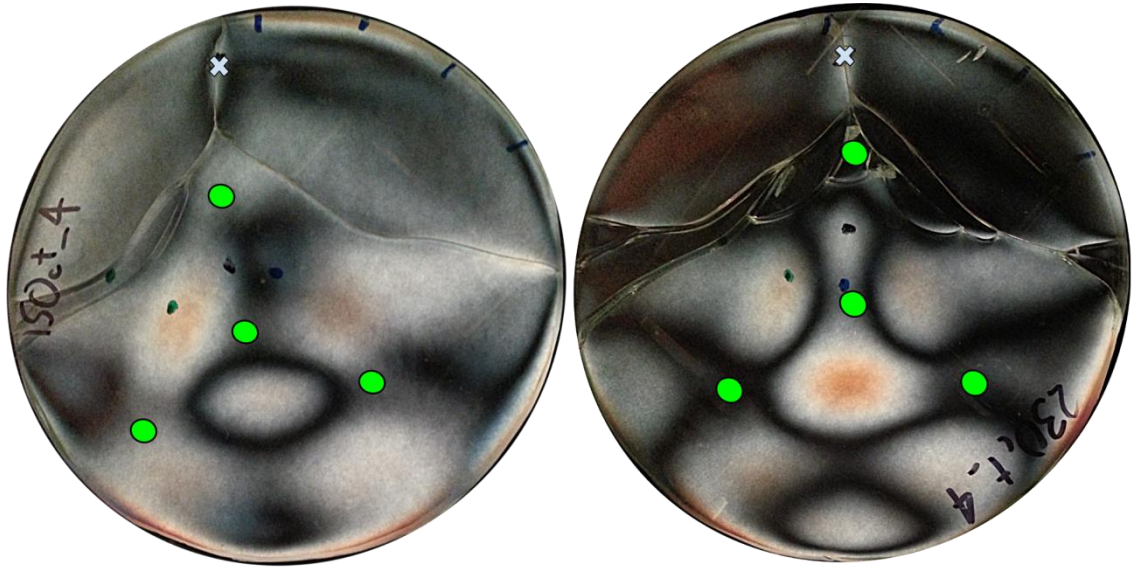


**Figure 8.8** – Example fracture patterns of punched disc samples subjected to a low cooling rate (left) and a high cooling rate (right), viewed in a plane polariscope. The fragments were held in place by adhesive tape, which may have affected the retardation of the source light. The alignment of the left sample was particularly affected by movement of the supporting wires during the heating stage of the tempering procedure. Green circles indicate jet impingement locations.

**Macroscopic fracture patterns due to impact:** All 6 disc samples fractured with the fracture origin location directly below the impact location on the opposite glass surface to impact. The resulting fracture patterns and corresponding failure energies are shown in Figure 8.9. Samples subjected to a high cooling rate showed an overall greater fragmentation density, although this was also affected by the greater impact energies required to cause failure for some samples. The size of fragments varied significantly across each impacted sample, as did the included angles of the fragments as viewed on the y-z plane.

A high frequency of cracks in each sample diverted from a straight propagation path in the y-z plane and showed a tendency to create curved and rounded fragments. Rounded fragments appeared to correlate to at least one impinging jet location on each sample as indicated in Figure 8.9. However, such fragments were also present in other areas around the sample periphery. This was contrary to the expectation that compressive membrane stresses would only develop at the impinging jet locations, resulting in larger fragments. It is possible that jet interaction effects occurred that may have increased the magnitude of convective heat transfer elsewhere on the glass surfaces. However, investigation into the airflow interaction and the resulting distribution of convective heat transfer coefficients on the sample surfaces was beyond the scope of the current study.

The majority of fragments had cracks which had not fully propagated through the thickness of the glass, and so the actual fragment count was less than that as observed from photographs. Fragments were prone to further fragmentation at these cracks, which necessitated careful handling of the samples during the fragment sampling process.

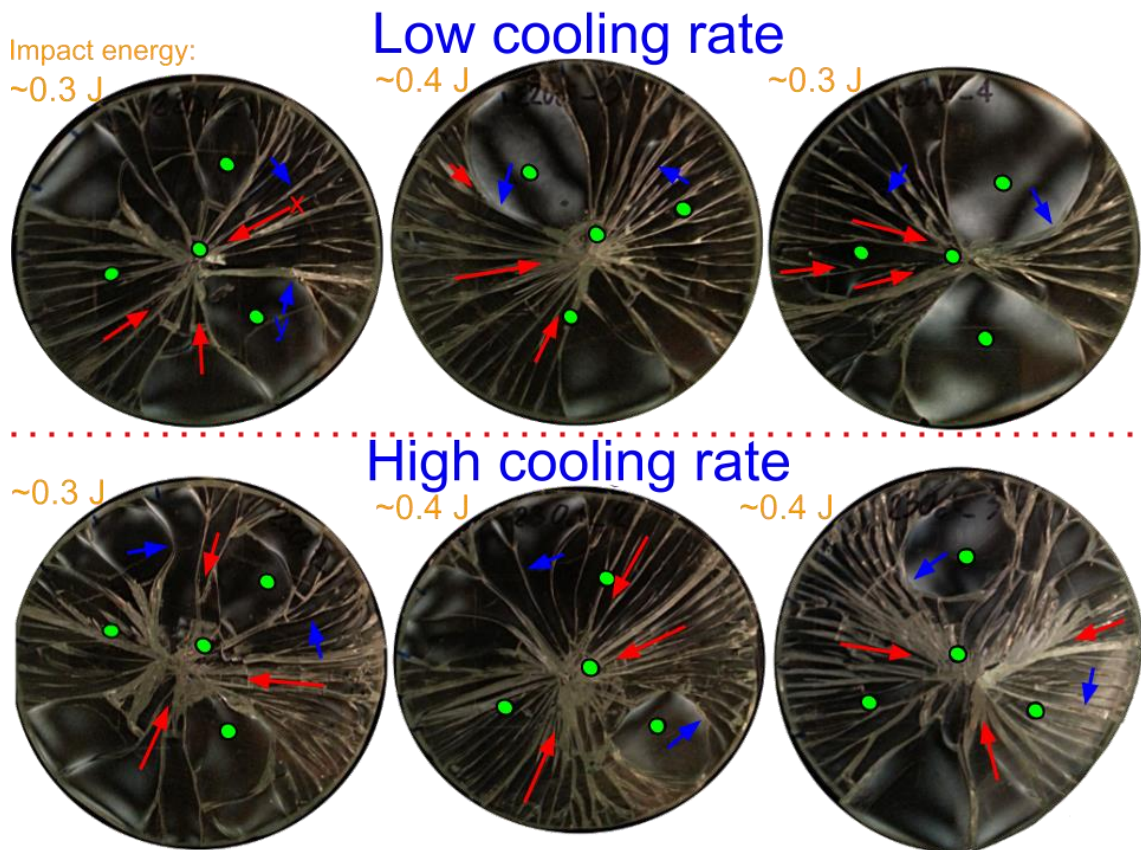


Figure 8.9 – Non-uniformly tempered glass discs broken by impact as per sub-section 3.6.1.4. Impingement locations are indicated by the green circles. Red and blue arrows denote sampling locations for x-axis and y-axis edges, respectively. Impact fracture energy (calculated using equation 3.5) shown in orange font.

**Fracture surfaces:** A radial fragment with one near-straight edge was taken from each sample, and the fracture surface corresponding to the straight edge was observed with a stereo optical microscope. Example fracture surfaces are shown in Figure 8.10. The fracture surface features were similar to those of the tempered rectangular fragments in section 7.3, and indicated a crack front that initially led at the tensile surface and tended towards the mid-plane as it propagated away from the origin location. This effect occurred for samples subjected to both low and high cooling rates. Some fracture surfaces at curved cracks were also viewed. These fracture surfaces had central regions of shear hackle and twist hackle near the edges, but were overall less detailed than the radial regions.

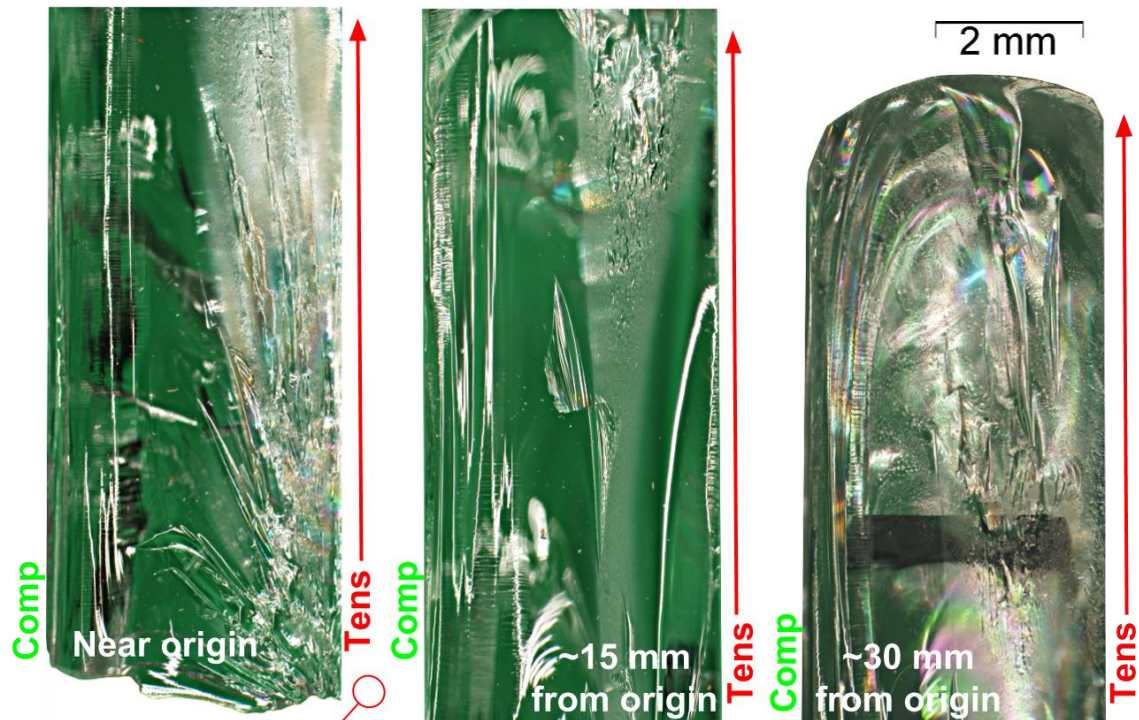


Figure 8.10 – Three example fracture surfaces of non-uniformly tempered disc fragments broken by impact with tensile and compressive sides labelled, at various propagation lengths. Red circle denotes origin location, which is not shown in the figure.

This sub-section has detailed the pre-sharpness assessment analysis conducted for non-uniformly thermally tempered glass discs. Results from the sharpness assessments conducted are detailed in the following sub-section.

**8.3.3 Sharpness assessment: overview**

A summary of the sharpness assessment tests and analyses conducted on fragments from non-uniformly tempered glass disc samples is given in Table 8.8 below.

<p>x-axis edges</p>	Optical profile analysis	Selected fragment profiles (18)
	SEM analysis (tip radii)	None
	Penetration testing	Selected fragments (18)
<p>y-axis edges</p>	Micro-CT cross-sections (included angles)	Selected fragments (2)
	Replica sections (edge radii)	None
	Slash test	Selected fragments (12)

Table 8.8 – Sharpness analysis summary table for investigation of sharpness as affected by lateral temper stresses.

**X-axis edges:** 3 fragments were taken from each impacted disc sample for x-axis edge assessment. The location of each assessed x-axis edge is indicated by the red arrows in Figure 8.9. Fragments were initially sampled at locations in between impinging jet locations. However, it proved difficult to remove some fragments without causing further damage. Consequently, the intact fragment in closest proximity to the desired fragment location was selected for testing. Each of these fragments was then subjected to optical profile analysis and penetration testing.

Rounded fragments were not included in this assessment as they were not considered to pose great penetration potential. Instead, rounded fragments were prioritised for y-axis assessment.

**Y-axis edges:** 2 fragments were taken from each impacted disc sample for y-axis edge assessment. The location of each assessed y-axis edge is indicated by the blue arrows in Figure 8.9. An edge of a rounded fragment and an edge of a straighter fragment were taken from each sample and their performance in slash tests was compared. This was done to investigate whether the edges of the rounded fragments posed less cutting potential. Only y-axis edges on the tensile side of each fragment were assessed in order to simplify the analysis. As with previous sections, the tensile side was chosen. This was because the compressive side was in contact with the adhesive tape, and any further bending of the glass sample after fracture may have damaged the compressive side edges.

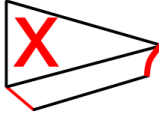
#### **8.3.4 Sharpness assessment: x-axis edges**

A summary of measured geometrical parameters for x-axis edges from non-uniformly tempered discs broken by impact are shown in Table 8.9. The results in the table are categorised according to sample cooling rate alongside the overall mean values. Similar to other x-axis profile analyses in this thesis, a large level of variation was observed for each parameter value measurement, with the largest variation found for tip radii measurements. This is likely to be a result of the vulnerability of tips to damage during handling and preparation, as discussed in section 7.3.4.2.

The fragments from samples of both cooling rates performed similarly in penetration tests, with average penetration forces of ~11 N. This is comparable to the penetration forces of fragments from the top region of tempered pint glasses in the previous section, and the penetration forces of annealed pint glass fragments. This may therefore suggest that the level of temper for both sample types was low. However, it should be noted that only out-out edges

were selected for testing here, which generally have relatively small free surface included angles.

As with the measured penetration forces, no statistically significant differences were found at a 5% significance level between the majority of geometrical parameters for samples of both cooling rates. The full results of the Student's *t*-tests are given in Appendix N. This is reflected in the average profile shapes as shown in Figure 8.11, which all show a similar level of flatness.

	Low cooling rate (n = 9)	High cooling rate (n = 9)	All fragments (n = 18)
<b>Fracture surface parameters</b>			
Tip radius / $\mu\text{m}$ (manual)	347 $\pm$ 297 (86)	61 $\pm$ 60 (98)	204 $\pm$ 258 (126)
Near included angle / $^{\circ}$ (manual)	107.0 $\pm$ 48.8 (46)	102.7 $\pm$ 35.6 (35)	104.9 $\pm$ 42.7 (41)
Thickness 1mm from piercing point /mm	3.5 $\pm$ 0.6 (17)	3.0 $\pm$ 1.0 (33)	3.3 $\pm$ 0.9 (27)
Protrusion length /mm	1.2 $\pm$ 0.6 (50)	1.6 $\pm$ 0.7 (44)	1.4 $\pm$ 0.7 (50)
Average protrusion length /mm	0.7 $\pm$ 0.4 (57)	1.0 $\pm$ 0.5 (50)	0.9 $\pm$ 0.5 (56)
Lateral distance to comp. edge /mm	1.3 $\pm$ 1.2 (92)	1.9 $\pm$ 1.2 (63)	1.6 $\pm$ 1.2 (75)
Root mean square roughness, Rq /mm	0.53 $\pm$ 0.22 (42)	0.82 $\pm$ 0.44 (54)	0.67 $\pm$ 0.38 (57)
<b>Free surface parameters</b>			
Tip radius / $\mu\text{m}$ (manual)	24 $\pm$ 21 (88)	28 $\pm$ 27 (96)	26 $\pm$ 24 (92)
Near included angle / $^{\circ}$ (manual)	53.7 $\pm$ 30.2 (56)	63.3 $\pm$ 38.7 (61)	58.5 $\pm$ 35 (60)
Far included angle / $^{\circ}$	44.9 $\pm$ 18.7 (42)	40.3 $\pm$ 14.6 (36)	42.6 $\pm$ 16.9 (40)
Thickness 1mm from piercing point /mm	1.0 $\pm$ 0.5 (50)	1.1 $\pm$ 0.5 (45)	1.1 $\pm$ 0.5 (45)
Root mean square roughness, Rq /mm	0.15 $\pm$ 0.06 (40)	0.16 $\pm$ 0.07 (44)	0.16 $\pm$ 0.07 (44)
<b>Penetration testing</b>			
Penetration load /N	12 $\pm$ 4 (33)	10 $\pm$ 5 (50)	11 $\pm$ 4 (36)

**Table 8.9 – Summary of parameter data collected for out-out x-axis profiles of non-uniformly tempered disc fragments. In each case the average value is shown  $\pm$  the standard deviation. The percentage of the standard deviation compared to the average value is shown in parentheses. All parameters listed in this table are described and illustrated in section 6.4.2.**

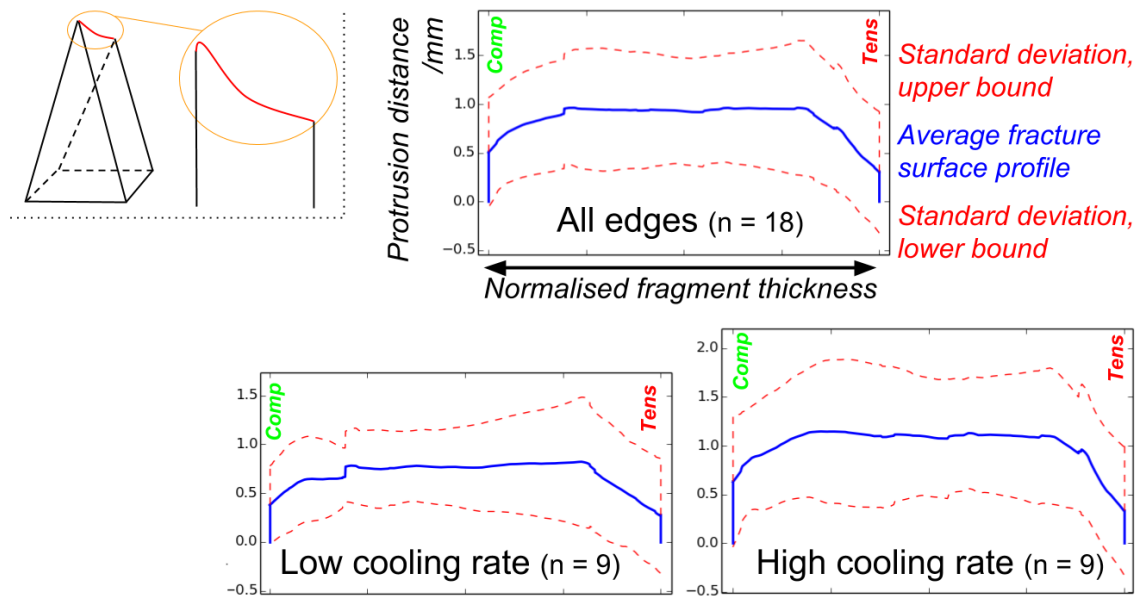


Figure 8.11 – Average profile morphology of x-axis edges from selected non-uniformly tempered rigid disc fragments. Vertical axes are in units of mm. Average profiles are plotted with a solid blue line. Upper and lower standard deviation profile bounds are plotted with dashed red lines. Inset shows x-axis profile context.

This section has discussed the results of x-axis edge sharpness assessments on non-uniformly tempered discs.

### 8.3.5 Sharpness assessment: y-axis edges

This sub-section presents and discusses the results of slash test sharpness assessments of y-axis edges on selected straight and rounded fragments from non-uniformly tempered disc samples. The exact fragments used for this analysis are shown in context in Figure 8.9. All slash test results gathered for this investigation are shown in Table 8.10.

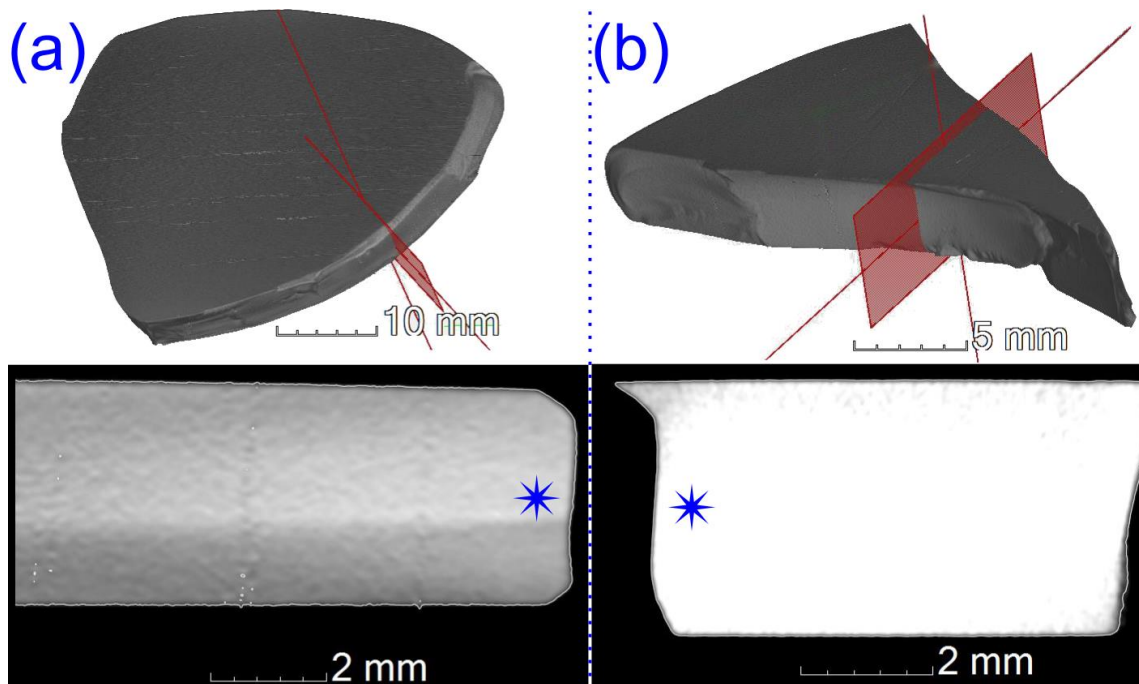
	Straight edges	Rounded edges
<b>Fragment cutting/slashing tests</b>		
Penetration depth /mm	0.61 ± 0.22 (36)	0.41 ± 0.38 (93)
Average load in steady state /N	3.7 ± 0.4 (11)	4.8 ± 0.8 (17)
Friction coefficient	0.45 ± 0.05 (11)	0.58 ± 0.09 (16)

Table 8.10 – Summary of slash test data collected for y-axis edges of straight and rounded fragments from non-uniformly tempered glass discs. In each case the average value is shown ± one standard deviation. The percentage of the standard deviation compared to the average value is shown in parentheses. All parameters listed in this table are described in section 6.5.

Round-edged fragments were found to require a significantly larger steady cut propagation force compared to straight edged fragments. Additionally, the penetration depth of rounded fragment edges was on average less than for straight fragment edges. This suggests that

round-edged fragments from non-uniformly tempered glass pose less injury potential than for straight-edged fragments.

Figure 8.12 shows cross section images from micro-CT scans of a round-edged fragment and a fragment previously adjacent to it in the macroscopic fracture pattern. These cross sections are in corresponding locations. It can be seen that the rounded fragment has rounded edges in both the y-z and x-y fractographic planes. However, the corresponding fragment has a protruding feature at one edge which corresponds to the rounded edge of the round fragment. The opposite side of the corresponding fragment is rounded, which implies that some damage was caused to at least one of the fragments during fracture. This suggests that any decrease in the sharpness of one fragment must be accounted for by an increase in the sharpness of an adjacent fragment or broken away.



**Figure 8.12 – Micro-CT 3D renders and cross sections of (a) a round-edged fragment and (b) a corresponding fragment previously adjacent to fragment (a). The cross sections closest to the blue asterisks are the corresponding cross section locations.**

This sub-section has presented the main results from this sharpness investigation. The following sub-section overviews the conclusions from this work.

### 8.3.6 Conclusions

Section 8.3 has discussed the results of pre-sharpness assessments, fracture patterns, and sharpness assessments of fragments from non-uniformly tempered glass discs broken by impact.

The main conclusions of this investigation are as follows:

- All fractured non-uniformly tempered discs had fragments of a range of different sizes and shapes. Specifically, large rounded fragments were produced in locations that roughly corresponded to the positions of cooling jets during tempering, and smaller straight-edged fragments with acute included angles were encountered elsewhere.
- No significant differences were found between the x-axis parameters of straight-edged fragments from samples subjected to low and high cooling rates. The penetration forces of these samples were similar to those measured for fragments from annealed pint glasses.
- Significant differences were found between the performance of rounded fragments and straight-edged fragments during slash tests. Rounded fragments were found to penetrate to a lower depth than straight edge fragments, and required a greater force to propagate the cut.
- Micro-CT scans showed that edges of rounded fragments were rounded in both the x-y and y-z fractographic planes. However, this meant that adjacent fragments had pointed features. These were in some cases delicate, and may break off in practical circumstances. Overall it was observed that non-uniformly tempered glass produced fragments with a range of levels of injury potential.

Recommendations for how the investigation could be improved or extended are given below.

- Changing the spacing between cooling jets would alter the lateral spread of residual stresses. This would enable the effects of non-uniform tempering on sharpness properties to be more fully characterised.
- Investigating the application of a non-uniform tempering process to pint glasses could determine whether fragments with lower injury potential could be produced in critical areas of the pint glass.

## **8.4 Sharpness properties of fragments from thermally and chemically tempered glass**

### **8.4.1 Introduction**

This section details an investigation into the sharpness properties of fragments from thermally and chemically tempered flat glass broken by ring-on-ring testing. Annealed samples were also tested for comparison. The specific aims of this investigation were to:

- Investigate whether the high localised compressive surface stress state present in chemically tempered glass significantly affects the sharpness properties of the resulting fragments when broken.
- Investigate the effects of large loading stresses on fragment sharpness, achieved by fracturing glass samples in their as-received state (no surface pre-damage applied).
- Assess the use of equibiaxial ring-on-ring testing for use as part of a standardised sharpness assessment method.

The thermally and chemically tempered glass discs used for this investigation were tempered externally, as detailed in section 3.3.2. The thermally tempered discs were more uniformly tempered than those detailed in the previous section, and enabled a more representative assessment of commercially tempered glass. Although the chemical tempering of pint glasses is not performed commercially, it is considered here to further elucidate whether glass surface treatments affect the inherent sharpness of the resulting fragments when broken, rather than the glass loading conditions being the main influencing factor.

The structure of this section follows that of previous sections in this chapter. The following sub-section overviews the pre-sharpness assessment stage of the investigation, which is followed by the results of the sharpness assessment tests conducted. An overall discussion of the results is presented at the end of the section.

#### 8.4.2 Pre-sharpness assessment analysis and fracture

A summary of the pre-sharpness analysis stage of this investigation is given in Table 8.11 below.

Glass samples:	30 3.82 mm thick flat discs: 10 x annealed (75 mm diameter), 10 x chemically tempered (75 mm diameter), 10 x thermally tempered (80 mm diameter)
Tempering/annealing processes:	As-received (annealed), thermally and chemically tempered as per sub-section 3.3.2
Residual stress assessment:	SCALP, punch test.
Surface pre-damaging:	Vickers indentation as per sub-section 3.5.1 for disc samples
Fracture method:	Ring-on-ring as per sub-section 3.6.1.3

**Table 8.11 – Pre-sharpness analysis summary table for investigation of sharpness of fragments from equibiaxially fractured discs.**

A total of 30 discs were used for ring-on-ring tests, which included 10 annealed, 10 thermally tempered and 10 chemically tempered samples. Despite the discrepancy in sample dimensions for the thermally tempered samples, both disc sizes detailed in Table 8.11 were eligible for the

same ring-on-ring testing configuration according to the ASTM C1499 standard method [2]. A summary of key measured and calculated values is given in Table 8.12 below.

	Mean surface compression /MPa	Vickers hardness (0.5 kgf) /GPa ‡	Flaw size (2c) / $\mu\text{m}$	Indented samples failure stress /MPa	As-received samples failure stress /MPa
Annealed	$-9 \pm 2$ *	$5.73 \pm 0.2$	$73 \pm 5.9$	$130.2 \pm 5.9$	$285.6 \pm 68.9$
Thermally tempered	$-150 \pm 14$	$5.61 \pm 0.13$	$38.8 \pm 4.3$	$278.3 \pm 60.2$	$349.7 \pm 12.9$
Chemically tempered	$\sim -557$ †	$6.03 \pm 0.06$	$40.7 \pm 4.5$	$163.9 \pm 9.2$	$842.8$ $\psi$

**Table 8.12 – Residual stress, indentation, flaw size, and strength data for flat glass disc samples. Values shown are the mean  $\pm$  the standard deviation.**

\* Taken from measurements of the same glass sheets detailed in section 7.2.2.2.

† Estimated from failure stress of a validly fractured as-received chemically tempered sample minus the average failure stress of as-received annealed disc samples. It is therefore subjected to a high degree of error, likely to be within the region of  $\pm 100$  MPa.

‡ Calculations based on measurements of spare disc samples, not the central Vickers indentations used as an initiating flaw.

$\psi$  Failure stress of the only valid fracture reported.

**Residual stress assessment:** The residual stress was evaluated quantitatively by SCALP measurement only for thermally tempered discs. The SCALP is unsuitable for the measurement of chemically tempered glass, because the compressive layer case depth is likely to be much smaller than the diameter of the laser beam used for the measurement of the scattered light intensity [3].

SCALP measurements were taken at the centre of 10 thermally tempered discs prior to conducting ring-on-ring tests. 5 repeat measurements were taken for each sample, and the peak central tensile stress and the near-surface (surface at the laser entry side) compressive stress values were noted. It was found from initial measurements that the variation between values taken at perpendicular orientations was less than the overall sample-to-sample standard deviation. The discs were therefore assumed to have an isotropic stress distribution at the measurement location, and one orientation was used to characterise the residual stress state. The results from these measurements are summarised in Table 8.12.

The overall average near surface compressive stress was  $-150 \pm 14$  MPa, and the overall central peak tensile stress was  $65 \pm 7$  MPa. A spare thermally tempered sample subjected to a punch test is shown in Figure 8.13, which showed a far greater fragmentation density and a more consistent fragment size than the non-uniformly thermally tempered glass in the previous section.

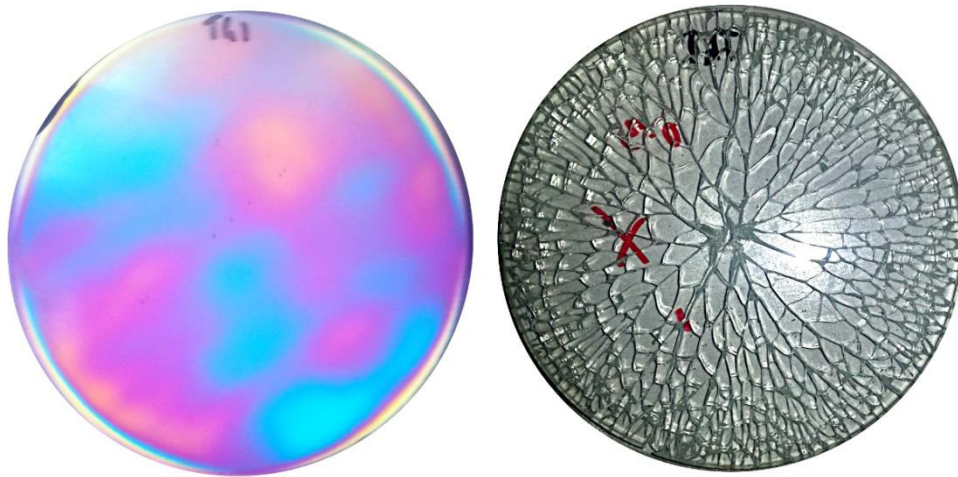


**Figure 8.13 – Photoelastic pattern as viewed in a plane polariscope with a tint plate (left) and fracture pattern due to a punch test (right) of a uniformly thermally tempered glass disc sample. The punch location was at the centre of the disc.**

**Pre-damaging by Vickers indentation:** 5 samples of each type (annealed, thermally tempered, and chemically tempered) were indented centrally (as demonstrated previously in Figure 3.13) with a nominal load of 0.5 kgf prior to ring-on-ring testing. In addition to simulating real-life wear, this was done as an attempt to regulate the fracture stress over the various samples. The remaining 15 samples were left in their as-received condition.

Due to a technical error, the actual applied load for Vickers indents was lower than the nominal load of 0.5 kgf. The measurements from the Vickers indents imparted centrally to each sample were therefore not used for the calculations of the Vickers hardness values shown in Table 8.12. Instead, an array of 5 indents at an actual load of 0.5 kgf was imparted onto a spare sample of each type for the reported Vickers hardness values.

An indentation load of 0.5 kgf was chosen because this appeared to result in the least overall variation in the flaw size without causing significant lateral crack effects in the chemically tempered glass samples. An example indent for each glass type is shown in Figure 8.14. The flaw sizes reported in Table 8.12 were calculated by taking the average length of  $2c$  (see Figure 3.12) parallel to each indent diagonal. The flaw sizes were relatively consistent between chemically and thermally tempered samples. The flaw sizes for the annealed samples were greater than for the other sample types, primarily due to the larger propagation lengths of the median/radial cracks.

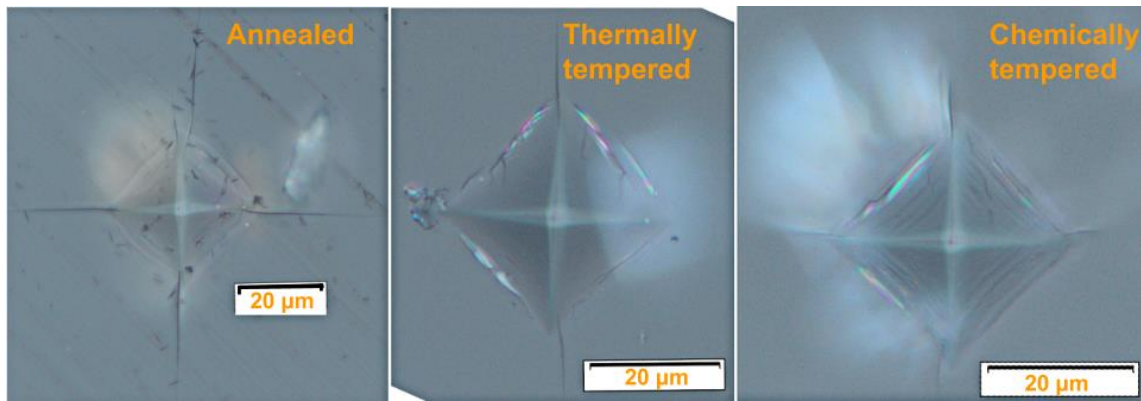


**Figure 8.14 – Example Vickers indents imparted into annealed, thermally tempered, and chemically tempered flat glass samples.**

**Macroscopic fracture patterns:** An example fracture pattern of a sample from each test category is shown in Figure 8.15. A summary of the failure stresses from the ring-on-ring tests is given in Table 8.12, which were calculated using equation 3.4. For this equation to be valid, the fracture origin location must be within the span of the central loading ring. All indented samples broke from the indentation location and were therefore valid. Additionally, all as-received annealed and thermally tempered discs fractures were valid. However, for the as-received chemically tempered samples, only 1 out of 5 discs constituted a valid failure. The other 4 discs fractured from edge flaws at failure stresses between 403-681 MPa.

Indented chemically tempered samples showed only a modest increase in strength compared to indented annealed samples, and the two had similar fracture patterns. This was expected since the case depth of the compressive stress layer was likely to be smaller than the indentation depth. Indented thermally tempered glass samples were on average able to withstand twice the external tensile stress than indented annealed glass samples, and exhibited extensive fragmentation. However, the fragments near the centre of the discs were elongated compared to fragments outside the span of the support ring.

The failure stresses for all as-received samples were greater than for all indented samples. The one valid fracture of the as-received chemically tempered glass discs resulted in the largest tensile failure stress recorded over the course of testing (~843 MPa). Fractured as-received samples were accompanied by a high frequency of very small fragments within the span of the support ring, particularly for the chemically tempered samples. Additionally, as-received samples showed secondary fractures that appeared to correspond to the circumference of the support ring. Thermally tempered as-received samples showed similar fragmentation characteristics to the indented thermally tempered samples, although a greater level of fragmentation was observed in the central region of the former.

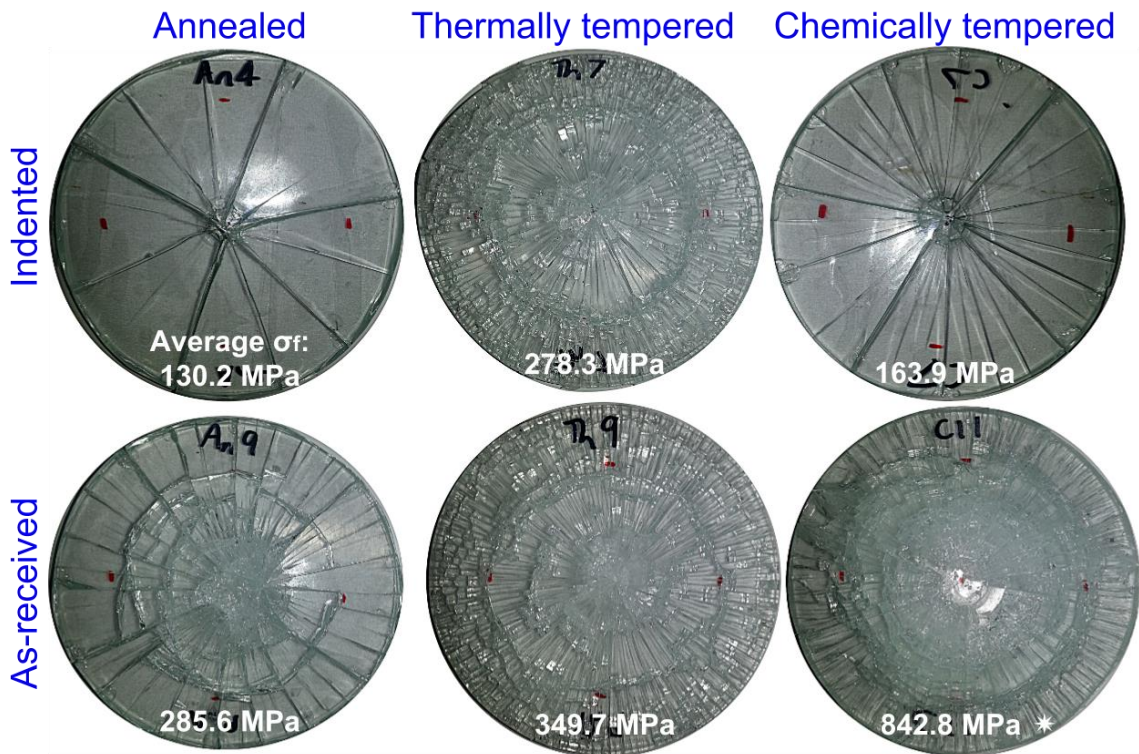


Figure 8.15 – Example fracture pattern for each test category for the investigations detailed in section 8.4, with average failure stresses labelled for convenience. Other sample data is summarised in Table 8.12. \* Value based on one sample due to others resulting in non-valid fractures.

**Fracture surfaces:** Example fracture surfaces of fragments from annealed, thermally tempered and chemically tempered samples are shown in Figure 8.16. Annealed and thermally tempered fragments showed generally similar fracture features to those detailed in previous sections (sections 7.2, 7.3, 8.3) and are therefore not discussed in detail here. However, most fracture surfaces of all types showed a featureless region near the tensile side that corresponded to the location of the support ring. This is indicated by a yellow asterisk in Figure 8.16. This is likely to be due to localised compressive stresses imposed by the support ring. The indented chemically tempered sample fracture surfaces appeared to be very similar to those of indented annealed samples, due to the similar breakage energies involved. However, as-received chemically tempered sample fracture surfaces showed thick and dense mist hackle regions as shown in Figure 8.16.

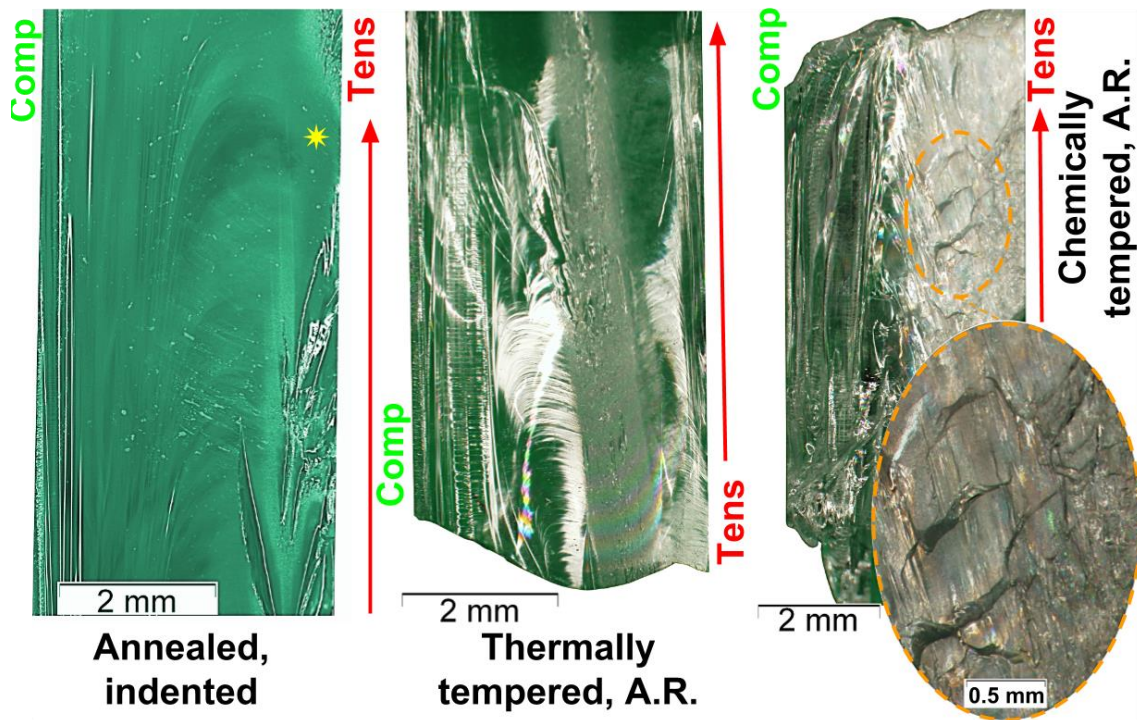


Figure 8.16 – Three example fracture surfaces from flat discs broken by ring-on-ring testing with tensile and compressive sides labelled. Yellow asterisk denotes location above support ring where the propagating crack decelerates.

This sub-section has detailed the pre-sharpness assessment analysis conducted for annealed, thermally tempered, and chemically tempered glass discs. Results from the sharpness assessments conducted are detailed in the following sub-section.

**8.4.3 Sharpness assessment: overview**

A summary of the sharpness assessment tests and analyses conducted on fragments from glass disc samples is given in Table 8.13 below.

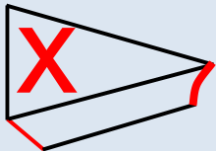
 <p>x-axis edges</p>	Optical profile analysis	Selected fragment profiles (4 x C)
	SEM analysis (tip radii)	None
	Penetration testing	Selected fragments (4 x C)
 <p>y-axis edges</p>	Micro-CT cross-sections and 3D analysis (included angles)	Selected fragments (6) and small as-received fragments (9)
	Replica sections (edge radii)	None
	Slash test	Selected fragments (8 x C)

Table 8.13 – Sharpness analysis summary table for investigation of sharpness of fragments from equibiaxially fractured discs. Tests used exclusively on fragments from chemically tempered glass are indicated by the letter C.

Fragments from chemically tempered glass disc samples were prioritised for sharpness analysis because sharpness tests on fragments from annealed and thermally tempered glass are detailed elsewhere in this thesis. However, because the majority of fragments from as-received chemically tempered discs had maximum lengths shorter than 10 mm, they were not eligible for penetration or slash tests. Therefore the penetration and slash tests detailed in the following sub-sections are only based on indented chemically tempered samples.

The as-received fractured samples all had a large quantity of small fragments located in the central region which corresponded to the loading ring location, as shown in Figure 8.15. Similar small fragments were noted for the pint glass fracture investigations in chapter 4, which were present alongside glass dust. Three of these small fragments were taken from each as-received sample type and subjected to micro-CT scans for a qualitative sharpness assessment. Additionally, larger fragments were taken for all sample types from the central region for micro-CT analysis to view cross sections and near-edge geometry in three dimensions.

#### **8.4.4 Sharpness assessment: x-axis edges of chemically tempered fragments**

Only the x-axis edges of four chemically tempered fragments were subjected to sharpness assessments, for the reasons discussed in the previous sub-section. The average profile plot of these fragments is shown in Figure 8.17, and full geometrical parameter data is given in Appendix O.

The profile shape was similar for each fragment, and shows a cantilever curl effect not unlike the x-axis profiles in section 7.3.4.2. This profile shape was similar to that found on annealed x-axis edges sampled at the same near-impact location. This was expected given the similarity in fracture patterns for both indented annealed and chemically tempered disc samples. The average penetration force of ~16 N is similar to that measured for annealed pint glass fragments and fragments in the top region of tempered pint glasses.

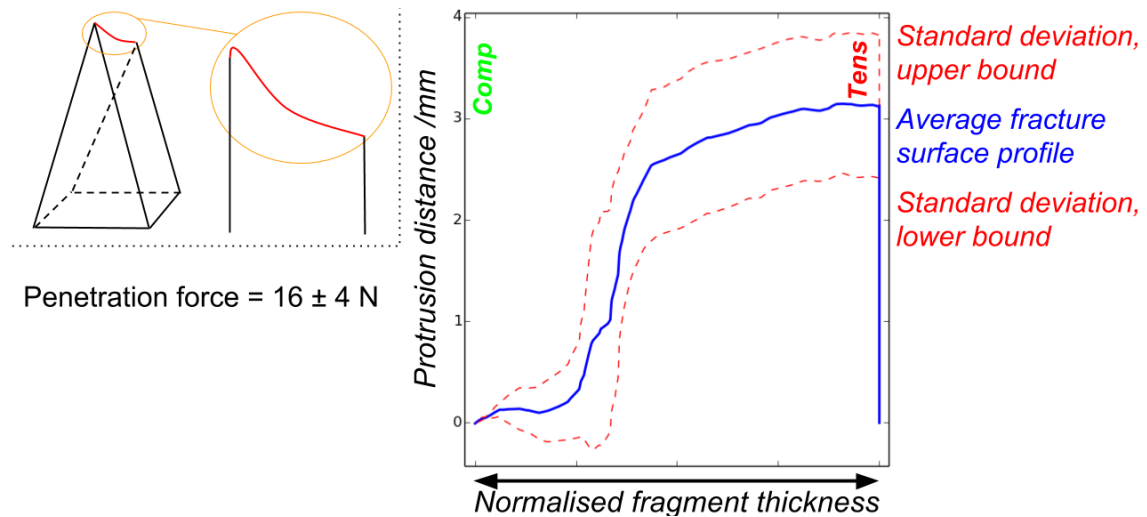


Figure 8.17 – Average profile morphology (solid blue line) of 4 selected near-origin out-out x-axis edges from indented chemically tempered discs. Upper and lower standard deviation profile bounds are plotted with dashed red lines. Inset shows x-axis profile context.

#### 8.4.5 Sharpness assessment: y-axis edges of chemically tempered fragments

This sub-section presents and discusses the results of slash test sharpness assessments of y-axis edges on glass fragments from indented chemically tempered glass disc samples. Both the compressive side edges and the tensile side edges were tested. All slash test results gathered in this analysis are shown in Table 8.14.

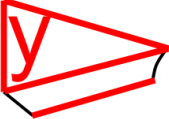
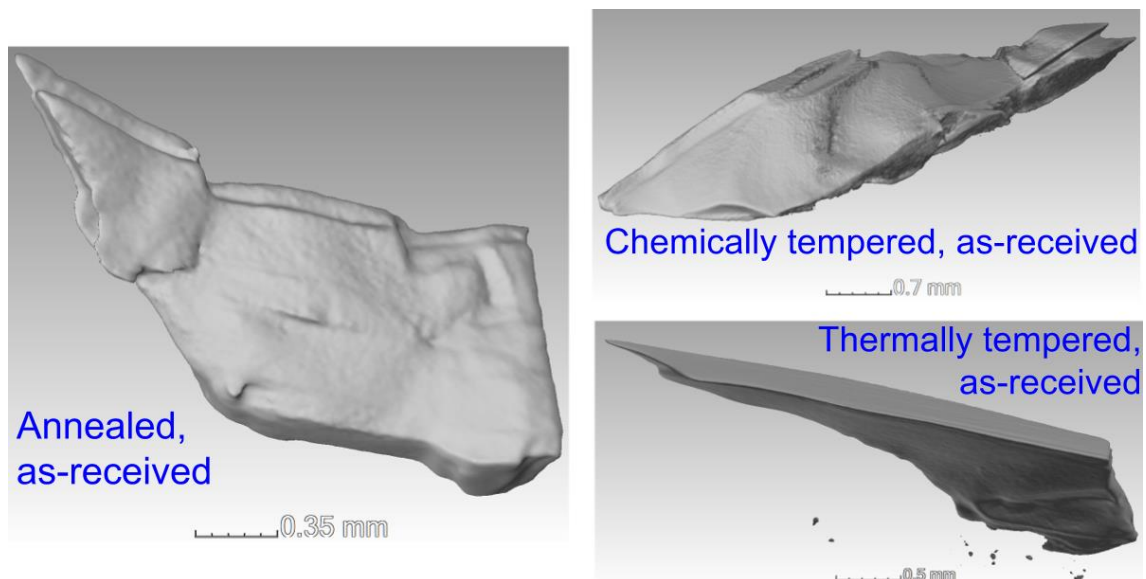
	Compressive side	Tensile side	All edges
	(n = 4)	(n = 4)	(n = 8)
<b>Fragment cutting/slashing tests</b>			
Penetration depth /mm	0.33 ± 0.20 (61)	0.62 ± 0.11 (18)	0.48 ± 0.22 (46)
Average load in steady state /N	3.0 ± 0.5 (17)	3.4 ± 0.2 (6)	3.2 ± 0.4 (14)
Friction coefficient	0.36 ± 0.06 (17)	0.41 ± 0.03 (7)	0.39 ± 0.05 (13)

Table 8.14 – Summary of slash test data collected for y-axis edges of fragments from indented chemically tempered discs broken by ring-on-ring loading. In each case the average value is shown ± one standard deviation. The percentage of the standard deviation compared to the average value is shown in parentheses. All parameters listed in this table are described in section 6.5.

Tensile side y-axis edges penetrated to a greater depth on average compared to compressive side edges, but this was not judged to be statistically significant by Student's *t*-tests with a 5% significance level. The average overall friction coefficient of 0.39 is among the lowest of the slash tests conducted in this thesis. However, since other fragments from different sample types broken by ring-on-ring testing were not subjected to the same tests, it is not possible to determine whether this is due to the chemical tempering process or the fracture method.

#### 8.4.6 Micro-CT analyses

Three examples of micro-CT images of small glass dust fragments are shown in Figure 8.18. The shape and sizes of all fragments varied considerably, and no differences in morphology due to sample type could be distinguished. The as-received thermally tempered fragment shown in the bottom right was taken directly from the tensile surface, as demonstrated by its one straight side. All fragments appeared qualitatively sharp, usually with one or more notably pointed edges. It would be expected that low forces would be required for skin penetration with these fragments, however, their potential for serious injury would be limited by their small size.



**Figure 8.18 – Examples of 3D renders of small ‘dust’ fragments from the central region of as-received fractured samples.**

Examples of micro-CT images of fragments from as-received disc samples are shown in Figure 8.19 and Figure 8.20. A large variation in profile morphology near to the compressive side was observed, similar to trends discussed in chapter 7. This was particularly noticeable in the cross sections shown in the top right image of Figure 8.19 and the top image of Figure 8.20. Both fragment types were fragile and prone to damage during handling, as indicated by the high frequency of cracks visible in the cross sections. The near-edge raggedness of the chemically tempered fragment in particular may be expected to increase the force required to propagate a cut during slashing. This raggedness is highlighted by the anaglyphs.

This sub-section has presented the main results from this sharpness investigation. The following sub-section overviews the conclusions from this work.

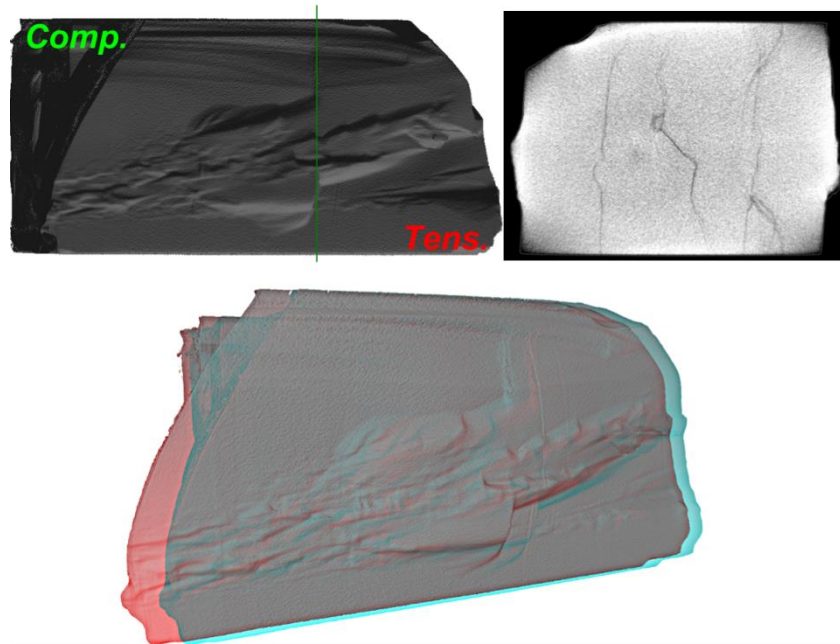


Figure 8.19 – Micro-CT images of a fragment from an as-received fractured thermally tempered glass disc. Top left: 3D render of the fragment. Top right: Cross section at green line in top left image, showing blunted corner of one edge, and protrusion from surface caused by mist hackle region. Bottom: Anaglyph to show fracture surface morphology. An optical micrograph of the same fracture surface is given in Figure 8.16.

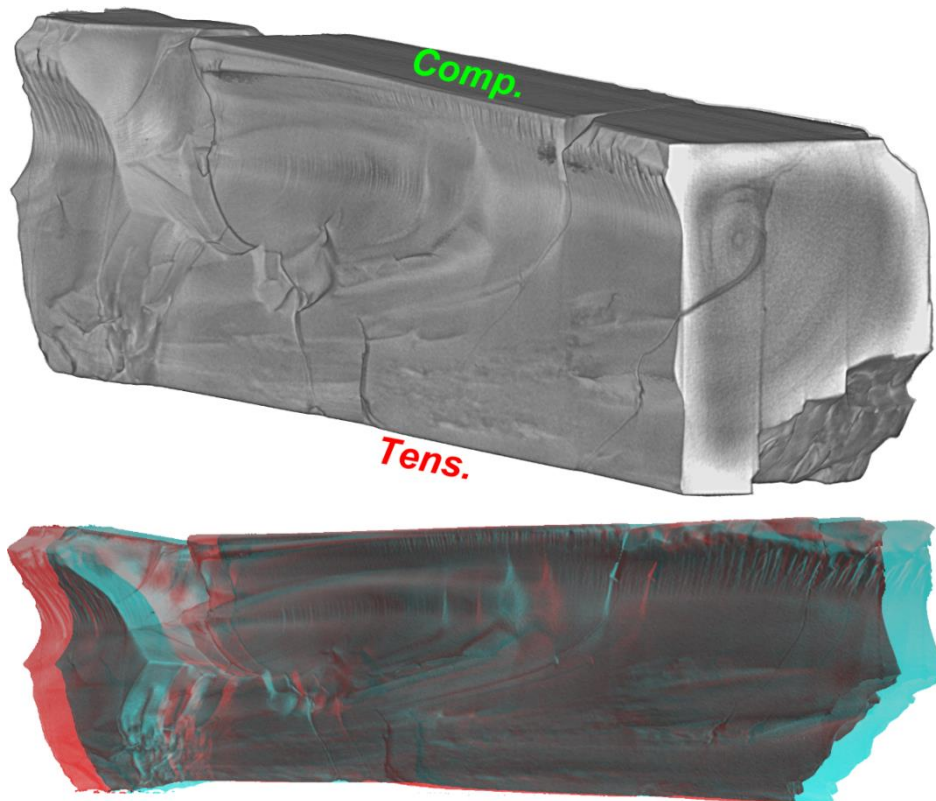


Figure 8.20 – 3D renders of a fragment from an as-received fractured chemically tempered glass disc obtained by a micro-CT scan. Top: Cross-sectioned image showing opposite cantilever curl effects near to the compression side. Bottom: anaglyph of the fracture surface, demonstrating the curved near-edge morphology.

### 8.4.7 Conclusions

Section 8.4 has discussed the results of pre-sharpness assessments, fracture patterns, sharpness assessments, and qualitative micro-CT sharpness assessments of fragments from glass discs broken by ring-on-ring loading.

The main conclusions of this investigation are as follows:

- The use of ring-on-ring loading to fracture glass discs produced fragments of various sizes, which corresponded to the fragment location relative to the loading and support rings in the macroscopic fracture pattern. This permitted the sharpness assessment of fragment edges created at different external loading stresses within the same sample. However, this effect was not observed for indented annealed and chemically tempered discs due to the low load involved to cause fracture.
- There was little evidence to show that the high localised compressive stress state present in chemically tempered glass resulted in fragment edges with different sharpness properties to fragments other glass types when broken. However, the high load required to cause fracture had a marked effect on the macroscopic fracture pattern which resulted in dense fragmentation local to the area of the highest externally applied stress. The resulting fragments appeared qualitatively sharp, but their injury potential would likely have been limited due to their small size.
- The  $\gamma$ -axis edge morphology of fragments varied significantly from sample to sample. This appeared to be due to cantilever curl effects.

Recommendations for how the investigation could be improved or extended are given below:

- Investigating the sharpness of fragments from different areas of the sample relative to the load and support rings would enable a comparison between sharpness properties of edges created by different levels of stress.
- Further sharpness assessments of corresponding areas of annealed and thermally tempered glass fragments would permit further comparison with chemically tempered glass fragments.
- Additional contact-based sharpness assessment methods (e.g. penetration and slash testing) suitable for assessing the sharpness of very small fragments present in broken thermally tempered glass and broken as-received chemically tempered glass would enable broader practical assessments of glass fragments.

## 8.5 Chapter summary

This chapter has presented three investigations into the sharpness properties and cutting performance of glass fragments from various glass samples. This included fragments from broken pint glasses, non-uniformly tempered glass discs, and chemically tempered glass discs. The measurement of sharpness of glass fragments is a complicated problem, and this chapter presents one approach for doing so.

Section 8.2 investigated the x-axis edge profile morphology and penetration force of fragments from pint glasses, alongside y-axis edge geometrical measurements, and the slashing ability of side-looping fragments (introduced in chapter 4). A modified Vickers indenting technique was used to reproducibly pre-damage pint glasses. It was found that fragments from tempered pint glasses near to the glass base required on average  $\sim 3$  times more force to penetrate a skin simulant. The penetration force of near-rim fragments from tempered glasses was comparable to that of annealed glass fragments, although the tempered fragments were notably smaller and therefore may not practically pose the same level of injury potential. Additionally, y-axis edges of annealed looping fragments penetrated to a depth 4-5 times greater than the equivalent edges of tempered looping fragments.

Section 8.3 investigated the sharpness properties of fragments from broken non-uniformly tempered glass discs. A large variation in fragment size and shape was noted, with larger rounded fragments present at locations that roughly corresponded to the location of cooling jets during tempering. Smaller straight-edged fragments with acute angles were encountered elsewhere. Rounded fragments were found to penetrate to a lower depth and required a greater force to propagate a cut compared to straight-edged fragments. Micro-CT scans showed that the reduced sharpness of rounded fragments may be offset by an increase in the sharpness of adjacent straight-edged fragments.

Section 8.4 involved the use of a ring-on-ring loading method to reproducibly fracture annealed, thermally tempered and chemically tempered glass discs. The fracture patterns of the discs corresponded to the external loading stress distribution imposed by the ring-on-ring method and provided opportunities for sharpness assessments of various fragment sizes. Cantilever curl effects were observed to influence the geometrical features near to the compressive side in micro-CT scan images. The results did not present enough evidence to determine whether the chemical tempering process results in different sharpness properties to annealed or thermally tempered glass fragments. However, the increased strength of as-

received chemically tempered glass resulted in notably small fragments after fracture, which limited their potential to cause serious injury.

The following chapter discusses the key findings from this chapter and the thesis as a whole, and places the findings in their real-life context.

## 8.6 Chapter references

- [1] R. Gardon, "Thermal Tempering of Glass," in *Glass: Science and technology, Volume 5, Elasticity and Strength in Glasses*, D. R. Uhlmann and N. J. Kreidl, Eds. Academic Press, New York, 1980, pp. 145–216.
- [2] ASTM C1499-09(2013), Standard Test Method for Monotonic Equibiaxial Flexural Strength of Advanced Ceramics at Ambient Temperature, ASTM International, West Conshohocken, PA, 2013, [www.astm.org](http://www.astm.org).
- [3] GlasStress Ltd., "Scattered Light Polariscopes SCALP-04, Instruction Manual ver 4.5.1." .

## 9 Conclusions and further work

### 9.1 Key findings and significance

This thesis has presented empirical research into the injury potential of pint glasses with particular emphasis on the effect of thermal tempering processes. Additionally, original methodologies and testing equipment have been detailed, which assisted the assessment of the injury potential of glass fragments from various annealed and thermally tempered glass articles. This section outlines the main findings from the work and discusses their contextual significance. These findings are outlined under three main headings: pint glass fracture properties, characteristics of glassing attacks, and the sharpness of glass fragments. A further sub-section is included which discusses the findings within the context of the establishment of a standard for tempered pint glasses.

#### 9.1.1 Pint glass fracture properties

The fracture of pint glasses was considered in the most detail in chapter 4 of this thesis. This involved fracturing glasses by external impact and punch tests, examining the fracture characteristics, and considering finite element simulations, glass shape, residual stress measurements, and wall thickness measurements. The key conclusions of this work are outlined below.

- Glasses broken by impact exhibit similar symmetrical fracture patterns. This pattern involves cracks propagating longitudinally near the impact location, looping around the sides of the glass, and propagating longitudinally 180° from the impact location.
- The base of an annealed glass usually remains intact after fracture. By contrast, the base of a thermally tempered glass usually fragments into small cube-shaped pieces. However, for thermally tempered stemmed glassware, the stem and base regions may remain intact after fracture by impact.
- Fragmentation density in the top region (near the glass rim) of annealed and tempered pint glasses is often similar. For thermally tempered glasses, this means that fragments in the top region are larger than fragments in the base region. This is a reflection of the higher level of residual stress in the base region, which itself reflects the greater wall thickness in this region.
- Failure is likely to occur from a critical flaw within the region of tensile stress on the opposite surface of the glass wall to the point at which the load is applied (inward

flexure), or at the glass rim. This was the area of peak imposed tensile stress in finite element simulations.

- Glasses worn from general usage (as opposed to the techniques used to replicate wear) are likely to fail from critical flaws located at the glass rim when subjected to external impact.

### 9.1.2 Characteristics of glassing attacks

Replications of glassing attacks were conducted, some with groups of volunteers, and some with a systematic drop tower methodology. The severity of the attacks and the effect of using different glasses were assessed by measuring the forces involved with the attacks, measuring the duration of the attack events, and the cut patterns made into layers of silicone. These results are considered in detail in chapter 5 of this thesis, and the key conclusions of this work are outlined below.

- Glassing attacks are likely to include a number of key impact events, most likely due to: initial impact force (which may or may not include breakage), a secondary impact with another portion of the glass (if not broken by initial impact force), and the follow-through of glass fragments and the attacking hand. Additional force peaks recorded in this study may have been due to impact/deflection of the glass-securing safety fixture. Force peaks were more apparent for attacks involving lower forces.
- The overall average maximum force from all glassing attacks by slapping (23 participants, 74 tests) was 706 N with a standard deviation of 346 N. However, this may be an overestimate of the true force involved with a slapping attack due to the added weight of the fixture used to hold the glasses for safety reasons. Additionally, forces in actual attacks may be lower due to the compliance of the target. Throws with intact pint glasses resulted in significantly less force (~120 N) than in attacks by slapping or thrusting.
- The majority of damage caused in a pint glass slapping attack is centred around the impact point and is largely affected by the dimensions of the impact target and how the glass is held. Glasses held over a wider area of the glass wall are more likely to cause a wider spread of damage during the follow-through event of the attack after glass fracture.
- Attacks with tempered pint glasses were seen to result in either more damage areas or an equal amount of damage areas to annealed pint glasses. However, the damage caused by annealed glass resulted in longer cuts and deeper punctures than tempered

glass, and resulted in more damage to the equipment used. The maximum cut/puncture length observed from a tempered glass was 20 mm, and 36 mm from and annealed glass.

### 9.1.3 The sharpness of glass fragments

Sharpness was used in this study as a means of qualitatively or quantitatively describing the ease at which an object can penetrate a target, thereby contributing to an understanding of the injury potential of a fragment. The assessment of the sharpness of glass fragments is complex and was discussed in depth in chapter 6 of this thesis. Methodologies were developed that enabled the forces involved with the penetration of glass fragments into a skin simulant to be estimated, as well as providing a comparative measure of the force required for various fragments to propagate a cut. These methodologies were used for the work in chapters 7 and 8 of this thesis, alongside a detailed geometrical analysis of sharpness.

Chapter 7 used a customised thermal tempering apparatus to enable a comparative assessment of fragments from glass of varying residual stress levels. Chapter 8 complemented these results by presenting investigations into the sharpness of fragments from pint glasses, and glass subjected to other treatments and loading conditions. The key conclusions of this work are outlined below.

- Although the small fragment sizes from broken tempered samples limited the available contact-based sharpness assessments, no significant differences were found between the measured geometrical parameters of fragments from samples of various temper level broken by three point bending.
- The comparison of fragments from annealed glass samples to fragments from tempered glass samples was complicated by the considerable differences in fragment sizes. However, limited SEM tip radii measurements of edges were similar for both fragment types, and generally ranged between  $\sim 1\text{-}11\ \mu\text{m}$ .
- The average forces required for pint glass fragments to penetrate a skin simulant varied from 16 N to 48 N. The lowest average penetration forces were recorded for fragments from annealed pint glasses and fragments from near to the rim of tempered pint glasses. Fragments closer to the base of tempered pint glasses required  $\sim 3$  times more force to penetrate the simulant. This is a reflection of observations from pint glass fracture assessments, where fragments near to the rim of tempered pint glasses were regularly comparable in size to those of annealed glasses. It should be noted however that the observed near-rim fragment sizes from tempered glasses tested in

this investigation were consistently smaller than corresponding fragments from annealed glasses.

- All fractured non-uniformly tempered glass samples contained fragments of a wider range of sizes and shapes than other types of glass samples. Specifically, large rounded fragments were produced in locations that roughly corresponded to the positions of cooling jets during tempering; and smaller straight-edged fragments with acute included angles were encountered elsewhere. Rounded fragments were found to produce shallower cuts compared to straight-edged fragments during slash tests, and require a greater force to propagate the cut.
- Geometrical parameters on the free surface side of fragments (y-z fractographic plane) were observed to be the most influential on penetration forces. Additionally, cantilever curl effects were consistently observed on fragment cross sections and may bear a significant influence on the cut propagation forces observed in slash tests.

#### **9.1.4 Establishment of a standard for tempered pint glasses**

In order to establish a thermally tempered pint glass standard for safety purposes, the fracture characteristics that constitute safe breakage need to be determined. However, there are no universally accepted desired breakage criteria for pint glasses, and in some cases, manufacturers may intentionally limit fragmentation to certain regions of an article<sup>††</sup>. The basis of safe breakage criteria may only be possible from field testing of pint glasses of known parameters and properties, or by biomechanical reconstructions of attacks with pint glasses.

It was shown in chapter 4 that fragmentation of the near-rim region of thermally tempered pint glasses was far less dense than fragmentation of the base region. Additionally, levels of residual stress appeared to correlate to the wall thickness of the glasses. Key aspects of a tempered pint glass standard may include the specification of a minimum fragment count for both the rim and base regions, as well as a minimum glass wall thickness. In addition, a minimum impact resistance with regulated impacting equipment would provide a means to ensure that an adequate strength increase has been achieved.

Chapters 5-8 further investigated injury potential, in order to provide a basis for the requirements prescribed by a standard method. Force measurements in chapter 5 showed that high forces can be involved in glassing attacks that considerably surpass the forces required for penetration of both annealed and tempered fragments into skin, as measured in

---

<sup>††</sup> Glass Technology Services, private communication.

chapters 6, 7, and 8. However, observations of cut damage patterns and depths in chapter 5 showed that the damage caused by tempered fragments is likely to be less severe.

The multi-layered silicone target tests detailed in chapter 5 may provide a good comparative test for pint glasses when considering their relative injury potential. These tests provide a more convenient means of determining injury potential than the cutting performance methodologies and geometrical assessments detailed in chapter 6. Furthermore, the multi-layered silicone target tests may be more appropriate as they give more of an indication of the effects on injury potential caused by fragment size.

## 9.2 Further work

This thesis has reviewed existing work relating to glass fracture and injury potential, has developed original methodologies and equipment for assessing the sharpness and injury potential of pint glasses, and has contributed empirical research pertaining to the injury potential of pint glasses. This work could serve as a foundation for a number of further studies, suggestions for which are given below.

- Field testing of tempered pint glasses with known properties (e.g. known residual stress distribution) would give an indication of whether specifications from current standards for tempered flat glass are suitable for reducing the injury potential of pint glasses. This would require the comparison of records of injuries/assaults with pint glasses (reported separately from incidents involving glass bottles) before and after the introduction of the tempered pint glasses.
- The multi-layered silicone target glassing tests detailed in section 5.4 of this thesis could be used or adapted to allow for a comparative assessment of the injury potential of various pint glasses. This could provide a further foundation for a tempered pint glass standard based on injury potential, using a maximum number of cuts and/or maximum cut depth that is considered acceptable.
- Adapting the glass fragment stab and slashing tests detailed in section 6.5 of this thesis to allow smaller fragments to be tested would improve the versatility of the methods. However, that smaller fragments could not be used with these tests is to some extent a reflection of their reduced injury potential in practice. Additionally, adapting the slash test so that fragments penetrate to the same depth prior to the slashing procedure would enable cut propagation forces to be better compared.
- The sharpness assessment of fragments from glass samples of variable temper levels detailed in section 7.3 of this thesis could be improved by using glass samples with a

wider range of residual stress. This would enable variations in fragment sharpness due to temper level to be more readily discernible. Additionally, testing fragments further from the area of maximum externally imposed tensile stress may be more representative of the majority of fragments from broken tempered glass articles.

- Extending the non-uniform thermal tempering method used for glass disc samples in section 8.3 of this thesis to pint glasses, and subsequently subjecting them to the multi-layered silicone target glassing tests, would enable the merits of this tempering method for reducing injury potential to be assessed.

### 9.3 Concluding remarks

Glass drinkware is widely used in the UK, but it has also been associated with incidents of violence, particularly with imperial pint glasses. This thesis aimed therefore to examine the injury potential of pint glasses and to provide a foundation for a future standard for tempered drinking glasses.

Detailed methods and processes for preparing comparable glass fragments were outlined in chapter 3. Assessments of pint glass fracture properties, residual stress levels and wall thickness variations were presented in chapter 4. The forces involved with glassing attacks with pint glasses and the subsequent severity and spread of damage were investigated in chapter 5. Methodologies to assess the sharpness of glass fragments were discussed in chapter 6. The sharpness of glass samples of different temper levels was compared in chapter 7. The sharpness of pint glass fragments, fragments from non-uniformly tempered glass, and highly-stressed glass was considered in chapter 8. Finally, the main conclusions of the work were outlined in this chapter and were considered alongside the establishment of a tempered drinking glass standard.

This work contributes to existing research into the effect of thermal tempering processes on the sharpness and injury potential of glass fragments. This could be used in the future for the basis of a pint glass standard, working towards a safer pint glass.

## Appendix A – Hot wire anemometer measurement of jet velocities

This appendix summarises the results from investigations into the air velocity field of the 4-port jet arrays and the flat fan nozzles described in chapter 3. The 4 port jet arrays were used in experimentation to temper glass disc samples, and the flat fan nozzles were used to temper rectangular glass samples.

### A.1 Experimental order and setup

The jet arrays were examined first. Two hot wire anemometers were used simultaneously to measure the air flow velocity through the jet array ports, for various initial compressor pressures. One anemometer was allocated to each jet array (Figure A.1, left), and for each alteration to the cooling routine/setup, measurements were taken from all four ports consecutively. This enabled both individual port velocities to be measured, and also the total difference in air velocity between the two jet arrays. A glass disc was placed centrally between the jet arrays in a slotted steel plate. The anemometers were held by retort stands and positioned 10 mm laterally from each jet array, with the hot wire positioned centrally in front of the port hole of interest. Therefore the velocity values, once calibrated, were taken as the nozzle exit velocities. The voltage output from each anemometer was recorded over a period of 40 seconds, and began logging after the compressor pressure had reached the desired initial value and the LabVIEW cooling routine program had been initiated. This enabled measurement of: the velocity peak from the outstroke of each actuator, the initial air velocity at the time of the jet arrays being switched on, and the rate of decrease of the air velocity following jet array switch-on. Adjustments were made to the pneumatic circuit based on these results to equalise the air flow velocity over the jet arrays (section A.3).



Figure A.1 – Hot wire anemometer setup. Left – anemometers set up to simultaneously take measurements from opposite ports of the jet arrays, right – the position of a single anemometer set up centrally in front of a port.

For flat fan nozzles, one anemometer was used and the air velocity was measured at 9 positions on a 3 x 3 rectangular grid, as shown in Figure A.2. The anemometer was positioned 10 mm laterally from one of the impingement surfaces of a rectangular fragment. Therefore the velocity values, once calibrated, were taken as the impinging velocities. The same voltage output recording procedure as that described for the jet arrays was conducted.

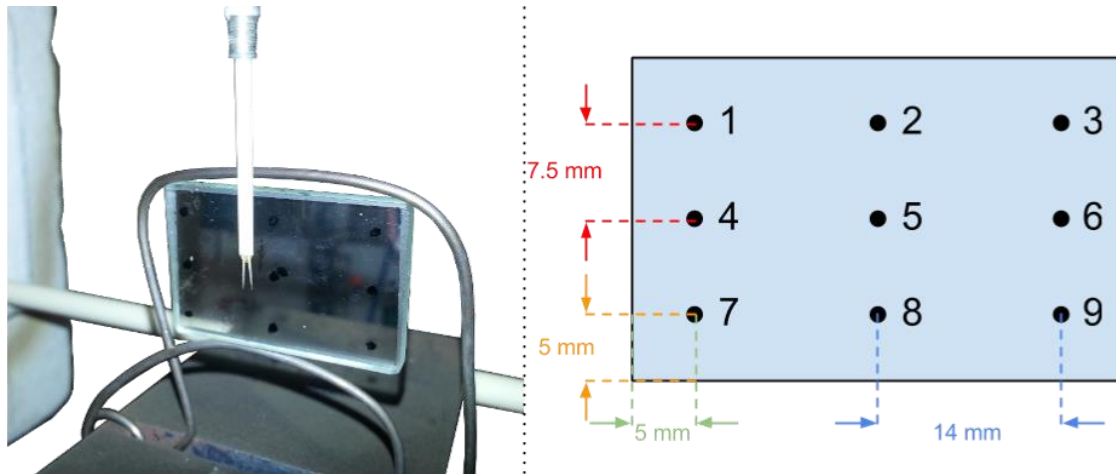


**Figure A.2 – Left: Anemometer positioned centrally in front of rectangular measurement grid. Right: Schematic of anemometer probing grid for measurement of flat fan nozzle velocity field.**

## A.2 Anemometer output and calibration

A graph showing the typical voltage output from an anemometer is shown by the blue line in Figure A.3. The voltage output was logged at a frequency of  $100 \text{ s}^{-1}$  – resulting in a total of 4000 data points per test run. Given that the air leaving each port was turbulent, and that there was air rebounding from the glass sample back towards the anemometer, the raw data output resulted in a rough profile on the voltage output/time graph. In order to extract key values from this raw data, a moving average was applied as shown by the green line in Figure A.3. A suitable number of points to take a moving average over was selected after conducting trials of various averaging interval lengths, and judging by eye the lowest-width interval that smoothed out the raw data line whilst accurately reflecting the general data trend. This was judged to be a moving average of 350 data points, meaning that 1.75 s of data before and after the point in question were averaged for any given data point. The maximum voltage over the time period was then taken as the initial voltage, and the voltages 5 s, 10 s, and 15 s or 20 s after this point were recorded for calculation of the air velocity drop gradient (although, the relationship between the anemometer voltage output and the actual air velocity is not linear).

The voltage output was then calibrated individually for each anemometer using a DISA type 55D41 miniature wind tunnel. The voltage output of the anemometer was measured at

velocities from  $10 \text{ ms}^{-1}$  to  $40 \text{ ms}^{-1}$  in  $2 \text{ ms}^{-1}$  intervals. This covered all voltage outputs measured whilst the jets were on. The data was then fitted to a fourth order polynomial. All reported velocities in this appendix are interpolated from this data.

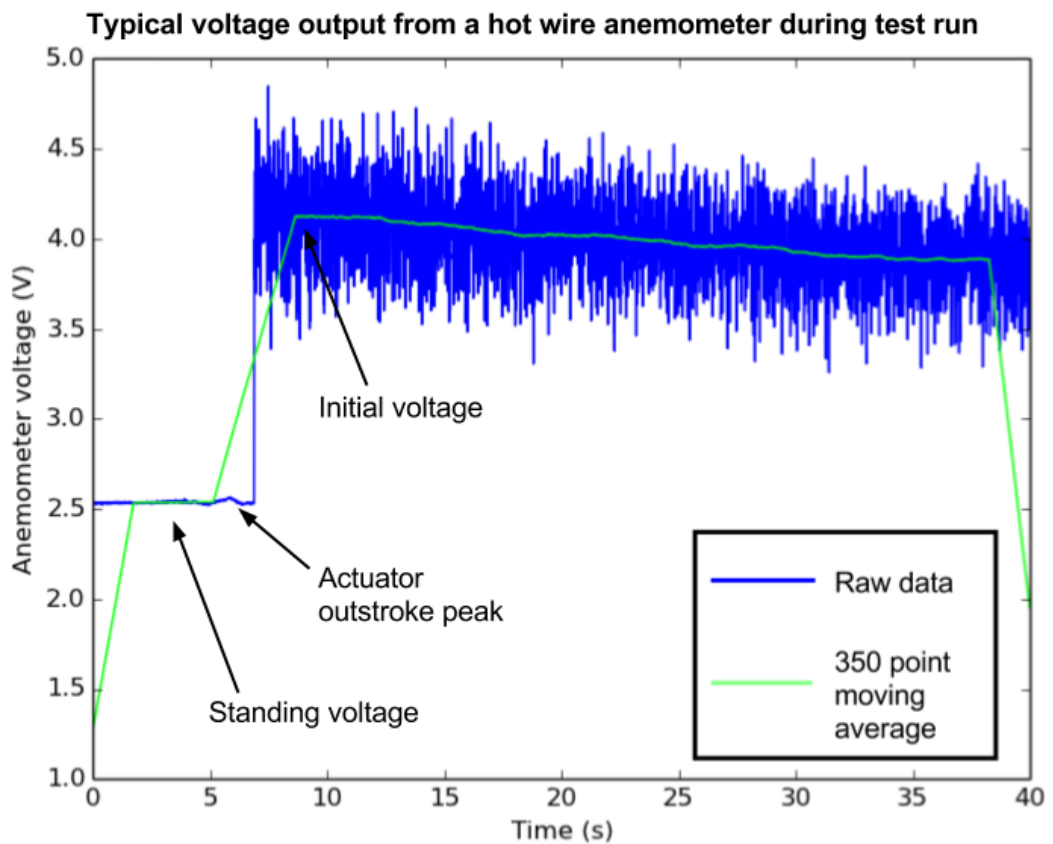


Figure A.3 – Anemometer output over a 40 second test run, shown as raw data and with a 350 point moving average.

### A.3 Equalisation of jet array airflow using tube clamps

Miniature G-clamps were attached to pneumatic tubing where necessary to equalise and regulate airflow through the ports of the 4-jet arrays (Figure A.4).

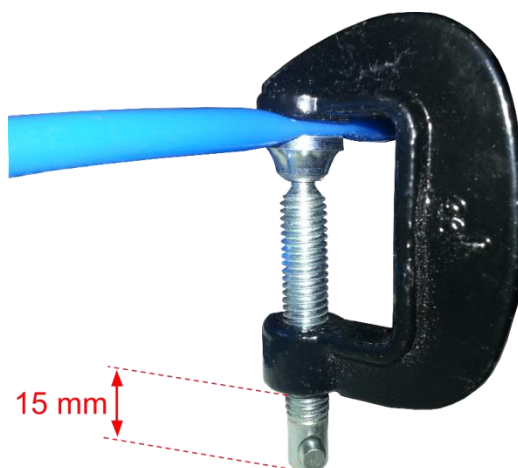


Figure A.4 – Clamp distance measure.

Initial test runs showed much higher velocities from two particular jet ports on each array, as highlighted by red circles in Figure A.5. Applying the clamps to the tubing behind these array ports, and tightening to the clamp distance measure of 15 mm illustrated in Figure A.4 was found to be effective in distributing the airflow. Some small further adjustments were made, and the final distribution of initial air velocities is shown in Figure A.5. This spread was deemed to be adequate with an initial compressor reservoir pressure of 0.3 MPa. The values shown in the figure are the average values over 3 separate measurement runs with the final clamp setup.

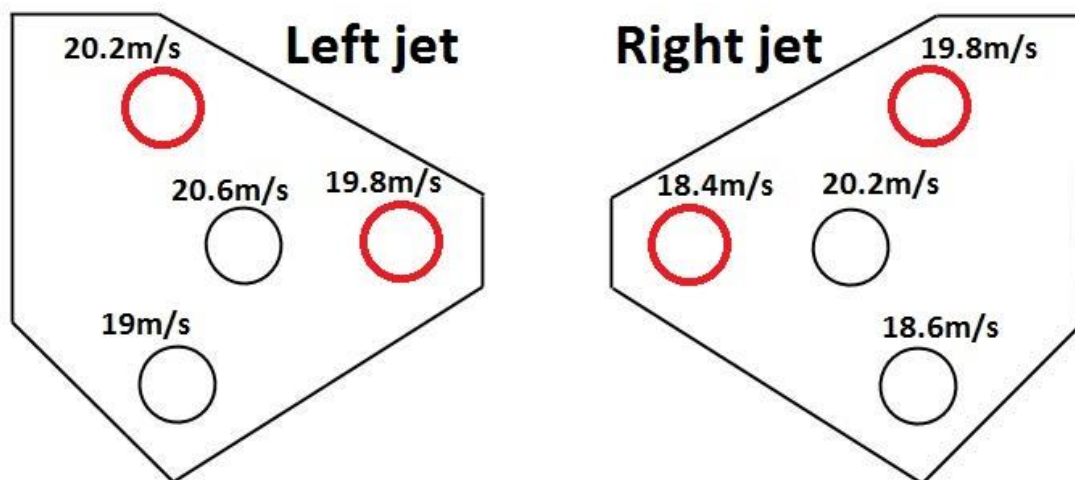


Figure A.5 – Initial air velocity through each port (initial pressure of 0.3MPa) on each jet array after using miniature G-clamps to regulate air flow. Ports highlighted in red indicate where clamps had been used.

#### A.4 Effect of initial compressor pressure changes for jet arrays

The compressor reservoir pressure at the time of jets being switched on was varied from 0.6MPa down to 0.35MPa in 0.05MPa increments. The air velocity was measured for the top port of the left jet array (in the orientation as shown in Figure A.5) and for each different initial reservoir pressure, the test run was repeated three times. The average initial velocity, and the average air velocity after 5, 10, and 20 seconds, are reported in Table A.1.

Test runs with higher initial compressor reservoir pressures resulted in a higher initial air velocity, but also a steeper velocity drop gradient.

Initial reservoir pressure at jet switch on time (MPa)	Initial velocity (ms <sup>-1</sup> )	Velocity after 5s (ms <sup>-1</sup> )	Velocity after 10s (ms <sup>-1</sup> )	Velocity after 20s (ms <sup>-1</sup> )
0.6	39.6	36.3	32.9	25.64
0.55	37	34.25	31.25	25.2
0.5	34.5	31.8	29.05	23.55
0.45	33.45	30.7	27.95	22.6
0.4	30.7	27.68	24.65	19.8
0.35	23.55	22	20.59	18.4

Table A.1 – Air velocities from the top port of the left jet array at varying initial compressor reservoir pressures.

### A.5 Effect of initial compressor pressure changes for flat fan nozzles

Initial compressor reservoir pressures of 0.3 MPa, 0.5 MPa, and 0.7 MPa at the time of jets being switched on were tested. These were the same three initial pressure values used during testing. Figure A.6 shows the initial air velocity measurements across the 3 x 3 measurement grid for each initial compressor reservoir pressure.

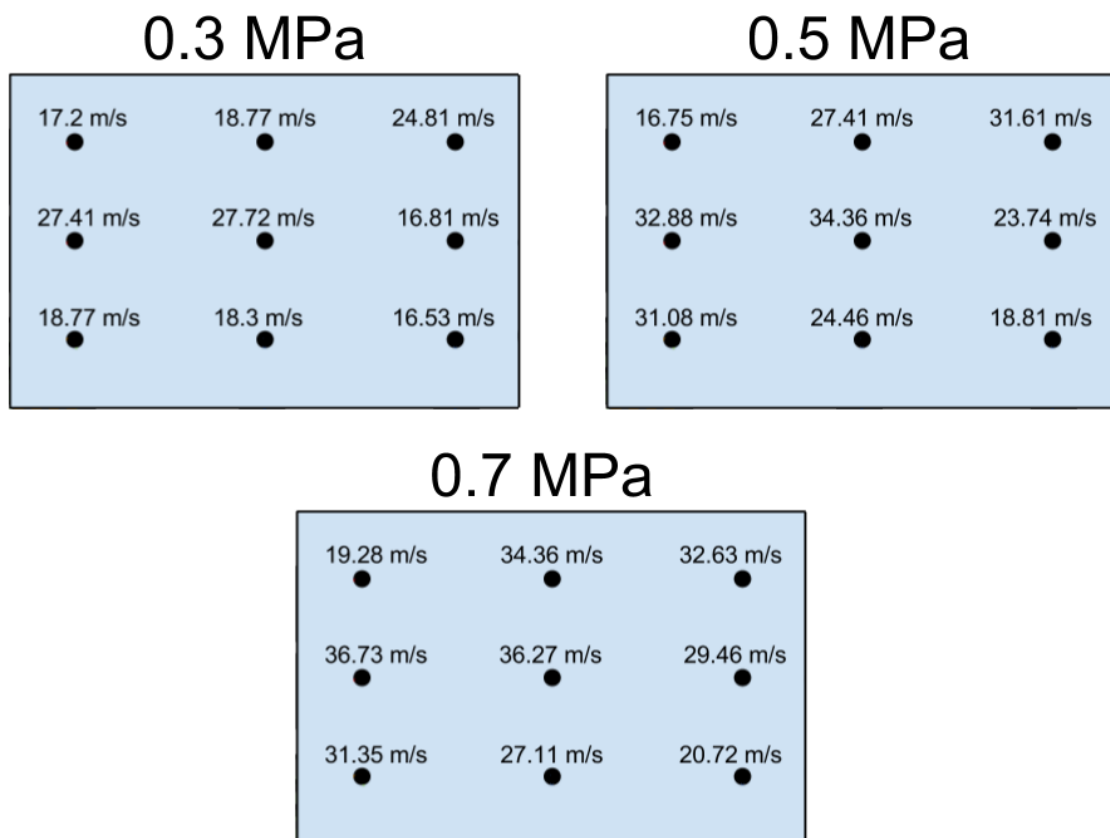


Figure A.6 – Initial air velocities across the 3 x 3 measurement grid for flat fan nozzles for initial compressor pressures of 0.3 MPa, 0.5 MPa, and 0.7 MPa.

The overall average initial velocity value was  $20.7 \text{ ms}^{-1}$ ,  $26.79 \text{ ms}^{-1}$ , and  $29.77 \text{ ms}^{-1}$  for initial pressures of 0.3 MPa, 0.5 MPa, and 0.7 MPa respectively. The velocity measurements at positions 1 and 9 were lower than expected for all initial compressor pressures. By inspection of the tempering apparatus after hot wire anemometer measurement, that the furnace door had been tilting slightly forward, and is likely to be the reason for the discrepancy. This was adjusted prior to tempering of rectangular samples, so that the nozzle line was parallel to the longer centre line of the sample. As such, the velocity values reported for flat fan nozzles in Table 3.1 (chapter 3) are taken as the average velocity from positions 4, 5, and 3. These positions can be considered as the location of the “adjusted” central impingement line, due to door tilt. The central line was chosen as the area local to the central line was of most interest in sharpness studies after breakage. This results in average centre-line velocities of  $24.65 \text{ ms}^{-1}$ ,  $32.95 \text{ ms}^{-1}$ , and  $35.21 \text{ ms}^{-1}$ .

Table A.2 reports the average initial velocity, and the average air velocity after 5, 10, and 15 seconds, at position 5 on the measurement grid for three initial pressures tested. As with measurements for the 4-jet arrays, test runs with higher initial compressor reservoir pressures resulted in a higher initial air velocity, but also a steeper velocity drop gradient.

<b>Initial reservoir pressure at jet switch on time (MPa)</b>	<b>Initial velocity (<math>\text{ms}^{-1}</math>)</b>	<b>Velocity after 5s (<math>\text{ms}^{-1}</math>)</b>	<b>Velocity after 10s (<math>\text{ms}^{-1}</math>)</b>	<b>Velocity after 15s (<math>\text{ms}^{-1}</math>)</b>
0.7	36.27	34.84	33.38	32.38
0.5	34.36	32.88	31.61	31.08
0.3	27.72	27.11	26.16	26.16

**Table A.2 – Air velocities at the central grid point (point 5 in Figure A.2) at varying initial compressor reservoir pressures.**

## **A.6 Other comments**

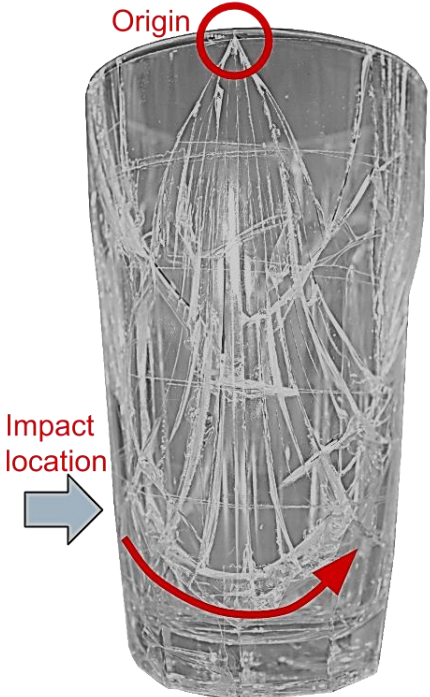
The voltage peak caused by the outstroke of the actuators was lower than the lowest voltage tested for during calibration. An estimate for the air velocity experienced by anemometer can be made by linearly interpolating below the lower calibration bound, which was 4m/s. This gave an estimate of 0.29m/s and 0.31m/s for the left actuator and right actuator respectively, when averaged over 5 test runs chosen at random.

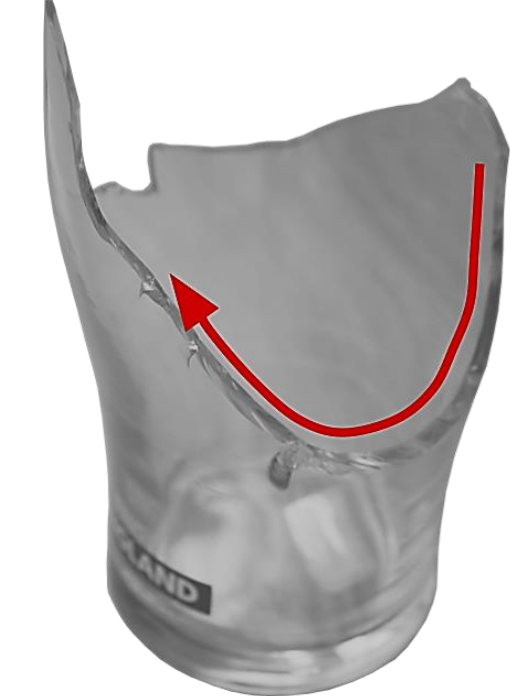
### Appendix B – Drinking glasses fractured for section 4.3

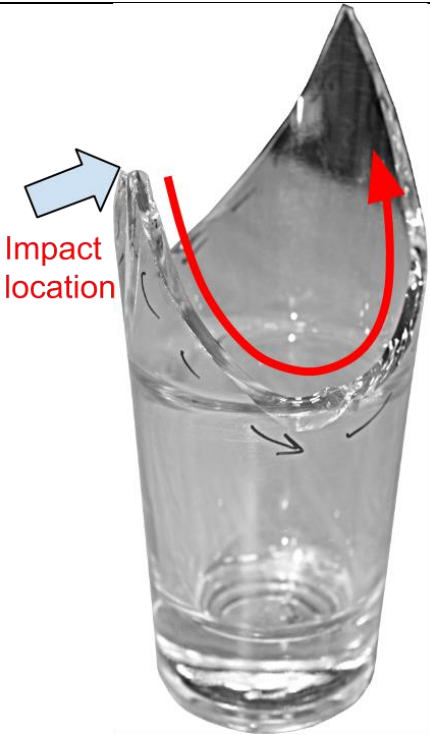
This appendix gives a full sample breakdown of all the glasses tested for the investigation into drinking glass fracture characteristics detailed in section 4.3 of this thesis (Table B.1). Following this are brief descriptions of the fracture characteristics of some of the drinking glasses not discussed in the main text.

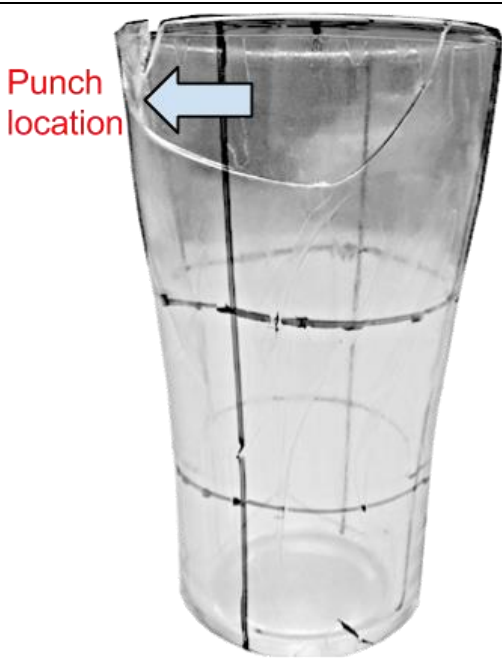
Impact type:	Sample breakdown:
Near-rim impacts	1 x Nonic – <b>NT, HS</b> , 1 x Perfect Pint – <b>NT, HS</b> , 1 x Ultimate Pint – <b>NT, HS</b> , 1 x Nonic – <b>HS</b> , 1 x Perfect Pint – <b>HS</b> , 1 x Ultimate Pint – <b>HS</b> ,
Mid-height impacts	2 x Nonic, 2 x Perfect Pint, 2 x Ultimate Pint, 1 x Nonic – <b>AR</b> , 1 x Perfect Pint – <b>AR</b> , 1 x Ultimate Pint – <b>AR</b> , 17 x various used annealed tumbler glasses (0.3-0.5 pint, see Appendix C), 2 x branded Tulip glasses, 4 x branded stemmed glasses, 1 x promotional Coca-Cola glass – <b>NT</b> , 1 x annealed panelled tumbler glass, 1 x promotional Tulip glass – <b>NT</b> , 2 x Duratuff Endeavour 12 oz glasses (Libbey, Ohio, USA), 2 x Duratuff Endeavour 12 oz glasses – <b>NT</b>
Manual impacts	3 x Nonic, 3 x Nonic – <b>A</b> , 3 x Perfect Pint, 3 x Ultimate Pint
Near-base impacts	1 x annealed panelled tumbler glass
Dropped glasses	3 x Nonic, 3 x Perfect Pint, 3 x Ultimate Pint
Selected punch tests	1 x Nonic – <b>AR</b> , 1 x Perfect Pint – <b>AR</b> , 1 x Ultimate Pint – <b>AR</b> , 4 x branded stemmed pint glasses (inside base and near rim) – <b>AR</b>

**Table B.1 – Testing overview for drinking glass fracture investigation. All glasses were taped and abraded (section 3.5.2.2) prior to fracture unless marked otherwise. Labels: A: annealed after received; HS: fracture observed with high speed video; AR – as-received; NT – glass not taped prior to fracture. Total:74 glasses.**

<b>B.2 Annealed panelled tumbler, abraded, near-base impact</b>	<b>Fracture description</b>
	<ul style="list-style-type: none"> <li>- <i>Failure energy:</i> ~ 8 J (dropped from 1.62 m with 0.5 kg impactor)</li> <li>- <i>Origin location:</i> rim, 90° from impact</li> <li>- <i>Source:</i> homeware store.</li> <li>- <i>Box description:</i> toughened panelled glass.</li> <li>- <i>Fracture characteristics:</i> Base intact, shows signs of annealed fracture. Some dense fragmentation in central region due to high impact energy.</li> </ul>

<b>B.3 Promotional tulip pint glass, abraded, mid-height impact</b>	<b>Fracture description</b>
	<ul style="list-style-type: none"> <li>- <i>Failure energy:</i> ~ 0.4 J (dropped from 0.08 m with 0.5 kg impactor)</li> <li>- <i>Origin location:</i> Inside wall opposite impact, within inward flexure region.</li> <li>- <i>Source:</i> supermarket.</li> <li>- <i>Box description:</i> England beer glass.</li> <li>- <i>Fracture characteristics:</i> Base intact, shows signs of annealed fracture. Fragments in top region of variable size, from 20 mm diameter to 90 mm diameter. Total fragment count (including base) of 15.</li> </ul>

<p><b>B.4 Duratuff Endeavour 12 oz glass, abraded, mid-height impact</b></p>	<p><b>Fracture description</b></p>
	<ul style="list-style-type: none"> <li>- <i>Failure energy:</i> ~ 0.6 J (dropped from 0.13 m with 0.5 kg impactor)</li> <li>- <i>Origin location:</i> Inside wall opposite impact, within inward flexure region.</li> <li>- <i>Source:</i> online retailer.</li> <li>- <i>Box description:</i> durable glassware with prolonged service life for the foodservice industry.</li> <li>- <i>Fracture characteristics:</i> Base intact, shows signs of annealed fracture. Fragments in top region of variable size, from 14 mm diameter to 70 mm diameter. Total fragment count (including base) of 13.</li> </ul>

<p><b>B.5 Ultimate Pint glass, as-received, punched 10 mm from rim</b></p>	<p><b>Fracture description</b></p>
	<ul style="list-style-type: none"> <li>- <i>Source:</i> online retailer.</li> <li>- <i>Description:</i> Ultimate Pint glass, subjected to a punch test as per 3.6.2.2 prior to systematic testing detailed in section 4.4.</li> <li>- <i>Fracture characteristics:</i> No spontaneous failure, localised fragmentation and one looping crack near the rim. Further investigation and discussion of these glasses by punch tests is detailed in section 4.4.</li> </ul>

### Appendix C – Flaw sizes a fracture data from a selection of used drinking glasses

Glass	Type	Impact energy	Number of origin locations	Origin location	Flaw width (2c)	Flaw depth
1	a	0.79	2	<b>Inward flexure</b>		
				Rim, 60 deg from impact (left)	144	68
2	a	0.4	1	<b>Rim, 180 deg from impact</b>	50	20
3	a	0.48	1	<b>Rim, 180 deg from impact</b>	14	7
4	a	0.56	3	<b>Rim, impact axis</b>	106	35
				Rim, 90 deg from impact (left)	148	64
				Rim, 90 deg from impact (right)	162	76
5	a	0.63	2	<b>Rim, impact axis</b>		
				Rim, 90 deg from impact (right)	492	165
6	b	0.48	2	<b>Inward flexure</b>		
				Rim, 45 deg from impact (right)	74	34
7	b	0.48	2	<b>Inward flexure</b>		
				Rim, 45 deg from impact (right)	110	24
8	b	0.71	1	<b>Rim, 180 deg from impact</b>	68	25
9	c	0.71	1	<b>Rim, impact axis</b>	134	83
10	d	1.35	1	<b>Rim, 180 deg from impact</b>	34	9
11	e	2.94	1	<b>Rim, impact axis</b>	54	5
12	f	0.87	1	<b>Inward flexure</b>		
13	f	1.11	2	Rim, 90 deg from impact (left)	206	153
				Rim, 90 deg from impact (right)		
14	g	2.46	1	<b>Inward flexure</b>	110	158
15	g	0.79	1	<b>Rim, 180 deg from impact</b>	166	80
16	h	1.35	1	<b>Inward flexure</b>		
17	h	1.27	1	<b>Inward flexure</b>		

Table C.1 – Fracture data for used drinking glasses broken by impact, discussed in section 4.3.4.3. Glass type refers to labels in Figures C.1 and C.2.



Figure C.1 – Photographs of used glasses a-d as referred to in Table B.1 and discussed in section 4.3.4.3.



Figure C.2 – Photographs of used glasses e-h as referred to in Table B.1 and discussed in section 4.3.4.3.

## Appendix D – Eye appraisal of wear on a selection of used pint glasses

A selection of pint glasses and other drinkware was donated by various pubs and hotels. The drinkware had been withdrawn from use at the discretion of the pubs and hotels. In all cases, visual appearance was cited as the reason for their dismissal. This sub-section discusses a brief appraisal of the surface condition of 20 donated used glasses from a local pub, as a means to make comparisons to methods used to impart surface wear onto new pint glasses. This included 10 small-bulge Nonic glasses, 4 large-bulge Nonic glasses, and 6 Tulip glasses, as featured in Figure D.1. All appraisal was conducted by eye.

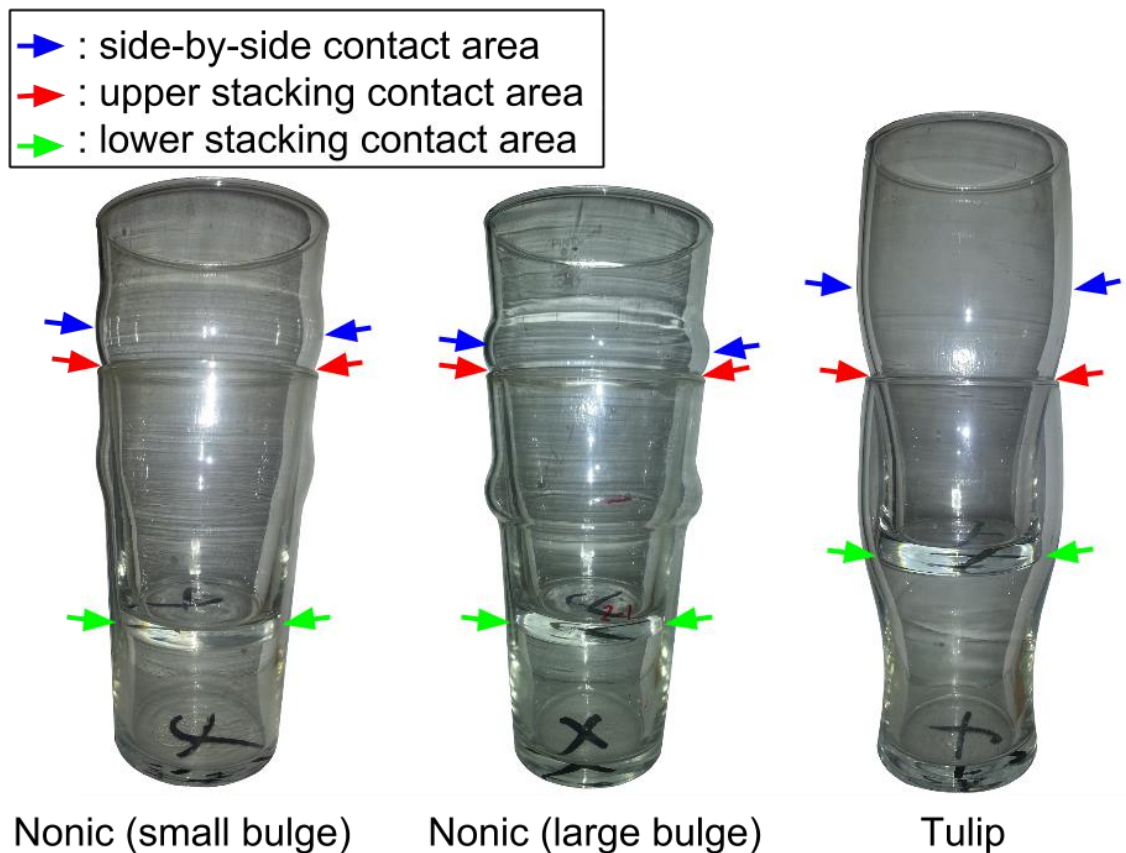


Figure D.1 – Areas of contact during stacking and side-by-side placement of 3 pint glasses.

Advice given by 21<sup>st</sup> Century Pint for publicans and bar staff lists the following as contributors to surface damage on pint glasses<sup>7</sup>:

- Stacking glasses inside one another.

<sup>7</sup> "Information for Publicans and Bar Staff," *21st Century Pint - Best Practice Guidelines*, Institute of Materials Minerals and Mining, Materials Knowledge Transfer Network, 2012. [Online]. Available: <http://21stcenturypint.org/information-publicans-and-bar-staff>. [Accessed: 21-Apr-2015].

- Putting cutlery inside glasses.
- Contact with beer taps.
- Rattling glasses together on shelves.
- Picking glasses up in groups like bouquets.
- Aggressive dishwasher cycles which can degrade glass surfaces and cause a cloudy appearance in the glass.

The location of contact areas when the glasses were stacked and when they stood side-by-side were therefore noted. These contact areas were then appraised for evidence of damage caused by the processes listed above. Each of the three areas of interest (rim area, stacking contact areas, side-by-side contact areas) of the 20 glasses was viewed, followed by a general check for surface damage or cloudiness elsewhere. This was first viewed by eye in daylight, and then viewed by eye in a dark room and lit using a desk lamp with a 60 W incandescent light bulb. The full outcome of the surface condition appraisal is tabulated in Table D.1.

Figure D.1 shows the position of the upper stacking contact area and the lower stacking area of a pint glass. The upper contact area involved contact between the rim of the lower glass and the outside wall of the upper glass. The lower contact area involved contact between the inside wall of the lower glass and the base of the upper glass. With the glasses stacked in the resting positions as shown in Figure D.1, the rim of the lower glass supported the upper glass. The base of the upper glass therefore did not contact the inside wall of the lower glass in this configuration. However, contact could be made on the inner wall by tilting the upper glass. The Tulip glass required the largest tilt for it to contact the inside wall of the lower glass during stacking. Half of the Tulip glasses had visible surface damage in this area. By contrast, only one of the 14 Nonic glasses examined had visible surface damage on the inner surface lower stacking area.

A number of Nonic glasses did not appear to have any damage at all, and the overall condition of the small-bulge Nonic glasses was better than the other glasses. The most consistent area for damage was the side-by-side contact area. Almost three quarters of the used glasses had visible damage in this area when viewed in daylight. Examples of surface damage in this area are shown in Figure D.2a and Figure D.2c. 11 of the 20 glasses had visible surface damage on the outside surface at the upper stacking area. This was more subtle than damage at the side-by-side contact area, and was not visible in daylight for 5 glasses.

15 of the 20 glasses had visible damage near the rim, which generally had a mottled appearance as shown in Figure D.2b. Most glasses also had scratches and scuffs at the base, and various isolated scratches distributed across the outside glass wall. The inside surface was generally in better condition than the outside glass wall.



**Figure D.2 – Examples of surface damage on used pint glasses. a: damage in side-by-side contact area on a large-bulge Nonic glass; b: mottled damage below rim on a large-bulge Nonic glass, c: close-up view of side-by-side area damage on a Tulip glass.**

It is difficult to draw clear conclusions on the typical degree of wear a pint glass is subjected to in practice from this appraisal, due to: the small number of samples, the variability of the location and concentration of damage, and the unknown time in circulation of each glass. However, the appraisal does make it clear that most surface damage was present on the outside wall of the glass, particularly at the side-by-side contact area and at the rim. In addition, the pattern of surface damage may depend to some extent on the shape of the glass, since this affects how the glasses can be stacked.

Sample	Rim		Upper stack area (outside wall)		Lower stack area (inside wall)		Side-by-side contact area		Other	
	VID	VBI	VID	VBI	VID	VBI	VID	VBI		
Nonic (small bulge)	1	✓		✓		✓	✓	✓	Deep diagonal scratch on outside wall, 3 cm above base, scuffs at base	
	2	✓					✓	✓	Scuffs at base, small dots of damage on outside wall above base and near rim	
	3									
	4		✓						Scuffs at base	
	5		✓	✓						
	6		✓						Scuffs at base	
	7									
	8		✓						Scuffs at base	
	9		✓	✓				✓	✓	Scuffs at base, vertical scratches ~ 5 cm above base
	10									
Nonic (large bulge)	1		✓	✓			✓	✓	Scuffs at base	
	2		✓	✓			✓	✓	Scuffs at base, considerable scuffs on outside wall ~ 4 cm above base	
	3		✓	✓			✓	✓	Large scuff below bulge ~ 1 cm diameter, scuffs at base	
	4									
Tulip	1		✓				✓	✓	Scuffs at base, diag. scratches ~ 1 cm below rim, outside wall	
	2	✓	✓	✓			✓	✓	Scuffs at base, numerable scratches distributed across outside glass wall	
	3	✓	✓	✓		✓	✓	✓	Scuffs at base	
	4		✓				✓	✓	Scuffs at base, small dots of damage between rim and bulge, inside wall	
	5	✓	✓	✓		✓	✓	✓	Scuffs at base	
	6	✓	✓			✓	✓	✓	Scuffs at base	

Table D.1 – Appraisal of surface condition of used glasses. VID = visible in daylight, VBI = visible by illumination.

## Appendix E – Full fragmentation counts for pint glasses subjected to punch tests

<b>Nonic glasses</b>										
Sample no.	1	2	3	4	5	6	7	8	9	10
Base	169	175	169	0	156	165	0	175	185	136
Bottom third	445	439	462	0	471	470	0	486	453	447
Middle third	29	21	36	0	59	41	0	46	38	31
Top third	11	3	8	0	7	4	0	11	8	14
Total	654	638	675	0	693	680	0	718	684	628
Largest fragment length /mm	280	280	170	-	280	250	-	240	280	175

**Table E.1 – Fragmentation counts for 10 Nonic glasses subjected to a punch test, as discussed in section 4.4.4.**

<b>Ultimate Pint glasses</b>										
Sample no.	1	2	3	4	5	6	7	8	9	10
Base	101	0	139	140	0	107	0	0	0	0
Bottom third	295	0	269	412	0	282	0	0	0	0
Middle third	168	0	232	252	0	197	0	0	0	0
Top third	9	5	13	27	4	20	5	2	5	9
Total	573	5	653	831	4	606	5	2	5	9
Largest fragment length /mm	260	-	100	65	-	80	-	-	-	-

**Table E.2 – Fragmentation counts for 10 Ultimate Pint glasses subjected to a punch test, as discussed in section 4.4.4.**

<b>Perfect Pint glasses</b>										
Sample no.	1	2	3	4	5	6	7	8	9	10
Base	72	82	0	0	96	87	90	86	82	68
Bottom third	343	375	0	0	355	371	361	379	372	378
Middle third	388	437	0	0	378	394	406	458	399	423
Top third	140	154	0	0	147	156	146	140	127	144
Total	943	1048	0	0	976	1008	1003	1063	980	1013
Largest fragment length /mm	140	52	-	-	90	75	60	150	150	150

**Table E.3 – Fragmentation counts for 10 Perfect Pint glasses subjected to a punch test, as discussed in section 4.4.4.**

## Appendix F – Dynamometer output for impacts without pint glasses

This appendix shows and discusses a number of force-time plots of single-impact events to the force plate dynamometer as described in section 5.3. These were conducted to enable comparison to impacts with pint glasses which appeared to show multiple impact events during attacks.

**Hammer impacts:** 6 impacts were conducted to the centre of the dynamometer face with a hammer at a range of forces. The resulting force-time plots are shown in Figure F.1. The time period over which the impact event occurs is determined by the same manner as that described in section 5.3.2.2 of this thesis (see orange bounds in Figure F.1). It is referred to as the impact event from this point onwards.

The general shape of the force-time plot during the impact event remained similar over the range of forces examined. Two distinctive peaks were observed within the impact event: the first one including the maximum recorded force; and the second one having a peak value of approximately half the maximum force. The second peak may be a dynamic effect due to the initial resonance of the aluminium dynamometer face. The remaining peaks were resonant peaks, which were captured by high speed video footage during slapping attacks (section 5.3). The average impact event duration was ~9.5 ms. The maximum force occurred on average ~2.8 ms into the impact event (31.1% of the average impact event duration).

**Restraining fixture impacts:** 6 impacts were conducted to the centre of the dynamometer face with the pint glass restraining fixture at a range of forces without a pint glass attached. The same technique was used as that for slapping attacks in section 5.3. The impact event was determined by the same criteria as that described above for hammer impacts.

As with hammer impacts, the general impact event peak remained a similar shape over the range of impact forces examined. However, unlike the hammer impacts only one distinctive peak was observed. The average impact event duration was ~11 ms, and showed greater variation than with hammer impacts. Additionally, the peak force value was achieved significantly later into the impact event than with hammer impacts: on average ~6.7 ms into the impact event (60.9% of the average impact event duration).

The shape and form of these force-time plots are used as a comparative tool to assess force-time plots of glassing attacks in section 5.3.

Single hammer impacts onto dynamometer face

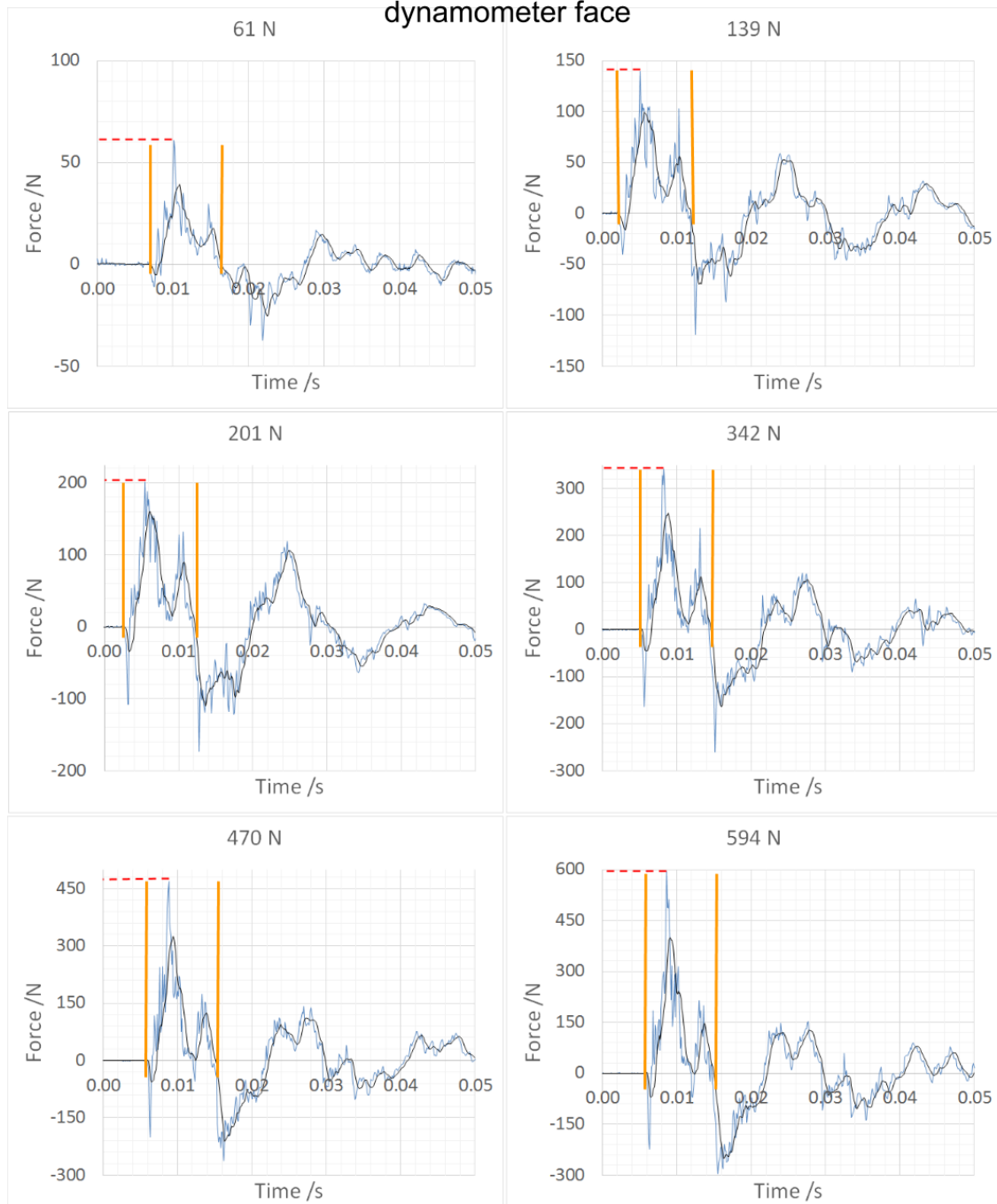


**Figure F.1 – Force time plots resulting from impacts by a hammer to the centre of the dynamometer face at 6 different forces. Blue line: raw data; black line: 10 point (1 ms) moving average; red dotted line: location of maximum force; orange lines: impact event bounds.**

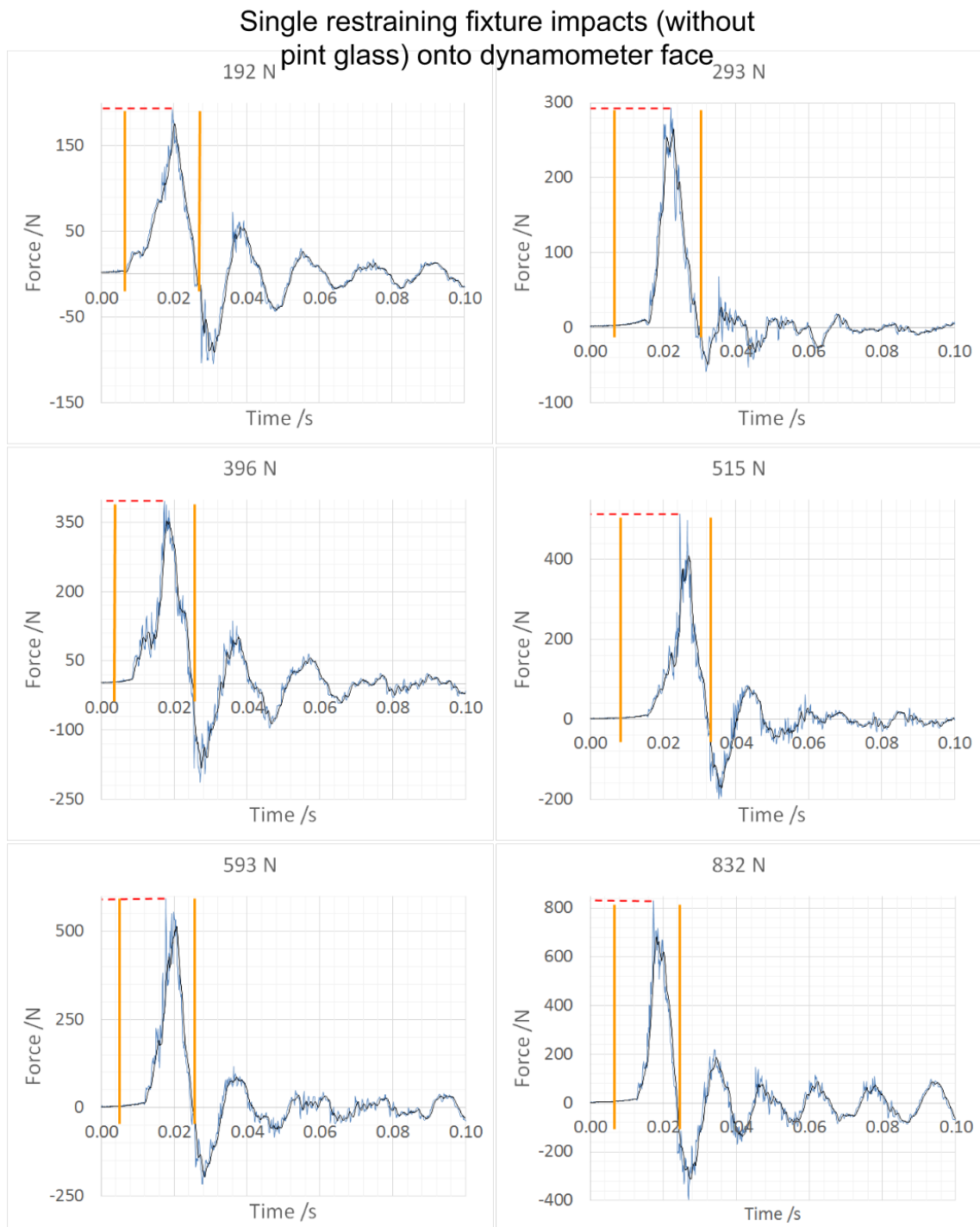


**Figure F.2 – Force time plots resulting from impacts by the pint glass restraining fixture (without a pint glass attached) to the centre of the dynamometer face at 6 different forces. Blue line: raw data; black line: 10 point (1 ms) moving average; red dotted line: location of maximum force; orange lines: impact event bounds.**

**Appendix G – Extended dynamometer results for slapping attack replications**

Participant	Gender (M/F)	Height (m)	Weight (kg)	Glass	Maximum force (N)	Approach velocity (ms <sup>-1</sup> )	Glassing event duration (ms)	Peak force time (ms)	% of peak force time to glassing event duration
A	M	1.8	70	N1	887	13.19	18.5	9.2	49.7
				N2	976	12.20	17.6	11.4	64.8
				T1	473	9.35	35.5	13	36.6
				T2	474	8.07	29	12.8	44.1
B	M	1.9	68	N1	1453	12.50	16.3	11.1	68.1
				N2	1322	11.62	15.8	10.6	67.1
				T1	678	8.07	23.1	14.3	61.9
				T2	937	10.7	18.9	13.7	72.5
C	M	1.7	70	N1	1247	15.00	14	11.8	84.3
				N2	936	12.93	16.9	12.1	71.6
				T1	1442	13.75	15.7	10.8	68.8
				T2	1208	16.69	11.2	4.7	42.0
D	M	1.8	63	N1	1385	12.02	13	7.8	60.0
				N2	992	10.36	13.6	6.8	50.0
				T1	1063	12.68	20.7	12.7	61.4
				T2	1363	9.43	15.8	11.1	70.3
E	F	1.6	48	N1	265	6.00	26.8	19	70.9
				N2	271	5.78	26.3	10.4	39.5
				T1	401	6.85	23	17.9	77.8
				T2	432	8.63	27.6	11.3	40.9
F	M	1.9	95						
				T1	1008	13.41	16.4	11	67.1
				T2	1283	13.53	17.5	11.4	65.1
G	M	2	103	N1	1680	11.43	9.9	4.6	46.5
				N2	1492	13.81	9.4	5.3	56.4
				T1	949	13.39	18.6	10.9	58.6
				T2	1070	11.17	15.9	11.4	71.7

**Table G.1 – Recorded parameters for glassing experimentation detailed in section 5.3.3.2. N1: First repeat with Nonic; N2: Second repeat with Nonic; T1: First repeat with Tulip; T2 Second repeat with Tulip. No attacks were conducted with Nonic glasses for participant F due to glass availability.**

Participant	Gender (M/F)	Attack type	Maximum force (N)	Glassing event duration (ms)	Peak force time (ms)	% of peak force time to glassing event duration	Notes
H	M	Free.	923	11.7	4.7	40.2	
		Hesi.	622	11.4	5.6	49.1	
		Agg.	434	16.8	10.1	60.1	P, L
I	M	Free.	455	13.2	6.7	50.8	P, L
		Hesi.	483	47.3	33.2	70.2	P, L
		Agg.	537	7.4	3.8	51.4	
J	M	Free.	454	185.1	37.3	20.2	L
		Hesi.	709	10.8	5	46.3	P
		Agg.	327	52.1	31.8	61.0	P, L
K	M	Free.	669	14.2	7.2	50.7	
		Hesi.	727	27.9	3.5	12.5	
		Agg.	677	23.8	20.4	85.7	P
L	M	Free.	416	49	36.3	74.1	
		Hesi.	497	45	33.6	74.7	
		Agg.	401	44.2	31.4	71.0	
M	M	Free.	315	158.1	37	23.4	L
		Hesi.	296	169.7	19.8	11.7	L
		Agg.	694	20.6	5.6	27.2	
N	M	Free.	406	23.7	18.7	78.9	P
		Hesi.	430	45.7	36.3	79.4	
		Agg.	655	12	5.9	49.2	
O	M	Free.	640	10.2	3.4	33.3	P
		Hesi.	556	49.2	31.2	63.4	P, L
		Agg.	430	39.8	32.8	82.4	

**Table G.2 – Recorded parameters for glassing experimentation detailed in section 5.3.3.3, table 1 of 2. Free: Freestyle attack; Hesi: Hesitant attack; Agg: Aggressive attack. Notes: P: perceived premature achievement of condition iii for the glassing event; L: evidence of leaning on the dynamometer face after initial impact.**

Participant	Gender (M/F)	Attack type	Maximum force (N)	Glassing event duration (ms)	Peak force time (ms)	% of peak force time to glassing event duration	Notes
P	M	Free.	456	10	4.6	46.0	P
		Hesi.	581	237.4	30.4	12.8	L
		Agg.	430	44.9	22.6	50.3	
Q	M	Free.	819	9.1	3.8	41.8	P
		Hesi.	853	32.1	21.4	66.7	
		Agg.	680	22.6	17.3	76.5	
R	F	Free.	907	8.6	4.3	50.0	
		Hesi.	508	43.7	33.6	76.9	
		Agg.	385	28.6	21.5	75.2	P
S	F	Free.	239	272.9	37.6	13.8	L
		Hesi.	391	48.3	37.2	77.0	
		Agg.	843	11	4.2	38.2	
T	F	Free.	431	38.7	17.8	46.0	
		Hesi.	418	43.9	20.1	45.8	
		Agg.	1022	19.6	5.5	28.1	
U	F	Free.	426	181.4	35.2	19.4	L
		Hesi.	444	44.9	30.6	68.2	P, L
		Agg.	718	8.1	3.1	38.3	
V	F	Free.	437	27.6	22	79.7	P
		Hesi.	456	52.1	33.2	63.7	P, L
		Agg.	427	43.8	31.2	71.2	

**Table G.3 – Recorded parameters for glassing experimentation detailed in section 5.3.3.3, table 2 of 2. Free: Freestyle attack; Hesi: Hesitant attack; Agg: Aggressive attack. Notes: P: perceived premature achievement of condition iii for the glassing event; L: evidence of leaning on the dynamometer face after initial impact.**

**Appendix H – Damage quantification data from section 5.4.3**

Test ref	Head damage			Hand damage		
	Area	Cut length (s) (mm)	Description	Area	Cut length (s) (mm)	Description
<b>Tempered Tulip</b>	I	-	Scratches	I	-	Large hole
	1	5	Cut	1	1	Puncture
	2	7	Cut	2	8	Cut
	3	15	Cut	3	4	Cut
	4	16	Cut + scratches	4	4	Cut
	5	6	Cut	5	3	Puncture
	6	1	Puncture	6	3	Puncture
				7	4	Puncture
$\bar{X} \pm \sigma$	8.33 ± 5.41			3.86 ± 1.96		
<b>Annealed Tulip</b>	I	-	Scratches	I	-	Large hole
	1	10	Cut	1	6	Cut
	2	2	Puncture	2	10	Cut
	3	14	Puncture, damage to PE head	3	4	Puncture
	4	15, 15	Cuts	4	11	Cut
	5	18	Cut	5	8	Cut
	6	5	Cut	6	20	Cut
	7	15, 5	15 mm cut with 5 mm branch	7	2	Puncture
	8	4	Cut			
	9	5	Cut			
$\bar{X} \pm \sigma$	9.82 ± 5.47			8.71 ± 5.47		

**Table H.1 – Quantitative damage data for the PE head and hand damage shown in Figure 5.14.**

Test ref.	Area	Cut length(s) (mm)	Description	Test ref.	Area	Cut length(s) (mm)	Description
<b>a</b>	1	15, 10	15 mm x 10 mm flap at the point of impact	<b>b</b>	I	1, 12	1 mm puncture, 12 mm cut
	2	5, 18	Two punctures in single line		1	15	
	3	14			2	11	
	4	14			3	17	
	5	4			4	8	
	6	7	Irregularly shaped		5	15, 10	15 mm x 10 mm flap
	7	Many	Numerous small cuts		6	4, 10	4 mm x 10 mm flap
	8	4			7	6	
	9	12			8	4	
	10	4			9	3	
	11	2			10	5	
$\bar{X} \pm \sigma$	9.08 ± 5.17				11	7,5	7 mm x 5 mm flap
<b>c</b>	1	2-3	3 punctures		12	4	
	2	1			13	2	
	3	26			14	4	
	4	8		15	12		
	5	5		$\bar{X} \pm \sigma$	7.75 ± 4.6		
	6	3					
	7	20					
	8	11					
	9	8					
	10	6					
	11	5					
$\bar{X} \pm \sigma$	7.73 ± 7.14						

Table H.2 – Quantitative damage data for silicone layers in Figure 5.15, (1/2).

Test ref.	Area	Cut length(s) (mm)	Description	Test ref.	Area	Cut length(s) (mm)	Description
<b>d</b>	I	12	One cut, numerous scratches	<b>e</b>	I	-	Numerous Scratches
	1	8			1	13	
	2	6			2	8	
	3	7			3	7	
	4	8			4	10	
	5	8			5	4	
	6	2			6	11	
	7	5			7	14	
	8	3			8	12	
	9	4			9	8	
	10	3			10	9	
	11	5			11	6	
	12	3			12	6	
	13	6			13	3	
	14	6			14	6	
	15	2			15	6	
16	9		16		3		
$\bar{X} \pm \sigma$	5.71 ± 2.67				17	5	
<b>f</b>	I	15,9,4			18	3	
	1	2			19	20, 20, 11	
	2	2		20	17		
	3	2		$\bar{X} \pm \sigma$	9.64 ± 5.69		
	4	2		<b>f</b>	13	10	
	5	6			14	9	
	6	2			15	10	
	7	10			16	4	
	8	5			17	11	
	9	12			18	11	
	10	13			19	3	
	11	8			20	6	
12	14		$\bar{X} \pm \sigma$	7.39 ± 4.19			

Table H.3 – Quantitative damage data for silicone layers in Figure 5.15, (2/2).

Sample ref:	Layer	Number of cuts	Cut length(s) (mm)	Number of punctures	Puncture length(s) (mm)
A1	1	Many		3	8, 13, 9
	2	1	6	1	8
A2	1	Many		5	7, 11, 8, 4, 15
	2	1	8	3	13, 10, 4
A3	1	Many		4	6, 12, 15, 7
	2	1	5	2	9, 3
A4	1	Many		6	7, 18, 5, 9, 4, 5
	2	2	14, 8	3	16, 6, 14
A5	1	Many		3	21, 5, 10
	2	0	0	1	7
A6	1	Many		5	7, 5, 9, 5, 4
	2	1	3	2	5, 3
A7	1	Many		4	24, 17, 15, 8
	2	0	0	1	11
A8	1	Many		8	36, 16, 21, 12, 9, 19, 32, 16
	2	2	21, 13	5	27, 17, 15, 19, 17
A9	1	Many		5	14, 7, 11, 5, 13
	2	1	8	2	12, 6
A10	1	Many		7	21, 5, 6, 18, 9, 5, 20
	2	2	11, 7	3	12, 7, 11

**Table H.4 – Quantitative damage data for annealed Nonic glasses broken onto two silicone layers as discussed in section 5.4.3.3. Layer 1: Silicone A, Layer 2: Silicone B.**

Sample ref:	Layer	Number of cuts	Cut length(s) (mm)	Number of punctures	Puncture length(s) (mm)
T1	1	Many		4	12, 4, 7, 14
	2	1	7	3	12, 3, 6
T2	1	Many		9	10, 2, 5, 3, 4, 5, 5, 3, 7
	2	2	2, 4	6	8, 3, 2, 4, 3, 6
T3	1	Many		2	2, 5
	2	0	0	1	3
T4	1	Many		5	9, 3, 2, 4, 3
	2	1	3	3	3, 6, 2
T5	1	Many		4	10, 12, 5, 4
	2	0	0	2	3, 5
T6	1	Many		5	9, 8, 4, 2, 6
	2	0	0	1	4
T7	1	Many		7	7, 2, 5, 4, 10, 2, 3
	2	1	2	4	2, 2, 2, 3
T8	1	Many		3	4, 4, 2
	2	0	0	0	0
T9	1	Many		6	7, 5, 10, 6, 3, 6
	2	1	3	4	8, 4, 2, 5
T10	1	Many		5	17, 13, 9, 7, 15
	2	0	0	2	4, 11

**Table H.5 – Quantitative damage data for tempered Nonic glasses broken onto two silicone layers as discussed in section 5.4.3.3. Layer 1: Silicone A, Layer 2: Silicone B.**

## Appendix I – Edge profile measurement scripts

The Python scripts shown below return x-axis edge profile measurements and free surface edge profile measurements, respectively, when co-ordinates of the edge profile are taken as an input. The coordinates must be saved as a text file, and formatted such that each row has an x-coordinate followed by a y-coordinate, separated by a tab-stop character. It also requires that the y-coordinates monotonically increase.

Standard practice when using the x-axis profile measurement code in this study involved:

1. Originally taking a micrograph of the fragment from the fracture surface side (Figure 6.7), oriented so the tensile and compressive edges were horizontal, with the compressive axis closer to the top of the figure.
2. Calibrating the image co-ordinate system to the scale bar, and then tracing the profile of the edge using imageJ software version 1.48.
3. Saving the traced edge profile line as a set of tab-separated XY coordinates in a text file.
4. Running the resulting text file through the program.

Standard practice when using the free surface profile measurement code in this study involved:

1. Originally taking a micrograph of the fragment from the free surface side (Figure 6.7), oriented so the free surface centre line was horizontal, with the tensile surface facing the objective lens (or the inside surface for pint glasses).
2. Calibrating the image co-ordinate system to the scale bar, and then tracing the profile of the edge using imageJ software version 1.48.
3. Saving the traced edge profile line as a set of tab-separated XY coordinates in a text file.
4. Running the resulting text file through the program.

**# X-AXIS PROFILE MEASUREMENT PROGRAM**

```

import numpy as np
import matplotlib.pyplot as plt
import scipy.interpolate as interp
import math

# 1. PROFILE MANIPULATION

# ask user whether x-axis profile is facing left or right in original figure.
# data is later transformed if it is facing left.
# compressive edge is already assumed to be the top edge.
orientation = 0
while orientation not in ("L", "R", "l", "r"):
    orientation = str(raw_input("Left or right facing? (L/R): "))

# initiate x and y lists
x = []
y = []

# open the coordinates text file and save x and y data as lists
with open("filename.txt", "r") as data:
    for row in data:
        datasplit = row.split("\t")
        if orientation in ("l", "L"):
            x.append(float(datasplit[0])*-1) # transforms to be right-facing
            y.append(float(datasplit[1].strip()*-1)
        else:
            x.append(float(datasplit[0]))
            y.append(float(datasplit[1].strip()*-1)

# values to calibrate to wedge line point
x_calibrate = min(x[0], x[-1])
y_calibrate = y[0]

# normalise data to wedge line point
c = 0
for each in x:
    x[c] = each - x_calibrate
    c += 1
c = 0
for each in y:
    y[c] = each - y_calibrate
    c += 1

# 2. INTERPOLATION

# define the 1-D interpolation function
f = interp.interp1d(y,x)
ynew = np.linspace(0,max(y), 1000)
# make the set of interpolated x-values
xnew = []
for each in ynew:
    xnew.append(f(each))

# 3. PROFILE MEASUREMENT

```

```

# glass thickness
thickness = max(ynew)
print "Glass thickness: %.2fmm" % (thickness)

# protrusion length
pro_length = float(max(xnew))
print "Wedge line protrusion length: %.2fmm" % (pro_length)

# high vertex protrusion length
high_vertex = max(xnew[0], xnew[-1])
high_pro_length = pro_length - high_vertex
print "Protrusion length from higher vertex: %.2fmm" % (high_pro_length)

# average protrusion length
average_pro_length = sum(xnew)/len(xnew)
print "Average protrusion length from wedge line: %.2fmm" % (average_pro_length)

# average roughness, Ra
baseline = np.linspace(high_vertex, 0, 1000)
c = 0
baseline_xnew = list(xnew)
for each in baseline_xnew:
    baseline_xnew[c] = math.fabs(each-baseline[c])
    c += 1
Ra = sum(baseline_xnew)/len(baseline_xnew)
print "Average roughness, Ra: %.2fmm" % (Ra)

# root mean square roughness, Rq
c = 0
squared_baseline_xnew = list(baseline_xnew)
for each in squared_baseline_xnew:
    squared_baseline_xnew[c] = each * each
    c += 1
Rq = math.sqrt(sum(squared_baseline_xnew)/len(squared_baseline_xnew))
print "Root mean square roughness, Rq: %.2fmm" % (Rq)

# pierce point distance to compressive edge
for x1, y1 in zip(xnew, ynew):
    if x1 == pro_length:
        y_at_pierce_point = y1
        comp_dist = thickness - y_at_pierce_point
print "Lateral distance to compressive edge: %.2fmm" % (comp_dist)

# thickness 1mm back from pierce point
if pro_length < 1: # to check whether protrusion length is below 1mm
    thickness_1mm = thickness
else:
    ref_1mm = pro_length - 1
    c = 0
    # find closest point lower side
    if (pro_length - xnew[0]) < 1: # check whether nearest terminal point is less than 1mm below pierce
point
        y_1mm_1 = ynew[0]
        c1 = 0
    else:
        while xnew[c] < pro_length: # condition to iterate over lower portion (right of pierce point)
            if c == 0:

```

```

    c += 1
    continue
elif xnew[c] == ref_1mm: # if there is an exact match
    y_1mm_1 = ynew[c]
    c1 = c
    c += 1
    continue
else:
    if (xnew[c] > ref_1mm) and (xnew[c-1] < ref_1mm): # if it's somewhere between two
        y_1mm_1 = (ynew[c] + ynew[c-1])/2
        c1 = c
        c += 1
        continue
    else:
        c += 1
        continue
# find closest point higher side
if (pro_length - xnew[-1]) < 1: # check whether nearest terminal point is less than 1mm below pierce
point
    y_1mm_2 = ynew[-1]
    c2 = 0
else:
    while c < (len(xnew) - 1):
        if xnew[c] == ref_1mm: # if there is an exact match
            y_1mm_2 = ynew[c]
            c2 = c
            break
        else:
            if (xnew[c] < ref_1mm) and (xnew[c-1] > ref_1mm): # if it's somewhere between two
                y_1mm_2 = (ynew[c] + ynew[c-1])/2
                c2 = c
                break
            else:
                c += 1
                continue
    thickness_1mm = y_1mm_2 - y_1mm_1
print "Thickness 1mm back from pierce point: %.2fmm" % (thickness_1mm)

# number of pierce points
c=0
number_peaks = 0
for each in xnew:
    if c == 0:
        if each > xnew[c+1]: # check to see if there is an edge peak at bottom
            number_peaks += 1
        c += 1
        continue
    elif c == 999:
        if each > xnew[c-1]: # check to see if there is an edge peak at top
            number_peaks += 1
        break
    elif (xnew[c-1] < each) and (xnew[c+1] < each): # condition to identify a peak
        number_peaks += 1
        c += 1
        continue
    else:
        c += 1

```

```
    continue
print "Total number of peaks (pierce points): %.0f" % (number_peaks)

# included angle 1mm back (far angle)
if thickness_1mm == thickness:
    farangle = 0
else:
    m1 = (ynew[c1+1]-ynew[c1-1])/(xnew[c1+1]-xnew[c1-1])
    m2 = (ynew[c2+1]-ynew[c2-1])/(xnew[c2+1]-xnew[c2-1])
    if (y_1mm_1 == ynew[0]) and (y_1mm_2 == ynew[-1]): # check to see whether profile is wedge in
1mm range
        farangle = 0
    elif (y_1mm_1 == ynew[0]) and (y_1mm_2 != ynew[-1]): # check whether lower side edge terminal
point is below 1mm of pierce point
        farangle = math.degrees(math.atan(m2 * -1))
    elif (y_1mm_1 != ynew[0]) and (y_1mm_2 == ynew[-1]): # check whether higher side edge terminal
point is below 1mm of pierce point
        farangle = math.degrees(math.atan(m1))
    else:
        farangle = math.degrees(math.atan((m1-m2)/(1+(m1*m2))))
    if farangle < 0:
        farangle += 180
print "Included angle 1mm back from pierce point: %.2fdeg" % (farangle)
```

---

**# FREE SURFACE PROFILE MEASUREMENT PROGRAM**

```

import numpy as np
import matplotlib.pyplot as plt
import scipy.interpolate as interp
import math

# 1. PROFILE MANIPULATION

# ask user whether free surface profile is facing left or right in original figure.
# data is later transformed if it is facing left.
# tensile surface is assumed to be facing the objective lens.
orientation = 0
while orientation not in ("L", "R", "l", "r"):
    orientation = str(raw_input("Left or right facing? (L/R): "))

# initiate x and y lists
x = []
y = []

# open the coordinates text file and save x and y data as lists
with open("filename.txt", "r") as data:
    for row in data:
        datasplit = row.split("\t")
        if orientation in ("l", "L"):
            x.append(float(datasplit[0])*-1) # transforms to be right-facing
            y.append(float(datasplit[1].strip())*-1)
        else:
            x.append(float(datasplit[0]))
            y.append(float(datasplit[1].strip())*-1)

# values to calibrate to pierce point
x_calibrate = max(x)
for x1, y1 in zip(x, y): # y_calibrate is y at max of x, scan over both lists at once
    if x1 == x_calibrate:
        y_calibrate = y1

# normalise data to pierce point
c = 0
for each in x:
    x[c] = each - x_calibrate + 1
    c += 1
c = 0
for each in y:
    y[c] = each - y_calibrate
    c += 1

# 2. INTERPOLATION 1

# define the 1-D interpolation function
f = interp.interp1d(y, x)
ynew = np.linspace(min(y), max(y), 1000)
# make the set of interpolated x-values
xnew = []
for each in ynew:
    xnew.append(f(each))

```

## # 3. INTERPOLATION 2: EXTRACT TOP 1mm AND INTERPOLATE

```

# first need to find +y and -y at x=0
c = 0
while ynew[c] < 0: # condition to iterate over lower portion (right of pierce point)
    if c == 0:
        c += 1
        continue
    elif xnew[c] == 0: # if there is an exact match
        y_1mm_1 = ynew[c]
        c1 = c
        c += 1
        continue
    else:
        if (xnew[c] > 0) and (xnew[c-1] < 0): # if it's somewhere between two
            y_1mm_1 = (ynew[c] + ynew[c-1])/2
            c1 = c
            c += 1
            continue
        else:
            c += 1
            continue
# find closest 1mm point top side
while c < (len(xnew) - 1):
    if xnew[c] == 0: # if there is an exact match
        y_1mm_2 = ynew[c]
        c2 = c
        break
    else:
        if (xnew[c] < 0) and (xnew[c-1] > 0): # if it's somewhere between two
            y_1mm_2 = (ynew[c] + ynew[c-1])/2
            c2 = c
            break
        else:
            c += 1
            continue

# make the second set of interpolated x-values
ynew1 = np.linspace(y_1mm_1, y_1mm_2, 1000)
xnew1 = []
for each in ynew1:
    xnew1.append(f(each))

```

## # 4. PROFILE MEASUREMENT

```

# thickness 1mm back from pierce point
thickness_1mm = y_1mm_2 - y_1mm_1
print "Thickness 1mm back from pierce point: %.2fmm" % (thickness_1mm)

# number of pierce points
c=0
number_peaks = 0
for each in xnew:
    if c == 0:
        if each > xnew[c+1]: # check to see if there is an edge peak at bottom
            number_peaks += 1
        c += 1

```

```

    continue
elif c == 999:
    if each > xnew[c-1]: # check to see if there is an edge peak at top
        number_peaks += 1
    break
elif (xnew[c-1] < each) and (xnew[c+1] < each): # condition to identify a peak
    number_peaks += 1
    c += 1
    continue
else:
    c += 1
    continue
print "Total number of peaks (pierce points): %.0f" % (number_peaks)

# included angle 1mm back (far angle)
m1 = (ynew[c1+1]-ynew[c1-1])/(xnew[c1+1]-xnew[c1-1])
m2 = (ynew[c2+1]-ynew[c2-1])/(xnew[c2+1]-xnew[c2-1])
farangle = math.degrees(math.atan((m1-m2)/(1+(m1*m2))))
if farangle < 0:
    farangle += 180
print "Included angle 1mm back from pierce point: %.2fdeg" % (farangle)

# ROUGHNESS CALCULATIONS
# define top perfectly smooth line
topfraction = abs(y_1mm_2) / thickness_1mm
smoothx2 = np.linspace(1, 0, int(round(1000*topfraction)))

# define bottom perfectly smooth line
bottomfraction = abs(y_1mm_1) / thickness_1mm
smoothx1 = np.linspace(0, 1, int(round(1000*bottomfraction)) + 1)
new_smoothx1 = np.delete(smoothx1, -1) # I added one to smoothx1 and deleted it here, so smoothx1
does not end in 1, since smoothx2 needs to start with 1
totalsmooth = list(new_smoothx1) + list(smoothx2)

# average roughness, Ra
xnew1_list = list(xnew1)
xnew1_bottom = []
xnew1_top = []
c = 0
while c < int(round(1000*bottomfraction)):
    xnew1_bottom.append(xnew1_list[c])
    c += 1
while c < 1000:
    xnew1_top.append(xnew1_list[c])
    c += 1
c = 0
for each in xnew1_bottom:
    xnew1_bottom[c] = math.fabs(each - new_smoothx1[c])
    c += 1
c = 0
for each in xnew1_top:
    xnew1_top[c] = math.fabs(each - smoothx2[c])
    c += 1

Ra = (sum(xnew1_top) + sum(xnew1_bottom)) / 1000
print "Average roughness, Ra: %.2fmm" % (Ra)

```

```
# root mean square roughness, Rq
c = 0
squaredxnew1_bottom = list(xnew1_bottom)
squaredxnew1_top = list(xnew1_top)
for each in squaredxnew1_bottom:
    squaredxnew1_bottom[c] = each * each
    c += 1
c = 0
for each in squaredxnew1_top:
    squaredxnew1_top[c] = each * each
    c += 1
Rq = math.sqrt((sum(squaredxnew1_bottom) + sum(squaredxnew1_top))/1000)
print "Root mean square roughness, Rq: %.2fmm" % (Rq)
```

---

## Appendix J – Silicone/foam simulant verification

An investigation into the penetration load consistency of a complete silicone/foam block was conducted prior to experimentation with the skin simulants. The load frame and apparatus outlined in section 6.5.1 was used for this investigation. The variation of penetration load with position on the simulant, proximity to other puncture holes, and proximity to the edge was investigated.

A glass shard was cut from a sheet of 4mm thick float glass and machined to have a free surface included angle of  $\sim 25^\circ$ , a free surface tip radius of  $\sim 0.83$  mm and a wedge x-axis edge profile, before being mounted in polyester resin. This shard was used for all penetrations and the free surface was always positioned parallel the shorter length of the simulant block.

The block was designated x and y axes as indicated in Figure J.1, and initially punctures were made at all intersections of the  $x/4$ ,  $y/4$ ,  $x/2$ ,  $y/2$ ,  $3x/4$  and  $3y/4$  lines (where x and y are the width and length of the silicone layer respectively) to give an indication of the area dependence on penetration load (Figure J.1i). Punctures were made firstly in between the existing punctures in different frequencies (Figure J.1ii), secondly towards the edges, and finally in increments of  $x/8$  and  $y/16$  (Figure J.1iii) in the remainder of the silicone surface. The x increment was larger since the puncture holes extended further in the x-axis than the y-axis. The results are shown schematically in Figure J.2.

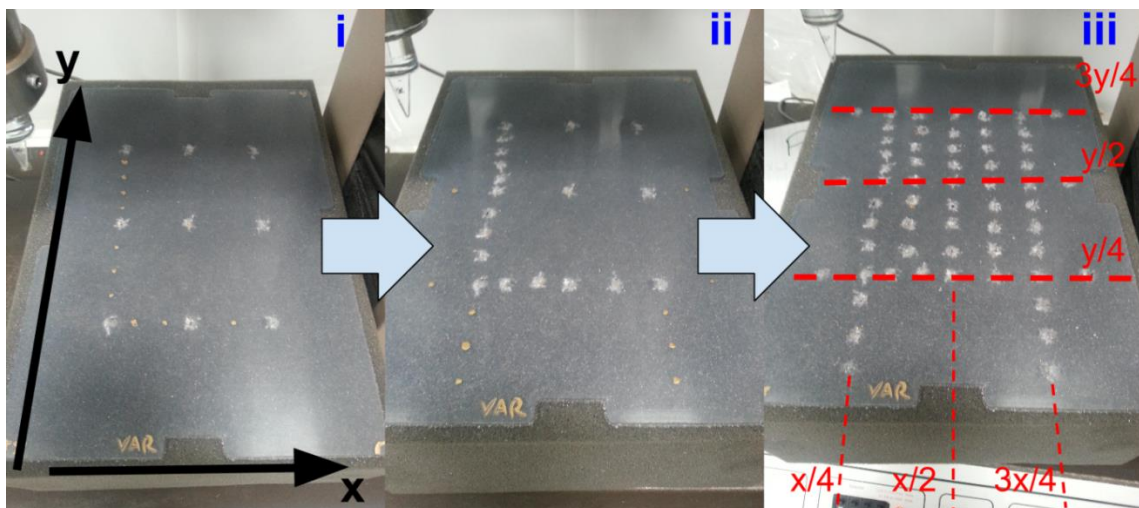


Figure J.1 – Order and position of verification test runs. The free surfaces of the penetrating fragment were parallel to the x-axis. After iii, the remainder of the silicone surface was punctured in  $x/8$  and  $y/16$  intervals.

The area-based punctures (runs 1 to 9) gave a mean penetration load of 55.6 N with a standard deviation (taken as population) of 3.64 N. The lowest overall penetration load value came from the centre point.  $x/8$  and  $y/16$  puncture intervals in general did not result in penetration loads more than one area-based standard deviation from the mean, but during intervals of  $y/20$ , run 18 gave a result more than 3 area-based standard deviations greater than the mean.  $x/12$  intervals were deemed too small as a crack in from the previous puncture ran towards puncture 12. Most runs made at points closer to the edges either failed to penetrate the silicone or resulted in very high penetration loads. As more punctures were made in subsequent runs over the remainder of the silicone surface, higher penetration loads were encountered and most runs made at points outside the  $[x/4, 3x/4, y/4, 3y/4]$  bounds failed to penetrate.

It is assumed that these effects occur due to the strain energy built up in the simulant as it is deflected prior to penetration. The lowest penetration load occurs at the direct centre of the simulant as most of the energy created by the fragment pushing into the simulant goes directly to deflecting the silicone underneath the fragment tip. As punctures get closer together more energy is used as surrounding punctures are stretched open, and in some cases cracks grow. This also accounts for the higher loads encountered when punctures were made within the  $[x/4, 3x/4, y/4, 3y/4]$  bounds from run 30 to run 57. Using a ruler, from run 30 onwards the radius of the silicone deflection was measured to be approximately 45 mm. Toward the edges, especially when the run was conducted to within 45 mm of an edge, folding in the silicone was observed alongside considerable compression of the underlying foam. This contributed to the low frequency of successful silicone layer penetrations with these runs.

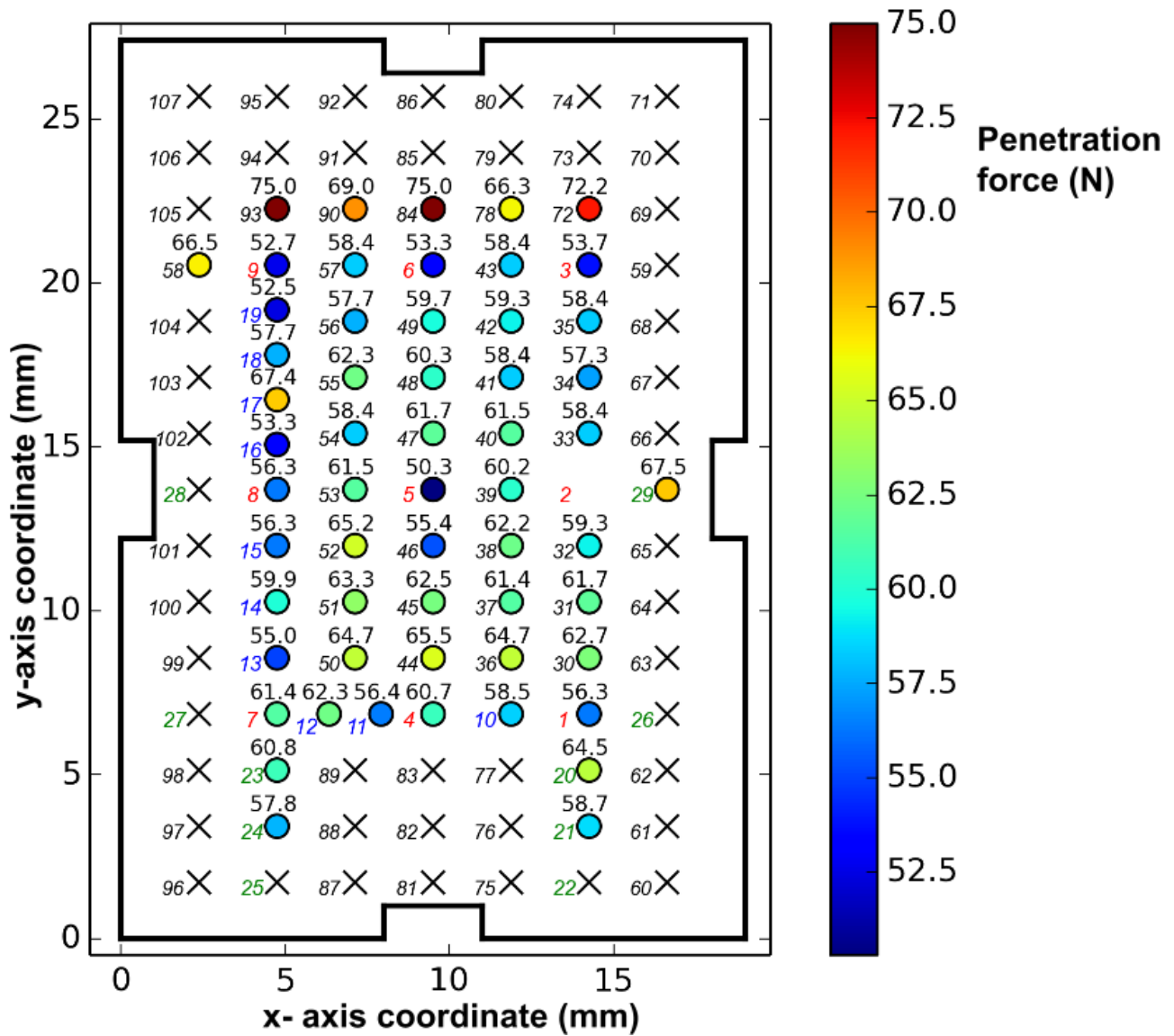


Figure J.2 – Results from simulant verification study. For all piercing points that failed to penetrate the simulant, their position is marked with an 'X'. For those that did penetrate, their position is marked with a circle colour-coded to the legend to the right of the figure. The penetration load is also displayed above each circle for convenience. The test run order is indicated by the numbers in italics next to each pierce point. Area-based points are displayed in red font, proximity-based points are displayed in blue, edge-based points in green font, and the remainder in black. Puncture 2 is not displayed due to a technical error.

## Appendix K – Further sharpness data from section 7.2

<b><i>Included angle t-test pairs</i></b> ↓	0.5 kgf samples	1 kgf samples	All samples
Far - near tens angle	0.37	<b>0.005</b>	<b>0.009</b>
Far - near comp angle	0.08	<b>0.00005</b>	<b>0.00006</b>
Near tens-comp angle	0.61	<b>0.008</b>	<b>0.03</b>
Far tens-comp angle	0.18	0.14	<b>0.05</b>
<b><i>Parameter t-test pairs</i></b> →	0.5 kgf samples - 1 kgf samples		
Near tensile side included angle		0.09	
Far tensile side included angle		0.71	
Near compressive side included angle		<b>0.03</b>	
Far compressive side included angle		0.96	
Penetration depth		0.39	
Average load in steady state		0.36	
Friction coefficient		0.36	

**Table K.1 – P-values obtained from Student's *t*-tests on y-axis annealed rectangular sample data sets. All values that are below a 5% significance level are shown in red font.**

**Appendix L – Further edge/surface profile plots and sharpness data from section 7.3**

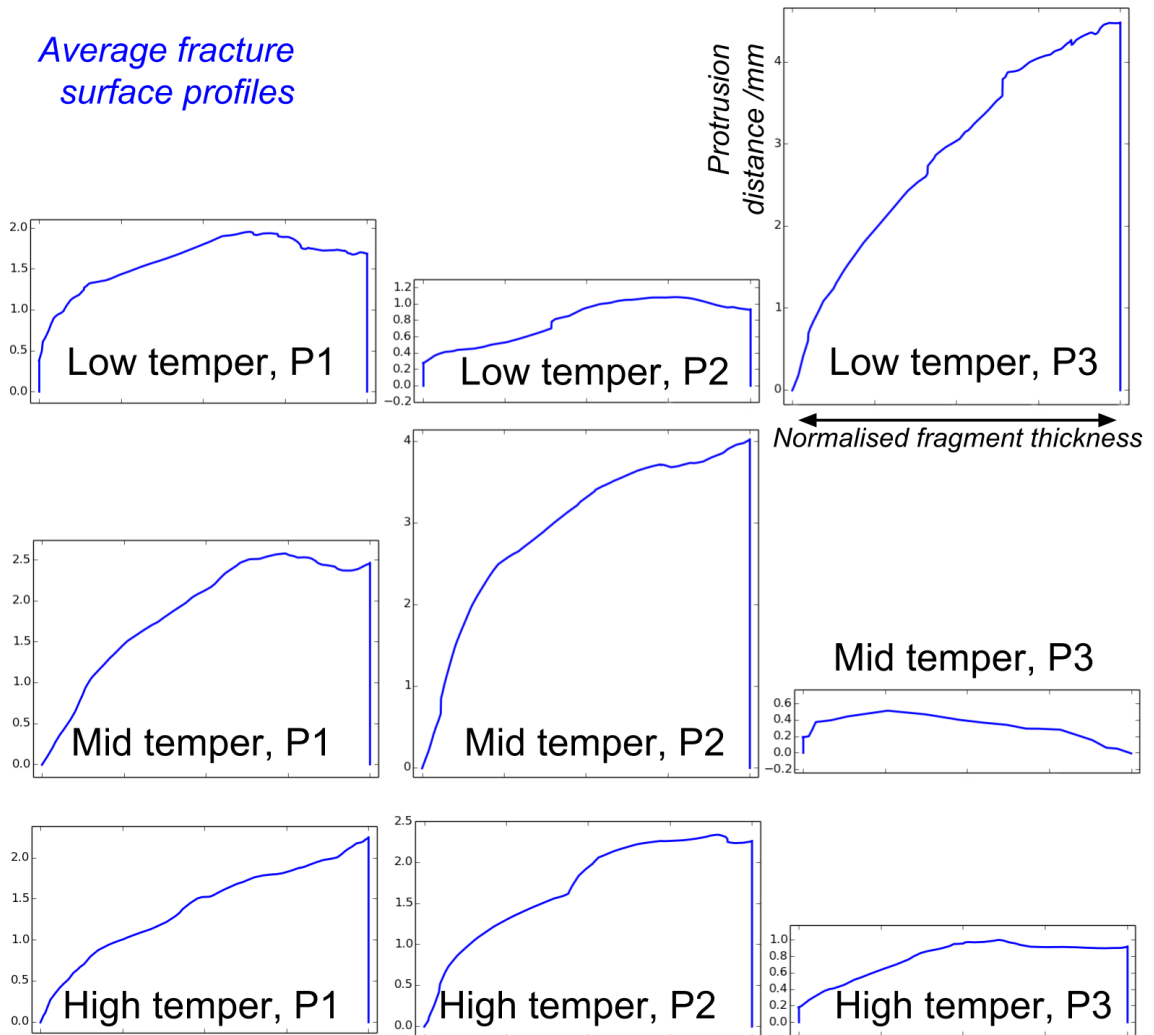


**Figure L.1 – Further categorisation of average x-axis profile morphology of out-out edges from the tempered rectangular samples shown in Figure 7.11.**

Student's <i>t</i> -test pairs→	Low-Mid	Mid-High	Low-High	P1-P2	P2-P3	P1-P3
<b>Fracture surface parameters</b>						
Tip radius / $\mu\text{m}$ (manual)	0.73	0.35	0.09	0.15	0.44	0.26
Near included angle / $^{\circ}$ (manual)	0.51	0.80	0.32	0.67	0.89	0.61
Thickness 1mm from piercing point /mm	0.47	0.28	0.77	0.68	0.99	0.78
Protrusion length /mm	0.44	0.06	0.32	0.70	0.96	0.81
Average protrusion length /mm	0.26	<b>0.03</b>	0.33	0.61	0.76	0.92
Lateral distance to comp. edge /mm	0.62	0.96	0.67	0.64	0.59	0.36
Root mean square roughness, Rq /mm	0.32	<b>0.02</b>	0.16	0.65	0.45	0.69
<b>Free surface parameters</b>						
Tip radius / $\mu\text{m}$ (manual)	0.40	0.92	0.29	0.34	0.45	0.16
Near included angle / $^{\circ}$ (manual)	0.81	0.59	0.71	0.35	0.60	0.89
Far included angle / $^{\circ}$	0.66	0.47	0.21	0.79	0.24	0.24
Thickness 1mm from piercing point /mm	0.49	0.92	0.53	0.06	0.73	0.36
Root mean square roughness, Rq /mm	0.79	0.76	0.96	0.22	0.47	0.16

**Table L.1 – P-values obtained from Student's *t*-tests on 6 pairs of tempered rectangular sample data sets. All values that are below a 5% significance level are shown in red font.**

<b>Included angle <i>t</i>-test pairs↓</b>	Low temper	Mid temper	High temper	All tempered
Far - near tens angle	0.46	0.16	0.07	<b>0.02</b>
Far - near comp angle	<b>0.02</b>	0.09	<b>0.005</b>	<b>0.00007</b>
Near tens-comp angle	0.31	0.21	0.87	0.18
Far tens-comp angle	0.08	0.66	0.08	<b>0.03</b>
<b>Parameter <i>t</i>-test pairs→</b>	Low-Mid	Low-High	Mid-High	All annealed – All tempered
Near tensile side included angle /deg	0.57	0.07	0.18	0.48
Far tensile side included angle /deg	0.84	0.71	0.54	0.91
Near compressive side included angle /deg	0.48	0.42	0.95	0.87
Far compressive side included angle /deg	0.33	0.52	0.61	0.44

**Table L.2 – P-values obtained from Student's *t*-tests on y-axis annealed rectangular sample data sets. All values that are below a 5% significance level are shown in red font.**

## Appendix M – Further edge/surface profile plots and sharpness data from section 8.2

### M.1 Further average profile data and Student's *t*-test data

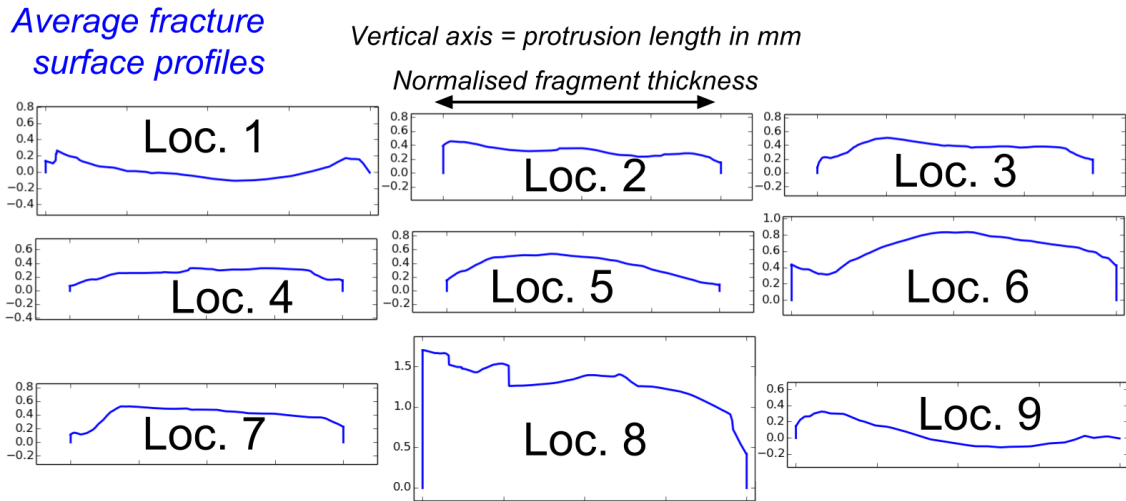


Figure M.1 – Further categorisation of average x-axis profile morphology of edges from tempered pint glass fragments detailed in section 8.2.

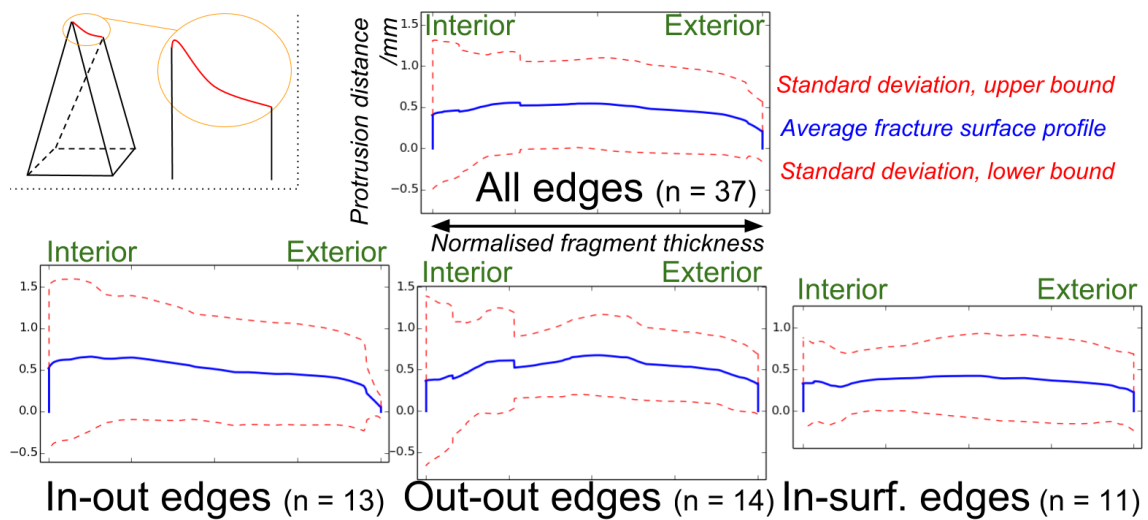
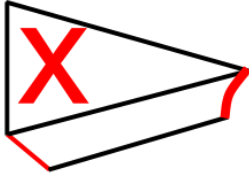


Figure M.2 – Average profile morphology of x-axis edges from selected pint glass fragments. Average profiles are plotted with a solid blue line. Upper and lower standard deviation profile bounds are plotted with dashed red lines. Interior and exterior surfaces of the pint glass are as labelled. Inset shows x-axis profile context.

	In-out (n =13)	Out-out (n = 14)	In-surface (n = 11)	All fragments (n=37)
<b>Fracture surface parameters</b>				
Tip radius / $\mu\text{m}$ (manual)	1649 $\pm$ 1981 (120)	2043 $\pm$ 2066 (101)	882 $\pm$ 1107 (126)	1438 $\pm$ 1703 (118)
Near included angle / $^{\circ}$ (manual)	144.2 $\pm$ 43.1 (30)	137.5 $\pm$ 41.0 (30)	96.2 $\pm$ 48.9 (51)	126.4 $\pm$ 48.5 (38)
Thickness 1mm from piercing point /mm	4.6 $\pm$ 1.2 (26)	4.4 $\pm$ 1.5 (34)	3.7 $\pm$ 1.4 (38)	4.3 $\pm$ 1.4 (33)
Protrusion length /mm	0.8 $\pm$ 0.9 (113)	1.0 $\pm$ 0.9 (90)	0.8 $\pm$ 0.5 (63)	0.9 $\pm$ 0.8 (89)
Average protrusion length /mm	0.5 $\pm$ 0.6 (120)	0.5 $\pm$ 0.4 (80)	0.4 $\pm$ 0.4 (100)	0.5 $\pm$ 0.5 (100)
Root mean square roughness, Rq /mm	0.39 $\pm$ 0.44 (113)	0.48 $\pm$ 0.51 (106)	0.43 $\pm$ 0.21 (49)	0.44 $\pm$ 0.42 (95)
<b>Free surface parameters</b>				
Tip radius / $\mu\text{m}$ (manual)	188 $\pm$ 434 (231)	140 $\pm$ 217 (155)	160 $\pm$ 228 (143)	166 $\pm$ 315 (190)
Near included angle / $^{\circ}$ (manual)	112.3 $\pm$ 25.0 (22)	71.9 $\pm$ 27.4 (38)	69.7 $\pm$ 30.1 (43)	86.3 $\pm$ 33.4 (39)
Far included angle / $^{\circ}$	111.5 $\pm$ 16.2 (15)	48.3 $\pm$ 14.0 (29)	57.7 $\pm$ 23.1 (40)	72.8 $\pm$ 33.8 (46)
Thickness 1mm from piercing point /mm	3.9 $\pm$ 1.4 (36)	1.4 $\pm$ 0.4 (29)	1.7 $\pm$ 0.8 (47)	2.4 $\pm$ 1.5 (63)
Root mean square roughness, Rq /mm	0.07 $\pm$ 0.04 (57)	0.12 $\pm$ 0.07 (58)	0.12 $\pm$ 0.06 (50)	0.10 $\pm$ 0.06 (60)
<b>Penetration testing</b>				
Penetration load /N	<b>56 <math>\pm</math> 13</b> (23) (n = 11, 2 damaged during preparation)	<b>33 <math>\pm</math> 13</b> (39) (n = 14)	<b>30 <math>\pm</math> 16</b> (53) (n = 9, 2 failed to penetrate )	<b>40 <math>\pm</math> 18</b> (46) (n = 33)

**Table M.1 – Summary of parameter data collected for in-out, out-out, and in-surface x-axis profiles of tempered pint glass fragments. In each case the average value is shown  $\pm$  one standard deviation. The percentage of the standard deviation compared to the average value is shown in parentheses. All parameters listed in this table are described and illustrated in section 6.4.2.**

Student's <i>t</i> -test pairs:	Top - mid	Top-bot	Mid-bot
<b><i>Fracture surface parameters</i></b>			
Tip radius / $\mu\text{m}$ (manual)	<b>0.0005</b>	<b>0.002</b>	0.11
Near included angle / $^\circ$ (manual)	<b>0.02</b>	0.53	<b>0.007</b>
Thickness 1mm from piercing point /mm	<b>3.95E-08</b>	<b>0.005</b>	0.75
Protrusion length /mm	0.72	<b>0.03</b>	<b>0.01</b>
Average protrusion length /mm	0.54	<b>0.02</b>	<b>0.02</b>
Root mean square roughness, Rq /mm	0.23	0.12	<b>0.04</b>
<b><i>Free surface parameters</i></b>			
Tip radius / $\mu\text{m}$ (manual)	0.39	0.08	0.18
Near included angle / $^\circ$ (manual)	0.08	0.09	0.98
Far included angle / $^\circ$	0.20	0.39	0.61
Thickness 1mm from piercing point /mm	0.21	0.23	0.95
Root mean square roughness, Rq /mm	0.41	0.12	0.36
<b><i>Penetration testing</i></b>			
Penetration load /N	<b>7.07E-05</b>	<b>2.22E-06</b>	0.83

**Table M.2 – P-values obtained from Student's *t*-tests on 3 pairs of tempered pint glass location-based x-axis profile sample data sets. All values that are below a 5% significance level are shown in red font. Top, mid, and bot refer to the top region, middle region, and bottom region of the pint glass respectively.**

Student's <i>t</i> -test pairs:	IO-OO	IO-IS	OO-IS
<b><i>Fracture surface parameters</i></b>			
Tip radius / $\mu\text{m}$ (manual)	0.63	0.27	0.099
Near included angle / $^\circ$ (manual)	0.69	<b>0.025</b>	<b>0.04</b>
Thickness 1mm from piercing point /mm	0.65	0.12	0.29
Protrusion length /mm	0.52	0.82	0.59
Average protrusion length /mm	0.78	0.62	0.30
Root mean square roughness, Rq /mm	0.64	0.82	0.72
<b><i>Free surface parameters</i></b>			
Tip radius / $\mu\text{m}$ (manual)	0.73	0.85	0.83
Near included angle / $^\circ$ (manual)	<b>0.0007</b>	<b>0.002</b>	0.86
Far included angle / $^\circ$	<b>2.63E-10</b>	<b>8.54E-06</b>	0.27
Thickness 1mm from piercing point /mm	<b>4.86E-05</b>	<b>0.0003</b>	0.25
Root mean square roughness, Rq /mm	0.08	<b>0.04</b>	0.85
<b><i>Penetration testing</i></b>			
Penetration load /N	<b>0.0004</b>	<b>0.002</b>	0.63

**Table M.3 – P-values obtained from Student's *t*-tests on 3 pairs of tempered pint glass edge type-based x-axis profile sample data sets. All values that are below a 5% significance level are shown in red font. IO: in-out; OO: in-out; IS: in-surface.**

## M.2 Regression analysis summary

### Pint glass fragments Regression Analysis: Penetration vs. measured geometrical parameters

#### Analysis of Variance

Source	DF	Adj SS	Adj MS	F-Value	P-Value
Regression	13	9440.4	726.187	8.83	0.000
<b>Free near angle (deg)</b>	<b>1</b>	<b>421.8</b>	<b>421.759</b>	<b>5.13</b>	<b>0.035</b>
Free thickness 1mm back (mm)	1	9.0	8.975	0.11	0.745
<b>Free far angle (deg)</b>	<b>1</b>	<b>706.1</b>	<b>706.087</b>	<b>8.59</b>	<b>0.009</b>
<b>Free Rq</b>	<b>1</b>	<b>644.9</b>	<b>644.889</b>	<b>7.84</b>	<b>0.011</b>
Frac tip rad (microns)	1	6.6	6.611	0.08	0.780
Frac near angle (deg)	1	3.0	2.971	0.04	0.851
<b>Frac fragment thickness (mm)</b>	<b>1</b>	<b>679.3</b>	<b>679.260</b>	<b>8.26</b>	<b>0.010</b>
Frac protrusion length (mm)	1	60.0	60.029	0.73	0.403
Frac average pro. length (mm)	1	0.4	0.430	0.01	0.943
Frac Rq	1	12.4	12.356	0.15	0.703
Frac lat. comp. edge dist. (mm)	1	1.6	1.606	0.02	0.890
<b>Frac thickness 1 mm back (mm)</b>	<b>1</b>	<b>387.7</b>	<b>387.685</b>	<b>4.72</b>	<b>0.043</b>
Frac far angle (deg)	1	3.1	3.074	0.04	0.849
Error	19	1562.1	82.218		
Total	32	11002.6			

#### Model Summary

S	R-sq	R-sq(adj)	R-sq(pred)
9.06742	85.80%	76.09%	46.53%

#### Coefficients

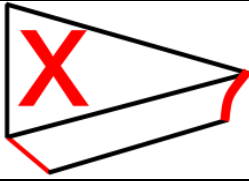
Term	Coef	SE Coef	T-Value	P-Value	VIF
Constant	-27.9	13.2	-2.12	0.048	
<b>Free near angle (deg)</b>	<b>0.240</b>	<b>0.106</b>	<b>2.26</b>	<b>0.035</b>	<b>4.49</b>
Free thickness 1mm back (mm)	-0.93	2.80	-0.33	0.745	6.32
<b>Free far angle (deg)</b>	<b>0.310</b>	<b>0.106</b>	<b>2.93</b>	<b>0.009</b>	<b>4.79</b>
<b>Free Rq</b>	<b>94.8</b>	<b>33.9</b>	<b>2.80</b>	<b>0.011</b>	<b>1.87</b>
Frac tip rad (microns)	-0.00039	0.00137	-0.28	0.780	2.35
Frac near angle (deg)	0.0111	0.0582	0.19	0.851	2.92
<b>Frac fragment thickness (mm)</b>	<b>22.82</b>	<b>7.94</b>	<b>2.87</b>	<b>0.010</b>	<b>30.35</b>
Frac protrusion length (mm)	-15.1	17.7	-0.85	0.403	87.72
Frac average pro. length (mm)	1.1	15.3	0.07	0.943	25.72
Frac Rq	-7.1	18.4	-0.39	0.703	25.27
Frac lat. comp. edge dist. (mm)	0.18	1.31	0.14	0.890	1.68
<b>Frac thickness 1 mm back (mm)</b>	<b>-16.59</b>	<b>7.64</b>	<b>-2.17</b>	<b>0.043</b>	<b>40.93</b>
Frac far angle (deg)	-0.022	0.115	-0.19	0.849	2.80

### Appendix N – Further sharpness data from section 8.3

Student's <i>t</i> -test pairs:	Low cooling rate - High cooling rate
<b><i>Fracture surface parameters</i></b>	
Tip radius / $\mu\text{m}$ (manual)	<b>0.03</b>
Near included angle / $^{\circ}$ (manual)	0.84
Thickness 1mm from piercing point /mm	0.23
Protrusion length /mm	0.18
Average protrusion length /mm	0.17
Lateral distance to comp. edge /mm	0.37
Root mean square roughness, $R_q$ /mm	0.13
<b><i>Free surface parameters</i></b>	
Tip radius / $\mu\text{m}$ (manual)	0.77
Near included angle / $^{\circ}$ (manual)	0.59
Far included angle / $^{\circ}$	0.60
Thickness 1mm from piercing point /mm	0.69
Root mean square roughness, $R_q$ /mm	0.82
<b><i>Penetration testing</i></b>	
Penetration load /N	0.42

**Table N.1 – P-values obtained from Student's *t*-tests on x-axis parameter data of non-uniformly tempered glass discs, subjected to low and high cooling rates. All values that are below a 5% significance level are shown in red font.**

## Appendix O – Further sharpness data from section 8.4

	A	B	C	D	$\bar{X} \pm \sigma$ (% $\sigma$ of $\bar{X}$ )
<b>Fracture surface parameters</b>					
Tip radius / $\mu\text{m}$ (manual)	70	26	38	70	$51 \pm 19$ (37)
Near included angle / $^\circ$ (manual)	144.5	115.1	114.2	134.9	$127.2 \pm 13.0$ (10)
Far included angle / $^\circ$	69.4	5.9	10.6	10.3	$24.1 \pm 26.2$ (109)
Thickness 1mm from piercing point /mm	2.4	2.8	2.4	2.2	$2.4 \pm 0.2$ (8)
Protrusion length /mm	2.4	3.6	2.6	4.2	$3.2 \pm 0.7$ (22)
Average protrusion length /mm	1.4	2.3	1.5	2.6	$2.0 \pm 0.5$ (25)
Lateral distance to comp. edge /mm	3.5	3.8	3.3	3.4	$3.5 \pm 0.2$ (6)
Root mean square roughness, $R_q$ /mm	0.48	0.80	0.66	1.04	$0.75 \pm 0.20$ (27)
<b>Free surface parameters</b>					
Tip radius / $\mu\text{m}$ (manual)	12	5	12	70	$25 \pm 26$ (104)
Near included angle / $^\circ$ (manual)	36.0	30.9	36.2	60.8	$41.0 \pm 11.6$ (28)
Far included angle / $^\circ$	44.7	48.6	37.7	37.4	$42.1 \pm 4.7$ (11)
Thickness 1mm from piercing point /mm	0.7	0.8	0.8	1.0	$0.8 \pm 0.1$ (13)
Root mean square roughness, $R_q$ /mm	0.08	0.05	0.09	0.18	$0.10 \pm 0.05$ (50)
<b>Penetration testing</b>					
Penetration load /N	14	14	23	14	$16 \pm 4$ (25)

**Table O.1 – All parameter data collected for near-origin out-out x-axis profiles of 4 chemically tempered disc fragments. In the rightmost column, the average value is shown  $\pm$  the standard deviation. The percentage of the standard deviation compared to the average value is shown in parentheses. All parameters listed in this table are described and illustrated in section 6.4.2.**

**Appendix P – The Effect of Tempering and Wall Thickness on the Fracture of Pint Glasses International Journal of Applied Glass Science, 6 [2] 196–207 (2015)**

*International Journal of Applied Glass Science, 6 [2] 196–207 (2015)*  
DOI:10.1111/ijag.12099

INTERNATIONAL JOURNAL OF  
**Applied Glass**  
SCIENCE

**The Effect of Tempering and Wall Thickness on the Fracture of Pint Glasses**

Richard W. Earp and Sarah V. Hainsworth\*

*Department of Engineering, University of Leicester, University Road, Leicester, LE1 7RH, UK*

David A. Eustice, Catherine Robinson, and Malcolm D. Glendenning

*Glass Technology Services Ltd., 9 Churchill Way, Sheffield, South Yorkshire, S35 2PY, UK*

This study presents a comprehensive analysis of the effect of tempering and wall thickness on the fracture of tempered drinking glasses typically used in bars and pubs in the United Kingdom. The fracture patterns are related to the manufacturing process, the glass geometry, and the level of residual stress. The bulk of experimentation was split into two categories: Firstly, an assessment of the residual stress was conducted, followed by an assessment of the fracture response of the glass in practical applications. Drinking glasses have a variable wall thickness as a consequence of their design and manufacture. This has a direct effect on the level of residual stress in the article, which in turn produces glasses that break to give fragments of variable sizes, with large sharp-edged fragments nearer the glass rim. It is also shown that tempered glasses broken by impact have a characteristic fracture pattern. The results show that to control the fracture of glasses to produce small fragments similar to those in tempered flat glass, the wall thickness and resulting level of residual stress need to be optimized.

**Introduction**

Tempered drinking glasses, in particular pint glasses, are widely used in bars and pubs in the United Kingdom for safety reasons. However, there are few studies which examine and compare the nature of annealed and tempered drinkware fractures.

The fracture pattern of a glass article is determined mainly by the distribution of stress in the article at the time of failure. This resultant stress field is the sum of

the residual stresses present in the article prior to failure, and the external stresses brought about by loading. Residual stresses are elastic stresses within a body that exist in the absence of external forces.<sup>1</sup> Such stresses become present in glass, when it is cooled below its transition temperature, and can be minimized by cooling the glass at a controlled rate to achieve temperature equilibrium throughout the article: a process known as annealing.<sup>2</sup> Conversely, in a process known as tempering, the glass surfaces are rapidly cooled through the glass transition temperature to create temperature gradients in the article, with the aim of creating a parabolic residual stress distribution with compressive stress at the glass surfaces, balanced by a central core tensile

The authors would like to acknowledge funding provided by EPSRC and Glass Technology Services, South Yorkshire, UK.

\*rv2@le.ac.uk

© 2014 The American Ceramic Society and Wiley Periodicals, Inc

stress. As glass fails only in tension and usually from a flaw at the surface, the maximum level of tensile stress that a tempered glass can withstand is increased by the compressive stress that perpetually acts on surface flaws, increasing the amount of tensile stress necessary to initiate a crack. A distinguishable feature of tempered glass is its extensive fragmentation into smaller, blunter pieces than that of standard annealed glass.<sup>3</sup> The visual difference between tempered and annealed glass can be almost indistinguishable without photoelastic assessment.

The tempering of flat glass has been practised commercially since the early 20th century. However, the application of this process to more complex-shaped articles is difficult, due to the challenges of removing spent air surrounding cooling jets and achieving consistent cooling over a curved surface. Nevertheless, in response to safety concerns with the use of annealed glasses, the tempering of drinking glasses was achieved commercially in the late 1990s.<sup>4</sup> Commercial experience over the following period for a variety of glass designs has shown that the principle causes of failure to tempered glasses are as follows: impact damage, poor design, uneven tempering, and reduced strength through abrasion during use.<sup>5</sup> While nickel sulfide inclusions are often found to act as an initiating flaw for spontaneous failure in tempered flat and architectural glass, they have not to date been identified as the principle cause of failure of tempered pint glasses.<sup>5</sup>

The issues related to uneven tempering have led to calls for a standard for the process on glass drinkware<sup>6</sup> as faultily tempered glass products can be weaker and consequently more likely to break than annealed glass products. This is usually in cases where the tempering process has not been properly controlled to develop a favorable residual stress distribution.

A number of standards exist for testing the performance of annealed glass containers (such as bottles or jars) under different testing conditions such as thermal shock and internally applied pressure,<sup>7-9</sup> but there are no standard test methods specifically concerning the external impact of tempered drinking glasses. By contrast, numerous standards exist for assessing the performance of tempered flat glass.<sup>10-16</sup> One reason for the lack of standardization for drinking glass manufacture is the complication added by both the conical shape of the glass and the varying thickness along its height. This thickness variation is

a consequence of the blow molding process used during manufacture,<sup>17</sup> which usually results in a greater wall thickness at the base of the glass than the rim. Furthermore, the conical shape of a drinking glass leads to the development of a complex distribution of residual stress in the manufactured glass. Not only does the residual stress vary parabolically through the thickness, but additional stresses are created due to the continued contraction of the thicker base of the glass after thinner regions nearer the rim have already cooled beyond the glass transition temperature, known as form stresses.<sup>18</sup> Furthermore, there are no universally accepted desired breakage criteria for glass drinking vessels, and in some cases, manufacturers may intentionally limit fragmentation to certain regions of an article.

Preston was the first to examine the stress systems developed in bottles and glasses due to external loading<sup>19</sup> and identified that the crack branching angle can be used to assess the stress state acting on the crack.<sup>20</sup> These findings were extended by Mould,<sup>21</sup> who identified the so-called hinge stresses present in a cylindrical glass articles subjected to impact, using thin brittle coatings that crack under the influence of tensile stress. Beneath the point of impact, the glass wall is deflected inwards which leads to the formation of tensile stresses on the inside surface. Should the stress intensity factor,  $K_I$ , exceed the fracture toughness,  $K_{IC}$  of the glass at any point, these stresses will initiate fracture of the article. In response to this inward deflection, there is an outward deflection either side of the impact point, which is the cause of additional separate regions of tensile stress (as illustrated in Fig. 1). Kepple and Wasyluk claimed that hinge stresses were five times lower in magnitude than that of inward flexure.<sup>22</sup> A Hertzian contact stress also develops which circles the impact point and is proportional to the stiffness of the glass.<sup>23</sup> As the walls of drinking glasses can be thin (often ~2-mm width near the rim), the glass is more likely to bend, and this contact stress can usually be assumed to be negligible. There is also a region of tensile stress at 180° opposite the impact point, on the inside of the glass wall, but this is lower in magnitude than inward flexure.

The present work is a comprehensive study of pint glass fracture and attempts to fully explore how fracture relates to the design and the manufacturing process.

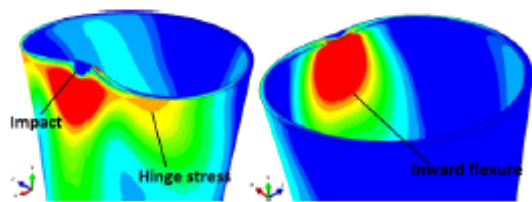


Fig. 1. Finite element static stress analysis of a conical pint glass subjected to impact at its rim. Red portions of higher first principal stress concentration. Made with Abaqus finite element software.

## Materials and Methods

### Glass Samples and Preparation

A range of pint glasses were examined, some of which were new, and some of which had been used in bars, pubs, or hotels.

The main focus of experimentation was on three particular imperial pint glasses (20 fl. oz., or 568 mL in volume) obtained new from an Internet wholesaler: the tempered nonic, the ultimate pint, and the perfect pint (see Fig. 2). The latter two were developed in response to the UK Home Office's Design Our Crime programme.<sup>24</sup>

To compare the performance of the tempered article to its annealed counterpart, a selection of these glasses were annealed prior to testing which required an appropriate annealing schedule to be determined.<sup>25</sup> The glasses were heated to the annealing point of 550°C at

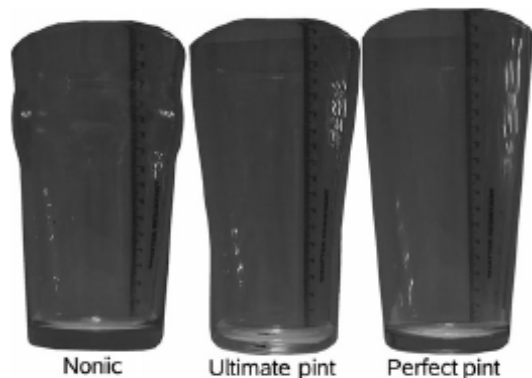


Fig. 2. Glasses examined in this study.

a rate of 8°C/min, then held at this temperature for an hour, and subsequently cooled at a rate of 2°C/min until the glass was far below its strain point (~500°C) to prevent the reintroduction of temper stresses.

The tensile failure stress of glass is dependent upon the presence, magnitude, and frequency of flaws and singularities, and for this reason, a degree of wear was applied to each specimen before breakage. The entire surface of each glass was abraded by hand with an applied force of ~3N with 220 grit SiC paper. Firstly, the glass was held horizontally and the paper was placed along the inside wall profile of the glass from directly below the rim to the base. A hand was pressed on the paper, and the glass was rotated fully three times. Secondly, this process was repeated for the outside wall profile. Thirdly, the rim was abraded, by placing a small piece of SiC paper around the circular rim profile and fully rotating the glass three times. Fourthly, the base of the glass was abraded, by holding the glass upside-down and pressing the paper over the base, and then rotating the glass fully three times. While this does not precisely replicate the wear encountered by the glass in practice, it provides a convenient means of creating a flaw distribution in the article.

### Residual Stress Assessment and Measurement of Wall Thickness

The level of internal temper of the glass is mainly dependent on the rate of quenching of the outer surfaces, but it is limited by the thickness of the sample.<sup>26</sup> CT scans were conducted to determine any circumferential and vertical variation in thickness, using a Toshiba Aquilion 64 detector scanner (Toshiba, Crawley, UK). Each scan was conducted at 120 kV and 100 mA with a 1-mm slice thickness, with reconstructions at 0.5 mm. The images were stored as DICOM files and analyzed using OsiriX version 4.1.2 (<http://www.osirix-viewer.com> last visited November 2013). Additionally, some cross-sections of annealed pint glasses were prepared by breaking the glass along a scribe line, which were then measured optically.

To directly measure the residual stresses, photoelastic measurements were taken of the glass samples using an integrated polariscope suited to analyzing cylindrical glass articles (Automatic Transmission Polariscope AP-07, Glasstress Ltd, Tallinn, Estonia). The pint glass is placed in a tank filled with immersion fluid that is mixed to have the same refractive index of the glass,

and a beam of polarized light is shone tangentially through the glass wall. The retardation of the light beam is measured by CCD camera and analyzed with Glasstress software to determine a residual stress profile using stress-optic theory.<sup>27</sup>

To confirm that a significant level of residual stress was present in the article, a punch test was conducted. This involved hammering a sharp point into the glass 1 cm from its rim (as shown in Fig. 3) and assessing the level of fragmentation using a procedure adapted from that outlined in section 8 of British Standard EN 12150.<sup>12</sup>

### Impact Testing

A reproducible impacting method was used for the assessment and comparison of strength and fracture characteristics of various glasses. This involved systematically increasing the height of an impactor in a drop tower, and subsequently letting it fall by its own weight onto the glass specimen which was loosely restrained onto a wooden block (see Fig. 4).

Two impactors of identical dimensions, one made of aluminum and the other steel, of mass 0.5 kg and 0.8 kg, respectively, were used. The impactor radius was 1.25 mm, to match glass vessel pendulum-based impact testing equipment available that use a 2.5-mm diameter ball bearing to impact the glass wall (Impact Tester, AGR International, Butler, PA). The heavier

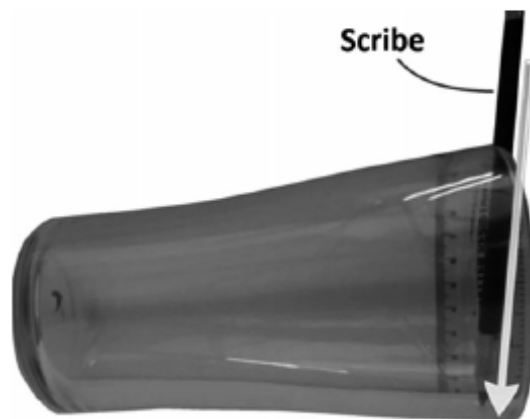


Fig. 3. Rim punch test. The glass is laid on its side on a firm surface, and a sharp tungsten carbide scribe is punched 10 mm from the glass rim using a 50-g hammer.

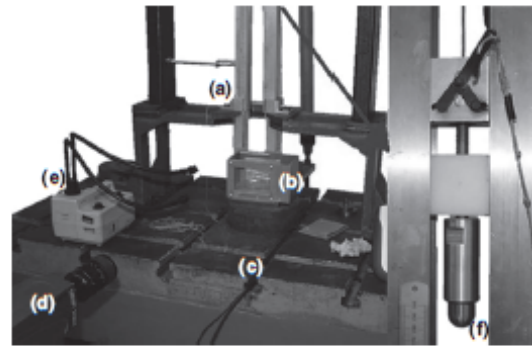


Fig. 4. Experimental setup used for systematic impact testing. (a) drop tower guide rails (extending beyond the top of the picture to a maximum height of 3.5 m), (b) glass securing box, (c) cast iron table, (d) high-speed camera, (e) light source, (f) enlarged picture of steel impactor from higher up the guide rails.

steel impactor was manufactured and used exclusively to fracture new glasses, as the aluminum impactor could not gain enough energy for the glasses to fracture. The kinetic energy could then be calculated using the relation  $KE = m \cdot g \cdot h$ , where  $h$  is the height from which the impactor is dropped and  $g$  is the acceleration on the impactor mass due to gravity; frictional effects were neglected. The drop height (distance between the glass impact point and the impactor tip) was increased in 10-mm intervals until failure, and the number of impacts prior to failure was recorded. Impacts were made at a distance of 10 mm from the glass rim, normal to the glass wall. Each glass was secured in place beneath the drop tower guide rails (Fig. 4b). A number of impacts were recorded with a high-speed video camera (Fig. 4d) to examine fracture development. The breakage energy was recorded for 10 of each new and abraded nonic glasses, ultimate pints, perfect pints, and 10 annealed nonic glasses for comparison, totaling 70 glasses.

Additionally, some pint glasses were broken manually by holding the glass in hand near its base and aiming to hit the upper half of the outside glass wall against the edge of a cast iron table (Fig. 4c). For this, thick Kevlar gloves and face protection were worn.

The impacts were also simulated as a finite element model for each different glass, so the stress response dependent on the glass geometry could be compared with the fracture pattern.

**Results**

**Thickness Variation**

Measurements taken from CT scans show an approximately linear decrease in glass thickness from the base of the glass to the rim (Fig. 5). However, the thinnest of the three pint glasses on average, the nonic, has a minimum wall thickness on the bulge of the glass as seen in Fig. 6.

**Photoelastic Measurements**

Although the surface compression is generally used to infer the strength of the glass article, it is the center band of tension that determines the extent of fragmentation.<sup>28</sup> This is plotted against the height of each glass in Fig. 7. The pint glass with the largest wall thickness at any given height, the perfect pint, also shows the largest residual tensile stress at any given height. Near the rim of the pint glasses, photoelastic measurement of stresses becomes more difficult due to the increasing influence of form stresses, resulting in a greater variability of results. However, the ultimate pint appears to have similar mid-plane residual tensile stress to the nonic (~30 MPa) approaching the top 30 mm of the glass.

This same trend of perfect pint > ultimate pint ≥ tempered nonic was also found by analysis of the com-

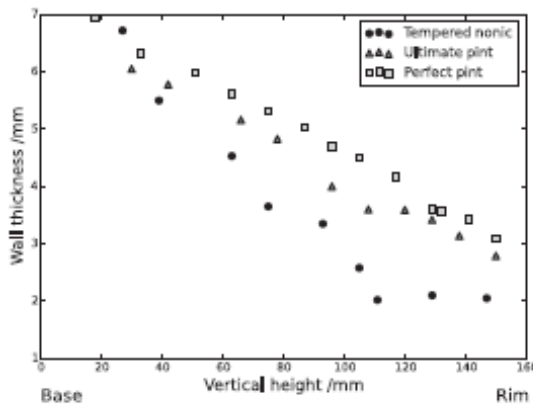


Fig. 5. Wall thickness with respect to vertical glass height for one of each glass. The perfect pint appears to be the most linear and on average, thickest. The tempered nonic reaches its minimum thickness at the glass bulge.

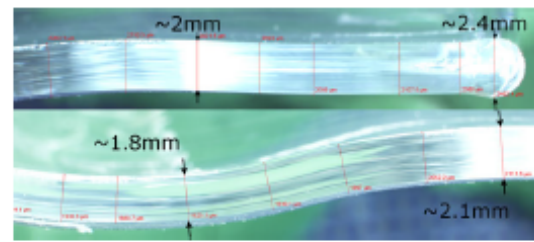


Fig. 6. The thickness of a nonic glass near its rim (top), illustrated by the profile of its fracture surface. The thickness in the wall is on average around 2 mm, rising to 2.4 mm at the rim at the right of the picture (bottom). Further to the left and across the bulge of the glass. The wall thickness at this feature is seen to decrease by ~15%.

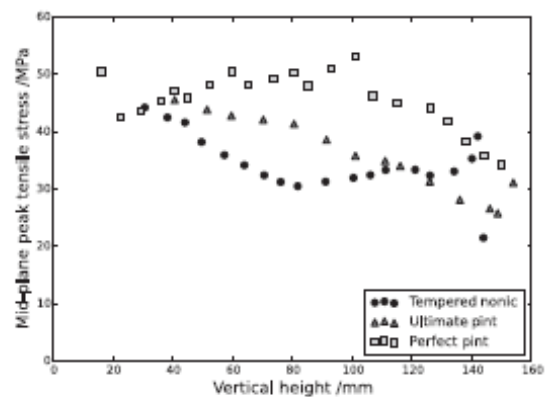


Fig. 7. A comparison of the perfect pint (squares), ultimate pint (triangles), tempered nonic (circles), and the mid-plane tensile stress from base to rim (left to right).

pressive stress values at the glass surfaces. Figure 8 shows this difference in compressive stress between the inside and outside walls of glass, which can be used as an assessment of the evenness of the quenching treatments.

**Fragmentation Density**

The fragmentation count due to a punch test for 10 of each of the three glasses examined in detail is shown in Fig. 9. The perfect pints exhibited the highest overall fragmentation. For both the perfect pint and the tempered nonic glasses, two out of the 10 samples did not completely fragment, but instead a rim chip or

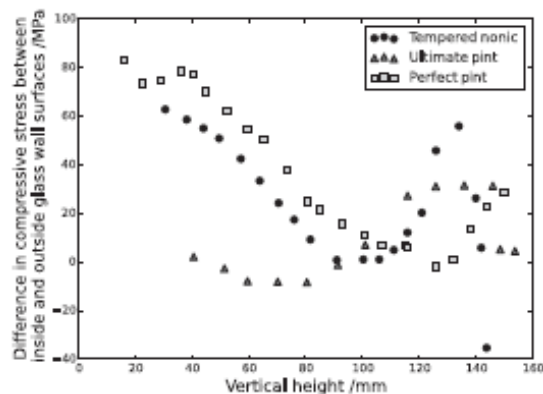


Fig. 8. A comparison of the perfect pint (squares), ultimate pint (triangles), tempered nonic (circles) and the difference between surface compressive stresses (inner stress—outer stress) from base to rim (left to right).

minor localized fragmentation was seen, driven mainly by the punch impact stress. By contrast, six out of the 10 ultimate pint samples did not completely fragment, suggesting a very low level of temper near to the rim. It is therefore more relevant to assess the fragmentation at the top of the glass, as demonstrated by the “X” markers in Fig. 9. The top region of the tempered nonic pints and ultimate pints performs similarly; producing fewer fragments than the perfect pints in the top region overall. This also means that larger shards are left remaining, particularly near the top of the glass.

### Impact Testing

The results for systematic impact tests for a total of 70 glasses are summarized in Table I. All of these 70 glasses were impacted 10 mm from the rim.

The perfect pint required the most impact energy to cause failure during testing. The performance of the ultimate pint was similar to that of the tempered nonic glass. The abraded glasses required approximately 20 times less energy for failure compared with their new counterparts.

In all tempered samples after impact, larger fragments were found nearer to the top of the glass and smaller fragments were found closer to the bottom. This is similar to the fracture behavior observed in punch tests. Frames from high-speed video footage (Fig. 10) further illustrate this tendency.

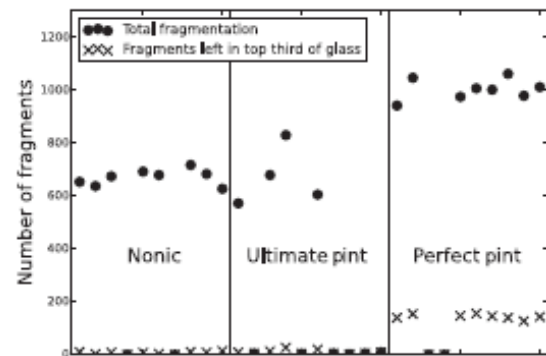


Fig. 9. Values of total fragmentation and top third fragmentation for all punch test samples. 0-values represent instances where the tensile band was not strong enough to initiate total fragmentation of the article.

The fracture behavior of the glasses broken by manual impact was similar to that of the drop tower tests, although a larger proportion of specimens failed by inward flexure directly below the impact point than those which failed due to rim stresses. Figure 11a shows an example of such a failure. Fractures originating from the rim generally produce characteristic triangular-shaped shards that divide the origin as shown in Fig. 12. Glasses broken by dropping, replicating accidental breakages, failed at the rim on 90% of occasions.

### Fracture Surfaces

In annealed glasses, the main propagating crack led on either the inside or the outside of the glass wall depending on the location of the maximum tensile stresses due to loading. In the majority of cases, the side on which the fracture initiated remained the side that the crack led on. However, in some cases the tensile stress acting on the opposite side to the leading crack was great enough to see the crack front move to the opposing side (Fig. 13).

Near the base of the glass, tempered samples were seen to have the crack lead centrally throughout the thickness, following the tensile mid-plane. An example of a centrally leading crack on a tempered glass surface is shown in Fig. 14. However, closer to the rim of the glass, the crack front led closer to a particular side. The crack's leading point tended toward the mid-plane as it traveled toward the base of the glass, (see Fig. 15).

**Table I. Results for Failure Impact Energies. The Remaining Percentages of Inward Flexure Failures were Hinge Failures**

Sample type	Average failure energy (J)	Standard deviation	% inward flex failures
Nonic – annealed, abraded	0.3	0.07	80
Nonic – abraded	0.5	0.08	90
Ultimate – abraded	0.5	0.12	100
Perfect – abraded	0.7	0.11	100
Nonic – new (steel impactor)	18.8	3.85	100
Ultimate – new (steel impactor)	19	3.18	100
Perfect – new (steel impactor)	25.8	2.52	100

## Discussion

### General Fracture Behavior

Annealed glasses produced sharp, relatively large shards. In most annealed fractures, the glass base remained intact with sharp protruding edges traveling out of it (Fig. 11c). When tempered pint glasses fractured, the base of the glass invariably underwent extensive fragmentation. As expected from FEA analyses, which suggested highest tensile stress concentrations near the top of the glass (Fig. 1), most fractures occurred via inward flexure or hinge stresses.

The higher fragmentation density of tempered articles occurs because the amount of stored elastic strain energy in the glass is proportional to the fracture stress squared.<sup>29</sup> For an applied surface stress to be the cause of fracture in tempered glass, it must overcome both the average level of compressive stress,  $\sigma_c$ , and the average failure stress of the glass in its inherent annealed state, that is,  $\sigma_f = \sigma_c + \sigma_{annealed}$  (Exceptions to this occur when a flaw depth is comparable in size to the compressive layer depth, and in cases whereby the tempering process affects the flaw distribution. In practice, the equation has been reported as  $\sigma_f = 1.18\sigma_c + \sigma_{annealed}$ <sup>30</sup>). This additional stress prior to fracture results in higher stored elastic strain energy prior to fracture, causing denser fragmentation along with the release of the residual stress. Furthermore, as worn glasses are effectively glasses with larger flaw sizes, less energy is required for breakage, and so the density of fragmentation is less.

A common feature of all pint glass fractures investigated was the tendency of the cracks to follow the same fundamental pattern. The development of a symmetrical stress system (Fig. 1) explains the symmetrical

fracture pattern, assuming that the glass is symmetrical. If the glass was not loaded along its diameter (which is highly unlikely under usual conditions), the fracture pattern would not be symmetrical about the impact point and would concentrate more on one side of the glass.

This recurring, and essentially symmetrical, pattern is demonstrated in Fig. 11a. From the point of impact, cracks traveled predominantly downward longitudinally, with cracks most leftward and rightward of impact deviating toward the circumferential orientation more than others. Subsequently, the cracks attempted to loop back upwards in the longitudinal direction, directly opposite the impact point. This can produce many boomerang-shaped shards as can be seen below the curved arrow in Fig. 11a and isolated in Fig. 11b. As a crack will always propagate normal to the maximum tensile stress at the crack tip, the change in direction implies a gradual rotation of maximum stress orientation. Specifically, the principal stress at the impact point was maximum in a circumferential (hoop) direction, switching to a longitudinal direction nearer the hinge stresses at an acute angle from impact, before becoming predominantly longitudinal again on the opposite side, 180 degrees from impact.

Cracks forced to loop around the side of the glass require more energy for propagation, as the crack orientation necessitates the development of a mode III stress component as opposed to cracks that propagate directly in the longitudinal direction.<sup>31</sup> As a result, it is not uncommon to see cracks in annealed pint glasses stall after or during looping.

Where the glass wall impacted a hard object, or vice versa, either from a manual break or an impactor

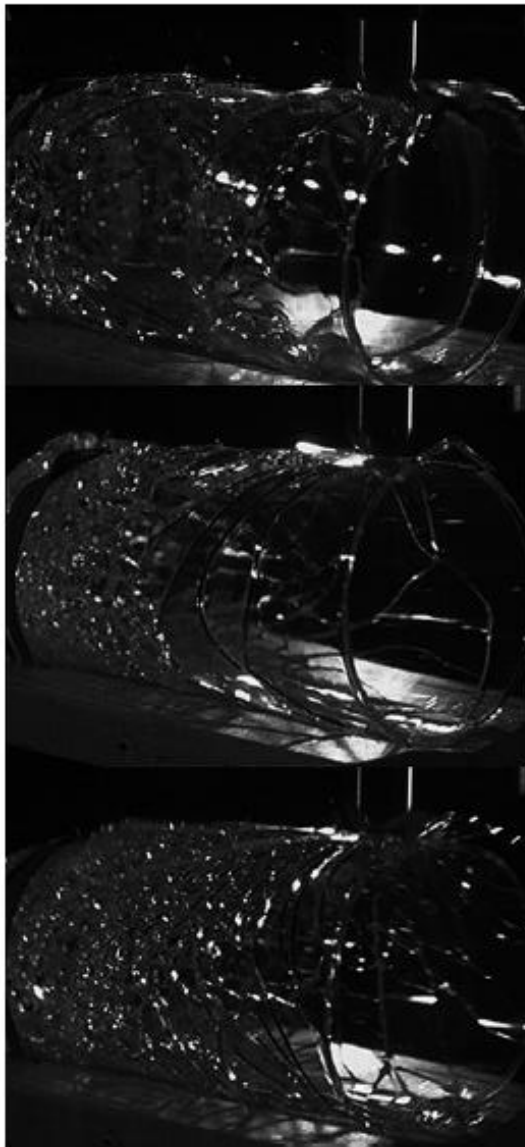


Fig. 10. High-speed video stills of pint glass fracture subject to controlled impact testing. Taken at 1000 frames per second (top). Frame from a tempered nomic break. A large portion of the rim remains intact, although the base still fragments completely (middle). Frame taken from high-speed video footage of an ultimate pint fracture. Near the base of the glass, the tempering process is effective and the glass breaks into small shards (bottom). Frame from a perfect pint fracture, which breaks into comparably equal-sized fragments, but still some larger fragments remain toward the rim.

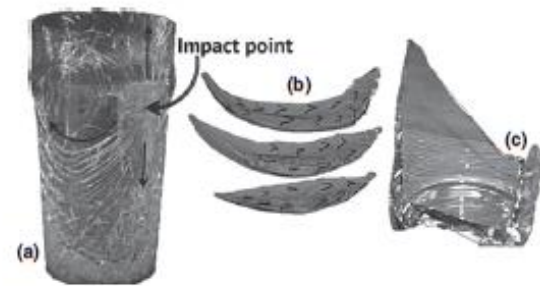


Fig. 11. (a) A tempered nomic glass broken by manual impact. The glass is oriented such that the swooping nature of the cracks is emphasized (curved arrow). Longitudinal arrows illustrate the predominantly longitudinal cracking direction. The pattern is approximately symmetrical. (b) Curved boomerang-shaped shards isolated for emphasis. (c) Half-impact annealed nomic glass base postfracture.

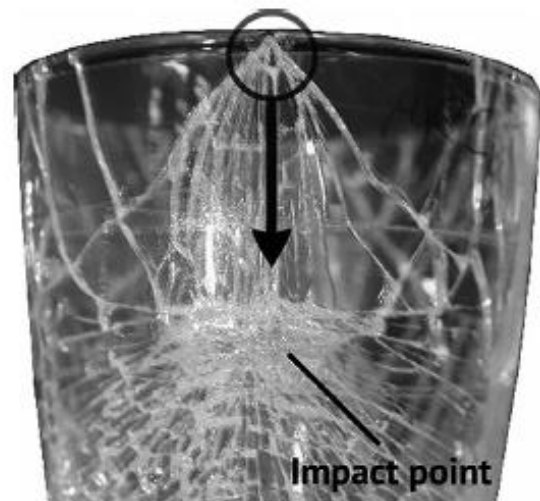


Fig. 12. A typical rim fracture showing triangular shards that divide the fracture origin in an ultimate pint. The origin is circled. The cracks propagate rapidly and unstably at their terminal velocity ( $\sim 1500$  m/s for soda lime glass) from the rim to the impact point, before propagating out from there.

from drop tower tests, very severe fragmentation and spallation was observed at the point of impact, occasionally making the origin of fracture impractical to recover. While inward flexure will be the likely cause for fracture initiation, the continued force of the

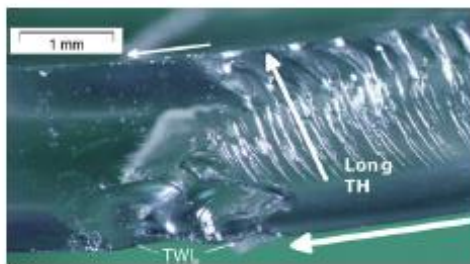


Fig. 13. A fracture surface observed in an annealed nionic glass subject to manual impact showing a crack leading on one side switch to the other. Traveling right to left, the crack is initially leading on the glass' outer surface before switching over to the inner surface where the magnitude of tension stress is greater.

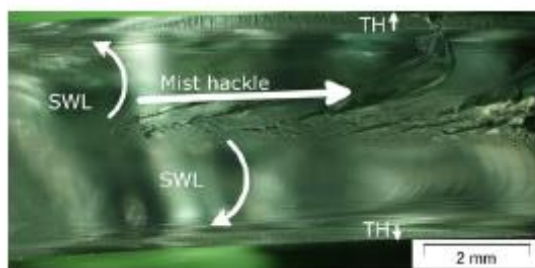


Fig. 14. A tempered glass fracture surface. The crack leads centrally along the tensile mid-plane and travels from left to right as indicated by the mist hackle. Secondary Wallner lines develop with the trailing parts of the crack front either side of the central mist hackle. Finally, twist hackle (TH) is formed as the least developed portion of the crack travels the previous zones of compression.

impacting object produces the further fragmentation. This continued applied force immediately after fracture causes broken fragments to have their fracture surfaces abraded against each other, creating a fine glass dust. The combination of contact stresses and inward flexure on the glass wall also causes secondary cracks to initiate on the impacting side.

The walls of the glass close to the base are generally ~3 times thicker than the walls nearer the rim. Due to this larger thickness, more residual stress is stored there from tempering; thus, the center tensile stress forms a thicker band. Cracks reaching this band are aided in their branching, causing significant dicing of the base. Fragments nearer the glass rim, where the wall thickness is less, were generally larger than those

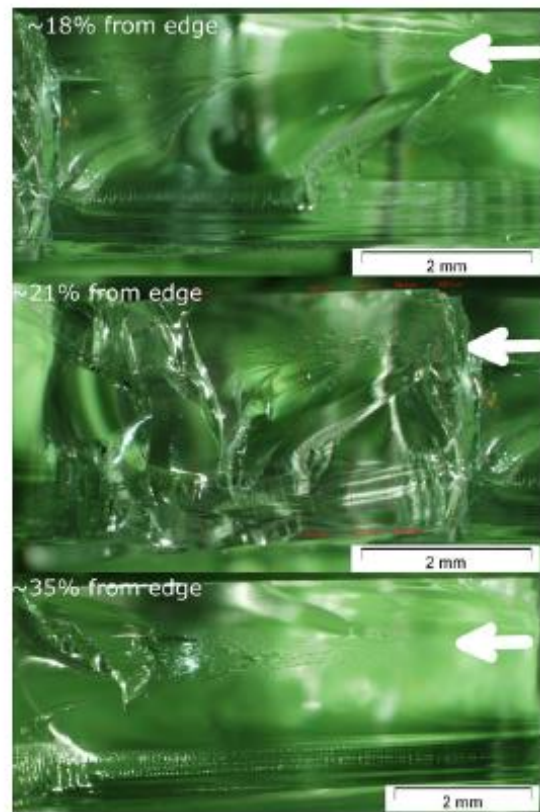


Fig. 15. Three fracture surfaces from the same broken glass, all showing the crack lead from right to left. Top image is the fracture surface 1.3 mm from the rim of the glass, middle image shows the fracture surface 1.6 mm from the rim, and the bottom image is 2 mm from the rim.

near the base and were very sharp, like fragments from annealed glass fracture.

Nearer the rim of tempered glasses, the crack front led closer to a surface instead of directly through the center (see Fig. 15). The location of the leading crack front is dependent on a competition between the applied stress and the stored residual stress. The greater the tensile stress on a particular surface due to loading, the further the interior band of tensile residual stress will tend toward that surface. Toward the bottom of the glass, the interior tensile stress is dominant and the crack is seen to lead and branch near the mid-plane (Fig. 14). This is because there is negligible externally applied stress at this point, and the

crack propagation is driven almost exclusively by the residual tensile stress. The result is a glass that breaks more like an annealed article toward the top and breaks in a way expected of a tempered article toward the bottom.

### Geometrical Influence on Fracture

An alternative view of the same glass as shown in Fig. 11a is presented in the left image of Fig. 16, along with a FEA simulation of the impact it was subjected to. It can be seen that a series of almost equidistant cracks (parallel to the arrow) are present over the glass bulge, which all branch when the crack front reaches the straight-walled portion of the glass near the rim. This suggests a decrease in stress intensity in the vicinity of the bulge before an increase just above it. The FEA image to the right of Fig. 16 supports this explanation, showing a region of higher tensile stress occurring at the point of branching. The fracture surface across this bulge (Fig. 17) shows deep twist hackle markings indicative of a mode III stress component at the crack tip and the high energy expenditure necessary to continue crack propagation.

### Individual Glasses

Of the two premium glasses investigated, the perfect pint generally broke into smaller, more consistent shards (Fig. 10, bottom). This is likely to be a result of the greater average wall thickness of the perfect pint,

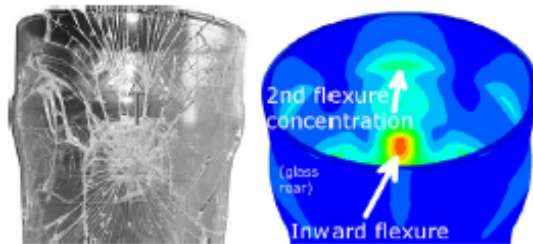


Fig. 16. (left) Front view of the impact point of the same tempered nonic glass in Fig. 11a. The fracture surface at the arrow is shown in Fig. 17. (right) FEA simulation showing the distribution of the inward flexure stress concentrations. Tensile stress concentration decreases over the bulge and increases just above it, creating a 2nd flexure concentration.

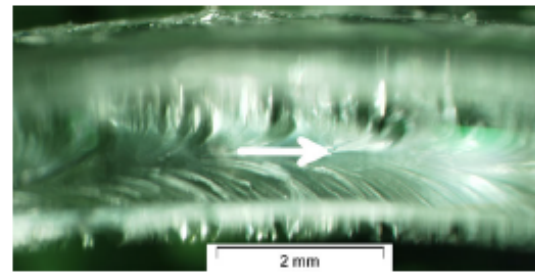


Fig. 17. Fracture surface from the tempered nonic glass as shown in Fig. 16. The crack leads from left to right with the crack front leading centrally as indicated by the arrow. It is closer to the inside surface than the outside, as the interior tensile stress acts on the growing crack front but the exterior tensile stress is still great enough to shift the main tensile band away to the surface. The top of the figure is out of focus because it lies closer to the microscope lens.

which is reflected in the higher mass of this pint glass (454 g) compared with the ultimate pint (417 g). The ultimate pint typically broke with fairly large shards nearer the glass rim (Fig. 10, middle), with the base in both glasses fragmenting extensively. Fracture surfaces were usually relatively featureless: The only visible markings were regions of mist prior to branching, small concentrations of twist hackle at the surfaces, and shear hackle around corners. Fragments from the bottom of each glass were generally blunt.

The difference in compressive stress values between the inner and outer surface of the glass wall is shown in Fig. 8. Due to limitations imposed due to available manufacturing methods, it is difficult to cool both surfaces evenly, especially with complex geometries. The nonic glass shows a large peak in this compression differential at the location of the glass bulge. The surface with the lower compressive residual stress is the inner surface, which is the surface subjected to the highest applied tensile stress under impact. This may pose less of an issue compared with other glass shapes due to the reduced likelihood of contact in this area from stacking glasses on top of each other. The straight-walled perfect pint shows the least difference in compressive values near the rim (the values closer to the base are of less interest, as the base is subjected to the least externally applied tensile stress). The stress also varies in magnitude around the glass circumference.

## Conclusions

The tempered glasses examined in this study had a varying wall thickness, greater toward the bottom than to the top, and consequently, less residual stress could be stored in the thinner regions through tempering. Under typical loading conditions, the greatest tensile stress concentrations occurred near the top of the glass. As a result, the glass was subject to the most tensile stress where the level of residual surface compressive stress was typically the lowest. This may explain why in most tempered glasses, shards similar to those expected in annealed glass fractures are found near the rim of the glass. Although the base of the glass shows dense fragmentation, large rim shards are often present. Additionally, the size and frequency of shards, particularly near the rim, can vary considerably between manufacturers.

The key fracture characteristics of glass drinking vessels are as follows:

- Glasses broken by impact exhibit similar symmetrical fracture patterns due to the development of a similar stress state, which is a result of their conical geometry.
- The critical flaw is highly likely to occur within the region of tensile stress opposite the point at which the load is applied.
- The base of an annealed glass usually remains intact after fracture.
- Typically, the base of tempered glasses fragments into small cube-shaped pieces.
- Large shards are often left near the rim of tempered glasses.
- Rim fractures can typically be identified by characteristic triangular-shaped shards that divide the origin.
- Impact occurring closer to the rim will require less energy for breakage than impact closer to the base.
- Typical energies to cause fracture of tempered glasses as received were 15-20 times greater than those with the degree of wear applied in this study.
- If a propagating crack appears to lead on a particular surface in a tempered glass, this usually means that a very high tensile stress is acting to pull the crack apart at the surface. It may, however, be the result of uneven or faulty tempering.
- Glasses with thicker walls are able to store more residual stress, thereby improving strength and fragmentation density.

## Acknowledgments

Mr. G. Nolan, Mr. C. Vivian, Mr. G. Clark, Mr. T. Forryan, and Mr. A. Wale are thanked for their technical assistance during experimentation.

## References

1. P. J. Withers and H. K. D. H. Bhadeshia, "Residual Stress. Part 1 - Measurement Techniques," *Mater. Sci. Technol.*, 17 [4] 355-365 (2001).
2. L. H. Adams and E. D. Williamson, "The Annealing of Glass," *J. Franklin Inst.*, 190 [5] 597-631 (1920).
3. G. Quinn, *Fractography of ceramics and glasses*. A NIST recommended practice guide; Special Publication 960-16, National Institute of Standards and Technology, Washington, DC, 2007.
4. "Toughened Glass. Press release, Brewers and Licensed Retailers Association, 42 Portman Square, London," BLRA, 1997.
5. Glass Technology Services, private communication.
6. J. P. Shepherd, R. H. Huggert, and G. Kidney, "Impact Resistance of Bar Glasses," *J. Trauma*, 35 [6] 936-938 (1993).
7. ASTM Standard C147, 2010, "Standard Test Methods for Internal Pressure Strength of Glass Containers," ASTM International, West Conshohocken, PA, doi:10.1520/C0147-86R10, www.astm.org.
8. ASTM Standard C148, 2012, "Standard Test Methods for Polariscopic Examination of Glass Containers," ASTM International, West Conshohocken, PA, doi:10.1520/C0148-12, www.astm.org.
9. ASTM Standard C149, 2010, "Standard Test Method for Thermal Shock Resistance of Glass Containers," ASTM International, West Conshohocken, PA, doi:10.1520/C0149-86R10, www.astm.org.
10. ASTM Standard C1036, 2011e1, "Standard Specification for Flat Glass," ASTM International, West Conshohocken, PA, doi:10.1520/C1036-11E01, www.astm.org.
11. ASTM Standard C1048, 2012e1, "Standard Specification for Heat-Strengthened and Fully Tempered Flat Glass," ASTM International, West Conshohocken, PA, 2003, doi:10.1520/C1048-12E01, www.astm.org.
12. "BS EN 12150-1:2000 - Glass in building. Thermally toughened soda lime silicate safety glass. Definition and description," British Standards Institution, 2000.
13. "BS EN 14179-1:2005 Glass in building. Heat-soaked thermally-toughened soda lime silicate safety glass," British Standards Institution, 2005.
14. "BS 6206:1981 Specification for impact performance requirements for flat safety glass and safety plastics for use in buildings," British Standards Institution, 1981.
15. "BS 6262-4:2005 Glazing for buildings. Code of practice for safety related to human impact," British Standards Institution, 2005.
16. "BS 857:1967 Specification for safety glass for land transport," British Standards Institution, 1967.
17. *Making Glass*, 4th edition, British Glass Manufacturers Confederation, 2007.
18. H. Aben and C. Guillemet, *Photostereicity of Glass*, 198-215, Springer-Verlag, Berlin, 1993.
19. F. W. Preston, "Bottle Breakage - Causes and Types of Fractures," *Am. Ceram. Soc. Bull.*, 18 [2] 35-60 (1939).
20. F. W. Preston, "The Angle of Fodking of Glass Cords as an Indicator of the Stress System," *J. Am. Ceram. Soc.*, 18 [1-12] 175-176 (1935).
21. R. E. Mould, "The Behavior of Glass Bottles Under Impact," *J. Am. Ceram. Soc.*, 35 [9] 230-235 (1952).

22. J. B. Kepple and J. S. Waslyk, "The Fracture of Glass Containers," *Fractography of Glass*, eds. R. C. Bradt and R. E. Tressler, Plenum Press, New York, 207–252, 1994.
23. V. D. Pâchetne, *Failure Analysis of Brittle Materials: Advances in Ceramics*, Vol. 28, 100–109. American Ceramic Society, Westerville, OH, 1990.
24. "Using design to reduce injuries from alcohol related violence in pubs and clubs," Home Office, Design Out Crime, 2010.
25. F. V. Tooley and S. R. Scholes, *The Handbook of Glass Manufacture*, Ashlee Publ., New York, 1984.
26. R. Gardon, "The Tempering of Glass by Forced Convection," Proc. Int. Congr. Glass, 7th, Institut. National du Verre, Chateauf, Belgique, [paper no. 79], 1965.
27. H. Aben, J. Anton, and A. Ernpert, "Modern Photoelasticity for Residual Stress Measurement in Glass," *Strain*, 44 [1] 40–48 (2008).
28. S. T. Gulati, "Frangibility of Tempered Soda-Lime Glass Sheet," Glass Processing Days, Tampere, Finland, 72–76, 1997.
29. R. C. Bradt, "The Fractography and Crack Patterns of Broken Glass," *J. Fail. Anal. Prev.*, 11 [2] 79–96 (2011).
30. A. S. Redner, E. Mogano, and M. Schiavonato, "Correlation between Strength and Measured Residual Stress in Tempered Glass Products," *J. ASTM Int.*, 2 [3] 85–94 (2005).
31. D. Hull, *Fractography: Observing, Measuring, and Interpreting Fracture Surface Topography*, 87–90, Cambridge University Press, Cambridge, 1999.